EVALUATION AND CALIBRATION OF A PROTOTYPE ACOUSTIC TEST SECTION FOR THE VIRGINIA TECH STABILITY WIND TUNNEL

Hugo E. Carmargo, Benjamin S. Smith, William J. Devenport and Ricardo A. Burdisso

Department of Aerospace and Ocean Engineering
and Department of Mechanical Engineering

Virginia Polytechnic Institute and State University Blacksburg, VA 24061, U.S.A.

Report VPI-AOE-294

May 2005

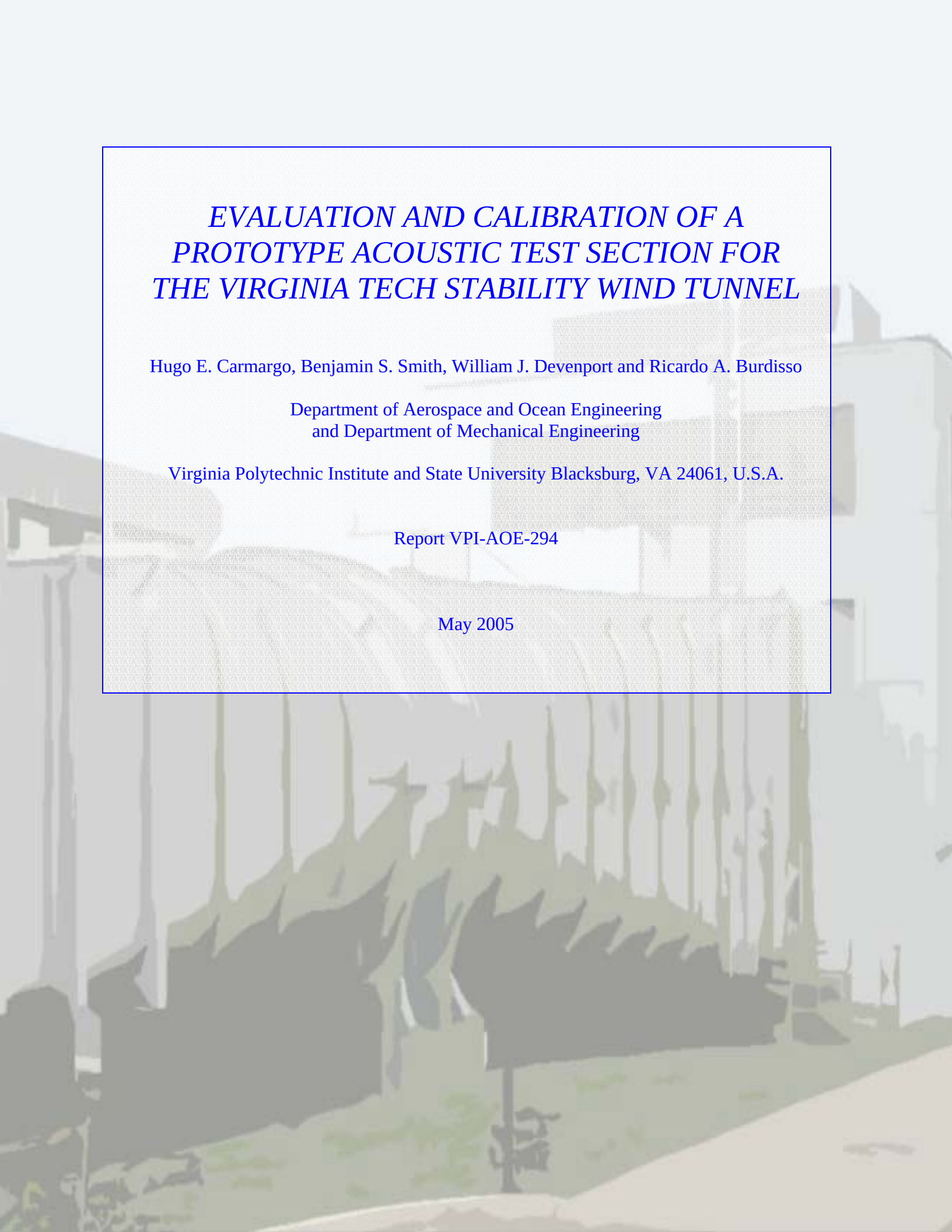

ABSTRACT

The preliminary development and testing of a new anechoic wind tunnel test section designed for the Virginia Tech Stability Wind Tunnel has been performed. The novel design uses large areas of ballistic Kevlar cloth to provide a stable flow boundary, eliminating the need for a free jet and jet catcher. To test this concept the current wind tunnel test section was modified to incorporate prototype acoustic treatment, two large Kevlar cloth side-walls and surrounding acoustic enclosures. A 63-microphone phased array system was designed and constructed to perform demonstration aeroacoustic measurements of large aspect ratio airfoils through these Kevlar acoustic windows.

An extensive program of experiments has been conducted to examine the performance of this new hardware under a range of conditions. These include baseline experiments that reveal the aerodynamic and aeroacoustic performance of the tunnel in its original configuration, wind tunnel tests to examine the effect of two different types of acoustic treatment, and measurements of the aerodynamics and aeroacoustics of a NACA 0012 airfoil model over a range of angles of attack and Reynolds numbers.

These measurements show the acoustically treating only the test section of the Stability Wind Tunnel provides a reduction of between 10 to 16dB, depending on frequency, in the in-flow background noise level. They also show that large Kevlar panels can be used to quietly and stably contain the flow eliminating the need for an open-jet and jet catcher system. Furthermore, they not only reduce lift interference, but appear to offer the prospect of actively controlling it. Measurements with the phased arrays reveal its correct operation and capabilities, demonstrate the acoustically

transparency of the Kevlar walls and the practicality of making noise measurements through them. Aerodynamic measurements with the NACA 0012 airfoil show its lift, drag and boundary layer characteristics at high Reynolds numbers to be consistent with expectations based on earlier studies. Acoustic measurements with the NACA 0012 airfoil clearly show the narrow-band and broadband trailing edge noise produced by trailing edge vortex shedding when the airfoil boundary layers are untripped. The broadband trailing edge noise spectra generated with fully turbulent trailing edge boundary layers, however, is barely measurable with the 63-microphone array used in this initial phase, due to residual background noise. It is expected that further reductions in background noise levels produced when the full conversion of the facility is complete, along with other treatment of the tunnel circuit and the development of a 128-microphone phased array, will make this measurement possible.

ACKNOWLEDGEMENTS

The authors would like to thank National Renewable Energy Laboratory, in particular Drs. Paul Migliore and Patrick Moriarty, for their support of this work under subcontract ZAM-4-3326-01. Motivation for this work was also provided by ONR DURIP Grant N00014-04-1-0493, administered by Dr. Ron Joslin, which is providing funding for the facility upgrade that has been prototyped in this study. The authors would also like to thank Patricio Ravetta for all his support with the development of the phased array system. In addition, the authors would like to thank Bill Oetjens for all of his help and advice during the tunnel modification process and Bruce Stanger and James Lambert for their expertise in fabricating hardware used in the test. Without the help of these individuals, the results in this report could not have been obtained. Finally, the authors would like to thank everyone in the ATFRG and everyone in VAL who volunteered their time to help.

TABLE OF CONTENTS

1. INTRODUCTION

The aeroacoustic noise produced by wind turbines is perhaps the most significant environmental factor affecting their deployment and operation. Quieter wind turbines can be sited closer to the population centers where their power is needed, and can be deployed in greater numbers. To make such turbines possible requires not only better physical understanding of the sources and mechanisms of noise production, but also the development of an experimental database - a database of measurements that allow designers to balance aerodynamic and aeroacoustic performance when selecting an airfoil, and one that can be used to improve and validate aeroacoustic prediction methods. One of the principal hurdles in initiating and expanding such a database, and in providing long term experimental support needed to improve understanding, is the lack of anechoic wind tunnels in the United States. The list of such facilities that can test sufficiently large aspect ratio airfoil sections (2 or greater), at realistic Reynolds numbers (>3 million), is very short indeed. Use of these select facilities can involve prohibitive costs and administrative hurdles. The absence of facilities is not an indication that aeroacoustic testing is no longer relevant to other applications. The understanding and prediction of leading, trailing and side-edge noise remain at substantial issues in the design and development of surface ships, submarines, helicopters and aircraft engines.

This report is part of a research program with the following overall goals:

1. To obtain landmark measurements of the aeroacoustic properties of 3 airfoils over a range of conditions, providing the foundation of the aeroacoustic database needed by wind-turbine designers.

2.To upgrade, calibrate and prove the wind tunnel needed to perform these and future wind turbine aeroacoustic tests, and to make this facility readily available for future testing at low cost.

The wind tunnel referred to here is the Virginia Tech Stability Wind Tunnel.

This report describes the first phase of this program in which we have developed and tested some of the hardware needed for the acoustic upgrade of this facility. This hardware has included wind tunnel test section acoustic treatment and enclosures, a 63 microphone phased array system and a new technology for containing the test section flow. This technology involves the use of large panels of ballistic Kevlar cloth to form the side walls of the wind tunnel.

An extensive program of experiments has been conducted to examine the performance of this new hardware under a range of conditions. These include baseline experiments that reveal the aerodynamic and aeroacoustic performance of the tunnel in its original configuration, wind tunnel tests to examine the effect of two different types of acoustic treatment, and measurements of the aerodynamics and aeroacoustics of a NACA 0012 airfoil model over a range of angles of attack and Reynolds numbers.

These measurements show the acoustically treating only the test section of the Stability Wind Tunnel provides a reduction of between 10 to 16dB, depending on frequency, in the in-flow background noise level. They also show that large Kevlar panels can be used to quietly and stably contain the flow eliminating the need for an open-jet and jet catcher system. Furthermore, they not only reduce lift interference, but appear to offer the prospect of actively controlling it. Measurements with the phased arrays reveal its correct operation and capabilities, demonstrate the acoustically

transparency of the Kevlar walls and the practicality of making noise measurements through them. Aerodynamic measurements with the NACA 0012 airfoil show its lift, drag and boundary layer characteristics at high Reynolds numbers to be consistent with expectations based on earlier studies. Acoustic measurements with the NACA 0012 airfoil clearly show the narrow-band and broadband trailing edge noise produced by trailing edge vortex shedding when the airfoil boundary layers are untripped. The broadband trailing edge noise spectra generated with fully turbulent trailing edge boundary layers, however, is barely measurable with the 63-microphone array used in this initial phase, due to residual background noise. It is expected that further reductions in background noise levels produced when the full conversion of the facility is complete, along with other treatment of the tunnel circuit and the development of a 128-microphone phased array, will make this measurement possible.

2. APPARATUS AND INSTRUMENTATION

2.1 Stability Wind Tunnel

All tests were performed in the Virginia Tech Stability Wind Tunnel. This facility is a continuous, single return, subsonic wind tunnel with a 7.3-m long removable rectangular test section, with a square cross section 1.83m on edge. The general layout is illustrated in Figure 2-1.

The tunnel is powered by a 0.45-MW variable speed DC motor driving a 4.3-m propeller at up to 600 r.p.m. This provides a maximum speed in the test section of about 80m/s and a Reynolds number per meter up to about 5,300,000. The fan (figure 2-2) has 8 Clark Y section blades that rotate clockwise as seen from upstream. Some 0.9m upstream of the fan a 'model catcher' made from fine wire mesh netting is stretched across the flow protecting (and generating turbulence that flows into) a circular segment of the fan disc that subtends an angle of some 90 degrees at the fan axis. At a distance of 0.25m downstream of the fan trailing edge plane (measured at the tip) the flow passes through a set of stator vanes spaced at intervals of 6.8^o ($360^o \div 53$) around the fan axis. The array of stator vanes is interrupted beneath fan by two streamlined struts that support the motor. The approximately radial struts are offset some 38 degrees from the vertical. This arrangement results in fundamental frequencies for tone noise generation equal to the blade passing frequency of the fan at $8f_f$ and its harmonics, where f_f is the fan rotation rate. A possibly strong harmonic might be associated with rotor-stator interaction at $424f_f$.

The tunnel forms a closed loop, but has an air exchange tower open to the atmosphere to allow for temperature stabilization. The air exchange tower is located

downstream of the fan and motor assemblies. Downstream of the tower the flow is directed into a 5.5×5.5m settling chamber containing 7 turbulence-reducing screens each with an open area ration of 0.6 and separated by 0.15m. Flow exits this chamber through the 9:1 contraction nozzle which further reduces turbulence levels and accelerates the flow to test speed. At the downstream end of the test section flow passes into a 3-degree diffuser. Sixteen 0.16m high vortex generators arranged at intervals of 0.39m around the floor, walls and ceiling of the flow path at the entrance to the diffuser (see figure 2-3) serve to mix momentum into the diffuser boundary layer, minimizing the possibility of separation and the consequent instability and inefficiency. The four corners in the flow path (two between the air exchange tower and settling chamber, and two between diffuser and fan) are equipped with a diagonal arrays of shaped turning vanes. Spacing between the vanes is 0.3m except in the corner immediately ahead of the settling chamber where the spacing is 0.076m.

The test section itself is located in a hermetically sealed steel building (figure 2-1). The pressure inside this control room is equalized with the static pressure in the test section flow, this being below atmospheric by an amount roughly equal to the dynamic pressure. Pressure is equalized through a small adjustable door in the tunnel side wall at the upstream entrance to the diffuser. This 0.4x0.3-m rectangular door is hinged at its upstream end and is free to swing in or out of the flow according to the pressure difference. The hole within which the door is mounted is a simple rectangle in the steel plate of the diffuser wall, with no aerodynamic fairing.

The 7.3-m long test section used for the present work is depicted in figure 2-4. The test section is built around a steel beam structure with members that define a series of

rectangular frames to which panels can be bolted to form the internal walls of the test section. In the original test section configuration these panels, most of which are 1.83×0.91m or 1.83×0.76m (and thus span the full width or height of the test section), are constructed from either 3.18-mm thick steel plate or Plexiglas. Plexiglas is used in selected panels on the starboard side of the test section (as windows from the control room) and the test section ceiling (to allow lighting of the test section from outside). The panel edges and the countersunk heads of the bolts used to attach them provide some roughness on the interior walls of the test section with a typical scale of about 2mm. There is shallow rectangular cavity that runs around the periphery of the interior walls at the downstream end of the test section, with a streamwise scale of about 30-mm. (This cavity is part of an interchangeable test section system and provides the clearance needed for the test section to be removed and installed). This configuration will be referred to throughout the remainder of this report as the 'hardwall configuration', to distinguish it from the acoustically treated configurations described below.

Flow through the empty hardwall test section is both closely uniform and of low turbulence intensity. Table 2-1 shows measurements made by Reynolds (1982) and Choi and Simpson (1987) detailing the flow uniformity and streamwise turbulence intensity as functions of flow speed. Choi and Simpson also measured the lateral integral scales of the streamwise velocity in both the horizontal L_z and vertical L_y directions. They found L_z=56mm for 15m/s and 28mm for 37.5m/s and L_y=122mm for 15m/s and 25mm for 37.5m/s.

There have been several measurements of flow angularity in the empty test section at speeds from 10 to 60m/s, (Choi and Simpson, 1987, Bereketab *et al.*, 2000,

Mason, 1971) but these measurements are likely to have been influenced by the in-test-section traverse gear used. Both Choi and Simpson (1987) and Bereketab *et al.* (2000) argue that residual flow angularity due to boundary layer growth on the parallel test section walls is likely to be close to 0.1 degrees. This convergence is associated with a slightly favorable streamwise pressure gradient in C_p of 0.09% per foot.

2.2 Acoustic treatment

A major objective of this study was to examine the effectiveness of various test section modifications designed (a) to enable sound generated in the flow to escape from the test section and be measured external to the test section and (b) to reduce background noise levels in the flow.

2.2.1 Acoustic windows

The conventional way to allow sound to escape the flow is to completely remove the walls of the test section to produce a free jet. This results in a flow that is both acoustically open (sound radiation passes freely out of the flow) and aerodynamically open (free flow boundary). Such a solution has several problems. A jet catcher is required that must be designed and tested with some care to avoid generating excessive noise and producing a 'pumping' instability associated with the impingement of the jet free shear layer. Modifying a large scale existing facility in this way poses particular difficulties. This open-jet configuration is also particularly sensitive to lift interference in airfoil tests. Limiting the size of these corrections means limiting the size of airfoil models and thus, unfortunately, the maximum Reynolds number at which they can be tested.

Because of these problems a different approach was developed and tested here. This novel approach involves replacing sections of the wind-tunnel wall with large areas of tensioned Kevlar cloth. The Kevlar is transparent to sound but at the same time largely contains the flow. It thus offers the potential to produce an acoustically open test section without the need for a jet catcher and while eliminating at least a fraction of the lift interference effect. The use of tensioned Kevlar cloth as an acoustic window was pioneered by Jaeger *et al.* (2000). They were investigating different means of shielding a phased array microphone system embedded in the wall of a test section. They found that tensioned thin weave Kevlar 120® (7.9grams/cm^2) (mass produced for surf board and bullet-proof vest manufacture) transmitted sound with very little attenuation up to at least 25kHz, and to be much more durable than metal weave or fiberglass. They then compared measurements made with their phased array system recessed behind a Kevlar sheet and flush with the wind tunnel wall, demonstrating much greater signal to noise ratio in the former case.

While Jaeger *et al.* (2000) demonstrated the usefulness of Kevlar cloth as a covering for a wall-mounted phased array system, our goal was to used this material to replace entire sections of the wind tunnel wall, in other words, to use the Kevlar cloth as a replacement for the free-jet boundary that is conventionally used in acoustic wind tunnels. Scaling up this technology involved some questions and risk. Specifically, it was not immediately clear how a tensioning frame of the size and shape needed could be built, and we were concerned that excessive tension would be required to avoid flapping or other instability in the cloth. For this reason, we began with the small scale prototype pictured in figure 2-5 which was designed to test the concept aerodynamically by

replacing an area equivalent to a single steel panel in the existing test section with Kevlar. To mount and tension the material an OLEC Corporation Large Format Roller Chase® Frame (type RCLF 1.75B), was used. This type of frame is manufactured for use in the screen printing industry. The cloth is tensioned using 4 rollers (figure 2-6) one on each side of the frame – a system that can apply tensions as large as 1 tonne per linear meter of the frame length. This type of frame also holds the cloth slightly above of the rest of the frame, allowing one side of the cloth to be used as the flow surface, without any part of the frame projecting into the test section. The only apparent disadvantage of this system is that small square sections of cloth (typically 0.1×0.1m) at the corners of the frame remain untensioned.

The small prototype frame had internal dimensions of 1.83×0.76m. Plain weave Kevlar 120® cloth was mounted in the frame and tensioned and the frame mounted to the test section wall. The Kevlar provided a smooth and subjectively rigid flow surface. The step from the inside of the test section to the Kevlar surface (no more than 6mm) was faired using 0.89-mm thick aluminum sheet and 0.13-mm thick aluminum tape to provide a smooth transition for the tunnel test section flow (see figure 2-6). The aerodynamic behavior of this acoustic window was examined by varying flow speed through the empty test section from zero to 50m/s while monitoring the deflection at its center using a dial indicator mounted on the outside of the wind tunnel. Generally the Kevlar frame performed well with no overall instability or flapping. There was a slight deflection at the center of the window inward into the test section that increased with flow speed (0.13mm at 21m/s, 0.38mm at 32m/s and 0.56mm at 40m/s), apparently resulting from the residual imbalance between the pressure in the control room at that in the flow. Vibration of the

Kevlar was minimal and appeared to have an amplitude of about $1/10^{th}$ of the mean deflection.

With the success of these preliminary tests, two much larger Kevlar windows needed for aeroacoustic testing were chosen and assembled (figure 2-7). Each of these identical windows used larger versions of the same OLEC Corporation Large Format Roller Chase® Frame (Type RCLF 2.0C). These frames had internal dimensions of 1.83×2.49m. The intention hand been to use 2-m width Kevlar cloth in these frames, but widths over 1.52m (while often advertised) are quite hard to obtain. Instead, each frame used two pieces of 1.52-m wide cloth seamed together. The vertical 1.83-m long seam was sewn at a local upholstery shop using T-50 Atlantic Thread Kevlar in a standard overlap stitch. The flow side of the seam was taped with aluminum tape and resulted in a smooth ridge roughly 1.6mm high thick running vertically from top to bottom of the acoustic windows. The Kevlar fabric was stretched to a tension of between 25 to 30 N/cm measured using a Newman Frames tension meter (model ST-Meter-1E).

When in use, the two frames were mounted on either side of the test section, as illustrated schematically in figure 2-8, placing the leading edge of both Kevlar windows 2.2 to 2.4m downstream of the test section entrance (the exact location was different for the empty test section and NACA 0012 model tests discussed in this report). To install the frames several of the vertical members of the steel frame structure of the test section had to be removed from both sides. Both measurements and an ANSYS computation of the resulting deflection of the weakened test section were made and found to be negligible (<3mm). Additional computations estimating the deformation of the facility in

this state with over 1 tonne of aerodynamic load were performed and found to be less than 13mm.

As with the small frame the steps from the inside of the test section to the Kevlar surfaces at the downstream and upstream ends of the frames (no more than 6mm) were faired using 0.89-mm thick aluminum sheet and 0.13-m thick aluminum tape.

2.2.2 Acoustic absorbers and flow surfaces

To reduce background noise levels in the flow for aeroacoustic testing, almost all the remaining steel panels of the test section walls were replaced with acoustic absorbers designed and built by Mish (2003), see figure 2-8. Most of these absorbers, designed to fit in the panel locations, consisted of rectangular boxes 1.73-m in length and between 0.71 and 0.84-m in width, surrounded by an aluminum flange used for mounting. Most boxes were 0.51-m deep except those used where space was restricted where 0.2-m deep boxes were used. As shown in figure 2-9, the boxes were fabricated from 9.5-mm MDF board or 6-mm honeycomb composite paneling and filled with layers of Owens Corning 701 fiberglass insulation. The fiberglass was capped by a 1-inch thick layer of acoustic foam, to eliminate any possibility of wind erosion of the fiberglass. Mish designed the 0.51-m deep boxes to provide their peak attenuation of acoustic reflections between 100 and 200Hz. However, they were expected to produce noise absorption over a much broader frequency range.

To provide the flow surface when the boxes are installed in the wind tunnel, Mish lined the entire test section with perforated steel sheet. He concluded, however, that at higher frequencies (>500Hz) the perforations actually increased the background noise

level (presumably due to scrubbing or roughness noise) and so two alternative approaches were tested here to alleviate this problem.

The first approach was simply to cover the acoustic absorbers with the same Kevlar 120® used in the acoustic windows. It was assumed that the same properties that made it suitable for use as an acoustic window would also make it suitable as a quiet and acoustically transparent flow surface. Given the number of absorbers, however, it was not possible to use a sophisticated tensioning system so a much simpler scheme, illustrated in figure 2-10 was devised. The Kevlar cloth was simply wrapped around the mounting flanges of the absorbers taped to the sides of the boxes under manual tension. When installing the absorbers in the test section frame the Kevlar was trapped around the flange so as to provide some additional tension. With the acoustic absorbers installed in the test section the Kevlar flow surface thus generated was not completely continuous, but interrupted by gaps between adjacent boxes. These gaps, typically 30-mm wide and 3-mm deep, were smoothed by using aluminum foil tape. The overall effect of the Kevlar flow surface thus generated can be seen in figure 2-11a. One of the smaller-sized acoustic absorbers covered with Kevlar cloth is shown in figure 2-12.

The second approach was to use compressed fiberglass board as the flow surface. Specifically we used 25mm-thick Johns Manville Whispertone Wallboard XG (figure 2-12). This material is used in interior design to attenuate environmental noise, particularly over 1kHz. It has a fibrous surface that is sufficiently rugged to function, at least for limited times, as a flow surface. The fiberglass board was used to line the walls of the test section and was mounted directly over the Kevlar covered acoustic absorbers and attached using silicon gel. The board was supplied 1.22×2.44m sheets, but edges could be

closely aligned eliminating significant gaps and the need to use tape. The overall appearance of this covering is shown in figure 2-11b. Because of the 25mm-thickness of the board, the effective cross-section of the test section was slightly reduced by this treatment. Wooden fairings of wedge cross section were used to smooth the 25-mm steps from this flow surface to the Kevlar of the acoustic windows. The wedges were attached to both the fiberglass board and Kevlar with foil tape.

2.2.3 Acoustic enclosure and baffle

A temporary acoustic enclosure and baffle were on constructed on the outside of the test section to provide an anechoic housing for the phased array microphone systems, and an acoustically absorbent backing for the acoustic window opposite the phased array. The enclosure and baffle (figure 2-13), were constructed from 0.46-m high acoustic foam wedges glued to 19-mm thick MDF boards using standard urethane adhesive. These wedges, measuring 0.31×0.62m at the base, were arranged in a checkerboard pattern.

The acoustic baffle was 2.43m-high and had a width of 3.66m (for empty tunnel tests) and 3.36m (for tests with the NACA 0012 airfoil mode). It was positioned with the tips of the wedges almost touching the surface of the port-side Kevlar window and so as to completely cover the window (figure 2-13). The baffle had no sides – gaps between the wedges and the roller chase frame were stuffed with acoustic foam and fiberglass insulation to reduce contamination of the sound field in the test section from ambient noise in the control room.

The acoustic enclosure consisted of a similar 3.66×2.43m array of wedges but with two additional 1.37m×2.43m forming sidewalls arranged on the outside of the

starboard-side acoustic window, as shown in figure 2-13. This enclosure effectively created a small anechoic chamber, with horizontal internal dimensions of 2.7m×0.89m, where the phased array microphone systems could be housed. Due to space limitations, wedges were not used on the floor and ceiling of the enclosure, which instead used acoustic foam and compressed fiberglass board to limit acoustic reflections and contamination from the surrounding control room.

2.2.4 Assembly

Figures 2-14 to 2-17 show the stages involved in assembling the acoustic treatement, Kevlar windows and acoustic baffle and enclosure as seen from the port side of the test section. Installation begins with the removal of the steel panels forming the test section walls and of the vertical support struts in the area where the acoustic windows are to be located (compare figures 2-14 and 2-15). Acoustic absorbers (figure 2-15) are then installed followed by the Kevlar windows (figure 2-16) which are clamped to the frame structure of the test section. Finally the acoustic baffle and enclosure are installed on the outside of the windows (figure 2-17).

2.3 Airfoil model

Aerodynamic and acoustic measurements were performed on an NACA 0012 airfoil model, figure 2-18. The model, constructed by Novakinetics LLC, was designed to span the complete vertical height of the test section. It has a 1816mm span, 914mm chord and 110mm maximum thickness. The model is built around 88.9-mm diameter steel tube that forms a spar centered on the quarter chord location, and a series of 6 ribs. The model

has a fiberglass composite skin and a fill of fiberboard and polyurethane foam. The steel tube projects 166mm from each end of the airfoil and was used for mounting. Novokinetics proof tested the load strength of the model to a load of 27kN evenly distributed across the span – this being much larger than the maximum expected aerodynamic load. Deflection at this load at center span was approximately 5mm.

The model was instrumented with a total of 82 pressure taps of 0.5mm internal diameter located near the midspan. The nominal coordinates of the pressure taps, measured from the midspan leading edge (see figure 2-18) are listed in table 2-2. The taps appeared free from burrs and other defects, although a number were later discovered to be blocked and were eliminated from measurements. The taps were connected internally to 1.6mm Tygon tubing that exited the model through the center of the steel tube. In order to provide access to the interior of the model in the area of the pressure taps, a hatch was provided on one side of the model as illustrated in figures 2-18 and 2-19. The hatch was fixed in place using a series of flathead bolts countersunk into the airfoil surface. Both bolt heads and the slight step at the edge of hatch were covered with 0.13-mm thick aluminum tape during testing.

The shape of the model was measured in the AOE Machine shop by comparing the model section at the ¼, ½ and ¾ span locations with a measured reference thickness distribution. The measured distribution shape (table 2-3) is compared with the theoretical NACA 0012 geometry in figure 2-20. Deviations from this profile were found to be less than ±0.13mm at all locations, except over the hatch at midspan where the deviations were less than ±0.3mm. The reference profile itself shows the airfoil to be slightly thicker than the intended shape by about 0.15% chord at most stations. Two-dimensional

vortex-panel method calculations of the flow over the airfoil, using 150 panels, were performed to examine the aerodynamic significance of this. Results of these calculations, in terms of pressure distributions at zero and 8 degrees angle of attack, are shown in figure 2-21. They appear to show no significant effect of the extra thickness. The thickness of the slightly-rounded trailing edge the model was measured separately and found to be 2.33mm, 2.35mm and 2.39mm at the ¼, ½ and ¾-span locations, measuring the span from the tip of the airfoil that appears at the bottom of figure 2-18.

The model was supplied with three pairs of removable end plates. The end plates, which were designed to fill the gap between the ends of the model and the test section walls, had the same shape and size as the model section, figure 2-22, and were constructed from a 12.7-mm thick layer of foam capped with a 1.6mm steel sheet. The three different pairs of endplates were supplied with different types of foam material.

The model was also supplied with two adjustable boundary layer fences (figure 2-23), designed to isolate the flow across most of the span of the airfoil from the wind tunnel wall boundary layers. Each fence consisted of 6.35-mm thick aluminum plate with a rounded external edge cut to the shape of an ellipse with a major axis of 1.118m and a minor axis of 229mm. A hole matching the NACA 0012 section of the airfoil was cut into the center of the plate with the major axis of the ellipse aligned with the chord line of the airfoil, and the center of the plate located at mid chord. The plate was split in two halves for mounting on the airfoil which were then bolted back together to slightly compress the airfoil and fix the fence at the desired spanwise station. Because of concerns over the sound that might be generated by the plates they were only installed for

a limited set of runs. For these runs both plates were located 0.305m inboard from the model tips.

The NACA 0012 model was mounted vertically in the test section, as shown in figure 2.24, with its leading edge (at zero angle of attack) 2.92m downstream of the test section entrance. For all tests the endplates with the firmest foam were attached. The overall model span with endplates was still slightly less than the test section height and, as a result a gap of approximately 5mm was left between the top end of the NACA0012 section and the ceiling of the test section. In this position the steel mounting tube projected through the test section ceiling and floor. The acoustic absorbers at this location were removed and replaced with 3.2mm steel panels with holes cut to accommodate the tubes. The top and bottom of the tube were then held on the outside of the test section using assemblies of the type shown in detail in figure 2-25. In each assembly a split aluminum block with containing a hole of slightly larger diameter than the mounting tube is used to clamp the tube firmly at a fixed angle of attack. The block itself is fixed to a 152-mm steel C-section beam welded directly to the principal test section support beams, the fixture allowing some minor adjustment to the sweep and lean of the model. Sweep and lean of the model were determined by fitting the mounting tube through the precision cut holes in the upper and lower steel panels.

The zero angle of attack of the model was determined using the measured pressure distribution, as will be discussed in chapter 4. Angles relative to zero were set by using a caliper and scribe lines on the steel floor plate immediately beneath the model. The accuracy of this process was estimated to be ±0.2 degrees.

For certain measurements the model boundary layer was tripped to ensure a stable and spanwise uniform transition location and a fully turbulent boundary layer at the trailing edge. The trip was made using several layers of aluminum tape cut with pinking shears to create a serrated edge (figure 2-26). The trip thickness of 0.38mm was selected based upon criteria given by Barlow *et al.* (1999) to ensure that the trip would be fully effective down to flow speeds of 23m/s. Laminar boundary layer calculations using the Thwaites Walz method, and a 200-panel vortex panel method calculation (to provide the pressure distribution), were also performed to check the trip size. These showed that the trip height would remain significantly greater than the approaching pressure side boundary layer displacement thickness for angles of attack through 16 degrees.

Photographs of the model mounted in the test section with the hatch open, and with the boundary layer fences installed are shown if figures 2-27 and 2-28.

2.4 Aerodynamic instrumentation

During all measurements various tunnel flow conditions were monitored. Flow speed was monitored using an 8-mm diameter reference Pitot static probe located in the forward part of the test section. For tests performed in the original test section configuration (the 'hard-wall' case) the mouth of the Pitot probe was located 0.28m downstream of the test section entrance, 1.51m from the floor and 0.23m from the port-side wall. For tests with acoustic treatment these positions were 1.6m, 1.5m and 0.18m from the starboard wall respectively. Pressure difference was sensed using a Setra Model 239 pressure transducer. Temperature in the test section was monitored using an Omega

Thermistor type 44004 (accuracy ±0.2°C) and the ambient absolute pressure was determined using a Validyne DB-99 Digital Barometer (resolution 0.01" Hg),

A series of Setra model 239 pressure transducers (with ranges of ±5" H_2O, ±15" H_2O and ±2.5 p.s.i.) were used to measure static pressures on the airfoil surface, and to operate the Pitot-static probes used to measure boundary layers and wakes. These transducers were zeroed and calibrated against the wind tunnel transducer to minimize errors associated with difference in offset and sensitivity. Pressures from the 82 pressure taps on the airfoil model surface were directed through a Scanivalve system for measurement. The pressure from each tap, converted to voltage by the transducer, was measured simultaneously with the reference dynamic pressure using a 12-bit DT 2801-A A/D converter installed in an IBM AT computer. Using a sampling frequency of 100Hz 10 seconds of data were recorded to form time average values.

The two-axis wind tunnel traverse shown in figure 2-29 was used to position probes in the test section. The traverse, which is capable of positioning a probe to within about 0.025mm (see Zsoldos, 1992), mounts inside the test section. The traverse produces an overall solid blockage of about 10% and so probes are supported upstream to avoid accelerations associated with this. The round 1.5-mm diameter Pitot-static probe used to perform measurements of the wind-tunnel wall boundary and airfoil wake is illustrated, with its support, in figure 2-30. A sting places the probe tip 1.24m upstream of the body of the traverse. The probe tip is also offset from the axis of the sting by 0.182m by a lateral section of the 1.5-mm diameter probe stem, located 22mm downstream of the tip. Absolute position of the probe for wall boundary layer measurements was determined by directly observing the traverse location at which the probe tip just contacted the wall.

Outputs from the transducers connected to the Pitot-static probe were measured simultaneously with those from the reference Pitot-static using an Agilent E1432 16-bit digitizer. Outputs were sampled at a rate of 1600Hz in 5 bursts of 1000 samples over a total sampling time of some 10 seconds to yield resolved time average values of the velocity and the static and stagnation pressure coefficients. The same sampling scheme was used for wall boundary layer and airfoil wake measurements.

The flattened Pitot probe shown in figure 2-31 was used to measure trailing edge boundary layer properties on the airfoil at x/c=0.98. The mouth of the probe has the form of a flattened oval with an opening 0.25mm high and exterior dimensions of 1.32×0.51mm. Measurements were made with the shorter of these dimensions across the boundary layer velocity gradient. Absolute probe position was determined by electrical contact of the probe tip with a spanwise strip of 0.13mm-thick aluminum tape attached to the airfoil surface just upstream of the trailing edge. Electrical contact was judged using a resistance meter. The flattened Pitot probe was supported on a streamwise support in-line with the probe sting connected to the model traverse. This support placed the probe tip 1.33 m upstream of the bulk of the traverse gear. Pitot pressures sensed by the probe were recorded simultaneously with pressures from the reference Pitot static in order to form a stagnation pressure coefficient. Voltage outputs were sampled using the Agilent system at a rate of 1600 Hz in 5 bursts of 200 samples over a total sampling time of some 20 seconds to yield resolved time average values. Velocity was then determined using static pressure coefficients measured on the airfoil using the tap located at x/c=0.98.

A single straight TSI type 1210-T1.5 hot-wire probe (figure 2-32) was used to make spectral measurements of velocity fluctuations just downstream of the airfoil

trailing edge. The hot wire sensor was held parallel to the trailing edge and supported from downstream on an elongated probe stem that placed the sensor 1.51 m upstream of the traverse gear. The sensor was operated at an overheat of 1.7 using a Dantec 56C17/56C01 anemometer and bridge unit. Velocity calibration (employing a least-squares fit to King's law with an exponent of 0.45) was performed in the wind tunnel free stream against the reference Pitot static probe. Output voltages from the anemometer were recorded using the Agilent digitizer. Time averaged spectra were formed by averaging 10 records of 1024samples each measured at a rate of 6400Hz or 12800Hz over a total sampling time of some 3 seconds.

2.5 In flow microphones

Measurements of noise levels in the test section flow were made using Brüel & Kjær 1/8th and ¼ -inch diameter condenser microphones, models 4138 and 4939 respectively. These microphones were fitted with nose cones (models UA 0355 and UA0385) and mounted to a model 2670 preamplifier (using a model UA 0160 adapter in the case of the 1/8th inch). The microphones were aligned with the free stream and supported, using the symmetrical airfoil strut shown in figure 2-33, some 756mm above the center of the test section floor. The microphone cable was allowed to hang loose after it was found that taping it to the trailing edge of the strut promoted vortex shedding and produced a measurable narrow band sound. The 1/8th inch microphone was operated using a B&K NEXUS 2690 conditioning amplifier, and the ¼ inch using a B&K model model 5935 conditioning amplifier. For both microphones signals were recorded using the Agilent digitizer at a sampling rate of 51.2kHz with anti-alias filtering above 20kHz.

Most acoustic spectra were formed by averaging 250 records of 8192 samples, resulting in a frequency resolution of 6.25Hz. In a few cases with the ¼ inch microphone a record length of 1024 samples was used giving a frequency resolution of 50Hz.

Both microphones were calibrated using a B&K model 4231 pistonphone, and were found to have sensitivities of 0.610 mV/Pa (1/8th inch) and 4.54 mV/Pa (1/4 inch). The pistonphone only has adaptors for microphones down to ¼-inch diameter, and so the 1/8th inch microphone was calibrated using the ¼-inch adaptor with a small piece of acoustic foam filling the gap. To check this method of calibration the calibrated microphones were then used to measure the same sound spectrum in the flow, shown in figure 2-34. These measurements show the calibrated microphones to be almost identical for frequencies up to 1kHz. Between 1kHz and 10kHz noise levels measured by the ¼ inch microphone rise slightly above those measured with the 1/8th. The reverse is true at frequencies above 10kHz. We believe these differences are due to differences in the behavior of the nose cones. In particular, differences in the wind noise they generate. Because the 1/8th inch microphone appeared quieter in the frequency range of most interest this microphone was used for most measurements.

The noise floor of the microphones was also investigated by making measurements with no-flow through the test section. Because of the lower sensitivity of the 1/8th inch microphone this noise floor (which appeared to be predominantly electrical noise) was a significant contributor to noise measurements below 20m/s. To minimize this contamination, no-flow spectra were subtracted from all 1/8th inch data before plotting or integration.

2.6 The 63-microphone phased array system

In order to perform trailing-edge noise measurements with the NACA 0012 airfoil model, a new 63-microphone phased array was developed. Phased array systems have long been used in fields such as sonar and radio astronomy. However, it was not until the early 1990s that phased array systems were adapted for aeroacoustic measurements. Most of the development and application of microphone phased arrays took place in wind tunnel testing (Mueller, 2002). In such hostile environments where the presence of wall boundary layers and the effect of reverberation make acoustic measurements difficult, phased arrays proved very efficient especially for source location.

The hardware of phased array systems is composed of an array of N microphones, and a data acquisition system capable of sampling data simultaneously for all the microphones. The microphone signals are processed using beamforming algorithms to "steer" the array to potential noise source locations. In this section, the design process for the microphone phased array is presented. The data processing with the beamforming algorithm will be described in chapter 4.

The phased array design for the present project started with the identification of the following test constraints: 1) Availability of a data acquisition system with a maximum of 64 channels, 2) A test section with a height of 1.83m, and 3) A frequency range of interest of 500-2000 Hz. This last constraint was obtained from predictions of trailing edge noise using the method developed by Brooks *et al.* (1989) for the NACA0012 airfoil model dimensions and test parameters.

The first constraint dictates the maximum sensor count; i.e. number of microphones. According to Underbrink (2002), the average sidelobe power level with

respect to the main lobe is related to the number of microphones, N, as: 10log(1/N)+3dB. Thus, the sidelobe power level is expected to be approximately 15 dB down from the mainlobe for a 63 microphone phased array to be implemented in this initial phase. This sensor count was considered appropriate for the initial phase of the project.

The last two constraints determine the resolution of the array defined as the spot size or dimension of the mainlobe in the beamforming maps. In this particular design, the main challenge was to obtain the best possible resolution at the lowest frequency of interest; i.e. 500 Hz. This requirement was accomplished by setting the outside radius of the array equal to the maximum physically allowed radius. Since the test section height is 1.83m, and the expected boundary layer thickness on the top and bottom walls is approximately 0.15m, the maximum diameter for the array was set to 1.52m.

Regarding the distribution of the microphones on the array, three patterns were investigated: 1) Equal-arc-length logarithmic spiral; 2) equal-arc-length multiarm logarithmic spiral; and 3) equal-aperture-area multiarm logarithmic spiral. These patterns were selected because spiral arrays and multi-arm spiral arrays were previously studied by Dougherty (2002) and Underbrink (2002), respectively. From these studies, these arrays revealed effective sidelobe control over a broad frequency range.

With the maximum number of microphones and outside diameter defined as the initial parameters, a trial and error process was carried out to determine the best microphone distribution pattern. To this end, the Point Spread Function, PSF, of each array pattern at various frequencies of interest were obtained. The PSF is analogous to the unit impulse concept; that is, it is the response of the array to a known point source. In

other words, the PSF defines how a point source would appear in the beamform output of the array.

The PSF for each array candidate was obtained using a MATLAB code that performs beamforming for a simulated point source 1.32m above the array. This source location represents the position of the airfoil model with respect to the phased array during the wind tunnel experiments. The beamform outputs at 500 Hz for the three microphone distribution patterns tested are shown in figure 2-35. It can be seen that the equal-aperture-area displays a better performance compared to the logarithmic spiral and the equal-arc-length multiarm.

The array resolution is defined as the ability of the array to resolve direction of propagation. It is usually specified by the size of the main lobe on a plane 3 dB down from the peak of the main lobe of the PSF. The 3 dB-down plane of the PSF for each of the three array designs at 500 Hz is presented in Figure 2-36. From this figure it can be seen that the logarithmic spiral and the equal-arc-length multiarm have a spot size of 26 inches. However, the equal-aperture-area has a spot size of 24 inches.

As the frequency increases, the array resolution improves. However, the peak sidelobe level also increases, which causes the signal-to-noise ratio of the array to decrease. Therefore, the PSF of the three array designs should be checked for sidelobe suppression at the highest frequency of interest. Figure 2-37 shows the PSF for the three candidate array designs. From this figure it can be seen that the equal-arc-length multiarm and the equal-aperture-area multiarm have a better sidelobe control. The corresponding spot size for this frequency is shown in figure 2-38.

Based on the resolution at the lowest frequency of interest, and the sidelobe control at the highest frequency of interest, the equal-aperture-area pattern was selected for the construction of the array. Therefore, for this particular test a 63-microphone phased array with an equal-aperture-area multiarm logarithmic spiral pattern was implemented. The array has 7 arms with 9 microphones per arm. This array is shown schematically in figure 2-39.

For the construction of the phased array, aluminum honeycomb panels 6.4-mm thick were used. These panels were available in 1.22x3.05m sheets, and had to be joined side by side by means of riveted L-shape beams before being cut in a circular geometry of 1.73-m outside diameter. However, in order to have a completely flat and flush front face, the joining beams were only placed on the back side of the panels.

The microphones used on the array were model WM-61A Panasonic omnidirectional back Electret condenser microphone cartridges, with a sensitivity of -35±4dB (0dB=1V/Pa, 1kHz). These microphones were mounted on nylon adapters as shown in figure 2-40. A total of 100 microphones with adapters were assembled. Each microphone was then calibrated in both magnitude and phase at 1000 Hz using a pistonphone. The results of this calibration were then tabulated and sorted by phase angle. The microphones to be used in the array were the set of 63 microphones with the smallest phase variation, i.e. matching the phase was main criteria for microphone selection.

Note that a hole at the center of the array was made for the placement of a laser pointer. The pointer was adjusted so that the laser beam was perfectly normal to the front face of the array. This laser pointer is used to shine a spot on the test model, and to

accurately determine the position of this model with respect to the phased array. Figure 2-41 shows a picture of the completed phased array.

2.7 Laser vibrometer and range finder

Static deflection of the Kevlar acoustic windows was measured using a Leica model Disto Pro[4]a laser range finder, with an accuracy of ±3mm. A laser vibrometer was used to measure vibration of the tensioned Kevlar. This vibrometer consists of a Polytec OFV-2600 Vibrometer Controller connected to a Polytec OFV-501 Fiber Interferometer. The interferometer detects the motion of the surface of interest by allowing this motion to modulate the path lengths travel by the laser beams. The output of the interferometer is processed by the Vibrometer Controller which is provided by a low pass filter with a 3dB-frequency specified at 100 kHz. The most important feature of the laser vibrometer is that it allows to perform non-contact vibration measurements, which is desired in the case of the tensioned Kevlar.

Freestream Velocity	**RMS Streamwise Fluctuations (at center section)**		**Mean flow uniformity**
U_∞ **[m/s]**	**Reynolds**	**Choi and Simpson**	
5	0.018%		
12	0.018%		
15	0.022%	0.041%	1.2%
20	0.028%		
30	0.045%		
37.5	0.072%	0.072%	1.3%
60			1.5%

***Table 2-1**. Flow quality in the Stability Wind Tunnel*

Table 2-2. *Pressure tap locations on the NACA 0012 airfoil model*

Hatch Side		Opposite Side	
x/c	*z/c*	*x/c*	*z/c*
0.0000	0.1032	0.0000	0.2302
0.0025	0.1038	0.0025	0.2296
0.0050	0.1043	0.0050	0.2290
0.0075	0.1049	0.0075	0.2284
0.0100	0.1055	0.0100	0.2278
0.0125	0.1061	0.0125	0.2273
0.0150	0.1066	0.0150	0.2267
0.0175	0.1072	0.0175	0.2261
0.0200	0.1078	0.0200	0.2255
0.0250	0.1089	0.0250	0.2244
0.0500	0.1147	0.0500	0.2186
0.0750	0.1205	0.0750	0.2128
0.1000	0.1263	0.1000	0.2071
0.1250	0.1320	0.1250	0.2013
0.1500	0.1378	0.1500	0.1955
0.1750	0.1436	0.1750	0.1898
0.2000	0.1494	0.2000	0.1840
0.2250	0.1551	0.2250	0.1782
0.2500	0.1609	0.2500	0.1724
0.2750	0.1667	0.2750	0.1667
0.3000	0.1724	0.3000	0.1609
0.3250	0.1782	0.3250	0.1551
0.3500	0.1840	0.3500	0.1494
0.3750	0.1898	0.3750	0.1436
0.4000	0.1955	0.4000	0.1378
0.4250	0.2013	0.4250	0.1320
0.4500	0.2071	0.4500	0.1263
0.4750	0.2128	0.4750	0.1205
0.5000	0.2186	0.5000	0.1147
0.5500	0.2302	0.5500	0.1032
0.6000	0.2186	0.6000	0.1147
0.6500	0.2071	0.6500	0.1263
0.7000	0.1955	0.7000	0.1378
0.7500	0.1840	0.7500	0.1494
0.8000	0.1724	0.8000	0.1609
0.8500	0.1609	0.8500	0.1724
0.9000	0.1494	0.9000	0.1840
0.9200	0.1447	0.9200	0.1886
0.9400	0.1401	0.9400	0.1932
0.9600	0.1355	0.9600	0.1978
0.9800	0.1309	0.9800	0.2025

x/c	t/c	x/c	t/c	x/c	t/c	x/c	t/c
0.0139	0.0357	0.2639	0.1211	0.5139	0.1054	0.7639	0.0617
0.0278	0.0542	0.2778	0.1215	0.5278	0.1036	0.7778	0.0587
0.0417	0.0658	0.2917	0.1217	0.5417	0.1016	0.7917	0.0556
0.0556	0.0746	0.3056	0.1216	0.5556	0.0996	0.8056	0.0526
0.0694	0.0821	0.3194	0.1214	0.5694	0.0976	0.8194	0.0495
0.0833	0.0885	0.3333	0.1210	0.5833	0.0954	0.8333	0.0463
0.0972	0.0938	0.3472	0.1206	0.5972	0.0931	0.8750	0.0365
0.1111	0.0984	0.3611	0.1199	0.6111	0.0907	0.8889	0.0331
0.1250	0.1024	0.3750	0.1192	0.6250	0.0884	0.9028	0.0297
0.1389	0.1058	0.3889	0.1184	0.6389	0.0861	0.9167	0.0262
0.1528	0.1089	0.4028	0.1174	0.6528	0.0836	0.9306	0.0227
0.1667	0.1114	0.4167	0.1163	0.6667	0.0811	0.9444	0.0188
0.1806	0.1137	0.4306	0.1151	0.6806	0.0784	0.9583	0.0146
0.1944	0.1156	0.4444	0.1137	0.6944	0.0758	0.9722	0.0103
0.2083	0.1172	0.4583	0.1122	0.7083	0.0731	0.9861	0.0059
0.2222	0.1186	0.4722	0.1107	0.7222	0.0703		
0.2361	0.1197	0.4861	0.1090	0.7361	0.0675		
0.2500	0.1205	0.5000	0.1073	0.7500	0.0646		

Table 2-3. *Measured thickness distribution for NACA 0012 model*

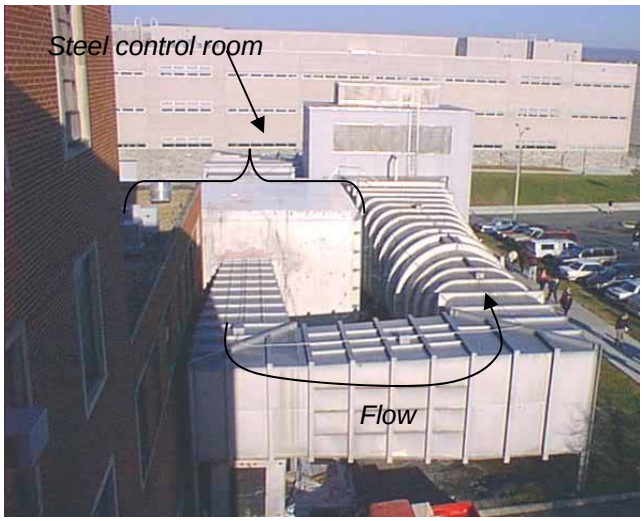

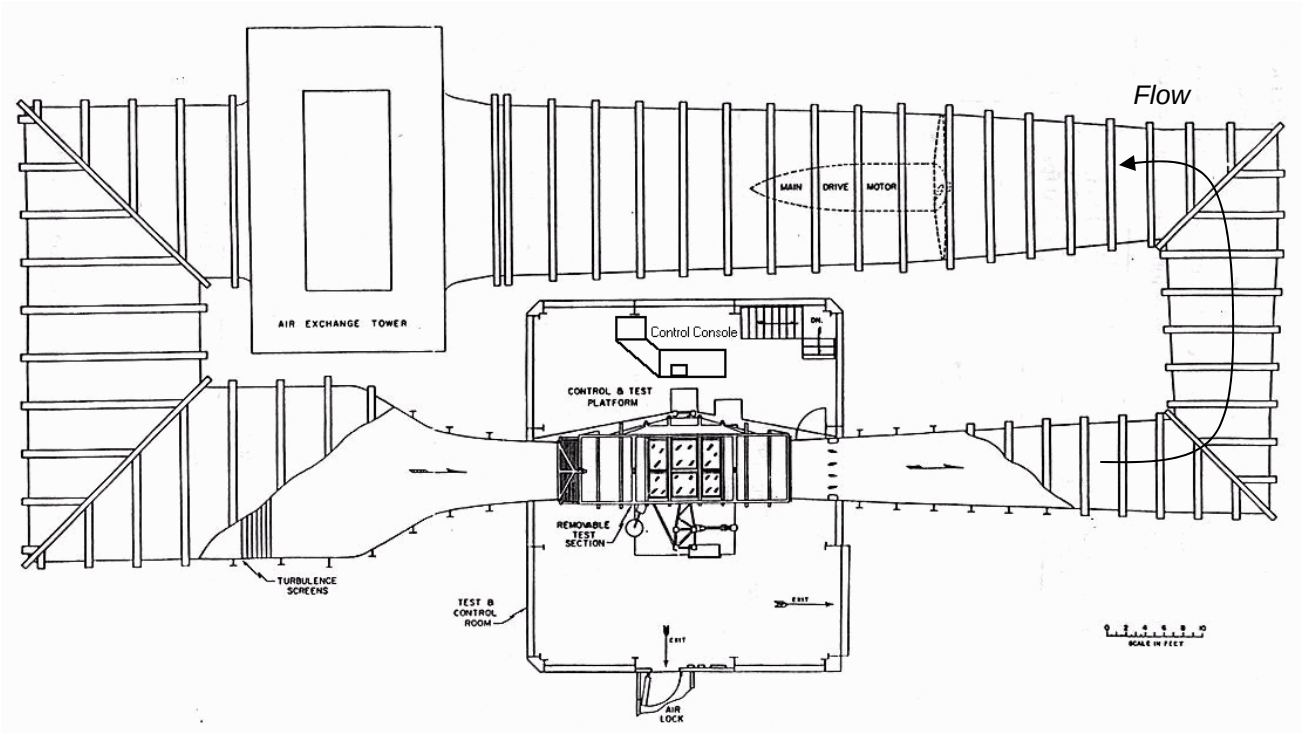

Figure 2-1. *(a) Photograph and (b) plan view schematic of the Virginia Tech Stability Tunnel. Photo shows connection to Randolph Hall through metal building at center of picture. This pressure sealed steel room, which contains both the test section and operating console.*

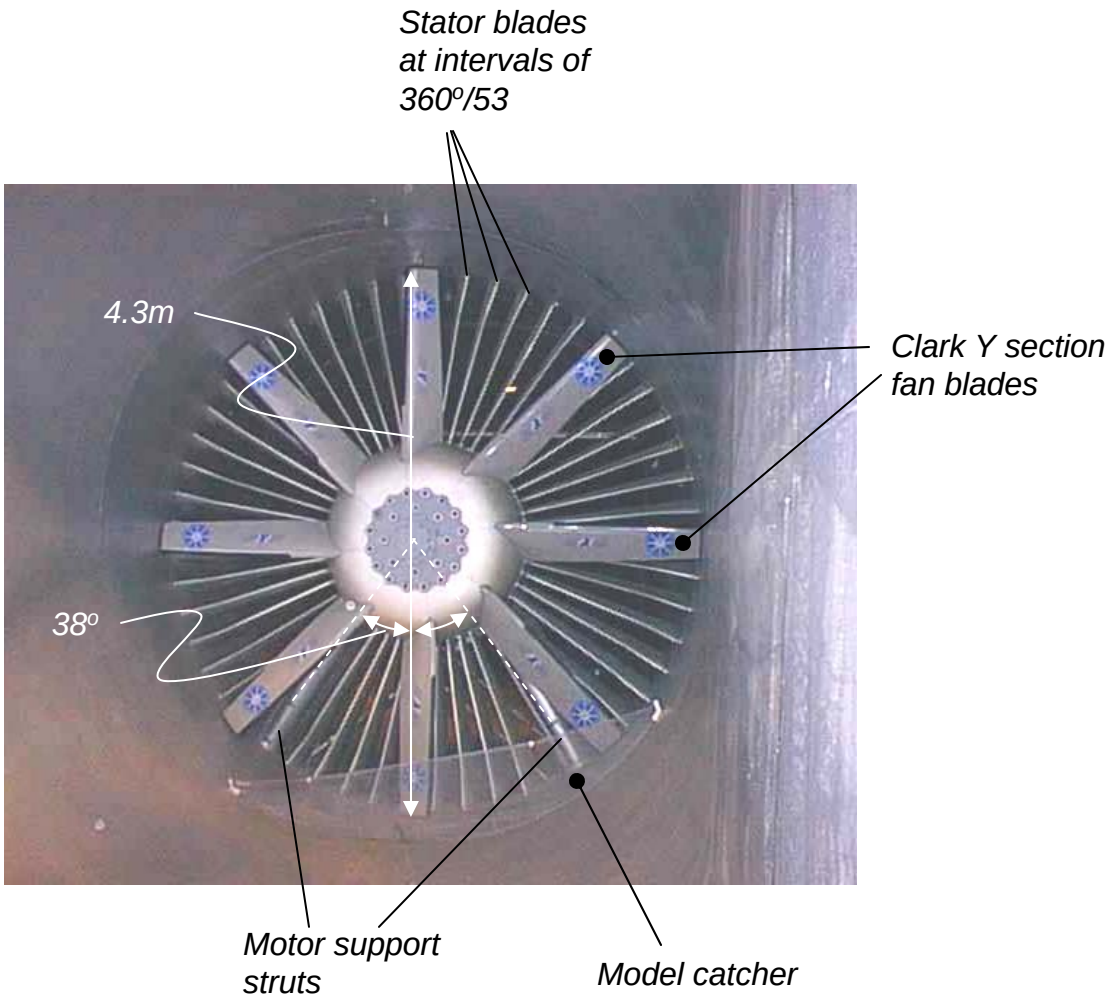

Figure 2-2. *Photograph of the Stability Wind Tunnel fan as seen from upstream.*

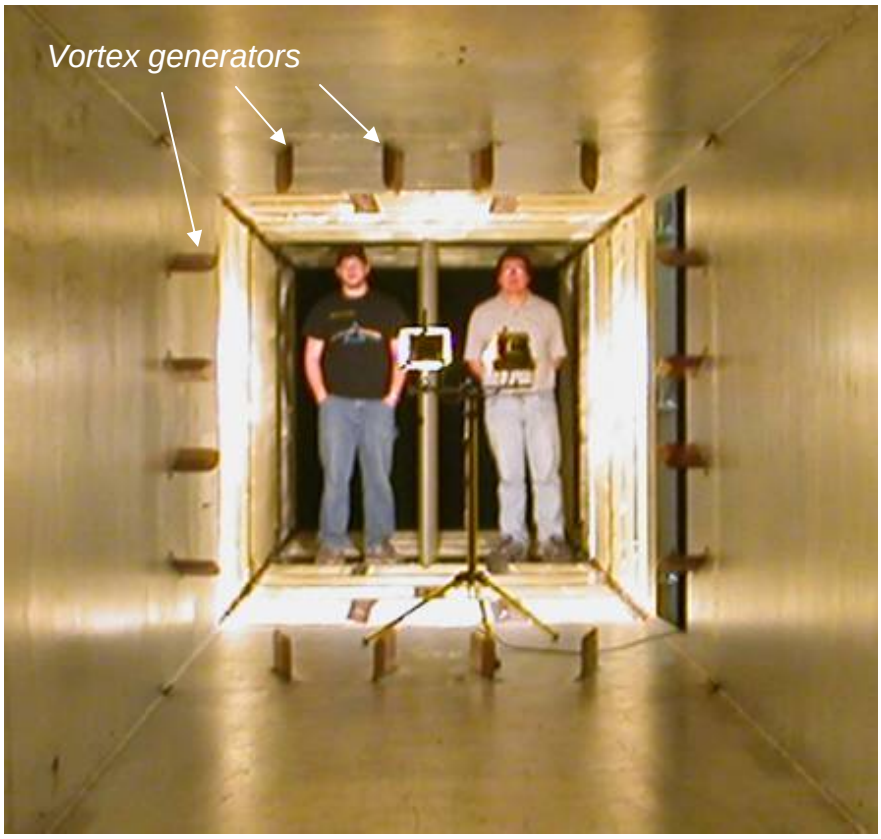

Figure 2-3. *Photograph of the Stability Wind Tunnel diffuser looking upstream into the test section (lamp and engineers removed for test).*

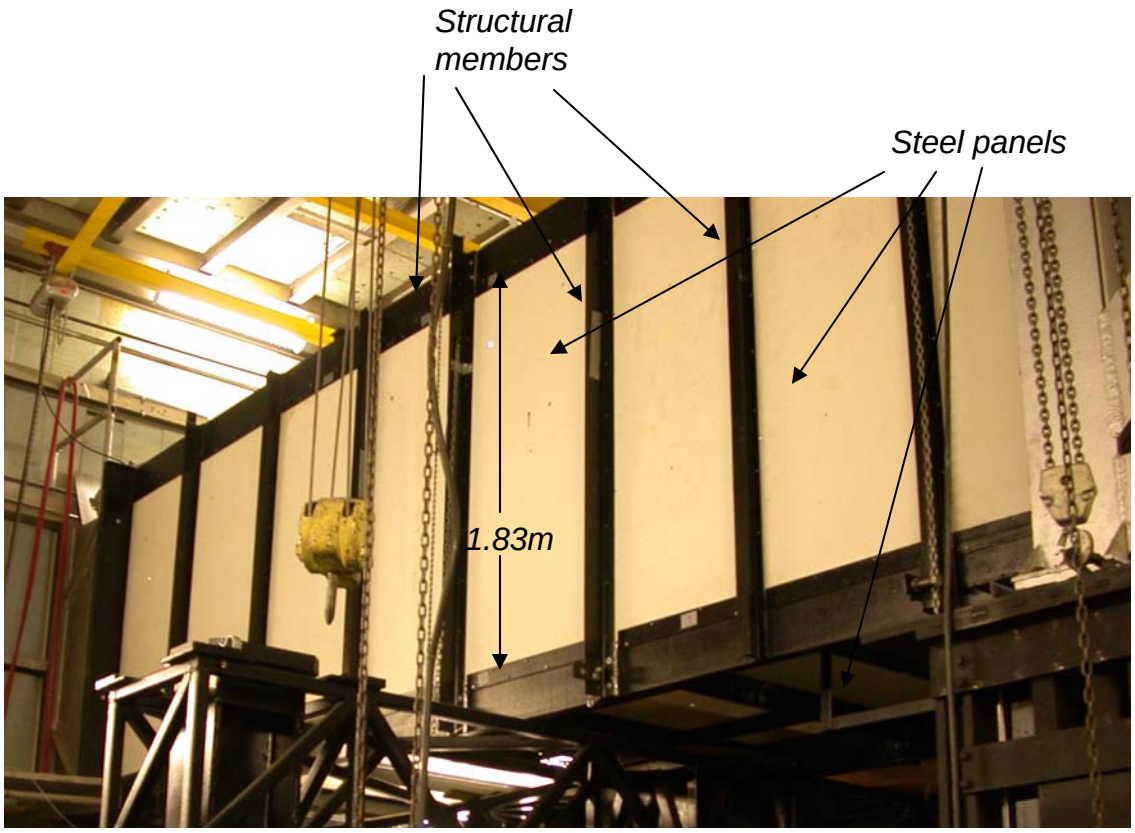

Figure 2-4. *Photograph of the port side of the Stability Wind Tunnel test section looking upstream*

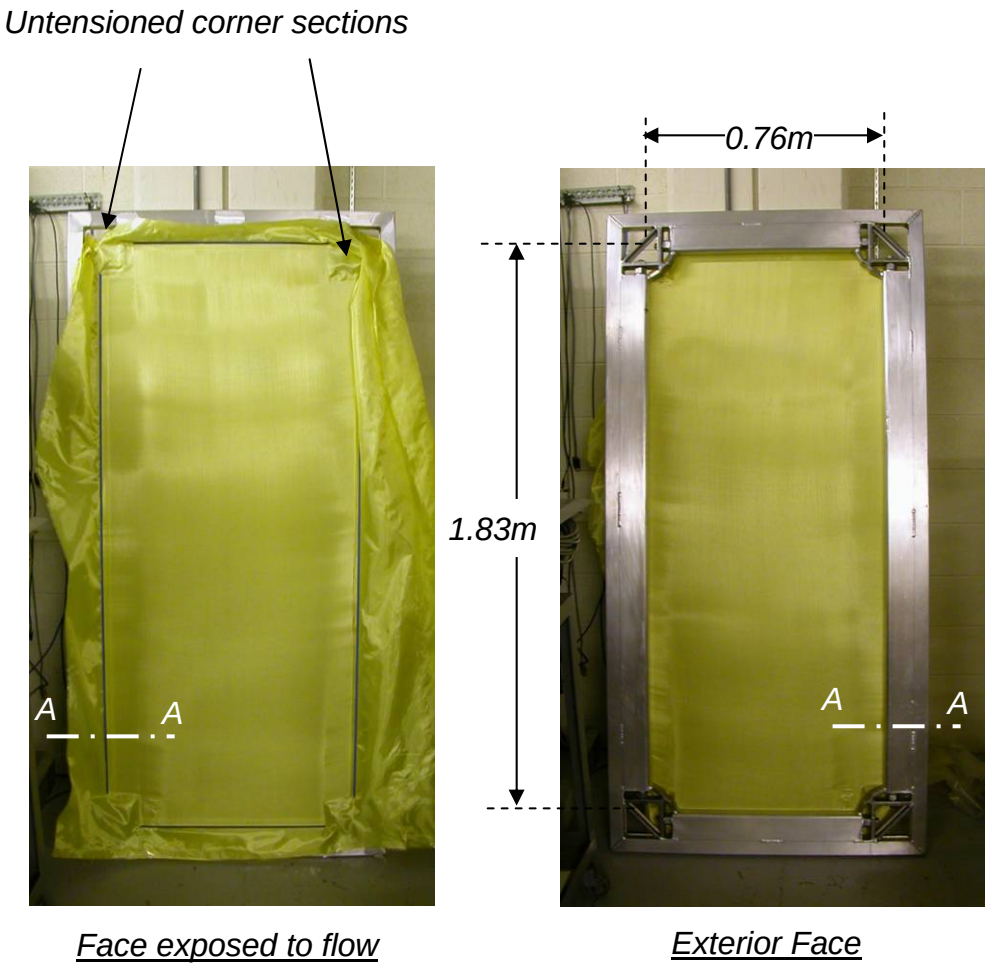

Figure 2-5. *Small scale roller chase frame used in preliminary testing of the Kevlar wall concept.*

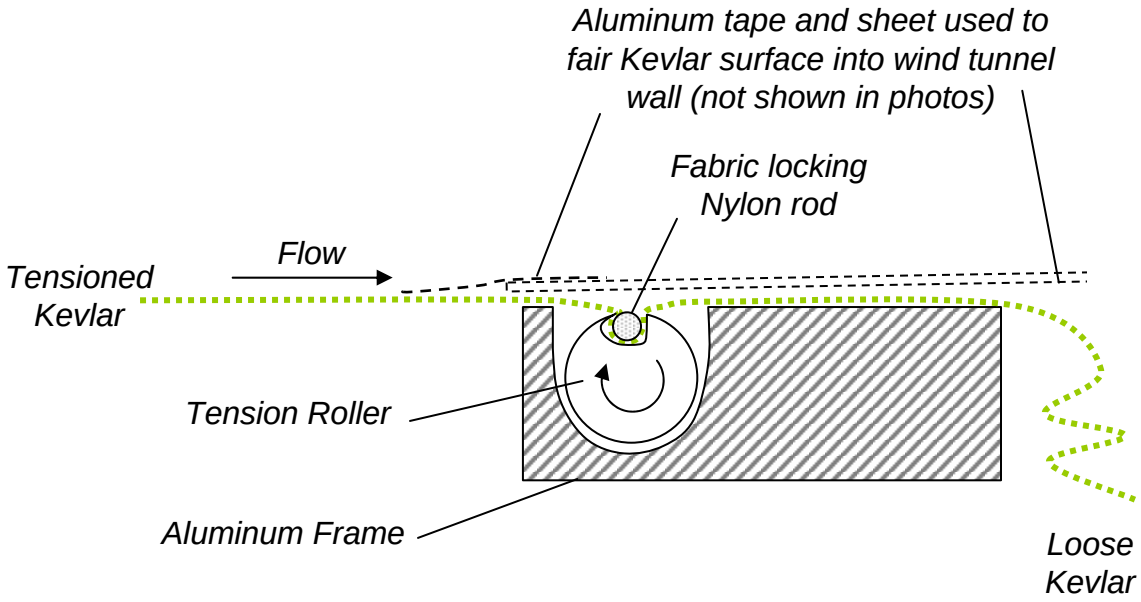

Section A-A (from Figure 2-5)

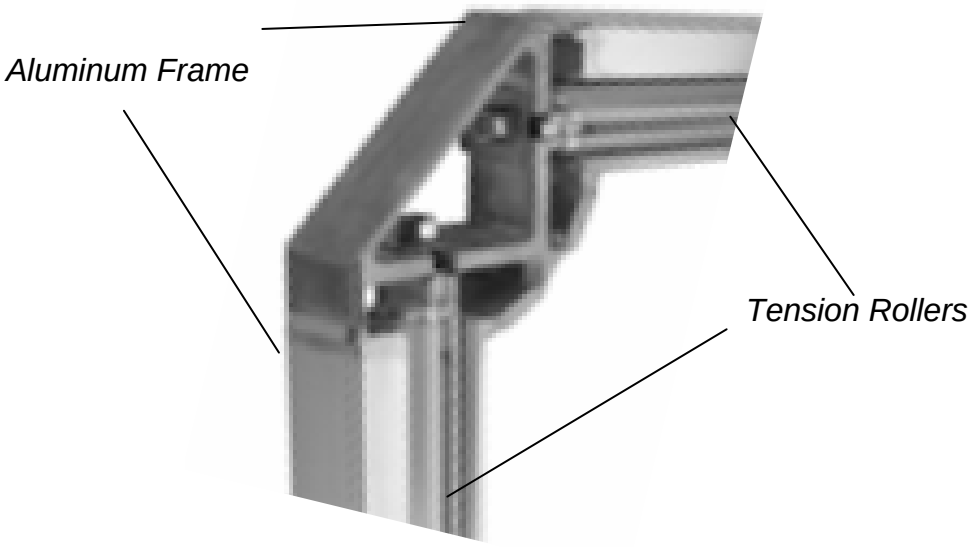

Frame corner detail (w/o Kevlar), flow side

Figure 2-6. *Kevlar mounting arrangement and roller chase frame details.*

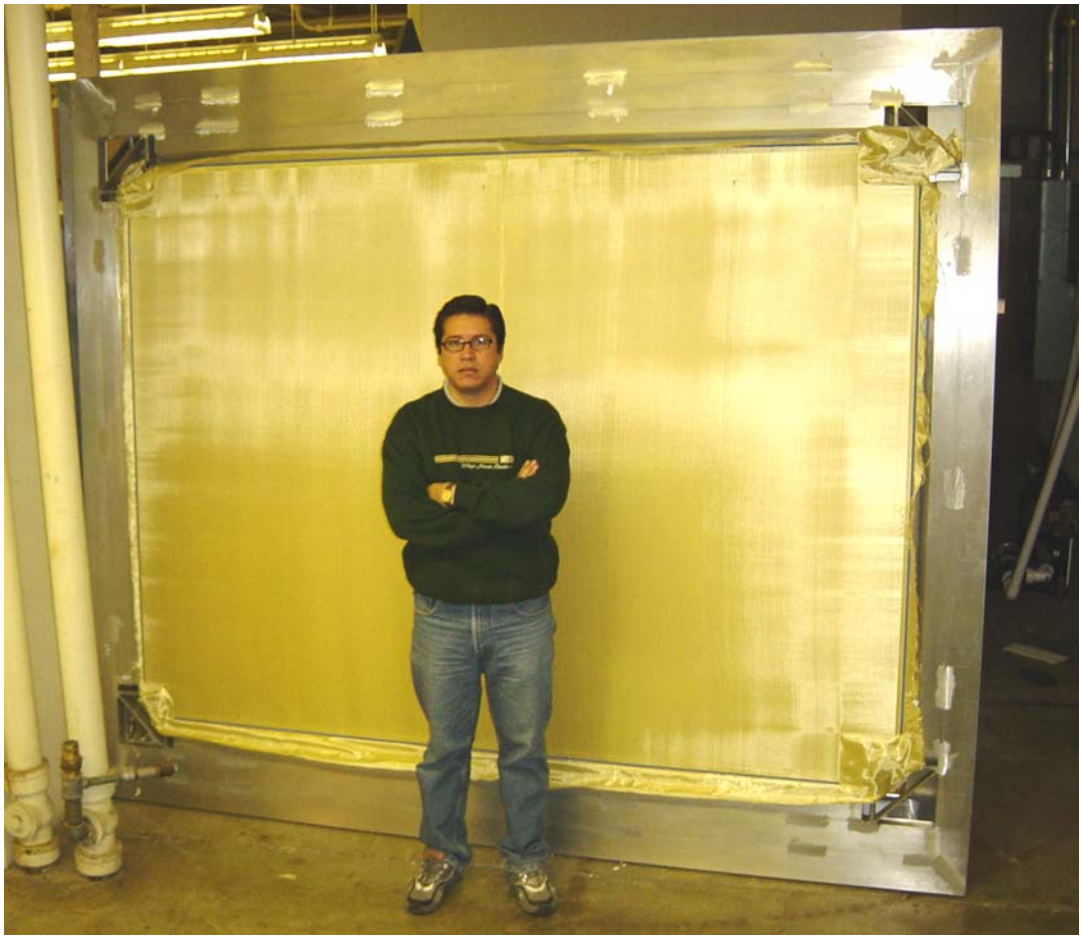

Figure 2-7. *Large scale roller chase frames used for the bulk of testing.*

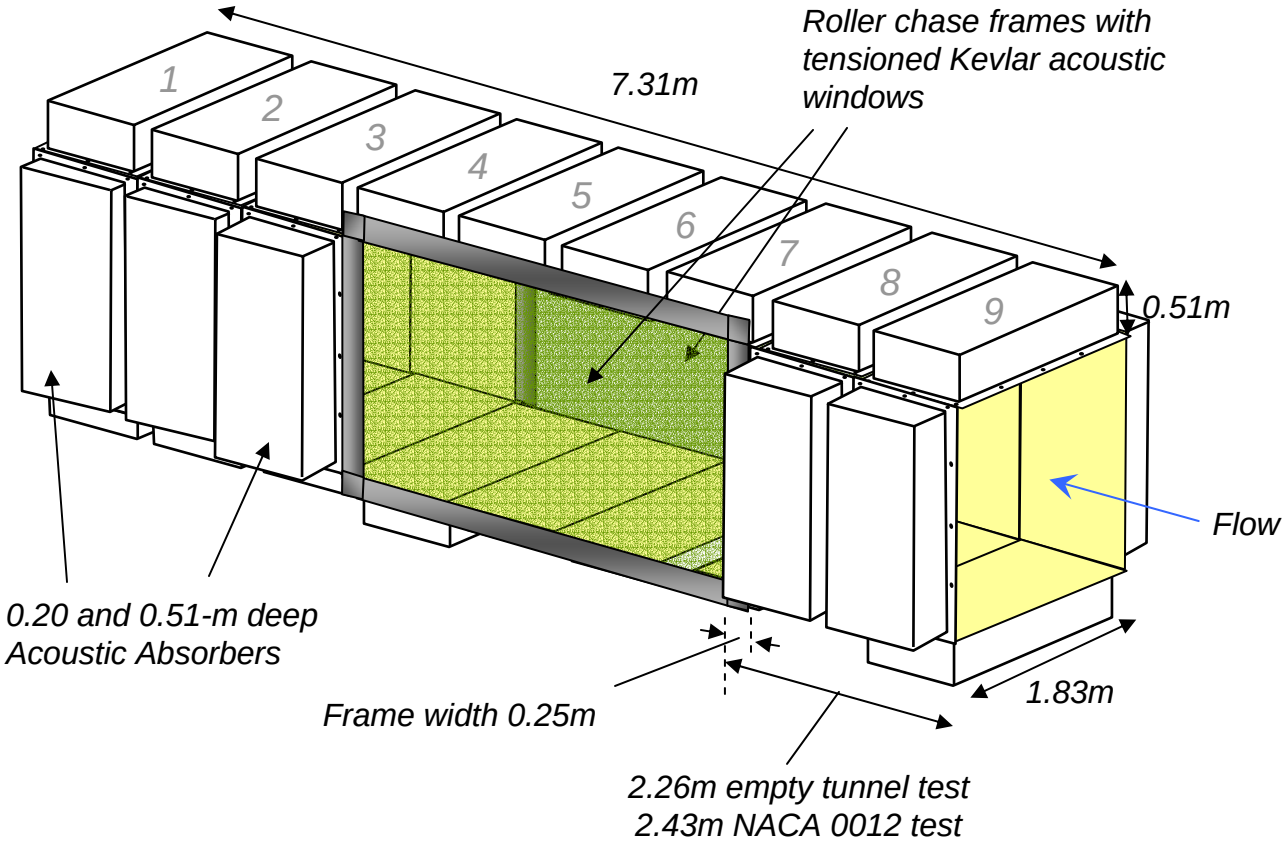

Figure 2-8. *Schematic showing the arrangement of acoustic absorbers and Kevlar acoustic windows used in the acoustically treated empty test section measurements.*

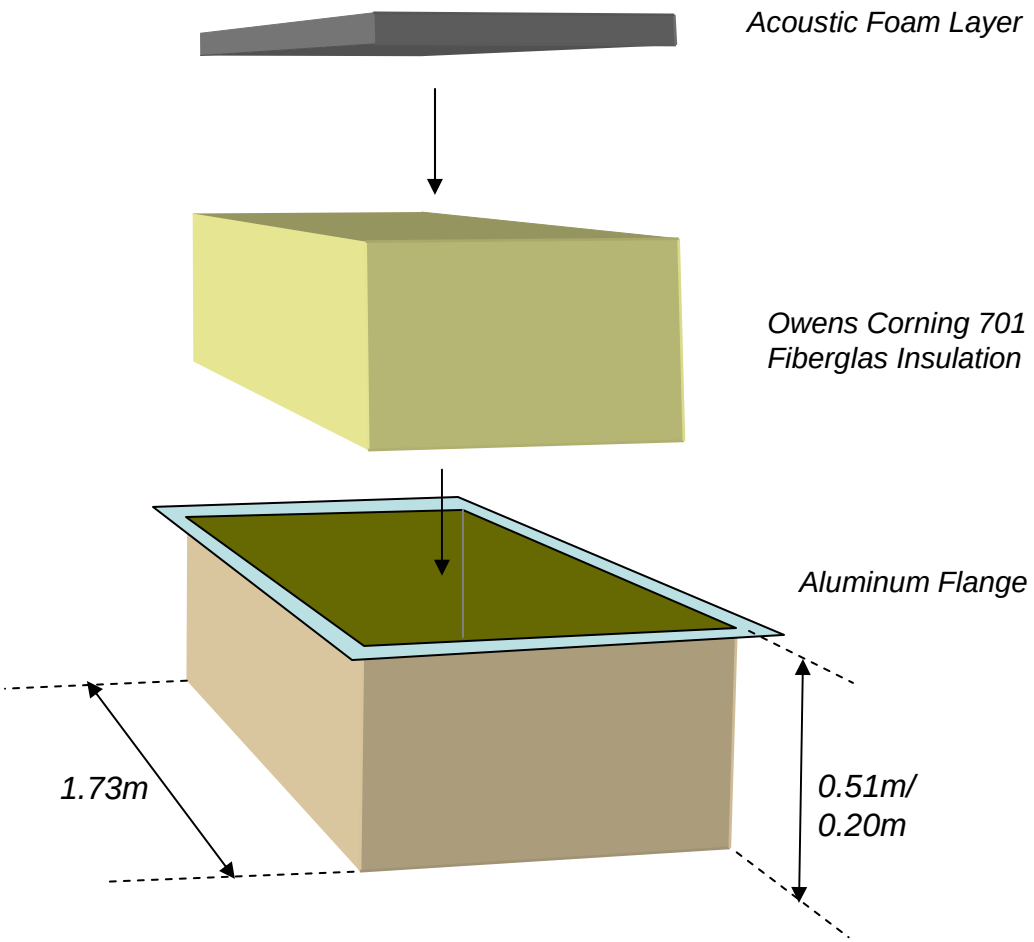

Figure 2-9. *Schematic showing construction of acoustic absorbers*

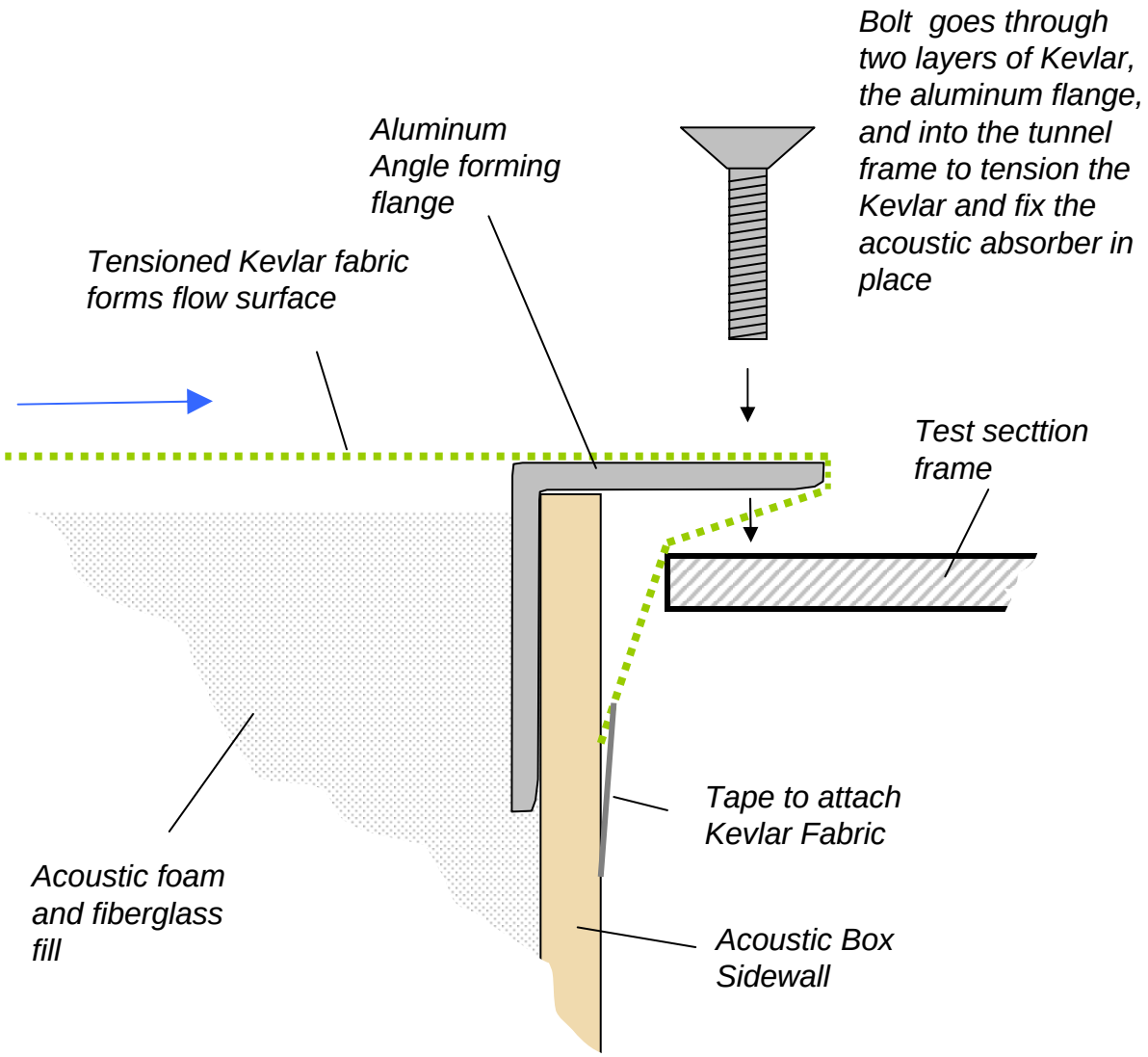

Figure 2-10. *Scheme used to cover acoustic absorbers with tensioned Kevlar cloth.*

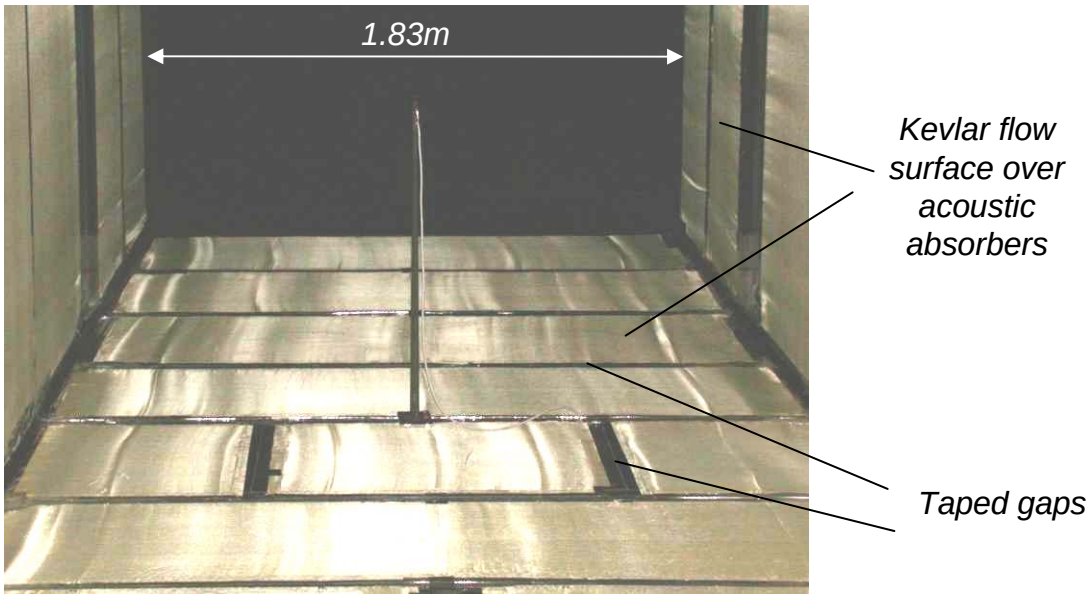

(a) Kevlar flow surface

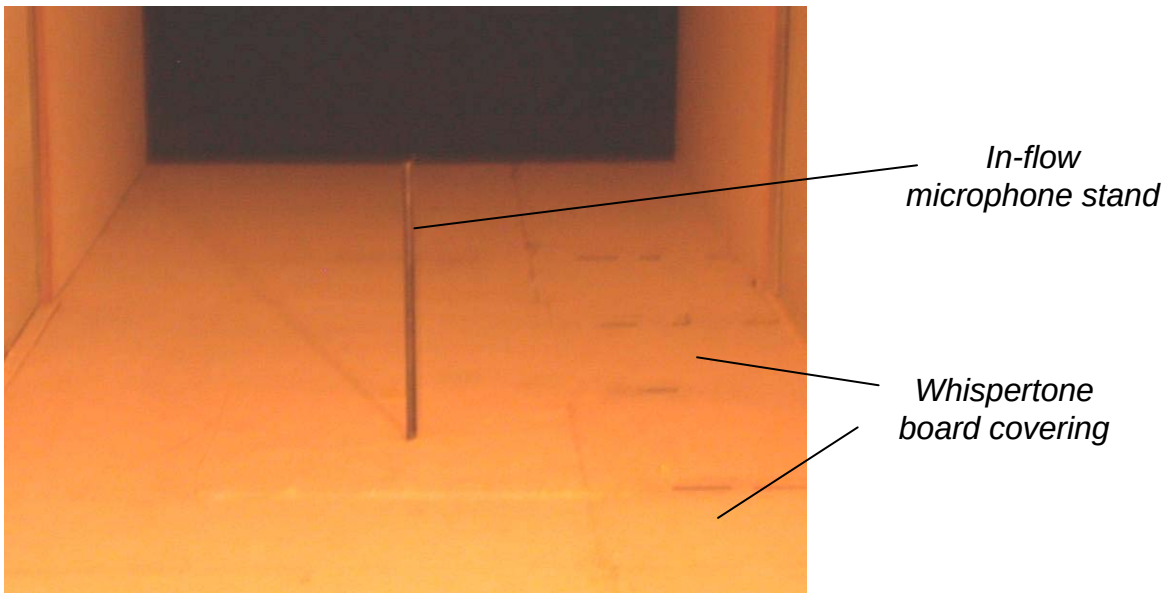

(a) Whispertone flow surface

Figure 2-11. *Photographs of the interior of the test section looking upstream.with the in-flow microphone stand installed.*

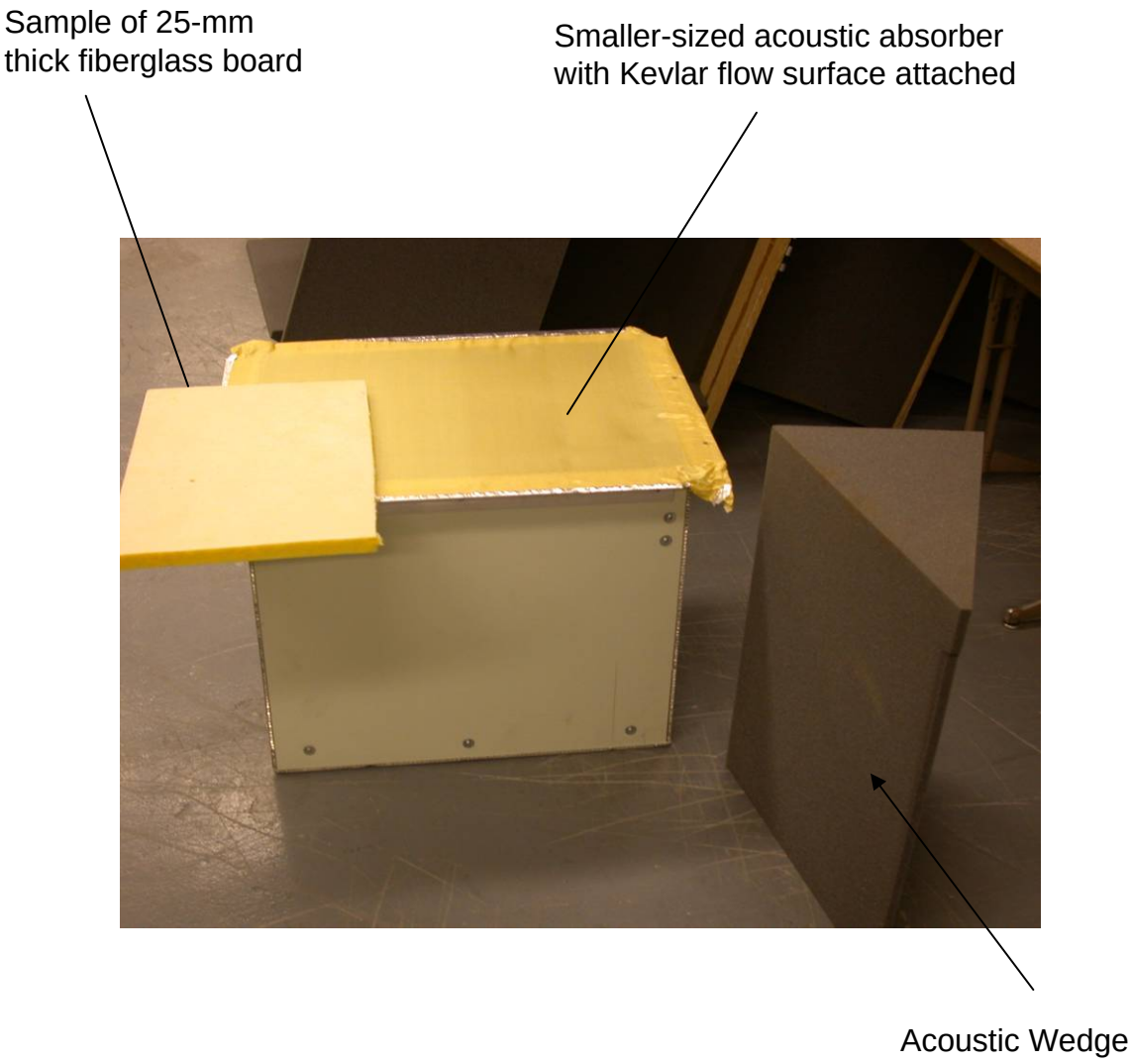

Figure 2-12. *Photograph of an acoustic absorber, acoustic wedge and sample of fiberglass board.*

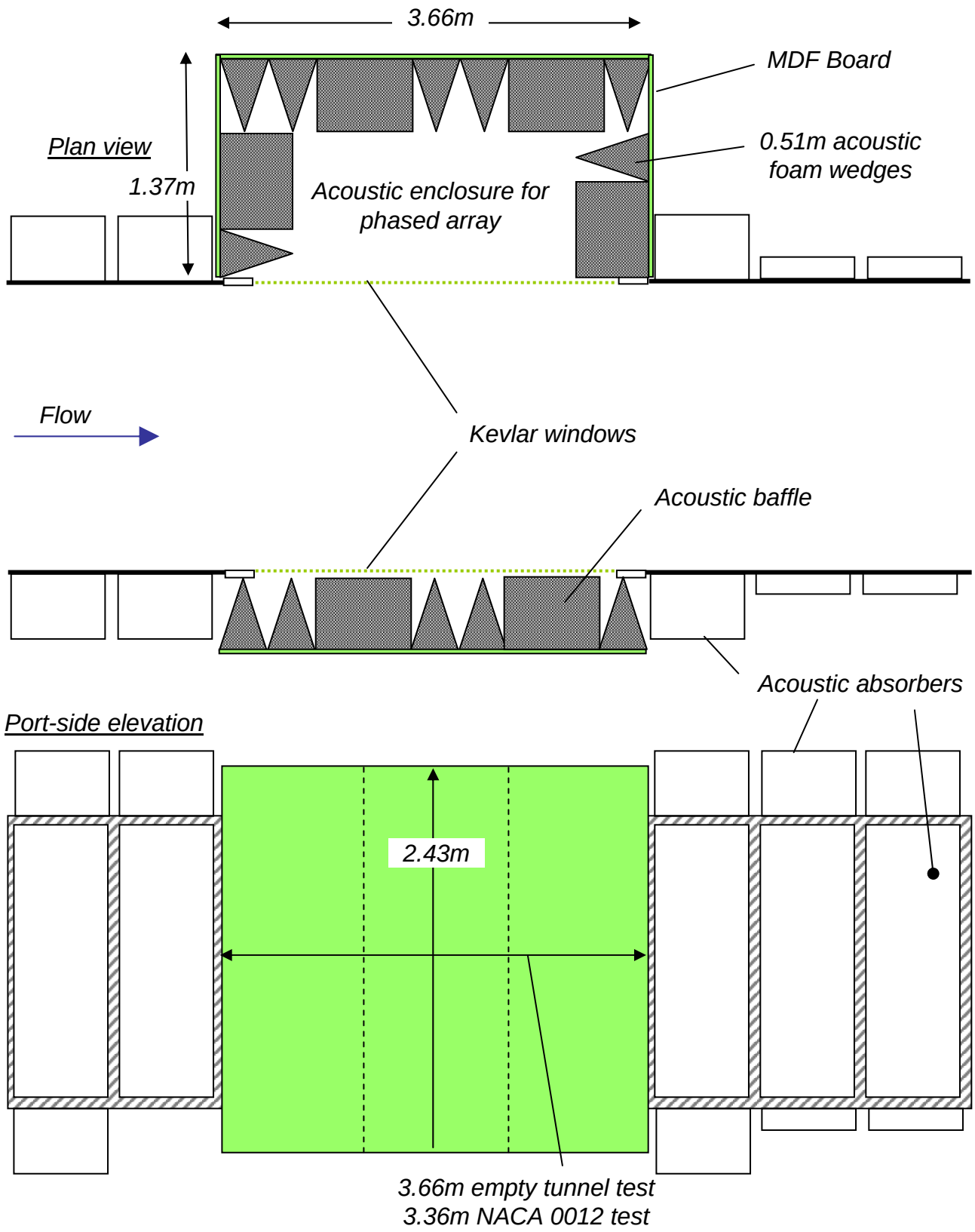

Figure 2-13. *Plan and elevation schematics showing the size and placement of the acoustic enclosure and baffle.*

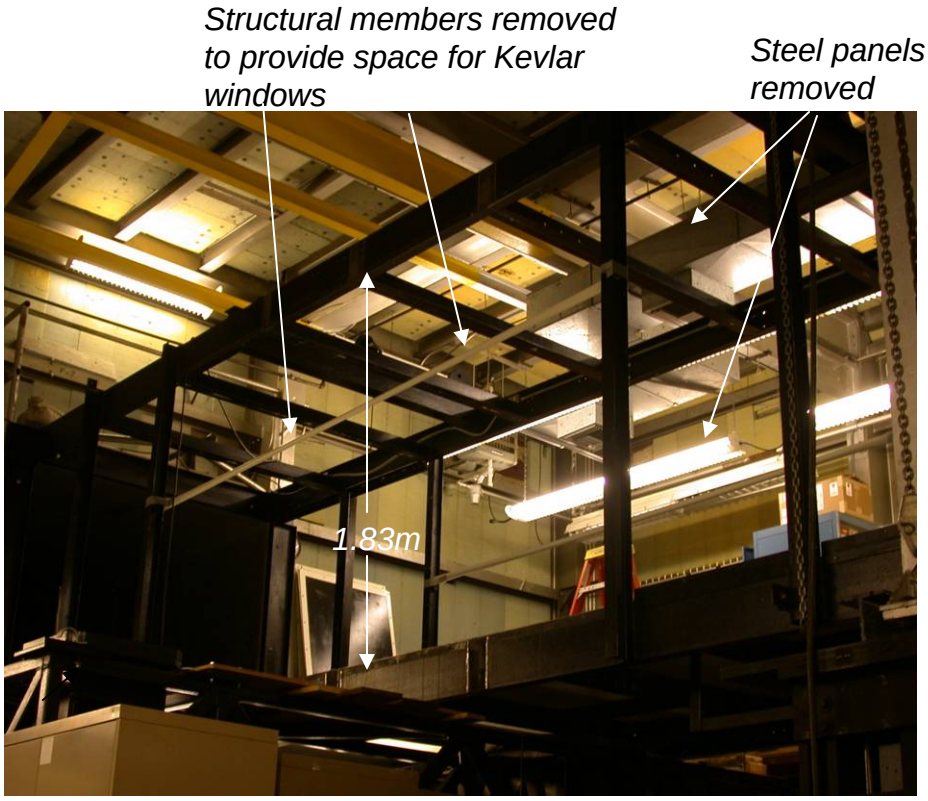

Figure 2-14. *Photograph showing the test section with steel panels and vertical struts removed in preparation for installation of the acoustic treatment*

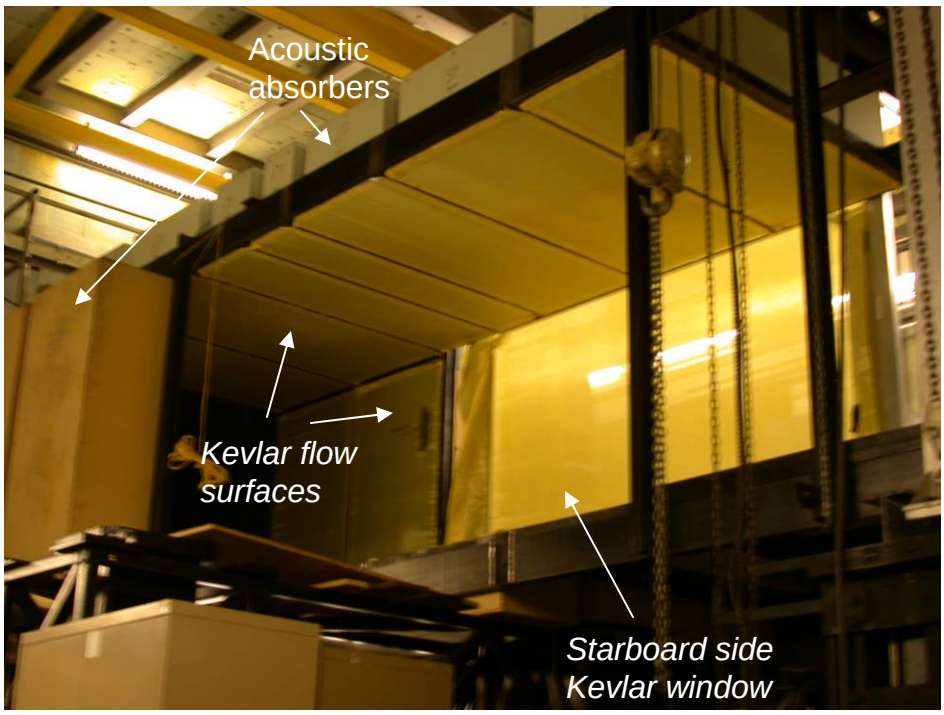

Figure 2-15. *Photograph showing the acoustic absorbers with Kevlar flow surfaces in the process of installation.*

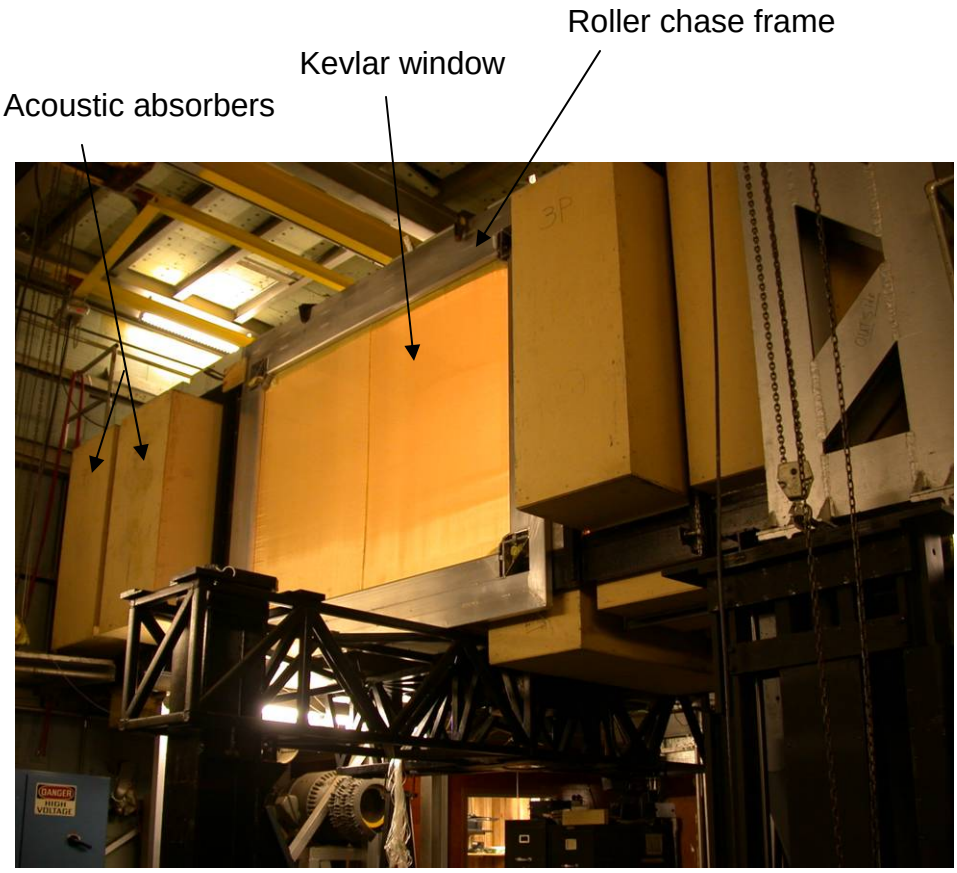

Figure 2-16. *Photograph showing the port-side Kevlar window installed*

Figure 2-17a. *Photograph showing the port-side acoustic baffle installed*

Figure 2-17b. *Photograph into the starboard-side acoustic enclosure with sidewall, floor and ceiling treatment removed. The picture also shows the 63-microphone phased array system is mounted next to the Kevlar acoustic window*

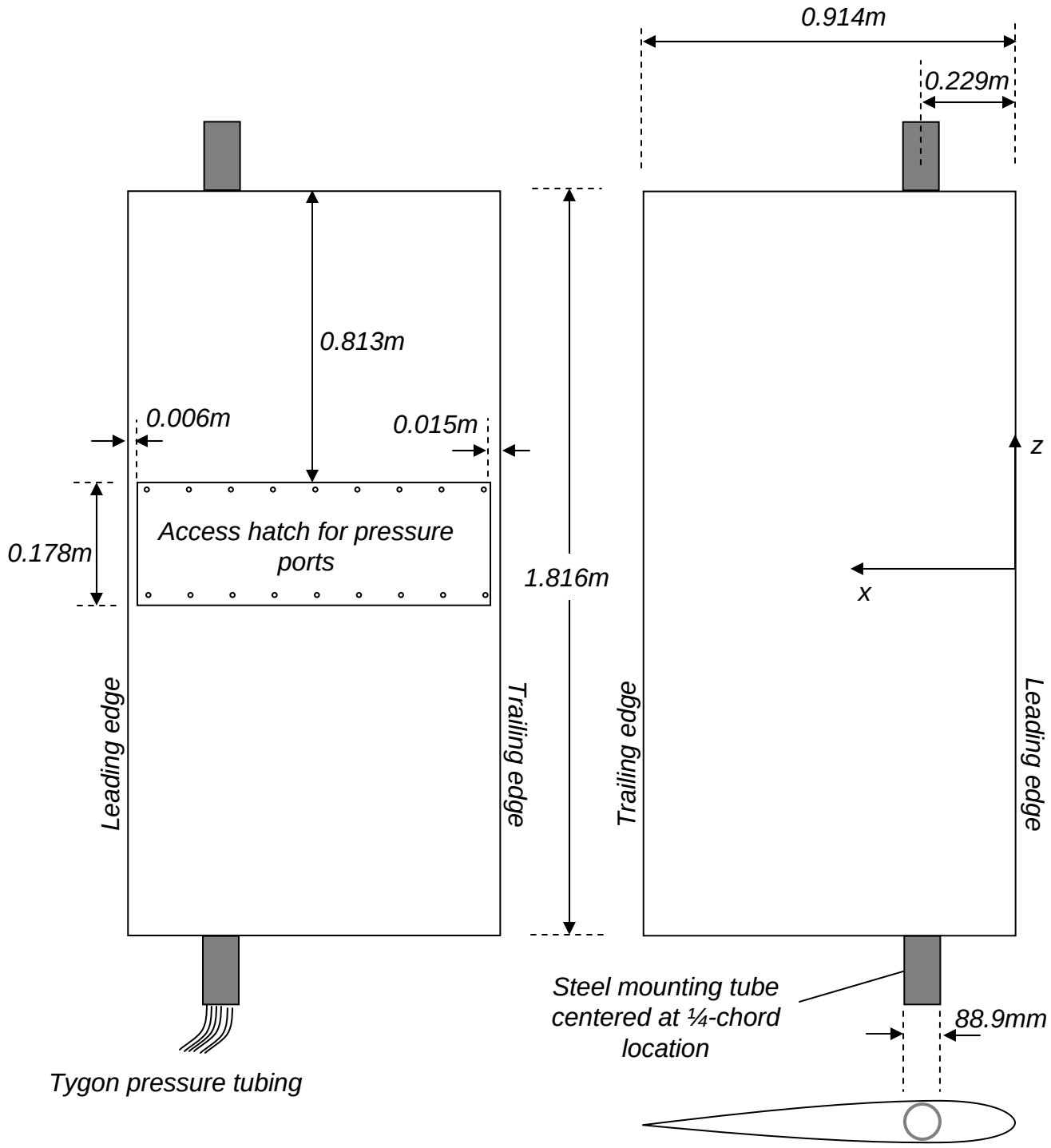

Figure 2-18. *Schematic of the NACA 0012 airfoil model.*

Figure 2-19. *Photographs of the NACA 0012 airfoil model showing the access hatch (courtesy Novakinetics, LLG).*

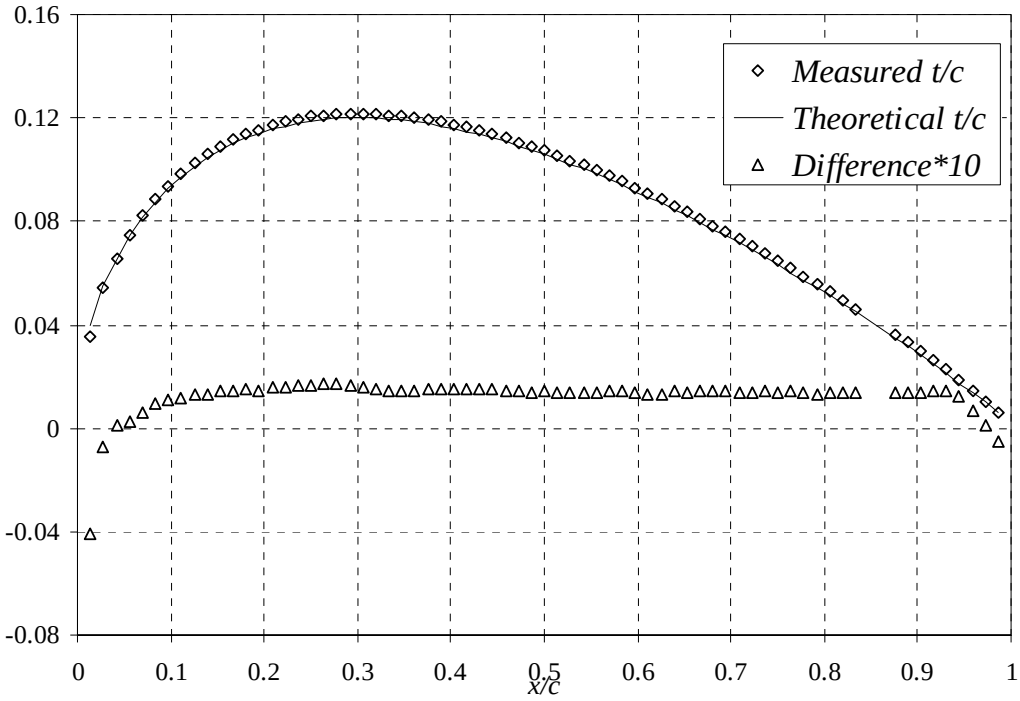

Figure 2-20. *NACA 0012 measured reference thickness profile compared with theoretical shape from Abbot and von Doenhoff (1959).*

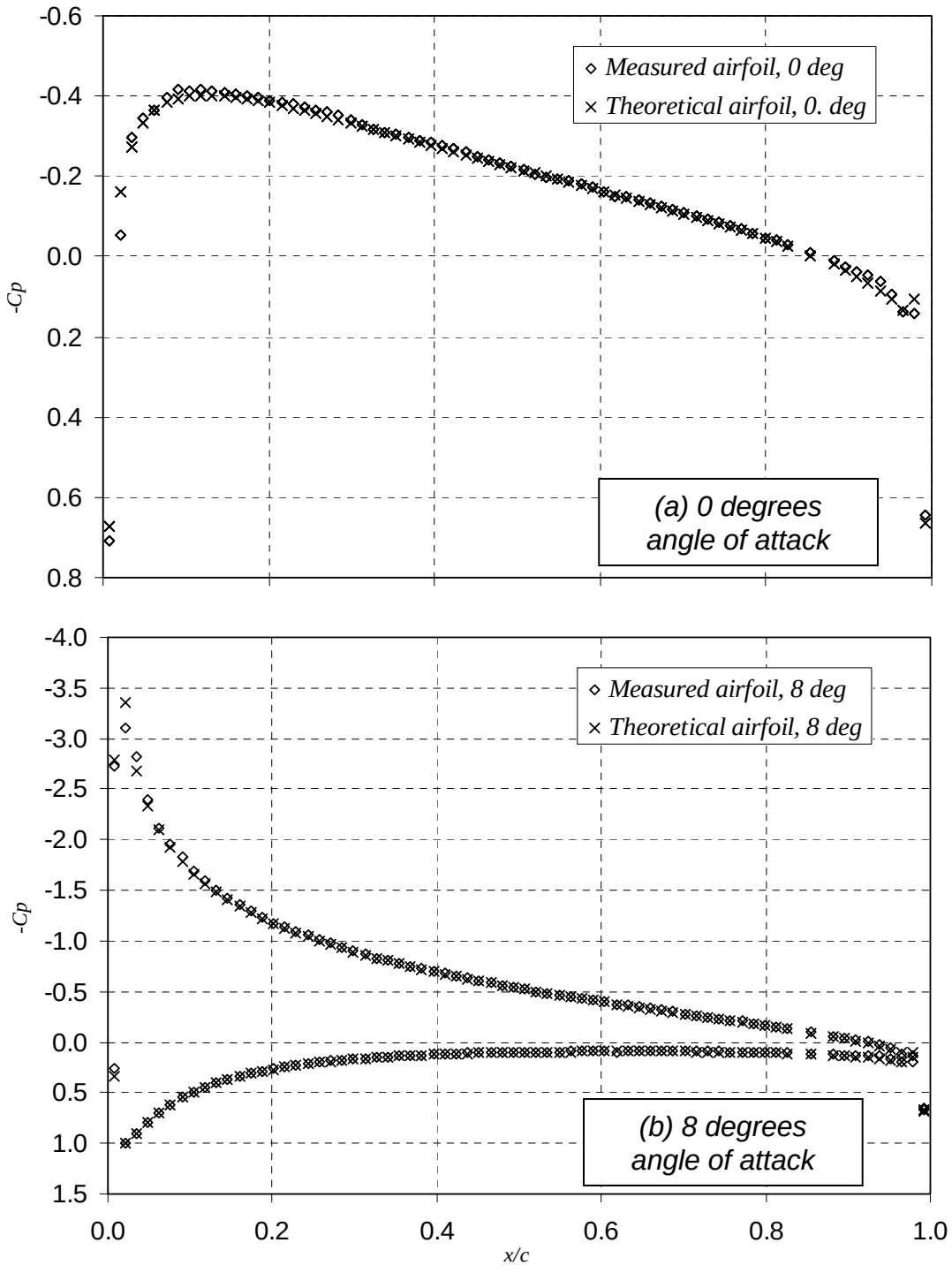

Figure 2-21. *Comparison of pressure distributions calculated using the vortex panel method for the theoretical and measured NACA 0012 shape.*

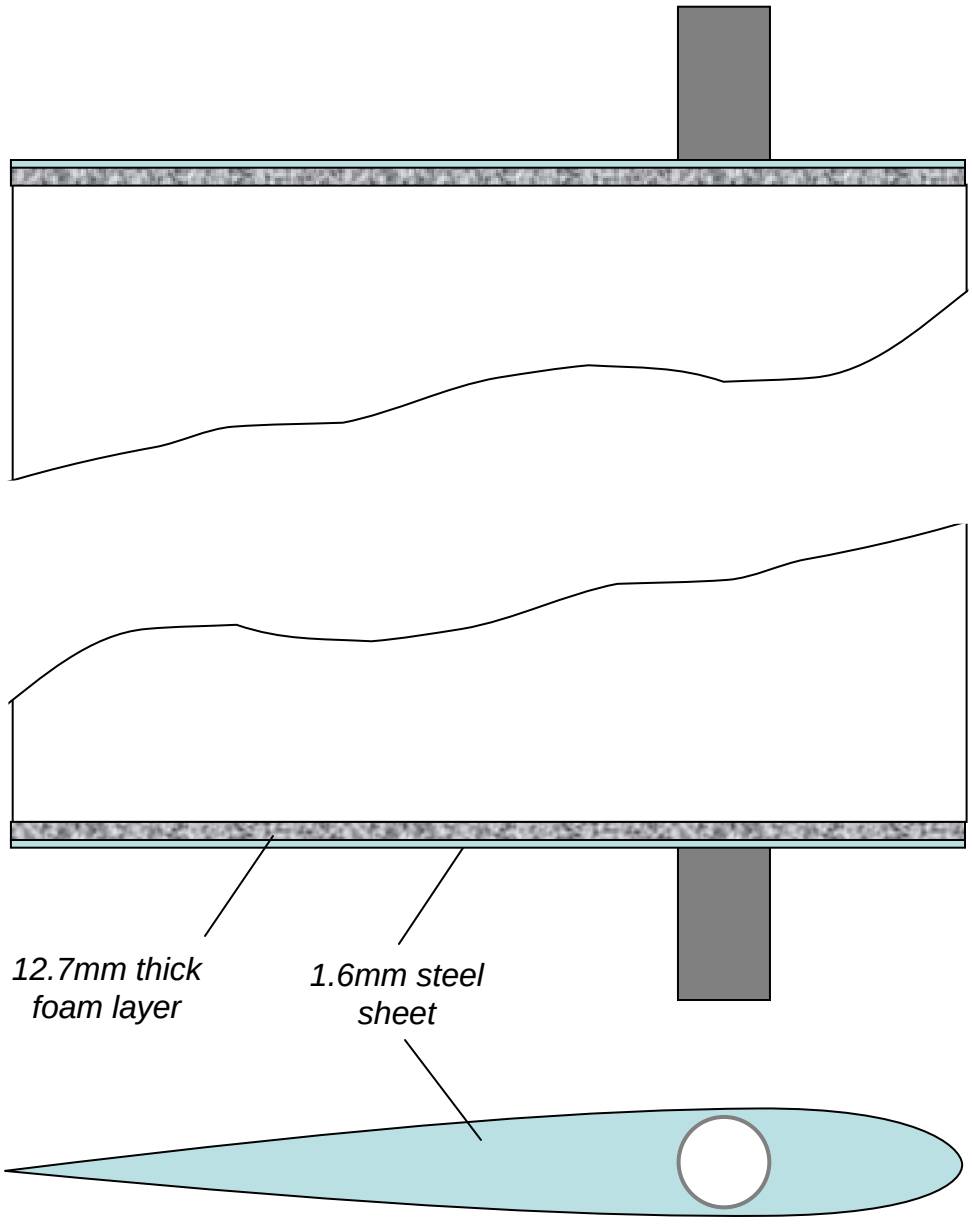

Figure 2-22. *Model endplates*

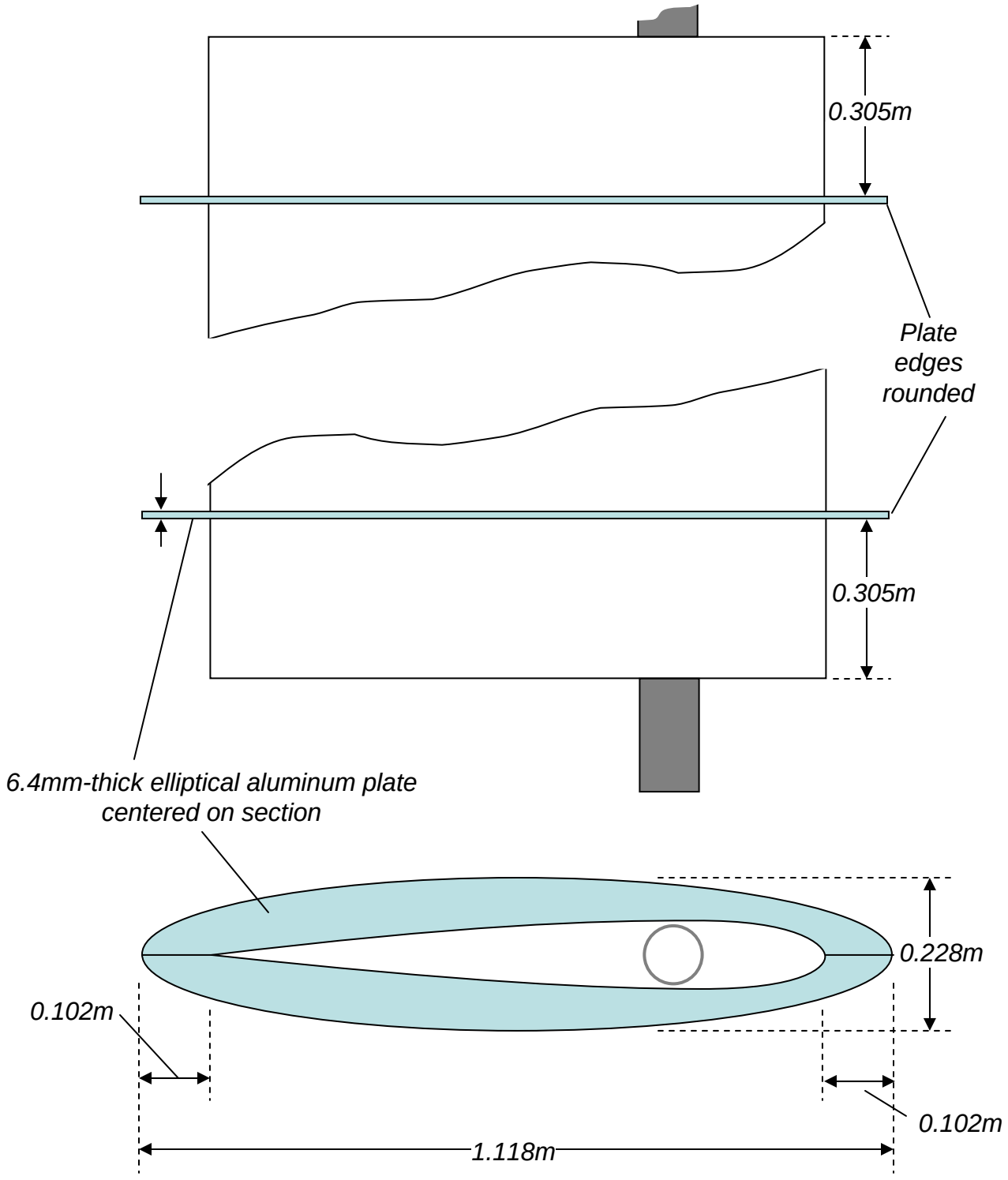

Figure 2-23. *Removable boundary layer fences, and mounting location*

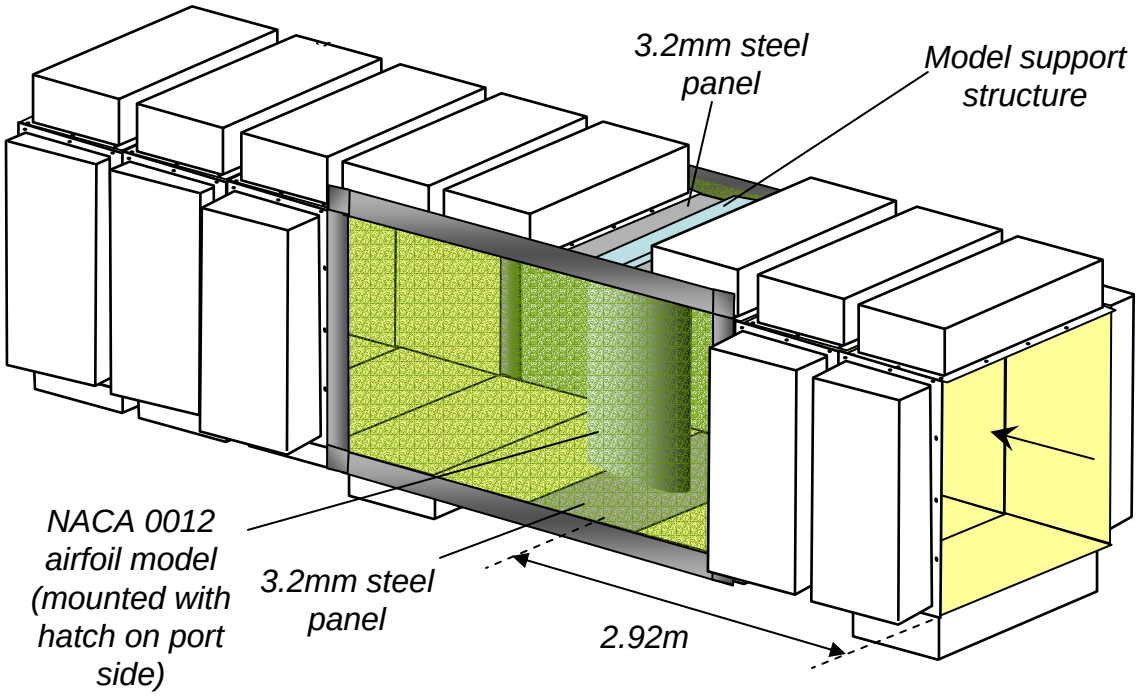

Figure 2-24. *Test section with acoustic treatment with NACA 0012 model mounted*

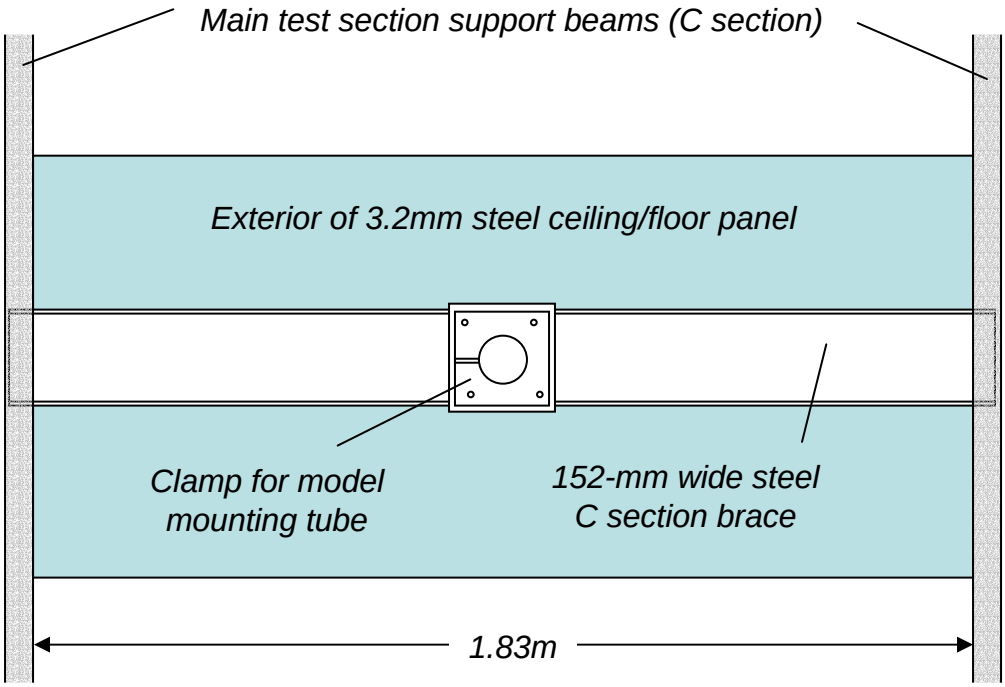

View of model support from outside tunnel

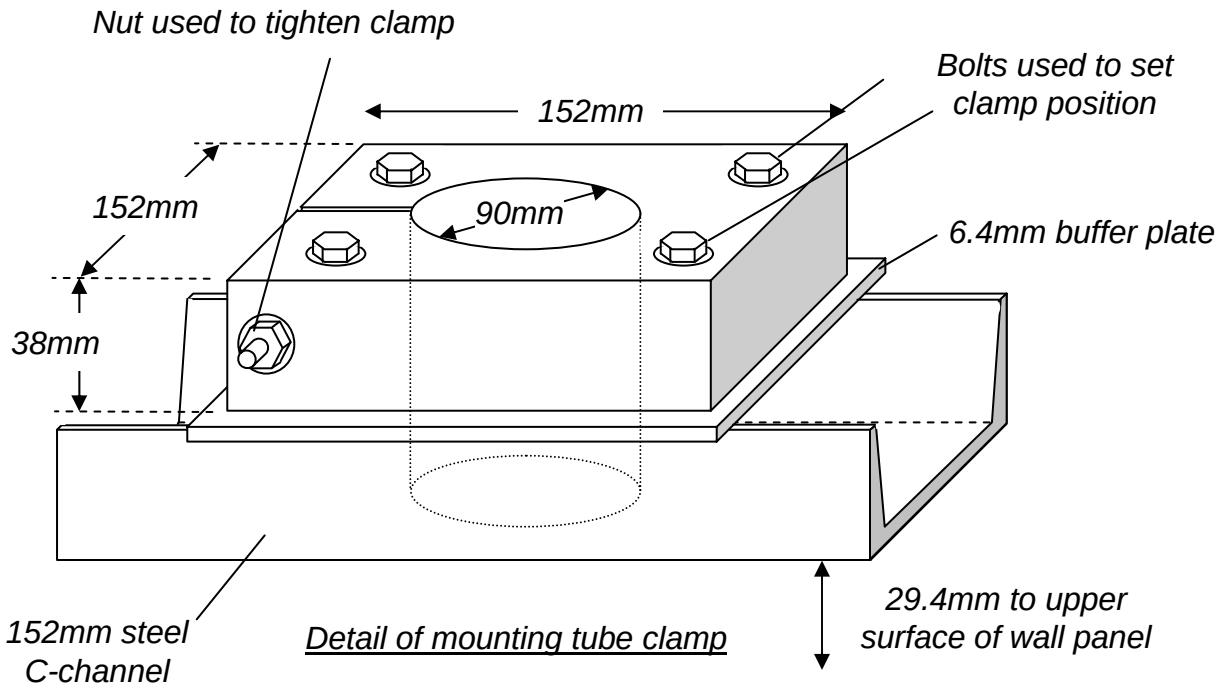

Figure 2-25. *Diagram of clamps used to mount NACA 0012 model to the test section structure*

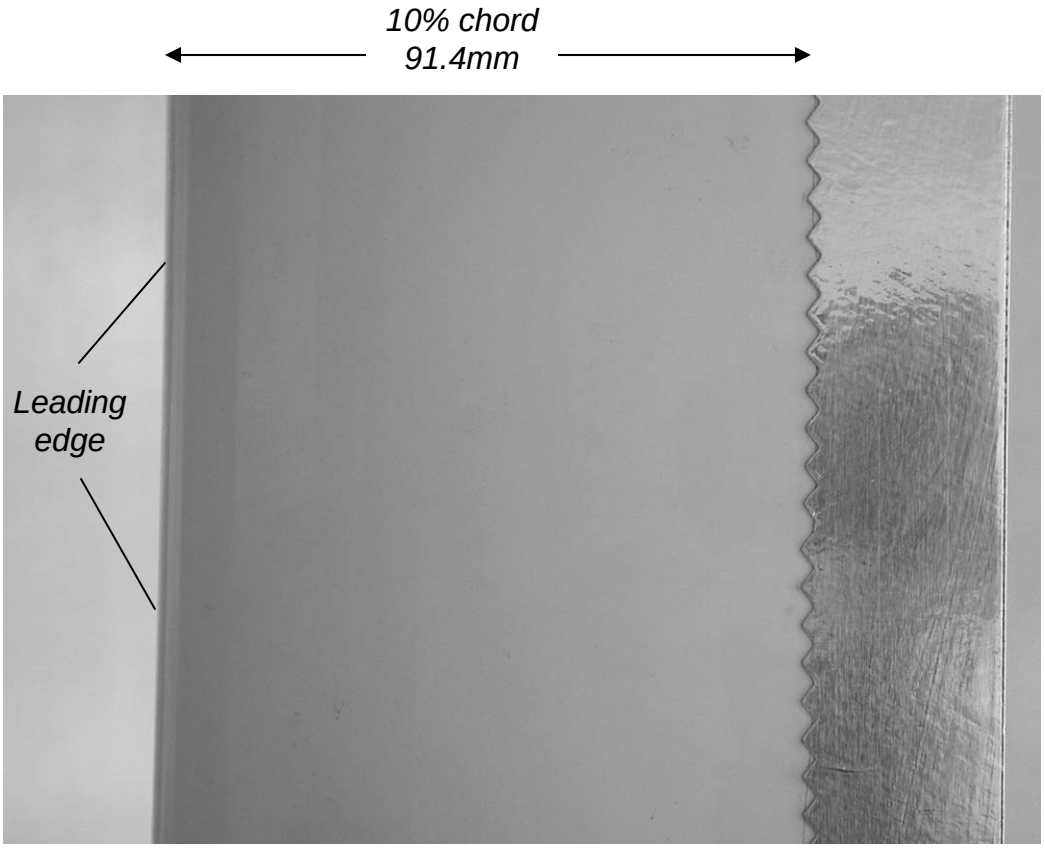

Figure 2-26. *Photograph of part of the leading edge showing the boundary layer trip and its placement.*

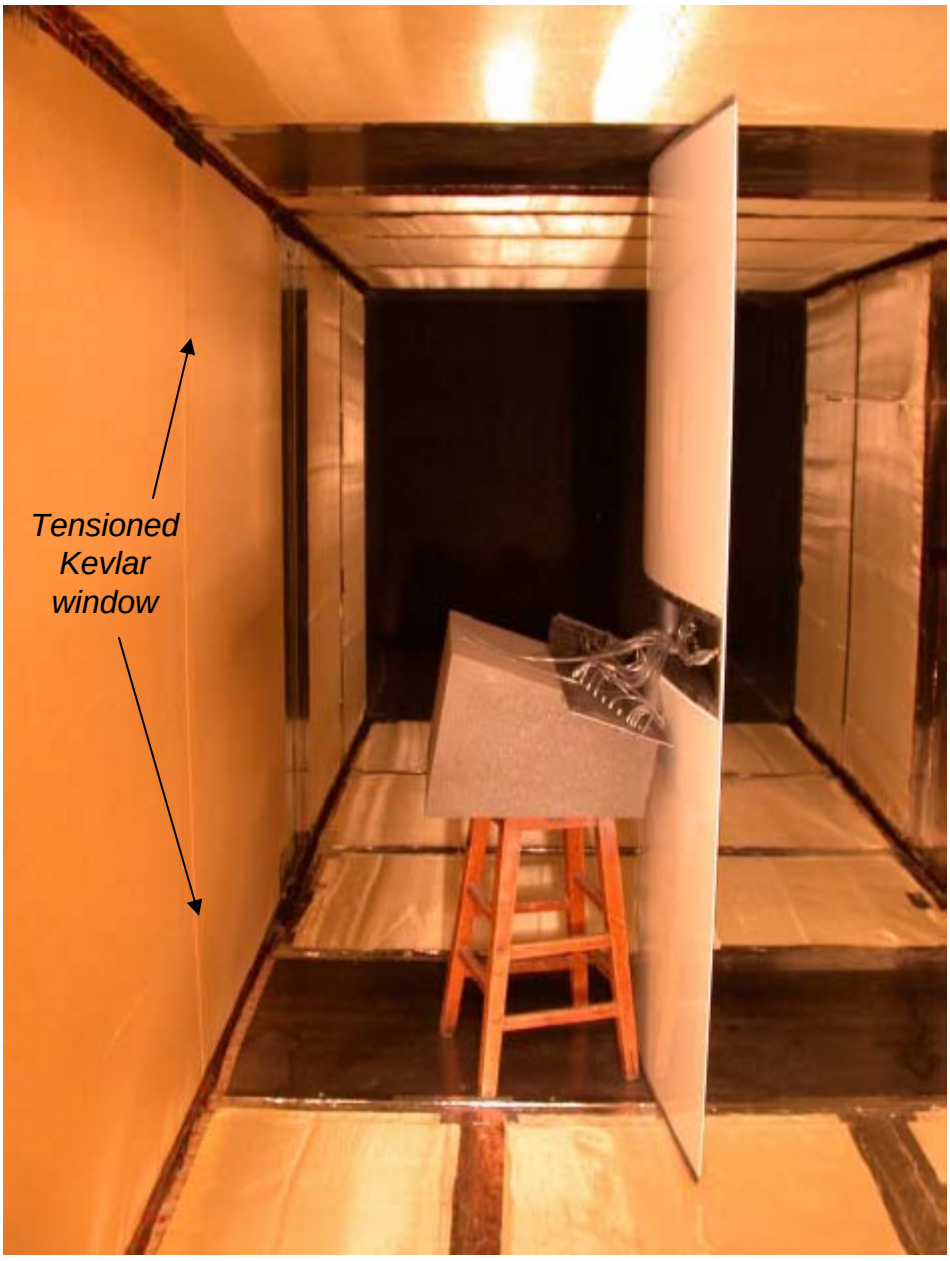

Figure 2-27. *Photograph showing the NACA 0012 model mounted in the test section, with the access hatch open. View from downstream.*

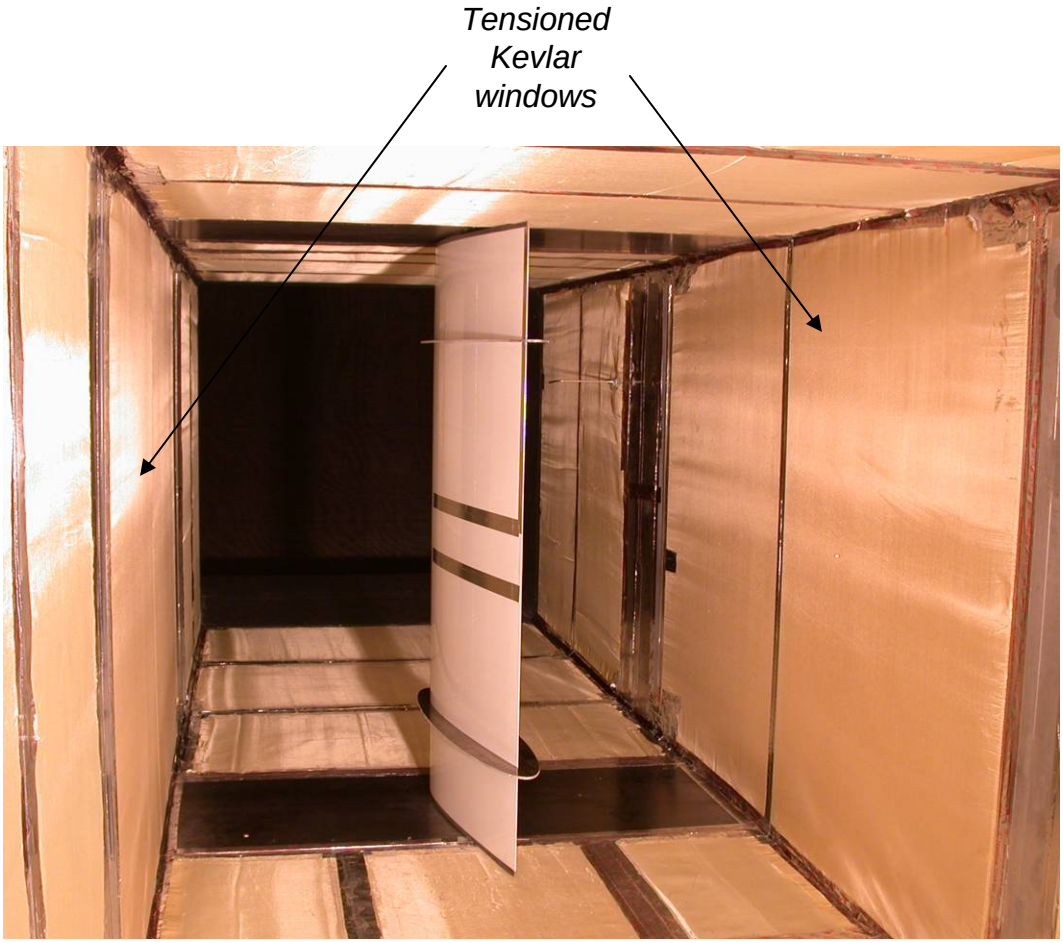

Figure 2-28. *Photograph showing the NACA 0012 model mounted in the test section, with the boundary layer fences installed. View from downstream.*

Figure 2-29. *Photograph showing the NACA 0012 model mounted in the test section, with in-section traverse gear in the foreground. View from downstream.*

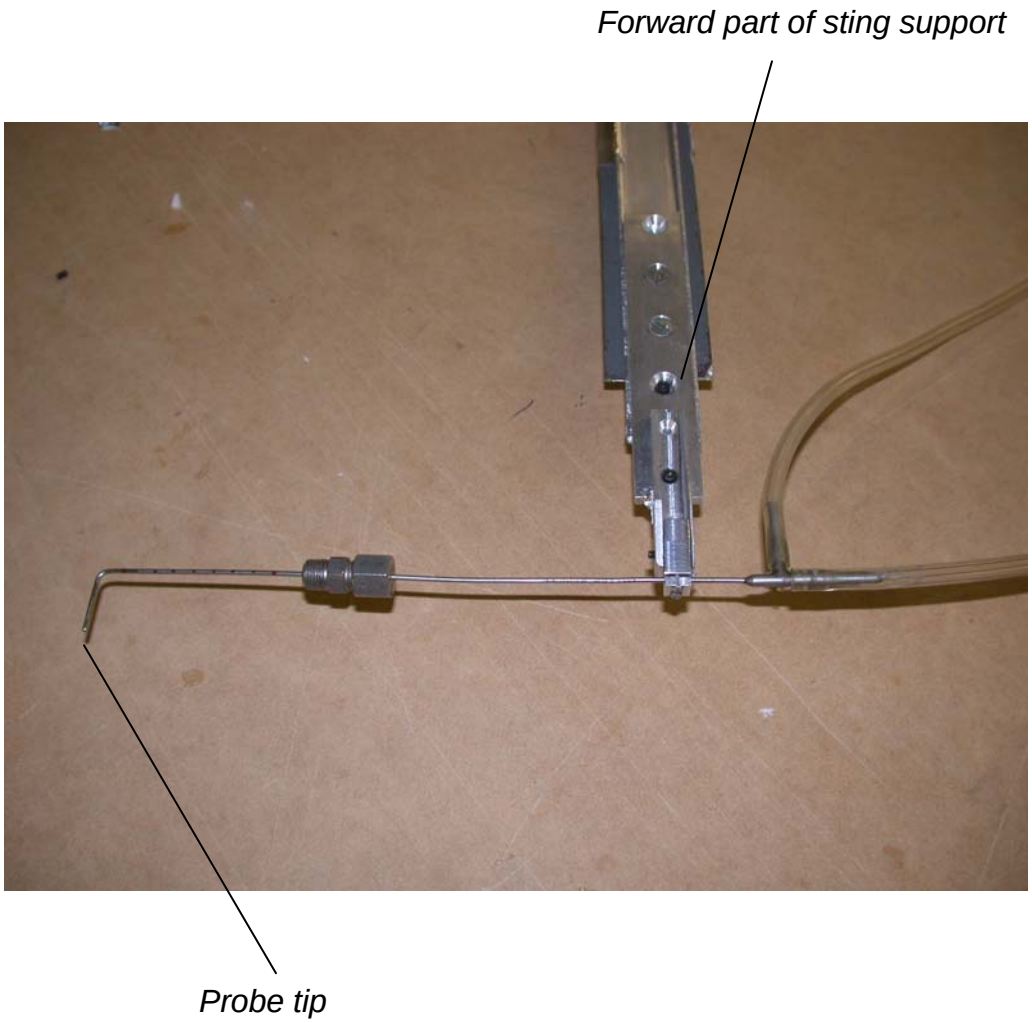

Figure 2-30. *Pitot-static probe used for test section wall boundary layer measurements*

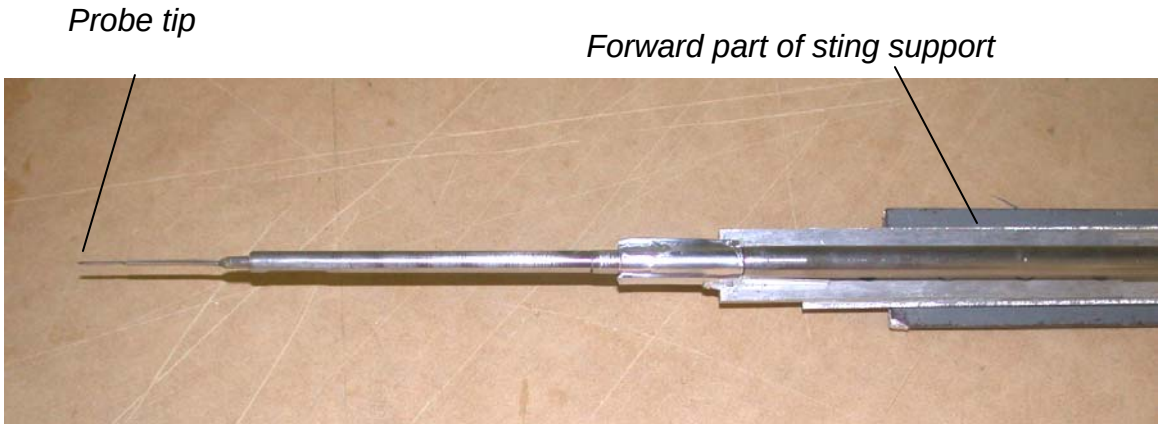

Photograph showing the probe and mount

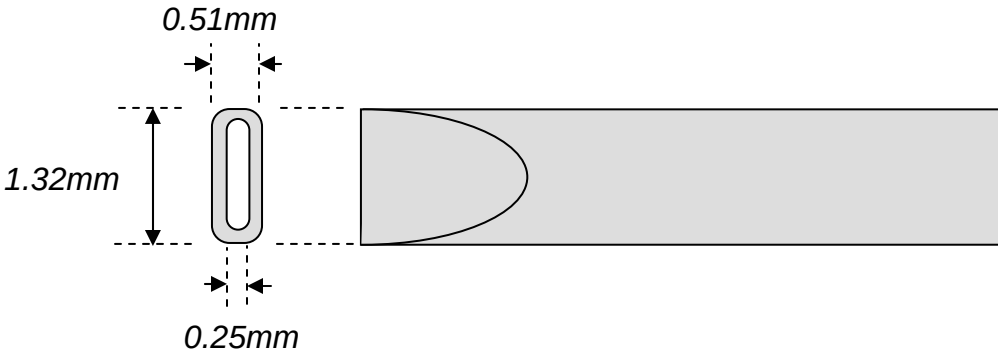

Detail of the probe tip

Figure 2-31. *Pitot-static probe and support used for airfoil trailing edge boundary layer and airfoil wake measurements*

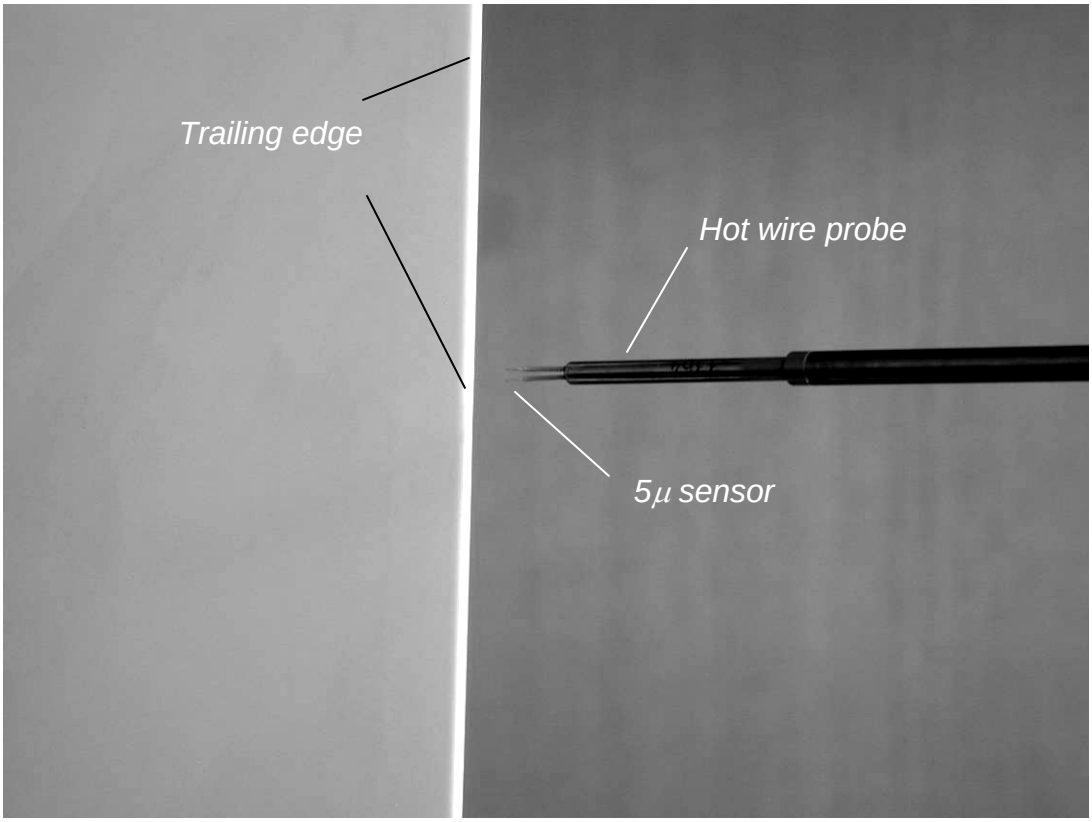

Figure 2-32. *Photograph showing the TSI 1210T1.5 hot wire probe adjacent to the trailing edge of the NACA 0012 model.*

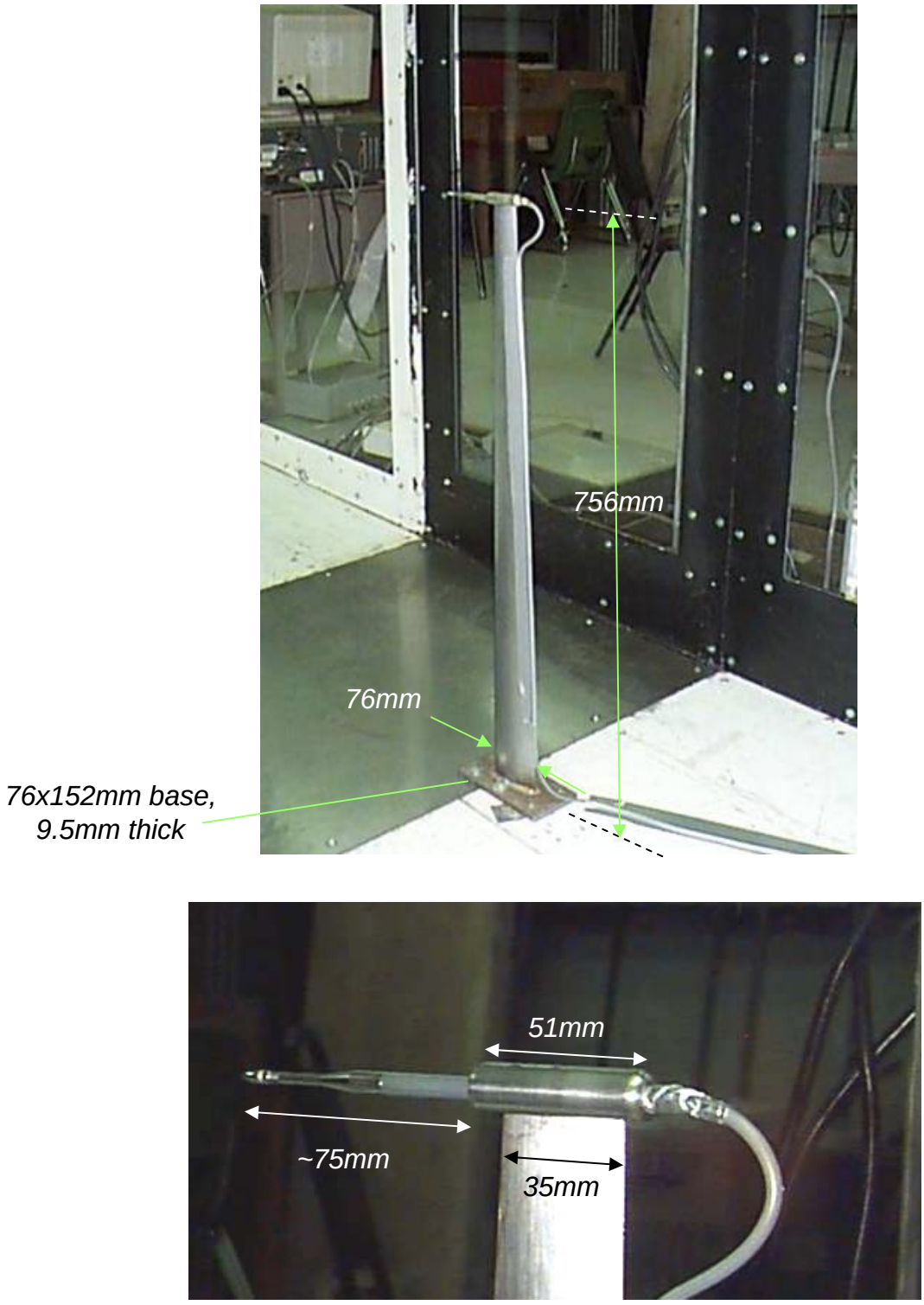

Figure 2-33. *Photographs showing the in-flow microphone support with the B&K 1/8th inch microphone mounted inside the test section in the hardwall configuration. Note that the microphone cable was not taped to the strut trailing edge for measurements presented here.*

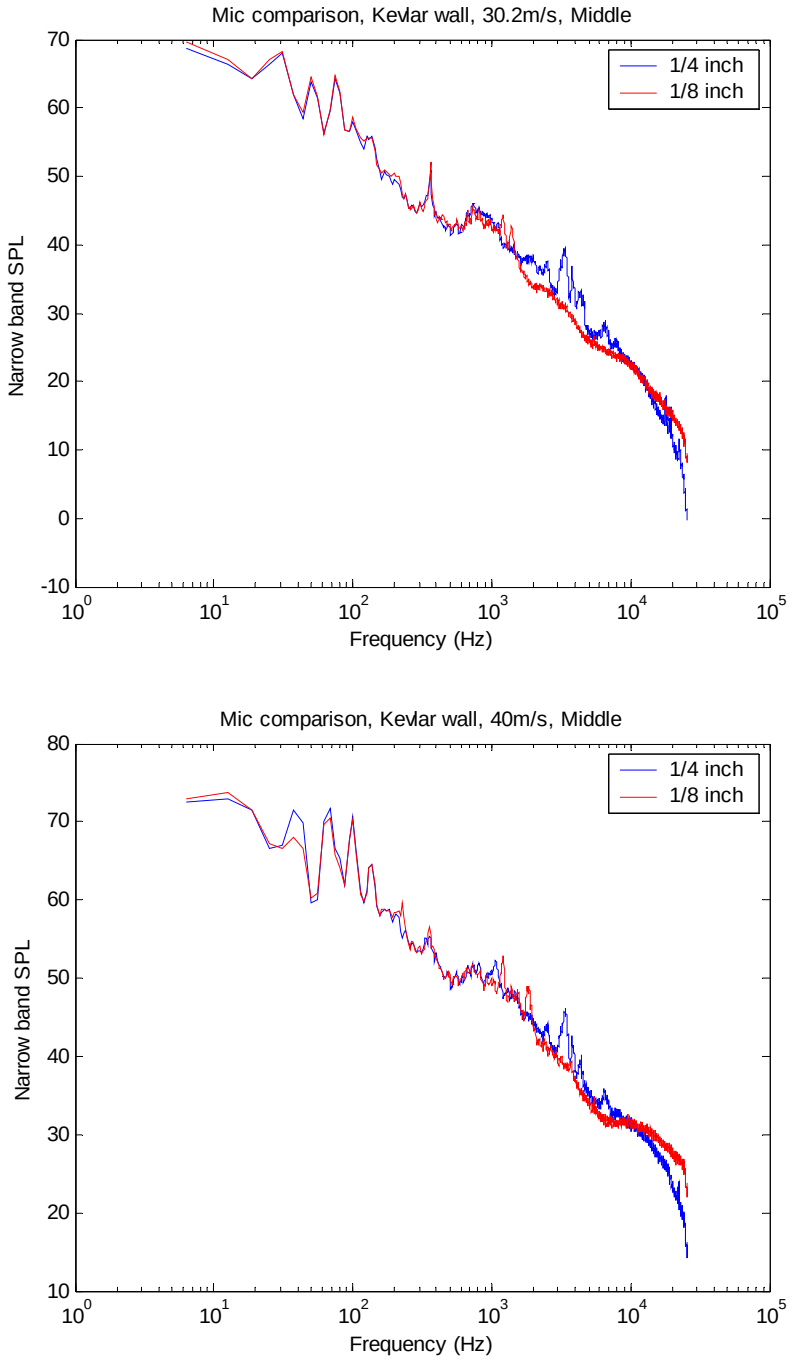

Figure 2-34. *Comparison of 1-Hz bandwidth spectra sound measured under identical conditions with the B&K 1/8th and ¼ inch microphones mounted inside the test section in the Kevlar wall configuration.*

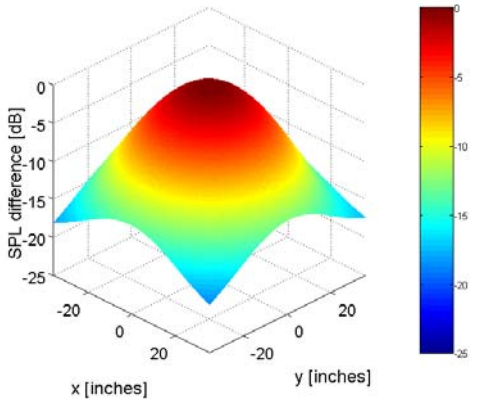

(a) Logarithmic spiral.

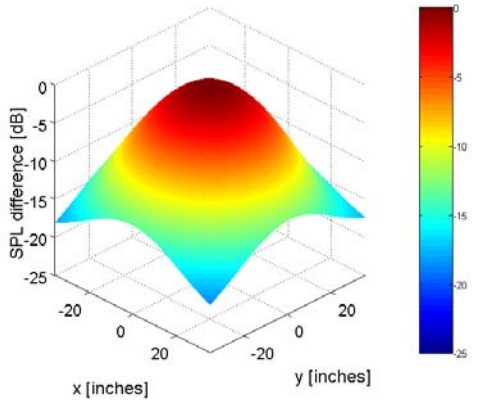

(b) Equal-arc-length.

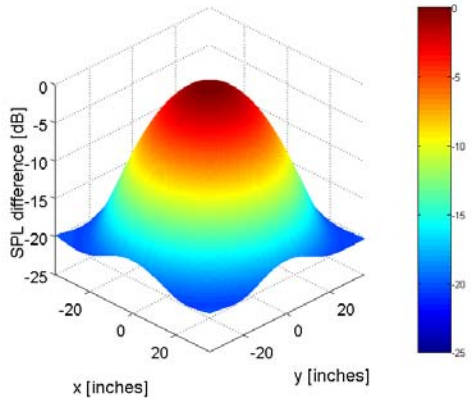

(c) Equal-aperture-area.

Figure 2-35. *Point Spread Function for the three array designs at 500 Hz.*

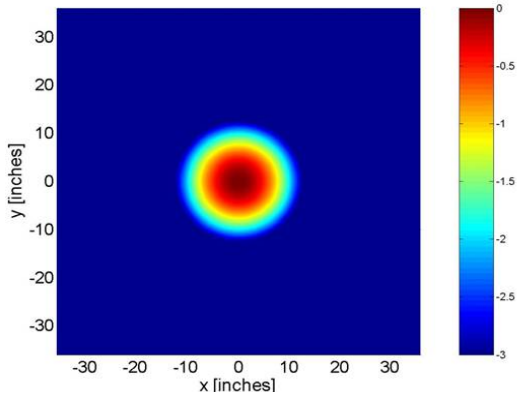

(a) Logarithmic spiral.

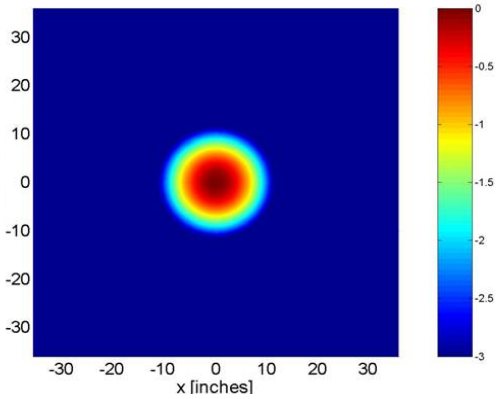

(b) Equal-arc-length.

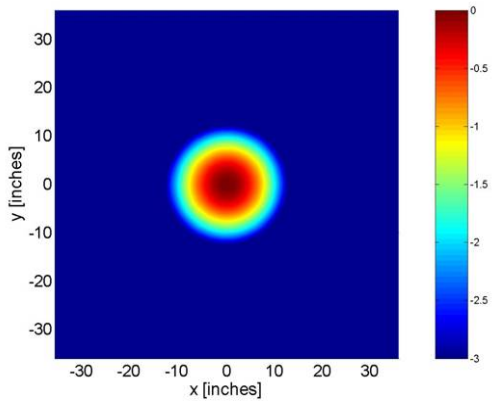

(c) Equal-aperture-area.

Figure 2-36. *Spot size for the three candidate array configurations at 500 Hz.*

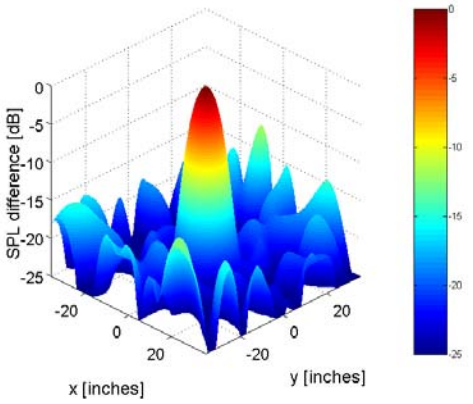

(a) Logarithmic spiral.

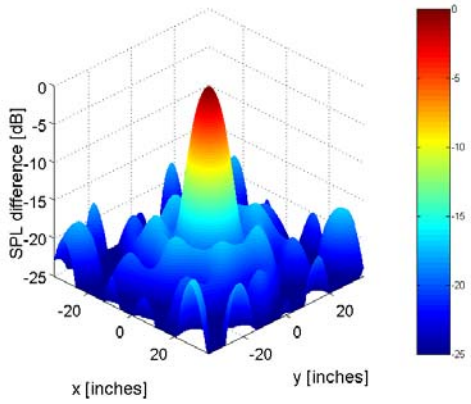

(b) Equal-arc-length.

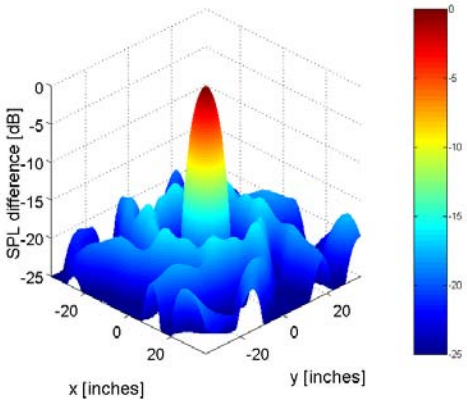

(c) Equal-aperture-area.

Figure 2-37. *Point Spread Function for the three array designs at 2000 Hz.*

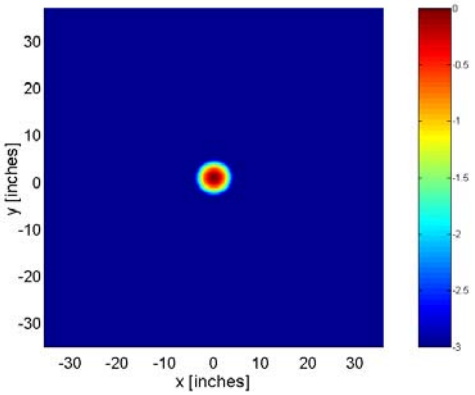

(a) Logarithmic spiral.

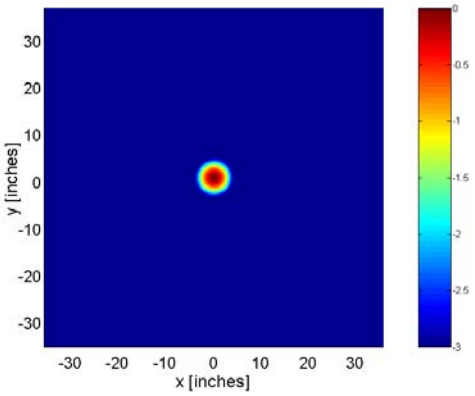

(b) Equal-arc-length.

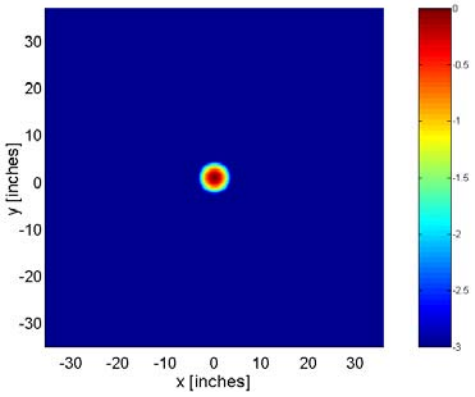

(c) Equal-aperture-area.

Figure 2-38. *Spot size for the three candidate array configurations at 2000 Hz.*

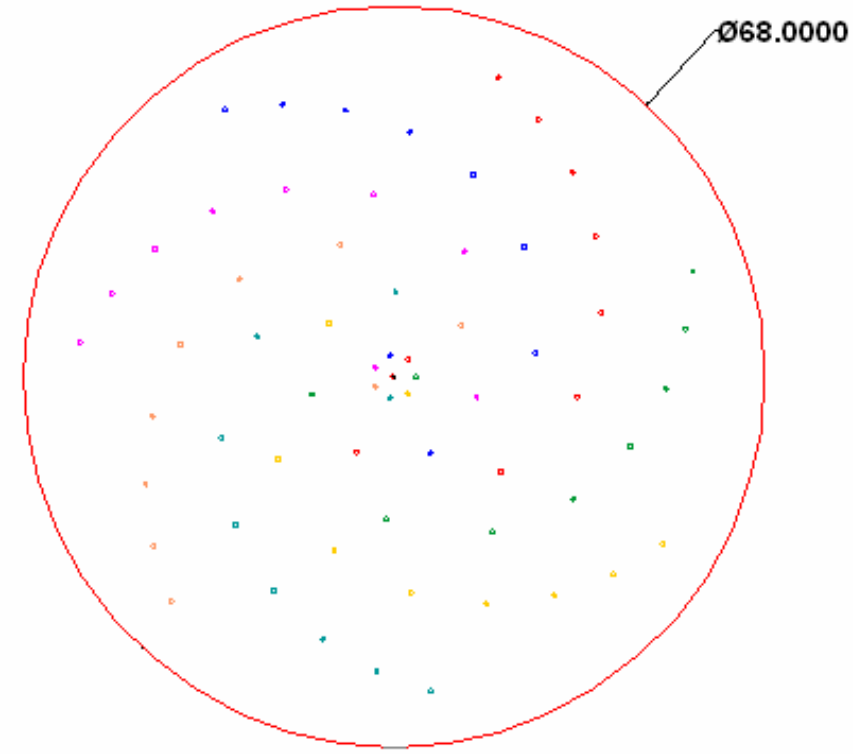

Figure 2-39. *Final array design.*

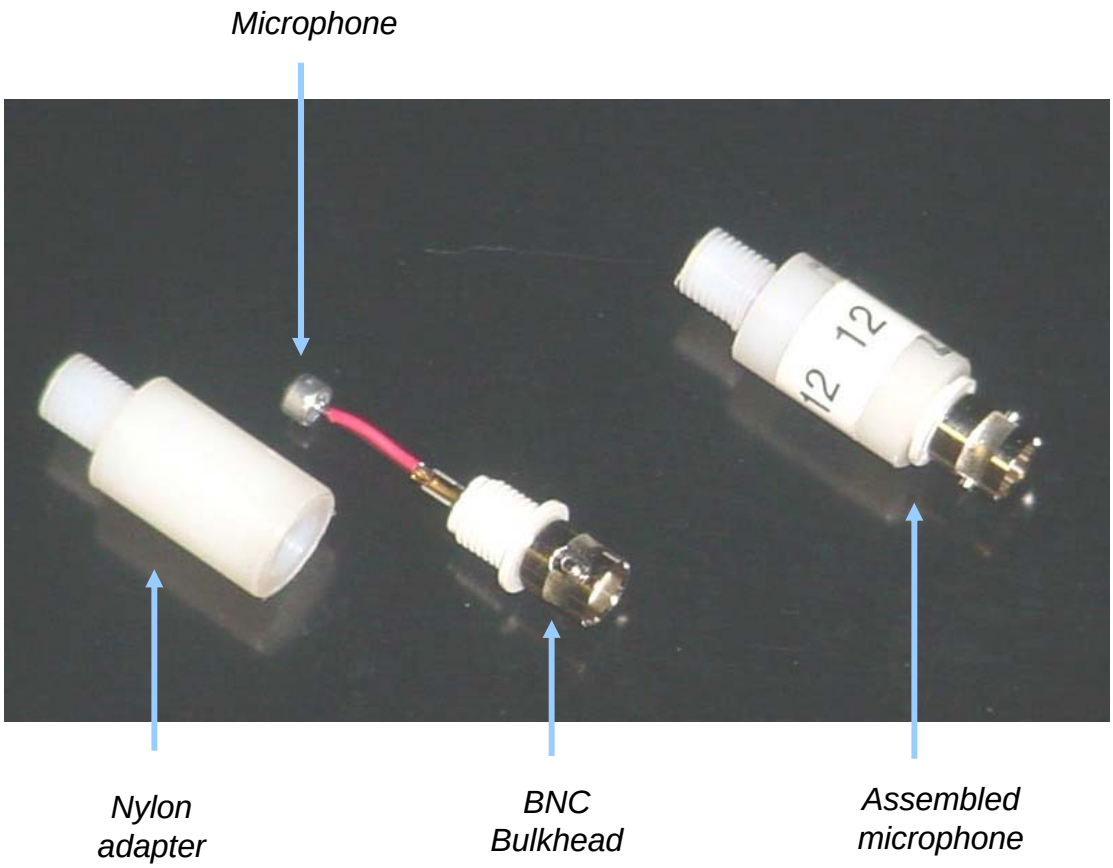

Figure 2-40. *Detail of the microphones used on the phased array..*

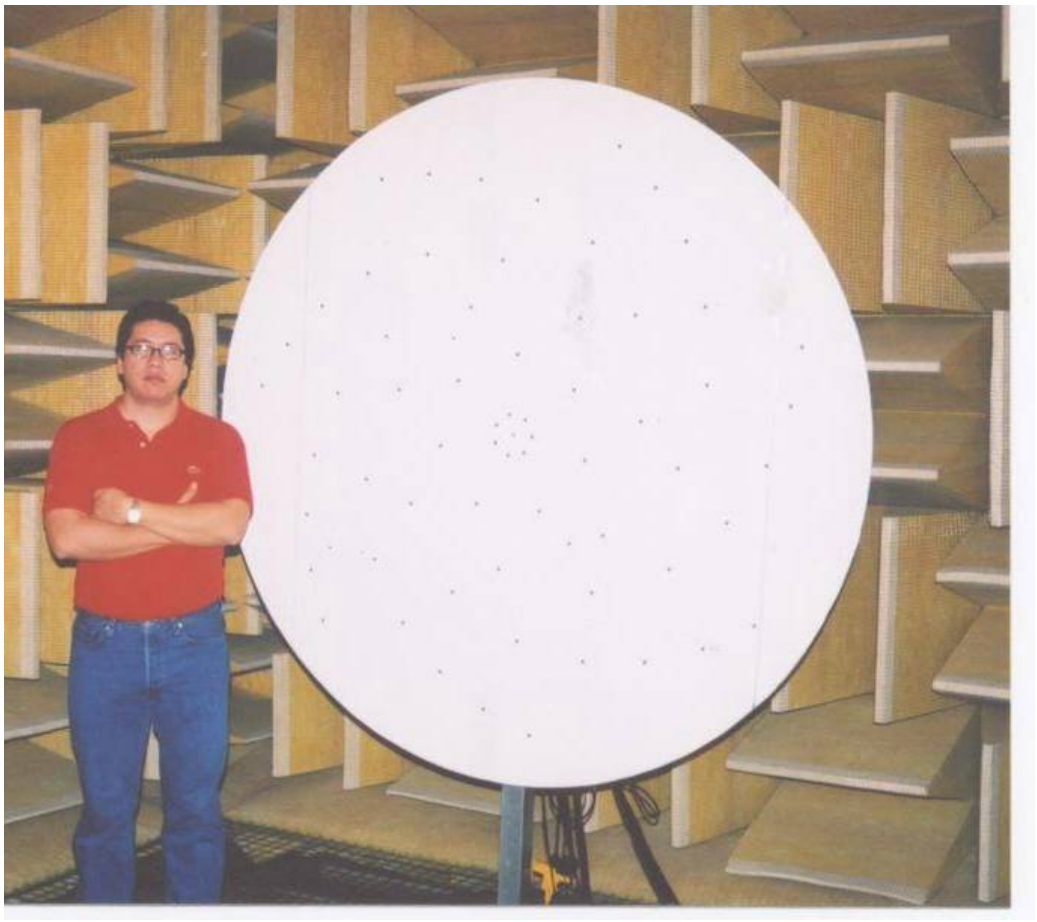

Figure 2-41. *Completed 63-microphone phased array.*

3. RESULTS AND DISCUSSION - EMPTY TEST SECTION

Measurements in the empty test section were made over a range of conditions primarily to compare the acoustic properties of the three different test section configurations, to assess the aerodynamic and acoustic performance of the Kevlar acoustic windows, and to demonstrate the capabilities of the 63-microphone phased array system.

3.1 In-flow noise levels

One of the simplest metrics of the acoustic environment is the in-flow noise measured using a single microphone. The 1/8th and 1/4-inch diameter microphones described in chapter 2 were used for this purpose. The useful test matrix from these measurements is shown in table 3-1. Measurements were made from 10 to 64m/s with each treatment with the microphone located 3.51m downstream of the test section entrance. As shown in figure 3-1 this location, referred to as mid-section, is close to half-way down the length of the test section and just aft of the streamwise center of the Kevlar windows. Measurements in this position in the hard-wall configuration are listed as cases 14 to 19 in table 3-1. Measurements in this position with the acoustic treatment with Whispertone walls are cases 21 to 27. Those with Kevlar walls are cases 28-45. Included in this latter set are 5 tests performed with minor modifications to the test section configuration (cases 32 to 36). These modifications, listed in table 3-2, include such things as removal of the diffuser vortex generators, and taping closed the pressure equalizing door in the diffuser. In addition to these, measurements were also made with

the hard wall to examine the streamwise variation in the sound field. These measurements were made 1.83m downstream of the test section entrance (the ‘upstream location’, cases 1-6) and 5.18m downstream of the entrance (the ‘downstream location’, cases 7 to 13), locations also illustrated in figure 3-1.

For each case, table 3-1 lists the overall sound pressure level relative to 20μPa (OSPL) and the overall A-weighted sound pressure level (OASPL) relative to the same reference. The table also lists the various conditions of each test, including flow speed through the test section and fan RPM. Plotting these two parameters against each other, as has been done in figure 3-2 provides some insight into the effects of the acoustic treatments on overall tunnel operation and thus some useful background to the noise results. This plot shows, not surprisingly, a very closely linear relationship between fan RPM and flow speed. In the hard-wall configuration the flow gains about 13m/s for every 100RPM of fan rotation rate. Current operational procedures (though not necessarily physical limitations of the system) dictate that the fan be run no faster than 600RPM, implying a top speed of 78m/s. These procedures are currently being reviewed. Installing the acoustic treatment with Kevlar flow surfaces into the test section has almost no effect on the overall RPM/speed relationship, suggesting that the acoustic treatment added no significant drag to the test section in this case. This is entirely consistent with the observed behavior of the Kevlar surfaces covering the acoustic absorbers and the Kevlar acoustic windows. Both sets of Kevlar surfaces remained extremely stable throughout the speed range. There was no significant mean deflection or flapping of these surfaces (detailed information on the acoustic window vibration is given in section 3.3). This was particularly surprising for the Kevlar covering of the acoustic absorbers, given the

relatively low tension of these covers and the crude way in which the tension was applied. With the Whispertone flow surfaces installed the efficiency of the facility drops slightly, the RPM needed to generate a given flow speed on average a few percent higher in this case. We believe that this was simply the a result of the thickness of the Whispertone board which created 25mm steps at the leading and trailing edges of the test section and the acoustic windows. While these steps were faired it seems likely that they fractionally increased the overall drag of the test section walls. The Kevlar acoustic windows appeared just as stable when the Whispertone board was used.

3.1.1 Sound spectra and overall noise levels

Figures 3-3 through 3-5 compare sound spectra measured at different flow speeds at the mid-section location (cases 14 to 31 and 42 to 45). Each plot shows results for a different test section configuration. Spectral levels for a 1Hz bandwidth are plotted in terms of sound pressure level relative to 20μPa vs. frequency in Hz. Figures 3-6 to 3-11 show the same data replotted to compare sound spectra measured with the different configurations for each of the flow speeds.

Consider first the spectra measured in the original hard-wall configuration (figure 3-3), which show a number of distinct features and regions. At the very lowest frequencies (0 to 20Hz) relatively high spectral levels are seen that increase in amplitude with flow speed but remain fixed in frequency. The implied wavelengths (17m and greater) are on the scale of the whole facility. Between 20 and 300Hz show a series of peaks that are become more distinct and increase in frequency as the flow speed is increased. These are likely tones associated with the wind tunnel fan (as will be further

discussed below). At 190Hz all the spectra show a sudden increase in spectral levels (illustrated by the dashed line on the plot), followed by a broadband roll off. We suspect this likely associated with resonances across the tunnel test section. Super-imposed on the broadband is a rooster-tail peak that increases in frequency with flow speed, from about 700Hz at 11m/s to 3kHz at 64m/s.

The upward shift of the spectra in figure 3-3 with flow speed is reflected in the overall sound pressure levels plotted in figures 3-13 and 3-14. OSPL increases from 88.1dB at 11m/s 115.0dB at 64m/s. The increase is greater in the A-weighted levels (from 67 to 109.4dB) because these are biased to spectral levels around 1kHz, where the spectra show the most rapid increase with flow speed. Ignoring the data at 11m/s (which may include some residual electrical noise levels and are most susceptible to contamination by ambient noise from outside the tunnel), the variations with flow speed are almost linear on the log scales of these graphs, implying a $U^{5.0}$ variation for the OSPL and a $U^{6.0}$ variation for the OASPL.

Both the Kevlar or Whispertone acoustic treatments substantially reduce noise levels in the test section across the spectrum at all speeds (figures 3-6 through 3-12). The reduction is greatest, about 16dB, between 500 and 1000Hz, and somewhat less at lower and higher frequencies. The spectra measured with the acoustic treatments show all the same features as those measured with the hard wall (compare figures 3-4 and 3-5), with the exception of the sudden rise in spectral levels at 190Hz. We suspect this feature associated with acoustic resonances across the test section which would be greatly reduced or eliminated by the acoustic treatments. Spectra measured with the Kevlar treatment at speeds of 35m/s and at 49m/s and greater (figures 3-4 and 3-9 to 3-12) do not

appear to show the distinct tones at low frequency attributed to the fan, but this is only because this particular set of spectra were measured at lower resolution (50Hz), insufficient to resolve these features.

Spectral levels measured with the Kevlar and Whispertone flow surfaces are very similar, but not identical. For speeds of 11, 20 and 30m/s (figures 3-6 to 3-8), where identical instrumentation was used to make measurements with the two treatments, spectral levels with the Kevlar flow surface appear slightly (1-3dB) below those measured with the Whispertone at most frequencies. The situation appears to reverse for speeds of 35m/s and above (figures 3-9 to 3-12) with the Whispertone flow surface appearing slightly quieter. However, for these speeds the Kevlar-wall measurements were made using the ¼-inch microphone which is believed to have been more susceptible to wind noise generated by the nose cone. It therefore seems plausible that measurements under identical conditions would have shown the slight advantage of the Kevlar persisting to higher speeds. In that case this advantage may simply be explained by differences in fan speeds needed to achieve the same flow with the two acoustic treatments (figure 3-2). In other words, if the Whispertone board had been mounted flush with the test section wall (rather than on top of it so as to create a step) it is quite possible that its performance would be identical to that of the Kevlar.

Overall sound pressure levels with the treatments are plotted alongside the hardwall data in figures 3-13 and 3-14. OSPL and OASPL levels are between 8 and 15dB lower than those in the hard-wall configuration. At higher speeds (>30m/s) noise reductions are all more than 10dB, by both measures. Again ignoring the 11 m/s data the variations with flow speed are almost linear but the slopes are different than in the hard-

wall configuration. With the Kevlar treatment OSPL and OASPL increase as $U^{4.7}$ and $U^{6.5}$, respectively, whereas for the Whispertone these variations are $U^{4.3}$ and $U^{6.5}$, respectively.

The effects of various minor modifications to the tunnel configuration to the in-flow noise spectrum measured mid-section with the Kevlar treatment are illustrated in figure 3-15. The effects of all the modifications are small if not negligible and appear, if anything, to slightly increase noise level. The largest increase (of 1 to 2dB) was produced by removing the vortex generators at the entrance to the diffuser, and this is likely because of the slightly higher fan RPM needed to maintain the flow speed in this case (see table 3-1). (Removing the generators likely makes the diffuser less efficient, necessitating this increase in fan power). It is interesting that removing the generators has its greatest effect on the noise peak at 30Hz, which is close to the blade-passing frequency of the 8-bladed fan in this case. This may indicate that flow non-uniformity into the fan is a significant noise source since this would likely be increased by the removal of the vortex generators.

The variation in noise levels with streamwise position in the test section for the hard-wall configuration is illustrated for the range of flow speeds in figures 3-16 to 3-21. (The streamwise positions at which these measurements were made are illustrated in figure 3-1.) The noise spectra are almost independent of streamwise location at higher speeds. At lower speeds (11 and 20m/s) there is a slight increase in the tones associated with the fan as the downstream end of the test section is approached, resulting in a 2 to 3dB increase on OSPL, but almost no change on OASPL (see table 3-1).

3.1.2 Spectral scaling

In this section we examine the scaling, with speed, of the noise spectra in figures 3-3 to 3-6 measured at the middle of the test section in its hard-wall and acoustically treated configurations. Figures 3-22, 23 and 24, show these spectra plotted against frequency normalized on the fan rotation rate f_f = RPM/60. As discussed in chapter 2, we would expect signals at harmonics the blade passing frequencies of the fan ($8f_f$) . For all three wall conditions the spectra show low frequency peaks at all speeds at, or close to this frequency. They also show peaks that scale with the fan speed at frequencies of around 12, 18 and 25 times f_f . While there is little doubt that these are fan related these are not exactly harmonics of the blade passing frequency. All the spectra also show peaks between 250 to 350 times f_f which is of the same order as (but not equal to) the expected stator rotor interaction frequency.

Overall, scaling the frequency on fan rotation rate lines up almost all the spectral features, with the exception of the very low-frequency modes and the sudden jump in spectral levels seen at 190Hz in the hard-wall configuration. It is therefore tempting to try to also scale the spectral levels. Figures 3-25 to 3-30 show attempts to scale the spectral level on the 4^{th} and 5^{th} powers of the flow velocity. Note that scaling on the 4^{th} or 5^{th} powers of the fan tip speed would produce almost identical results because of the closely linear relationship between the two shown in figure 3-2. These plots exclude the 11m/s spectra since the additional noise in this low speed data obscures the other spectra when they are scaled in this way.

Spectra measured with the hard-wall configuration (figures 3-25 and 3-28) scale closely to the same curve at frequencies over $60f_f$ when normalized on the 4^{th} power of

the velocity. In particular, the broadband region of elevated spectral levels that follows the sudden rise at 190Hz seen with the hard-wall configuration collapses almost perfectly under this scaling. In contrast the sound spectra measured with the either acoustic treatment, which don't have the 190Hz feature, also don't scale in this way (figures 3-26 and 3-27). Instead these appear to scale best when normalized on the 5^{th} power of the velocity, at least for frequencies above $20f_f$ (figures 3-29 and 3-30). The different scaling behavior suggests that different sources dominate noise spectra measured with the acoustic treatments. Indeed, we believe that the broadband component of the hard-wall noise spectra are dominated by test section resonances, whereas that part of the Kevlar or Whispertone spectra gives every indication of being dominated by broadband fan noise.

3.1.3 Comparison with the results of earlier studies and other facilities

Measurements from the present study can be compared with those performed previously by Larssen and Devenport (1999) and Mish (2003). Both of these prior studies made in-flow noise measurements using the same $1/8^{th}$ inch microphone system and stand employed in the present investigation, but both used the manufacturers calibration for the microphone sensitivity (0.905 mV/Pa), as opposed to the measured sensitivity (0.610 mV/Pa) used here, which is believed more accurate. Sound pressure levels presented by Larssen and Devenport (1999) and Mish (2003) must be increased by 3.4dB to account for this difference. With this correction the measurements of Larssen and Devenport (1999) for the hard-wall case agree with the present results to within 1dB at most frequencies, see figure 3-31. The only significant difference is that this earlier data set does not show the rooster-tail feature around 1kHz, which may be a useful clue as to

its source. Accounting for the calibration change, OSPL and SPL levels reported by Devenport and Larssen fall within 1 or 2 dB of present measurements, with the latter generally being higher, perhaps because of the rooster tail feature.

Figure 3-31 also compares noise levels for the current acoustic treatments (using the acoustic windows and Mish's (2003) acoustic absorbers with Kevlar and Whispertone flow surfaces) with noise levels for the treatment employed by Mish (no acoustic windows, acoustic absorbers in all panels with perforated steel flow surface). Mish's results show that his acoustic treatment substantially attenuated sound levels at frequencies below 500Hz, but increased them by up to about 8dB at higher frequencies. Indeed eliminating this increase, which was believed to be due to scrubbing noise, was one reason for testing the Kevlar and Whispertone flow surfaces used in the present study. However, Mish's spectrum appears so different from those measured in the present study that we suspect that instrumentation problems may have been a factor (specifically subsequent findings suggest that the microphone diaphragm may have been damaged). As such it may be worth revisiting perforated steel sheet as a quiet flow surface.

Figure 3-32 shows overall A-weighted noise levels with the three different test section configurations compared with levels reported for other aeroacoustic wind tunnel facilities by Duell *et al.* (2002). In either of the acoustically treated configurations the Stability Wind Tunnel lies close to the main band with noise levels comparable to the NASA Glenn (Lewis) 9×15 wind tunnel. In interpreting figure 3-32 it is worth remembering that it shows the effects of only preliminary treatment the Stability Wind Tunnel test section. The other facilities shown on this figure presumably have acoustic treatment on the fan or in other parts of the circuit. Treating the Stability Tunnel in this

way, and finalizing the test section treatment, are likely to result in further noise reductions.

3.2 Boundary layers on the test section wall

The Pitot static probe described in chapter 2 was used to measure boundary layer profiles just below the mid height of the port-side test section wall (see figure 3-1). Measurements were made at locations 2.29 and 4.87m downstream of the leading edge of the test section entrance, these being near the leading location and just upstream of the trailing edge location of the Kevlar acoustic window when installed. The original intent was to make a complete set of boundary layer measurements at both locations covering the full speed range and for all 3 sets of acoustic treatment. However, due to instrumentation and traverse problems only a curtailed set of data for the hard wall test section configuration could be obtained. Fortunately, during the later NACA 0012 airfoil tests (which were performed with the Kevlar acoustic treatment), it was possible to make boundary layer measurements at the aft location, with the airfoil at zero angle of attack. It seems likely that the test section boundary layer properties would have been almost the same as those in the empty test section in this case so we present them here, together with the hard-wall empty section data, to show the effects of the acoustic windows on the wind tunnel boundary layer.

Table 3-3 shows the locations and conditions at which boundary layer profiles were measured. Measurements were made at the forward station in the hard-wall configuration for nominal flow velocities of 20, 40 and 60m/s. Measurements were made at the aft station in the hard-wall configuration and with the Kevlar acoustic treatment for

these same speeds. Boundary layer mean velocity profiles for these cases are shown in figures 3-33 to 3-35. Boundary layer parameters (thickness, displacement thickness, and momentum thickness) are listed in table 3-3.

In the hard-wall configuration (figures 3-33 and 3-34) the profiles measured at both stations have typical turbulent forms. The boundary layer thickness is 55 to 60mm at the forward station and increases to about 80mm at the aft station. The displacement thickness grows from around 8mm to 11 mm over the same distance. Note that in case 6 (table 3-3 and figure 3-34) the *y*-origin of the profile was not recorded and had to be assumed by comparison with the lower speed profiles. With the Kevlar acoustic treatment and acoustic window in place (figure 3-35) the boundary layer grows to around 110 mm in thickness at the aft station, and there is roughly a doubling of the displacement thickness. The additional boundary layer thickness is presumably a consequence of the increased wall roughness (including the gaps between acoustic absorbers and step at the leading edge of the Kevlar window) and some transpiration through the window itself. Interestingly, the boundary layer profile becomes less full as the flow speed is increased with the acoustic treatment (figure 3-35), the opposite of the normal trend. We are unsure why this is so, but believe it may be connected with the behavior of the pressure difference across the window with speed and the resulting magnitude of this transpiration. This issue of flow through the window will be discussed in more depth in chapter 4.

3.3 Performance of the Kevlar acoustic windows

As discussed above, the Kevlar acoustic windows appeared stable over the entire speed range of the tests. However, we were nevertheless concerned that the slight vibration of the Kevlar panels observed (~1-2mm amplitude) might be a source of sound or might couple with the ambient noise field in the test section. In order to study this, the following measurements were performed over the full range of tunnel flow speeds with the Kevlar acoustic treatment in place. The laser vibrometer described in chapter 2 was used to measure the vibration of the center of the starboard-side Kevlar window. Simultaneously, the acoustic pressure inside the test section with an in-flow microphone installed at the mid-section location was measured (figure 3-1). The coherence between the two was then computed. An example result is shown in figure 3-36 for a flow speed of 58m/s. No significant coherence between the Kevlar window vibration and the sound field inside the test section was observed at any speed, confirming that the vibration of the Kevlar does not contribute to or interact with the background noise.

3.4 Phased array measurements

In order to evaluate the effectiveness of making phased array measurements through the acoustic windows the following preliminary test was conducted for the Kevlar treatment. A 12.7-mm diameter pipe, 0.61m long was introduced through the bottom center of the test section at a point near the streamwise center of the Kevlar window. On the lower end of the pipe, outside the test section, a speaker was mounted and driven by a sinusoidal signal at 10 kHz. This resulted in a monopole source at the tube's end inside the test section. The tunnel was then run at 57 m/s (approximately Mach 0.17) and the phased array, mounted as shown in figure 3-1, was used to locate the

source. Figure 3-37 shows the resulting beamform map at a plane containing the pipe, and compares it with a measurement made as part of an earlier study (Ravetta *et al.*, 2004) for which the same array was mounted flush with the test section walls in the hard-wall configuration. In both figures, the air flow goes from left to right. It can be seen there is a dramatic improvement in the signal-to-noise ratio of the acoustic image with the acoustic treatment. Indeed the acoustic image formed through the Kevlar window is clear enough that it is easy to identify the sidelobes.

A second test was conducted to determine the shifting of the noise sources on the beamform maps due to the mean air flow speed. To this end, the speaker and pipe used to simulate a monopole source were used again. The speaker was driven by a random noise signal and data was acquired at the flow speeds of interest. Since the location and position of the pipe with respect to the phased array was known, the shifting distance was readily obtained from the beamform maps. These results were used to shift the maps for the airfoil experiments.

Case	Test section	Location	Fan RPM	Speed, m/s	Re per meter	Mic. size	OSPL	OASPL
1	Hard-wall	Upstream	95	10.9	670000	1/8"	87.8	69.2
2	Hard-wall	Upstream	176	20.1	1210000	1/8"	90.4	78.9
3	Hard-wall	Upstream	250	30.1	1810000	1/8"	96.9	88.4
4	Hard-wall	Upstream	298	36.3	2170000	1/8"	101.0	93.3
5	Hard-wall	Upstream	421	51.5	3050000	1/8"	109.7	103.2
6	Hard-wall	Upstream	504	62.5	3670000	1/8"	114.1	109.0
7	Hard-wall	Downstream	93	11.0	650000	1/8"	90.6	69.7
8	Hard-wall	Downstream	168	20.2	1200000	1/8"	92.9	78.6
9	Hard-wall	Downstream	245	30.3	1790000	1/8"	97.7	88.4
10	Hard-wall	Downstream	288	36.1	2120000	1/8"	101.7	93.2
11	Hard-wall	Downstream	400	51.2	2990000	1/8"	109.6	103.4
12	Hard-wall	Downstream	480	62.1	3600000	1/8"	113.9	108.5
13	Hard-wall	Downstream	497	64.4	3720000	1/8"	114.7	109.7
14	Hard-wall	Mid-section	89	10.8	680000	1/8"	88.1	67.0
15	Hard-wall	Mid-section	163	19.8	1250000	1/8"	89.4	78.5
16	Hard-wall	Mid-section	240	29.8	1860000	1/8"	97.9	89.4
17	Hard-wall	Mid-section	287	36.1	2240000	1/8"	102.5	94.6
18	Hard-wall	Mid-section	397	51.3	3140000	1/8"	109.8	103.4
19	Hard-wall	Mid-section	475	61.3	3710000	1/8"	113.8	108.5
20	Hard-wall	Mid-section	496	63.8	3830000	1/8"	115.0	109.4
21	Whispertone	Mid-section	88	10.8	680000	1/8"	74.7	52.3
22	Whispertone	Mid-section	164	19.9	1250000	1/8"	81.7	64.2
23	Whispertone	Mid-section	245	29.8	1870000	1/8"	88.1	75.9
24	Whispertone	Mid-section	280	34.3	2150000	1/8"	90.1	79.2
25	Whispertone	Mid-section	394	48.6	3030000	1/8"	98.0	88.9
26	Whispertone	Mid-section	475	58.6	3630000	1/8"	101.4	94.5
27	Whispertone	Mid-section	492	60.3	3730000	1/8"	102.3	95.5
28	Kevlar	Mid-section	85	11.1	670000	1/8"	72.7	53.0
29	Kevlar	Mid-section	155	20.1	1210000	1/8"	75.7	62.1
30	Kevlar	Mid-section	229	30.2	1810000	1/8"	85.1	74.7
31	Kevlar	Mid-section	304	40.2	2400000	1/8"	90.7	82.6
32	Kevlar	Mid-section[1]	234	30.2	1800000	1/8"	85.5	74.7
33	Kevlar	Mid-section[2]	234	30.2	1800000	1/8"	85.3	74.9
34	Kevlar	Mid-section[3]	234	30.2	1800000	1/8"	85.4	74.9
35	Kevlar	Mid-section[4]	234	30.3	1800000	1/8"	85.3	74.8
36	Kevlar	Mid-section[5]	239	30.3	1800000	1/8"	88.6	75.6
37	Kevlar	Mid-section	85	11.1	680000	1/4"	71.7	55.0
38	Kevlar	Mid-section	159	20.1	1220000	1/4"	77.9	64.8
39	Kevlar	Mid-section	235	30.2	1820000	1/4"	85.1	75.8
40	Kevlar	Mid-section	308	39.7	2450000	1/4"	91.1	83.1
41	Kevlar	Mid-section	251	31.6	1990000	1/4"	84.0	76.2
42	Kevlar	Mid-section	280	35.7	2240000	1/4"	87.6	79.6
43	Kevlar	Mid-section	393	49.3	3080000	1/4"	96.0	90.5
44	Kevlar	Mid-section	477	59.9	3720000	1/4"	99.3	96.1
45	Kevlar	Mid-section	492	63.7	3940000	1/4"	100.2	96.8

Table 3-1 *Test matrix for the in-flow microphone measurements (footnotes in table 3-2).*

1. Brackets removed
2. Base of microphone stand taped
3. Pressure equalization door taped shut
4. Open gap in panel section 3 of taped
5. Diffuser vortex generators removed

Table 3-2 *Test section modifications denoted by footnotes in table 3-1.*

Case	Test section	Location	Speed, m/s	Re per meter	δ_{99} (mm)	δ^*(mm)	θ (mm)
1	Hard-wall	Forward (2.59m)	19.8	1240000	57	8.7	6.3
2	Hard-wall	Forward (2.59m)	41.2	2480000	55	7.5	5.6
3	Hard-wall	Forward (2.59m)	60.3	3710000	59	8.3	6.3
4	Hard-wall	Aft (4.87m)	20.0	2170000	73	10.3	7.7
5	Hard-wall	Aft (4.87m)	40.8	1220000	79	11.5	8.8
6	Hard-wall	Aft (4.87m)	60.3	2470000	82[1]	15.0[1]	8.9[1]
7	Kevlar[2]	Aft (4.87m)	20.1	1330000	104	20.6	14.1
8	Kevlar[2]	Aft (4.87m)	39.7	2640000	107	19.7	13.1
9	Kevlar[2]	Aft (4.87m)	53.9	3580000	125	34.1	21.0

[1] Displacement and momentum thicknesses may be inaccurate here due to lack of near wall data.
[2] NACA 0012 model at zero angle of attack mounted in test section

Table 3-3 *Test matrix for the test section boundary layer measurements*.

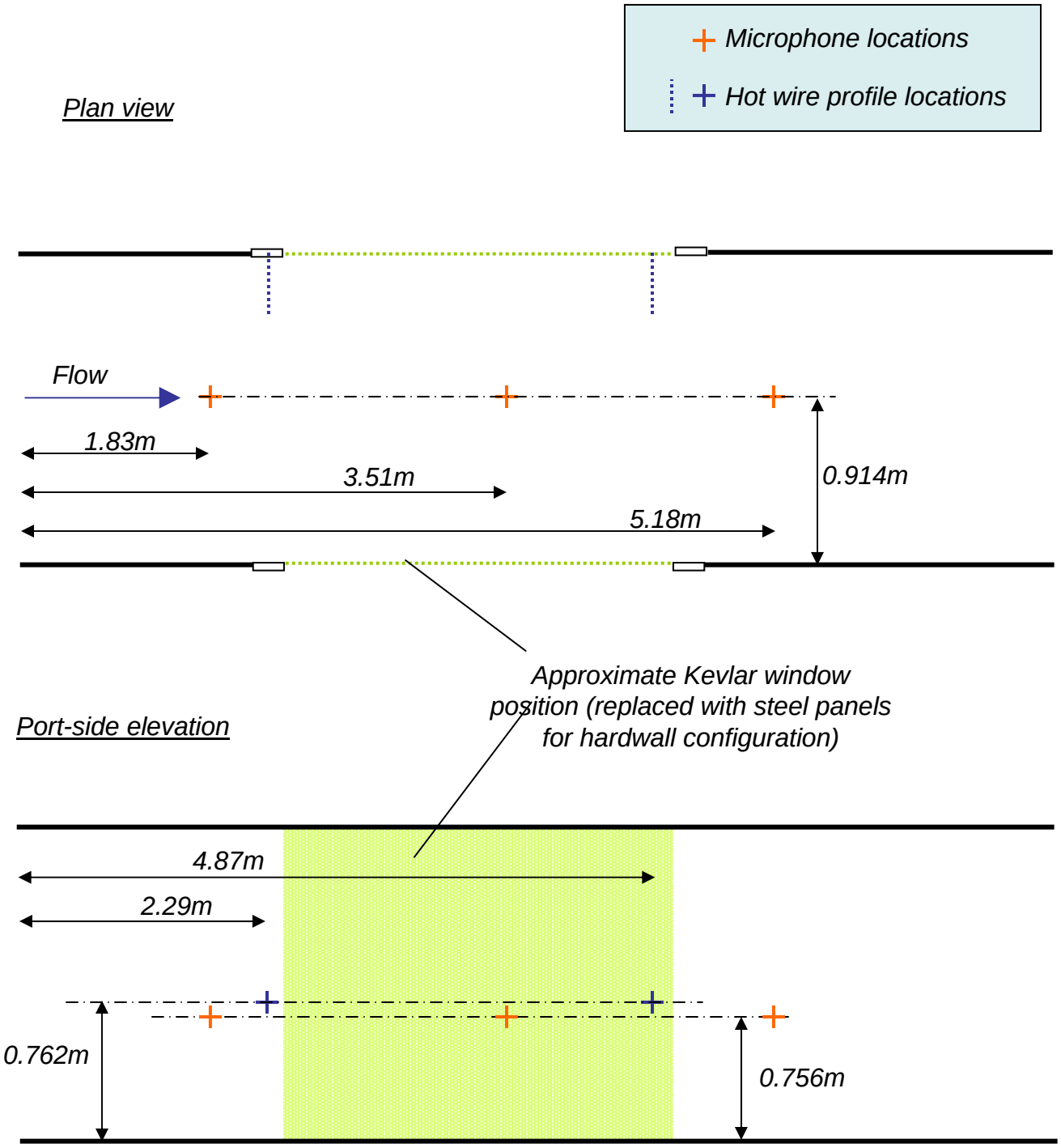

Figure 3-1. *Measurement locations relative to the tunnel test section and Kevlar acoustic windows (when installed).*

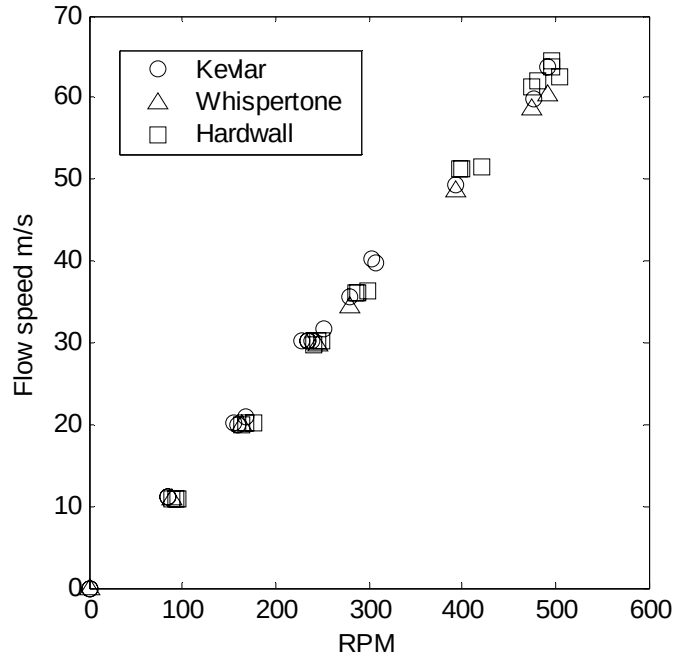

Figure 3-2. *Comparison of 1-Hz bandwidth spectra sound measured under identical conditions with the B&K 1/8th and ¼ inch microphones mounted inside the test section in the Kevlar wall configuration.*

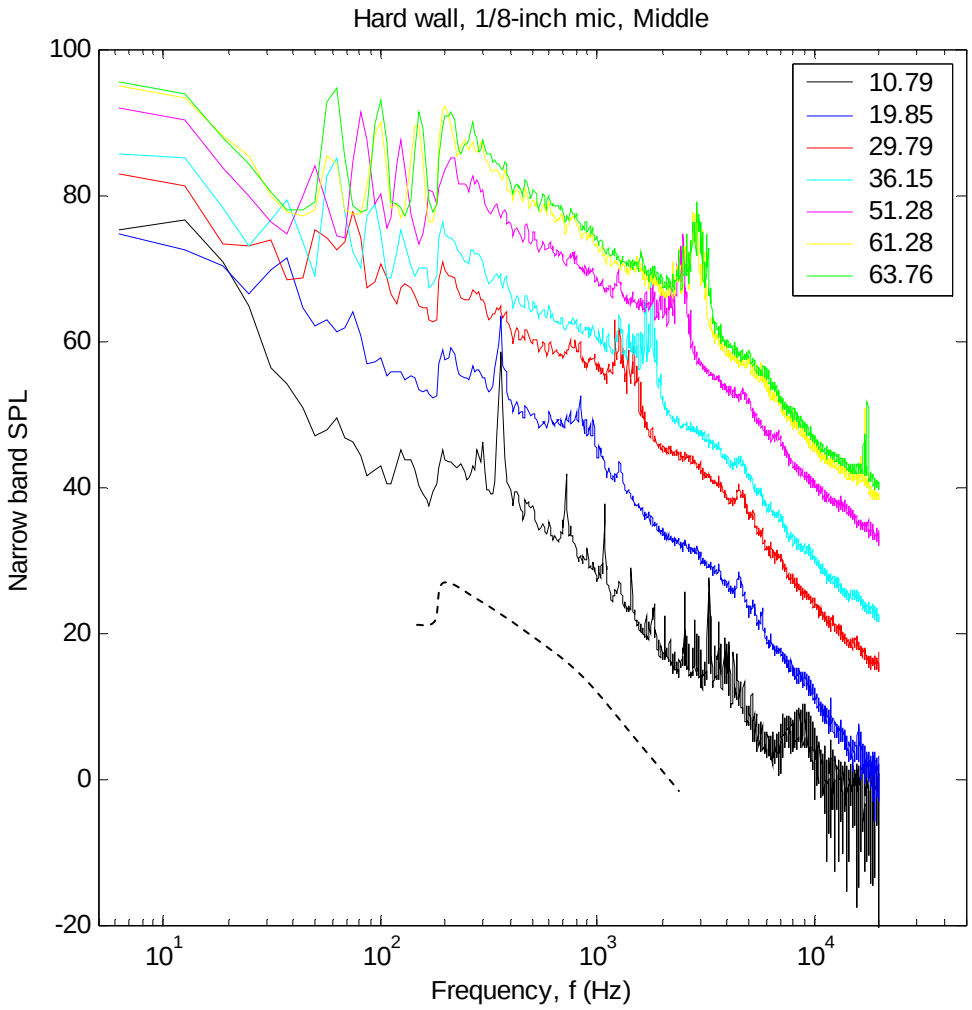

Figure 3-3. *In-flow noise spectra measured at mid-section location with the 1/8th-inch microphone in the hard-wall configuration.. Frequency resolution 6.25Hz*

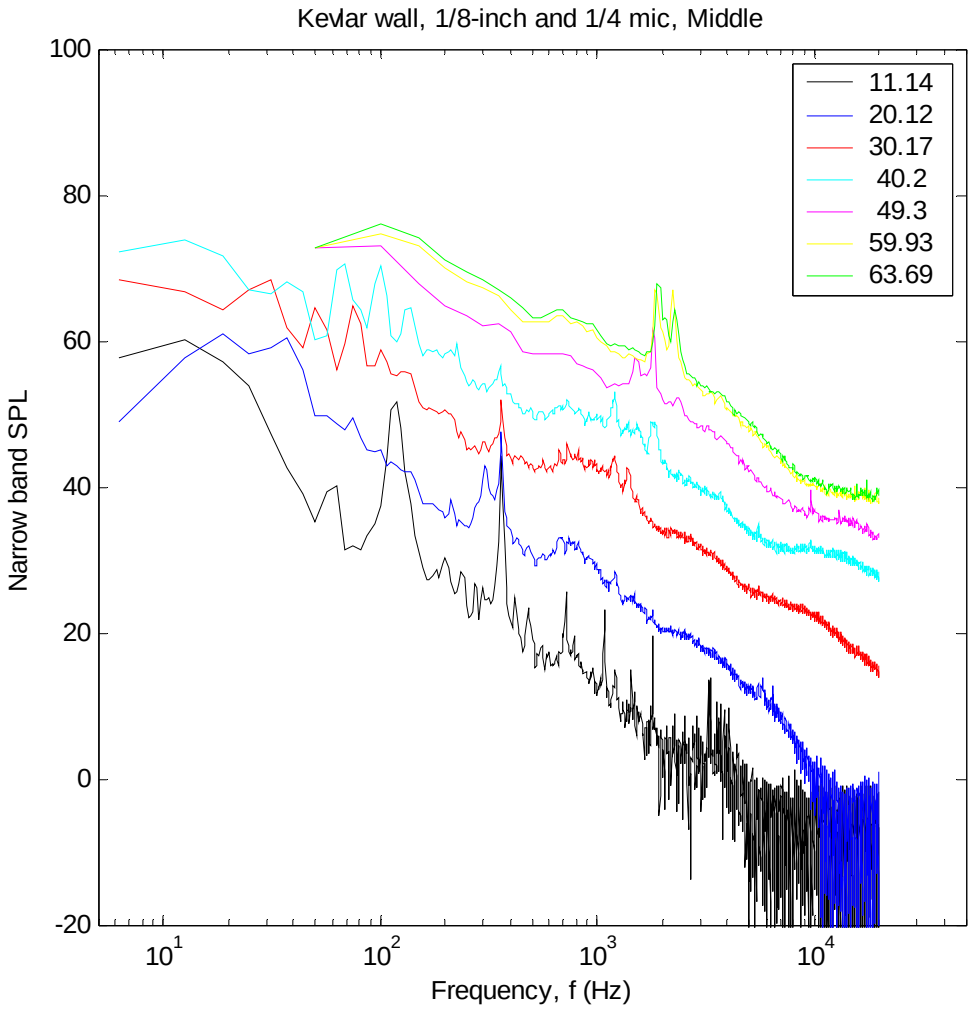

Figure 3-4. *In-flow noise spectra measured at mid-section location with the 1/8th-inch microphone (11-40m/s) and the ¼-inch microphone (49-64m/s) in the Kevlar-wall configuration. Frequency resolution 6.25Hz (11-40m/s) and 50Hz (49-64m/s)*

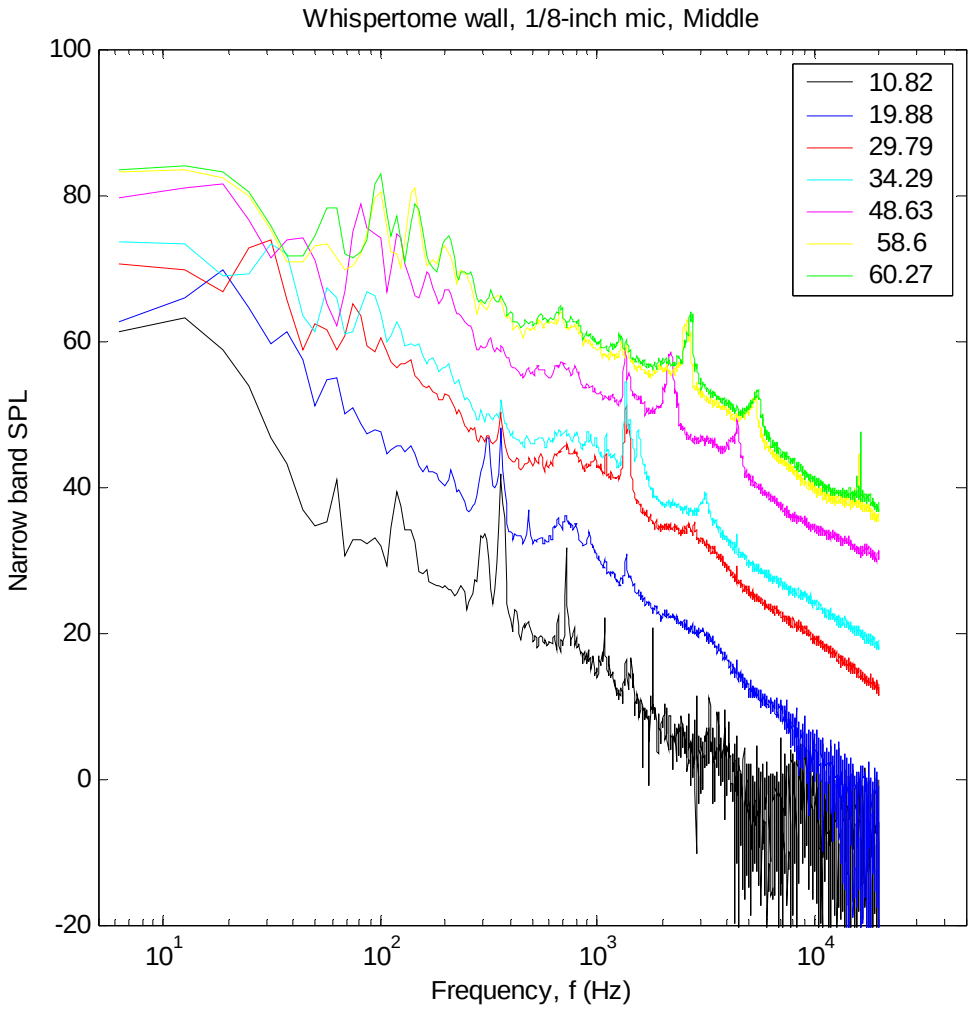

Figure 3-5. *In-flow noise spectra measured at mid-section location with the 1/8th-inch microphone in the Whispertone configuration.. Frequency resolution 6.25Hz*

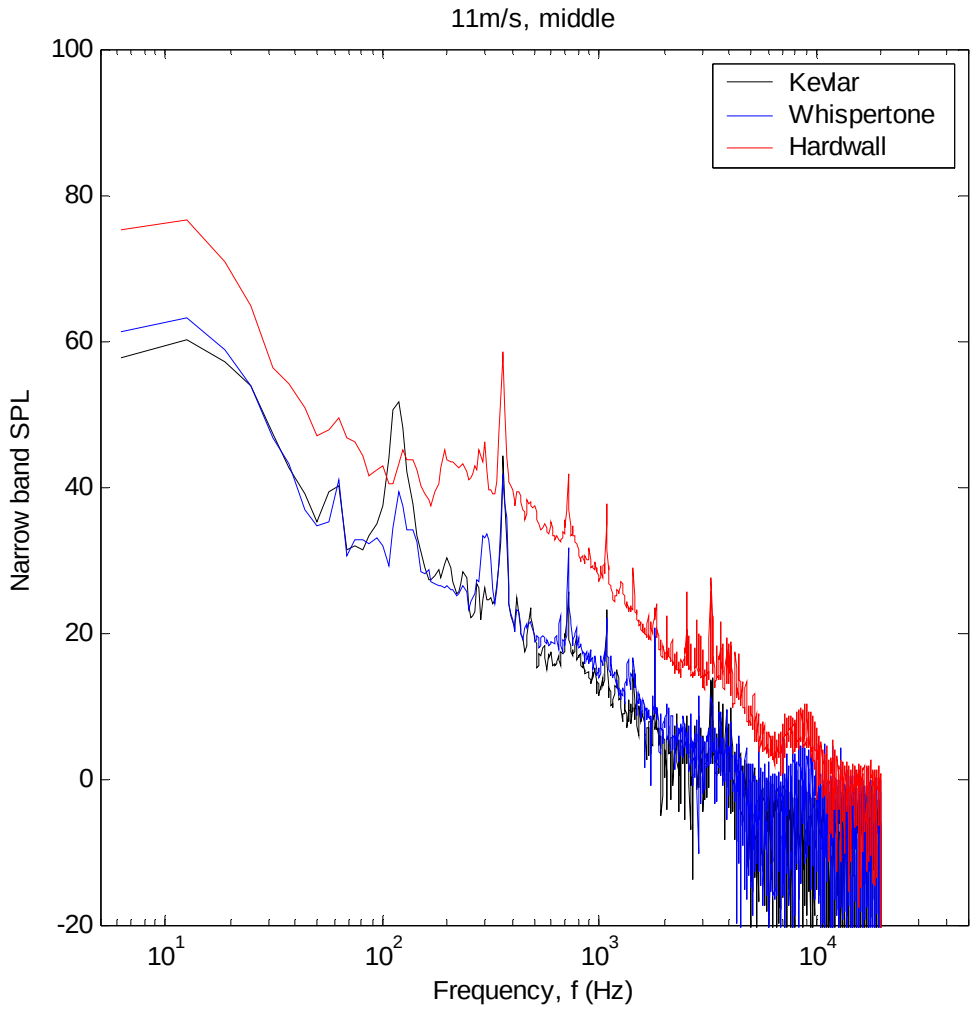

Figure 3-6. *Comparison of in-flow noise spectra measured at the mid-section location with different wall treatments. Flow speeds close to 11m/s. 1/8th-inch microphone. Frequency resolution 6.25Hz*

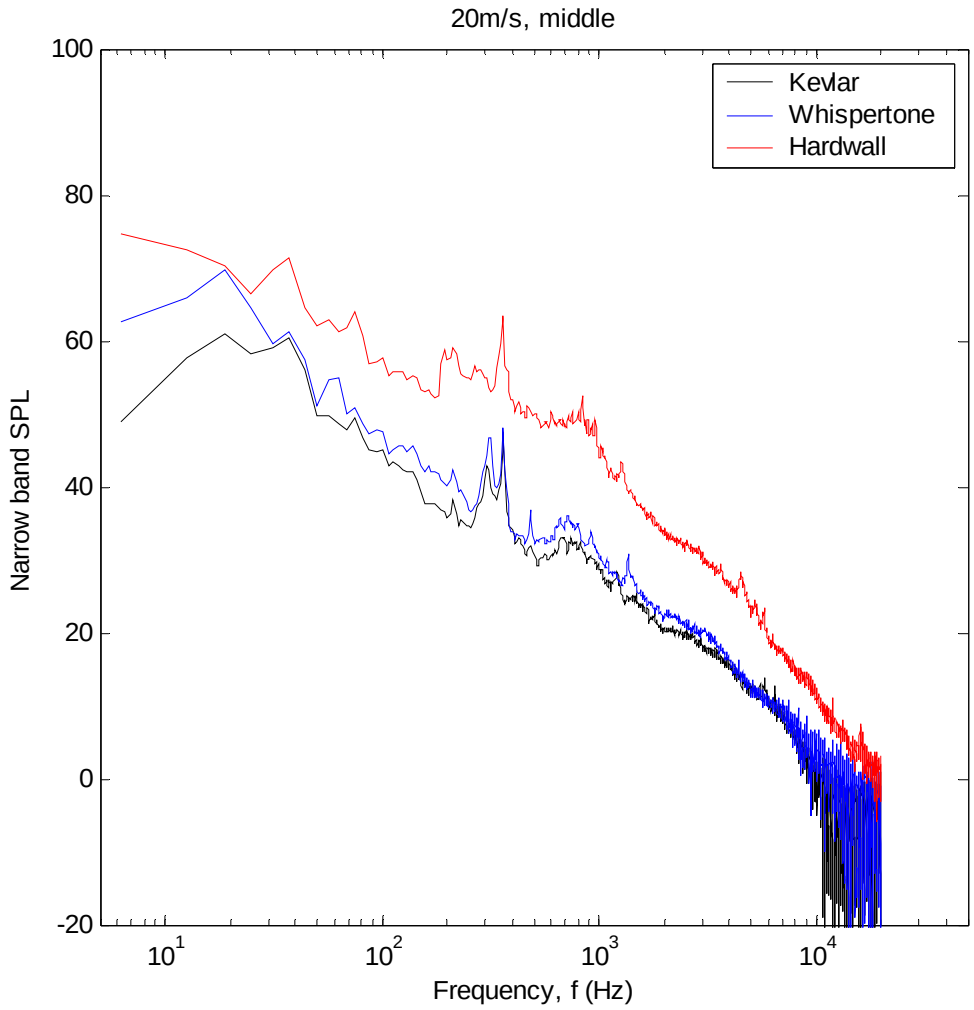

Figure 3-7. *Comparison of in-flow noise spectra measured at the mid-section location with different wall treatments. Flow speeds close to 20m/s. 1/8th-inch microphone. Frequency resolution 6.25Hz*

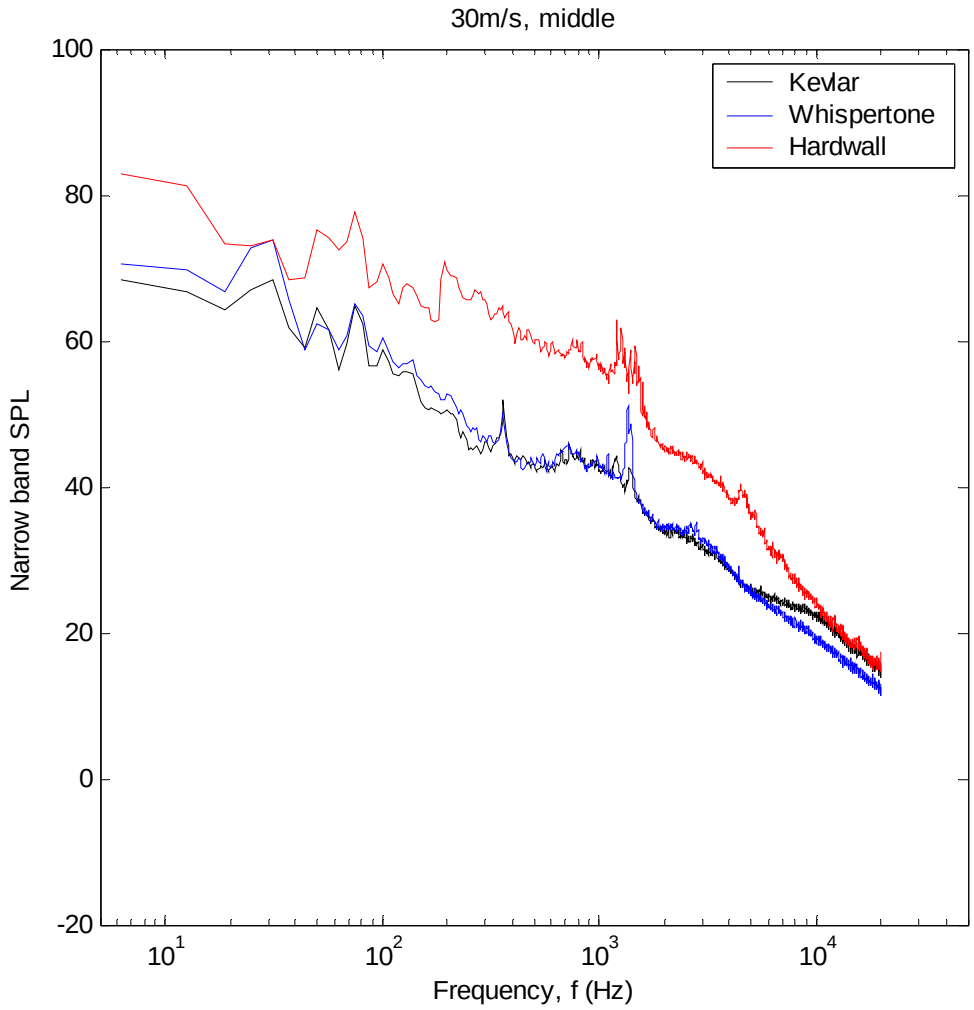

Figure 3-8. *Comparison of in-flow noise spectra measured at the mid-section location with different wall treatments. Flow speeds close to 30m/s. 1/8th-inch microphone. Frequency resolution 6.25Hz*

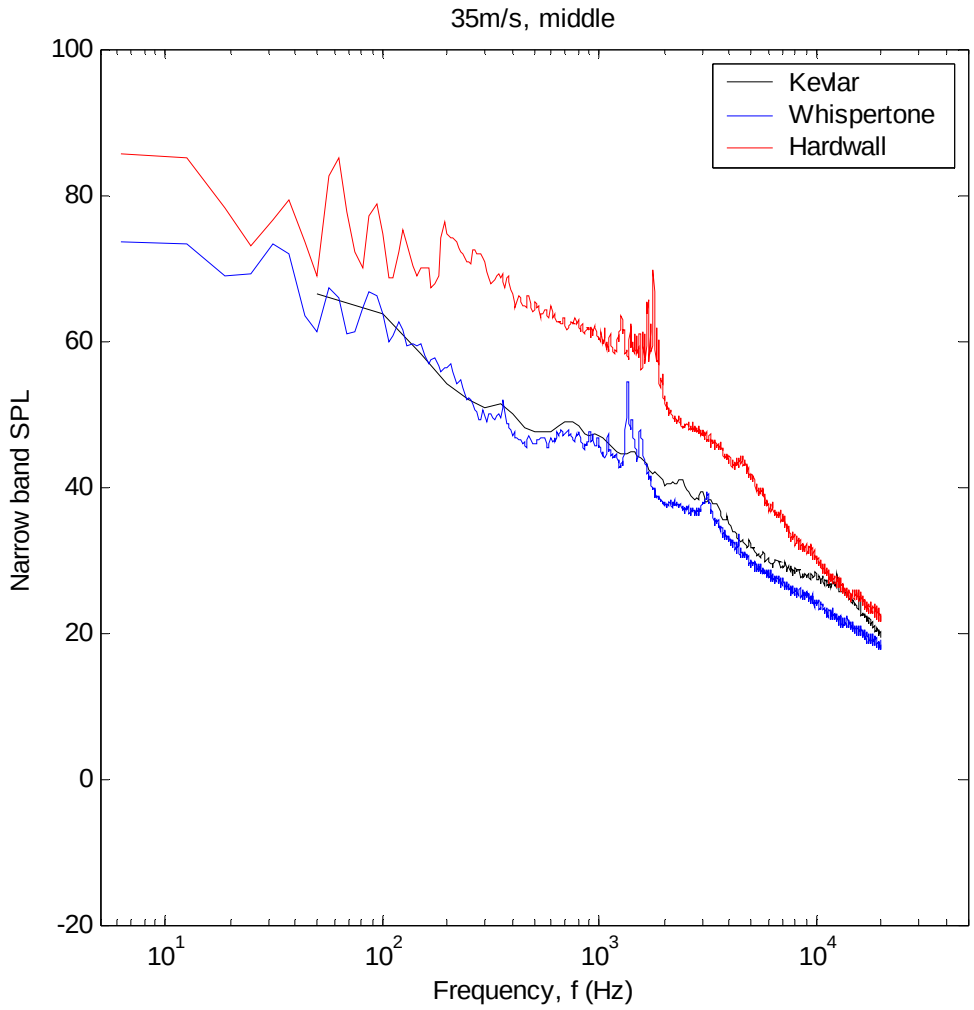

Figure 3-9. *Comparison of in-flow noise spectra measured at the mid-section location with different wall treatments. Flow speeds close to 35m/s. 1/8th-inch microphone with 6.25Hz frequency resolution (hard-wall and Whispertone). ¼-inch microphone with 50Hz frequency resolution (Kevlar)*

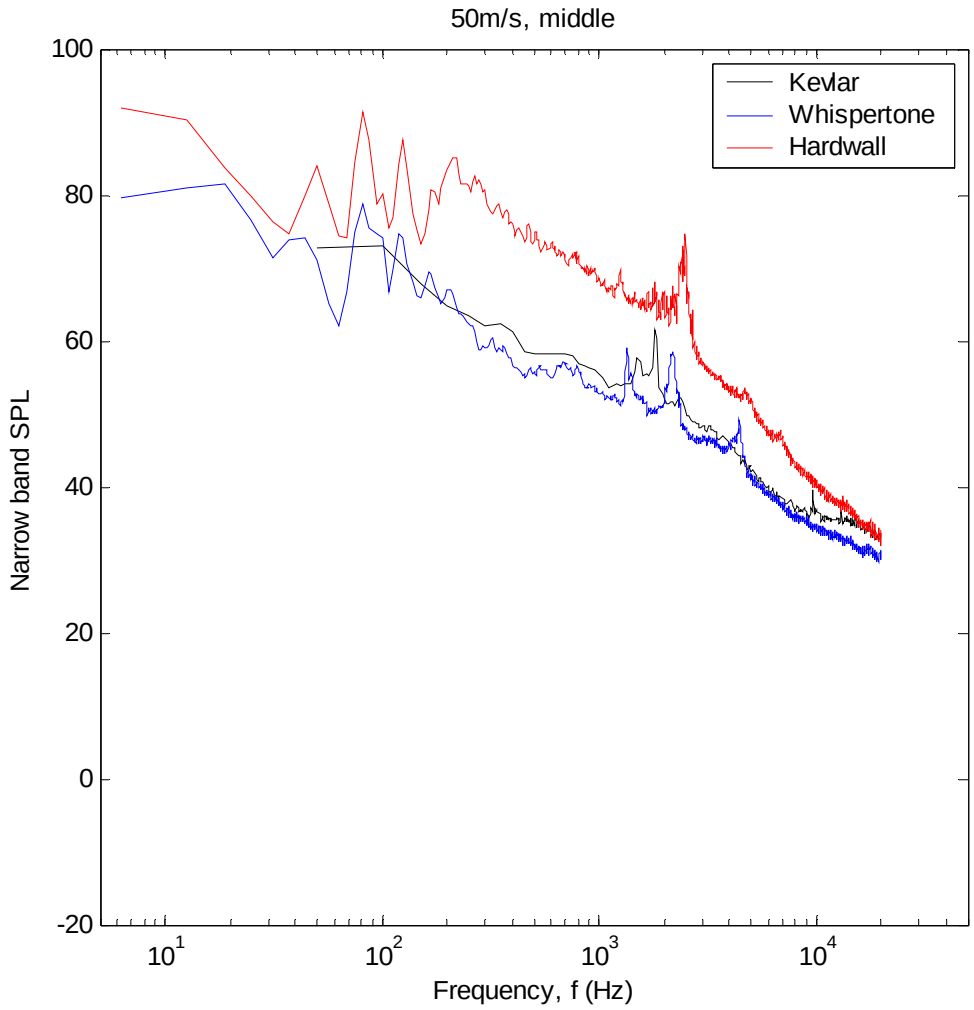

Figure 3-10. *Comparison of in-flow noise spectra measured at the mid-section location with different wall treatments. Flow speeds close to 50m/s. 1/8th-inch microphone with 6.25Hz frequency resolution (hard-wall and Whispertone). ¼-inch microphone with 50Hz frequency resolution (Kevlar)*

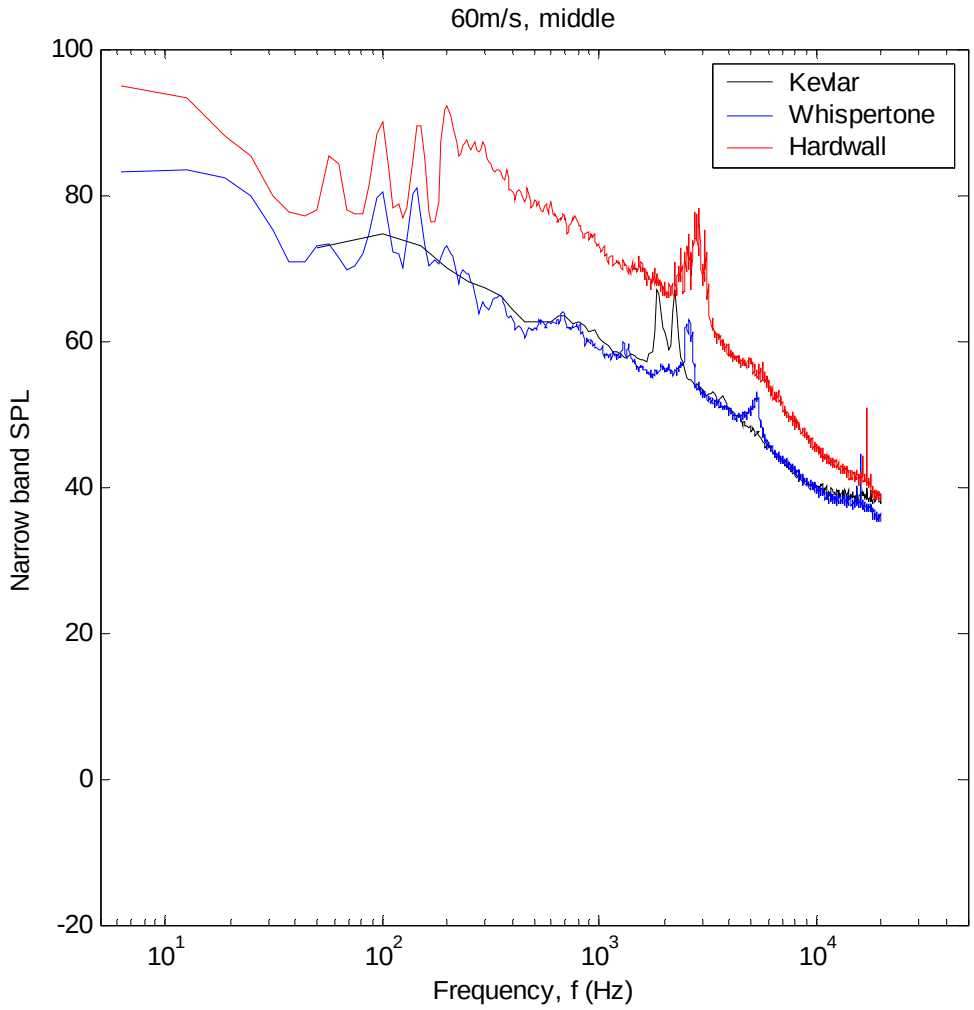

Figure 3-11. *Comparison of in-flow noise spectra measured at the mid-section location with different wall treatments. Flow speeds close to 60m/s. 1/8th-inch microphone with 6.25Hz frequency resolution (hard-wall and Whispertone). ¼-inch microphone with 50Hz frequency resolution (Kevlar)*

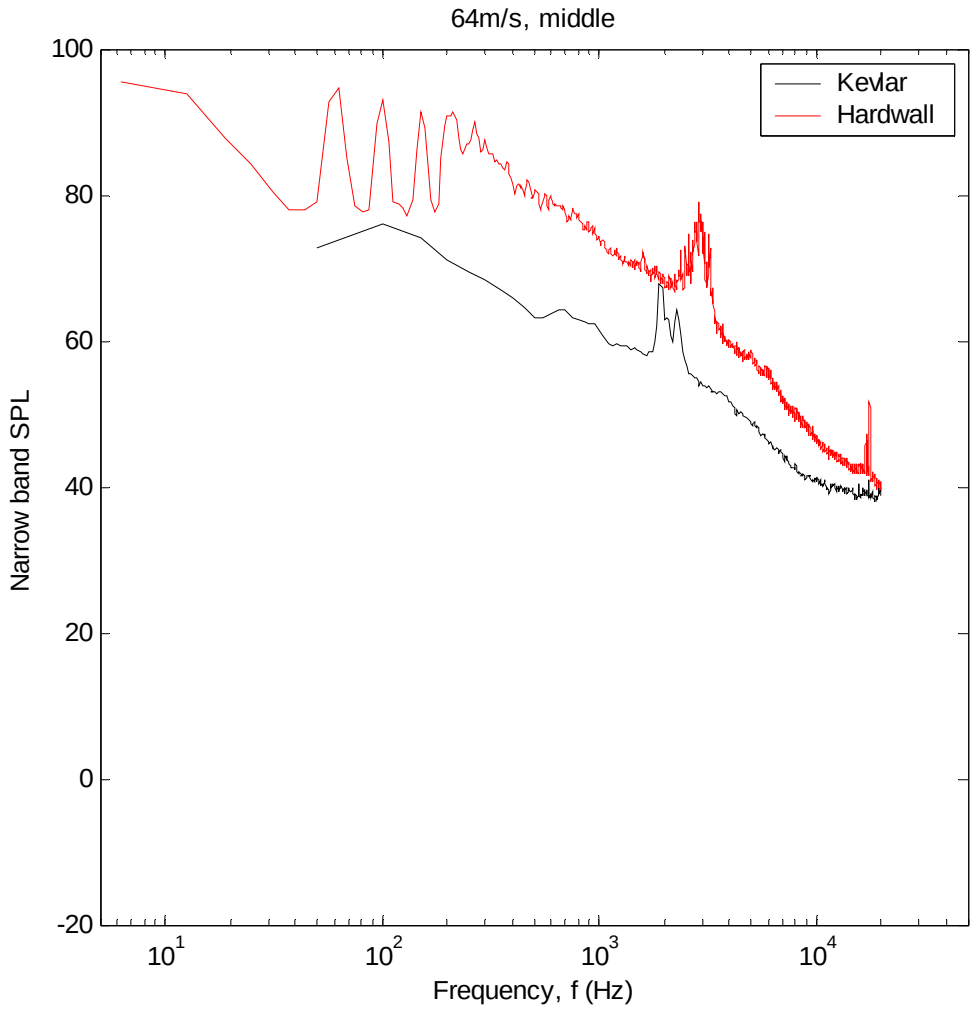

Figure 3-12. *Comparison of in-flow noise spectra measured at the mid-section location with different wall treatments. Flow speeds close to 60m/s. 1/8th-inch microphone with 6.25Hz frequency resolution (hard-wall and Whispertone). ¼-inch microphone with 50Hz frequency resolution (Kevlar)*

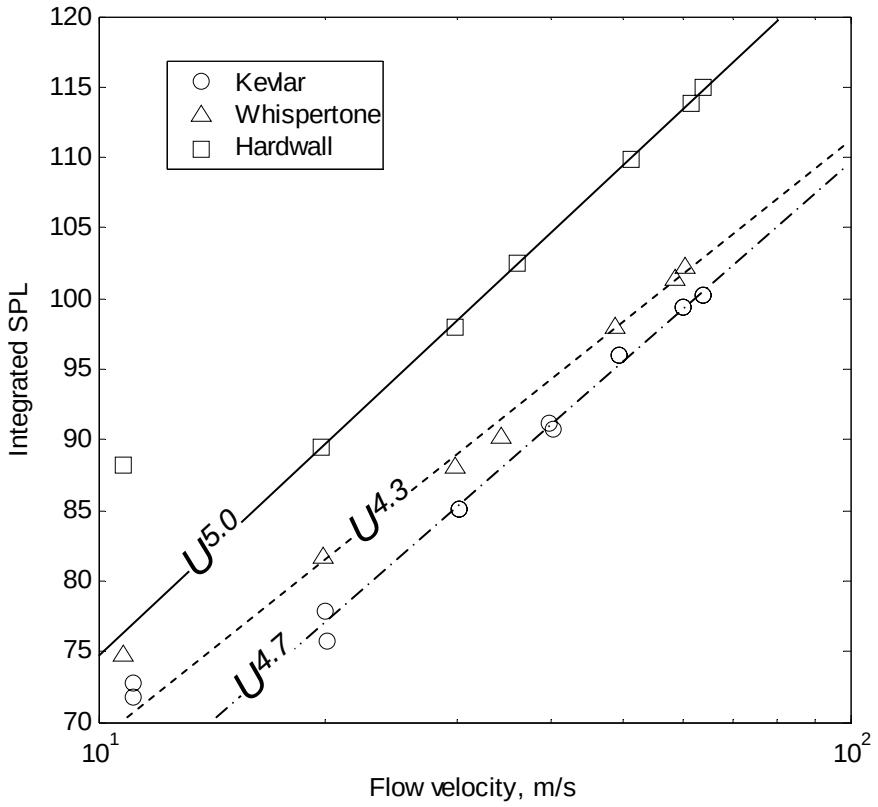

Figure 3-13. *Overall sound pressure levels measured at the mid-section location as a function of flow speed with different wall treatments.*

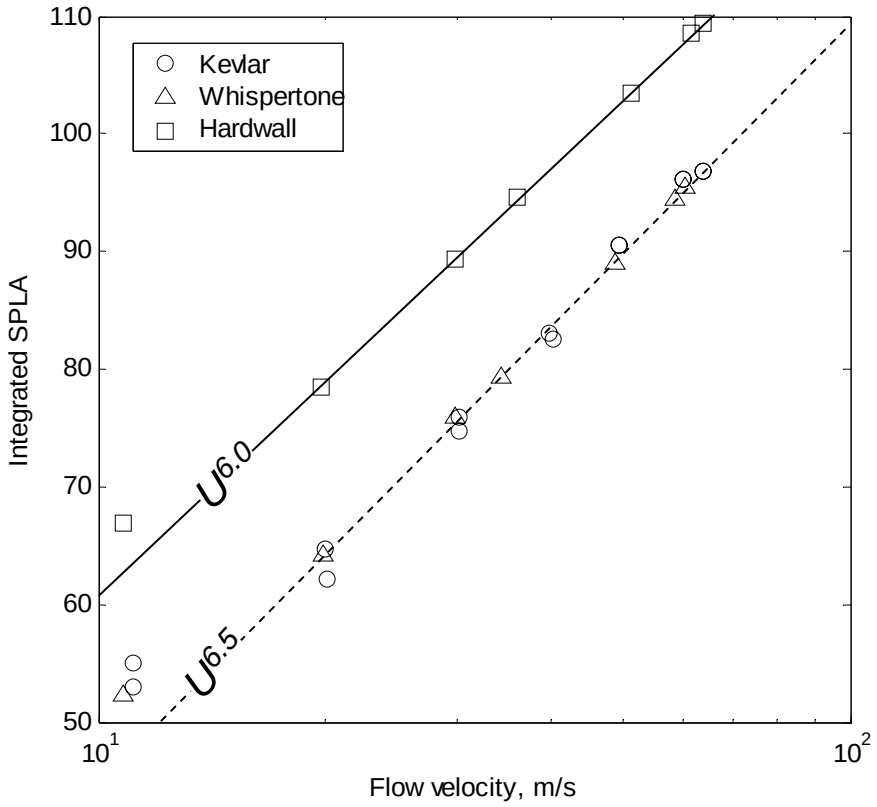

Figure 3-14. *Overall A-weighted sound pressure levels measured at the mid-section location as a function of flow speed with different wall treatments.*

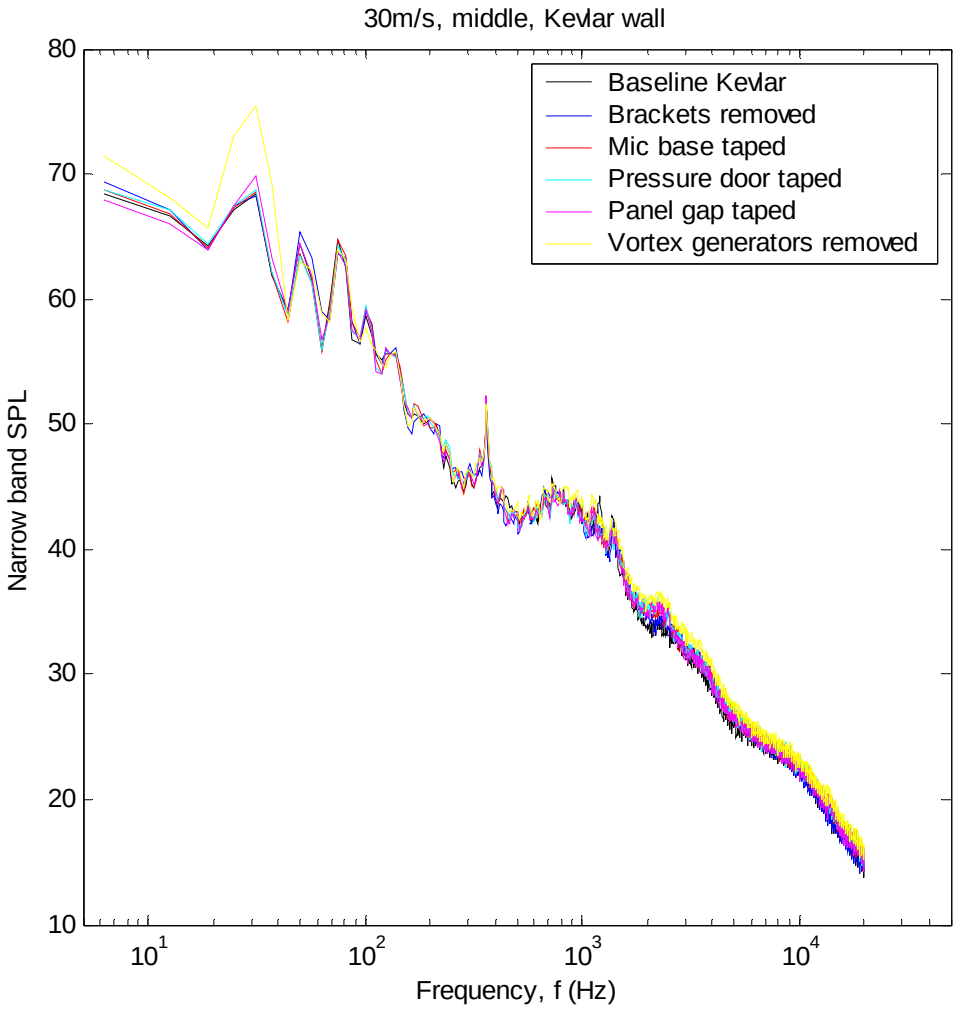

Figure 3-15. *Effect of various minor configuration modifications on the in-flow noise spectrum measured at the mid-section location wht the Kevlar acoustic treatment. Flow speed of 30m/s. 1/8th-inch microphone with 6.25Hz frequency resolution.*

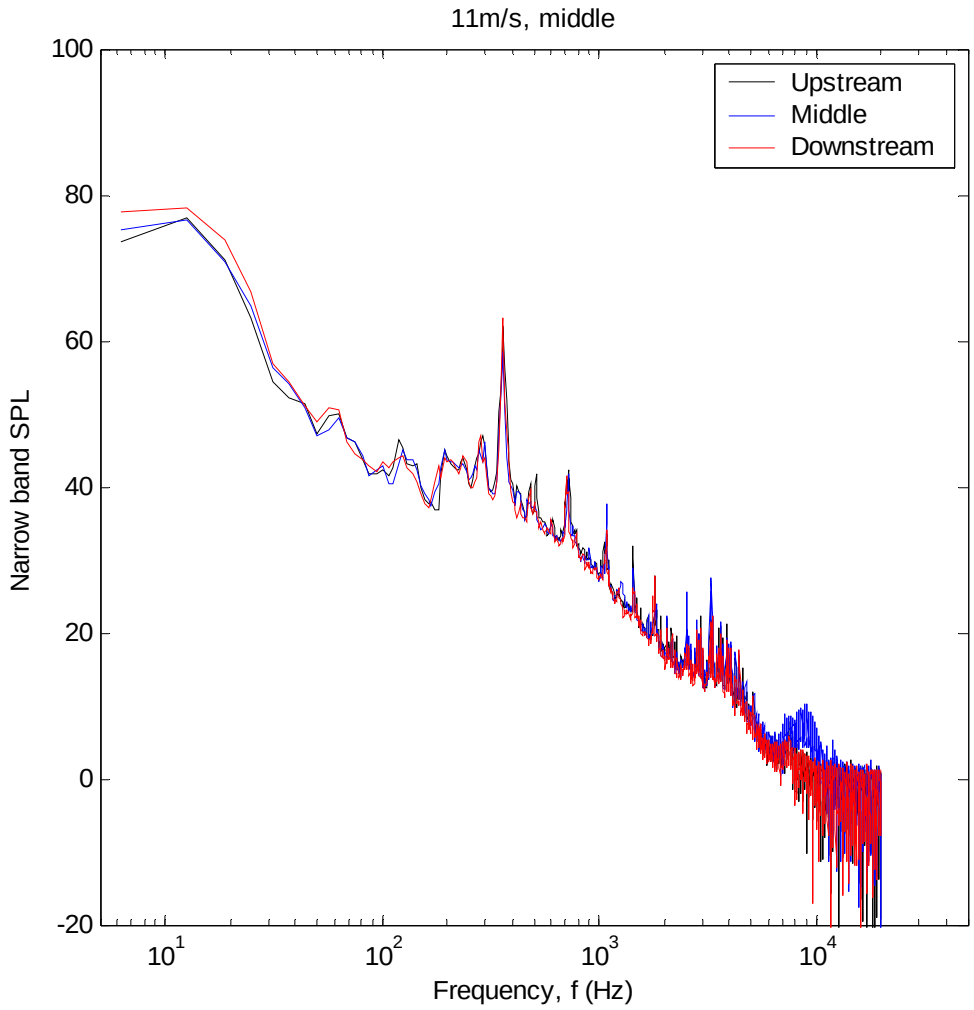

Figure 3-16. *Comparison of in-flow noise spectra measured at different streamwise locations in the hard-wall configuration. Flow speed of 11m/s. 1/8th-inch microphone with 6.25Hz frequency resolution.*

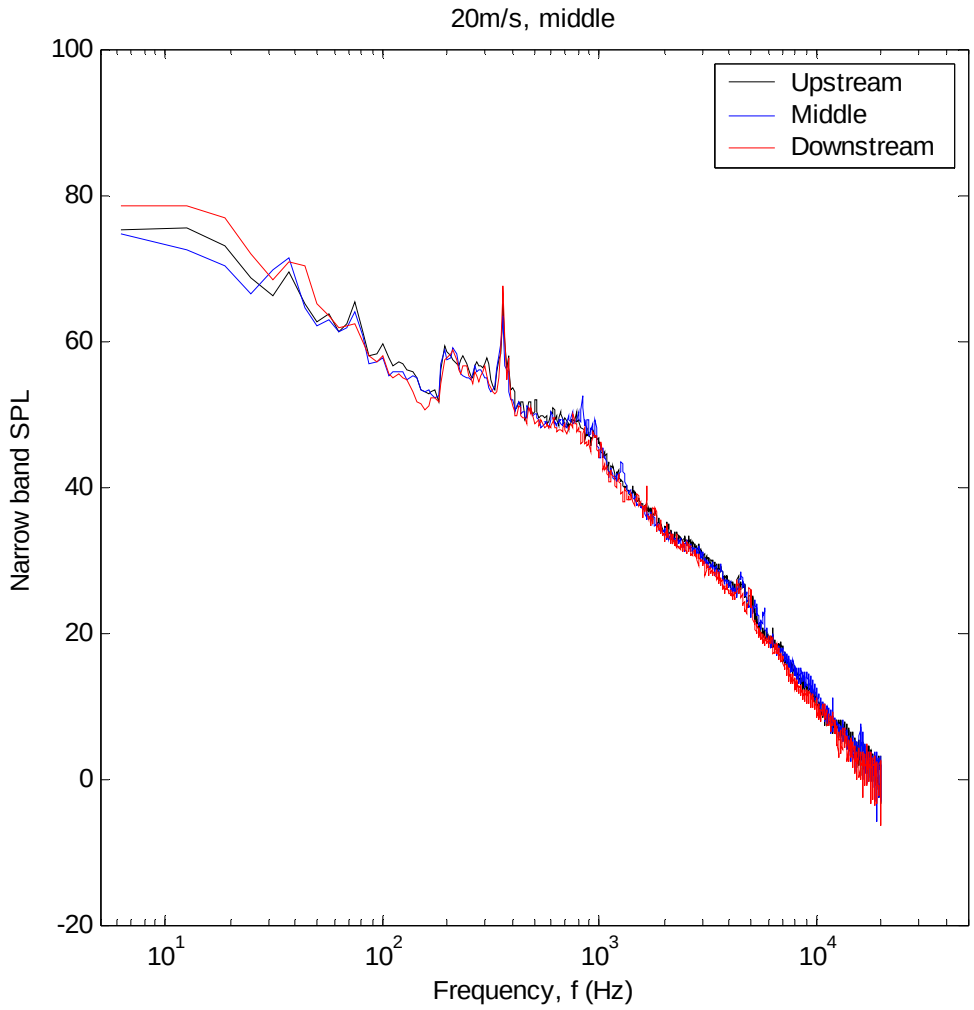

Figure 3-17. *Comparison of in-flow noise spectra measured at different streamwise locations in the hard-wall configuration. Flow speed of 20m/s. 1/8th-inch microphone with 6.25Hz frequency resolution.*

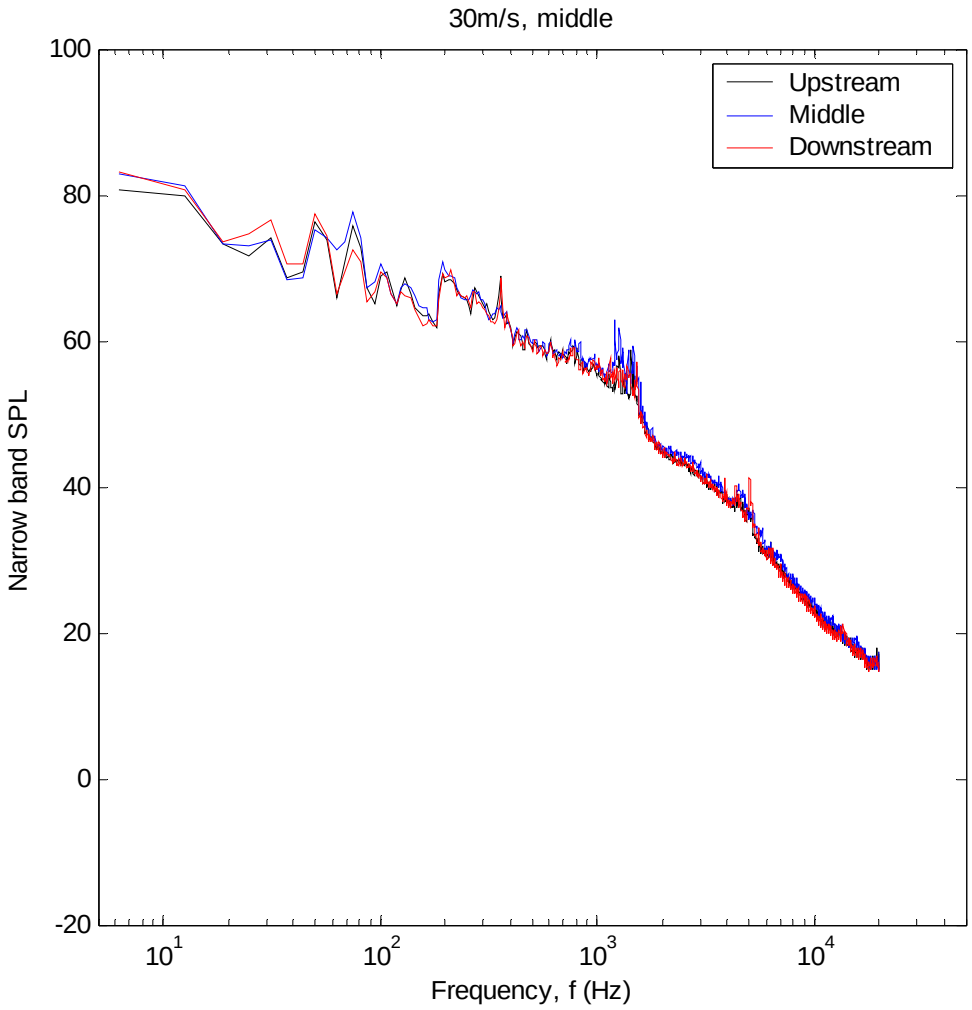

Figure 3-18. *Comparison of in-flow noise spectra measured at different streamwise locations in the hard-wall configuration. Flow speed of 30m/s. 1/8th-inch microphone with 6.25Hz frequency resolution.*

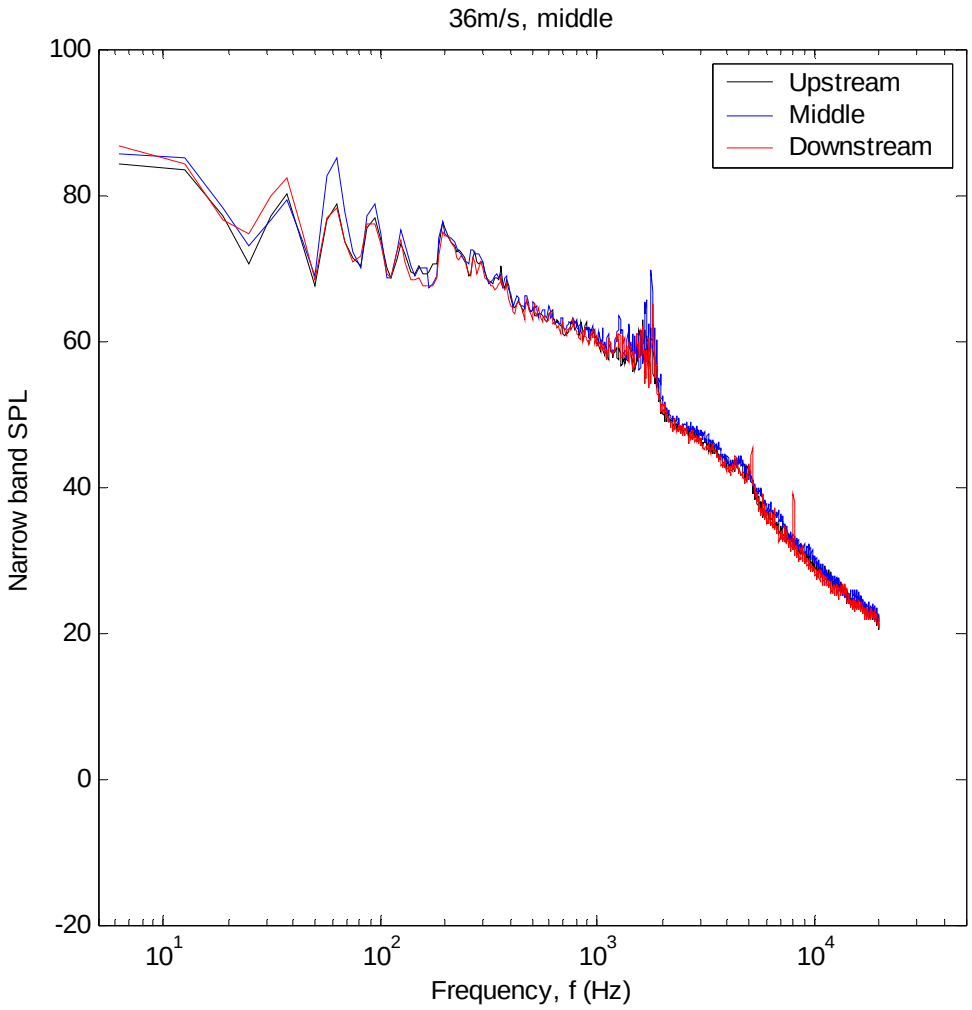

Figure 3-19. *Comparison of in-flow noise spectra measured at different streamwise locations in the hard-wall configuration. Flow speed of 36m/s. 1/8th-inch microphone with 6.25Hz frequency resolution.*

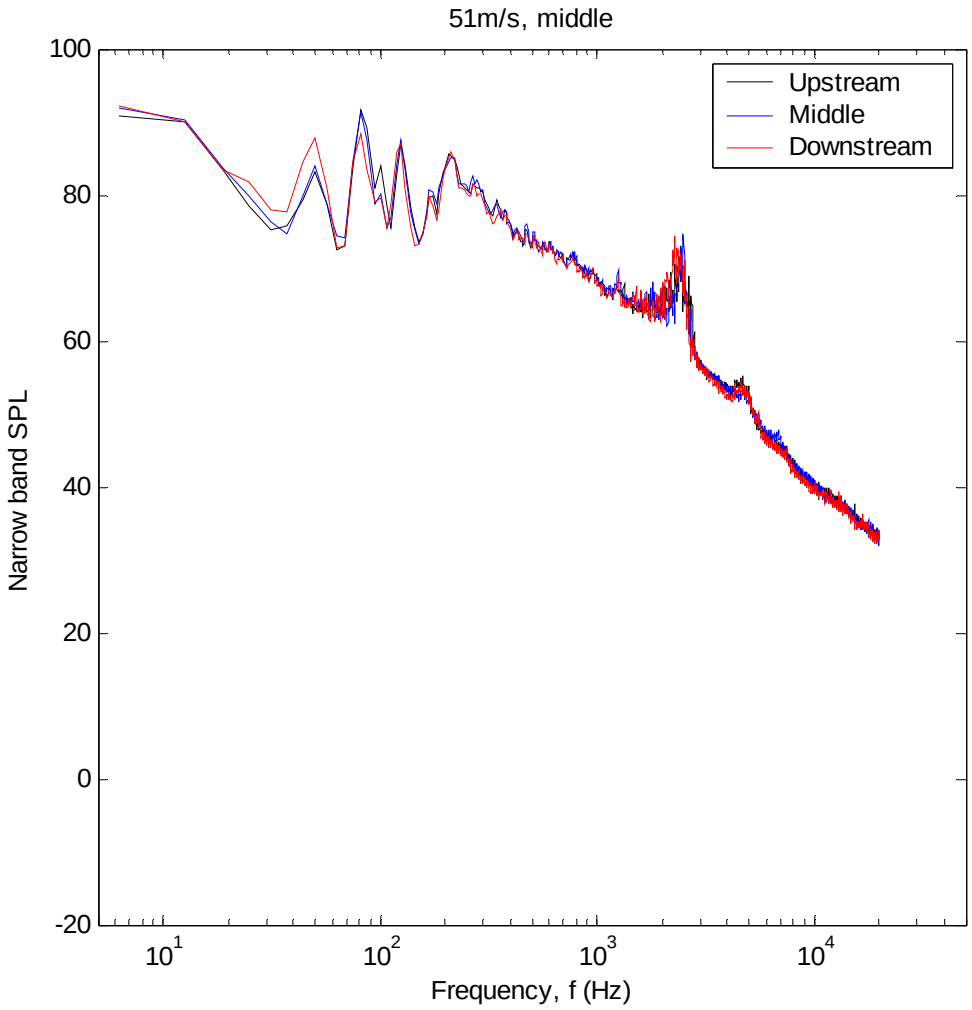

Figure 3-20. *Comparison of in-flow noise spectra measured at different streamwise locations in the hard-wall configuration. Flow speed of 51m/s. 1/8th-inch microphone with 6.25Hz frequency resolution.*

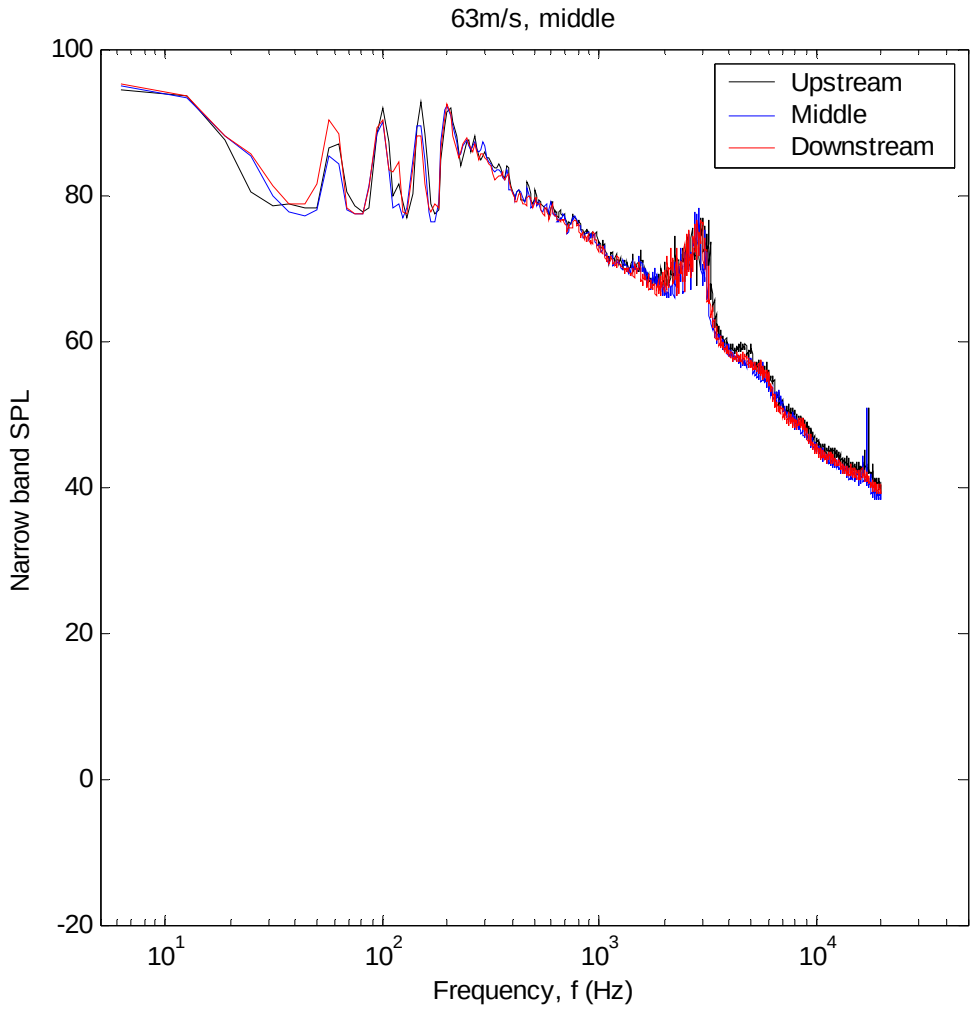

Figure 3-21. *Comparison of in-flow noise spectra measured at different streamwise locations in the hard-wall configuration. Flow speed of 63m/s. 1/8th-inch microphone with 6.25Hz frequency resolution.*

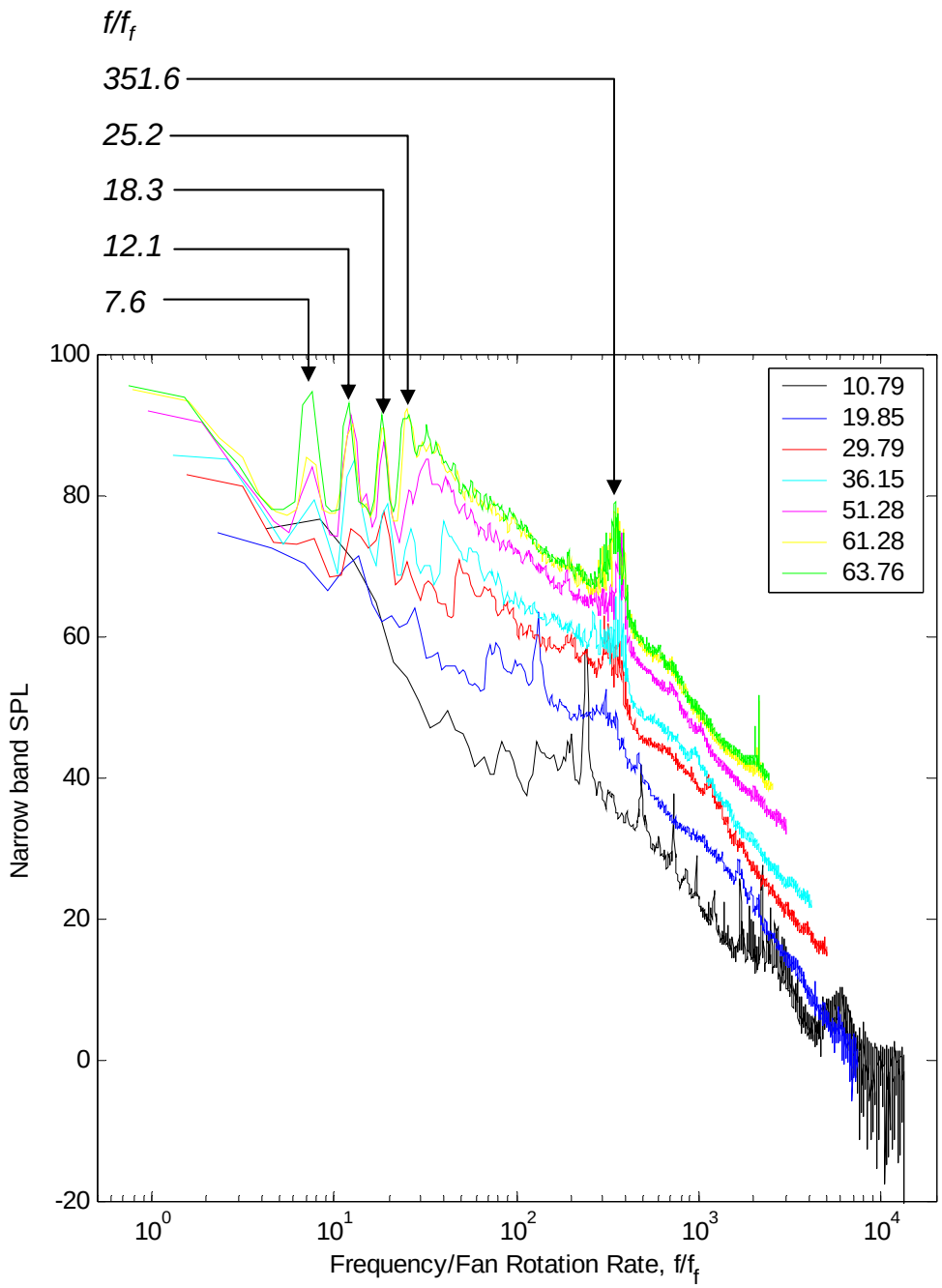

Figure 3-22. *In-flow noise spectra measured at mid-section location with the 1/8th-inch microphone in the hard-wall configuration with frequency scaled on fan rotation rate f_f. Frequency resolution 6.25Hz*

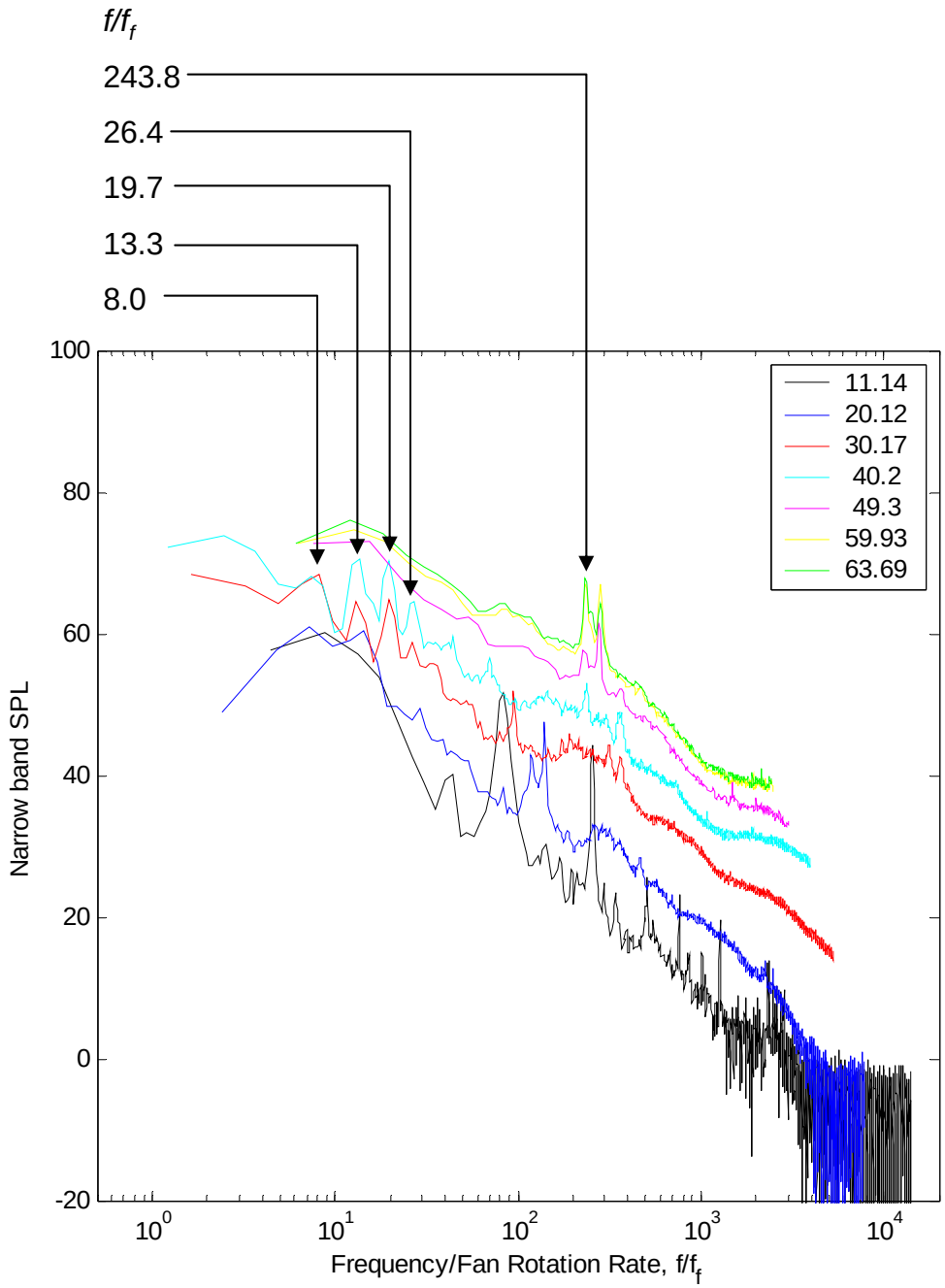

Figure 3-23. *In-flow noise spectra measured at mid-section location with the 1/8th-inch microphone (11-40m/s) and the ¼-inch microphone (49-64m/s) in the Kevlar-wall configuration with frequency scaled on fan rotation rate f_f. Frequency resolution 6.25Hz (11-40m/s) and 50Hz (49-64m/s)*

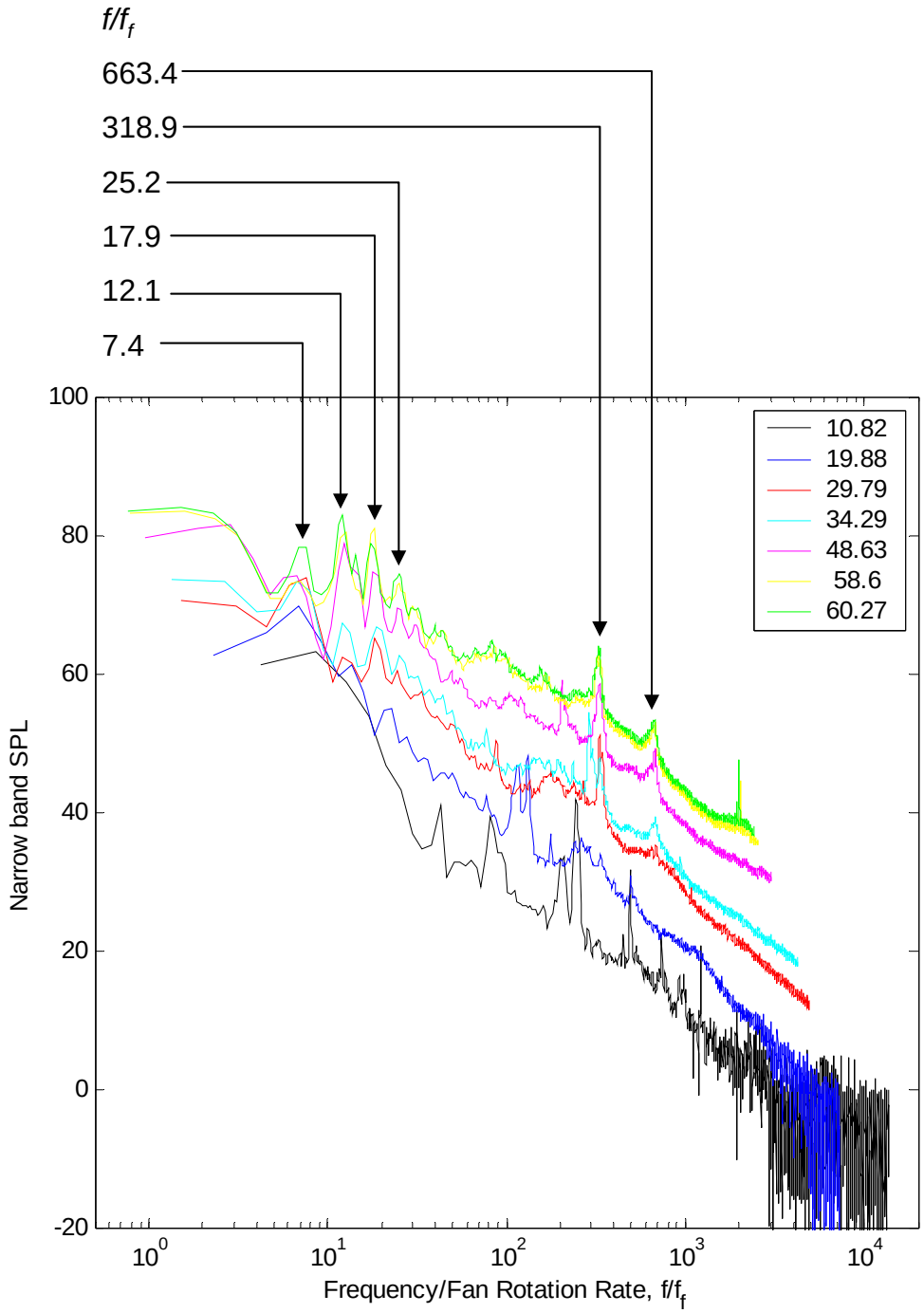

Figure 3-24. *In-flow noise spectra measured at mid-section location with the 1/8th-inch microphone in the Whispertone-wall configuration with frequency scaled on fan rotation rate f_f. Frequency resolution 6.25Hz*

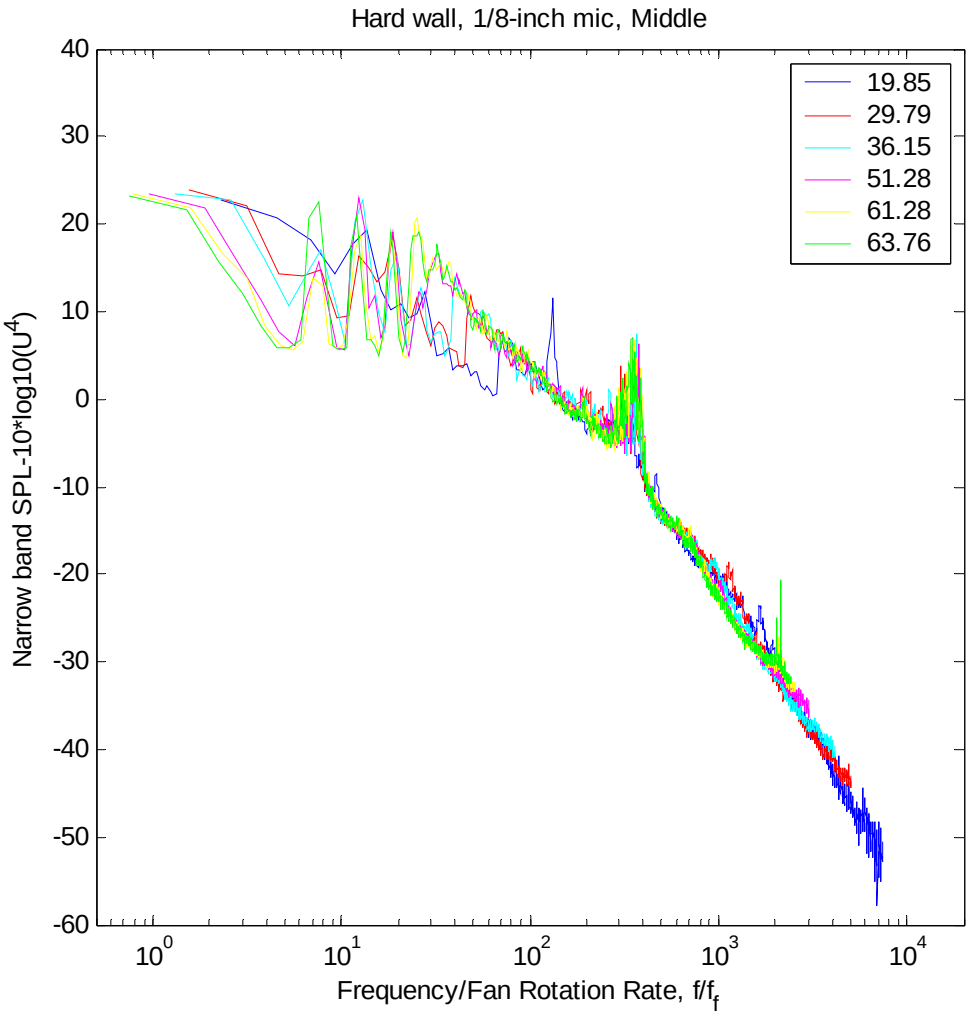

Figure 3-25. *In-flow noise spectra measured at mid-section location with the 1/8th-inch microphone in the hard-wall configuration with frequency scaled on fan rotation rate f_f. and spectral level scaled on the 4th power of the velocity. Frequency resolution 6.25Hz*

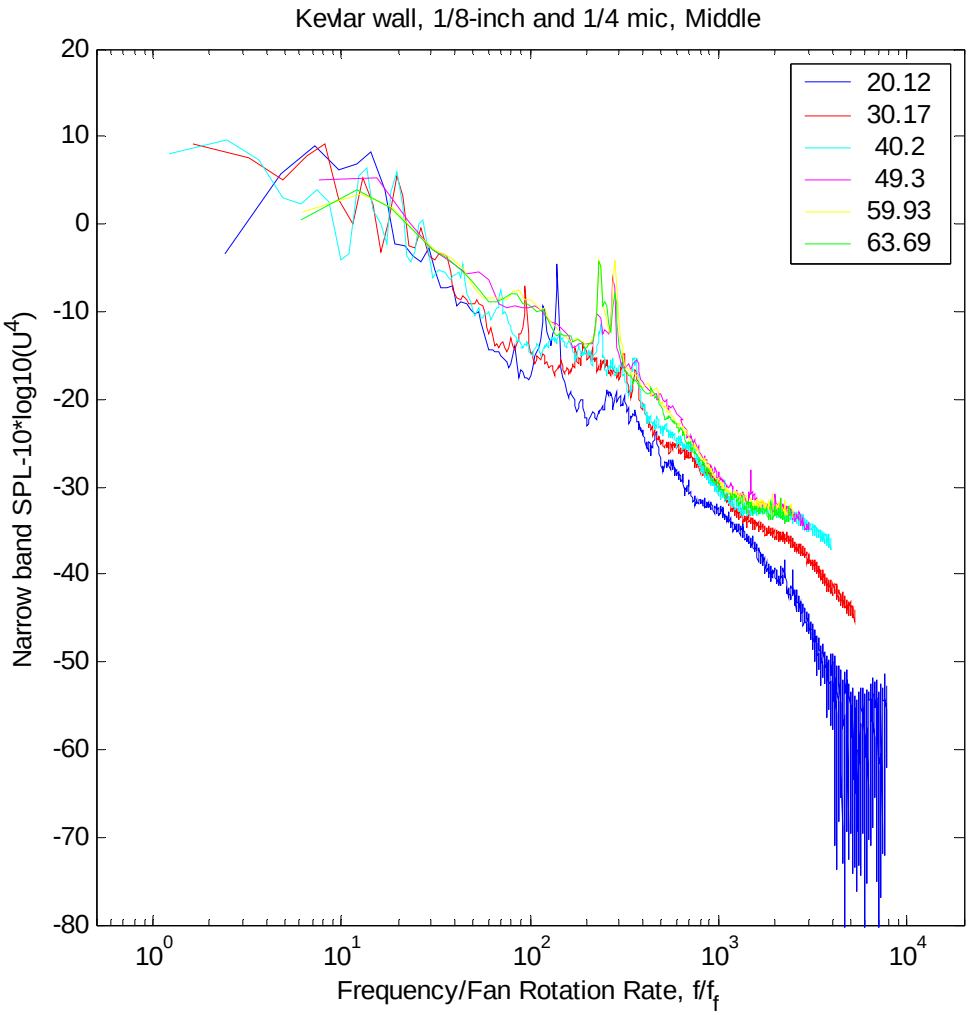

Figure 3-26. *In-flow noise spectra measured at mid-section location with the 1/8th-inch microphone (11-40m/s) and the ¼-inch microphone (49-64m/s) in the Kevlar-wall configuration with frequency scaled on fan rotation rate f_f. and spectral level scaled on the 4th power of the velocity. Frequency resolution 6.25Hz (11-40m/s) and 50Hz (49-64m/s)*

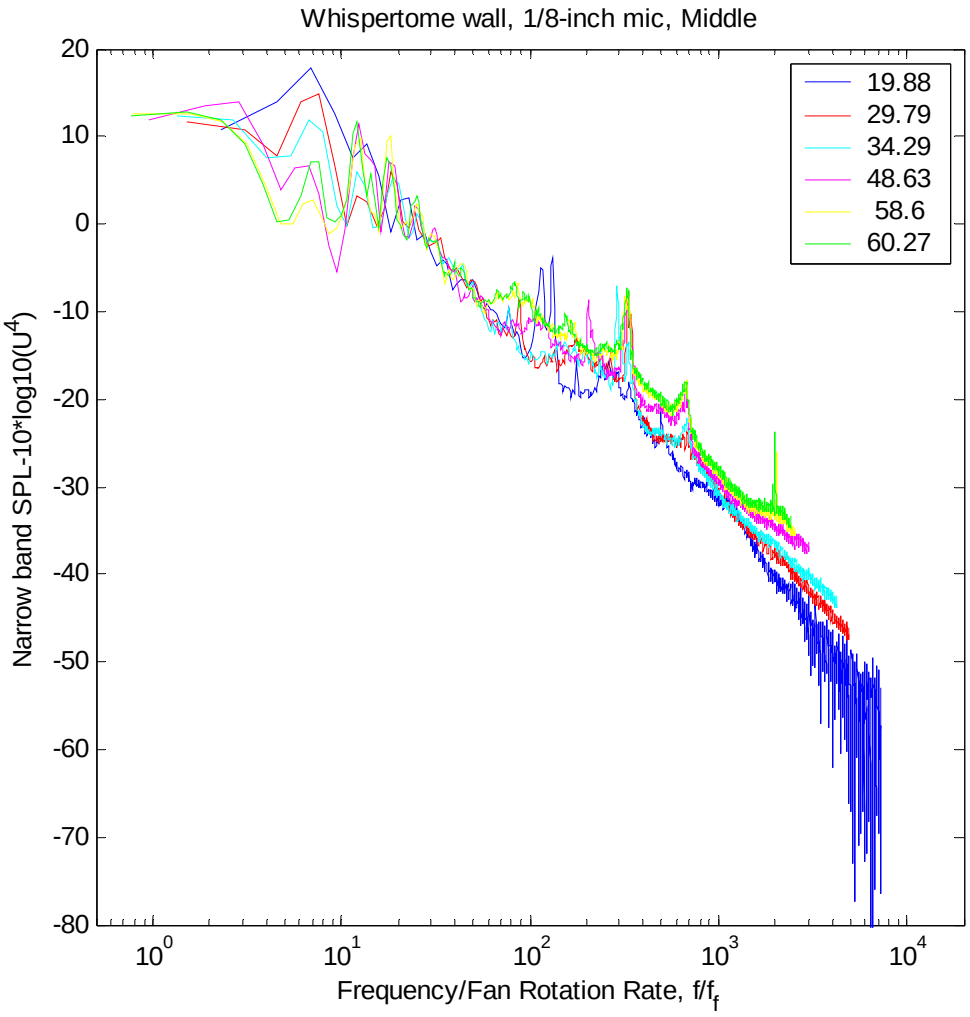

Figure 3-27. *In-flow noise spectra measured at mid-section location with the 1/8th-inch microphone in the Whispertone-wall configuration with frequency scaled on fan rotation rate f_f and spectral level scaled on the 4th power of the velocity. Frequency resolution 6.25Hz*

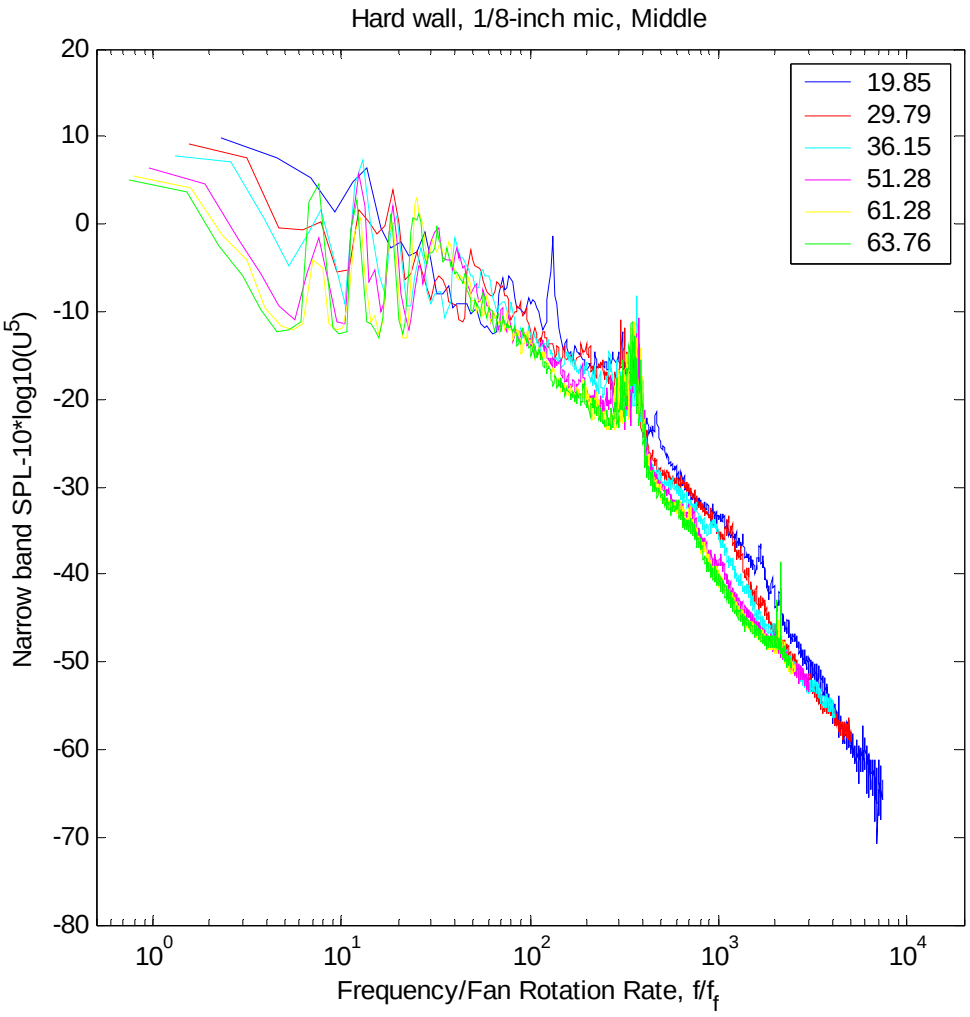

Figure 3-28. *In-flow noise spectra measured at mid-section location with the 1/8th-inch microphone in the hard-wall configuration with frequency scaled on fan rotation rate f_f. and spectral level scaled on the 5th power of the velocity. Frequency resolution 6.25Hz*

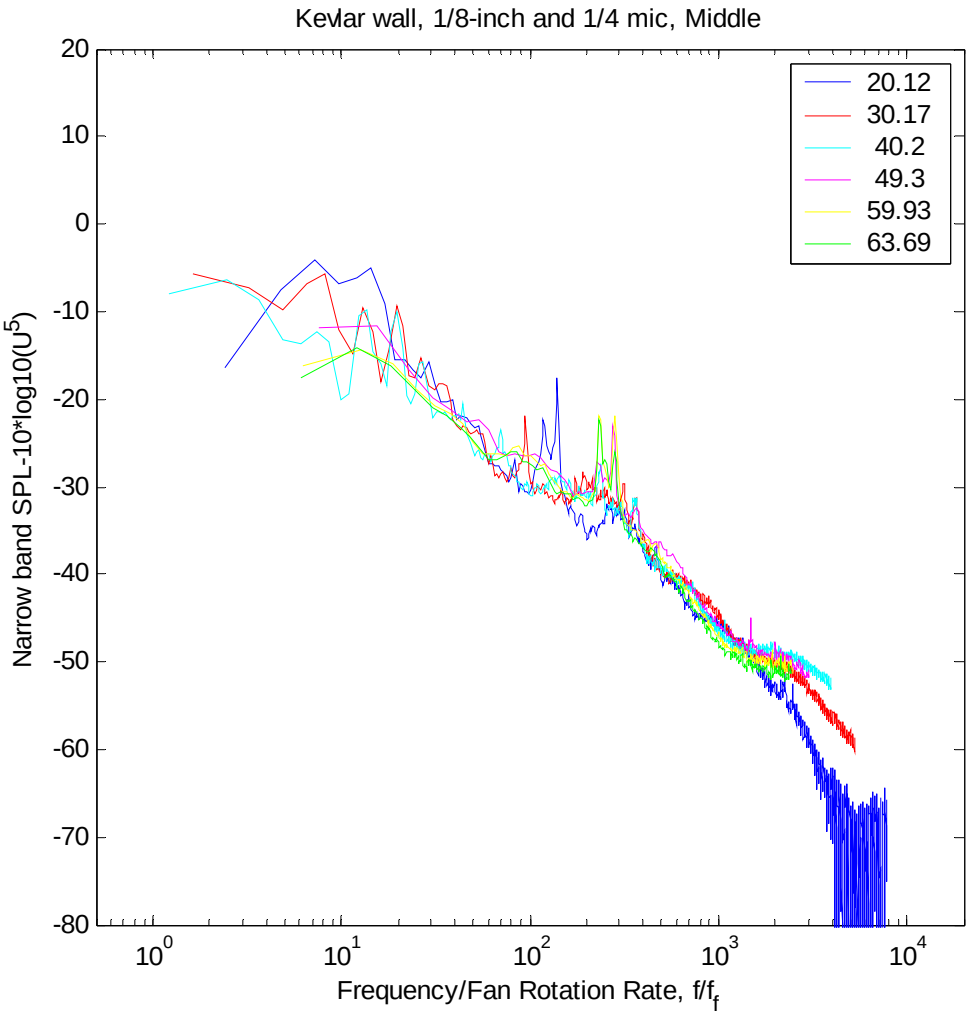

Figure 3-29. *In-flow noise spectra measured at mid-section location with the 1/8th-inch microphone (11-40m/s) and the ¼-inch microphone (49-64m/s) in the Kevlar-wall configuration with frequency scaled on fan rotation rate f_f, and spectral level scaled on the 5th power of the velocity. Frequency resolution 6.25Hz (11-40m/s) and 50Hz (49-64m/s)*

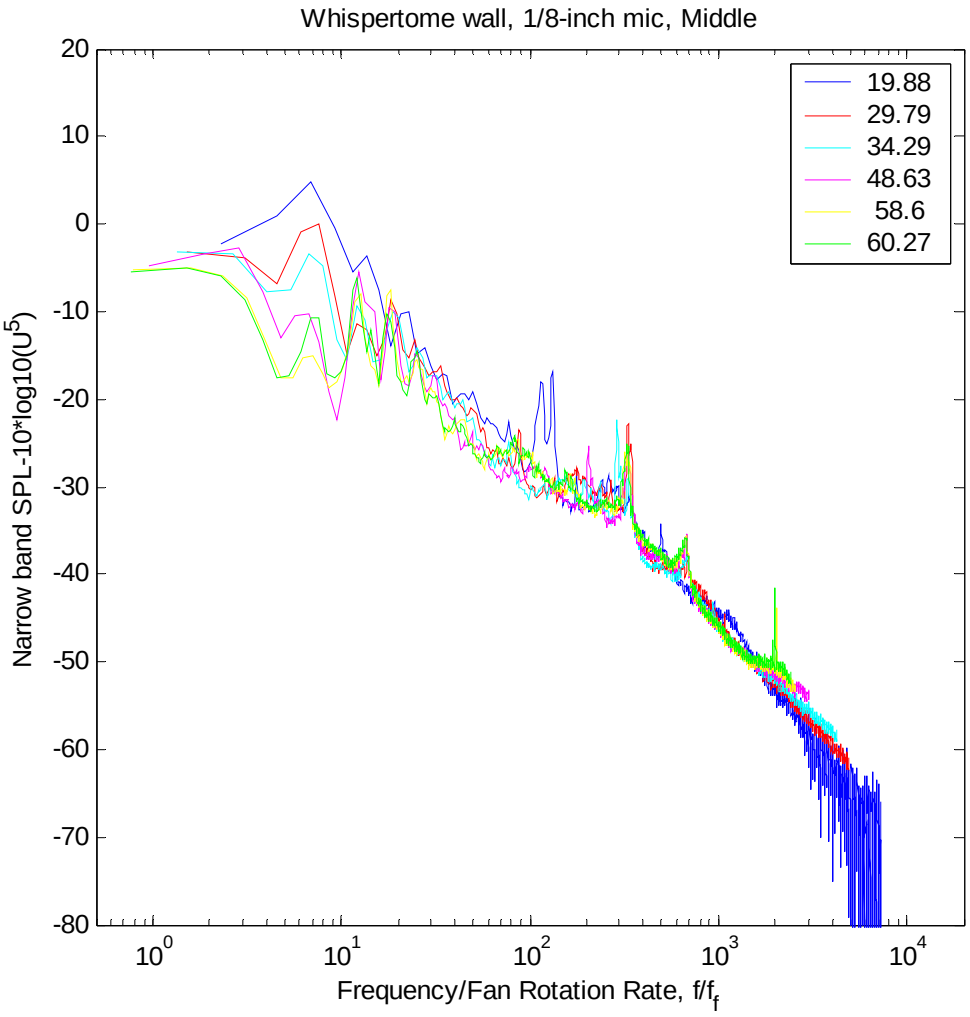

Figure 3-30. *In-flow noise spectra measured at mid-section location with the 1/8th-inch microphone in the Whispertone-wall configuration with frequency scaled on fan rotation rate f_f and spectral level scaled on the 5th power of the velocity. Frequency resolution 6.25Hz*

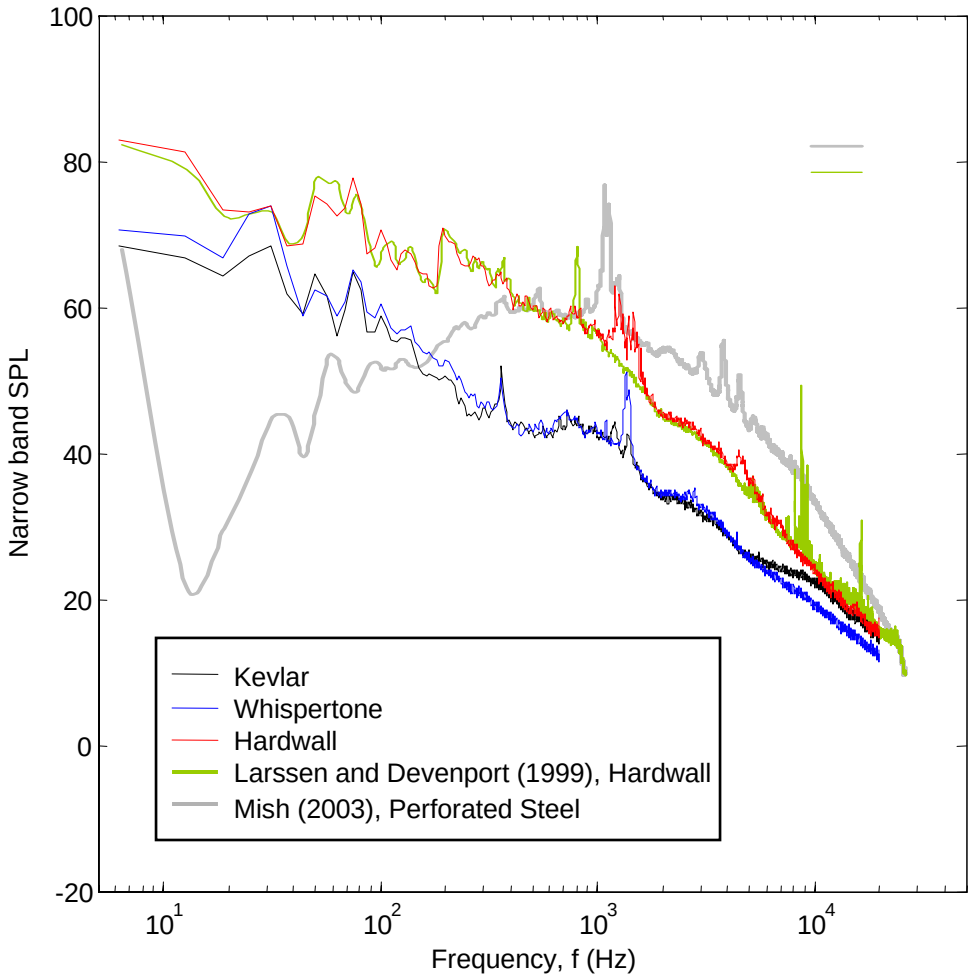

Figure 3-31. *Comparison of in-flow noise spectra measured at the mid-section location with different wall treatments including the perforated steel sheet flow surface used by Mish (2003). Flow speeds close to 30m/s. 1/8th-inch microphone. Frequency resolution 6.25Hz*

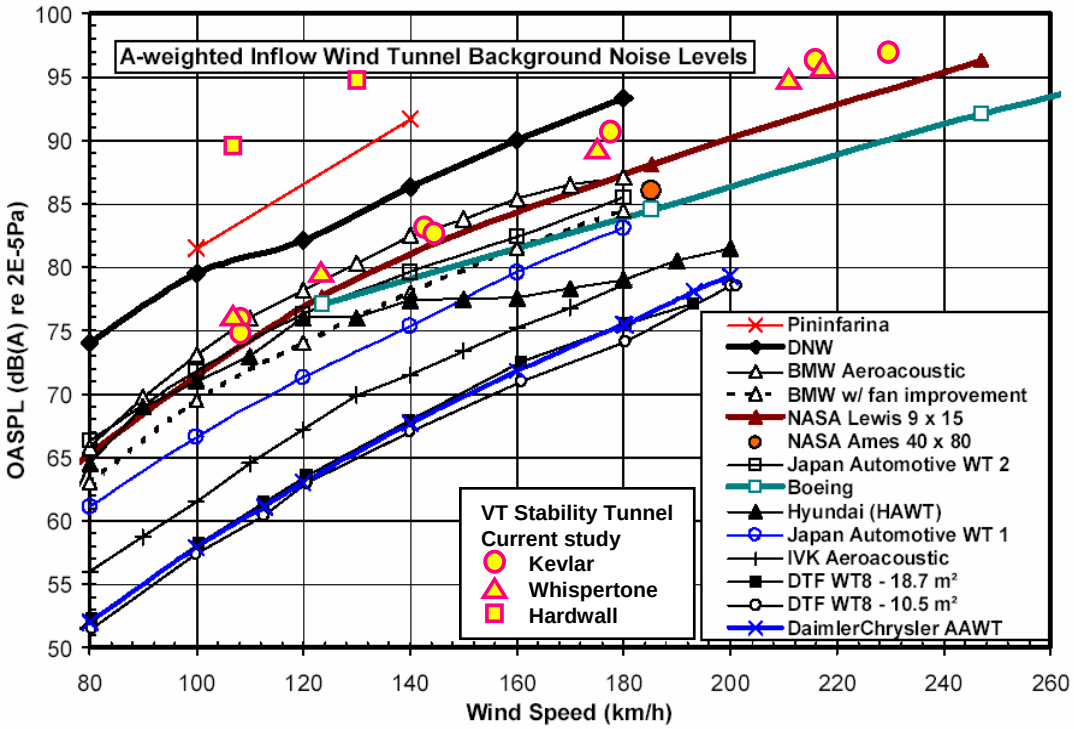

Figure 3-32. *A-weighted in-flow noise levels measured at the mid-section location with different wall treatments compared with other facilities. Plot adapted from Duell* et al. *(2002).*

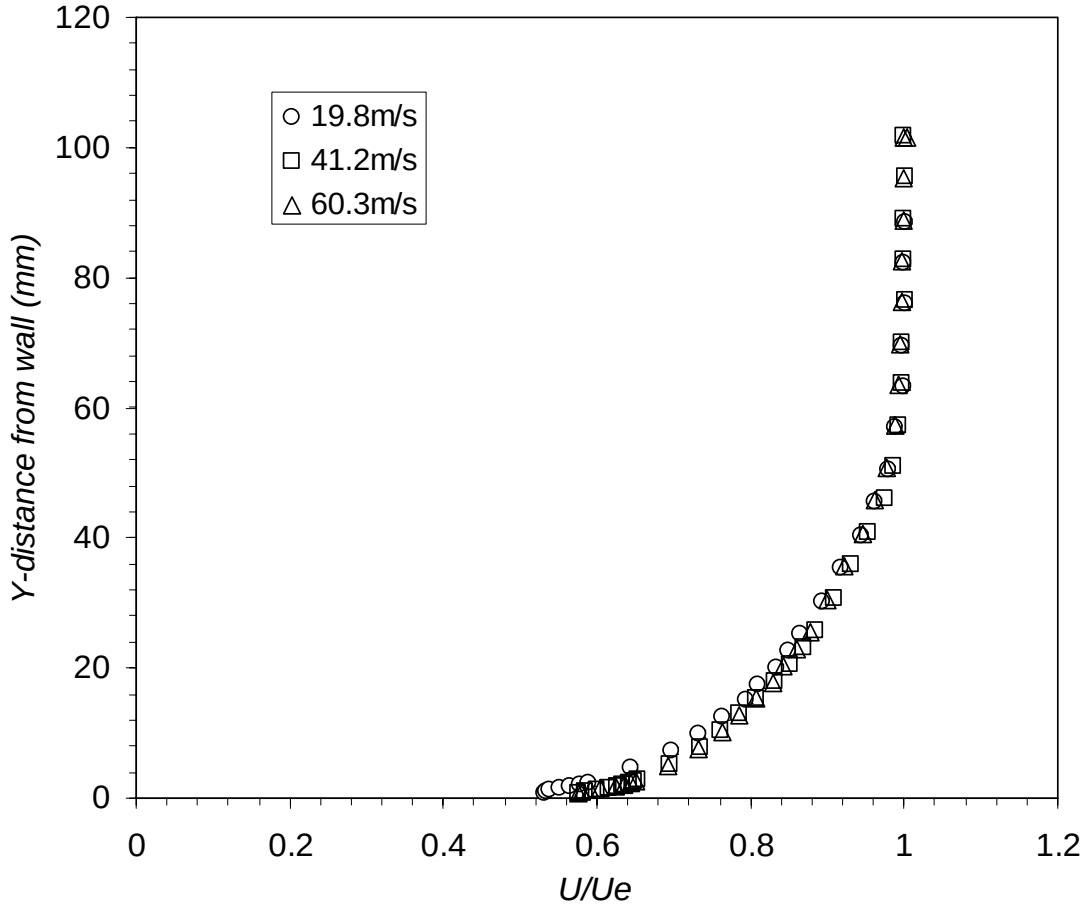

Figure 3-33. *Boundary layer mean velocity profiles measured at the forward station (x=2.59) in the hard-wall configuration*

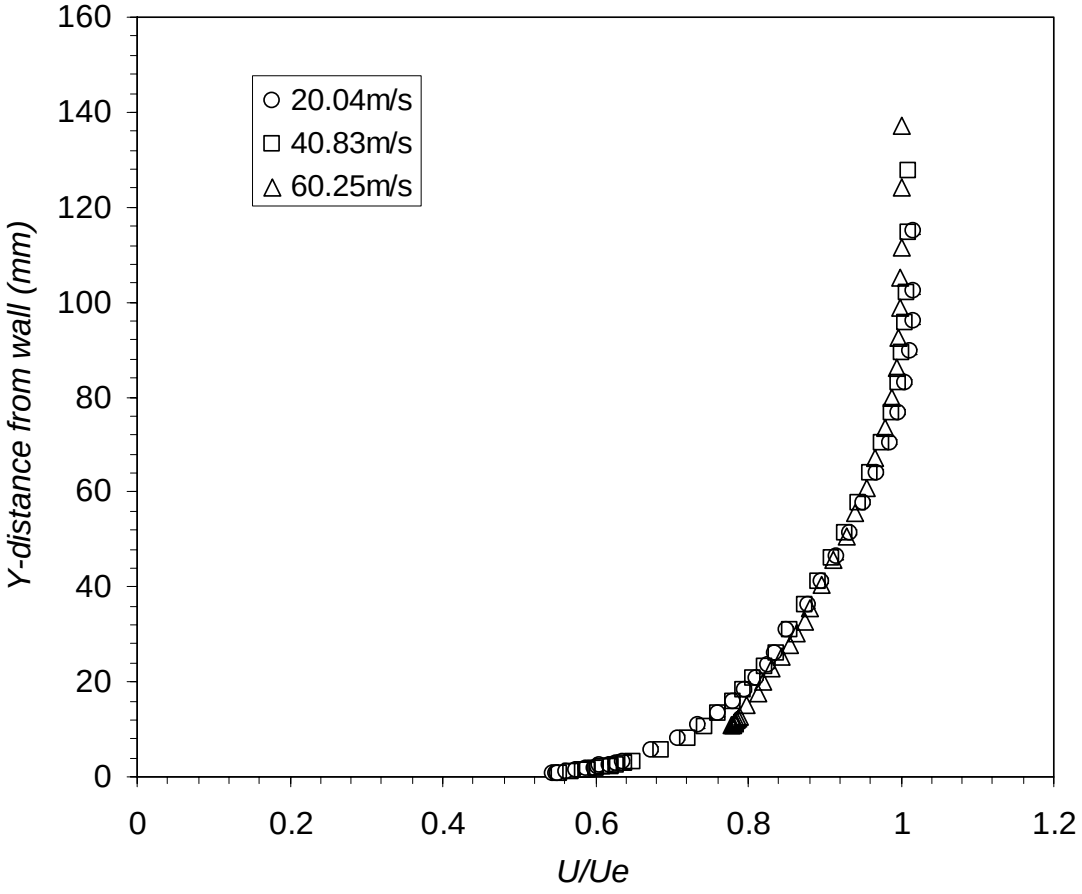

Figure 3-34. *Boundary layer mean velocity profiles measured at forward station (x=4.87) in the hard-wall configuration*

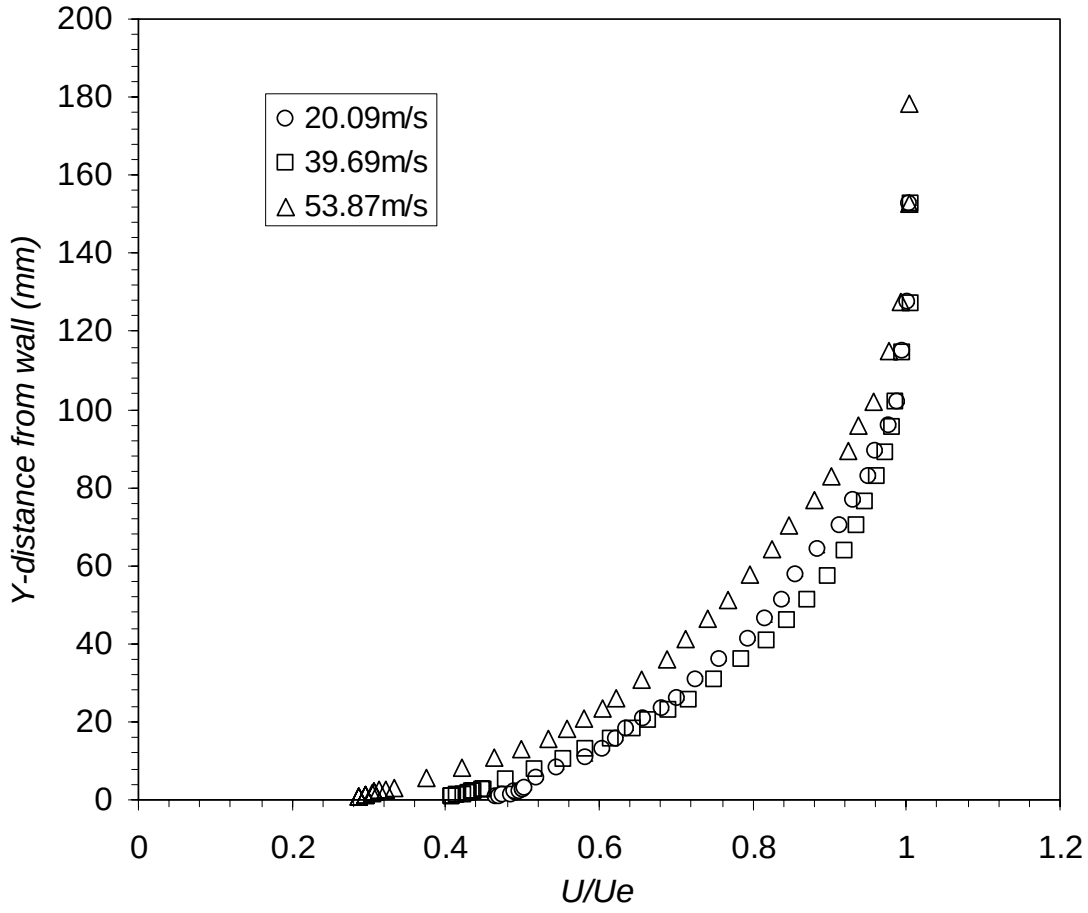

Figure 3-35. *Boundary layer mean velocity profiles measured at the aft station (x=4.87m) with the Kevlar acoustic treatment and the NACA 0012 airfoil installed at zero angle of attack.*

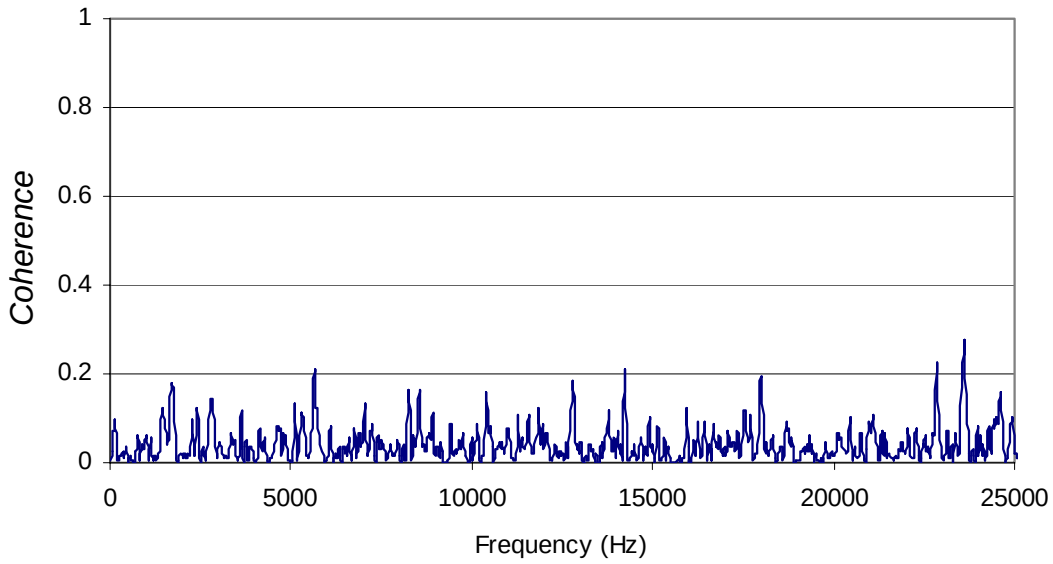

Figure 3-36. *Coherence between the vibration of the center of the starboard–side Kevlar window and in-flow microphone signal at the mid-section station for a flow speed of 58m/s.*

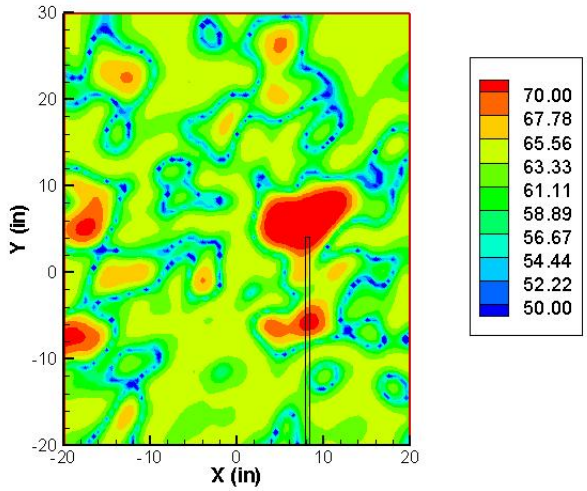

(a)

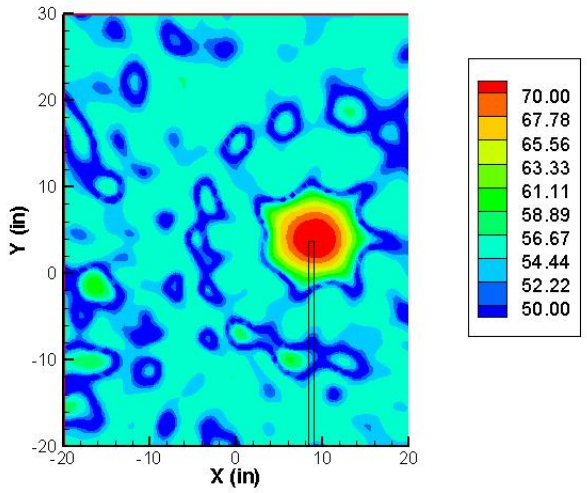

(b)

Figure 3-36. *Beamform maps at 9.7 kHz of monopole source (sound from a pipe inside the tunnel) at 57m/s (Mach 0.17) for a) hard walls and b) acoustically treated wind tunnel.*

4. RESULTS AND DISCUSSION – NACA 0012 AIRFOIL

Figure 4.1 shows the coordinate systems used in presenting the results of the NACA 0012 airfoil tests. The chord-aligned airfoil system (x,y) has its origin at the leading edge of the airfoil, that origin moving with the leading edge as the angle of attack α is varied. This system is used to present mean pressure distributions measured on the airfoil and to define the locations of the trailing edge boundary layer measurements. The tunnel fixed system (X,Y,Z) has its origin at the midspan of the leading edge when the airfoil is at zero angle of attack. This system is used for the wake and phased array measurements.

4.1 Behavior of the acoustic windows

The performance of the Kevlar windows was examined over a range of flow speeds and angles of attack. Measurements of the window deflection, vibration and of the relationship between fan speed and flow speed were made (an indicator of excessive drag) to judge their performance.

Figure 4-2 shows measurements made with the laser range finder of the static deflection of the center of the window to the suction side of the airfoil as a function of flow speed and airfoil angle of attack. At zero angle of attack the deflection remained small over the whole speed range, but increased significantly as the angle of attack of the airfoil was increased. It seemed very clear that the lower pressures generated over the suction side of the airfoil tended to suck the center of the window into the flow, producing this deflection. Indeed, we had the subjective sense that there was some air

was being drawn into the test section through the window – an observation that has some impact on the interference corrections discussed in the following section. While measurements were not made on the pressure side window we fully expect that it suffered similar deflections, but of opposite sign.

Figure 4-3 shows measurements of the vibration of the window at its center made using the laser vibrometer. The overall r.m.s. displacement of the suction-side Kevlar window is shown as a function of flow speed, and for various angles of attack. From this figure it can be seen that the rms displacements are very small indeed, confirming first hand observations that the windows remained stable and showed no significant flapping at all test conditions.

Table 4-1 includes a listing of the wind-tunnel fan speeds corresponding to different flow speeds and angles of angles of attack. These are plotted against each other and compared with the variation seen with the empty test section in figure 4-4. Although, there is some scatter in the data compared to the empty tests section (likely because of the large winter/summer difference in ambient conditions between these two tests) this plot shows that the airfoil does not have a dramatic impact on the fan speed required to produce a given flow speed. This implies that the overall drag of the tunnel circuit was not increased much by the presence of this very large model. This is an encouraging result because it implies not only well behaved flow over the airfoil but also well behaved flow over the Kevlar acoustic windows and treatment for these conditions.

4.2 Mean pressure distribution on the airfoil

Table 4-1 lists the cases for which the mean pressure distribution on the airfoil surface was measured. Measurements were made for chord Reynolds numbers between 1.9 and 4.3 million, and for geometric angles of attack of up to 15 degrees. Measurements were also made at negative angles of attack of -9 and -7 degrees to check for symmetry. For the -7 degree measurements the boundary layer fences were installed on the airfoil to examine their effect. No fences were used for any other measurements. Boundary layer trips (as described in chapter 2) were installed in all cases.

On of the main purposes of measuring these pressure distributions was to establish empirically the appropriate wind tunnel interference corrections for the Kevlar windows. In particular we were interested in seeing whether the interference correction could be characterized as a simple change in angle of attack, whether the interference corrections would remain a consistent fraction of the geometric angle of attack, and whether the magnitude of those corrections would be less than for a conventional open-jet configuration. To assess the effective angle of attack, and thus the correction, measured pressure distributions were compared with inviscid theory evaluated using an in-house code (the Vortex Panel Method Applet at http://www.engapplets.vt.edu/) and a 200-panel representation of the theoretical airfoil shape.

Measured and theoretical pressure distributions are plotted in figures 4-6 to 4-15 in terms of both chordwise distance x/c and edge-length s/c measured from the trailing edge in the clockwise direction (defined in figure 4-5). Plotting vs. s/c allows details of the pressure distribution around the leading edge to be revealed. Edge-length was determined from chordwise position using the theoretical NACA 0012 shape, which

implies a leading edge location of *s/c*=1.02. Pressures are plotted in terms of the coefficient

$$C_p = \frac{p - p_\infty}{p_{o\infty} - p_\infty} = \frac{p - p_\infty}{\frac{1}{2}\rho U_\infty^2}$$

where p is the local pressure, $p_{0\infty}$ and p_∞ are the reference freestream stagnation and static pressures and U_∞ is the free stream velocity.

Figure 4-6 shows the pressure distribution at zero degrees angle of attack. Plotting against *x/c* (figure 4-6a) the pressure distribution appears fairly symmetric at all Reynolds numbers and, indeed, it was this form of pressure distribution plot that was used to establish this orientation as the geometric zero angle of attack. At each Reynolds number two points between *x*/c=0.1 to 0.15 on the hatch-side of the airfoil (shaded symbols) stand away from the general trend, apparently because of the influence of the boundary layer trip installed at this station. In this form the measured pressure distributions appear to agree fairly well with theory for zero angle of attack. Plotted vs. edge length *s/c* (figure 4-6b and c) the measurements show surprisingly good consistency with theory in the vicinity of the leading edge, but some imperfections in symmetry further downstream. Specifically, pressure coefficients measured on the hatch side of the airfoil (indicated with the shaded symbols) are slightly lower than those on the opposite side at all Reynolds numbers, suggesting a small offset in the angle of attack.

The existence of such an offset (apparently about 0.2 degrees) seems to be confirmed in figures 4-14 and figure 4-15 which compare pressure distributions measured at +9 and -9, and +7 and -7, degrees angle of attack. Both plots show a slightly reduced loading for the negative angle of attack cases, consistent with the offset. Otherwise the distributions for positive and negative angles of attack are almost identical. Figure 4-15

also shows that the boundary layer fences had little or no discernable influence over these pressure distributions measured near midspan.

The overall variations in the pressure distribution with angle of attack and Reynolds number are visible in figures 4-6 through 4-13. The effects of angle of attack are, as one would expect, a rise in the magnitude of the peak negative pressure coefficient on the suction side of the airfoil, and a general flattening of the distribution on the pressure side. At the highest angle of attack (15 degrees, figure 4-13) the suction side pressure peak reaches a coefficient of -6, implying local flow velocities at the highest test speed greater than 140 m/s. There is no sign of stall at any angle of attack.

The theoretical pressure distributions plotted on top of these measurements indicate the effective angle of attack associated with each condition, at least to within the ¼-degree resolution at which the theoretical calculations were attempted. These plots clearly show that the interference can accurately be accounted for simply using an effective angle of attack. The magnitude of the correction is shown in figure 4-16 where effective angle of attack is plotted against geometric angle of attack. These data are also listed in table 4-1. The figure and table show that the effective angle correction is, as hoped, an almost constant fraction of the geometric angle. The constant of proportionality between the two is close to 0.72, implying a -28% correction. For an airfoil with a chord-length to tunnel with ratio c/h=0.5, as in the present case, the standard free jet interference correction suggested by Barlow *et al.* (1999) would be -44%. Lifting surface calculations by Brooks *et al.* (1980) suggest a correction of -50%. For a solid wall the correction would be close to +5%. We find, therefore, that the Kevlar windows do significantly decrease, but not eliminate, the open-jet interference correction. The

observed flow in through the Kevlar window on the suction side of the airfoil, and out on the opposite side, is believed to be responsible for most of the residual correction. Indeed, we believe that by controlling this mass flux (perhaps in the manner of Bernstein and Joppa, 1976) substantial further reductions in interference may be possible.

The measured pressure distributions were integrated to estimate the lift coefficient and pressure drag. To do this the distributions were first interpolated, in terms of edgelength and using a Hermite polynomial spline, to 1000 points evenly distributed around the airfoil contour. To improve the accuracy of the interpolation around the stagnation region (important for the pressure drag integration) a single data point, of unit pressure coefficient at the theoretically determined stagnation location, was added to the experimental data. Figure 4-17 shows a typical interpolated pressure distribution. Integrating the interpolation in terms of x and y yielded normal and axial force coefficients for the airfoil, which were then rotated using the effective angles of attack to obtain lift and drag coefficient C_l and C_d. These coefficients are plotted against geometric and effective angle of attack in figure 4-18. The lift coefficient shows the expected linear variation with a slope very close to 2π when the interference correction is accounted for. There are some slight effects of Reynolds number and some small, irregular departures from linearity, but we believe these are likely due to residual uncertainties in the setting of the angle of attack and associated with the large range of the pressure transducer used (±2.5p.s.i.) compared to measured range of surface pressures at lower speeds. Fortunately, both of these uncertainty sources are easy to reduce in future tests. The pressure drag estimates are quite likely dominated by uncertainty, but nevertheless are of

about the expected magnitude and show the qualitatively expected variation with angle of attack.

4.3 Trailing edge boundary layer properties

The flattened Pitot probe described in chapter 2 was used to measure boundary layer profiles at x/c=0.98 on both sides of the airfoil for angles of attack of 0, 3 and 9 degrees and for a range of Reynolds numbers with the boundary layer trips attached. Measurements were made 76mm above the midspan of the model (at Z/c=0.083, see figure 4-1) so as to be just clear of the section of airfoil surface disturbed by the hatch. The full test matrix is shown in table 4-2.

The original intention was to determine flow velocities from the measured Pitot pressures using the static pressure measured at the two ports on either side of the airfoil at x/c=0.98. However, after the test it was discovered that the static port on the side of the model opposite the hatch (usually the suction side) was blocked. As a result the pressure measured on the hatch side of the model at x/c=0.98 was used for the boundary layer profiles measured on both sides. As can be confirmed by examining the pressure distributions presented in the previous section, the static pressure difference across the airfoil this close to the trailing edge was very small, and likely within the measurement uncertainty.

Boundary layer velocity profiles from these measurements are presented in figures 4-19 through 4-21. Boundary layer thicknesses calculated from these profiles are listed in table 4-2 and plotted in figure 4-22 through 4-24 against effective angle of attack. Note that the profiles were actually measured perpendicular to the tunnel

centerline (in the *Y* direction, see figure 4-1) as opposed to perpendicular to the airfoil surface. The boundary layer thicknesses have been corrected for this by multiplying by the cosine of the angle between these two directions. Figures 4-22 through 4-24 include a comparison with curves suggested by Brooks *et al.* (1989) for boundary layer thicknesses on the tripped NACA 0012. These formulae were determined by curve fitting trailing edge boundary layer measurements that Brooks *et al.* had made as part of their trailing-edge noise study. For the Reynolds number range of the present study, they give the boundary layer thicknesses as zero angle of attack as

$$\delta_o / c = 10^{[1.892 - 0.9045 \log \mathrm{Re} + 0.0596 (\log \mathrm{Re})^2]}$$
$$\delta_o^* / c = 10^{[3.411 - 1.5397 \log \mathrm{Re} + 0.1059 (\log \mathrm{Re})^2]}$$
$$\theta / c = 10^{[0.5578 - 0.7079 \log \mathrm{Re} + 0.0404 (\log \mathrm{Re})^2]}$$

and the variations with angle of attack, relative to these values, as

$$\delta / \delta_o = 10^{[-0.04175 \alpha_{eff} + 0.00106 \alpha_{eff}^2]}$$
$$\delta^* / \delta_o^* = 10^{[-0.0432 \alpha_{eff} + 0.00113 \alpha_{eff}^2]}$$
$$\theta / \theta_o = 10^{[-0.04508 \alpha_{eff} + 0.000873 \alpha_{eff}^2]}$$

for the pressure side and

$$\delta / \delta_o = \begin{cases} 10^{0.0311 \alpha_{eff}} & (0 < \alpha_{eff} < 5^o) \\ 0.3468 \times 10^{0.1231 \alpha_{eff}} & (5^o < \alpha_{eff} < 12.5^o) \end{cases}$$
$$\delta^* / \delta_o^* = \begin{cases} 10^{0.0679 \alpha_{eff}} & (0 < \alpha_{eff} < 5^o) \\ 0.3810 \times 10^{0.1516 \alpha_{eff}} & (5^o < \alpha_{eff} < 12.5^o) \end{cases}$$
$$\theta / \theta_o = \begin{cases} 10^{0.0559 \alpha_{eff}} & (0 < \alpha_{eff} < 5^o) \\ 0.6984 \times 10^{0.0869 \alpha_{eff}} & (5^o < \alpha_{eff} < 12.5^o) \end{cases}$$

for the suction side.

The boundary layer profiles (figures 4-19 to 4-21) show behavior closely consistent with expectations based on Reynolds number and pressure gradients. The pressure gradients experienced by these boundary layers upstream of the trailing edge can be seen directly in figures 4-6, 4-8 and 4-11. On the pressure side of the airfoil the boundary layer profiles become thinner and fuller as the angle of attack is increased. This is because the adverse pressure gradient experienced along most of the airfoil surface at zero angle of attack (figure 4-6) is reduced at 3 degrees (figure 4-8) and almost completely eliminated at 9 degrees (figure 4-11). Interestingly, even at 9 degrees there is no region of favorable pressure gradient on the pressure side of the foil. On the suction side of the airfoil the same change in angle of attack produces a substantial steepening of the adverse pressure gradient, and predictably the boundary layer at the trailing edge becomes thicker and more inflected. In all cases the effect of increase in Reynolds is a slight reduction in thickness and filling out of the profile.

These effects are reflected in the boundary layer thicknesses which show trends with Reynolds number and angle of attack that appear to agree well with those implied by the formulae of Brooks *et al.* (1989). The measured boundary layers however are consistently about 50% thinner than those implied by these formulae. The reason, apparently, is the heavy tripping of the boundary layer in their case, which was accomplished using multiple strips of roughness from the leading edge to the 20% chord station. Indeed, if we replace the relations that Brooks *et al.* give for the thicknesses of a tripped boundary layer at zero angle attack with those they recommend for an untripped boundary layer

$$\delta_o / c = 10^{[1.659 - 0.9045 \log \mathrm{Re} + 0.0596 (\log \mathrm{Re})^2]}$$

$$\delta_o^* / c = 10^{[3.0187 - 1.5397 \log \mathrm{Re} + 0.1059 (\log \mathrm{Re})^2]}$$

$$\theta / c = 10^{[0.2021 - 0.7079 \log \mathrm{Re} + 0.0404 (\log \mathrm{Re})^2]}$$

while maintaining the rest of the formulae set for a tripped boundary layer, the parameters they predict fall much close to the present data at all the conditions measured, figures 4-25 to 4-27. We believe this is not because the present trips were ineffective, but simply because the present trips were sized to initiate transition but not otherwise significantly increase the boundary layer thickness or airfoil drag.

The viscous drag coefficient on the airfoil can be estimated from twice the sum of the two momentum thicknesses (suction and pressure) normalized on chord at each condition, see table 4-2. At Re=3.3×10^6 the resulting values of 0.0107 at 0^o angle of attack and of attack and 0.0129 at 9^o (6.5^o effective) are close (within .001) to those given for the total drag on a tripped NACA 0012 at Re=6×10^6 by Abbott and von Doenhoff (1959).

4.4 Wake measurements

Stagnation pressure, static pressure and mean velocity profiles were measured through the airfoil wake at *X/c*=2.5, 1.5 chordlengths downstream of the airfoil trailing edge at zero angle of attack. Measurements were made over the ranges of Reynolds number and angle of attack listed in table 4-3. Profiles of the pressure coefficients and

velocity normalized on approach free stream are plotted in figures 4-28 to 4-30 against *Y* position measured from the tunnel centerline.

At zero degrees angle of attack (figure 4-28) the wake has the symmetric form one would expect with an axial velocity deficit of close to 10%. There is a slight shifting of the wake upward as the Reynolds number is increased. We are not sure why this happens, but the overall shift is small – roughly equivalent to a shift of about 0.3 degrees in the angle of the flow leaving the trailing edge. The static pressure coefficient C_p is constant across the wake, invariant with Reynolds number and slightly negative, presumably because of the acceleration in the test section flow due to blockage produced by the airfoil wake and the growth of the wind tunnel boundary layers. As the angle of attack is increased (figure 4-29 and 4-30), the wake shifts down and becomes wider. A slight negative static pressure gradient with *Y* also develops suggesting some residual curvature of the free stream as it recovers from its interaction with the airfoil.

We have used these data to estimate the total airfoil drag through a straightforward momentum balance. Consider the control volume shown in figure 4-31. The difference of the mass flowing into the volume on the left and flowing out on the right, per unit span, is $\int \rho U_\infty - \rho U \, dY$. This, of course, is the mass flow out per unit span of the sides of the volume which we assume occurs with an average *X* component of velocity of $\frac{1}{2}(U_\infty + U_e)$ where U_e is the potential flow velocity on the right hand face of the volume. With this, the net *X*-momentum flux out of the volume per unit span is $\rho\int U^2 - U_\infty^2 \, dY + \frac{1}{2}\rho(U_\infty + U_e)\int U_\infty - U \, dY$ and the *X*-component of the pressure force

on the volume per unit span is $\int p_\infty - p \, dY$ where p is the pressure on the right-hand face. The total drag force per unit span on the airfoil located in the volume is thus

$$d = \rho \int U_\infty^2 - U^2 - \tfrac{1}{2}(U_\infty + U_e)(U_\infty - U) - \frac{p - p_\infty}{\rho} dY$$

and thus the drag coefficient is

$$C_d = \int 2 - 2\frac{U^2}{U_\infty^2} - (1 + \frac{U_e}{U_\infty})(1 - \frac{U}{U_\infty}) - C_p \, d(Y/c)$$

in terms of the stagnation and static pressure coefficients measured on the downstream face C_{p0} and C_p this becomes

$$\begin{aligned} C_d &= \int 2 - 2(C_{p0} - C_p) - (1 + \sqrt{1 - C_p})(1 - \sqrt{C_{p0} - C_p}) - C_p \, d(Y/c) \\ &= \int 2 - 2C_{p0} + C_p - (1 + \sqrt{1 - C_p})(1 - \sqrt{C_{p0} - C_p}) \, d(Y/c) \end{aligned}$$

Since the integrand is zero outside the viscous wake, the limits of the integral can be taken as the edges of the wake. Results of this integration, listed in table 4-3 seem generally consistent with expectations (e.g. Abbott and von Doenhoff, 1959) and the viscous drag estimates of table 4-2, except for the highest Reynolds number case at 9 degrees angle of attack. We believe the low drag estimate is erroneous and associated with the offset of the static pressure profile visible in this case figure 4-30. Other uncertainties in these estimates and the wake profiles derive from the unfamiliarity with the flow (resulting in points not being concentrated in the wake centers) and some of the instrumentation – sources that would be eliminated in future tests.

4.5 Measurements of untripped trailing edge vortex shedding

While the focus of the aerodynamic study of the NACA 0012 airfoil was on the tripped case, some phased array measurements described below were made without the

trip attached. Without the trip, vortex shedding at the trailing edge might be expected at some conditions leading to an easily identifiable acoustic signature. To support these acoustic measurements a single hot wire probe was used to search for evidence of vortex shedding in the fluctuating velocity just downstream of the trailing edge. Table 4-4 shows the full test matrix and the hot-wire locations. Measurements were made within 2% chord of the trailing edge, near the pressure-side of the wake (at slightly positive *y* for these negative angles of attack). At each location the velocity spectrum was measured, processed and then examined for the distinct peaks that would be produced by regular shedding.

Figure 4-32 shows three example spectra showing clear evidence of vortex shedding. Indeed two of these spectra show harmonics of the shedding frequency, an indicator of the non-sinusoidal nature of the associated velocity fluctuations. The dimensional frequencies of the shedding peaks and their harmonics, where they were observed are listed in table 4-4. The Reynolds number range over which shedding occurs clearly increases with angle of attack. For zero degrees no evidence of shedding was observed. For -3 and -7 degrees shedding was observed up to chord Reynolds numbers of 860000 and 2780000 respectively. For -9 degrees shedding was seen at thee highest Reynolds number tested of 3210000. The harmonic content also increases with angle of attack, with at least two peaks being visible for all the shedding cases at -9 degrees.

The fundamental shedding frequencies all lie between 92 and 796Hz, the frequency increasing some with flow speed. These frequencies can be used to infer the primary mechanism controlling the shedding. If the shedding were being stimulated by the acoustic feedback to the laminar part of the airfoil boundary layer we would expect to

see the frequency to roughly scale (at this low Mach number) on the sound speed and a distance related to the chord length. For purely aerodynamic shedding we would expect to see the Strouhal number based on the effective trailing edge size and the flow velocity to be nearly constant, and about 0.2. We can compute the effective trailing edge size Δ^* by adding the displacement thicknesses of the pressure and suction side boundary layers to the trailing edge thickness of 2.35mm. Since the displacement thicknesses of the untripped boundary layers were not measured, we used the formulae given by Brooks *et al.* (1989) to estimate them. Table 4-4 shows that the shedding frequencies normalized on Δ^* and U_∞ are almost constant at around 0.2 for all conditions. Conversely, a similar normalization using the sound speed and chordlength yields values that vary by an order of magnitude from case to case. Acoustic feedback is clearly not part of the shedding being observed here.

4.6 Phased array measurements

In this section measurements made using the 63-microphone phased array system (described in section 2.6.2) of the NACA0012 airfoil model are presented. The experimental setup for the aeroacoustic measurements is first described and then the aeroacoustic measurements are explained. These measurements are divided in two sets - measurements of the NACA0012 model with untripped boundary layer and measurements with the tripped boundary layer. In each set a few representative cases are presented and discussed. The beamform maps for all the tested cases are included in appendix 1.

4.6.1 Experimental Setup

Figure 4-33 shows a schematic drawing of the experimental setup used for the aeroacoustic measurements. This figure shows the position of the NACA0012 airfoil with respect to the phased array and the tensioned Kevlar windows. Figure 2-27 shows a picture of the NACA0012 mounted in the test section as well as the tensioned Kevlar windows. The phased array was mounted parallel to the direction of the flow, 0.41m from the tensioned Kevlar, as shown in figures 4-33 and 4-34.

Due to the symmetry of the airfoil cross section, data from both pressure and suction sides was acquired with the phased array fixed at this location. To this end measurements were made for both positive and negative angle of attack ranging from -15 to +15 degrees. To minimize the presence of extraneous noise sources generated by air flow into the test section, all gaps and orifices were sealed with aluminum tape as described in chapter 2.

For every measurement, 200 records of 16384 points each were acquired at a sampling frequency of 25600Hz using the Agilent E1432 data acquisition system with anti-aliasing filters.

4.6.2 Test matrix and data analysis

Table 4-5 presents the test matrix of the measurements performed on the NACA0012 model. This table shows the conditions at which the various configurations were tested. The geometric angle of attack, α, was varied from -15 to 15 degrees, the negative angles of attack giving the phased array a view of the pressure side of the airfoil. For geometric angles of attack of -1.5, 0 and 1.5 degrees angle of attack data was

acquired at four speeds: 30.8, 38.5, 54.2, and 70 m/s, which correspond to 0.09, 0.11, 0.16, and 0.2 Mach number, respectively. However, for angles of attack with magnitudes greater that 1.5-degrees, only the first three speeds were tested. This was due to a combination of blockage caused by the airfoil at higher angles of attack and the wear on the prototype acoustic treatment (particularly the tape used to cover the joints between acoustic absorbers).

The second step of the phased array measurements is associated with the processing of the data through the use of a beamforming algorithm. This data processing was carried out in the frequency domain. To this end, the 16384-point fast Fourier Transform, FFT, of each record of every microphone was obtained. These Fourier Transforms were then used to compute the Cross Spectral Matrix, CSM. To reduce the level of microphone self noise, the diagonal elements of this matrix were removed.

The beamform output, for each point in the grid is given by equation (1). For a detailed derivation of this expressions see Mueller (2002).

$$b(x_b) = \vec{w}^*(x_b) A \vec{w}(x_b) \tag{1}$$

In this equation A is the Cross Spectral Matrix, and $\vec{w}(x_b)$ is the microphone weight vector. The function of these weight vectors is to "steer" mathematically the array to the grid location x_b. Therefore, $\vec{w}(x_b)$ are also known as steering vectors, and are given by

$$\vec{w}(x_b) = \frac{\vec{C}(x_b)}{\left\| \vec{C}(x_b) \right\|}, \tag{2}$$

where $\vec{C}(x_b)$ are the propagation factors that model the propagation of acoustic rays from the source location, x_S, to the *n-th* microphone. This propagation factors have the form

$$C_n(x_S) = \frac{e^{-i\omega\sigma(x_n - x_S)}}{D(x_n, x_S)}, \tag{3}$$

where $\sigma(x_n - x_S)$ is the time required by the acoustic ray to travel from x_S to the microphone n, and $D(x_n, x_S)$ is a magnitude factor. When the distance from the source location to the array is large compared with the dimensions of the array, the variation of $D(x_n, x_S)$ will not be significant and the magnitude factor can be set equal to 1. However, this was not the case for the present test and the magnitude factors were taken into account in the computation of the propagation factors. Assuming spherical spreading of the acoustic waves, the magnitude factor is given by $4\pi r^2$, where r is the distance from the source location x_S to the *n-th* microphone.

Therefore, the beamform output is given for each point in the grid. However, a quantitative integrated result is also desired. This result is obtained through integration of the beamform output over the volume of interest that could include the entire model or only part of it. In this integration, the beamform output at each point in the grid is multiplied by the Point Spread Function, which was defined in section 2.6 as the response of the phased array to a point source. Note that this process is analogous to Green's Method. However, unlike the delta function used in the derivation of Green's functions, the PSF has sidelobes that would also enter in the integration process. To prevent sidelobes from entering the integration, all beamform outputs less than a certain threshold are excluded. For this process to be effective, the threshold should be higher than the maximum sidelobe peak level. The value of the threshold is commonly known as Cut-off level.

In this report, beamform maps of the trailing edge noise measurements will be presented in 1/3-octave and 1/12-octave frequency bands. All beamform maps will correspond to a plane parallel to the phased array, passing through the trailing edge. Each map is 2.56 m x 1.85 m, and the grid resolution is 2.54 cm. The integrated spectra of these beamform maps will be presented in the form of 1/3-octave band Sound Pressure Level. To compute these integrated spectra, three volumes of integration were considered. These volumes are shown in figure 4-35 and enclose the full, ¾ and ½ span-wise length of trailing edge region, all centered at the mid-span.

It is worthwhile to mention that neither the beamform maps nor the integrated spectra presented in this report are calibrated. That is, the levels on the maps and spectra do not necessarily correspond to the actual noise levels. However, these results can be compared between them to determine relative values between the plots. It should also be mentioned that for future work, a calibration procedure will be implemented so as to have actual noise levels in the beamforming results.

4.6.3 Untripped NACA0012 Trailing Edge Noise Measurements

Trailing edge noise, predominantly from the coherent vortex shedding observed with the hot-wire probe, was measured. Measurements here are presented for a typical test configuration to show the most important aspects of the aeroacoustic measurements. Specifically we examine the -7 degree angle of attack case (-5 degrees effective) for a flow speed of 38.5m/s (Mach 0.11). This configuration corresponds to case 17 of the hot-wire measurements (see table 4-3) which indicated well-defined vortex shedding at around 583Hz. The complete set of untripped boundary layer trailing edge noise

measurements are presented in appendix 1. These results are presented in 1/12-octave bands from 323 Hz to 1218 Hz since the contribution from TE noise is dominant in this frequency range

Figure 4-36 shows the beamform maps in 1/3-octave bands from 315 to 4000 Hz for this case. The noise directly produced by the vortex shedding can be clearly seen in the 1/3 octave bands with center frequencies of 500 and 630 Hz, which are shown in figures 4-36d and 4-36e, respectively. Even though the contribution from the vortex shedding mechanism peaks in the frequency range between 445 and 707 Hz, the broad-band component of the spectrum can be identified in the beamform maps up to approximately 2000 Hz but at lower levels, as it is shown in figures 4-36f, g, h and i. These results clearly demonstrate a capability to detect and measure trailing edge noise.

The acoustic maps at the lower frequency bands also reveal the presence of other noise sources in the tunnel both upstream and downstream of the model. Furthermore, it appears that the noise emanating from the downstream section is stronger than from the upstream section. The implication of these results is two fold: (a) the tensioned Kevlar wall concept was effective at reducing the test section boundary layer noise and (b) the acoustic characteristics could be further improved by reduce the tunnel noise present in the rest of the circuit, i.e. fan noise, turning vanes, etc.

Figure 4-37 presents the same data in terms of beamform maps on 1/12-octave bands. From this figure it can be seen that the contribution from the vortex shedding is dominant in the 1/12-octave bands with center frequencies of 542.5 and 574.7 Hz, as shown in figures 4-37f and g, respectively. Furthermore, the broadband component of noise can be identified in other frequency bands up to approximately 1990 Hz.

The integrated 1/3-octave band Sound Pressure Level for the present configuration is presented in figure 4-38 for three different cut-off levels. The integration was carried out over a volume enclosing the full span-wise length of the trailing edge region. This figure reveals both the tonal and broadband behavior trailing edge noise. The background integrated spectrum is also included in this figure as a reference, i.e. obtained from beamforming the empty tunnel with flow. It is worthwhile to mention that this shedding frequency agrees with predictions using the method of Brooks *et al.* (1989).

The dependence of the radiated sound on the flow speed is shown in figure 4-39 for 3 flow speeds corresponding to cases 16, 17 and 18 in table 4-3. At the two lowest speeds the peak frequency in the radiated sound spectra compare well with the frequencies of vortex shedding seen in the hot-wire data. At the highest flow speed, no shedding could be discerned in the hot-wire signal but interestingly trailing edge noise is still visible in the spectrum. Consistent with this there appears to be a general trend to a more broadband noise spectrum as the flow speed increases.

In figure 4-40, sound spectra for the airfoil at three different angles of attack are plotted. From this figure it can be seen that as the angle of attack increases, the SPL increases significantly and the radiated sound displays a strong tonal behavior.

4.6.4 Tripped NACA0012 Trailing Edge Noise Measurements

In this section, the measurements of the sound produced by the tripped airfoil boundary layers as they encounter the discontinuity at the trailing edge are presented. As in the previous section, a typical test configuration will be used to show the most important aspects of the aeroacoustic measurements. First we examine the -7 degree

angle of attack case (-5 degrees effective) for a flow speed of 38.5m/s (Mach 0.11), for which the pressure side of the airfoil was facing the phased array. Then we examine the +7 degree angle of attack case (±5 degrees effective) at the same flow speed to look at noise measurements on the side of the airfoil.

Figure 4-41 shows the beamform maps on 1/3-octave bands for the airfoil at -7 degrees angle of attack (phased array facing the pressure side) at 38m/s (M=0.11). In these acoustic maps, the presence of trailing edge noise is not as clear as in the untripped airfoil case. However, there is some indication of noise from the trailing edge in the 406 and 512 Hz 1/3-octave frequency bands as shown in Figures 4-41b and c, respectively.

Figure 4-42 shows the same data in terms of beamform maps on 1/12-octave bands. With this finer-scale frequency resolution the trailing edge noise can be identified in the bands with center frequencies of 430.5 and 456.1 Hz, as shown in figures 4-42b and c, respectively. Figure 4-42 also reveals the presence of extraneous noise sources upstream and downstream the airfoil model. Having treated acoustically the test section, this extraneous noise sources are attributed to other components of the tunnel circuit, particularly the fan (see discussion of in-flow noise measurements in chapter 3). Unfortunately, the contribution from these extraneous noise sources is significant in the low-frequency end of the spectrum, i.e. below 900 Hz, which coincides with the frequency range of interest for trailing edge noise measurements. Nevertheless, in spite of the presence of these extraneous noise sources, trailing edge noise was identified by virtue of the phased array beamforming algorithm that has the ability to “see” below the background noise.

The results also show that the level of the trailing edge noise is greater at the airfoil mid-span. Therefore, 1/3-octave integrated SPLs with a 3 dB cut-off level were obtained for three different volumes enclosing the full, ¾, and ½ span-wise length of the trailing edge region, as was explained earlier. These spectra are presented in figure 4-43. It can be seen that the noise levels for the half-span volume are higher that the levels for the full-span volume. Considering that the regions where the spanwise ends of the airfoil contact the tunnel test section's ceiling and floor are further from representing a smooth transition; these regions can introduce extraneous noise sources that can interfere with trailing-edge noise. For this reason, the integration over a volume enclosing the mid half-span of the airfoil is different from that enclosing the full span.

To analyze the effect of the integration cut-off level, the SPLs integrated over a volume enclosing the center half-span of the airfoil at 3, 5, and 8 dB cut-off were obtained. These spectra are shown in figure 4-44 which shows that as the cut-off level is increased the spectral levels tend to increase. This effect is due to the fact that as the cut-off level is increased, more frequency components are taken into account in the integration, with the result of increased levels of SPL.

The effect of the flow speed on the overall measured sound level can be seen in figure 4-45. The spectra shown in this figure correspond to the airfoil kept fixed at -7 degrees angle of attack, and the flow speed varied from 30 to 54.2m/s. As expected, figure 4-45 shows that as the flow speed is increased, the SPLs also increase. Furthermore, it was found that the scaling of these spectra on the flow speed is approximately on the order of M^5, as can be seen from figure 4-46 where the spectral levels have been normalized on M^5. This scaling approach is in agreement with the

studies of Brooks *et al.* (1989), who found that the flow speed dependence of SPL is the most sensitive parameter. However, in the present case this data undoubtedly contains some contribution from background noise levels.

To study the effect of angle of attack on the radiated sound, the integrated SPLs at four angles of attack maintaining all other parameters constant, is plotted in figure 4-47. This figure shows that as the angle of attack is varied, the frequency at which the spectral peaks in the measured noise occurs, remain unchanged. Nevertheless, there is a change in the spectrum in the frequency range between 900 and 2000 Hz for the airfoil at 15-degrees angle of attack, indicating a measure of trailing edge noise contribution.

Figure 4-48 shows beamform maps in 1/3-octave bands for the airfoil at +7 degrees angle of attack and the phased array now facing the suction side. From this figure there is some evidence of trailing edge noise in the frequency bands ranging from 362 Hz to 456 Hz and from 456 Hz to 575 Hz, as shown in figures 4-48b and c, respectively. Alternatively, figure 4-49 shows the beamform maps in 1/12-octave bands. From this figure, there is some evidence of trailing edge noise in the frequency bands ranging from 373 Hz to 395 Hz and 395 Hz to 418 Hz, as shown in figures 4-49b and c, respectively.

Following the same rationale used for the data obtained with the array on the pressure side, the 1/3-octave band SPLs of the airfoil at 7-degrees angle of attack was integrated over a volume enclosing ½-span length of the airfoil. These spectra are shown in figure 4-50. From this figure it can be seen that as the flow speed increases, the SPLs also increase. The spectra of figure 4-50 were scaled on M^5, and are presented in figure 4-51. The dependence of the SPL on the angle of attack is shown in figure 4-52. From this figure it can be seen that as the angle of attack is increased, the levels of the spectrum

increases, presumably indicating a significant trailing edge noise component. Note that this flow speed dependence is different from that observed at the pressure side where the peak levels remain approximately unchanged as the flow speed is increased.

Case	Angle of attack, α, deg.	U_∞	Chord Re	Fan r.p.m.	Effective angle of attack, α_{eff}, deg.	C_l	$C_d\|_{press}$
1	0	37.4	2339000	283	0	0.023	0.007
2	0	30.6	1916000	283	0	0.019	0.007
3	0	53.4	3314000	401	0	0.020	0.007
4	1.5	30.5	1925000	236	1	0.105	0.008
5	1.5	38.2	2391000	295	1	0.144	0.006
6	1.5	53.4	3320000	407	1	0.127	0.006
7	1.5	68.8	4251000	517	1	0.122	0.006
8	3	30.5	1920000	236	2.25	0.196	0.005
9	3	38.3	2407000	300	2.25	0.255	0.007
10	3	53.2	3348000	415	2.25	0.247	0.007
11	3	68.4	4269000	526	2.25	0.255	0.008
12	5	30.4	1928000		3.5	0.407	0.005
13	5	38.0	2397000		3.5	0.381	0.001
14	5	53.7	3351000	425	3.5	0.400	0.005
15	7	31.0	1955000	254	5	0.568	0.004
16	7	37.9	2390000	312	5	0.563	0.005
17	7	53.5	3352000	440	5	0.555	0.007
18	9	30.5	1920000	257	6.5	0.738	0.004
19	9	37.9	2387000	322	6.5	0.765	0.005
20	9	53.0	3322000	452	6.5	0.763	0.008
21	11	30.4	1922000	259	7.75	0.896	0.009
22	11	38.3	2405000	329	7.75	0.884	0.009
23	11	53.3	3333000	460	7.75	0.878	0.010
24	15	30.4	1906000	273	11	1.163	0.013
25	15	38.2	2381000	346	11	1.181	0.020
26	15	53.8	3304000	489	11	1.185	0.028
27	-9	54.2	3320000	447	-6.5	-0.702	0.023
28	-7	53.2	3190000	431	-5	-0.511	0.015

[1]Boundary layer fences installed

Table 4-1 *Test matrix for the NACA 0012 surface pressure measurements.*

Pressure (or hatch) side								
Angle of attack, deg	Flow speed (m/s)	Chord Re	Effective angle of attack, deg.	δ_{99} (mm)	δ^* (mm)	θ (mm)	θ/c	$C_d\|_{\text{visc}}$
0	30.8	1863943	0	17.23	3.98	2.42	0.0026	0.0123
0	38.5	2314731	0	17.33	4.22	2.58	0.0028	0.0121
0	54.0	3219847	0	17.23	3.65	2.32	0.0025	0.0107
3	30.8	1873333	2.25	16.84	3.42	2.25	0.0025	0.0122
3	38.6	2312658	2.25	16.84	3.30	2.20	0.0024	0.0104
3	54.1	3217399	2.25	16.94	3.73	2.32	0.0025	0.0117
9	30.7	1887587	6.5	12.50	2.06	1.45	0.0016	0.0141
9	38.4	2332681	6.5	13.00	2.15	1.50	0.0016	0.0140
9	53.9	3239953	6.5	11.90	1.95	1.30	0.0014	0.0129
Suction (or opposite) side								
Angle of attack, deg	Flow speed (m/s)	Chord Re	Effective angle of attack, deg.	δ_{99} (mm)	δ^* (mm)	θ (mm)	θ/c	
0	30.1	1917805	0	20.80	5.19	3.21	0.0035	
0	38.1	2366917	0	23.27	4.52	2.94	0.0032	
0	53.4	3306578	0	17.23	3.92	2.55	0.0028	
3	30.5	1913936	2.25	19.14	5.76	3.33	0.0036	
3	38.1	2383258	2.25	19.14	4.80	2.54	0.0028	
3	53.8	3284040	2.25	22.38	5.13	3.05	0.0033	
9	30.6	1902050	6.5	31.56	11.27	4.98	0.0054	
9	38.2	2363745	6.5	29.93	10.18	4.88	0.0053	
9	53.5	3271071	6.5	27.73	8.92	4.60	0.0050	

Table 4-2 *Test matrix for the NACA 0012 trailing edge boundary layer measurements at x/c=0.98.*

Case	Angle of attack, deg.	Flow speed (m/s)	Chord Re	Effective angle of attack, deg.	C_d
1	0	30.6	1859000	0	0.0143
2	0	38.3	2344000	0	0.0159
3	0	53.5	3310000	0	0.0145
4	3	30.5	1898000	2.25	0.0111
5	3	38.1	2387000	2.25	0.0146
6	3	53.3	3337000	2.25	0.0111
7	9	30.5	1909000	6.5	0.013
8	9	30.5	2387000	6.5	0.0134
9	9	38.0	3250000	6.5	0.0053

Table 4-3 *Test matrix for the NACA 0012 wake measurements at X/c=2.5.*

Case	Angle of Attack	U_∞	Chord Re	Effective Angle of Attack	*x/c*	*y/c*	Peak frequencies f_p, (Hz)			Peak frequencies $f_p\Delta^*/U_\infty$		
1	0	8.8	518000	0	1.012	0.015						
2	0	14.9	872000	0	1.012	0.015						
3	0	20.8	1214000	0	1.012	0.015						
4	0	31.1	1823000	0	1.012	0.015						
5	0	38.9	2274000	0	1.012	0.015						
6	0	47.0	2751000	0	1.012	0.015						
7	0	54.0	3159000	0	1.012	0.015						
8*	-3	8.8	518000	-2.25	1.022	0.015	177			0.289		
9	-3	14.7	863000	-2.25	1.022	0.015	311			0.274		
10	-3	21.2	1239000	-2.25	1.022	0.015						
11	-3	31.0	1815000	-2.25	1.022	0.015						
12	-3	38.6	2261000	-2.25	1.022	0.015						
13	-7	9.0	542000	-5	1.012	0.015	92			0.173		
14	-7	15.1	905000	-5	1.012	0.015	178	356		0.179	0.358	
15*	-7	20.7	1243000	-5	1.012	0.015	291	504		0.202	0.349	
16	-7	30.6	1836000	-5	1.012	0.015	412			0.182		
17	-7	38.6	2319000	-5	1.012	0.015	583			0.198		
18	-7	46.2	2775000	-5	1.012	0.015	688			0.191		
19	-7	53.3	3204000	-5	1.012	0.015						
20	-9	20.8	1243000	-6.5	1.015	0.008						
21*	-9	30.8	1839000	-6.5	1.015	0.008	477	841	1234	0.234	0.412	0.604
22	-9	38.5	2294000	-6.5	1.015	0.008	573	1126		0.218	0.429	
23	-9	46.3	2763000	-6.5	1.015	0.008	700	1327		0.216	0.410	
24	-9	53.9	3214000	-6.5	1.015	0.008	796	1509		0.208	0.394	

Table 4-4 *Test matrix for velocity spectra measured just downstream of the trailing edge of the NACA 0012 airfoil without boundary layer trip.*

Run Number	Angle of Attack		Phased Array side w.r.t to airfoil	Boundary Layer type	Flow Speed m/s	Mach Number	Chord Reynolds Number
	Geometric (deg)	Effective (deg)					
1	0	0	Pressure	Tripped	30.82	0.09	1879000
2	0	0	Pressure	Tripped	38.48	0.11	2346000
3	0	0	Pressure	Tripped	54.15	0.16	3301000
4	0	0	Pressure	Tripped	69.95	0.20	4264000
5	-1.5	-1	Pressure	Tripped	30.89	0.09	1883000
6	-1.5	-1	Pressure	Tripped	38.66	0.11	2357000
7	-1.5	-1	Pressure	Tripped	54.37	0.16	3315000
8	-1.5	-1	Pressure	Tripped	70.14	0.20	4276000
9	-3	-2.25	Pressure	Tripped	31.21	0.09	1902000
10	-3	-2.25	Pressure	Tripped	38.99	0.11	2377000
11	-3	-2.25	Pressure	Tripped	54.84	0.16	3343000
12	-5	-3.5	Pressure	Tripped	31.21	0.09	1903000
13	-5	-3.5	Pressure	Tripped	39.06	0.11	2381000
14	-5	-3.5	Pressure	Tripped	54.79	0.16	3340000
15	-7	-5	Pressure	Tripped	31.18	0.09	1901000
16	-7	-5	Pressure	Tripped	39.14	0.11	2386000
17	-7	-5	Pressure	Tripped	54.72	0.16	3336000
18	-9	-6.5	Pressure	Tripped	31.18	0.09	1901000
19	-9	-6.5	Pressure	Tripped	39.02	0.11	2379000
20	-9	-6.5	Pressure	Tripped	54.73	0.16	3337000
21	-11	-7.75	Pressure	Tripped	31.18	0.09	1901000
22	-11	-7.75	Pressure	Tripped	38.99	0.11	2377000
23	-11	-7.75	Pressure	Tripped	54.69	0.16	3334000
24	-15	-11	Pressure	Tripped	31.15	0.09	1899000
25	-15	-11	Pressure	Tripped	38.95	0.11	2374000
26	-15	-11	Pressure	Tripped	54.69	0.16	3334000
27	15	11	Suction	Tripped	30.85	0.09	1880000
28	15	11	Suction	Tripped	38.69	0.11	2358000
29	15	11	Suction	Tripped	54.23	0.16	3306000

Table 4-5 *Test matrix for trailing edge noise measurements made with the 63 microphone phased array (continued on following page).*

Run Number	Angle of Attack		Phased Array side w.r.t to airfoil	Boundary Layer type	Flow Speed m/s	Mach Number	Chord Reynolds Number
	Geometric (deg)	Effective (deg)					
30	11	7.75	Suction	Tripped	30.98	0.09	1889000
31	11	7.75	Suction	Tripped	38.87	0.11	2370000
32	11	7.75	Suction	Tripped	54.63	0.16	3330000
33	9	6.5	Suction	Tripped	31.09	0.09	1895000
34	9	6.5	Suction	Tripped	38.87	0.11	2370000
35	9	6.5	Suction	Tripped	54.58	0.16	3327000
36	7	5	Suction	Tripped	30.88	0.09	1883000
37	7	5	Suction	Tripped	38.99	0.11	2377000
38	7	5	Suction	Tripped	54.58	0.16	3327000
39	5	3.5	Suction	Tripped	31.09	0.09	1895000
40	5	3.5	Suction	Tripped	38.87	0.11	2370000
41	5	3.5	Suction	Tripped	54.58	0.16	3327000
42	3	2.25	Suction	Tripped	30.92	0.09	1885000
43	3	2.25	Suction	Tripped	38.84	0.11	2367000
44	3	2.25	Suction	Tripped	54.49	0.16	3322000
45	1.5	1	Suction	Tripped	31.03	0.09	1892000
46	1.5	1	Suction	Tripped	38.80	0.11	2365000
47	1.5	1	Suction	Tripped	54.44	0.16	3318000
48	1.5	1	Suction	Tripped	70.36	0.21	4289000
49	-3	-2.25	Pressure	Untripped	30.86	0.09	1881000
50	-3	-2.25	Pressure	Untripped	38.77	0.11	2363000
51	-7	-5	Pressure	Untripped	31.00	0.09	1890000
52	-7	-5	Pressure	Untripped	38.76	0.11	2363000
53	-7	-5	Pressure	Untripped	54.37	0.16	3315000
54	-9	-6.5	Pressure	Untripped	30.98	0.09	1888000
55	-9	-6.5	Pressure	Untripped	38.84	0.11	2368000
56	-7	-5	Pressure	Untripped	53.92	0.16	3287000

Table 4-5 *Test matrix for trailing edge noise measurements made with the 63 microphone phased array (completed).*

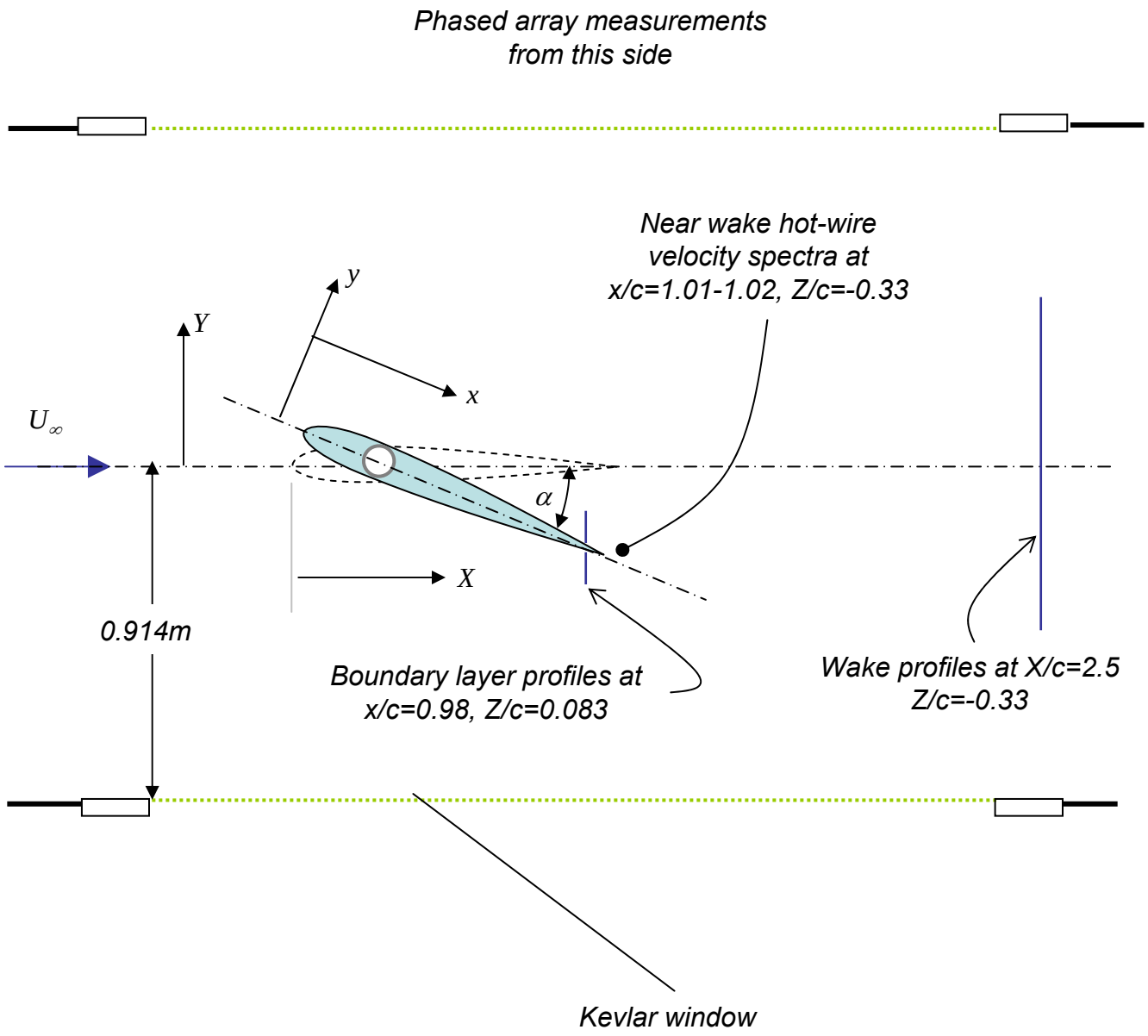

Figure 4-1. *Measurement locations and coordinate systems for the NACA 0012 test as seen in plan view. Z coordinate measured from center-span out of the paper*

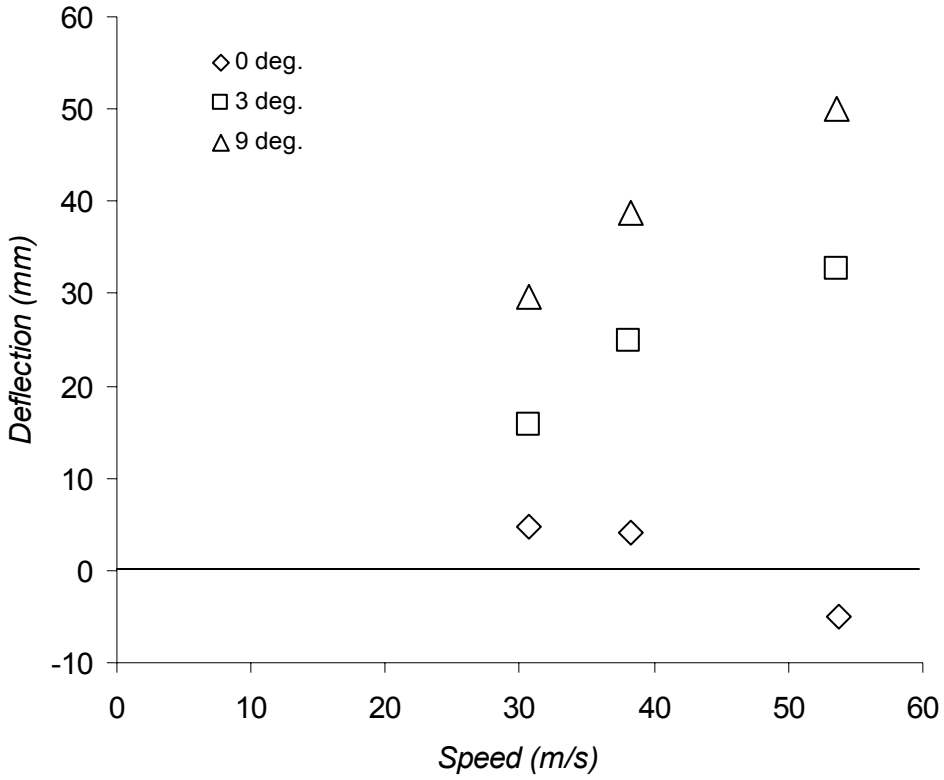

Figure 4-2. *Deflection of the center of suction-side Kevlar acoustic window with flow speed and model angle of attack. Positive deflection is into the wind tunnel test section.*

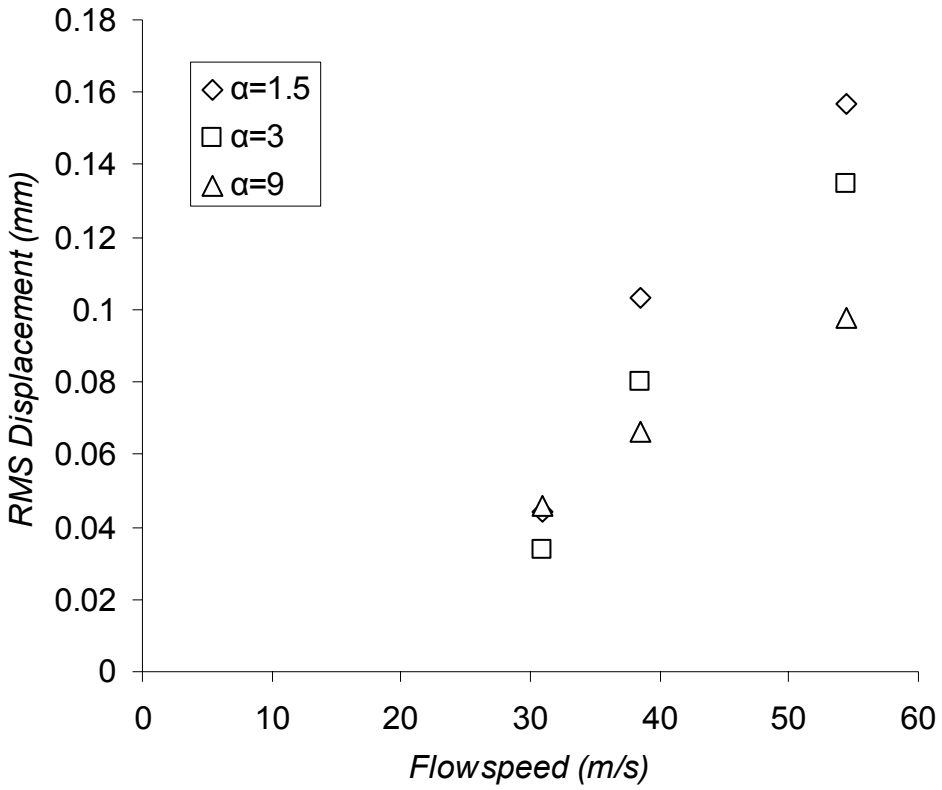

Figure 4-3. *RMS deflection of the center of suction-side Kevlar acoustic window with flow speed and model angle of attack measured using the laser vibrometer.*

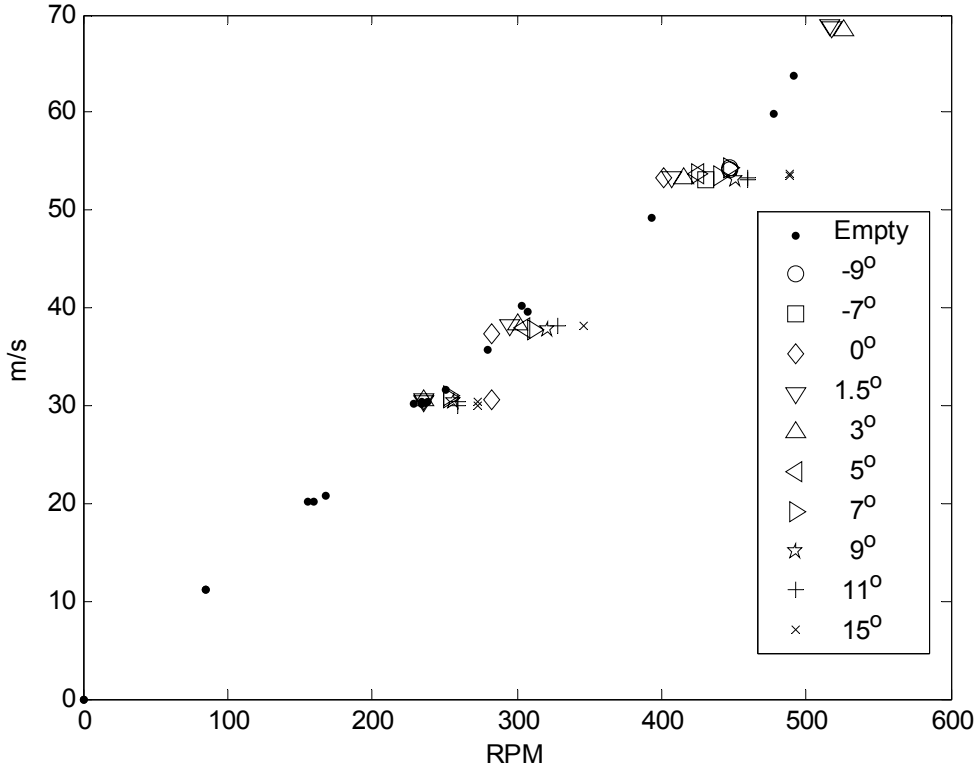

Figure 4-4. *Relationship between flow speed and tunnel fan RPM for measurements made with the NACA 0012 model compared with data from the empty test section.*

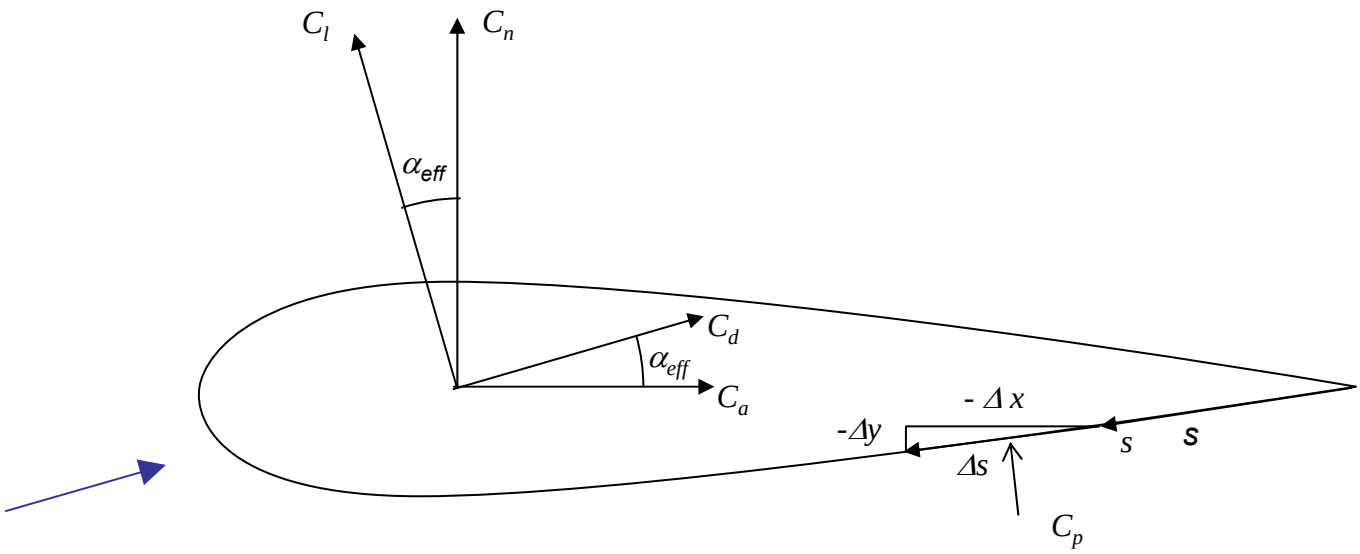

Figure 4-5. *Definition of the edge-length s and of the various force coefficients for the NACA 0012 model.*

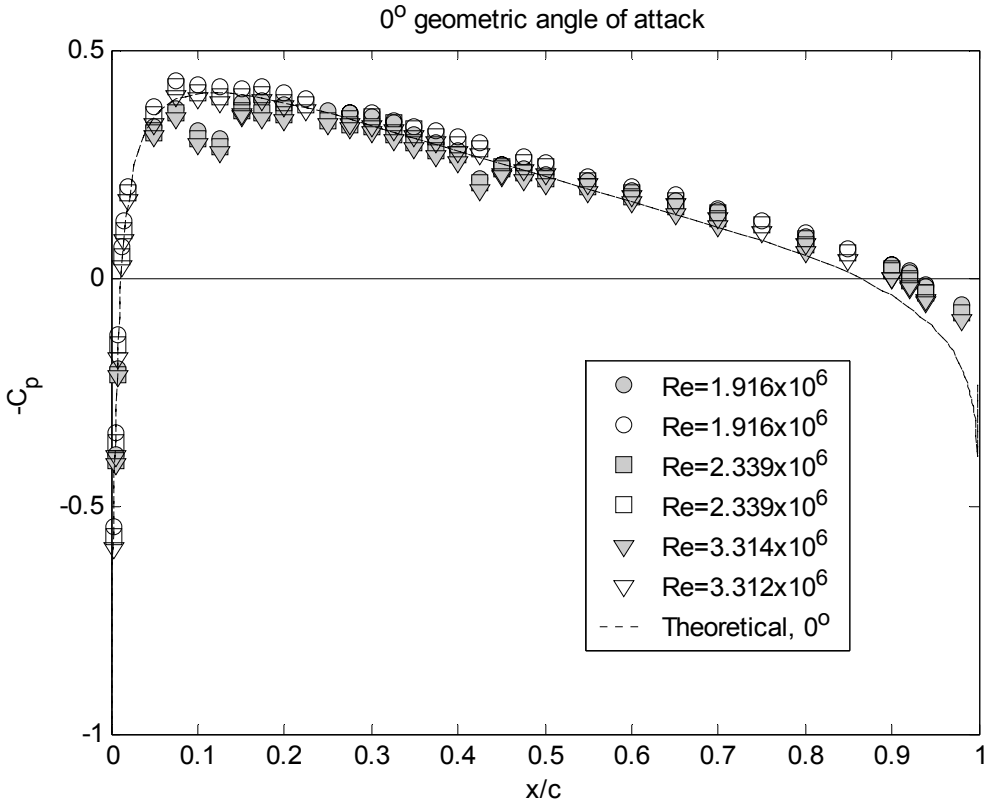

Figure 4-6. *Mean pressure distribution on the NACA 0012 airfoil at zero degrees geometric angle of attack as a function of Reynolds number. Filled symbols correspond to measurements made on the side of the model with the hatch. Open symbols are the opposite side. (a) Pressure plotted vs. chordwise distance x/c.*

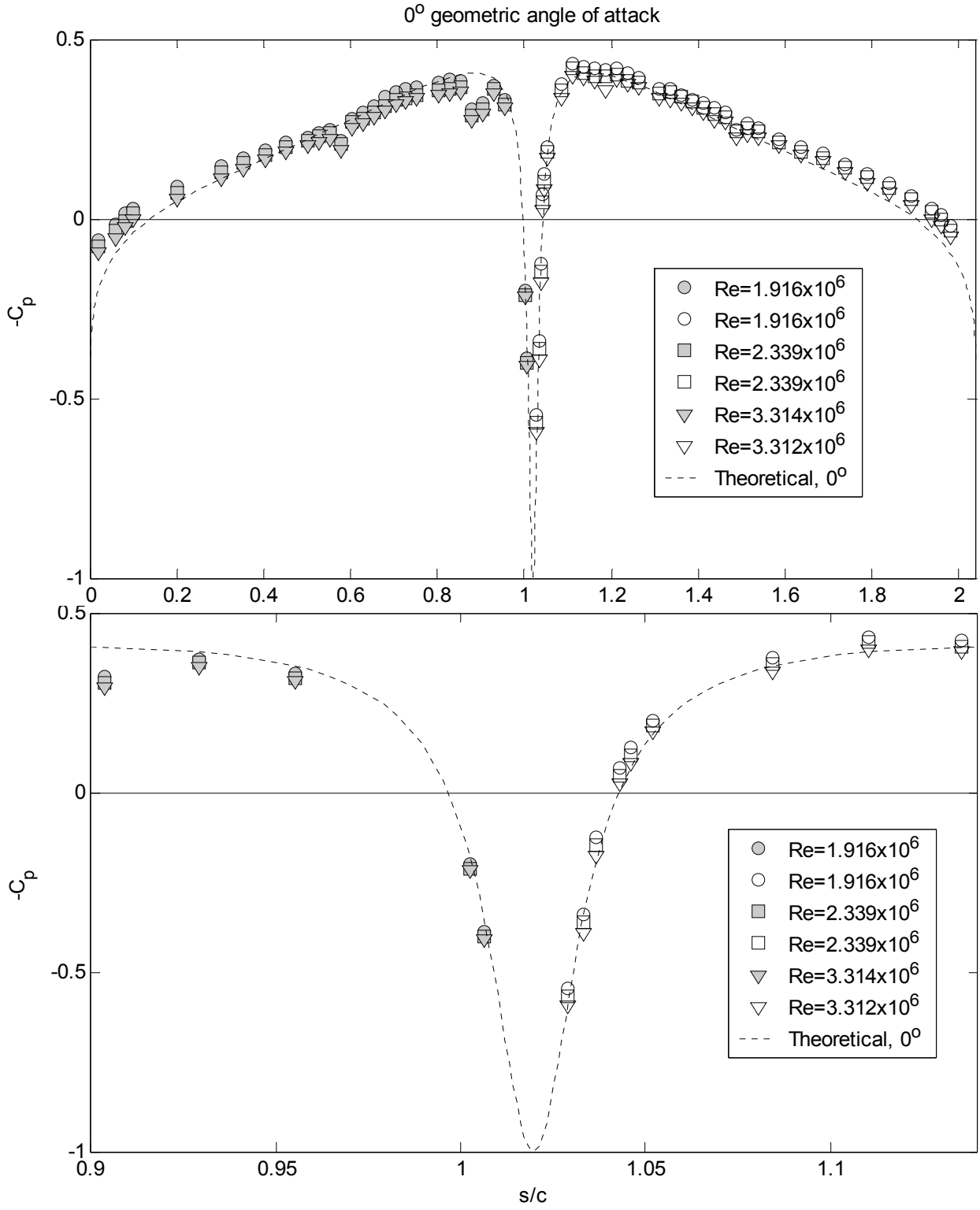

Figure 4-6. *Mean pressure distribution on the NACA 0012 airfoil at zero degrees geometric angle of attack as a function of Reynolds number. Filled symbols correspond to measurements made on the side of the model with the hatch. Open symbols are the opposite side. (b) and (c) pressure plotted vs. edge-length s/c.*

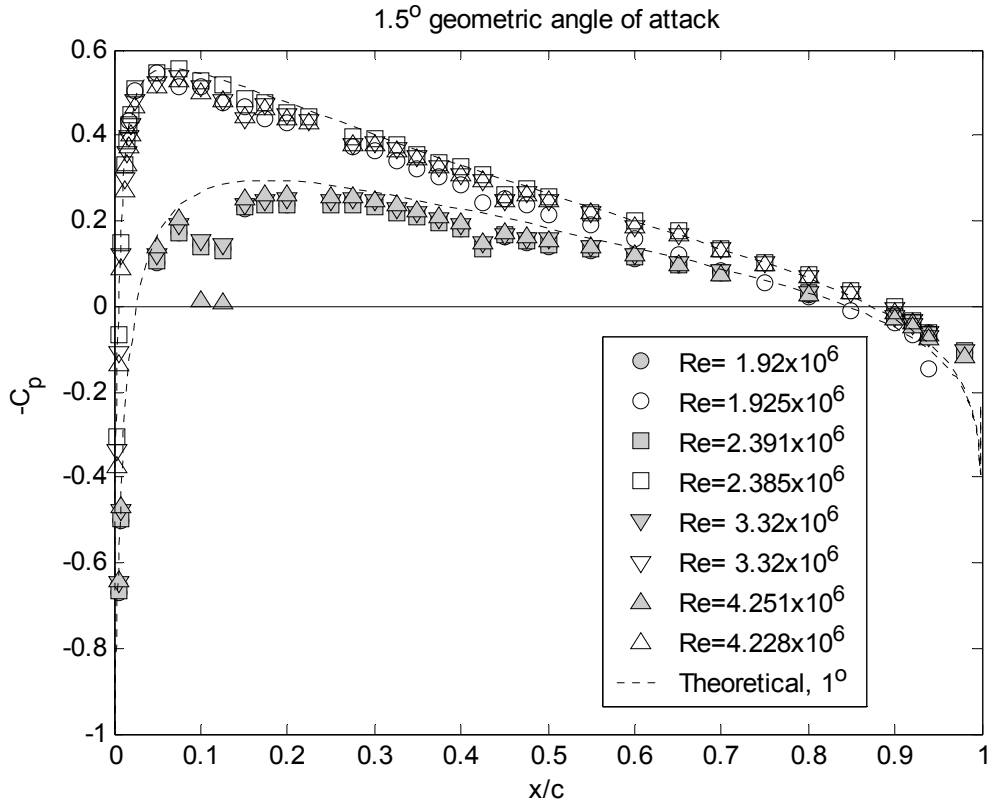

Figure 4-7. *Mean pressure distribution on the NACA 0012 airfoil at 1.5 degrees geometric angle of attack as a function of Reynolds number. Filled symbols correspond to measurements made on the side of the model with the hatch. Open symbols are the opposite side. (a) Pressure plotted vs. chordwise distance x/c.*

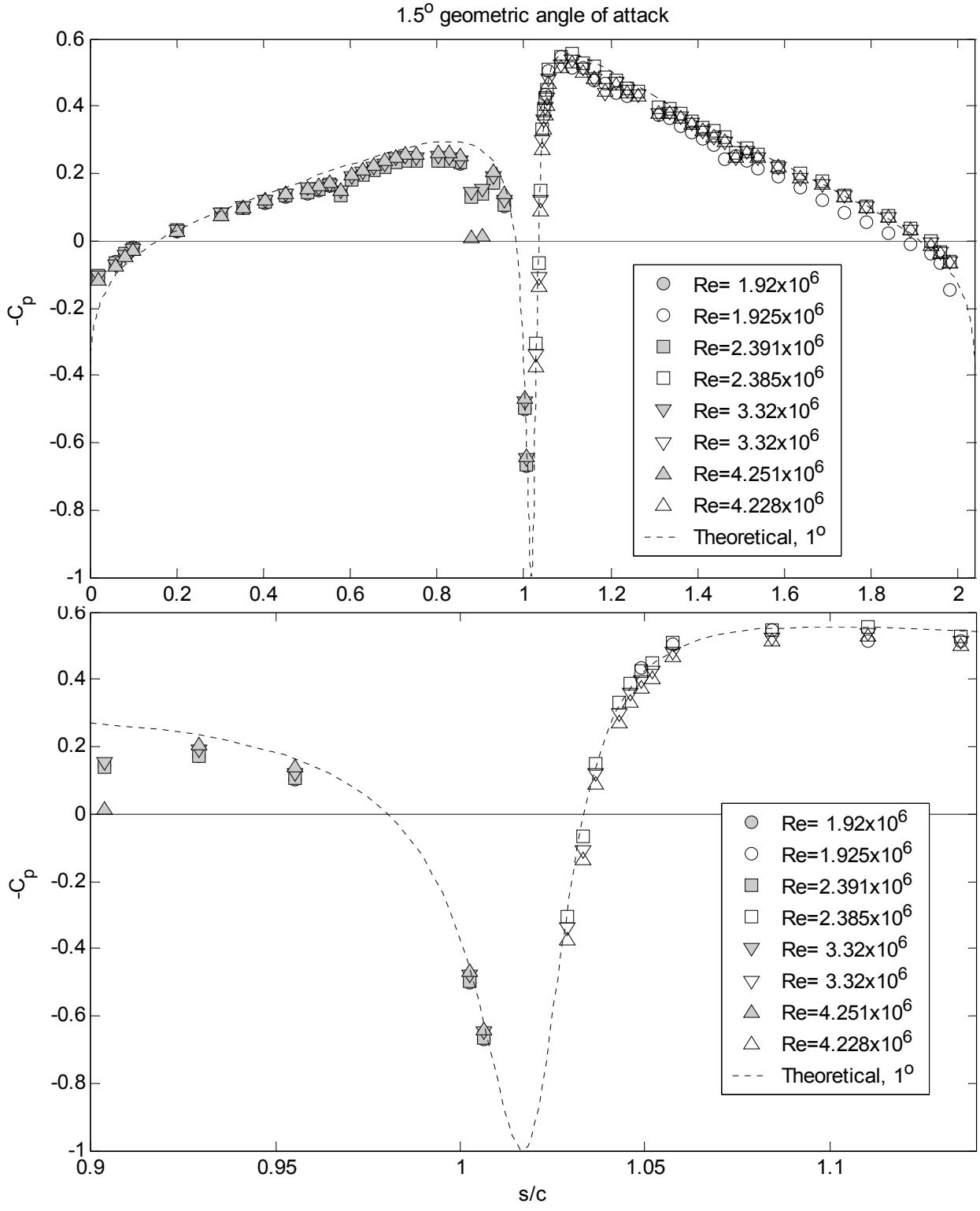

Figure 4-7. *Mean pressure distribution on the NACA 0012 airfoil at 1.5 degrees geometric angle of attack as a function of Reynolds number. Filled symbols correspond to measurements made on the side of the model with the hatch. Open symbols are the opposite side. (b) and (c) pressure plotted vs. edge-length s/c.*

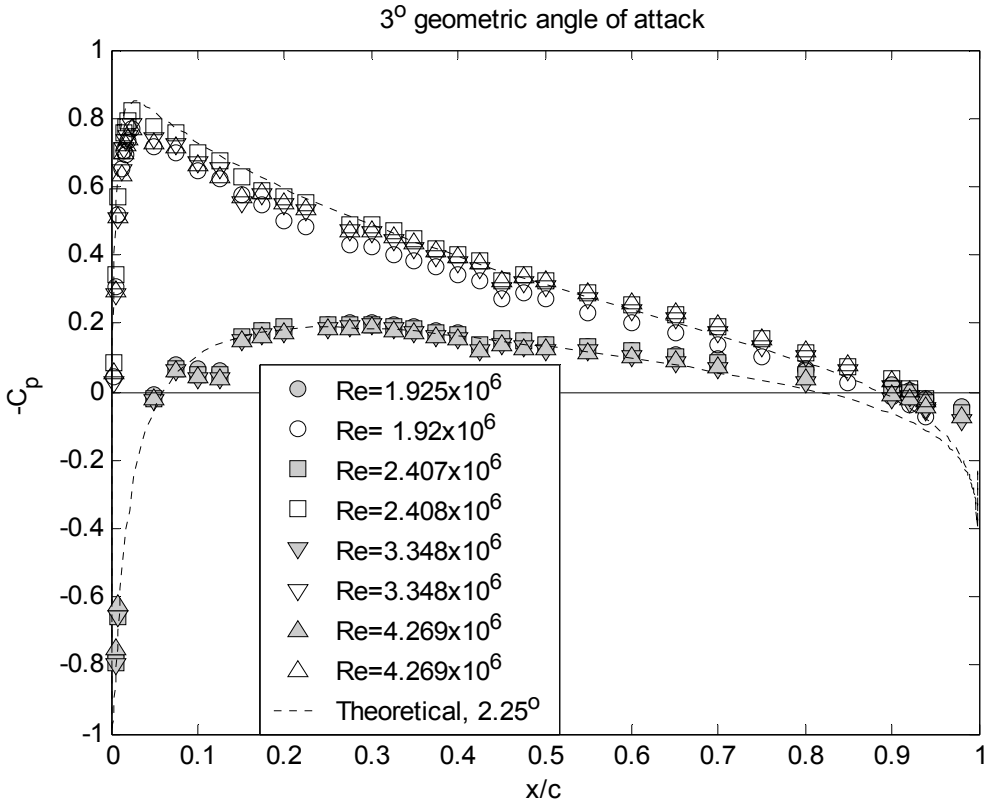

Figure 4-8. *Mean pressure distribution on the NACA 0012 airfoil at 3 degrees geometric angle of attack as a function of Reynolds number. Filled symbols correspond to measurements made on the side of the model with the hatch. Open symbols are the opposite side. (a) Pressure plotted vs. chordwise distance x/c.*

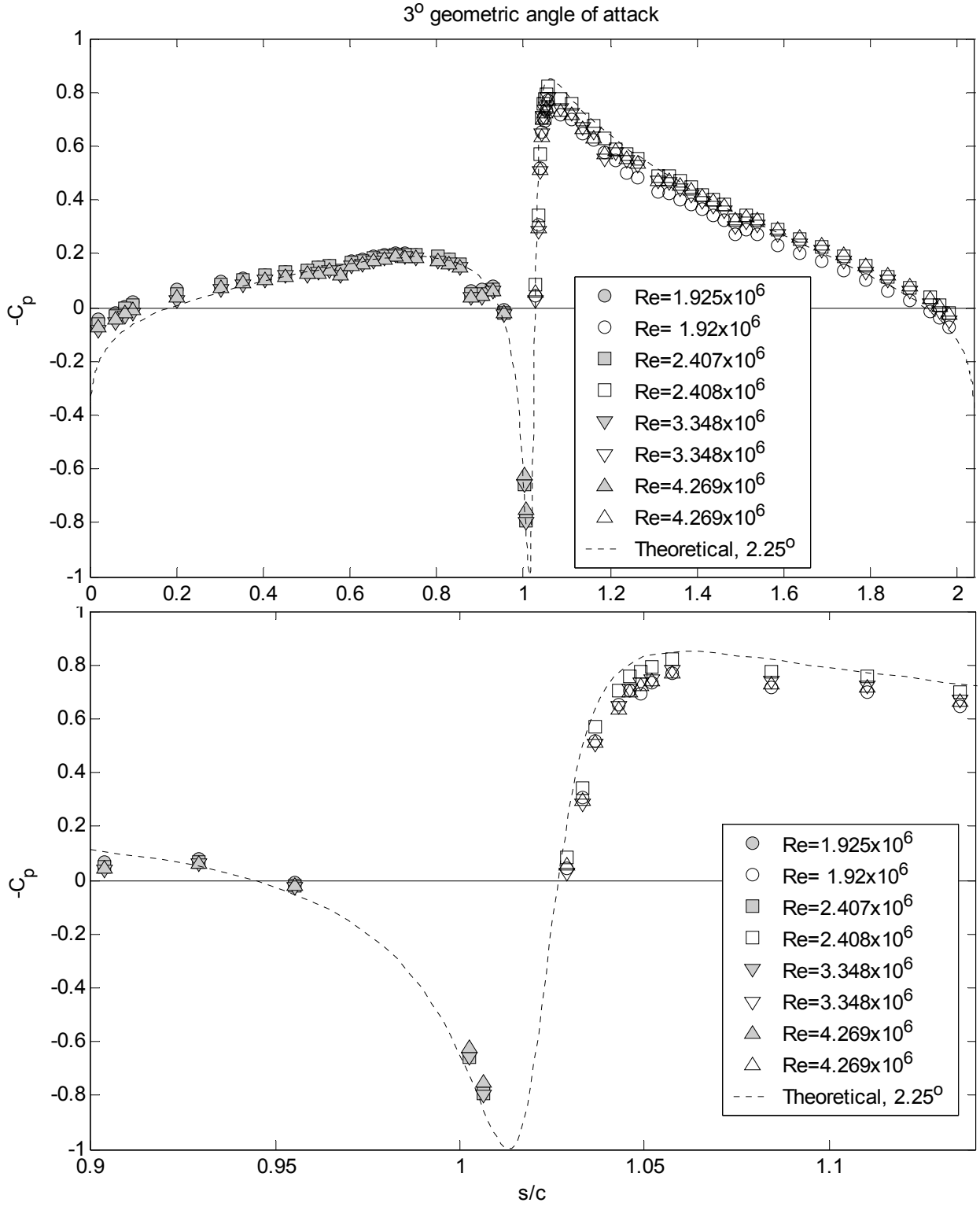

Figure 4-8. *Mean pressure distribution on the NACA 0012 airfoil at 3 degrees geometric angle of attack as a function of Reynolds number. Filled symbols correspond to measurements made on the side of the model with the hatch. Open symbols are the opposite side. (b) and (c) pressure plotted vs. edge-length s/c.*

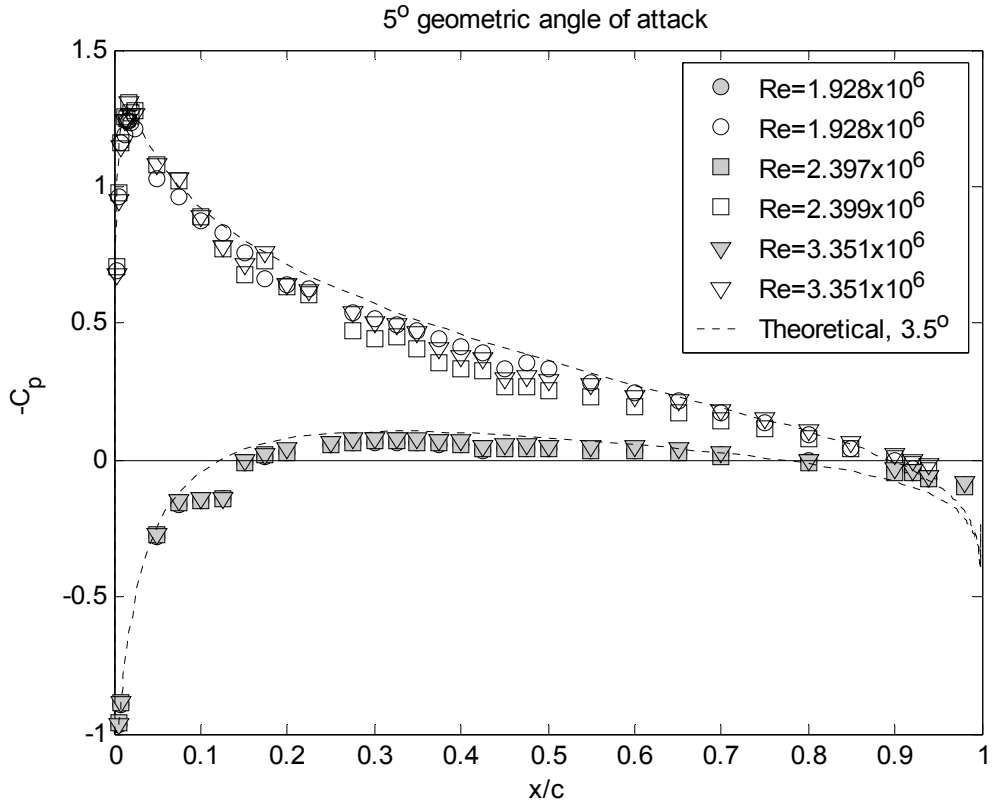

Figure 4-9. *Mean pressure distribution on the NACA 0012 airfoil at 5 degrees geometric angle of attack as a function of Reynolds number. Filled symbols correspond to measurements made on the side of the model with the hatch. Open symbols are the opposite side. (a) Pressure plotted vs. chordwise distance x/c.*

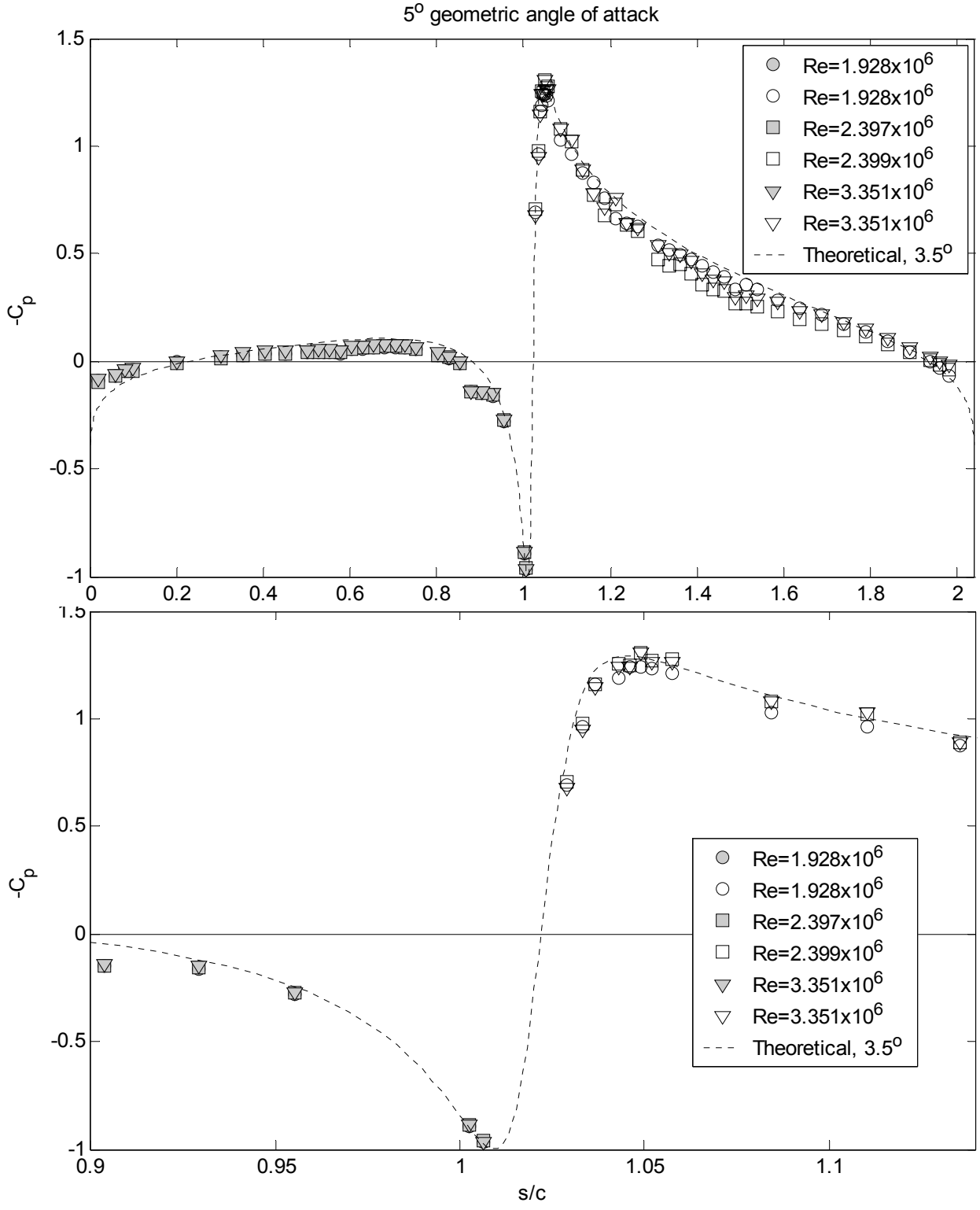

Figure 4-9. *Mean pressure distribution on the NACA 0012 airfoil at 5 degrees geometric angle of attack as a function of Reynolds number. Filled symbols correspond to measurements made on the side of the model with the hatch. Open symbols are the opposite side. (b) and (c) pressure plotted vs. edge-length s/c.*

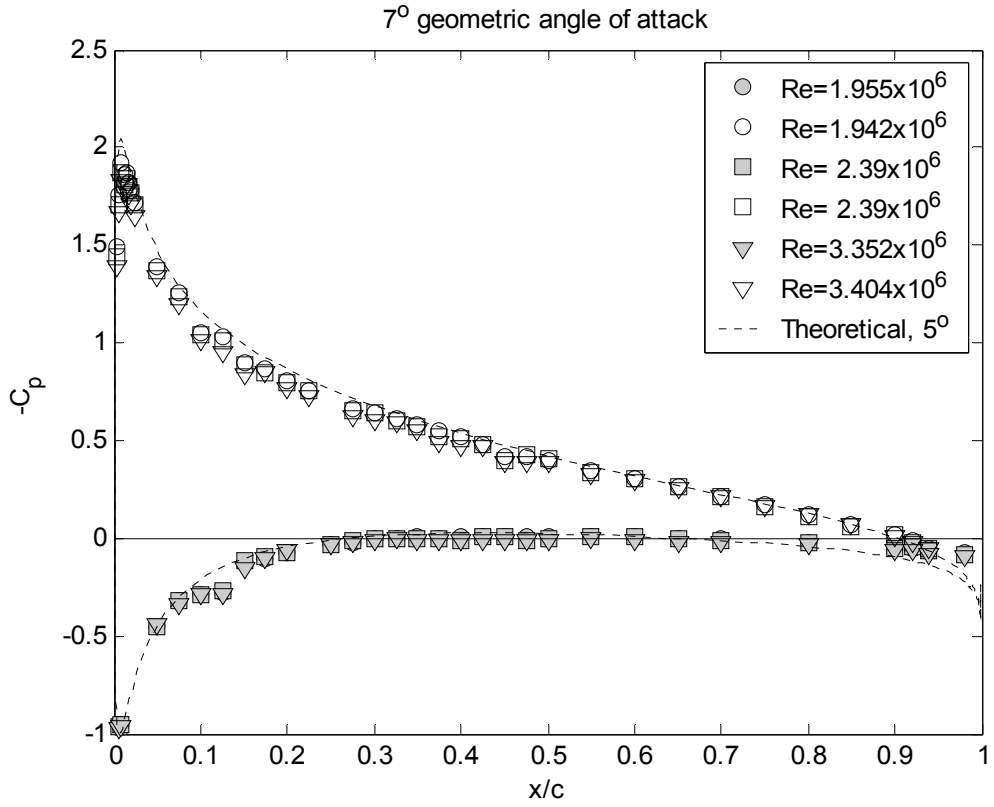

Figure 4-10. *Mean pressure distribution on the NACA 0012 airfoil at 7 degrees geometric angle of attack as a function of Reynolds number. Filled symbols correspond to measurements made on the side of the model with the hatch. Open symbols are the opposite side. (a) Pressure plotted vs. chordwise distance x/c.*

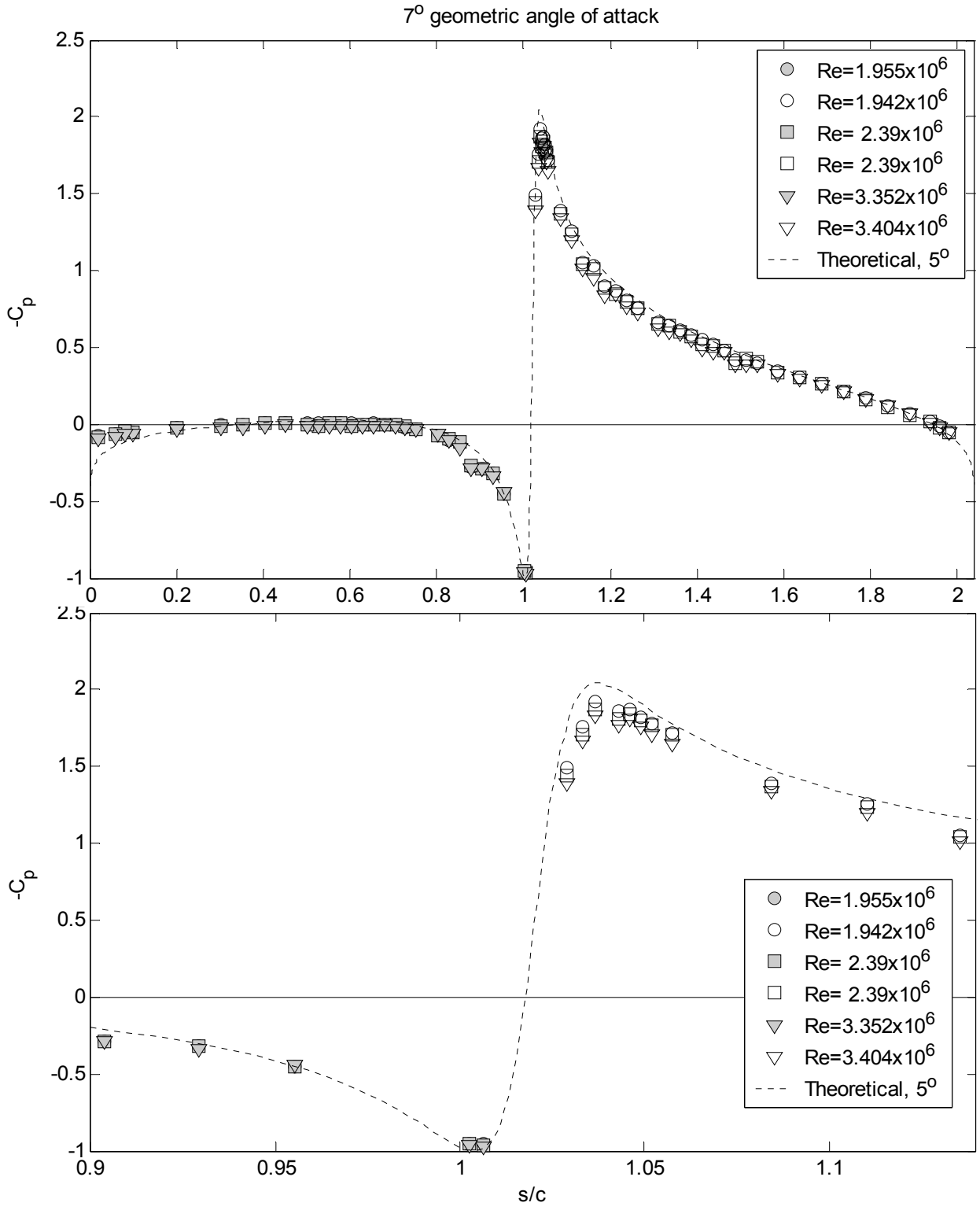

Figure 4-10. *Mean pressure distribution on the NACA 0012 airfoil at 7 degrees geometric angle of attack as a function of Reynolds number. Filled symbols correspond to measurements made on the side of the model with the hatch. Open symbols are the opposite side. (b) and (c) pressure plotted vs. edge-length s/c.*

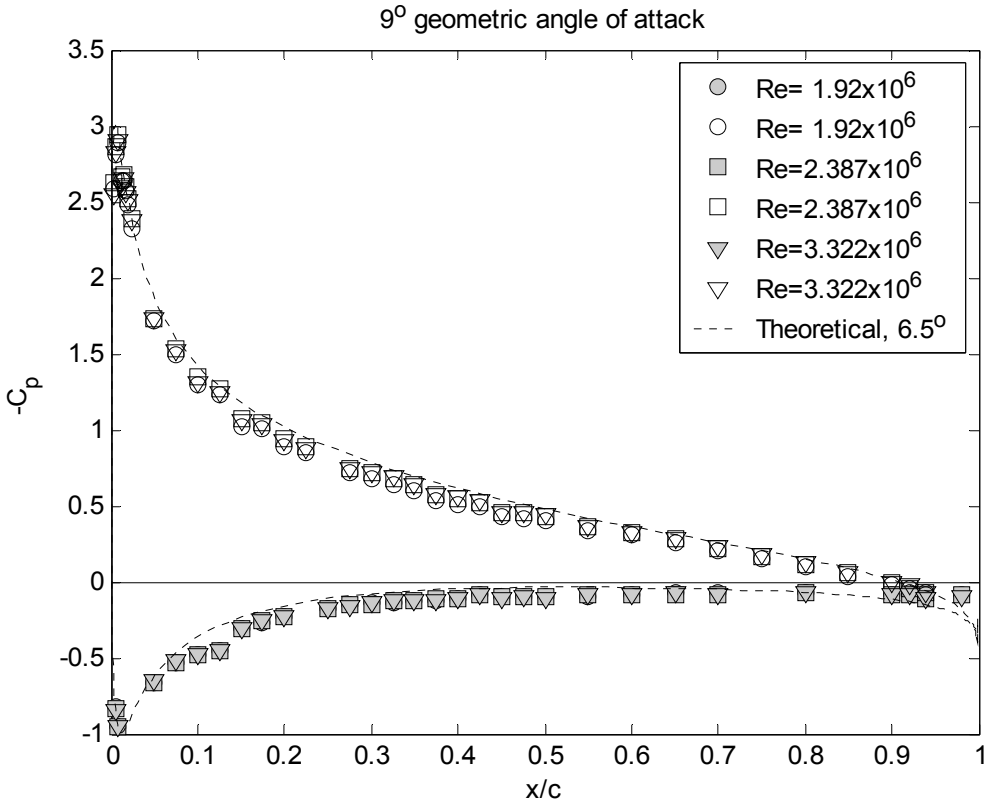

Figure 4-11. *Mean pressure distribution on the NACA 0012 airfoil at 9 degrees geometric angle of attack as a function of Reynolds number. Filled symbols correspond to measurements made on the side of the model with the hatch. Open symbols are the opposite side. (a) Pressure plotted vs. chordwise distance x/c.*

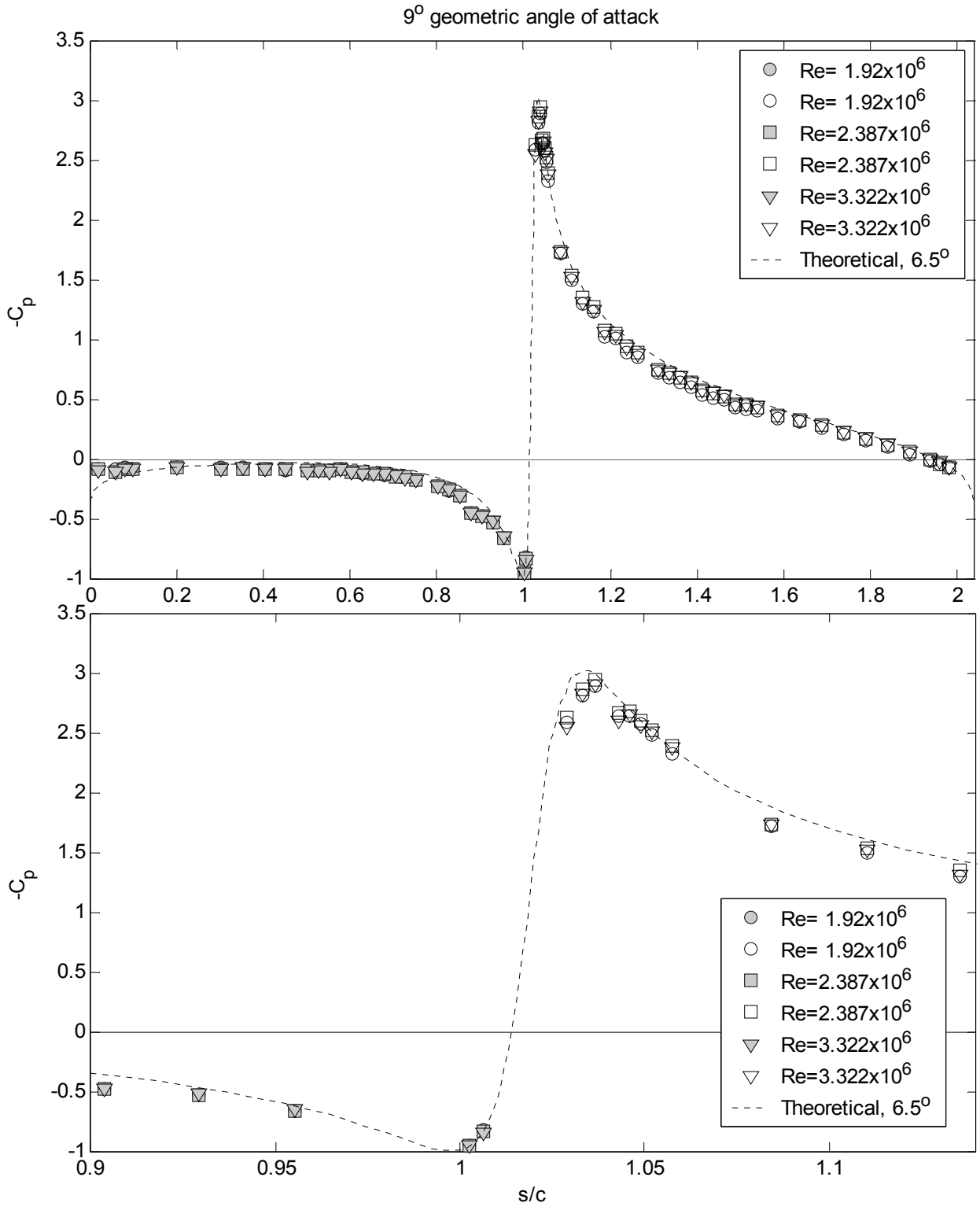

Figure 4-11. *Mean pressure distribution on the NACA 0012 airfoil at 9 degrees geometric angle of attack as a function of Reynolds number. Filled symbols correspond to measurements made on the side of the model with the hatch. Open symbols are the opposite side. (b) and (c) pressure plotted vs. edge-length s/c.*

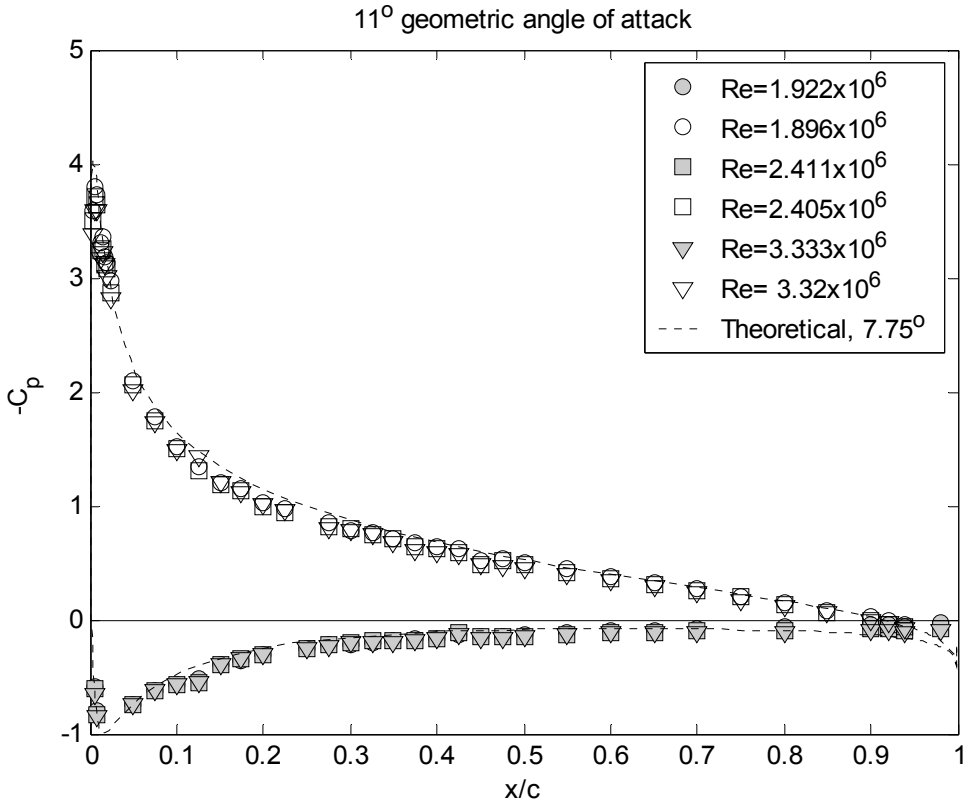

Figure 4-12. *Mean pressure distribution on the NACA 0012 airfoil at 11 degrees geometric angle of attack as a function of Reynolds number. Filled symbols correspond to measurements made on the side of the model with the hatch. Open symbols are the opposite side. (a) Pressure plotted vs. chordwise distance x/c.*

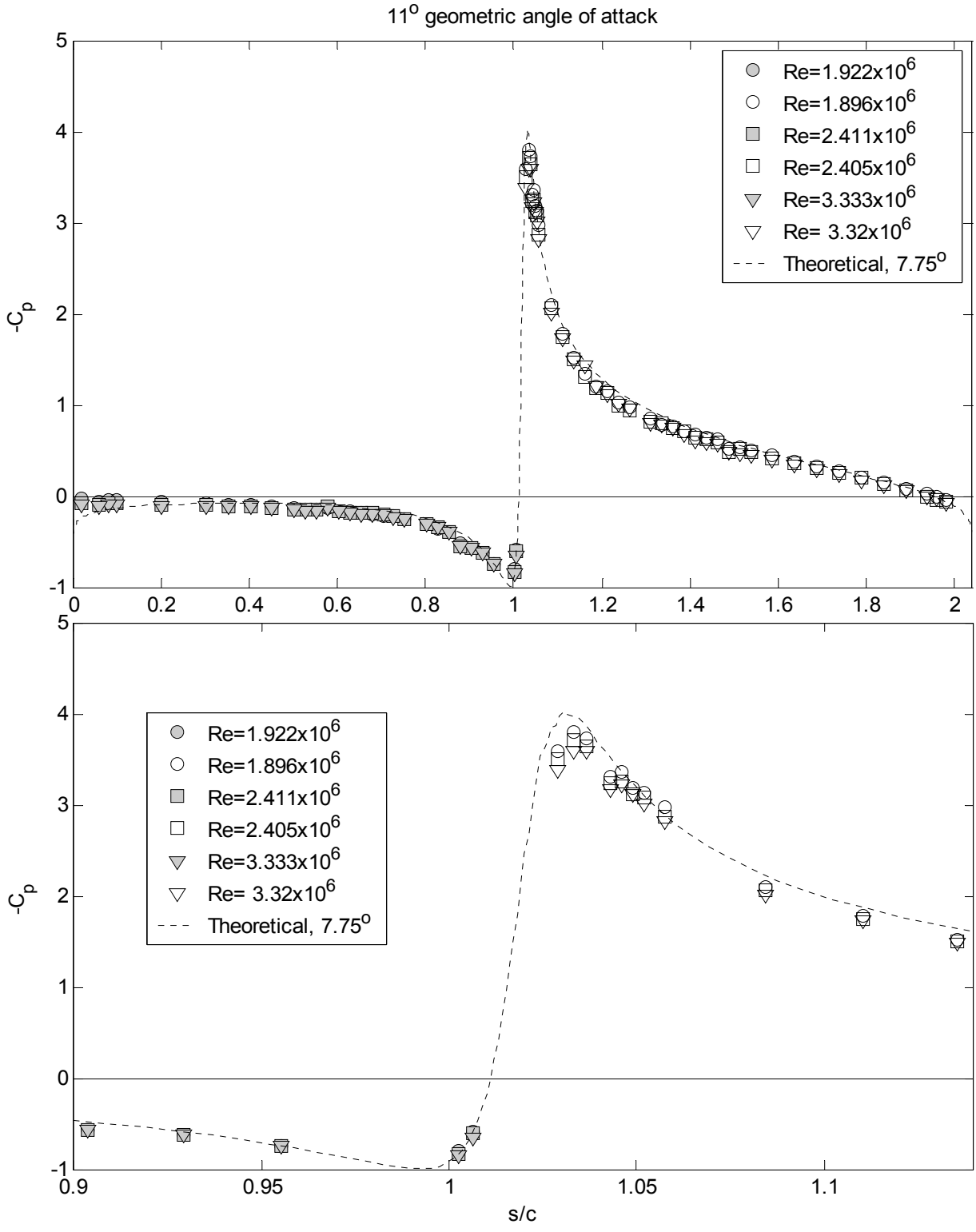

Figure 4-12. *Mean pressure distribution on the NACA 0012 airfoil at 11 degrees geometric angle of attack as a function of Reynolds number. Filled symbols correspond to measurements made on the side of the model with the hatch. Open symbols are the opposite side. (b) and (c) pressure plotted vs. edge-length s/c.*

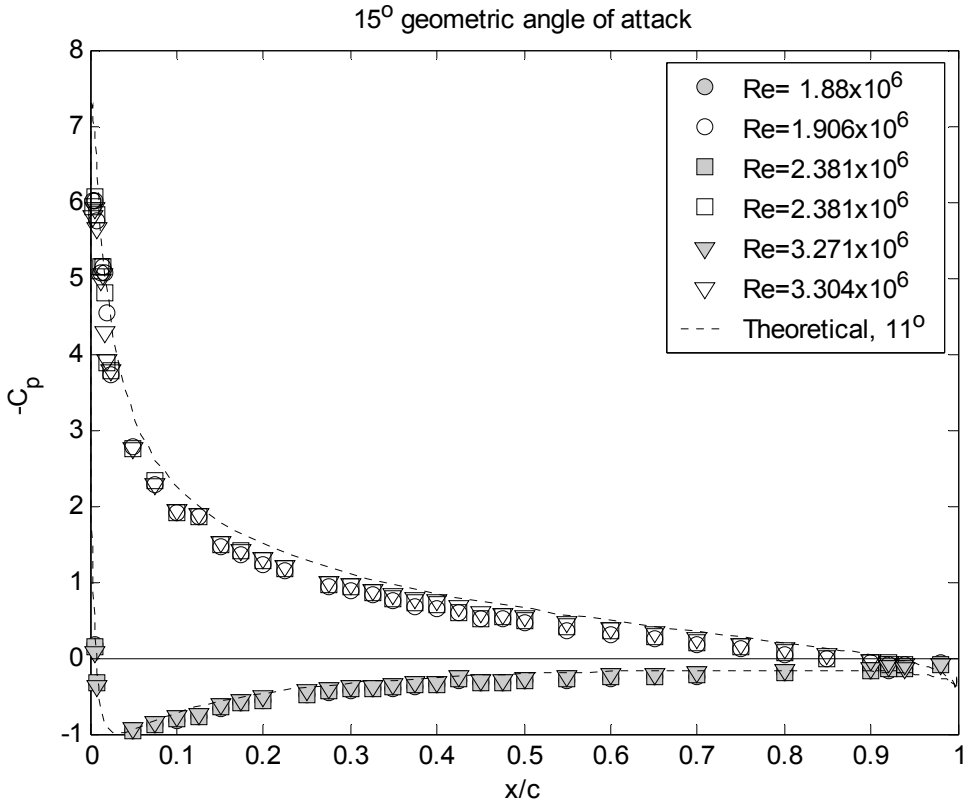

Figure 4-13. *Mean pressure distribution on the NACA 0012 airfoil at 15 degrees geometric angle of attack as a function of Reynolds number. Filled symbols correspond to measurements made on the side of the model with the hatch. Open symbols are the opposite side. (a) Pressure plotted vs. chordwise distance x/c.*

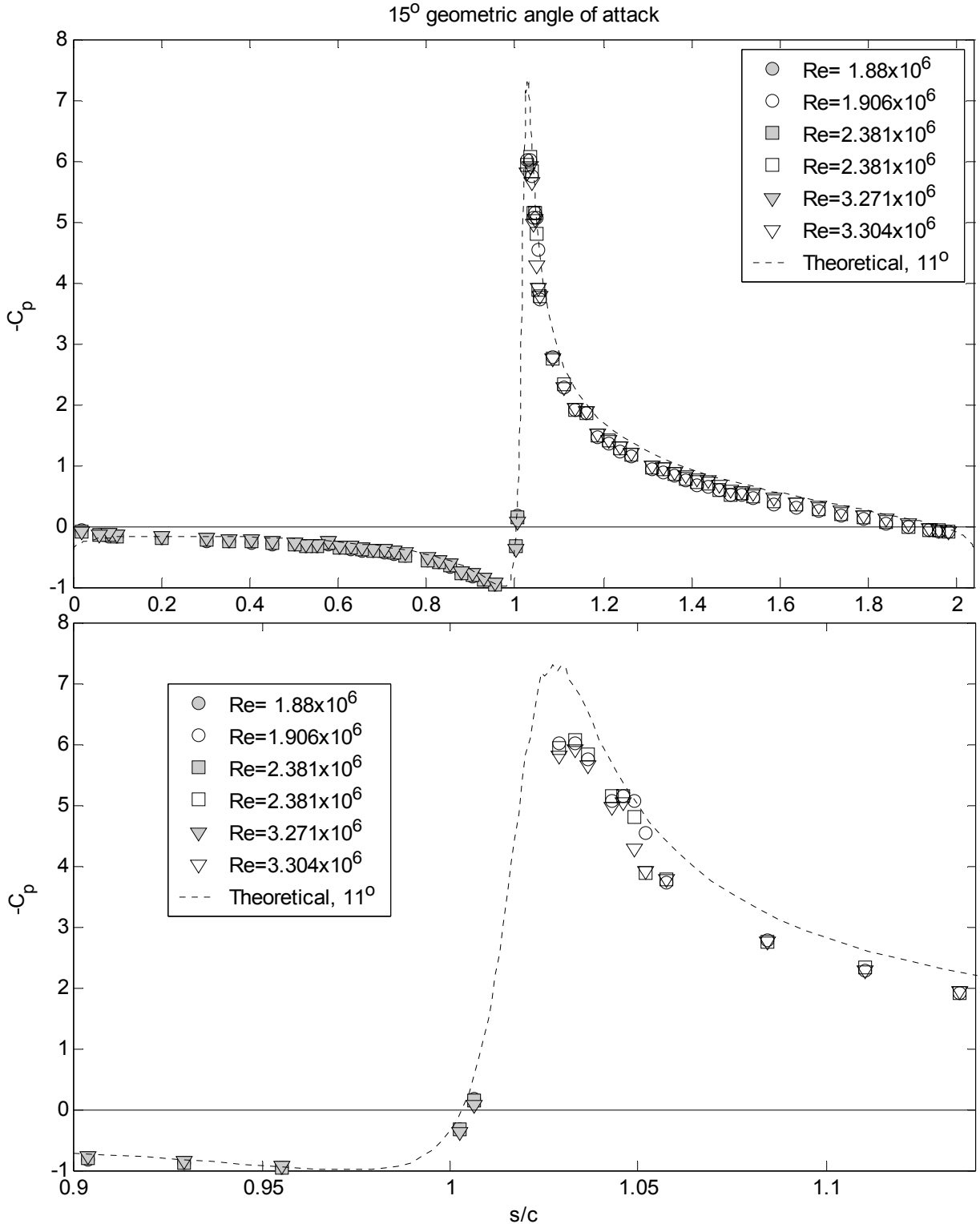

Figure 4-13. *Mean pressure distribution on the NACA 0012 airfoil at 15 degrees geometric angle of attack as a function of Reynolds number. Filled symbols correspond to measurements made on the side of the model with the hatch. Open symbols are the opposite side. (b) and (c) pressure plotted vs. edge-length s/c.*

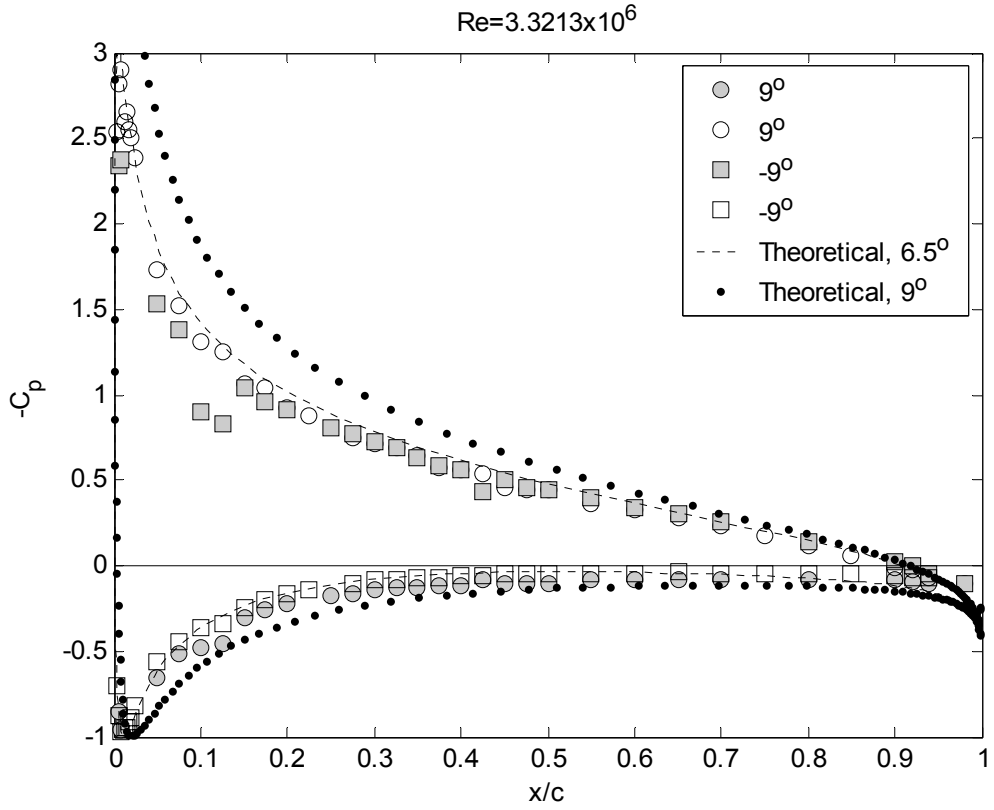

Figure 4-14. *Comparison of mean pressure distribution on the NACA 0012 airfoil at -9 and +9 degrees geometric angle of attack. Filled symbols correspond to measurements made on the side of the model with the hatch. Open symbols are the opposite side. Pressure plotted vs. chordwise distance x/c.*

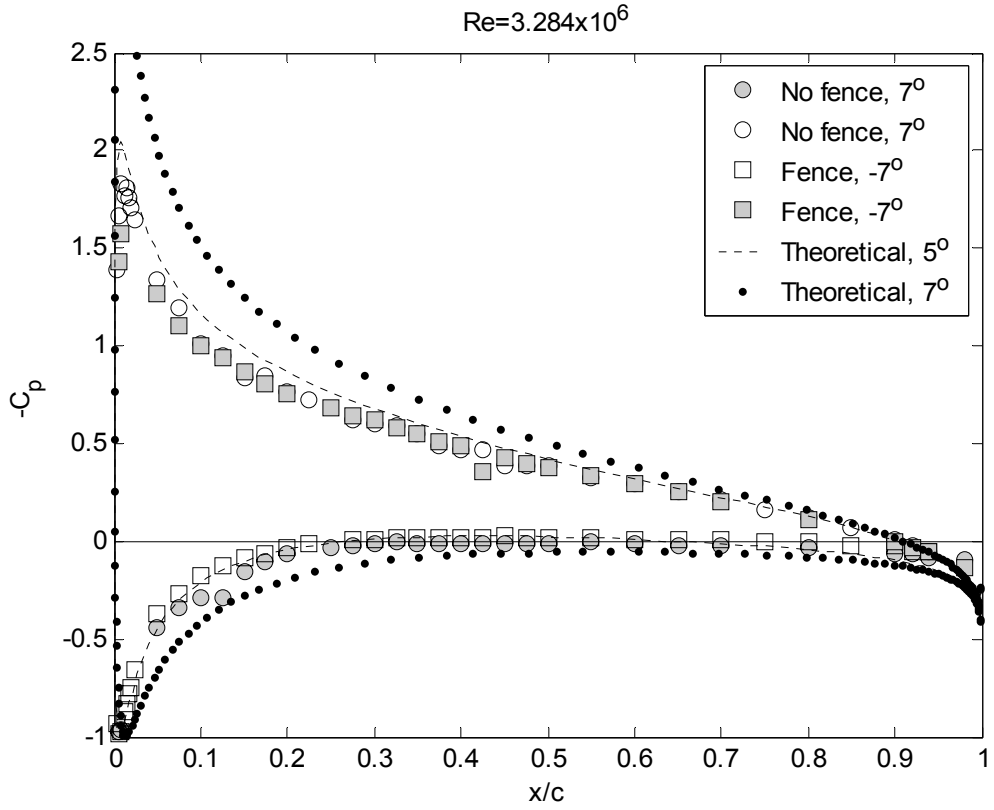

Figure 4-15. *Comparison of mean pressure distribution on the NACA 0012 airfoil at -7 and +7 degrees geometric angle of attack with and without boundary layer fences, respectfully. Filled symbols correspond to measurements made on the side of the model with the hatch. Open symbols are the opposite side. Pressure plotted vs. chordwise distance x/c.*

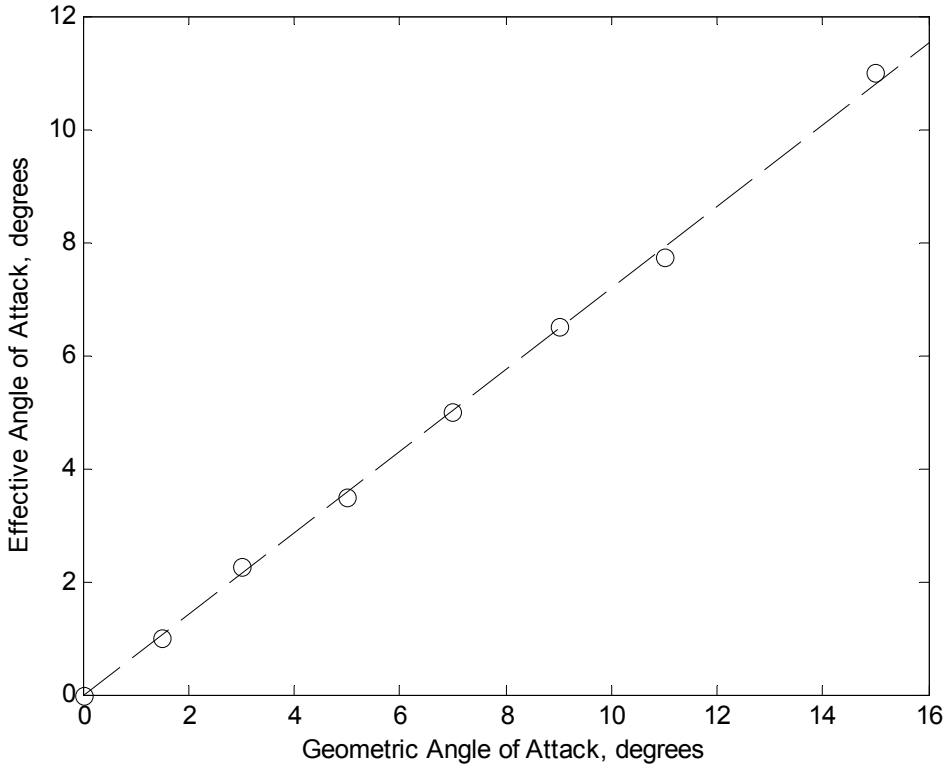

Figure 4-16. *Comparison of geometric and effective angles of attack for the NACA 0012 airfoil. Effective angles of attack determined by comparison with inviscid pressure distribution. Dashed line has a slope of 0.72.*

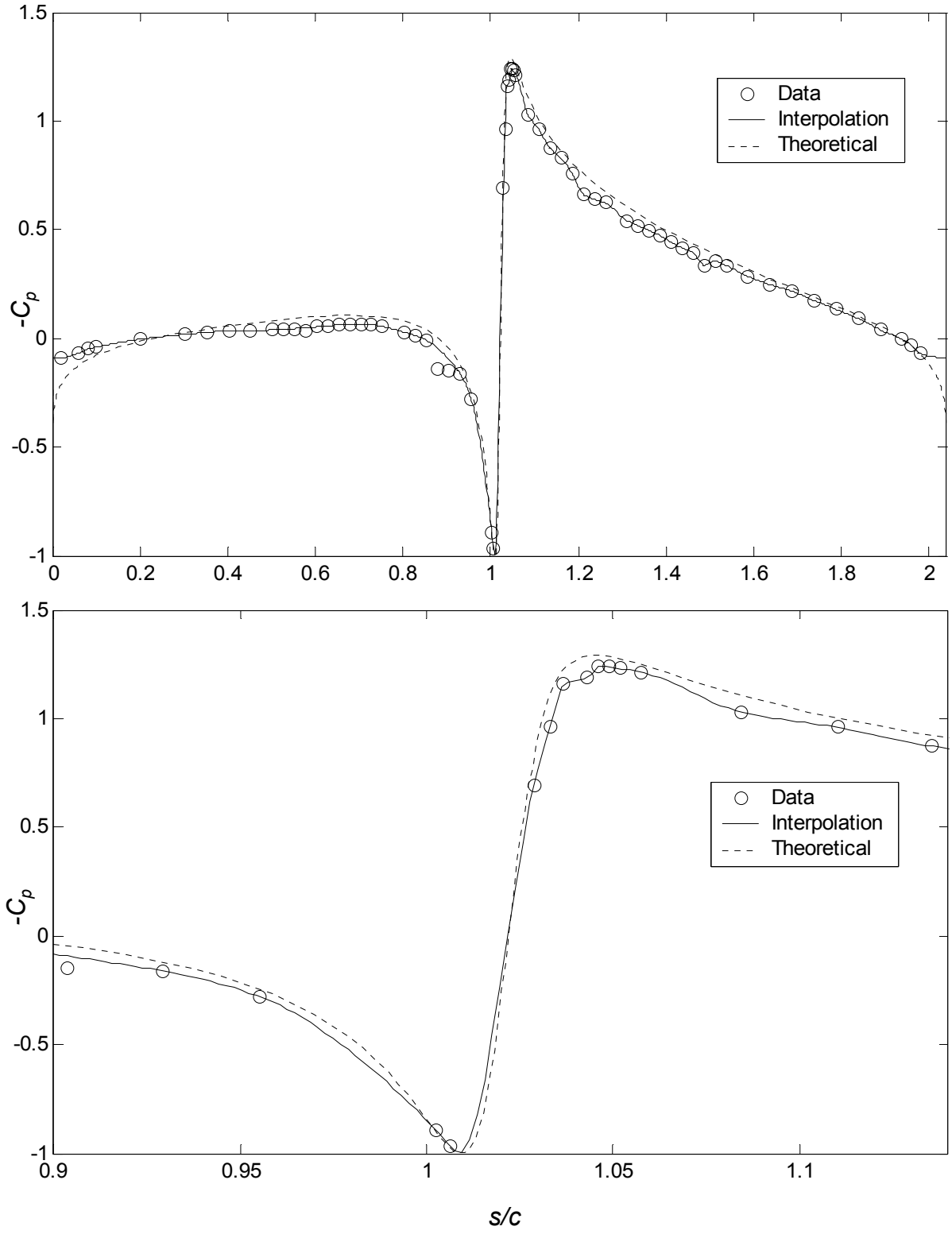

Figure 4-17. *Comparison of measured and interpolated pressure distributions for 5 degrees geometric angle of attack with the theoretical pressure distribution for an effective angle of attack of 3.5 degrees.*

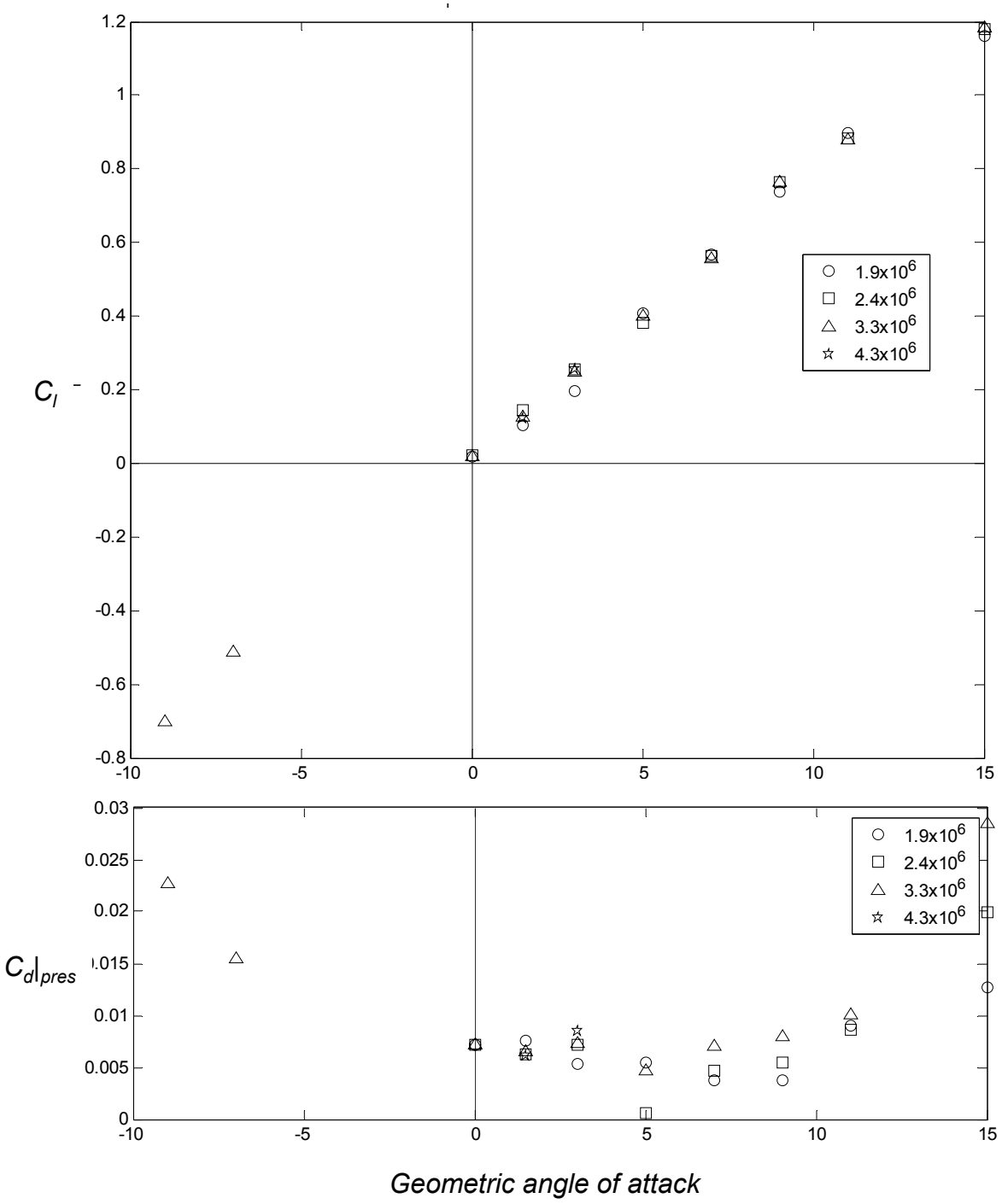

Figure 4-18. *Variation of lift coefficient and pressure drag coefficient (integrated from the measured airfoil pressure distributions) with geometric angle of attack for different Reynolds numbers.*

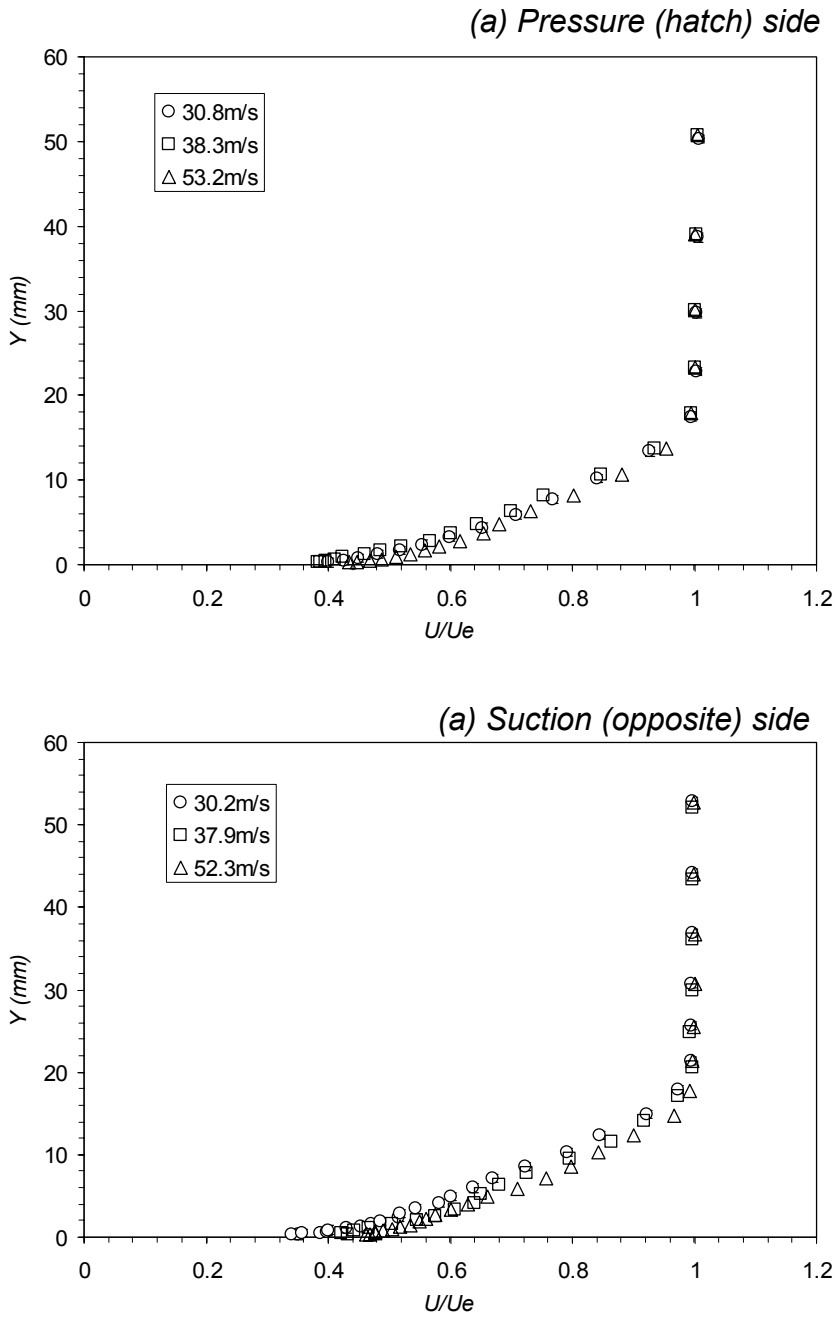

Figure 4-19. *Boundary layer profiles measured on the NACA 0012 airfoil at x/c=0.98 for zero degrees geometric angle of attack.*

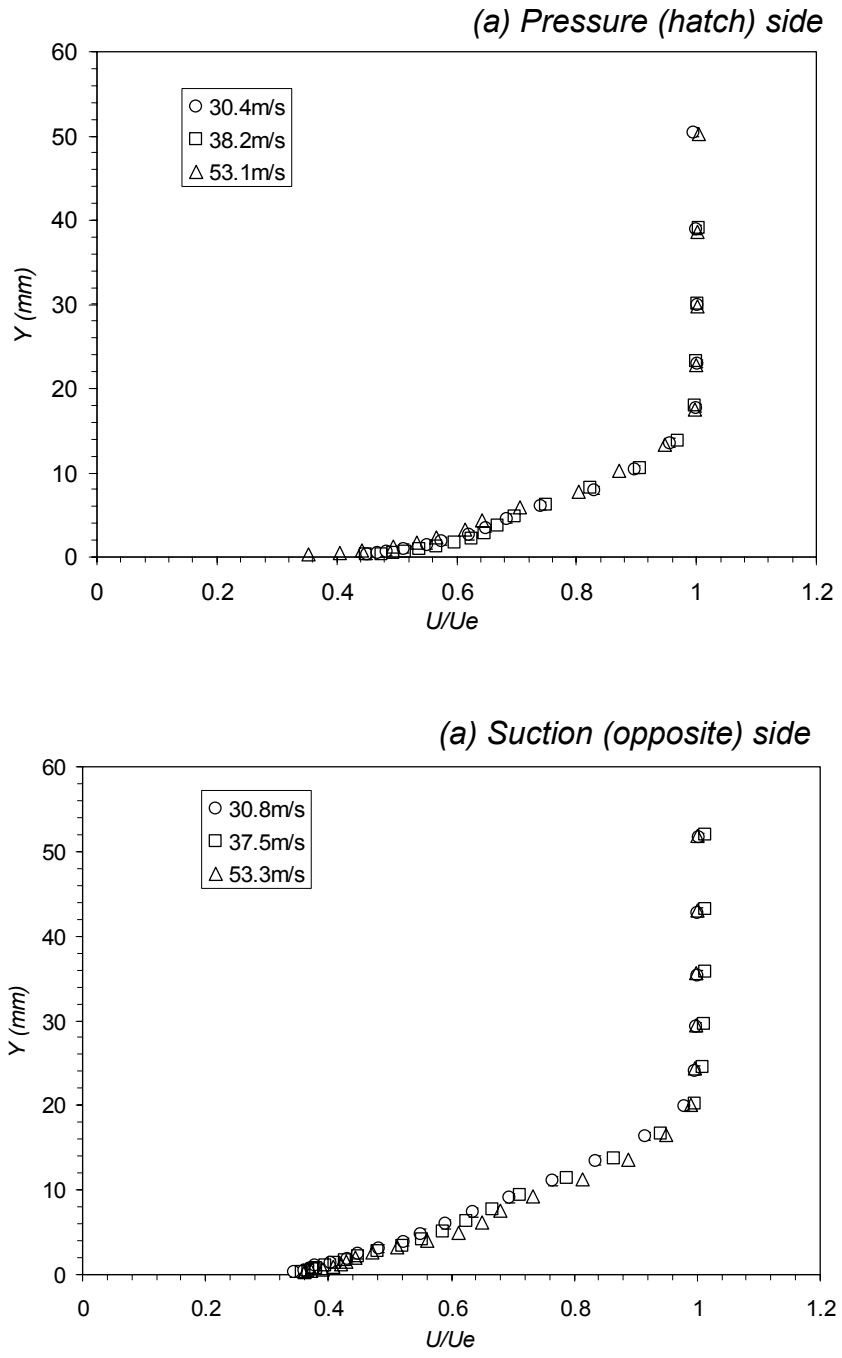

Figure 4-20. *Boundary layer profiles measured on the NACA 0012 airfoil at x/c=0.98 for three degrees geometric angle of attack.*

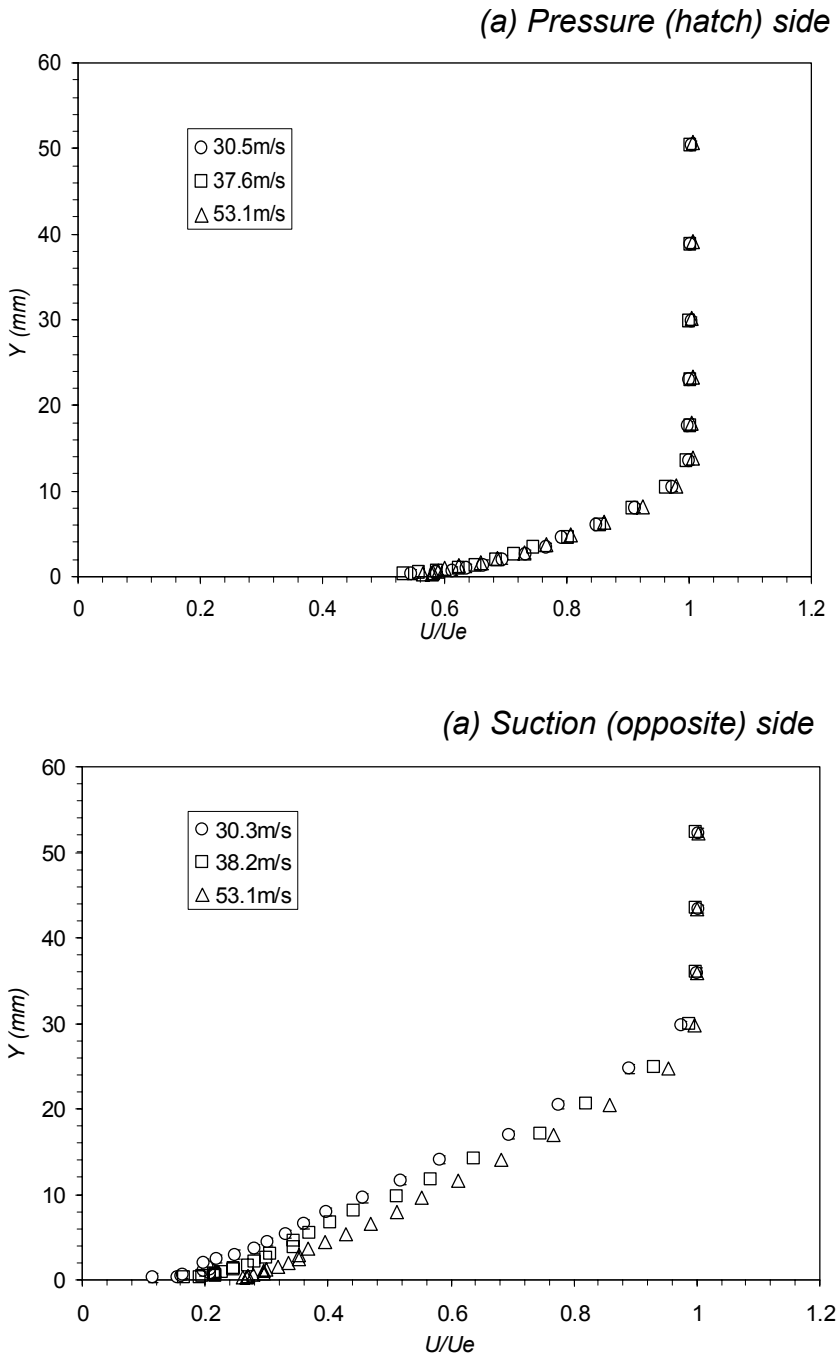

Figure 4-21. *Boundary layer profiles measured on the NACA 0012 airfoil at x/c=0.98 for nin degrees geometric angle of attack.*

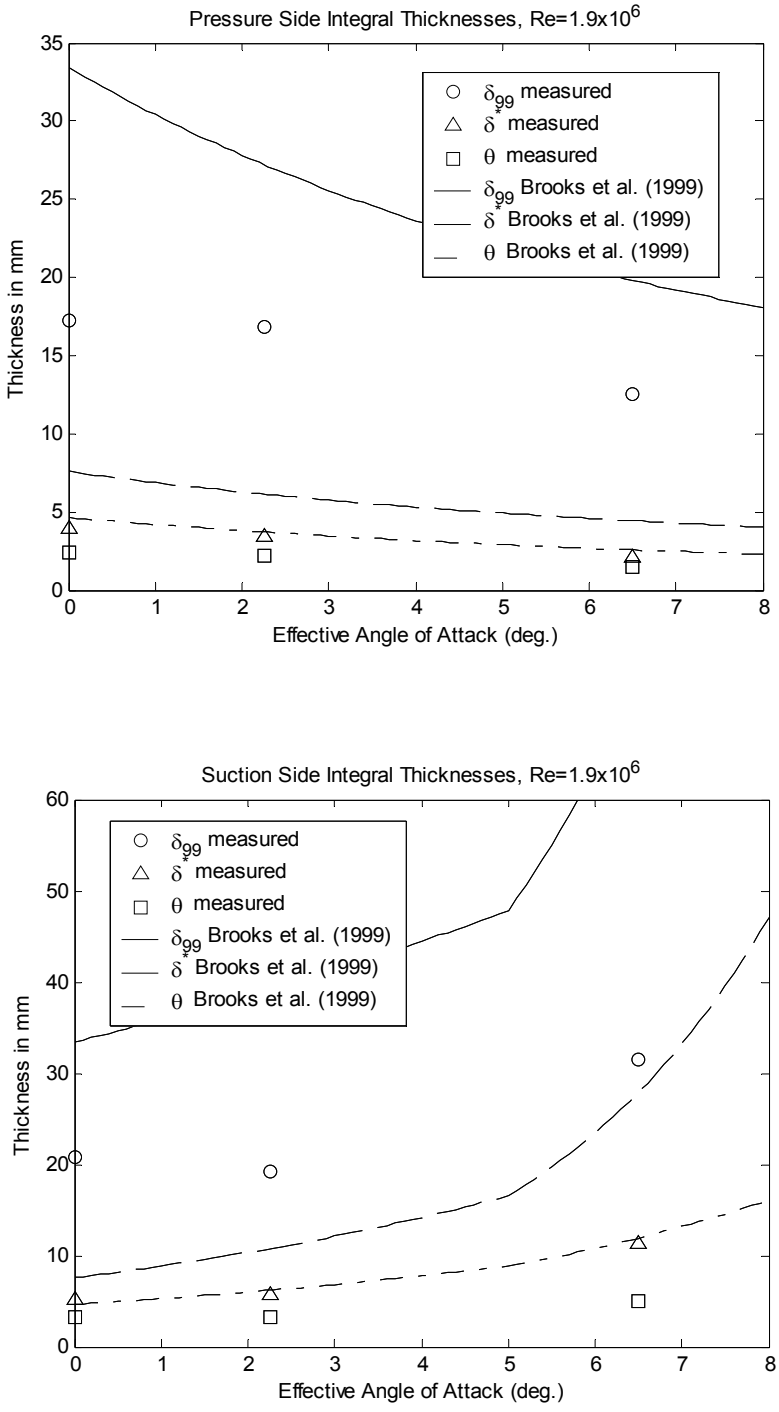

Figure 4-22. *Boundary layer thicknesses at x/c=0.98 for the NACA 0012 airfoil at Re=1.9x10^6 compared with empirical relations from Brooks et al. (1989).*

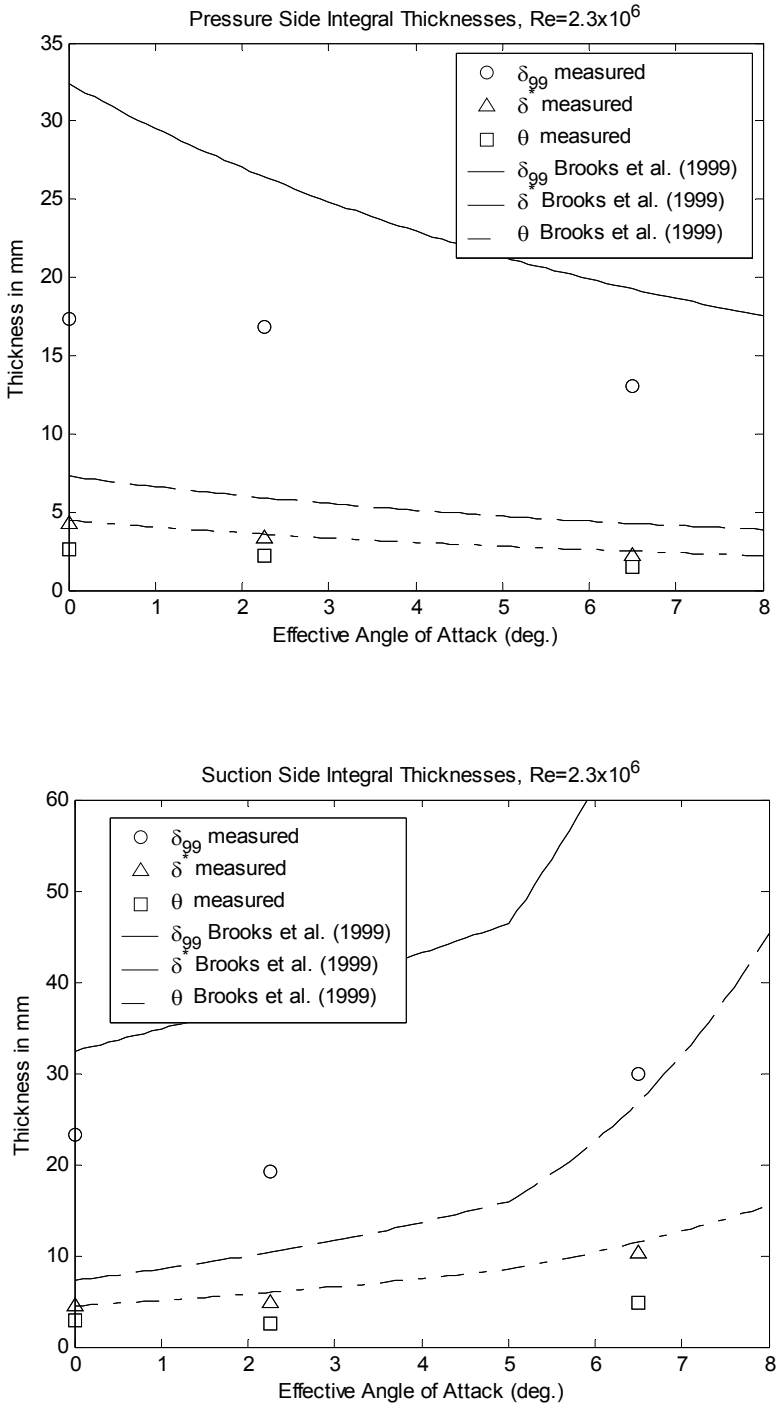

Figure 4-23. *Boundary layer thicknesses at x/c=0.98 for the NACA 0012 airfoil at Re=2.3x10^6 compared with empirical relations from Brooks et al. (1989).*

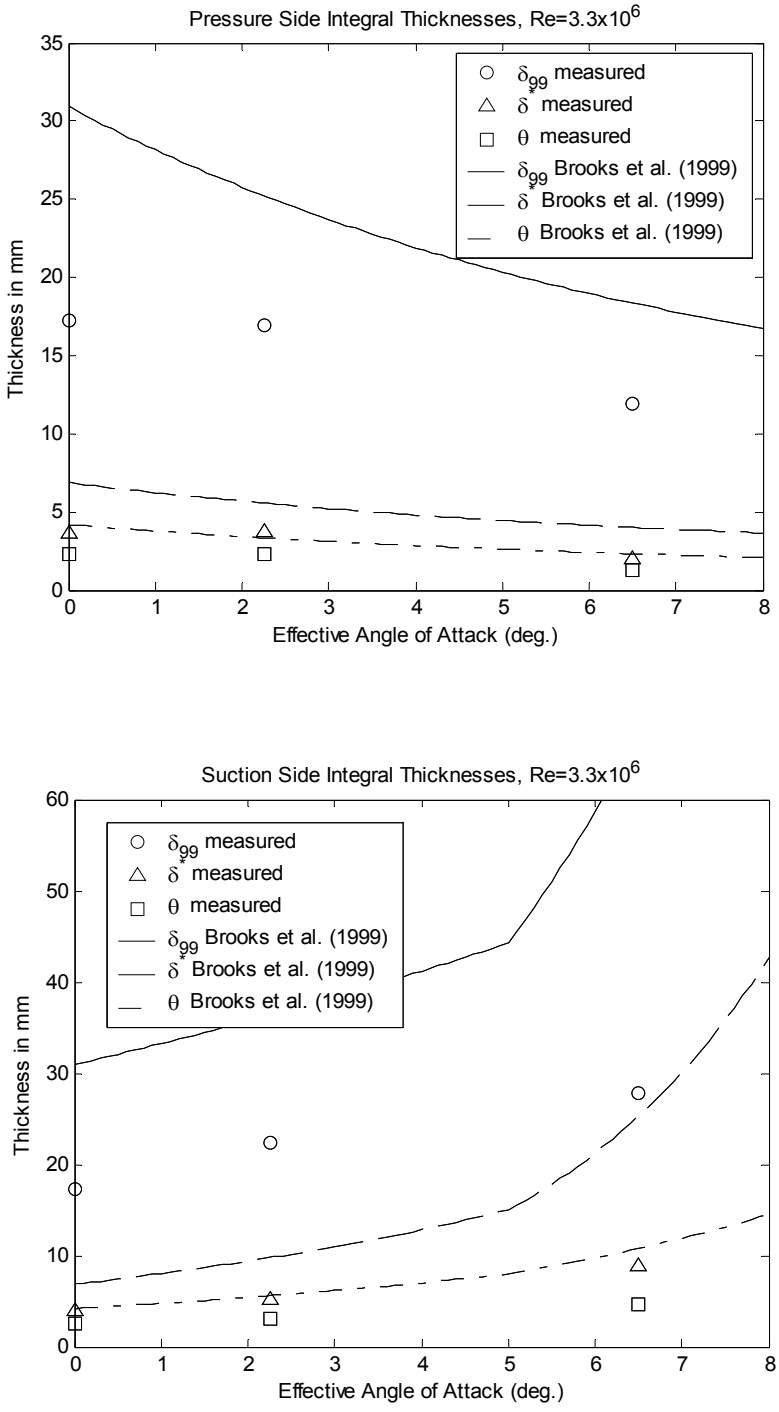

Figure 4-24. *Boundary layer thicknesses at x/c=0.98 for the NACA 0012 airfoil at Re=3.3x10^6 compared with empirical relations from Brooks et al. (1989).*

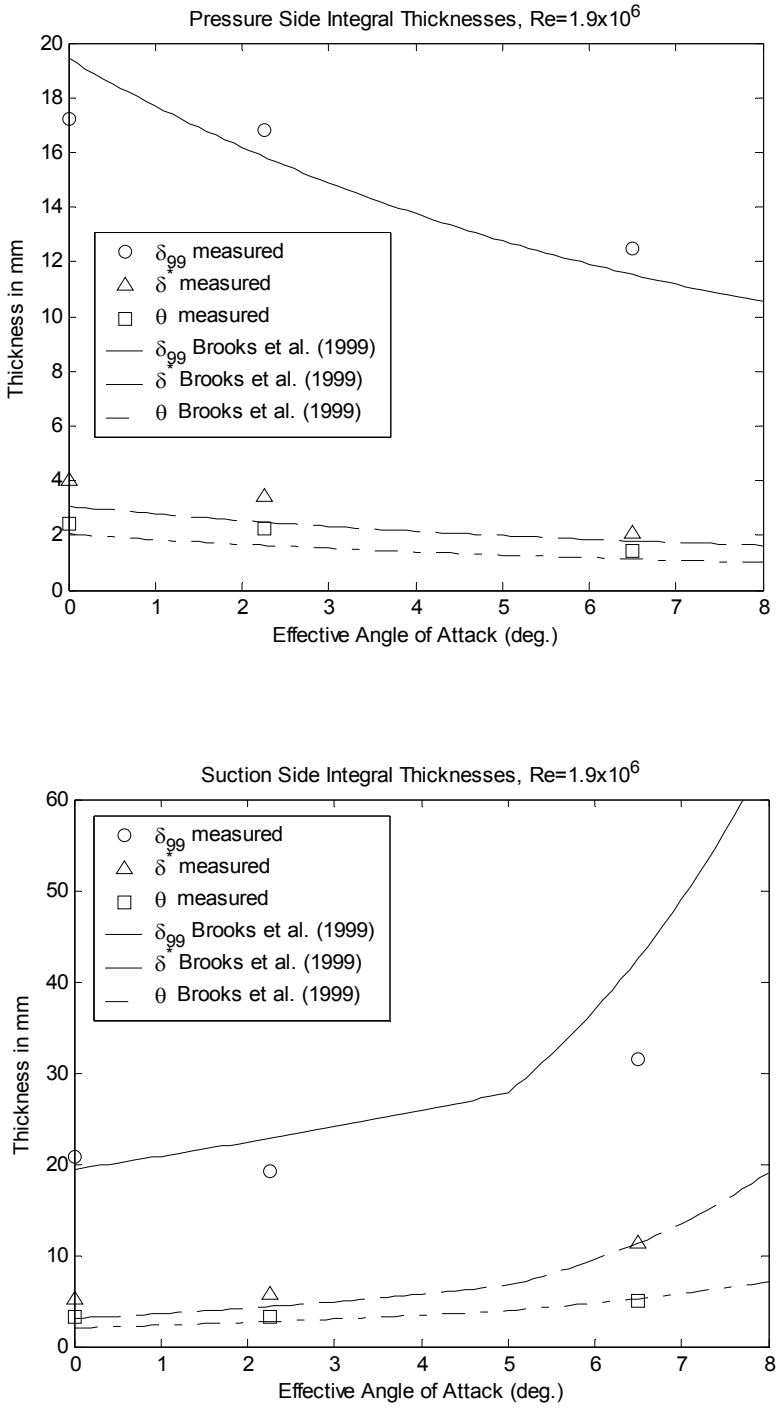

Figure 4-25. *Boundary layer thicknesses at x/c=0.98 for the NACA 0012 airfoil at Re=1.9x10^6 compared with empirical relations from Brooks et al. (1989) (untripped formula used for zero angle of attack values).*

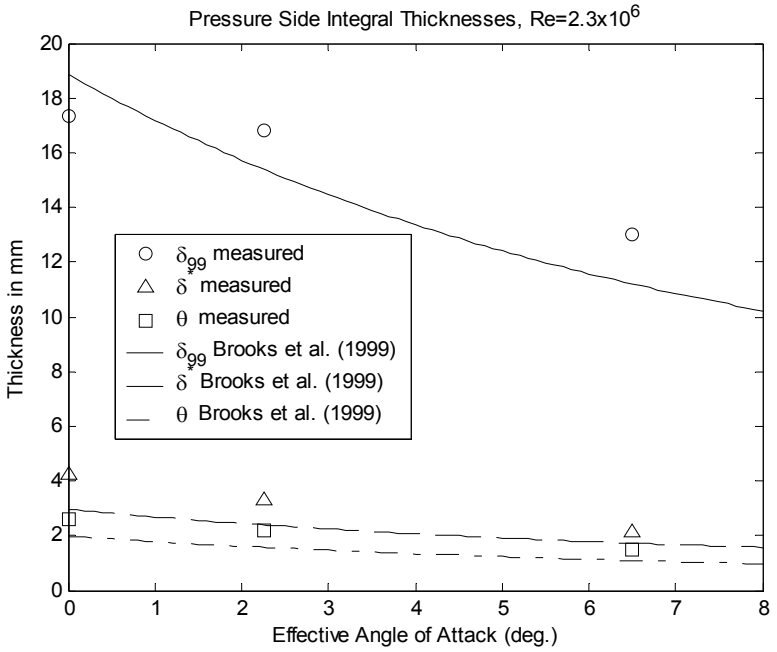

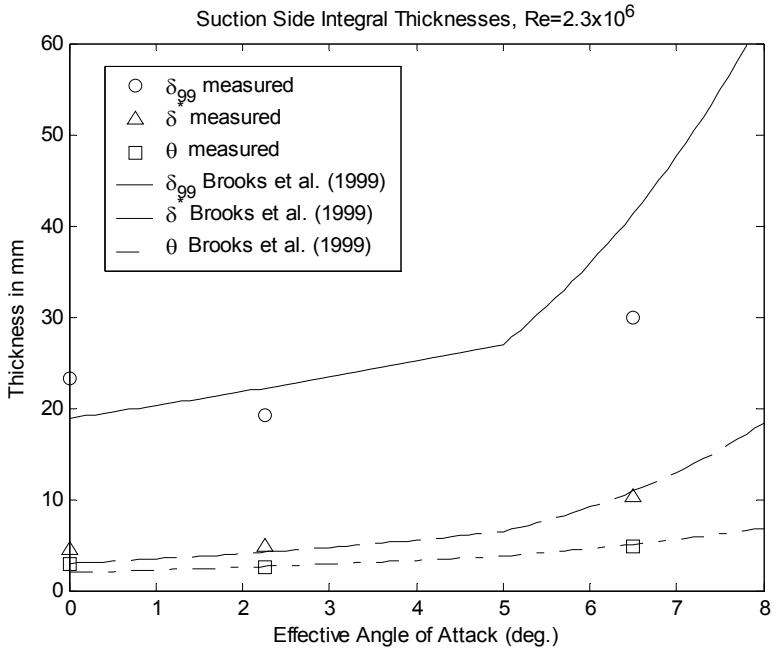

Figure 4-26. *Boundary layer thicknesses at x/c=0.98 for the NACA 0012 airfoil at Re=2.3x10^6 compared with empirical relations from Brooks et al. (1989) (untripped formula used for zero angle of attack values).*

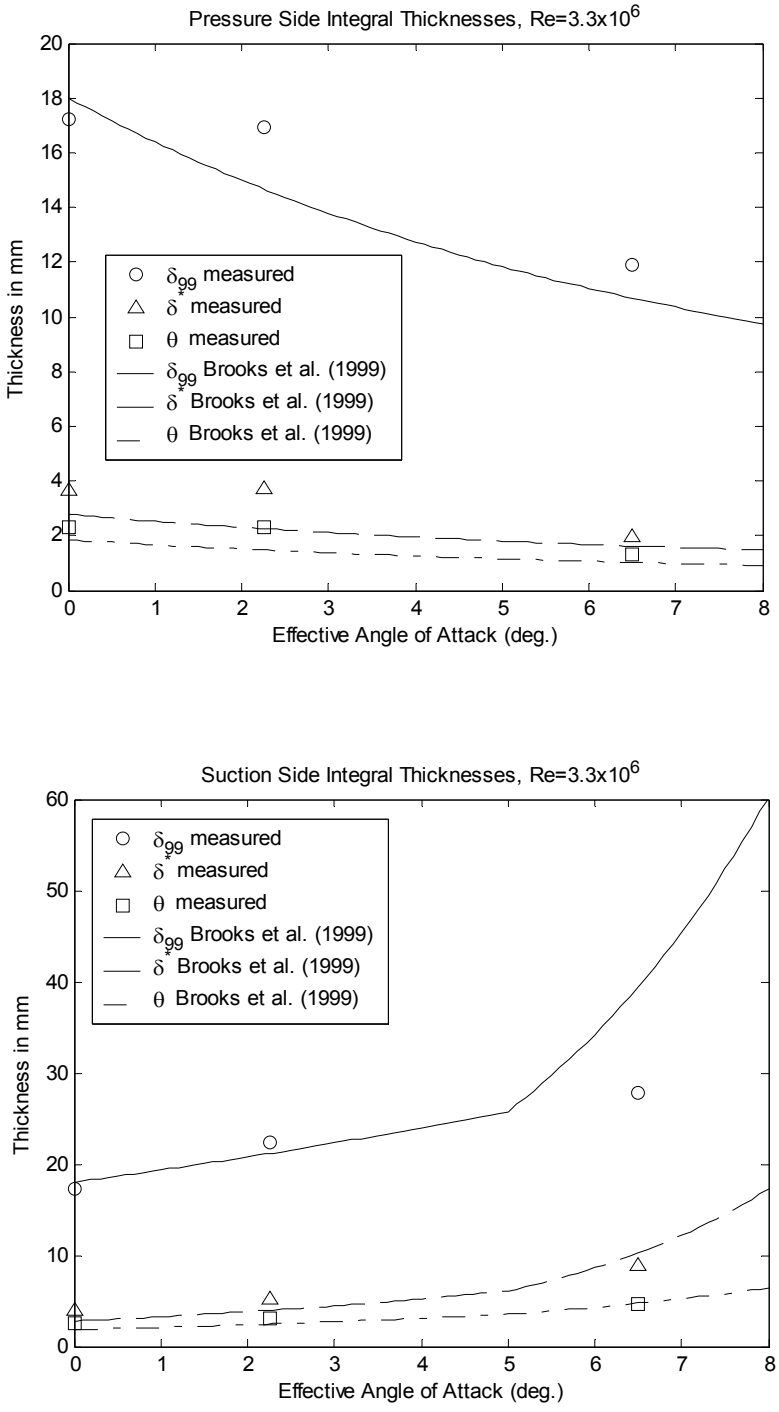

Figure 4-27. *Boundary layer thicknesses at x/c=0.98 for the NACA 0012 airfoil at Re=3.3x10^6 compared with empirical relations from Brooks et al. (1989) (untripped formula used for zero angle of attack values).*

.

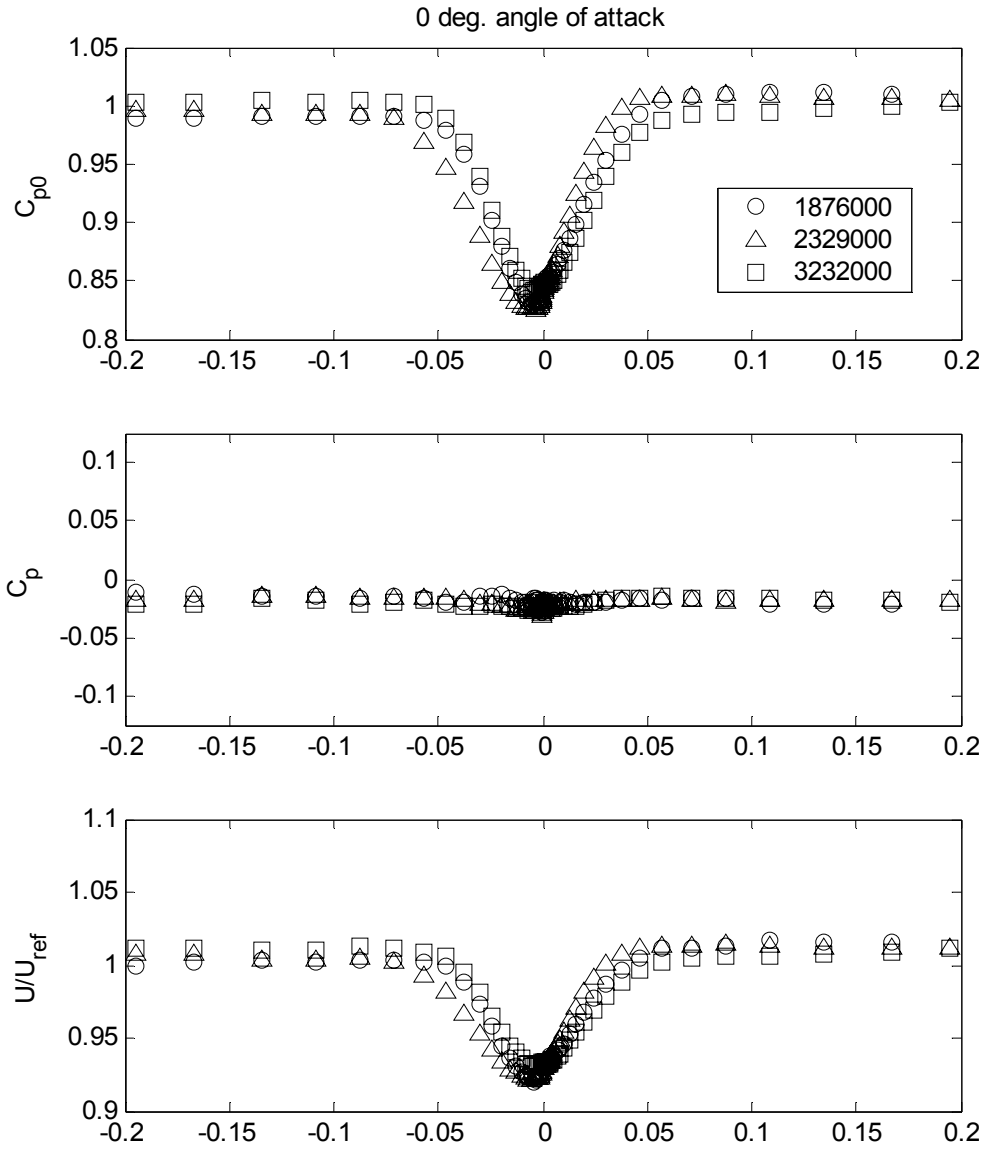

Figure 4-28. *Wake pressure and velocity profiles at X/c=2.5 for the NACA 0012 airfoil at zero degrees angle of attack as a function of Reynolds number*

.

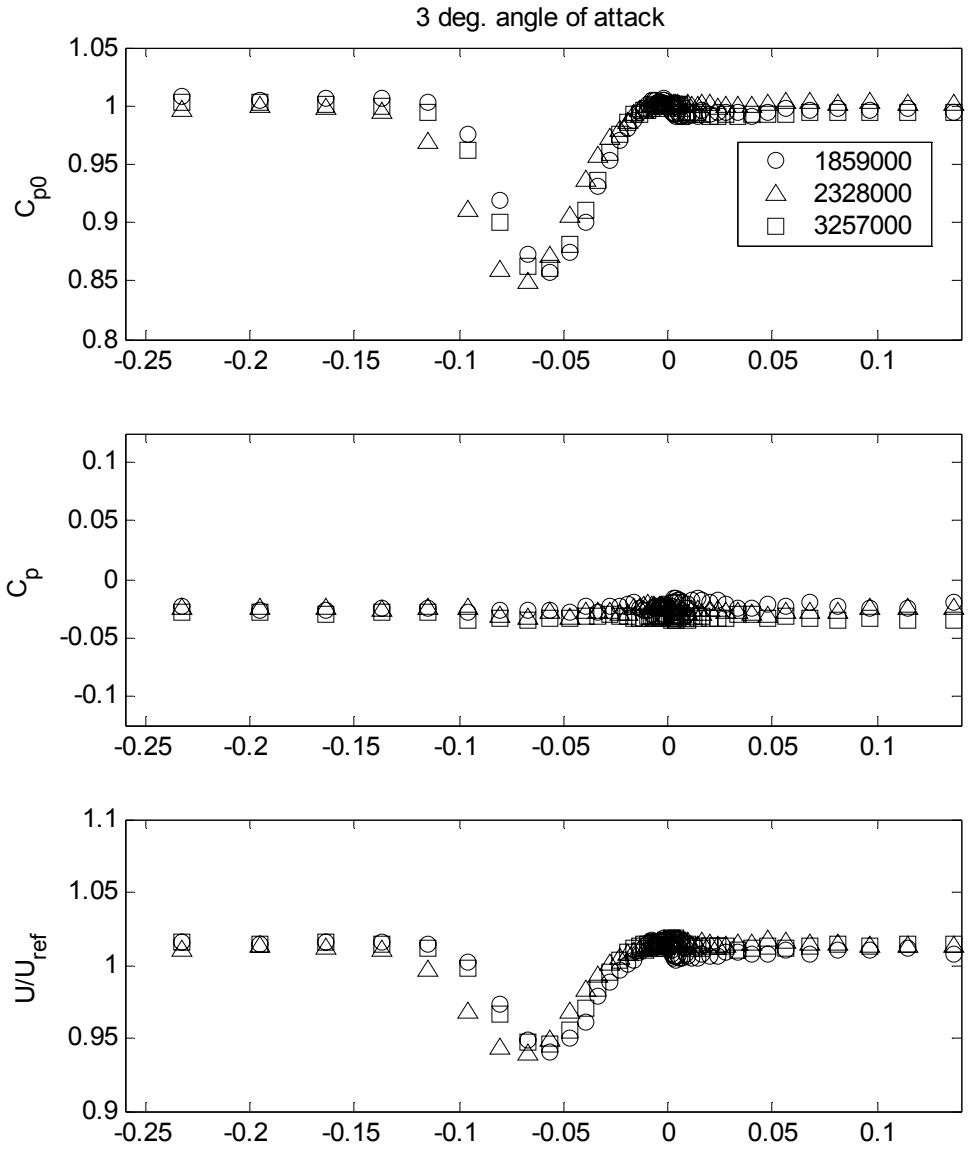

Figure 4-29. *Wake pressure and velocity profiles at X/c=2.5 for the NACA 0012 airfoil at 3 degrees geometric angle of attack as a function of Reynolds number*

.

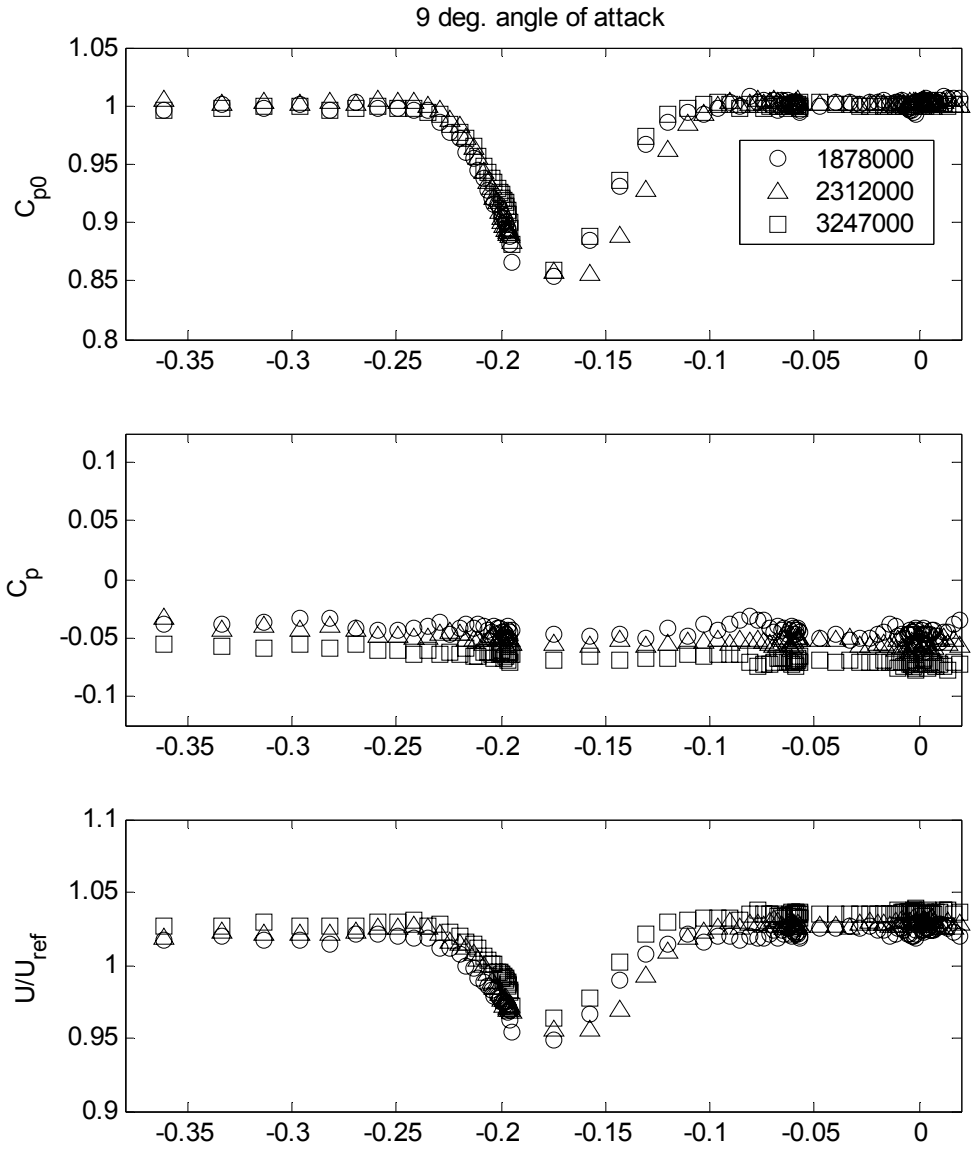

Figure 4-30. *Wake pressure and velocity profiles at X/c=2.5 for the NACA 0012 airfoil at 9 degrees geometric angle of attack as a function of Reynolds number*

.

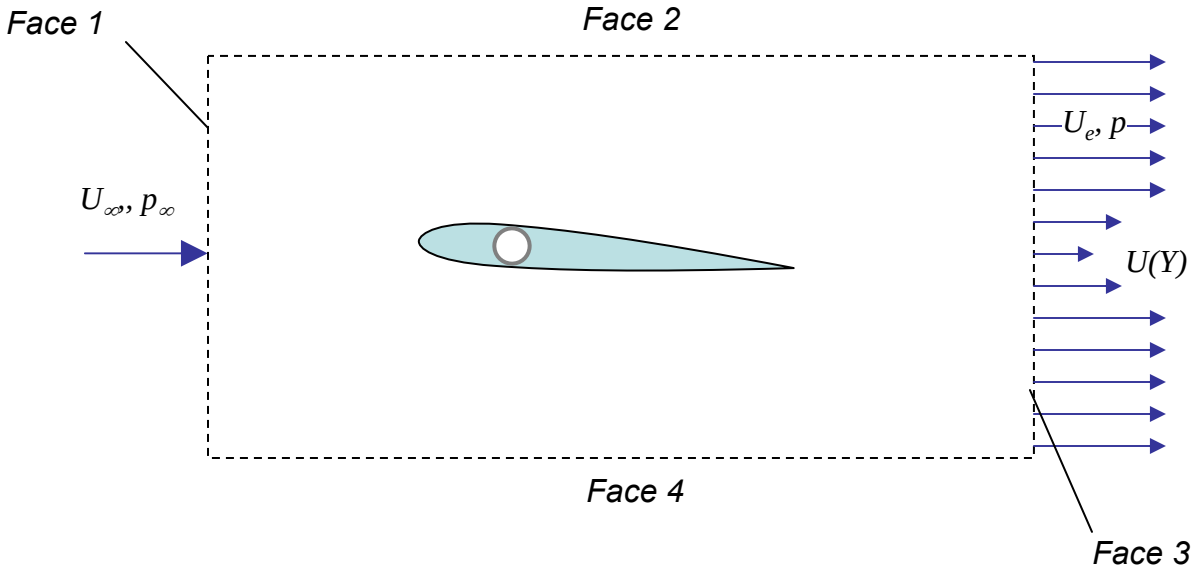

Figure 4-31. *Control volume used for drag analysis based on wake profiles.*

.

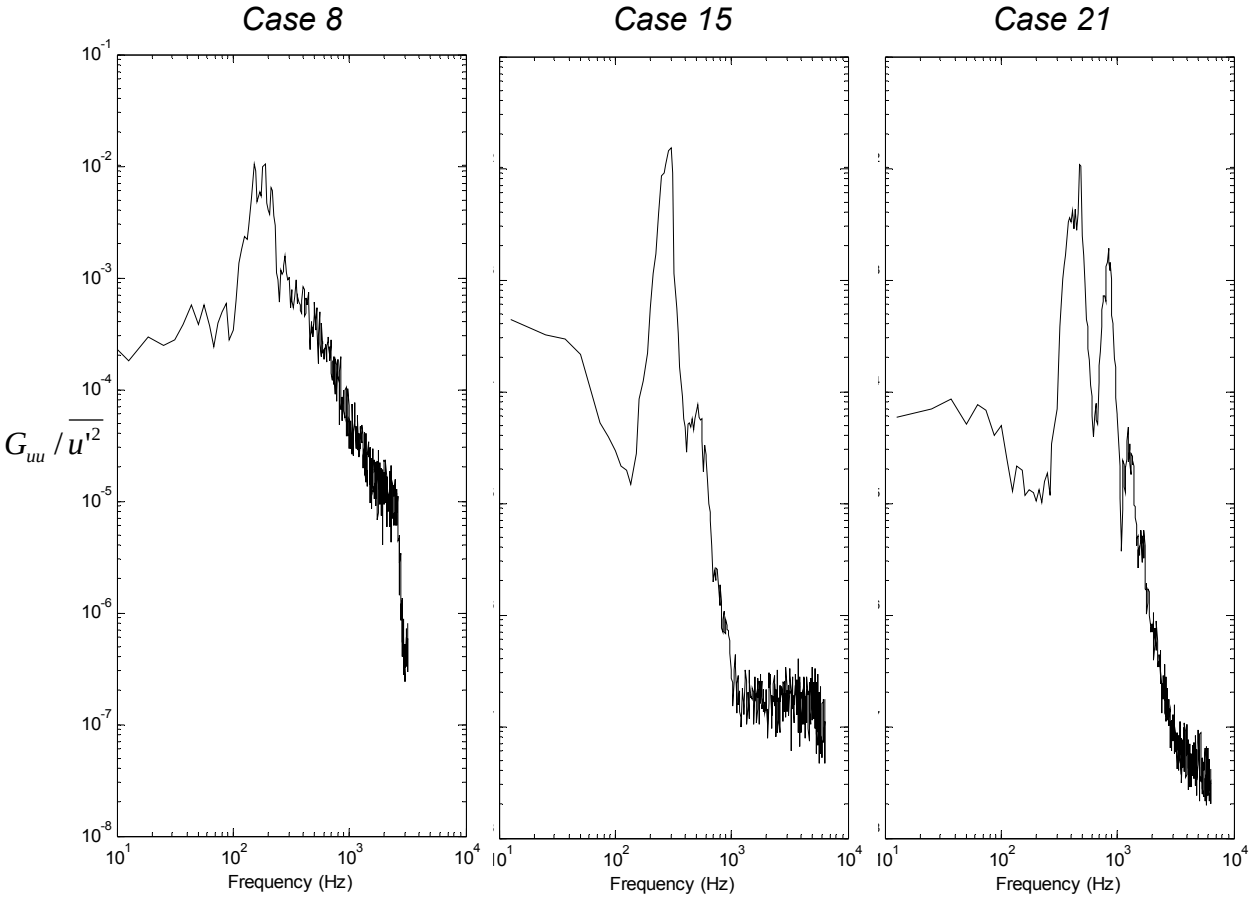

Figure 4-32. *Velocity spectra measured just downstream of the NACA 0012 trailing edge with no boundary layer trip. Case numbers refer to table 4-3.*

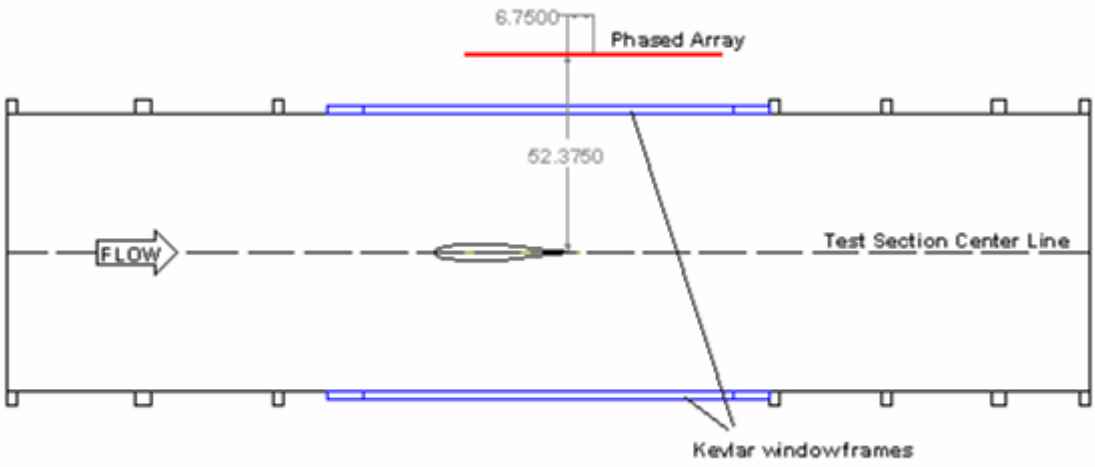

Figure 4-33. *Schematic drawing of the test setup for the aeroacoustic measurements (as seen from top). Dimensions in inches.*

(a) Front view of phased array.

Tensioned Kevlar

(b) Back view of phased array.

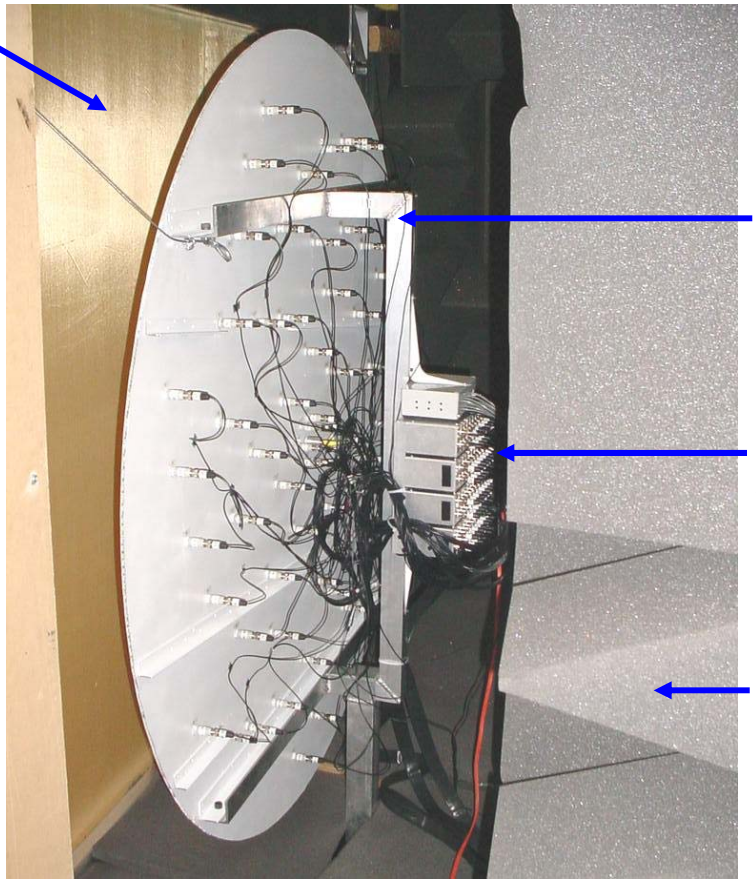

Figure 4-34. *Phased array installed in the acoustic enclosure behind the tensioned Kevlar window shown in figure 4-33.*

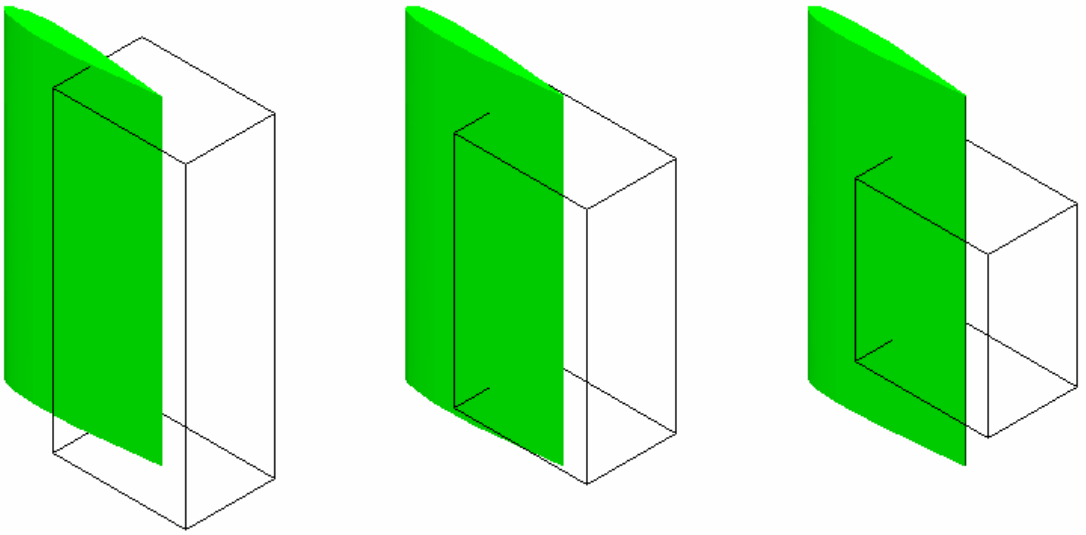

(a) Full span. (b) ¾-span. (c) ½ span.

Figure 4-35. *Volumes for the evaluation of the integrated SPL.*

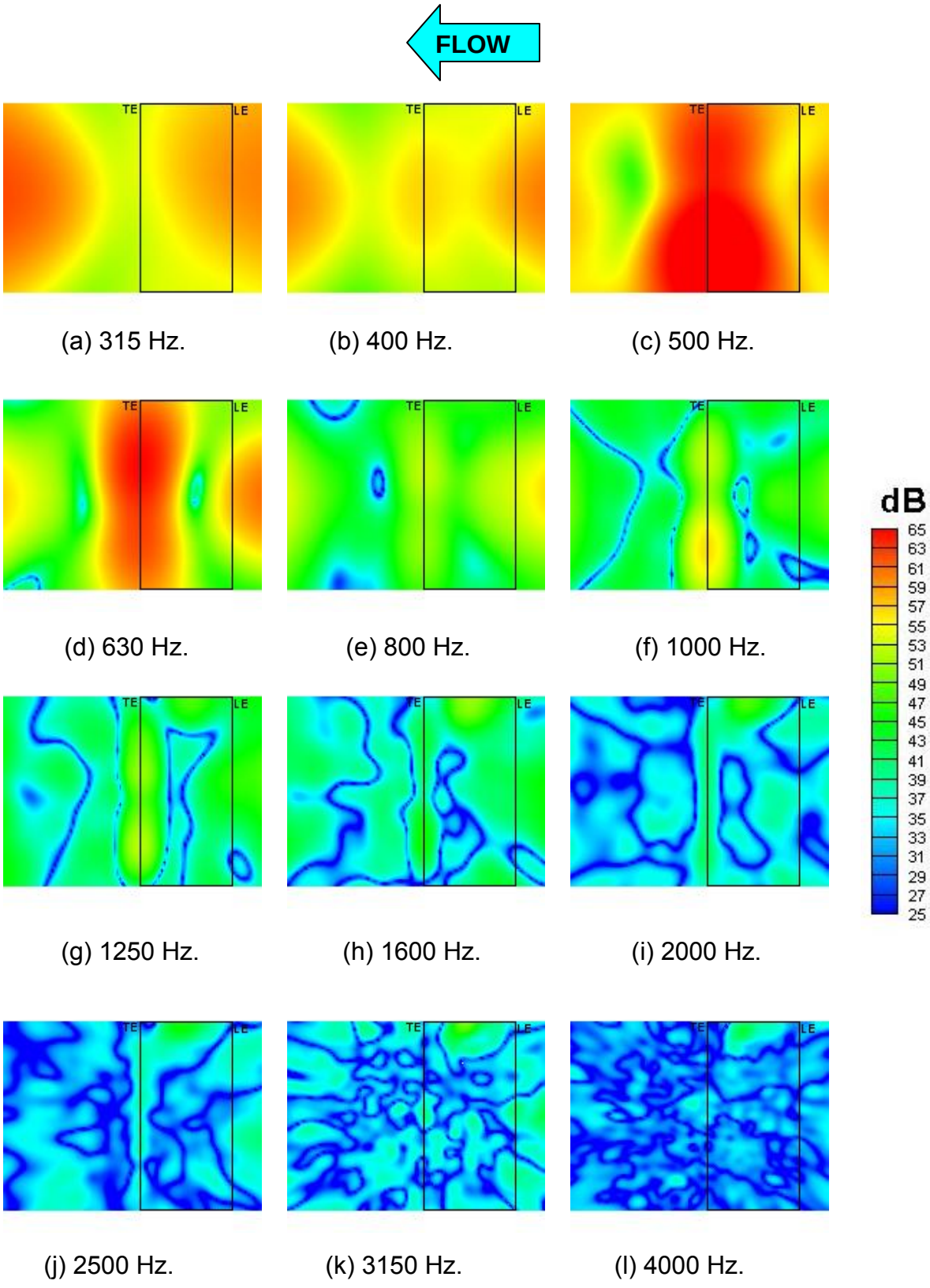

Figure 4-36. *1/3-Octave band beamform maps for the airfoil with untripped boundary layer, α=-7˚, Mach 0.11 (Re=2.38x10^6). Array on pressure side. Airfoil leading and trailing edges indicated by the vertical lines.*

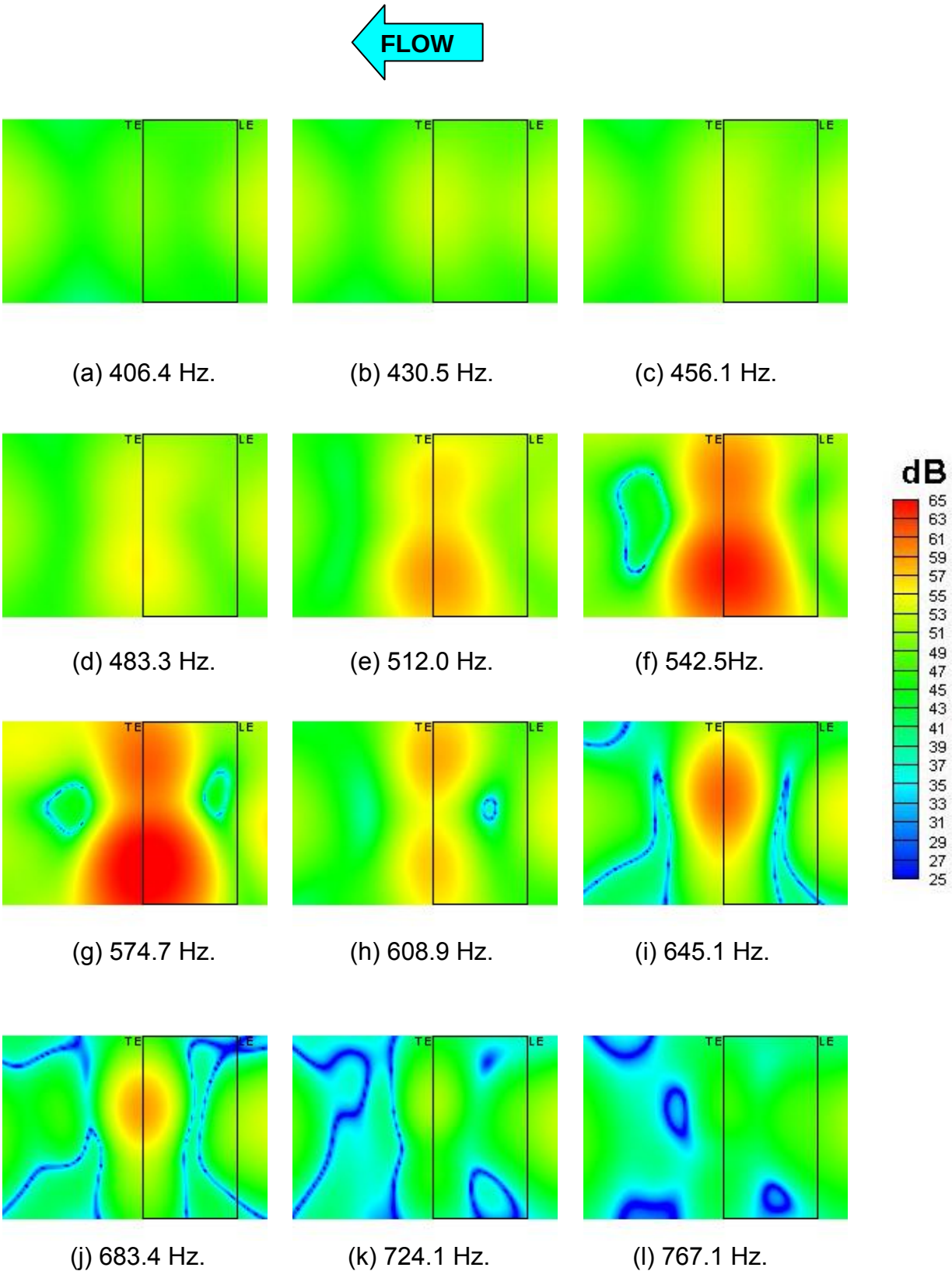

(a) 406.4 Hz. (b) 430.5 Hz. (c) 456.1 Hz.

(d) 483.3 Hz. (e) 512.0 Hz. (f) 542.5Hz.

(g) 574.7 Hz. (h) 608.9 Hz. (i) 645.1 Hz.

(j) 683.4 Hz. (k) 724.1 Hz. (l) 767.1 Hz.

Figure 4-37. *1/12-Octave band beamform maps for the airfoil with untripped boundary layer, α=7˚, Mach 0.11 (Re=2.38x10^6). Array on pressure side. Airfoil leading and trailing edges indicated by the vertical lines.*

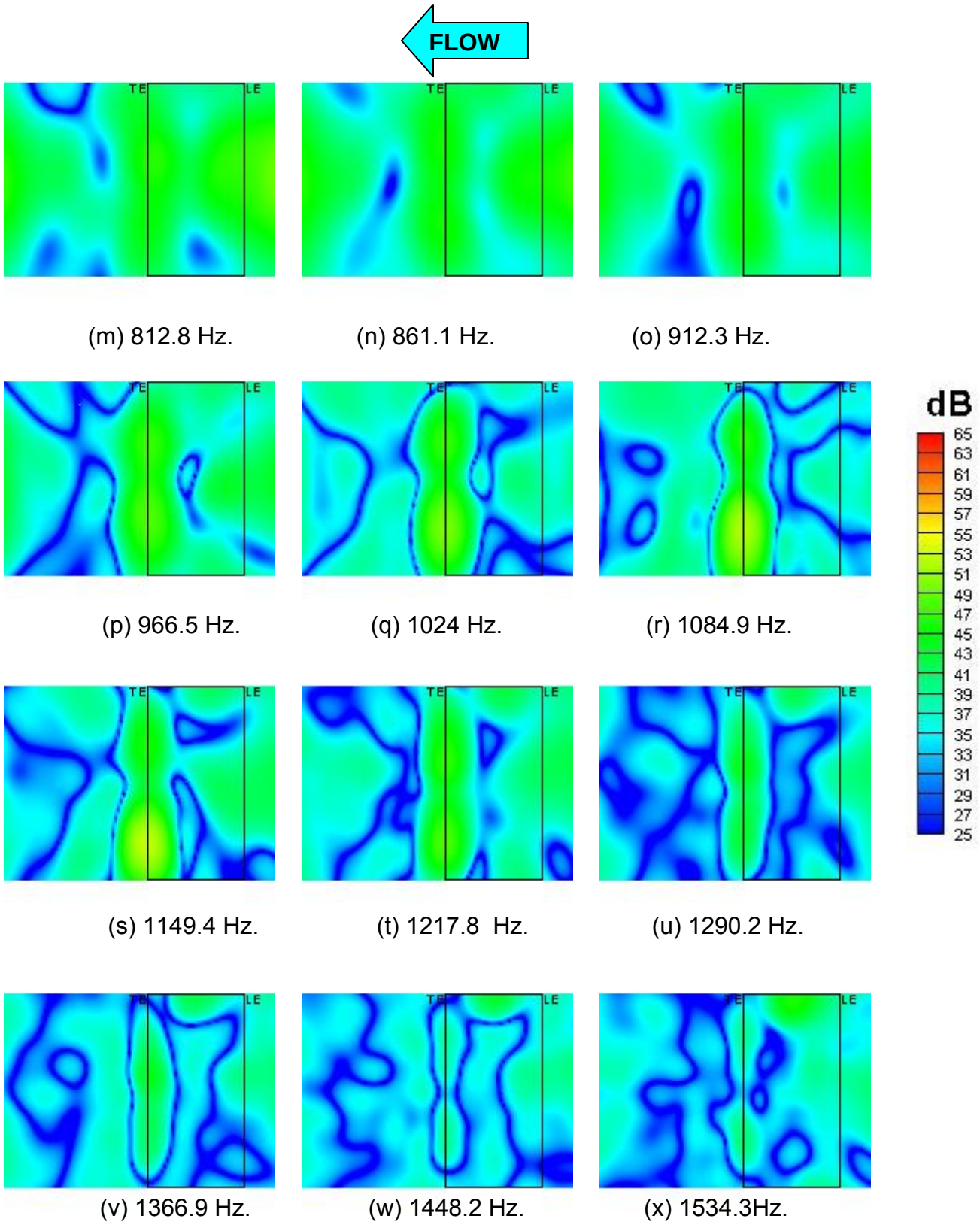

Figure 4-37. *1/12-Octave band beamform maps for the airfoil with untripped boundary layer, α=7˚, Mach 0.11 (Re=2.38x10^6). Array on pressure side. Airfoil leading and trailing edges indicated by the vertical lines.*

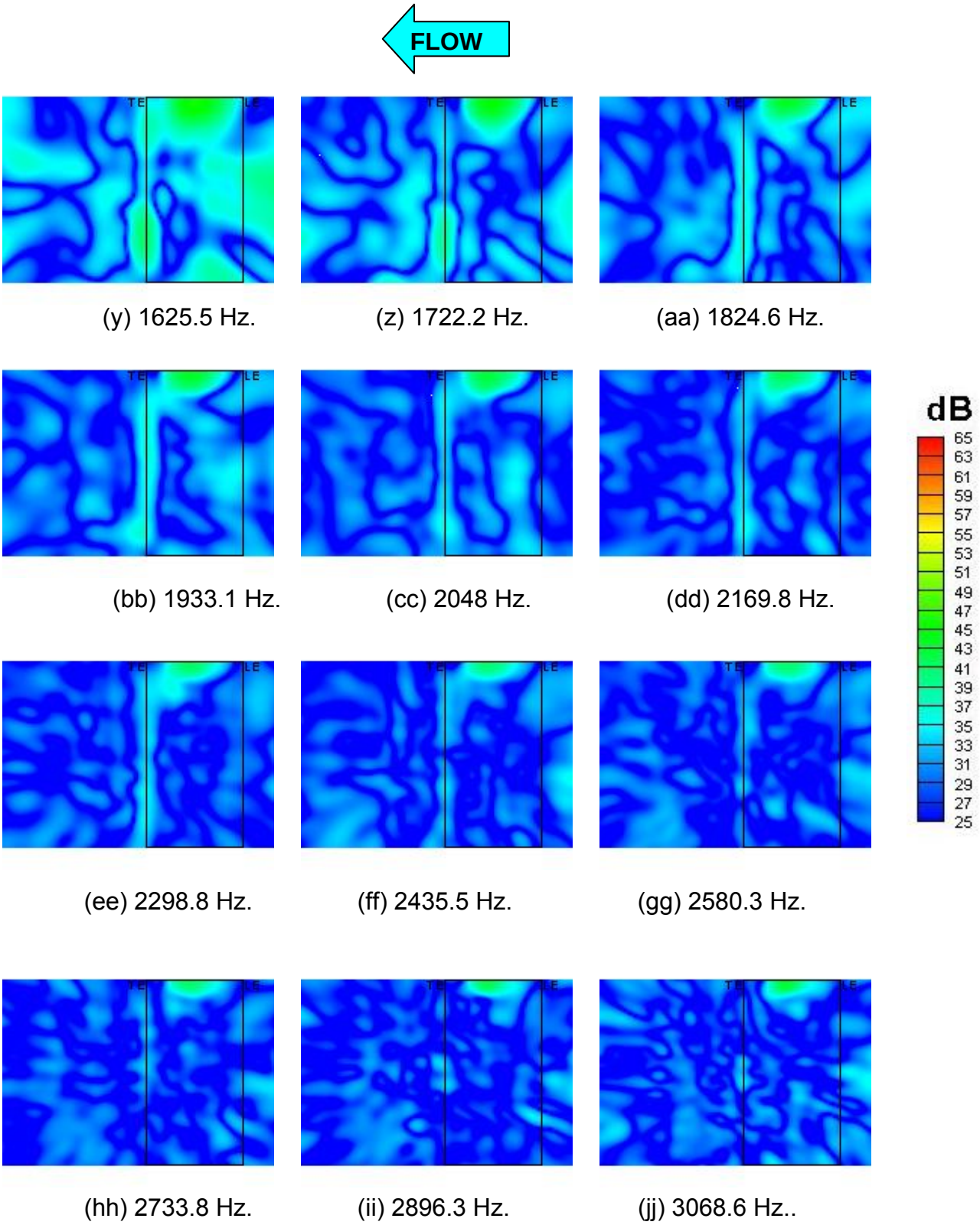

Figure 4-37. *1/12-Octave band beamform maps for the airfoil with untripped boundary layer, α=-7˚, Mach 0.11 (Re=2.38x10^6). Array on pressure side. Airfoil leading and trailing edges indicated by the vertical lines.*

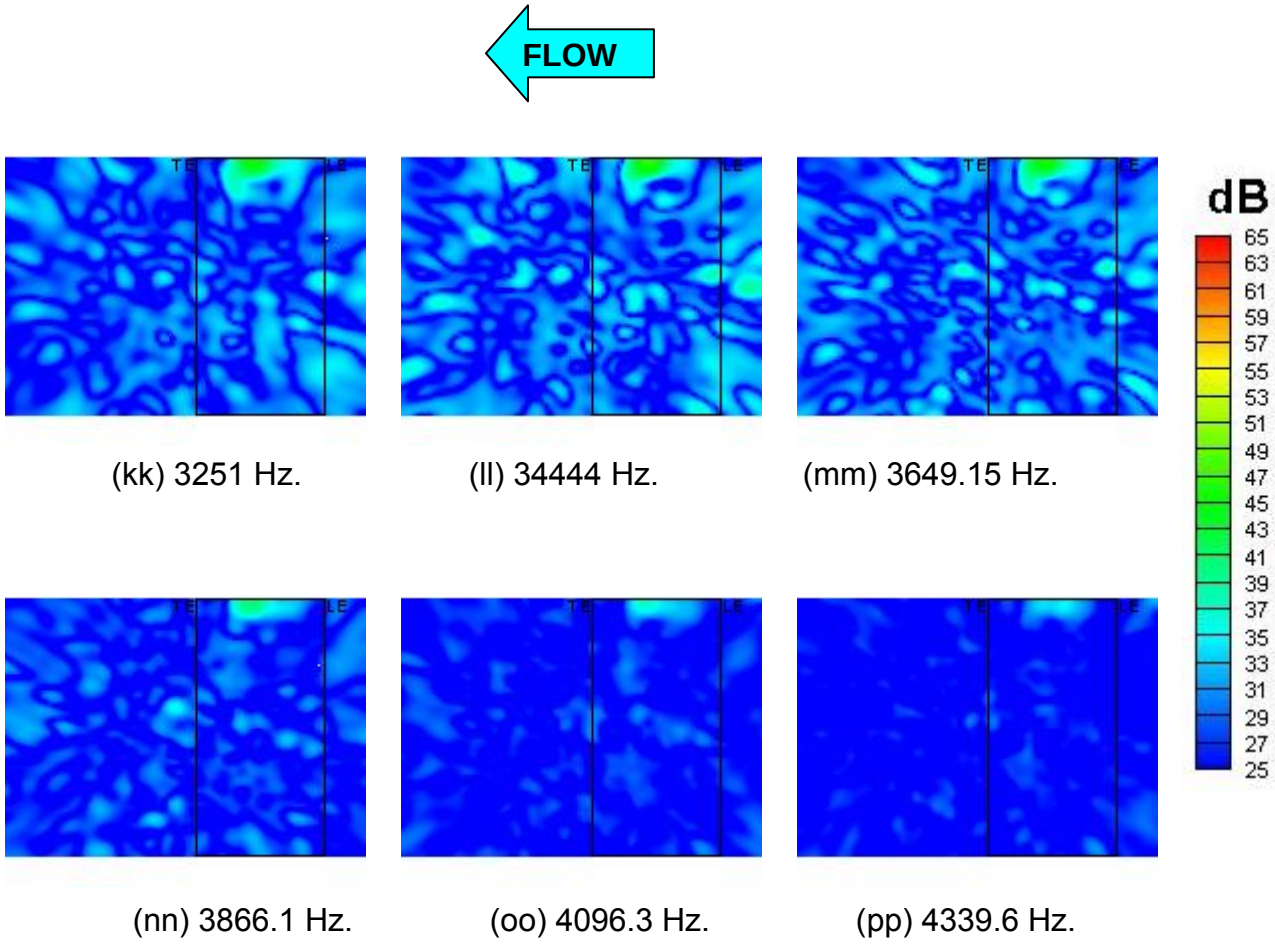

Figure 4-37. *1/12-Octave band beamform maps for the airfoil with untripped boundary layer, α=7˚, Mach 0.11 (Re=2.38x10^6). Array on pressure side. Airfoil leading and trailing edges indicated by the vertical lines.*

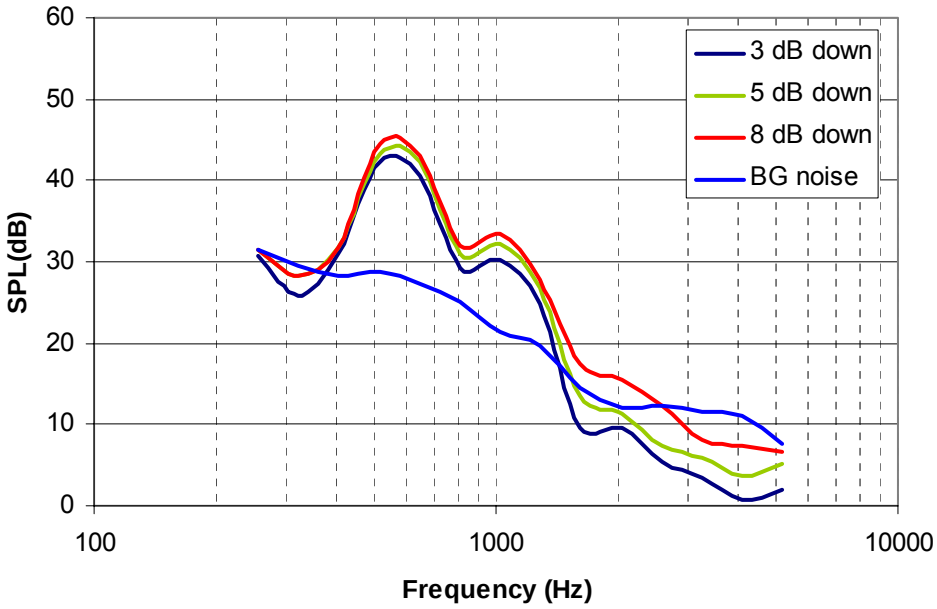

Figure 4-38. *Integrated 1/3-octave band spectrum for three different cut-off levels. Airfoil at -7 degrees angle of attack, geometric, 38m/s, Mach 0.11, array on pressure side.*

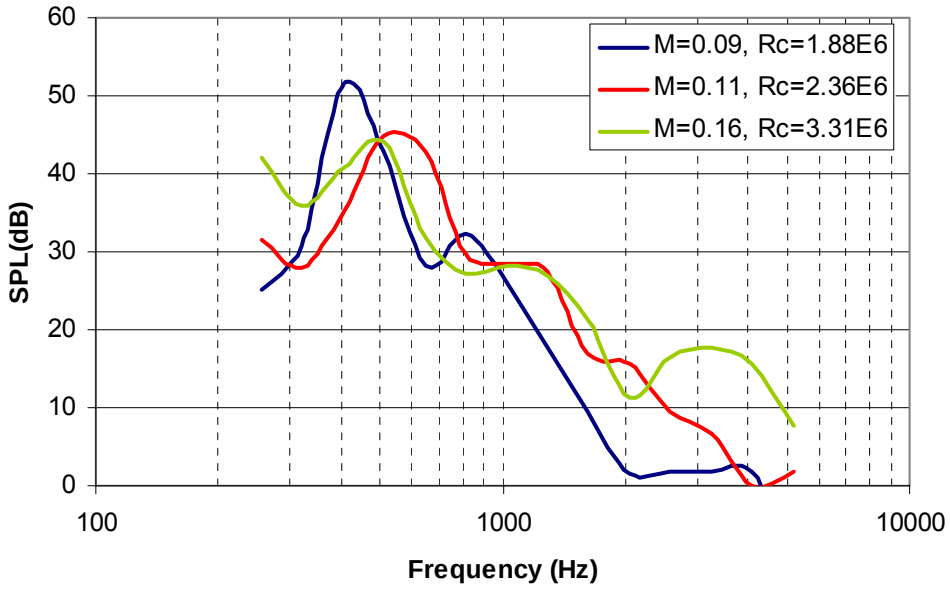

Figure 4-39. *Integrated 1/3-Octave band spectrum for various flow speeds (indicated here in terms of Mach number and Reynolds number). Airfoil at -7 degree angle of attack (geometric), phased array on pressure side.*

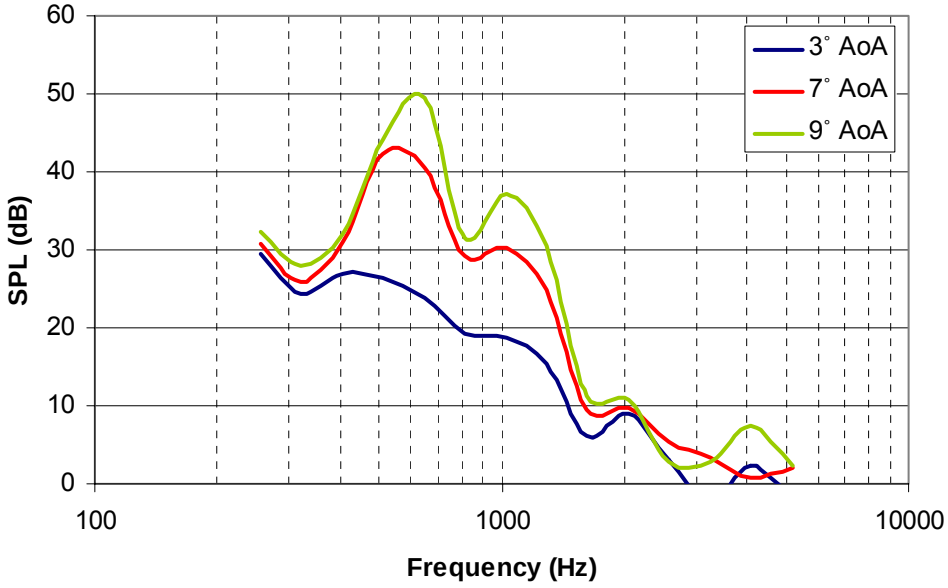

Figure 4-40. *Integrated spectrum in 1/3 octave bands for three angles of attack. Mach 0.11, Rc=2.36x10^6, array on pressure side. Indicated angles of attack are negative geometric. Corresponding effective angles of attack are -2.25, -5 and -6.5 degrees.*

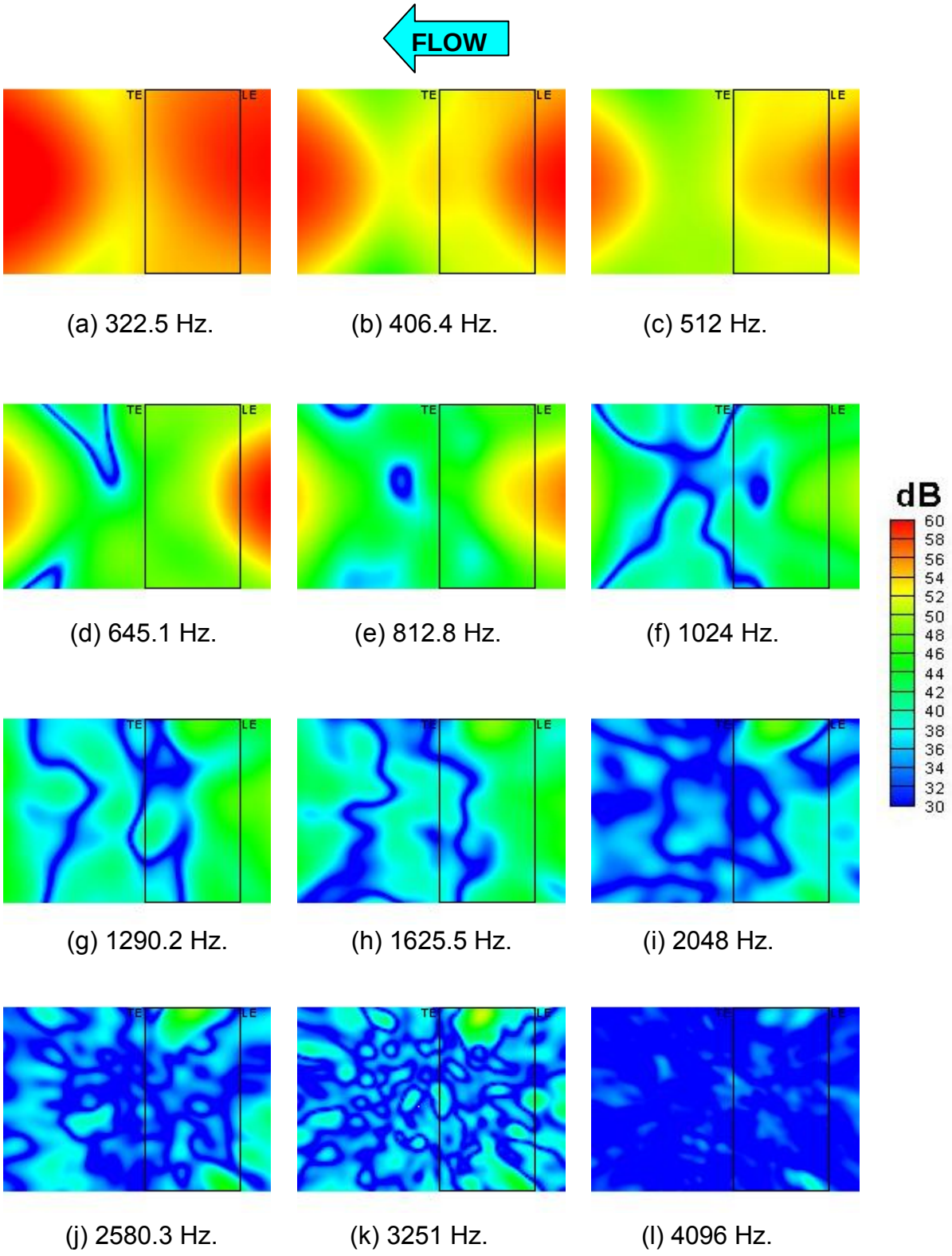

Figure 4-41. *1/3-Octave band beamform maps for the airfoil with tripped boundary layer, α=-7˚, Mach 0.11 (Re=2.38x10^6). Array on pressure side. Airfoil leading and trailing edges indicated by the vertical lines.*

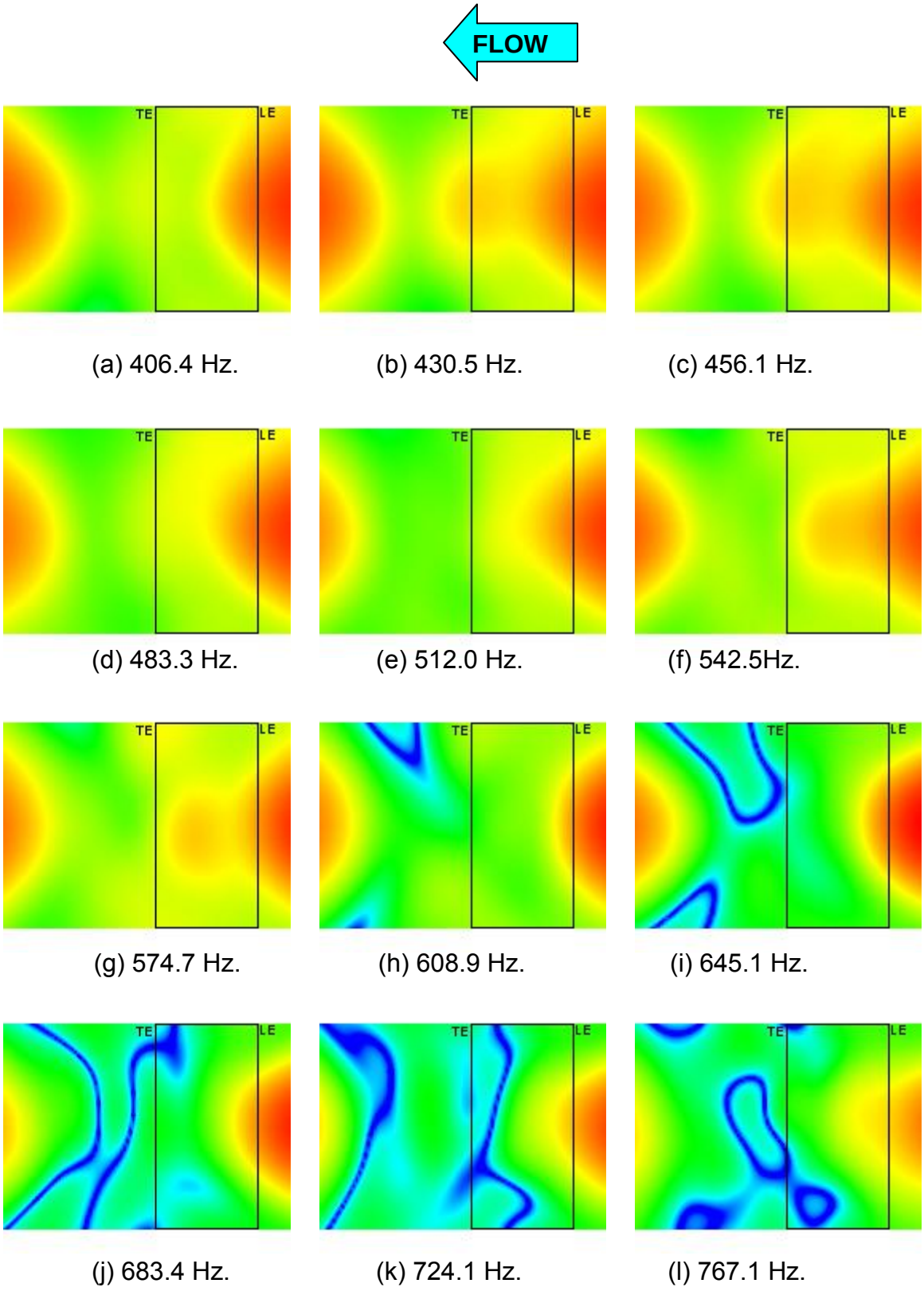

Figure 4-42. *1/12-Octave band beamform maps for the airfoil with tripped boundary layer, α=-7˚, Mach 0.11 (Re=2.38x10^6). Array on pressure side. Airfoil leading and trailing edges indicated by the vertical lines.*

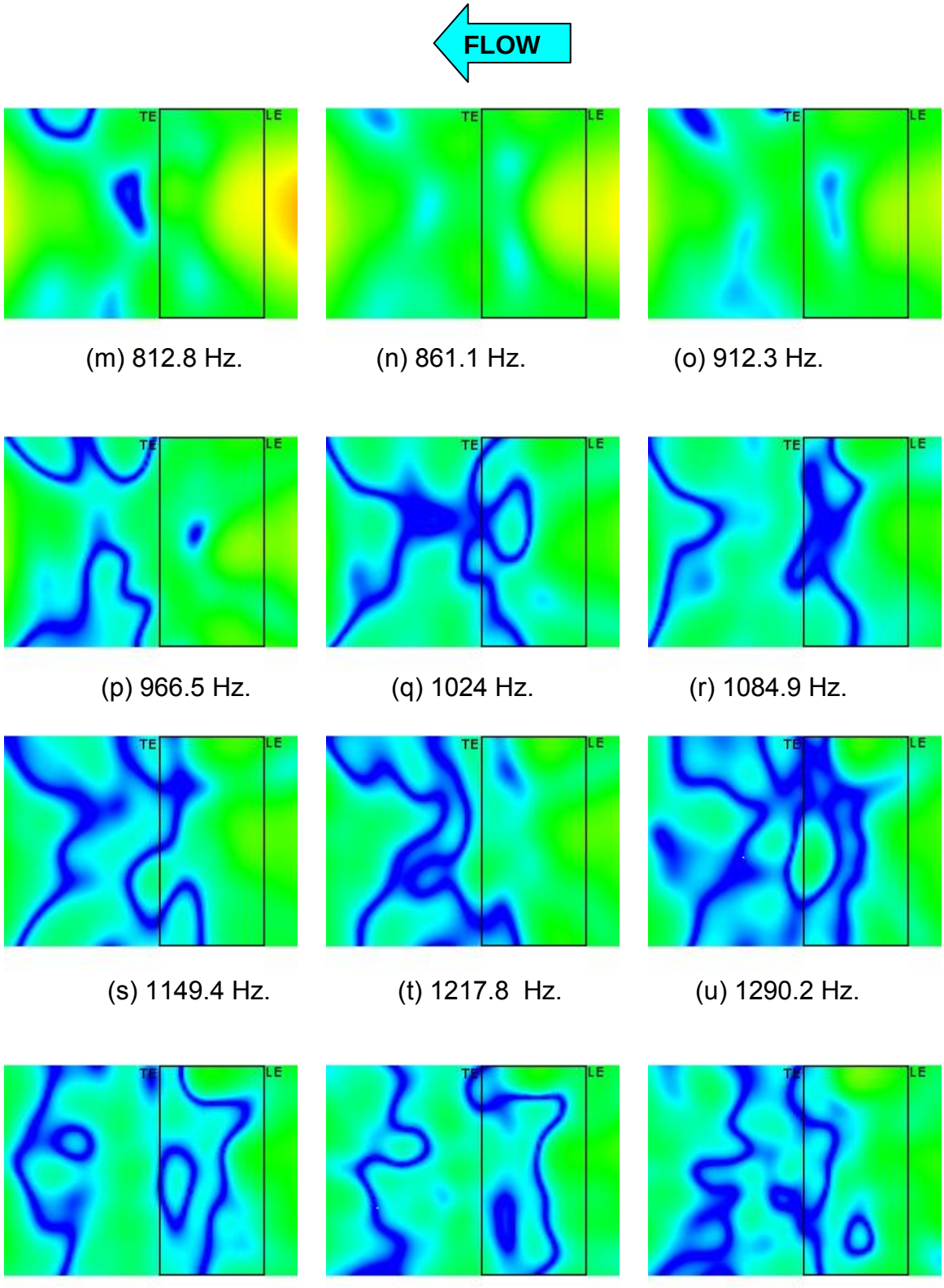

Figure 4-42. *1/12-Octave band beamform maps for the airfoil with tripped boundary layer, α=-7˚, Mach 0.11 (Re=2.38x10^6). Array on pressure side. Airfoil leading and trailing edges indicated by the vertical lines.*

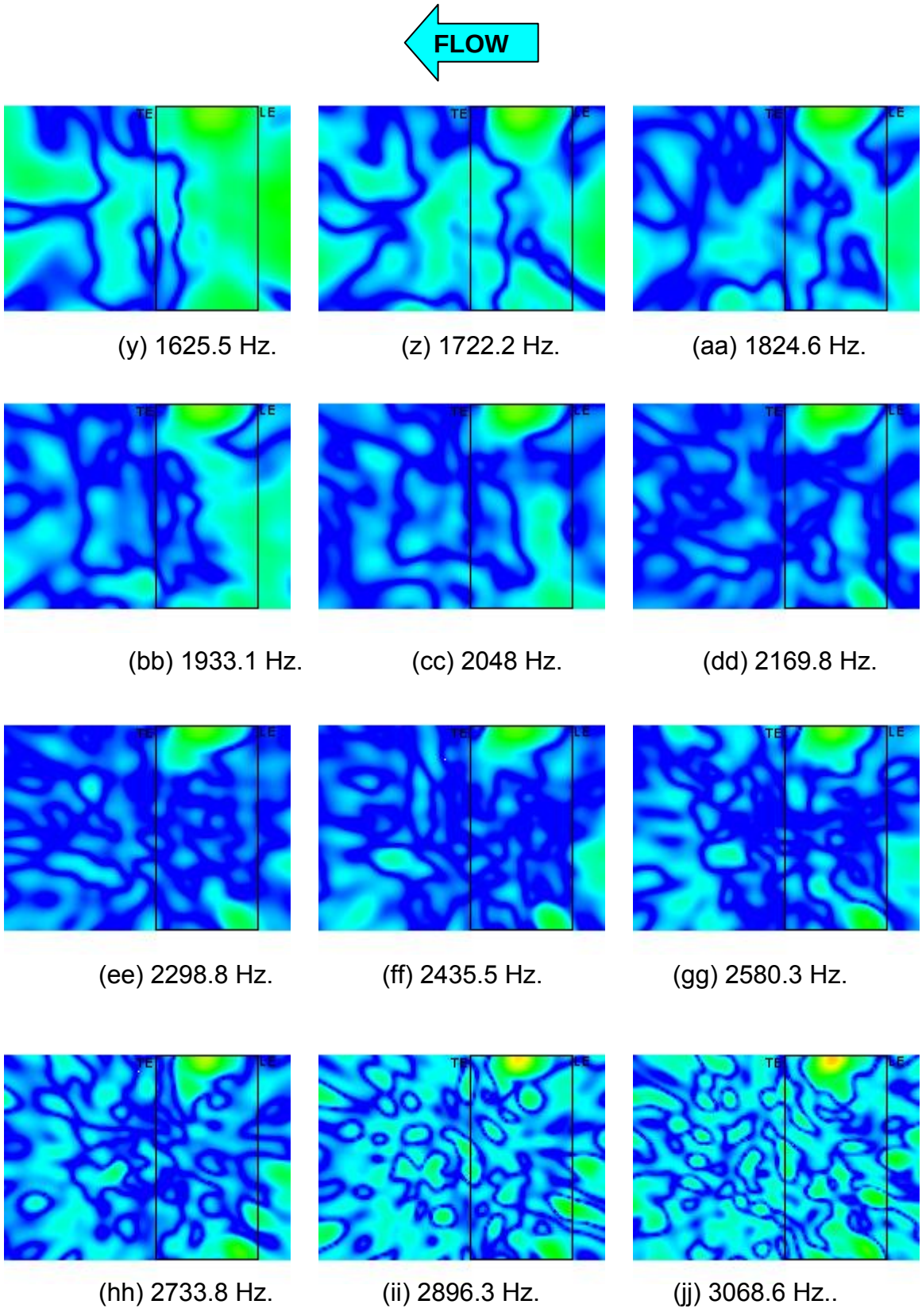

Figure 4-42. *1/12-Octave band beamform maps for the airfoil with tripped boundary layer, α=-7˚, Mach 0.11 (Re=2.38x10^6). Array on pressure side. Airfoil leading and trailing edges indicated by the vertical lines.*

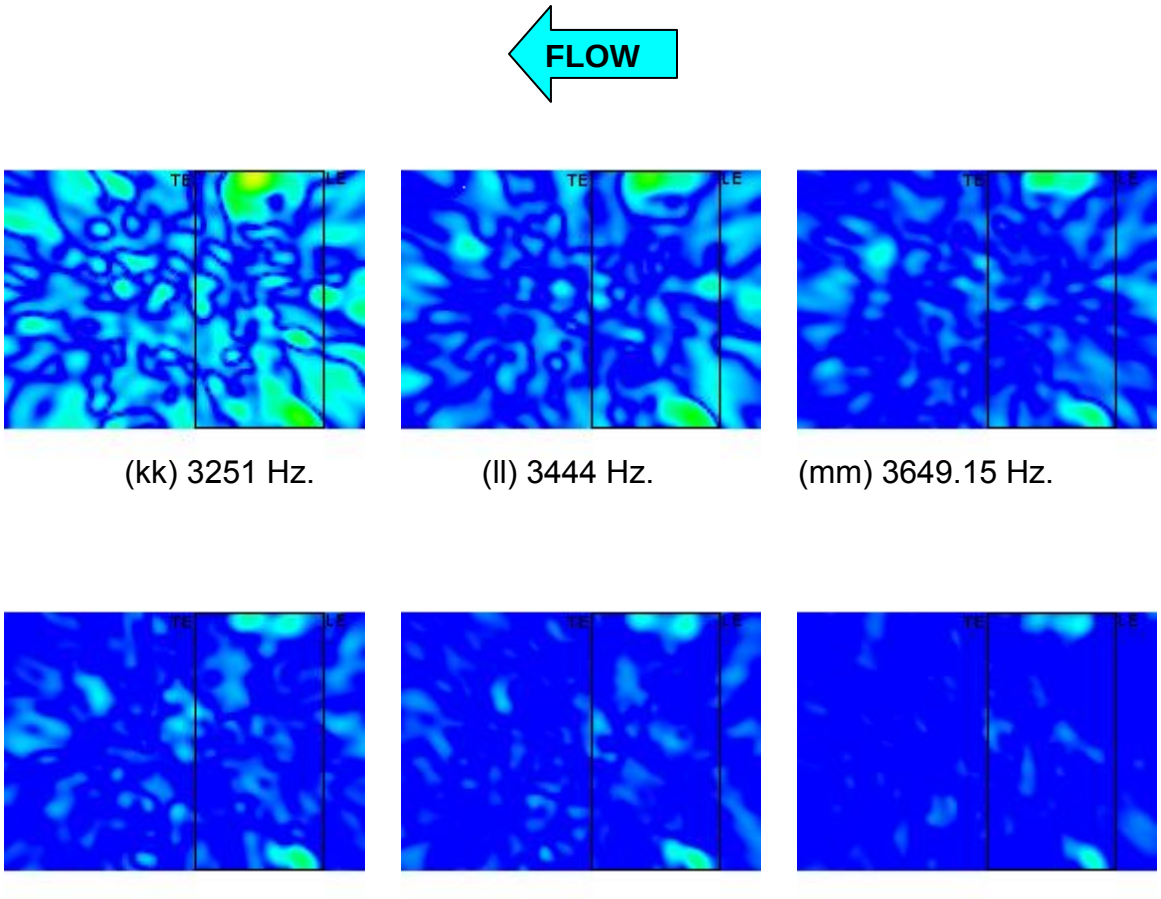

Figure 4-42. *1/12-Octave band beamform maps for the airfoil with tripped boundary layer, α=-7˚, Mach 0.11 (Re=2.38x10^6). Array on pressure side. Airfoil leading and trailing edges indicated by the vertical lines.*

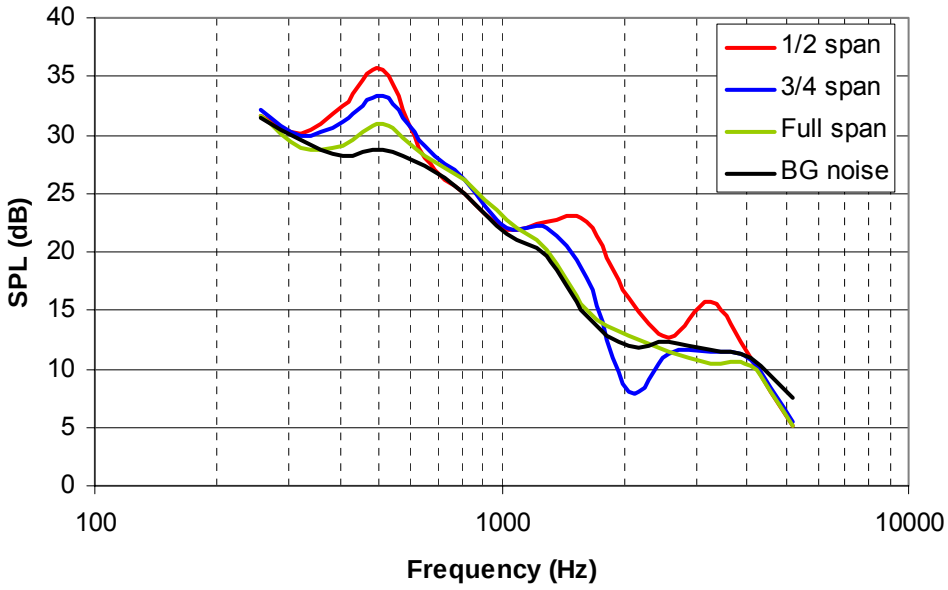

Figure 4-43. *Integrated 1/3-octave band spectrum for three volumes of integration. Airfoil at -7 degrees angle of attack , geometric, 38m/s, Mach 0.11, array on pressure side.*

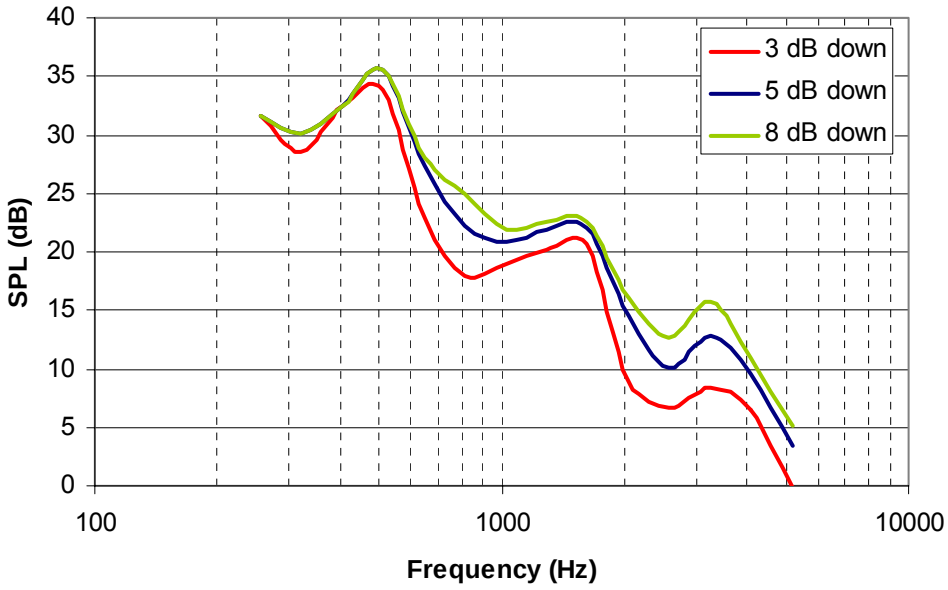

Figure 4-44. *Integrated 1/3-octave band spectrum for three cut off values.*
Airfoil at -7 degrees angle of attack , geometric, 38m/s, Mach 0.11, array on pressure side.

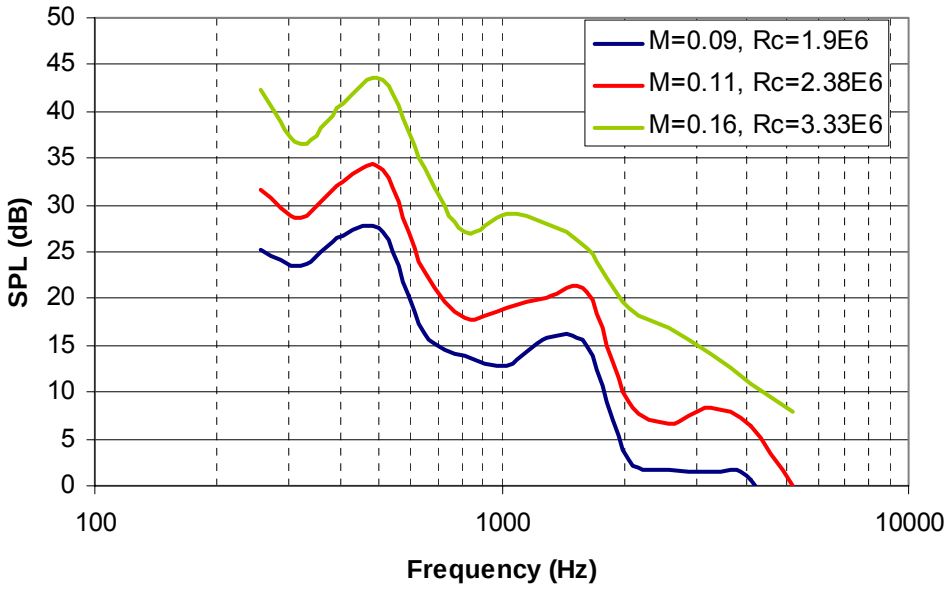

Figure 4-45. *Integrated 1/3-Octave band spectrum for various flow speeds (indicated here in terms of Mach number and Reynolds number). Airfoil at -7 degree angle of attack (geometric), phased array on pressure side.*

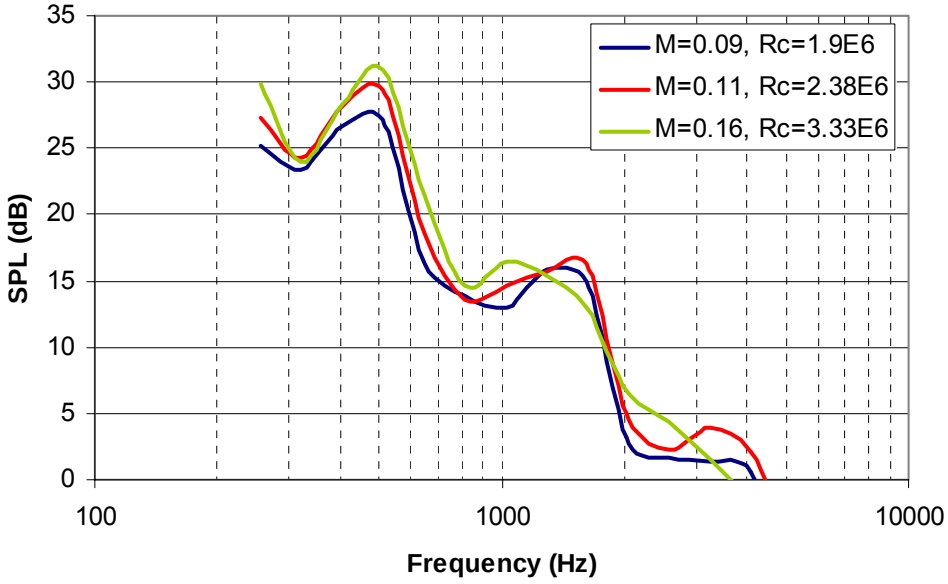

Figure 4-46. *Integrated 1/3-Octave band spectrum for various flow speeds (indicated here in terms of Mach number and Reynolds number) scaled on the 5th power of the Mach number. Airfoil at -7 degree angle of attack (geometric), phased array on pressure side.*

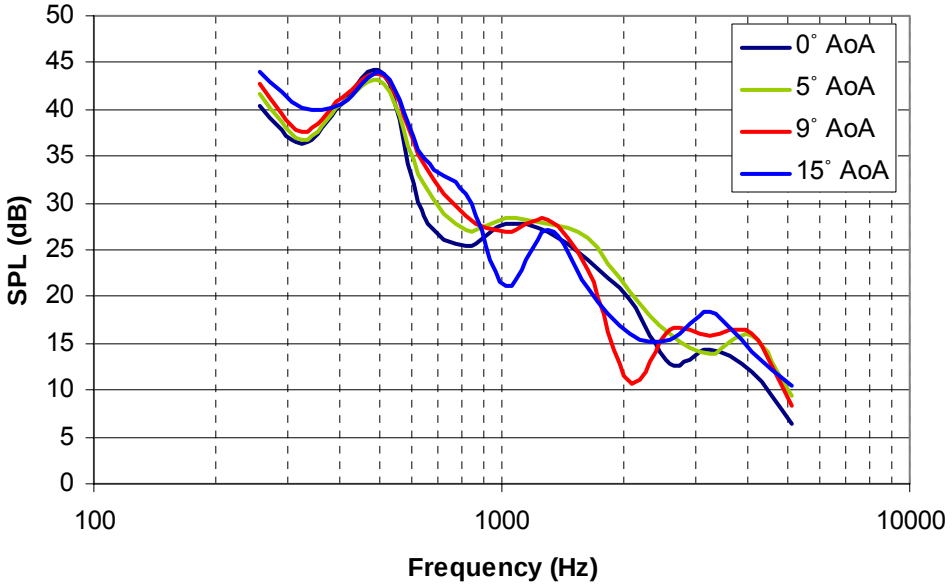

Figure 4-47. *Integrated spectrum in 1/3 octave bands for four angles of attack. Mach 0.16, Rc=3.32x10^6, array on pressure side. Indicated angles of attack are negative geometric. Corresponding effective angles of attack are 0, -3.5, -6.5 and -11 degrees.*

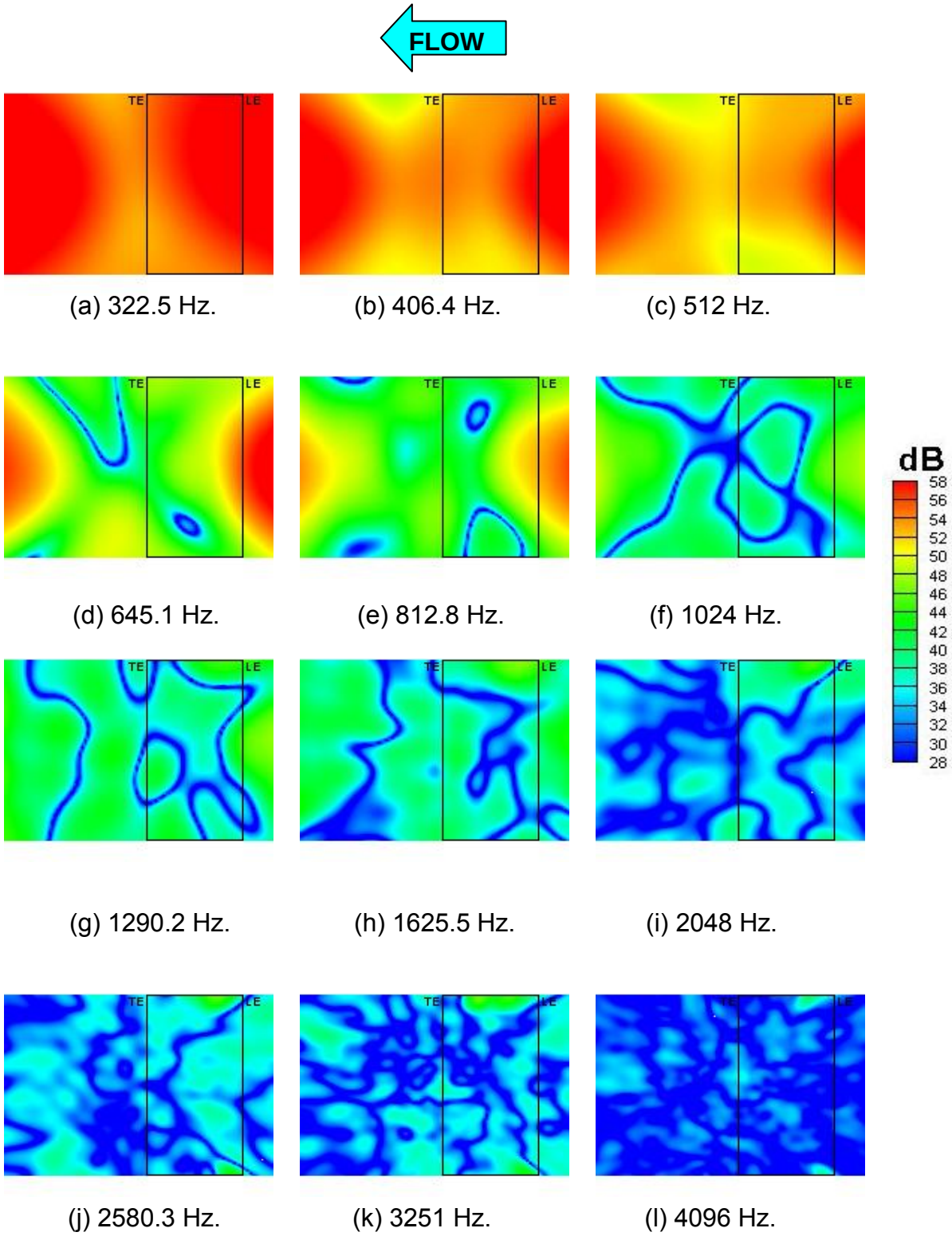

Figure 4-48. *1/3-Octave band beamform maps for the airfoil with tripped boundary layer, α=+7˚, Mach 0.11 (Re=2.38x10^6). Array on suction side. Airfoil leading and trailing edges indicated by the vertical lines.*

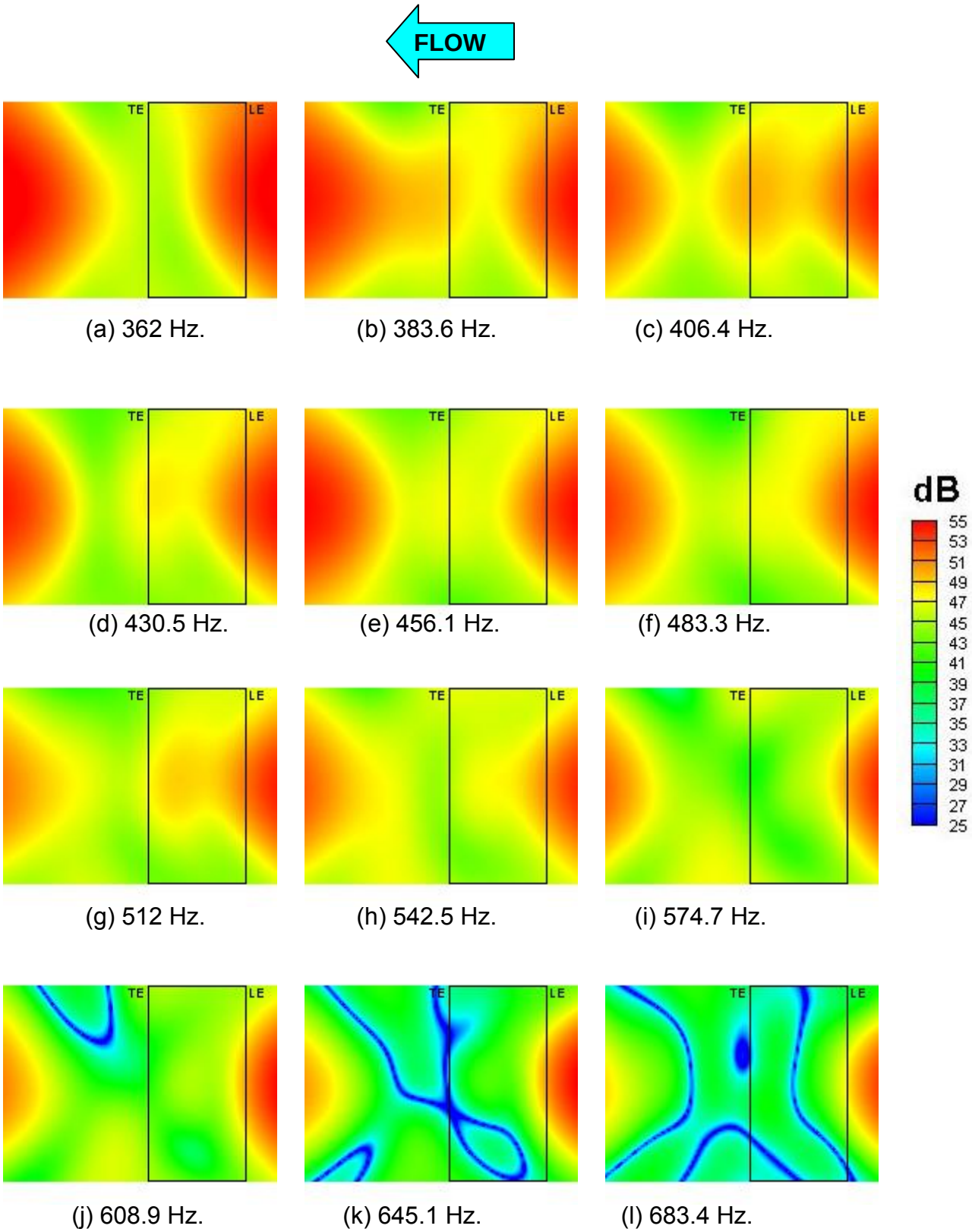

Figure 4-49. *1/12-Octave band beamform maps for the airfoil with tripped boundary layer, α=+7˚, Mach 0.11 (Re=2.38x10^6). Array on suction side. Airfoil leading and trailing edges indicated by the vertical lines.*

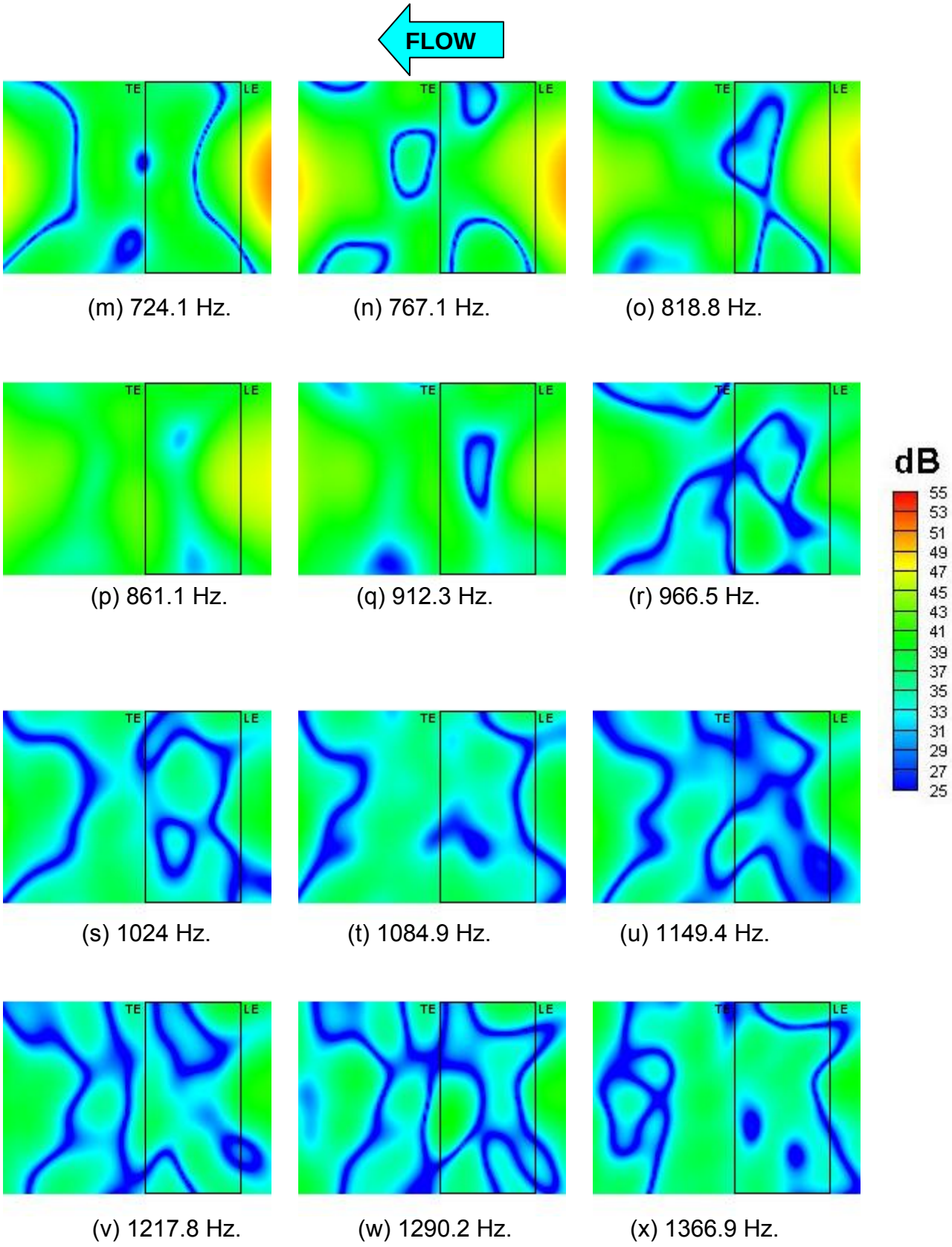

(m) 724.1 Hz. (n) 767.1 Hz. (o) 818.8 Hz.

(p) 861.1 Hz. (q) 912.3 Hz. (r) 966.5 Hz.

(s) 1024 Hz. (t) 1084.9 Hz. (u) 1149.4 Hz.

(v) 1217.8 Hz. (w) 1290.2 Hz. (x) 1366.9 Hz.

Figure 4-49. *1/12-Octave band beamform maps for the airfoil with tripped boundary layer, α=+7˚, Mach 0.11 (Re=2.38x10^6). Array on suction side. Airfoil leading and trailing edges indicated by the vertical lines.*

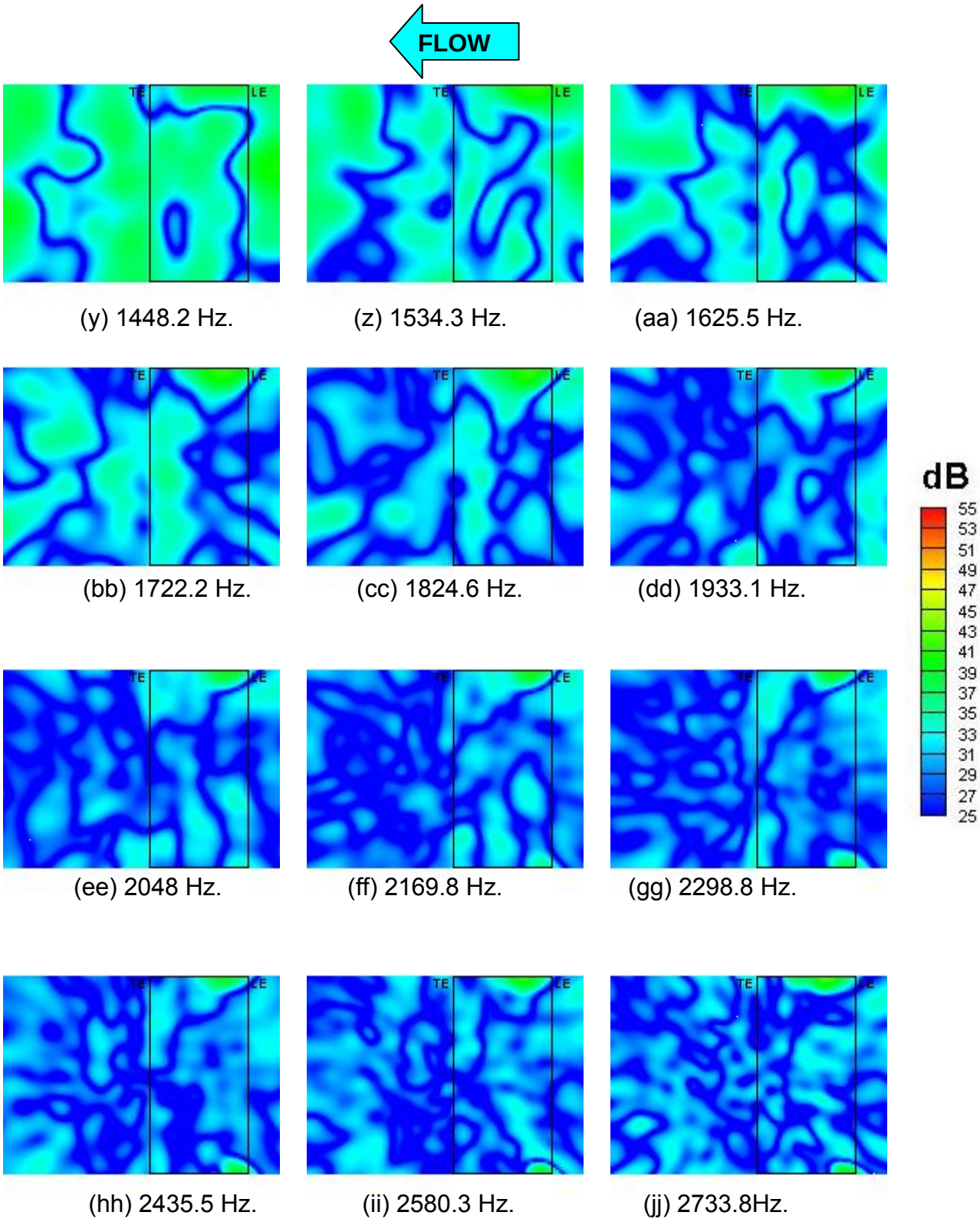

Figure 4-49. *1/12-Octave band beamform maps for the airfoil with tripped boundary layer, α=+7˚, Mach 0.11 (Re=2.38x10^6). Array on suction side. Airfoil leading and trailing edges indicated by the vertical lines.*

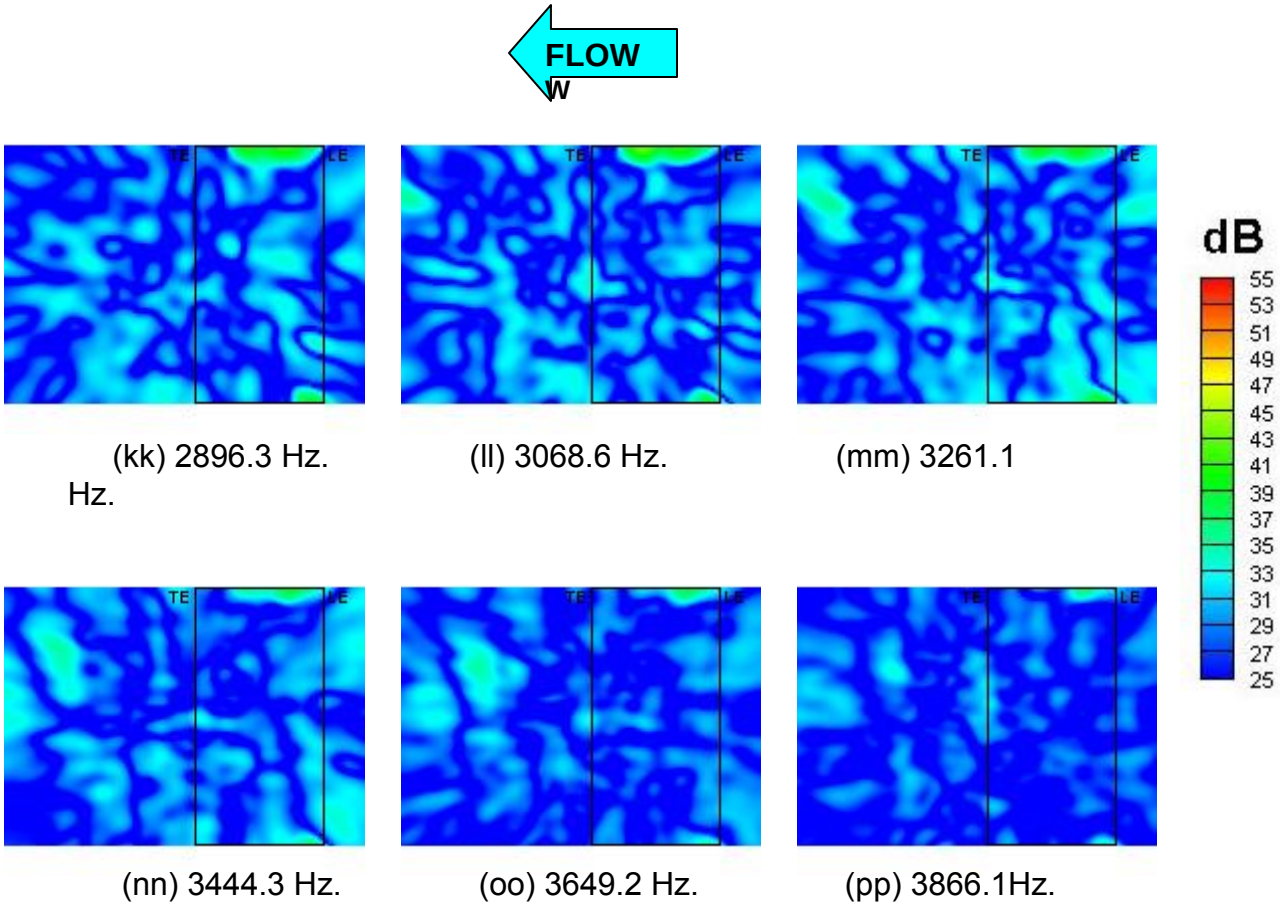

(kk) 2896.3 Hz. (ll) 3068.6 Hz. (mm) 3261.1 Hz.

(nn) 3444.3 Hz. (oo) 3649.2 Hz. (pp) 3866.1Hz.

Figure 4-49. *1/12-Octave band beamform maps for the airfoil with tripped boundary layer, α=+7˚, Mach 0.11 (Re=2.38x10^6). Array on suction side. Airfoil leading and trailing edges indicated by the vertical lines.*

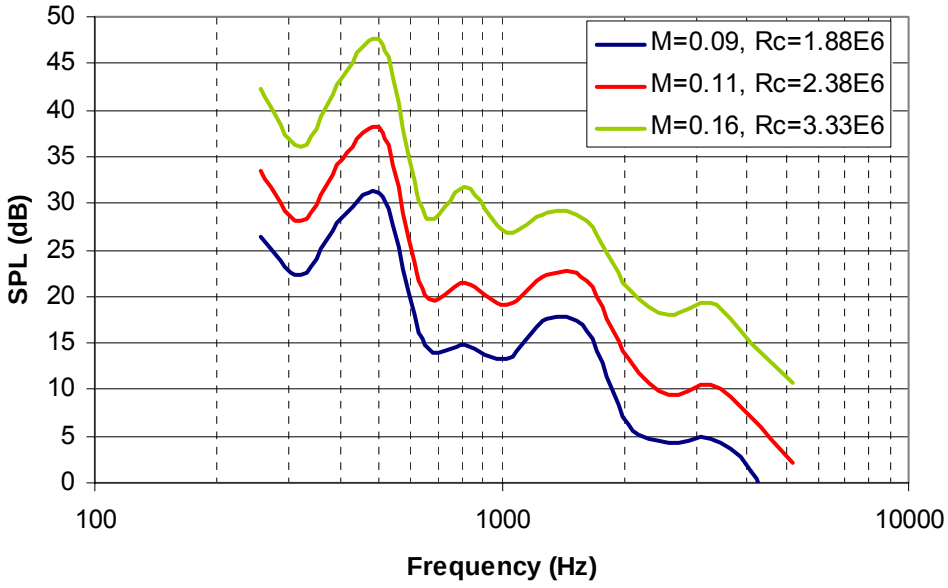

Figure 4-50. *Integrated 1/3-Octave band spectrum for various flow speeds (indicated here in terms of Mach number and Reynolds number). Airfoil at +7 degree angle of attack (geometric), phased array on suction side.*

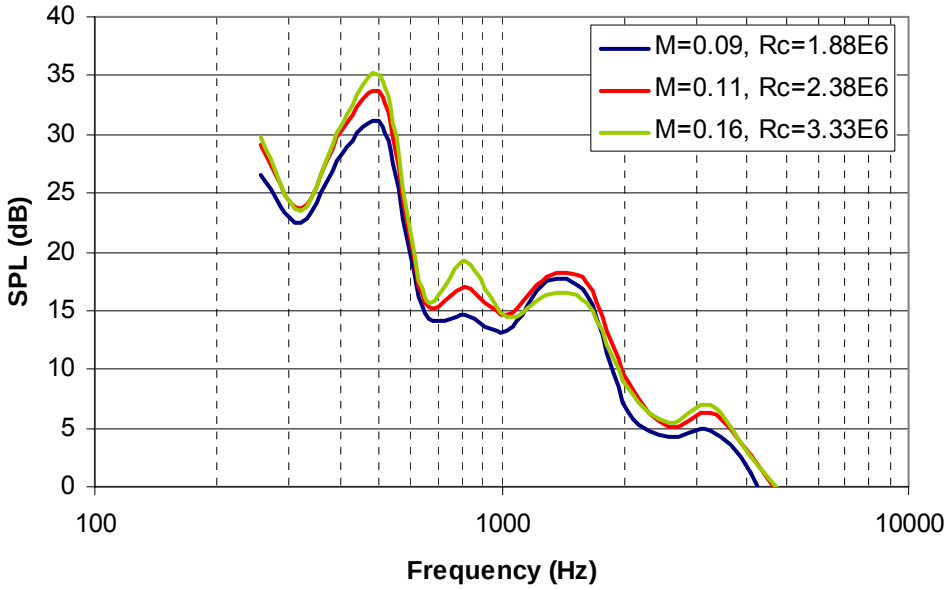

Figure 4-51. *Integrated 1/3-Octave band spectrum for various flow speeds (indicated here in terms of Mach number and Reynolds number) scaled on the 5th power of the Mach number. Airfoil at +7 degree angle of attack (geometric), phased array on suction side.*

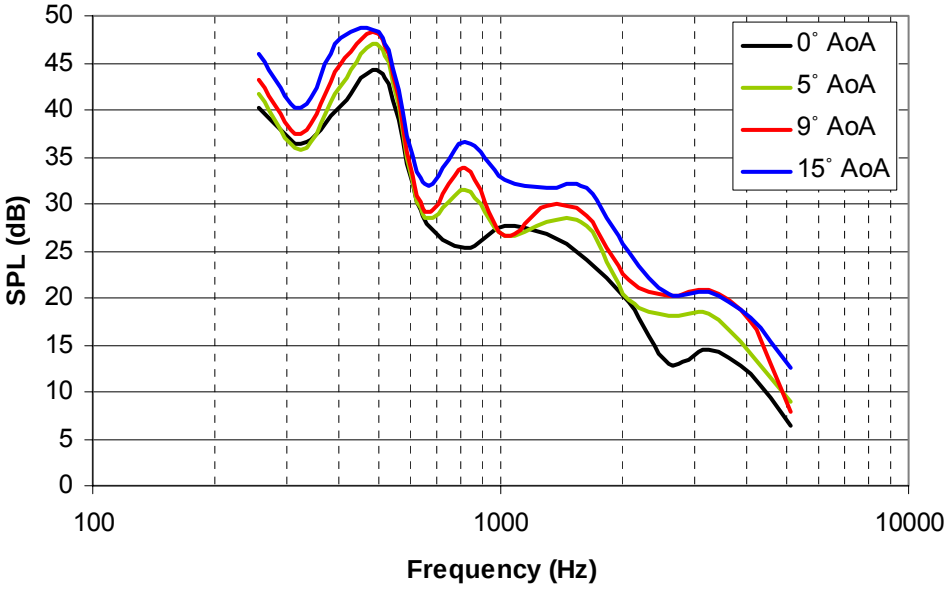

Figure 4-52. *Integrated spectrum in 1/3 octave bands for four angles of attack. Mach 0.16, Rc=3.32x10^6, array on suction side. Indicated angles of attack are positive geometric. Corresponding effective angles of attack are 0, 3.5, 6.5 and 11 degrees.*

5. CONCLUSIONS

The preliminary development and testing of a new anechoic wind tunnel test section designed for the Virginia Tech Stability Wind Tunnel has been performed. The novel design uses large areas of ballistic Kevlar cloth to provide a stable flow boundary. Sound generated in the flow can propagate through the Kevlar cloth into a surrounding anechoic chamber, where detailed noise measurements can be made. This approach offers the possibilities of providing anechoic capability without the complication and noise generated by a jet catcher and of reducing and controlling lift interference, which can be a large factor in open-jet wind tunnels.

To test this concept the current wind tunnel test section was modified to incorporate prototype acoustic treatment (with two different flow surfaces), two large Kevlar cloth side-walls and surrounding acoustic enclosures. A 63-microphone phased array system was designed and constructed to perform demonstration aeroacoustic measurements of large aspect ratio airfoils through these Kevlar acoustic windows.

An extensive program of experiments has been conducted to examine the performance of this new hardware under a range of conditions. Wind tunnel tests were performed to determine the aerodynamic and aeroacoustic performance of the empty test section in its original hard-wall configuration, and with the acoustic treatment and hardware installed, over the full speed range of the facility. These measurements included in-flow noise levels, test section wall boundary layer profiles, and documentation of the stability and deflection of the Kevlar windows.

A second series of tests were then performed with a large full span NACA 0012 airfoil model over a broad range of angles of attack (to 15 degrees geometric) and Reynolds numbers (to 4.3 million). The airfoil chord was half the width of the test section. Apart from further observations of the behavior of the Kevlar windows, measurements (including mean surface pressure distributions, trailing edge boundary layer profiles, wake profiles and near-wake spectra) were performed to document the aerodynamics of the airfoil flow in the presence of the Kevlar side walls. Of particular interest was the size and form of the interference correction. Finally, measurements with the phased array were performed through the Kevlar windows to document the trailing edge noise generated by the airfoil, and to demonstrate the ability to make useful aeroacoustic measurements with this novel test-section design.

The following conclusions are drawn:

1. **The Kevlar side walls replace the need for a free jet or jet catcher.** With and without the airfoil model installed the Kevlar walls appeared stable and quiet over the entire speed range. The wind tunnel boundary layer thickness downstream of the windows was roughly doubled compared to the original hard-wall test section. Vibration of the windows was of very small amplitude and was found to be un-correlated with the sound field inside the test section at all speeds. Static deflection of the windows was affected by the presence of the airfoil model, the Kevlar cloth being drawn inwards or pushed outwards slightly by the pressure field generated at angle of attack, which also appeared to produce some

transpiration of air through the cloth. Phased array measurements made with and without the airfoil demonstrated their acoustic transparency.

2. **The acoustic treatment greatly reduces noise levels in the tunnel, to a level comparable with other aeroacoustic facilities.** With the empty test section in the original hard-wall configuration in-flow noise levels are dominated by fan tones at low frequencies (<300Hz) and by broadband noise at high frequencies. Noise levels are almost independent of streamwise location at in the test section and overall A-weighted sound pressure levels increase as the sixth power of the flow velocity, reaching 109dB at 64 m/s. The prototype acoustic treatment and Kevlar acoustic windows, reduced overall levels in the test section by 10 to 16dB across the frequency range and from 8 to 15dB in terms of overall A-weighted SPL. In this configuration the Stability Wind Tunnel has noise levels comparable to a large number of other aeroacoustic facilities (e.g. NASA Glenn 9×15 wind tunnel) even though no it has no acoustic treatment outside the test section.

3. **The Kevlar side walls reduced lift interference when compared to a free jet.** Interference effects with the Kevlar side walls can accurately be accounted for using an effective angle of attack. The effective angle correction is a constant fraction of the geometric angle, -28% in the present case. The correction is significantly less than that expected for free jet correction of 44 to 50%. The observed transpiration through the Kevlar windows is believed to be responsible

for most of the residual correction. Indeed, we believe that by controlling this mass flux substantial further reductions in interference may be possible.

4. **The aerodynamic characteristics of an airfoil mode mounted in the Kevlar walled test section are closely consistent with expectations based on theory and prior studies.** Mean pressure distributions measured on the NACA 0012 airfoil at all angles of attack and Reynolds number agree well with inviscid calculations at the effective angles of attack. Mean properties of the trailing edge boundary layers (with trips installed) and their variations with Reynolds number and angle of attack conform closely to predictions using the formulae of Brooks *et al.* (1989), if the differences in the severity of the trip in that study are taken into account. Observations of shedding frequencies from the trailing edge (without trips installed) show an expected Strouhal number of 0.2 based on the effective trailing edge thickness. Wake and boundary layer profiles imply drag coefficients broadly consistent with prior studies.

5. **Phased array measurements of trailing edge noise through Kevlar side walls, including detailed source maps have been demonstrated and are practical.** With the boundary layer trips on the NACA 0012 airfoil removed, beamforming of measurements with the 63-microphone phased array revealed not only tone noise levels produced by the coherent trailing edge vortex shedding but also the lower intensity, higher frequency broadband component of the noise, and their variation with flow conditions.

6. **Further background noise reductions will be necessary before complete trailing edge noise measurements are possible, but are anticipated with the planned facility upgrade.** Phased array source maps measured with the airfoil boundary layer tripped barely show the broadband trailing edge noise in this case. The measurements are limited by extraneous noise sources upstream and downstream the airfoil model. It is expected that the further reductions in background noise levels produced when the full conversion of the facility is complete, along with other treatment of the tunnel circuit and the development of a 128-microphone phased array, will make this measurement possible.

REFERENCES

Abbot I H and von Doenhoff A E, 1959, *Theory of Wing Sections*, Dover, New York.

Barlow J B, Rae W H and Pope A, 1999, *Low Speed Wind Tunnel Testing*, Wiley, New York.

Bereketab S, Wang H, Mish P and Devenport W, 2000, "The Surface Pressure Response of a NACA 0015 Airfoil Immersed in Grid Turbulence. Volume 1: Characteristics of the Turbulence", Final Report to NASA Langley Under Grant Nag-1-1942, Department of Aerospace and Ocean Engineering, Virginia Tech.

Bernstein S and Joppa R G, 1976, "Development of minimum correction wind tunnels", Journal of Aircraft, vol. 13, pp. 243-247.

Brooks T F, Pope D S and Marcolini, 1989, "Airfoil Self Noise and Prediction", NASA RP 1218.

Choi, K., and Simpson, R.L., 1987, "Some Mean Velocity, Turbulence and Unsteadiness Characteristics of the VPI & SU Stability Wind Tunnel," Department of Aerospace and Ocean Engineering, Virginia Polytechnic Institute and State University, Blacksburg, Virginia 24061, Report VPI-Aero-161.

Dougherty R P, 2002, "Beamforming in Aeroacoustic Testing", *Aeroacoustic Measurements*, edited by T.J. Mueller, Springer Verlag, Berlin, pp 62-97.

Duell E, Yen J, Arnette S and Walter J, 2002, "Recent Advances in Large Scale Aeroacoustic Wind Tunnels", AIAA-2002-2503, 8th AIAA/CEAS Aeroacoustics Conference and Exhibit, Breckenridge, Colorado, June 17-19.

Jaeger S M, Horne W C and Allen C S, 2000, "Effect of Surface Treatment on Array Microphone Self Noise", AIAA Paper 2000-1937.

Larssen J V and Devenport W J, 1999 “Acoustic Properties Of The Virginia Tech Stability Wind Tunnel”, Department of Aerospace and Ocean Engineering, Virginia Tech, Report VPI-AOE-263. Available from http://www.aoe.vt.edu/research/facilities/stab/files/vpi-aoe-263.pdf

Mason W, 1971, “Farfield Structure of an Aircraft Trailing Vortex”, MS Thesis, Virginia Tech.

Mish P F, 2003, “An Experimental Investigation Of Unsteady Surface Pressure On Single And Multiple Airfoils”, Ph.D. Dissertation, Virginia Tech. Available from http://scholar.lib.vt.edu/theses/available/etd-03312003-173021/

Mueller, T. J., editor, *Aeroacoustic Measurements*, Springer Verlarg, Berlin, 2002,.

Paterson, R. W., Amiet, R. K., and Much, C. L., “Isolated Airfoil-Tip Vortex Interaction Noise”, AIAA Paper No. 74-194, Jan.-Feb. 1974.

Ravetta P, Burdisso R and Ng W, 2004, “Wind Tunnel Aeroacoustic Measurements on a 26%-Scale 777 Main Landing Gear”, AIAA-2004-2885, 10th Aeroacoustic Conference, Manchester UK.

Reynolds G A, 1982, “Experiments on the Stability of the Flat Plate Boundary Layer with suction”, PhD Dissertation, Virginia Tech.

Underbrink, J.R., 2002, “Aeroacoustic Phased Array Testing in Low Speed Wind Tunnels”, *Aeroacoustic Measurements*, edited by T.J. Mueller, Springer Verlag, Berlin, pp 98-217.

Zsoldos J S, 1992, “An experimental investigation of interacting wing-tip vortex pairs”, MS Thesis, Department of Aerospace and Ocean Engineering, Virginia Tech.

APPENDIX

1/12-Octave band beamform maps for all tested cases listed in Table 4.5

Note: Each map is on a plane that passes through the trailing edge of the airfoil in the stream flow direction. In all maps, air flows from right to left.

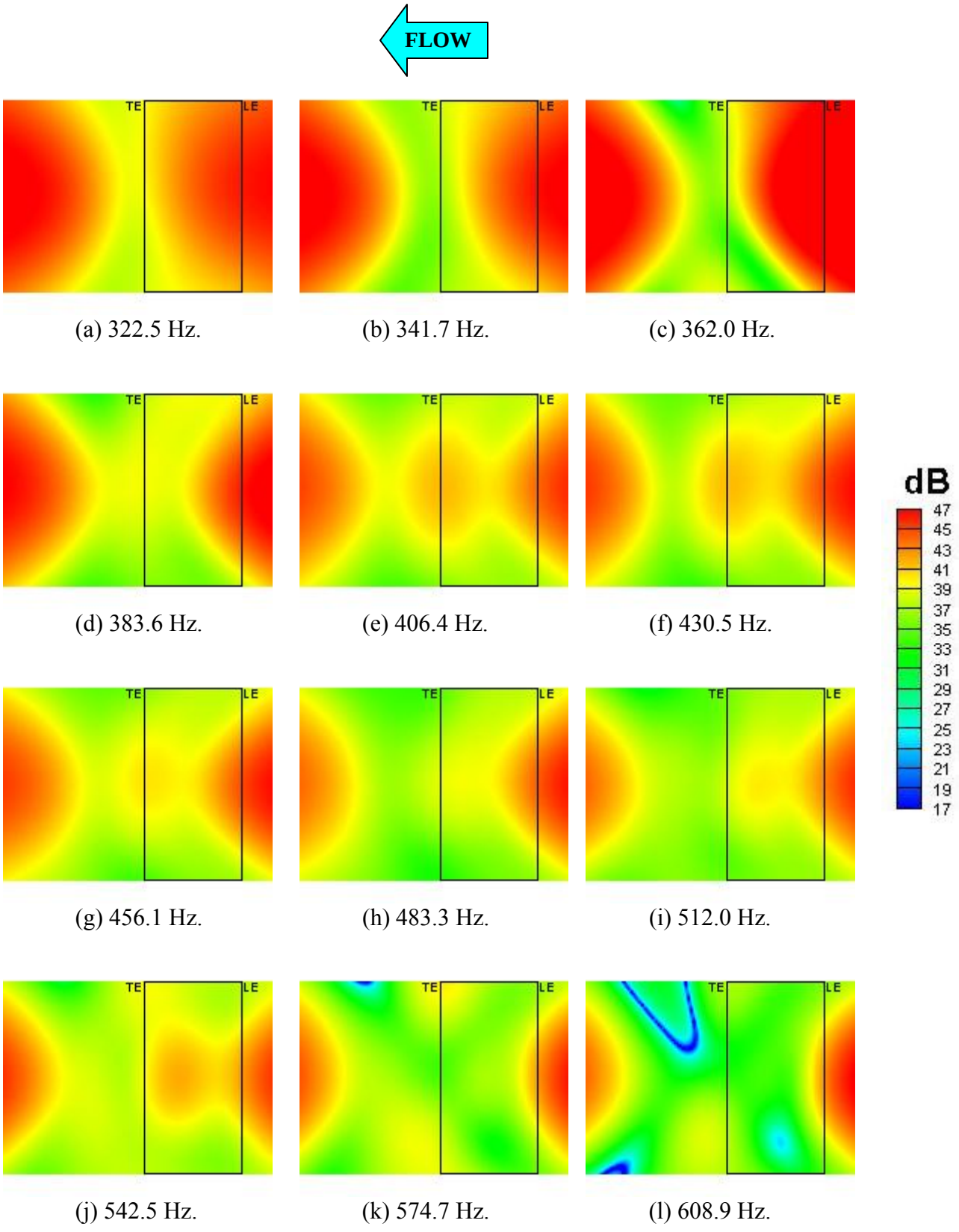

(a) 322.5 Hz. (b) 341.7 Hz. (c) 362.0 Hz.

(d) 383.6 Hz. (e) 406.4 Hz. (f) 430.5 Hz.

(g) 456.1 Hz. (h) 483.3 Hz. (i) 512.0 Hz.

(j) 542.5 Hz. (k) 574.7 Hz. (l) 608.9 Hz.

Figure 1. 1/12-Octave band beamform maps for Run001
(Airfoil at $\alpha = 0^{\circ}$, U=30.82 m/s, M = 0.09, Tripped BL, phased array on pressure side).

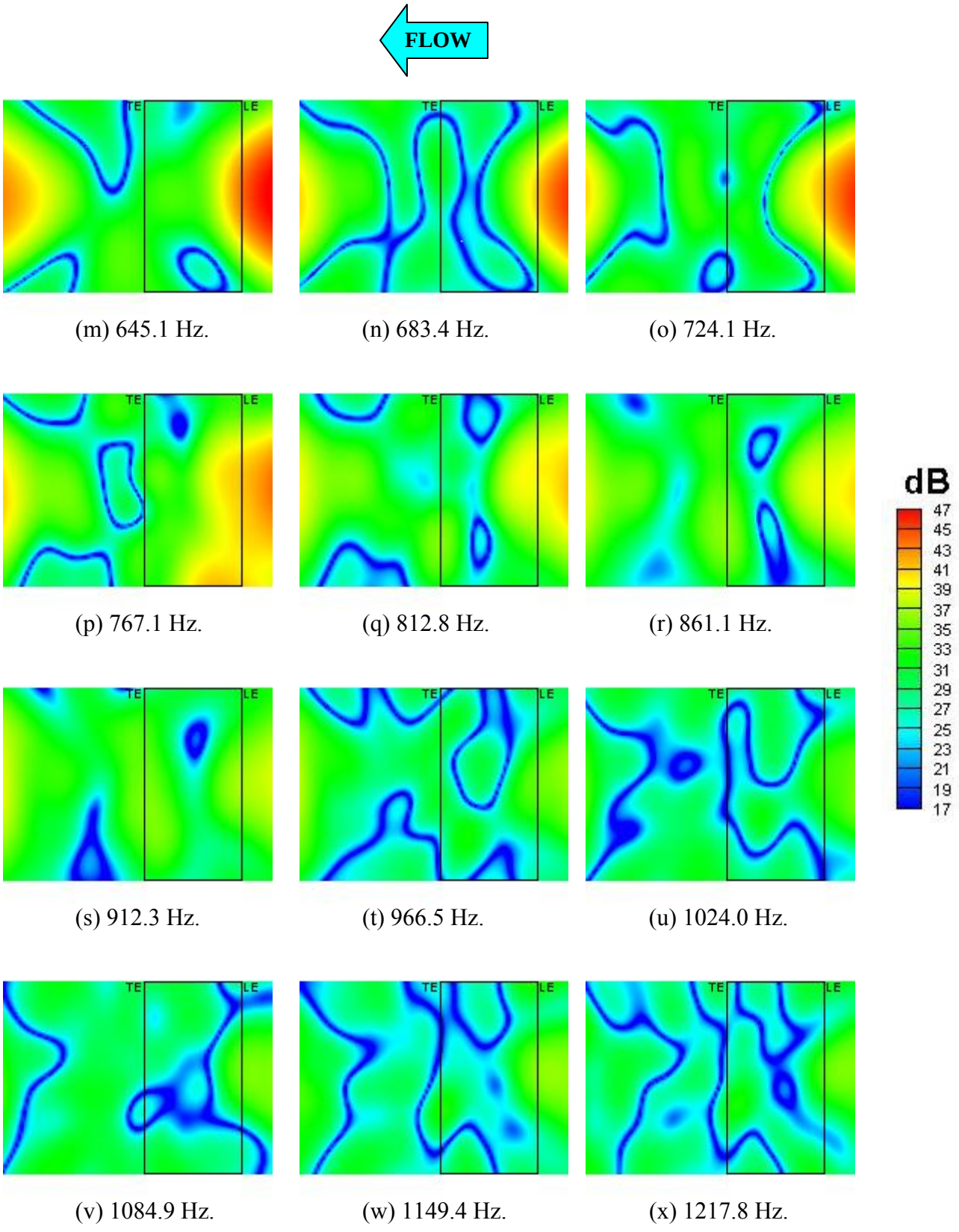

(m) 645.1 Hz. (n) 683.4 Hz. (o) 724.1 Hz.

(p) 767.1 Hz. (q) 812.8 Hz. (r) 861.1 Hz.

(s) 912.3 Hz. (t) 966.5 Hz. (u) 1024.0 Hz.

(v) 1084.9 Hz. (w) 1149.4 Hz. (x) 1217.8 Hz.

Figure 1. 1/12-Octave band beamform maps for Run001
(Airfoil at α = 0˚, U=30.82 m/s, M = 0.09, Tripped BL, phased array on pressure side).

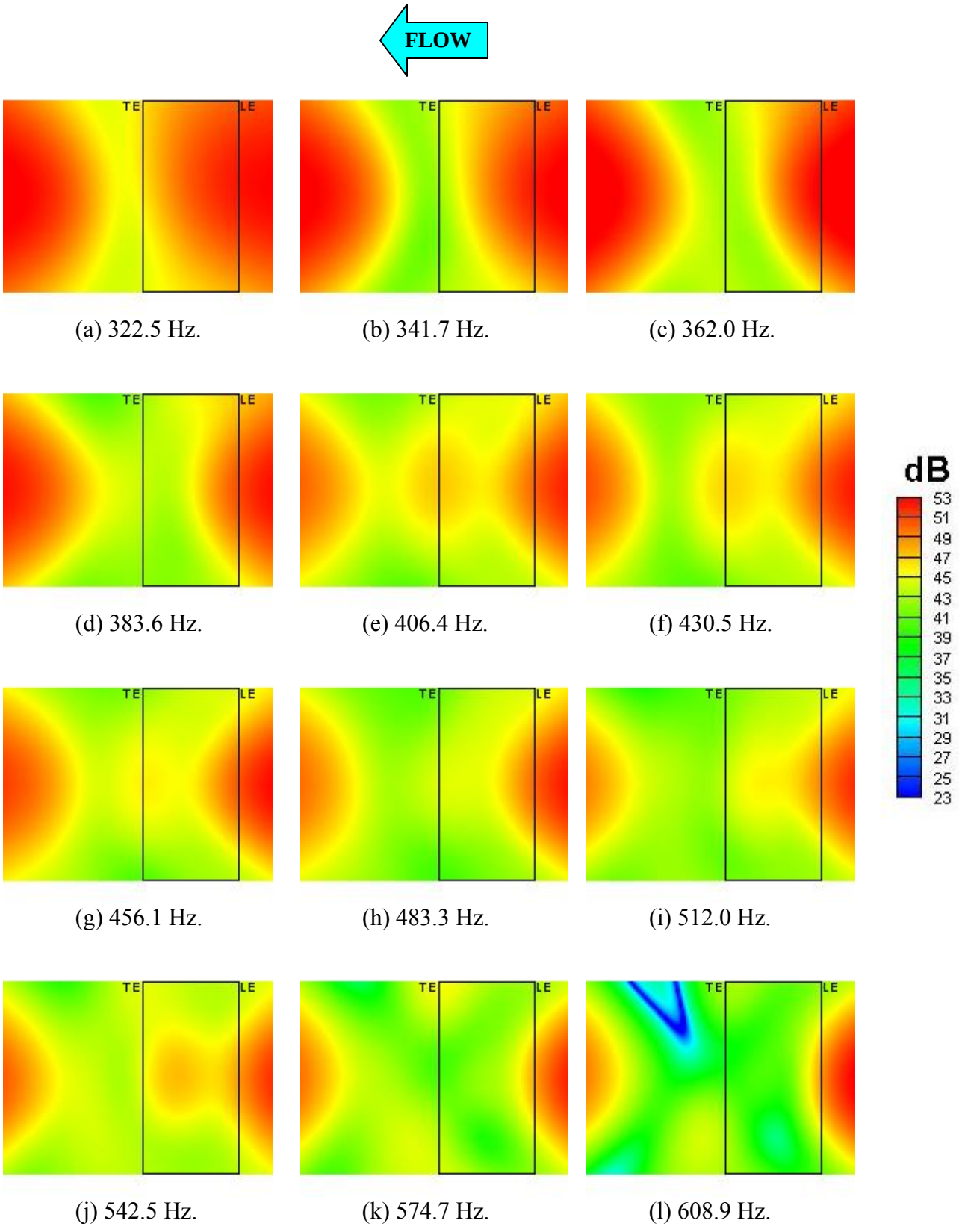

(a) 322.5 Hz. (b) 341.7 Hz. (c) 362.0 Hz.

(d) 383.6 Hz. (e) 406.4 Hz. (f) 430.5 Hz.

(g) 456.1 Hz. (h) 483.3 Hz. (i) 512.0 Hz.

(j) 542.5 Hz. (k) 574.7 Hz. (l) 608.9 Hz.

Figure 2. 1/12-Octave band beamform maps for Run002
(Airfoil at α = 0˚, U=38.48 m/s, M = 0.11, Tripped BL, phased array on pressure side).

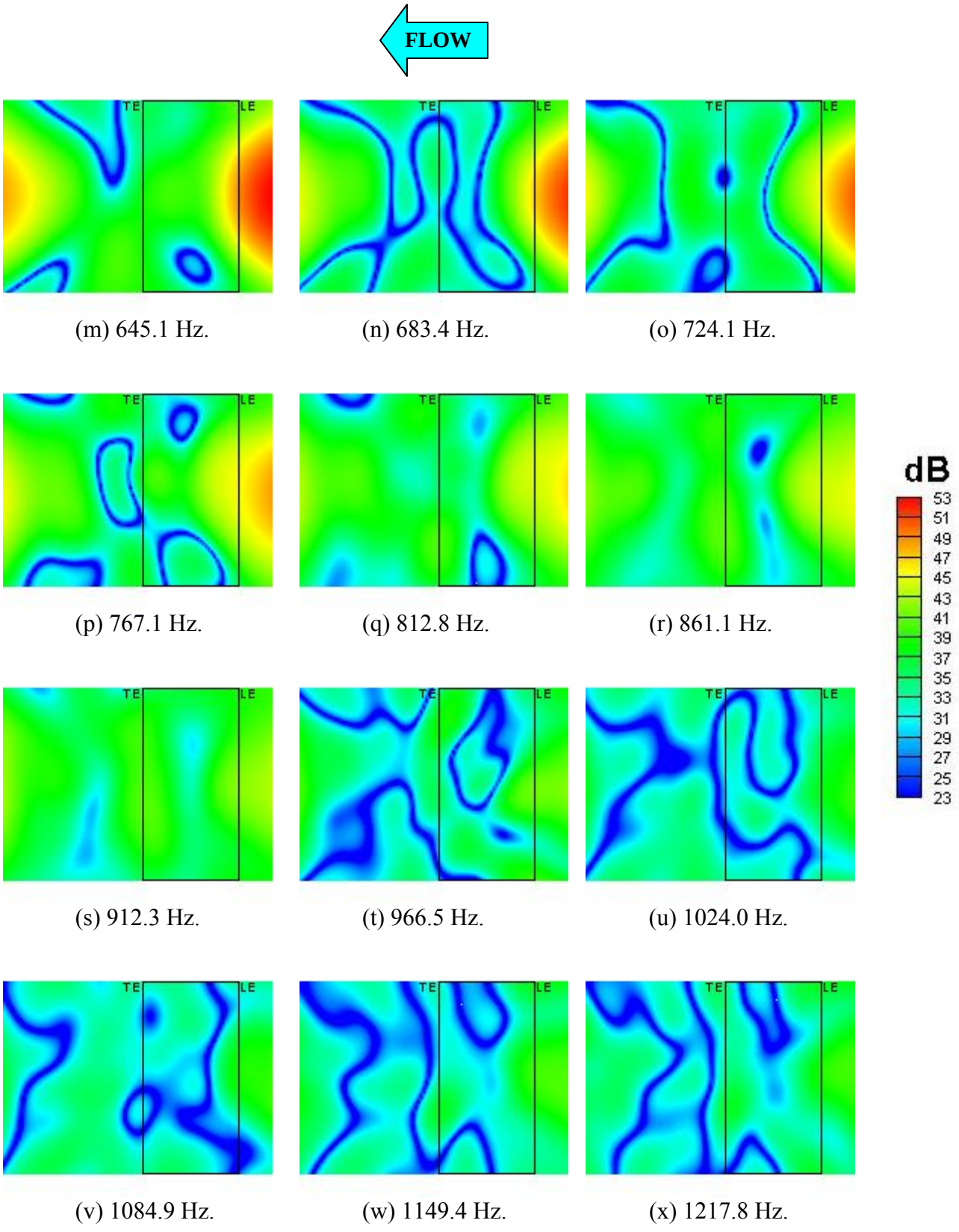

(m) 645.1 Hz. (n) 683.4 Hz. (o) 724.1 Hz.

(p) 767.1 Hz. (q) 812.8 Hz. (r) 861.1 Hz.

(s) 912.3 Hz. (t) 966.5 Hz. (u) 1024.0 Hz.

(v) 1084.9 Hz. (w) 1149.4 Hz. (x) 1217.8 Hz.

Figure 2. 1/12-Octave band beamform maps for Run002
(Airfoil at α = 0˚, U=38.48 m/s, M = 0.11, Tripped BL, phased array on pressure side).

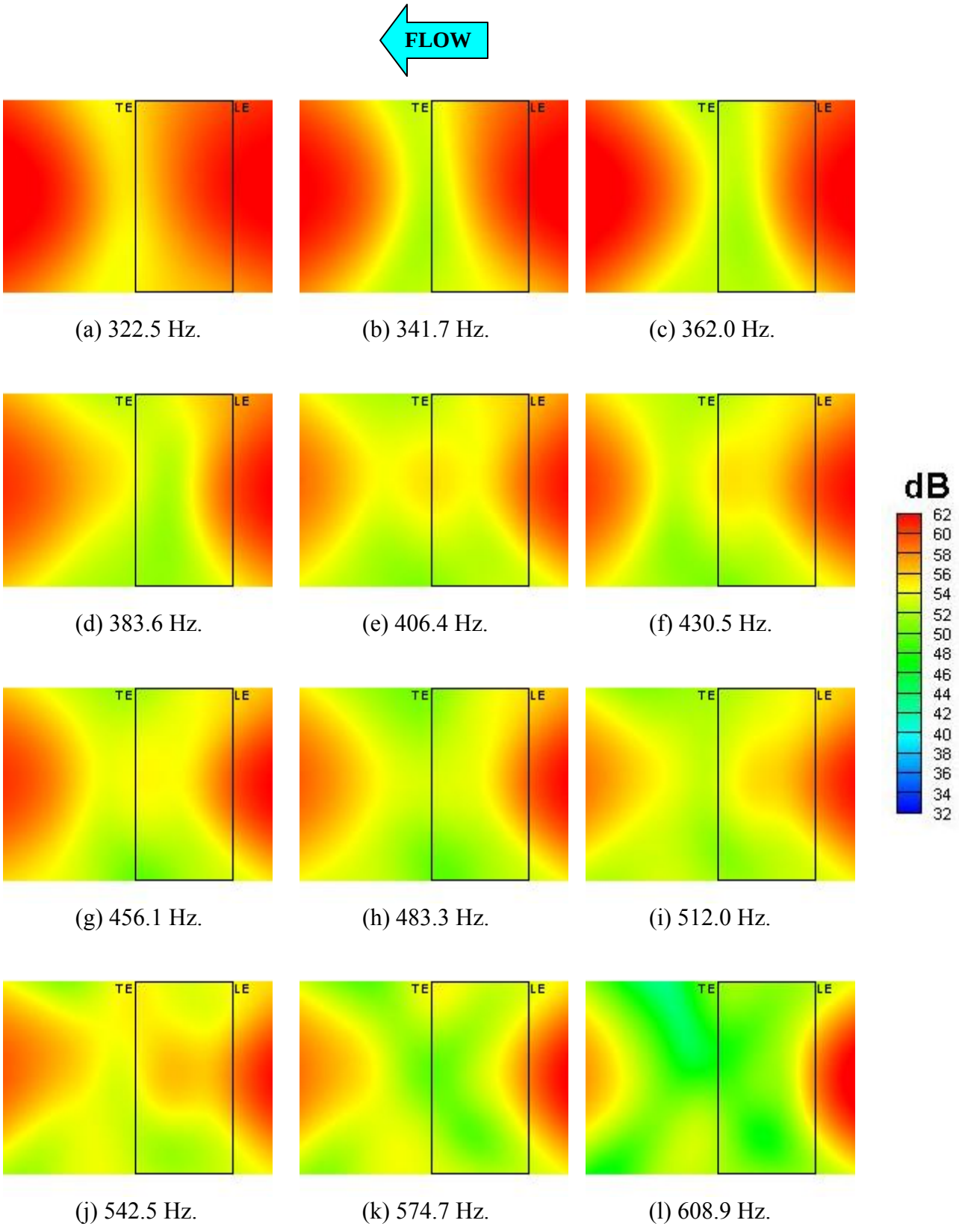

(a) 322.5 Hz. (b) 341.7 Hz. (c) 362.0 Hz.

(d) 383.6 Hz. (e) 406.4 Hz. (f) 430.5 Hz.

(g) 456.1 Hz. (h) 483.3 Hz. (i) 512.0 Hz.

(j) 542.5 Hz. (k) 574.7 Hz. (l) 608.9 Hz.

Figure 3. 1/12-Octave band beamform maps for Run003
(Airfoil at $\alpha = 0^{\circ}$, U=54.15 m/s, M = 0.16, Tripped BL, phased array on pressure side).

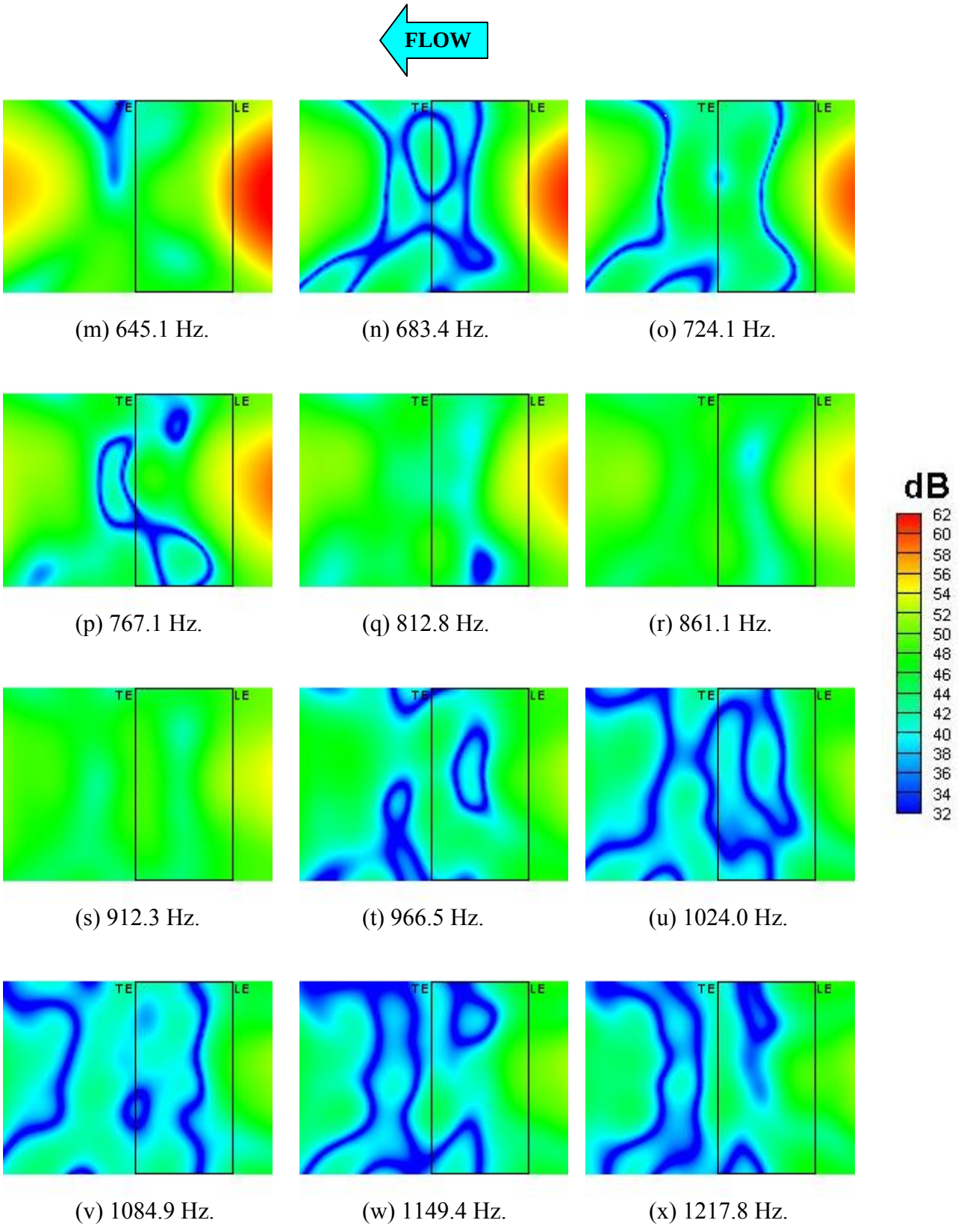

(m) 645.1 Hz. (n) 683.4 Hz. (o) 724.1 Hz.

(p) 767.1 Hz. (q) 812.8 Hz. (r) 861.1 Hz.

(s) 912.3 Hz. (t) 966.5 Hz. (u) 1024.0 Hz.

(v) 1084.9 Hz. (w) 1149.4 Hz. (x) 1217.8 Hz.

Figure 3. 1/12-Octave band beamform maps for Run003
(Airfoil at α = 0˚, U=54.15 m/s, M = 0.16, Tripped BL, phased array on pressure side).

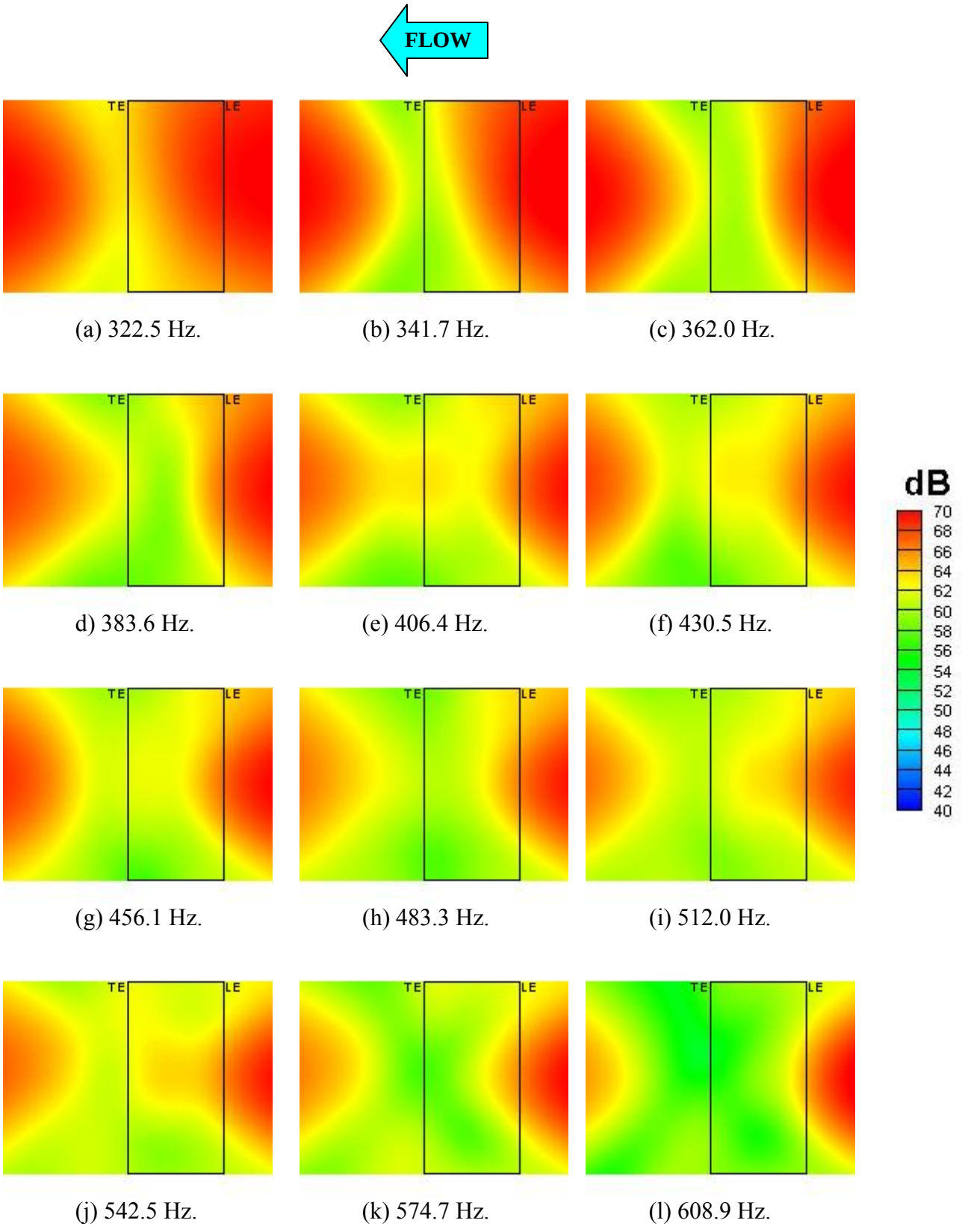

(a) 322.5 Hz. (b) 341.7 Hz. (c) 362.0 Hz.

d) 383.6 Hz. (e) 406.4 Hz. (f) 430.5 Hz.

(g) 456.1 Hz. (h) 483.3 Hz. (i) 512.0 Hz.

(j) 542.5 Hz. (k) 574.7 Hz. (l) 608.9 Hz.

Figure 4. 1/12-Octave band beamform maps for Run004
(Airfoil at α = 0˚, U=69.95 m/s, M = 0.20, Tripped BL, phased array on pressure side).

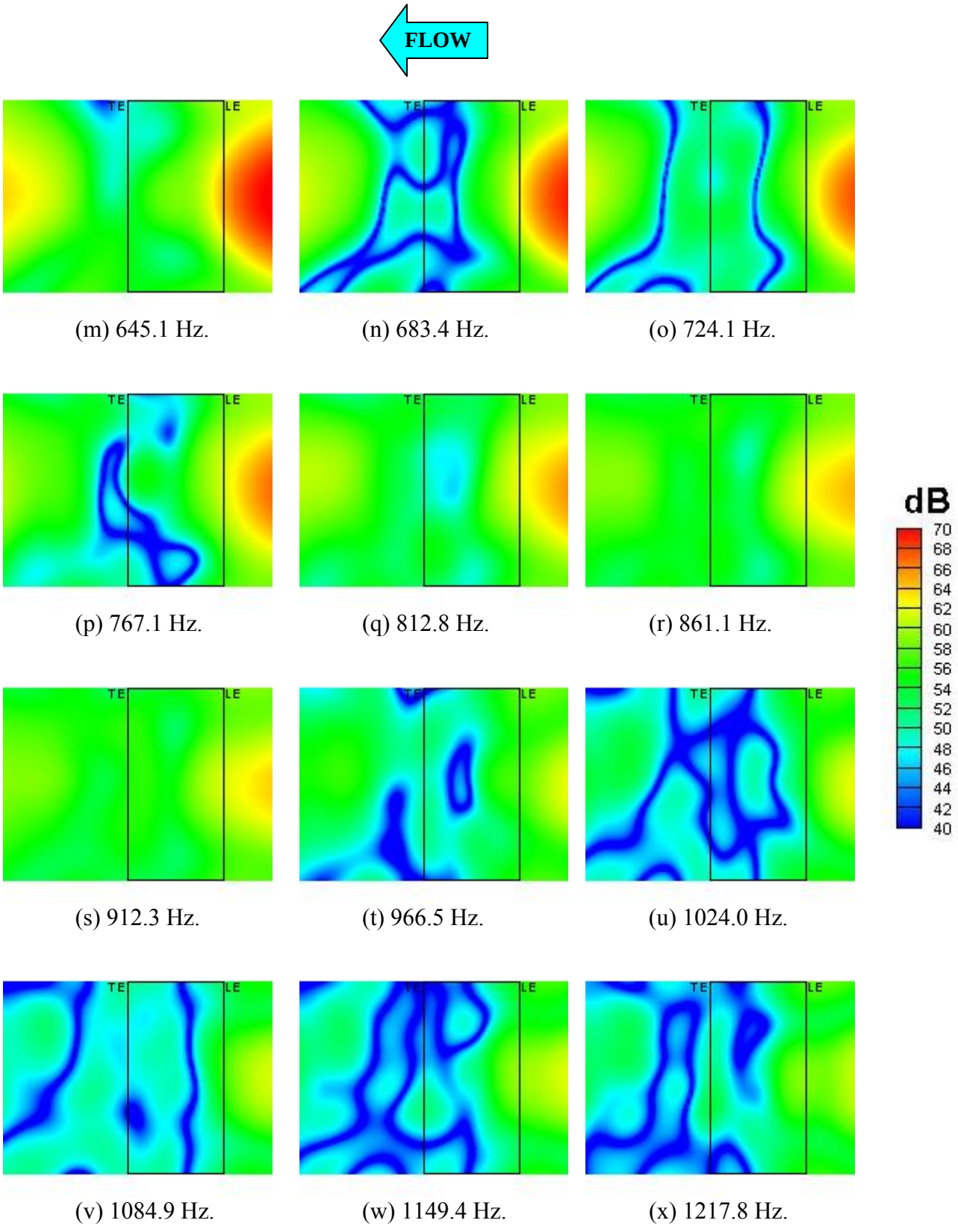

(m) 645.1 Hz. (n) 683.4 Hz. (o) 724.1 Hz.

(p) 767.1 Hz. (q) 812.8 Hz. (r) 861.1 Hz.

(s) 912.3 Hz. (t) 966.5 Hz. (u) 1024.0 Hz.

(v) 1084.9 Hz. (w) 1149.4 Hz. (x) 1217.8 Hz.

Figure 4. 1/12-Octave band beamform maps for Run004
(Airfoil at α = 0˚, U=69.95 m/s, M = 0.20, Tripped BL, phased array on pressure side).

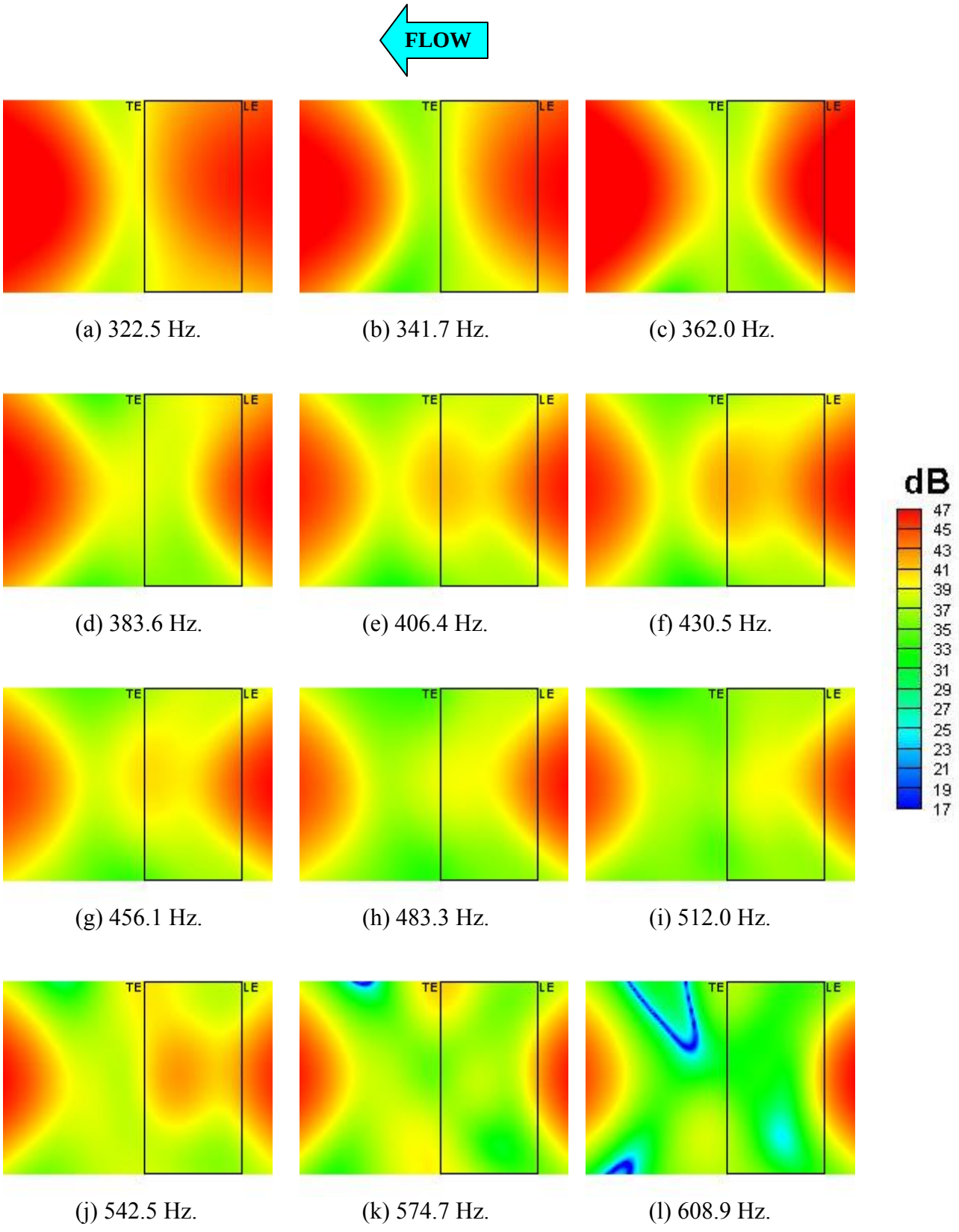

(a) 322.5 Hz. (b) 341.7 Hz. (c) 362.0 Hz.

(d) 383.6 Hz. (e) 406.4 Hz. (f) 430.5 Hz.

(g) 456.1 Hz. (h) 483.3 Hz. (i) 512.0 Hz.

(j) 542.5 Hz. (k) 574.7 Hz. (l) 608.9 Hz.

Figure 5. 1/12-Octave band beamform maps for Run005
(Airfoil at α = -1.5˚, U=30.89 m/s, Tripped BL, phased array on pressure side).

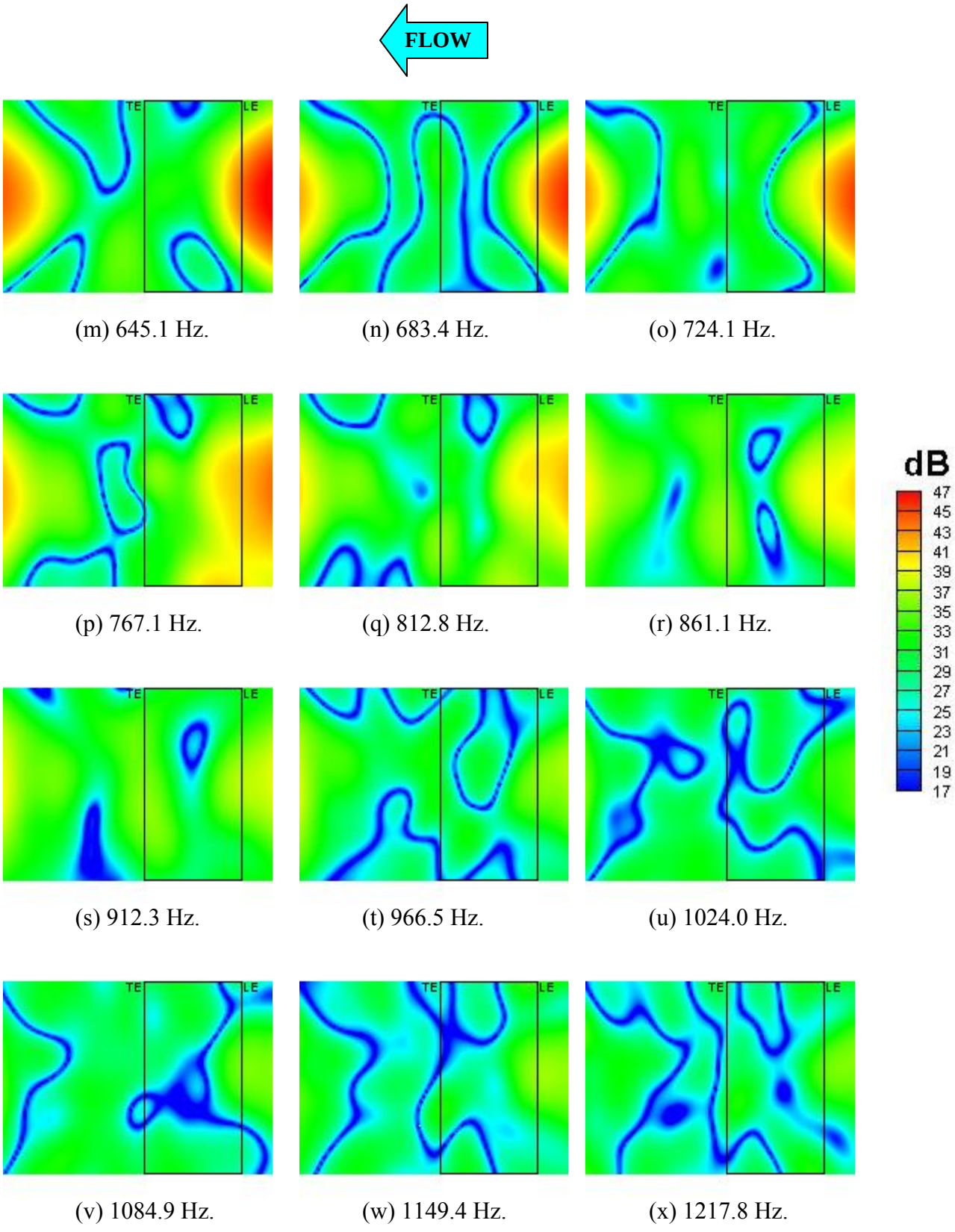

(m) 645.1 Hz. (n) 683.4 Hz. (o) 724.1 Hz.

(p) 767.1 Hz. (q) 812.8 Hz. (r) 861.1 Hz.

(s) 912.3 Hz. (t) 966.5 Hz. (u) 1024.0 Hz.

(v) 1084.9 Hz. (w) 1149.4 Hz. (x) 1217.8 Hz.

Figure 5. 1/12-Octave band beamform maps for Run005
(Airfoil at α = -1.5˚, U=30.89 m/s, Tripped BL, phased array on pressure side).

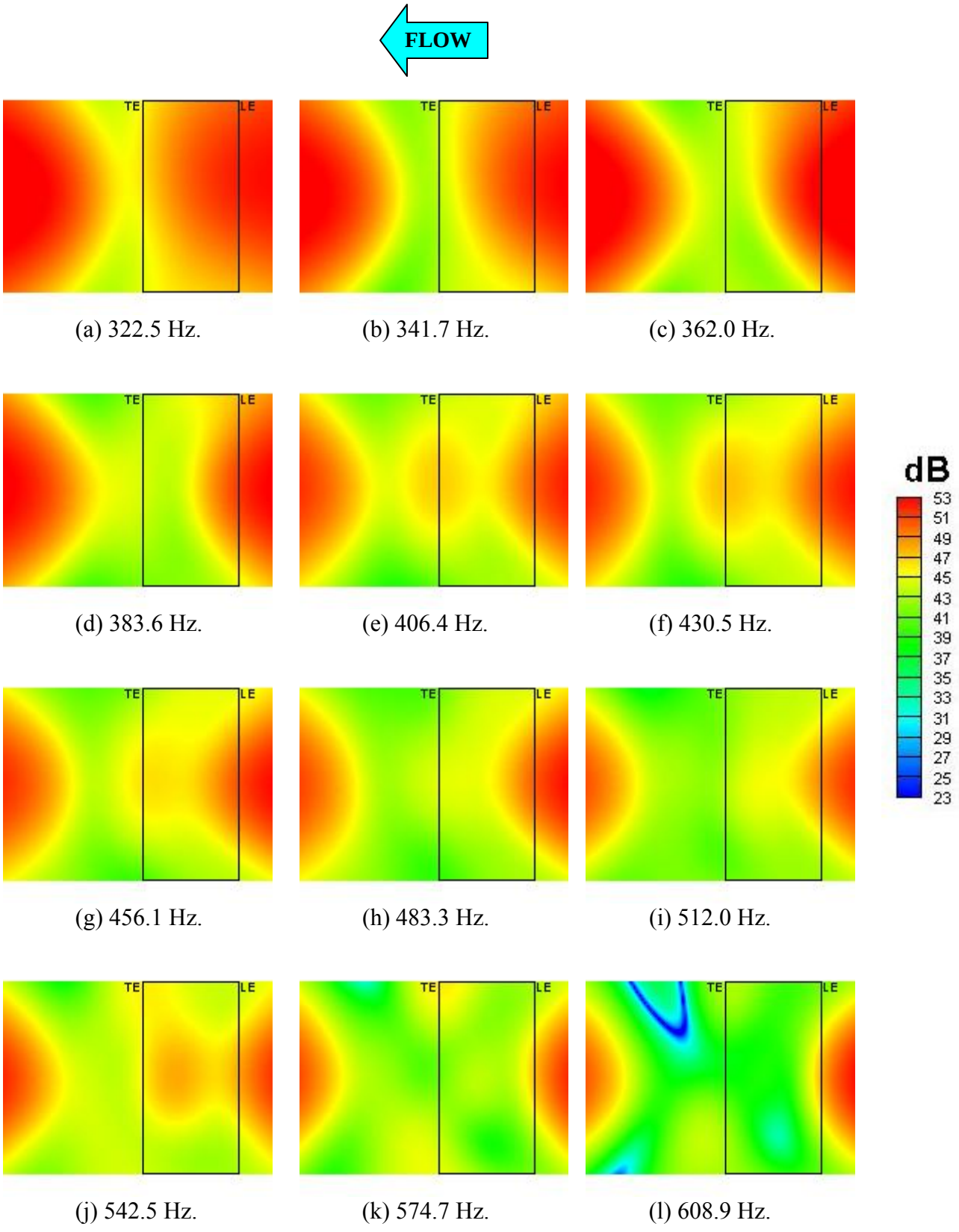

(a) 322.5 Hz. (b) 341.7 Hz. (c) 362.0 Hz.

(d) 383.6 Hz. (e) 406.4 Hz. (f) 430.5 Hz.

(g) 456.1 Hz. (h) 483.3 Hz. (i) 512.0 Hz.

(j) 542.5 Hz. (k) 574.7 Hz. (l) 608.9 Hz.

Figure 6. 1/12-Octave band beamform maps for Run006
(Airfoil at α = -1.5˚, U=38.66 m/s, Tripped BL, phased array on pressure side).

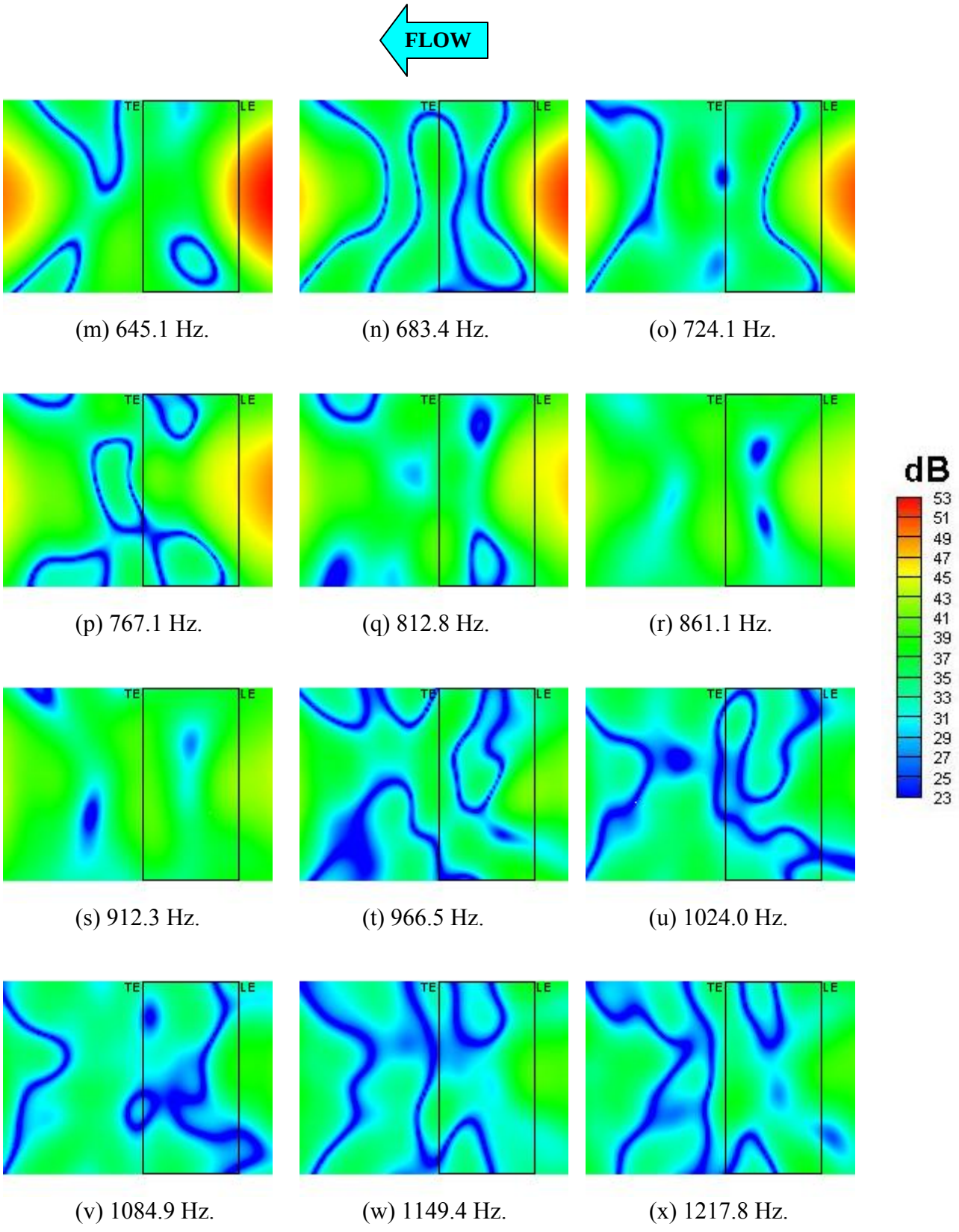

(m) 645.1 Hz. (n) 683.4 Hz. (o) 724.1 Hz.

(p) 767.1 Hz. (q) 812.8 Hz. (r) 861.1 Hz.

(s) 912.3 Hz. (t) 966.5 Hz. (u) 1024.0 Hz.

(v) 1084.9 Hz. (w) 1149.4 Hz. (x) 1217.8 Hz.

Figure 6. 1/12-Octave band beamform maps for Run006
(Airfoil at α = -1.5˚, U=38.66 m/s, Tripped BL, phased array on pressure side).

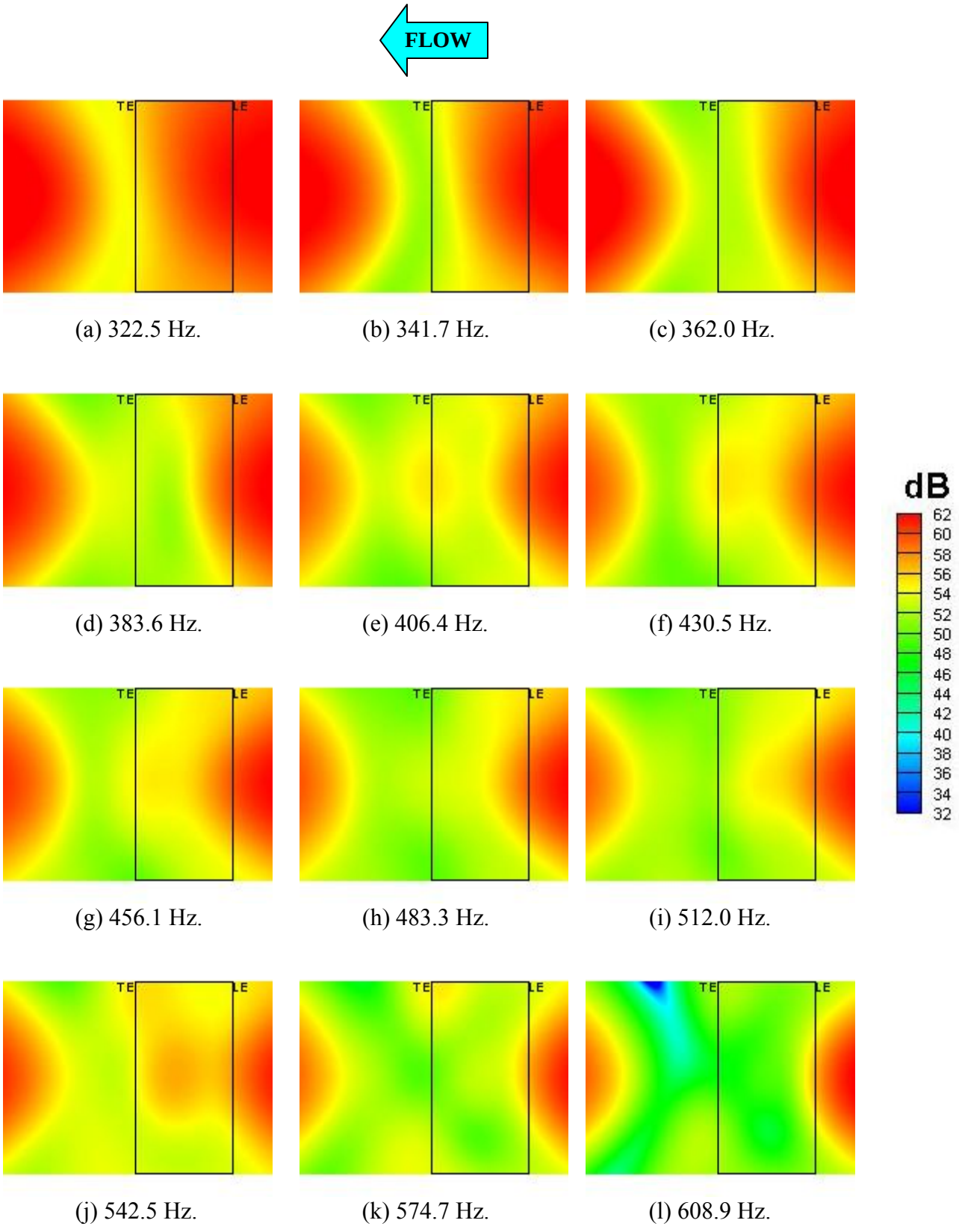

(a) 322.5 Hz. (b) 341.7 Hz. (c) 362.0 Hz.

(d) 383.6 Hz. (e) 406.4 Hz. (f) 430.5 Hz.

(g) 456.1 Hz. (h) 483.3 Hz. (i) 512.0 Hz.

(j) 542.5 Hz. (k) 574.7 Hz. (l) 608.9 Hz.

Figure 7. 1/12-Octave band beamform maps for Run007
(Airfoil at α = -1.5˚, U=54.37 m/s, Tripped BL, phased array on pressure side).

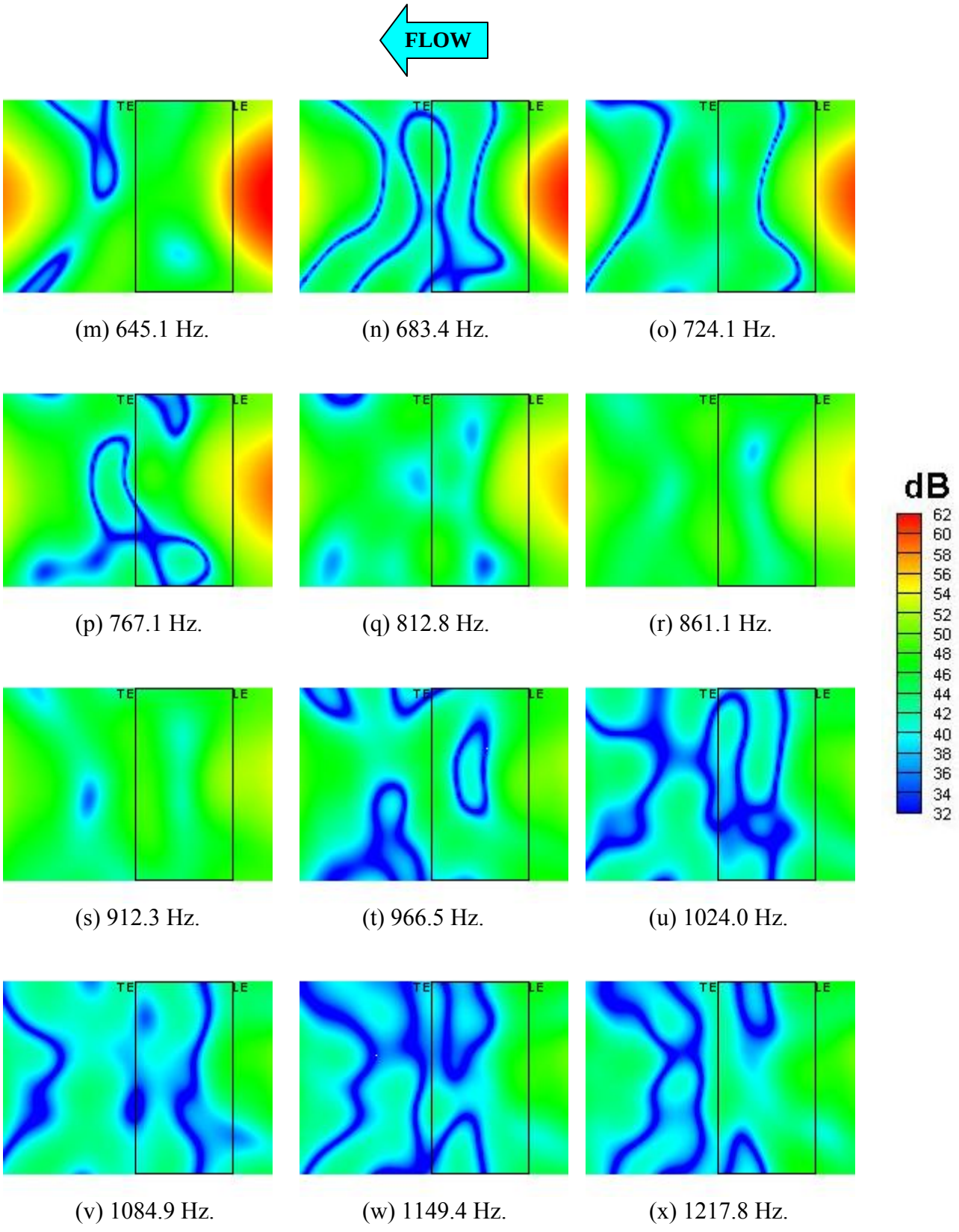

(m) 645.1 Hz. (n) 683.4 Hz. (o) 724.1 Hz.

(p) 767.1 Hz. (q) 812.8 Hz. (r) 861.1 Hz.

(s) 912.3 Hz. (t) 966.5 Hz. (u) 1024.0 Hz.

(v) 1084.9 Hz. (w) 1149.4 Hz. (x) 1217.8 Hz.

Figure 7. 1/12-Octave band beamform maps for Run007
(Airfoil at α = -1.5˚, U=54.37 m/s, Tripped BL, phased array on pressure side).

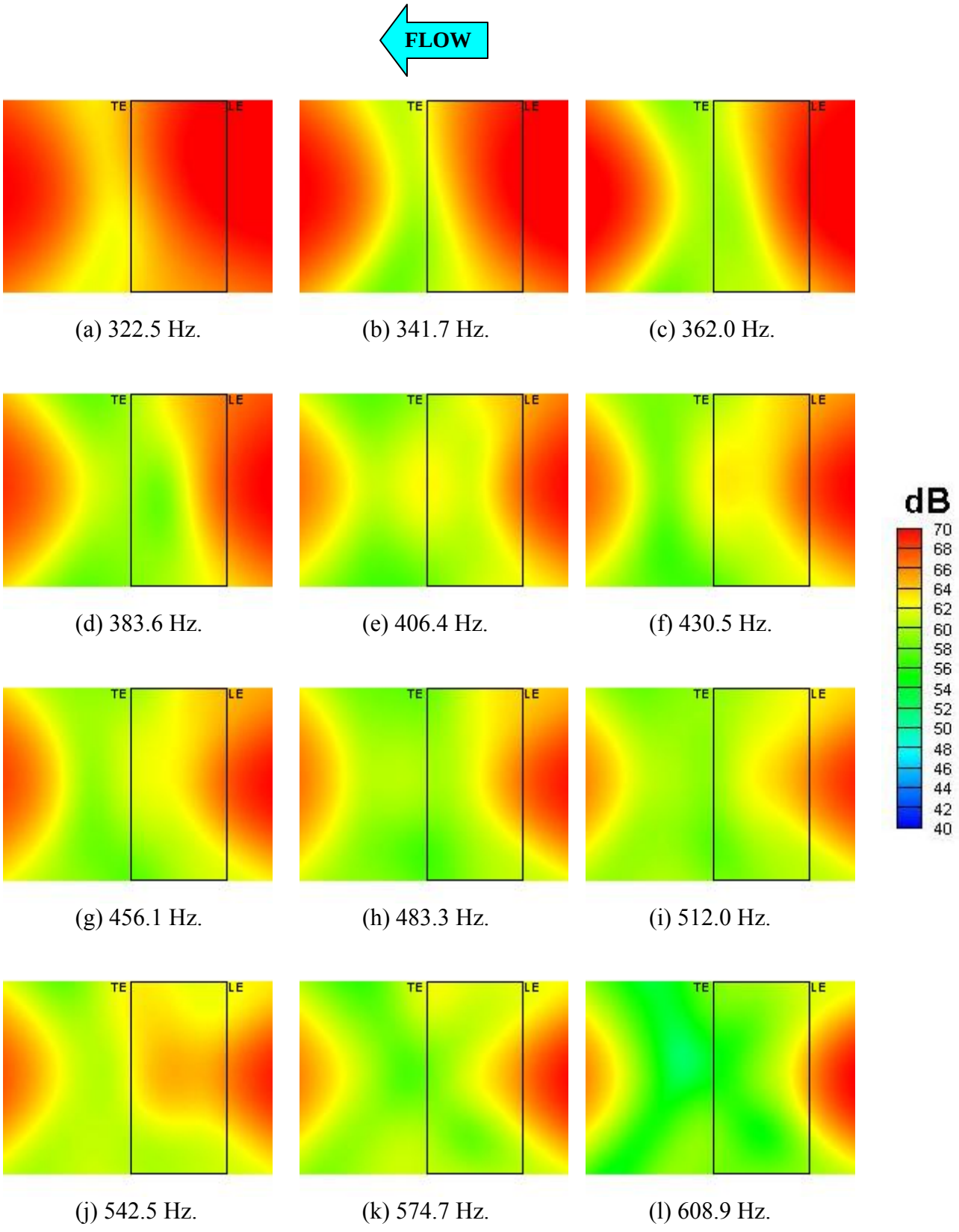

(a) 322.5 Hz. (b) 341.7 Hz. (c) 362.0 Hz.

(d) 383.6 Hz. (e) 406.4 Hz. (f) 430.5 Hz.

(g) 456.1 Hz. (h) 483.3 Hz. (i) 512.0 Hz.

(j) 542.5 Hz. (k) 574.7 Hz. (l) 608.9 Hz.

Figure 8. 1/12-Octave band beamform maps for Run008
(Airfoil at α = -1.5˚, U=70.14 m/s, Tripped BL, phased array on pressure side).

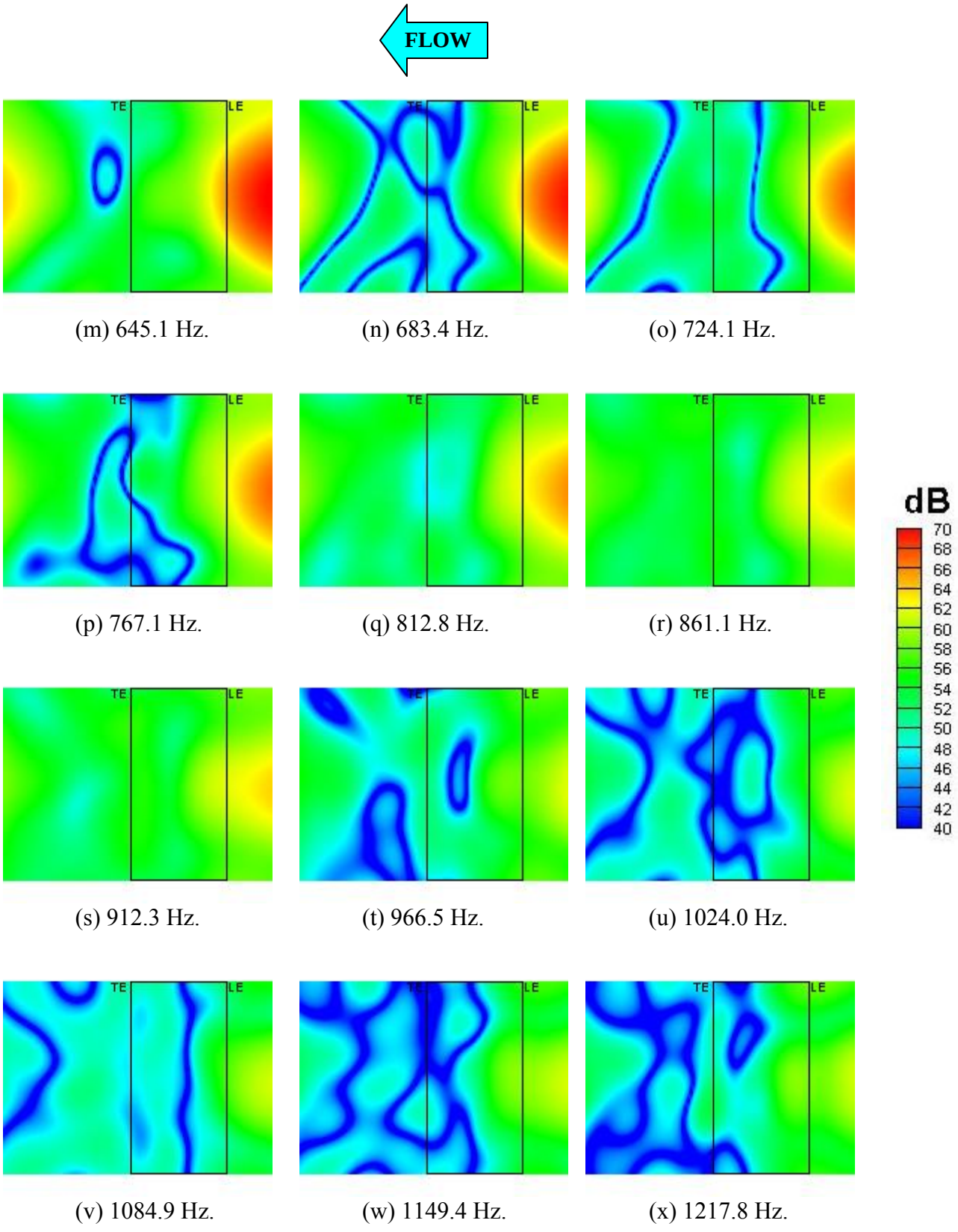

(m) 645.1 Hz. (n) 683.4 Hz. (o) 724.1 Hz.

(p) 767.1 Hz. (q) 812.8 Hz. (r) 861.1 Hz.

(s) 912.3 Hz. (t) 966.5 Hz. (u) 1024.0 Hz.

(v) 1084.9 Hz. (w) 1149.4 Hz. (x) 1217.8 Hz.

Figure 8. 1/12-Octave band beamform maps for Run008
(Airfoil at α = -1.5˚, U=70.14 m/s, Tripped BL, phased array on pressure side).

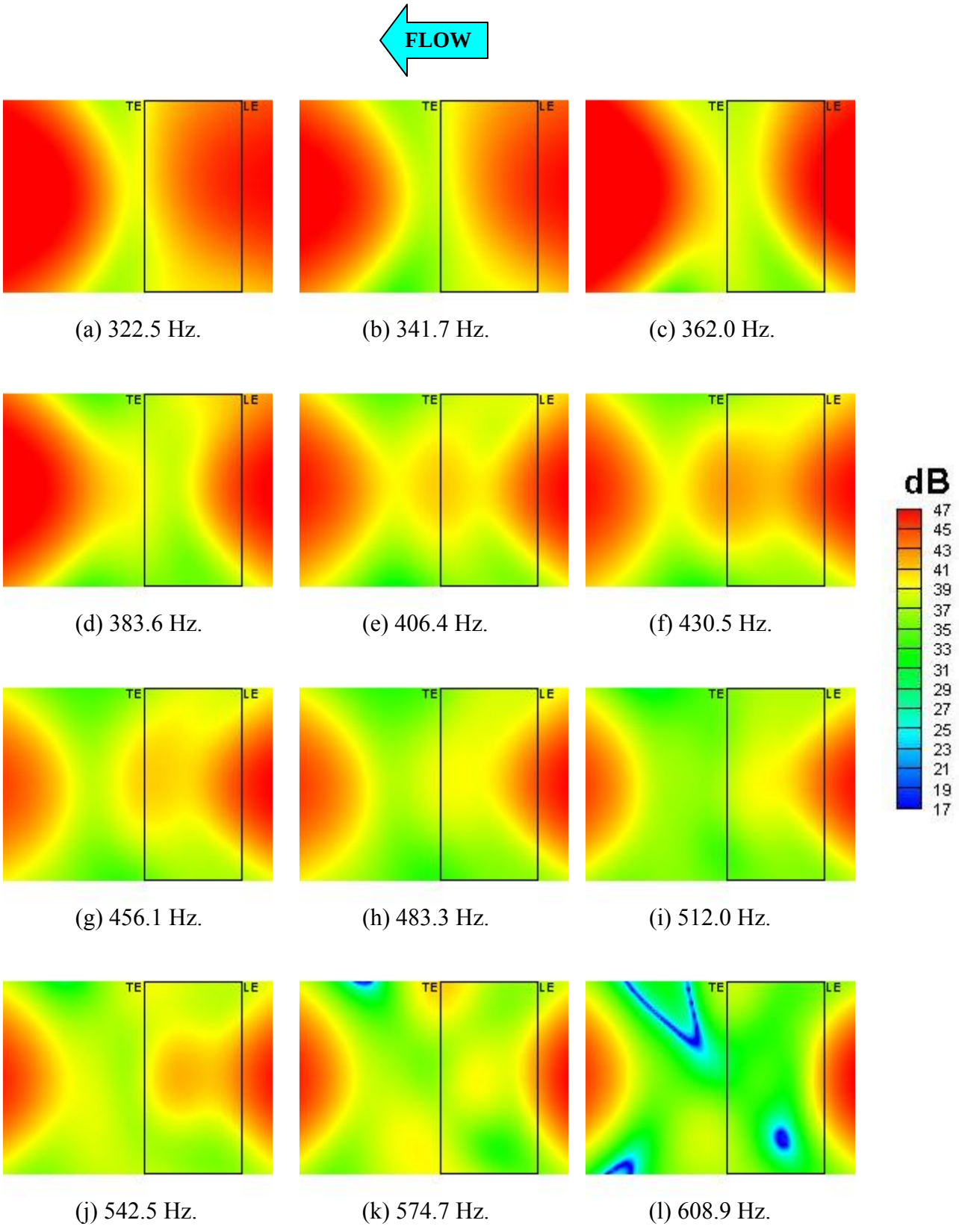

(a) 322.5 Hz. (b) 341.7 Hz. (c) 362.0 Hz.

(d) 383.6 Hz. (e) 406.4 Hz. (f) 430.5 Hz.

(g) 456.1 Hz. (h) 483.3 Hz. (i) 512.0 Hz.

(j) 542.5 Hz. (k) 574.7 Hz. (l) 608.9 Hz.

Figure 9. 1/12-Octave band beamform maps for Run009
(Airfoil at α = -3˚, U=31.21 m/s, Tripped BL, phased array on pressure side).

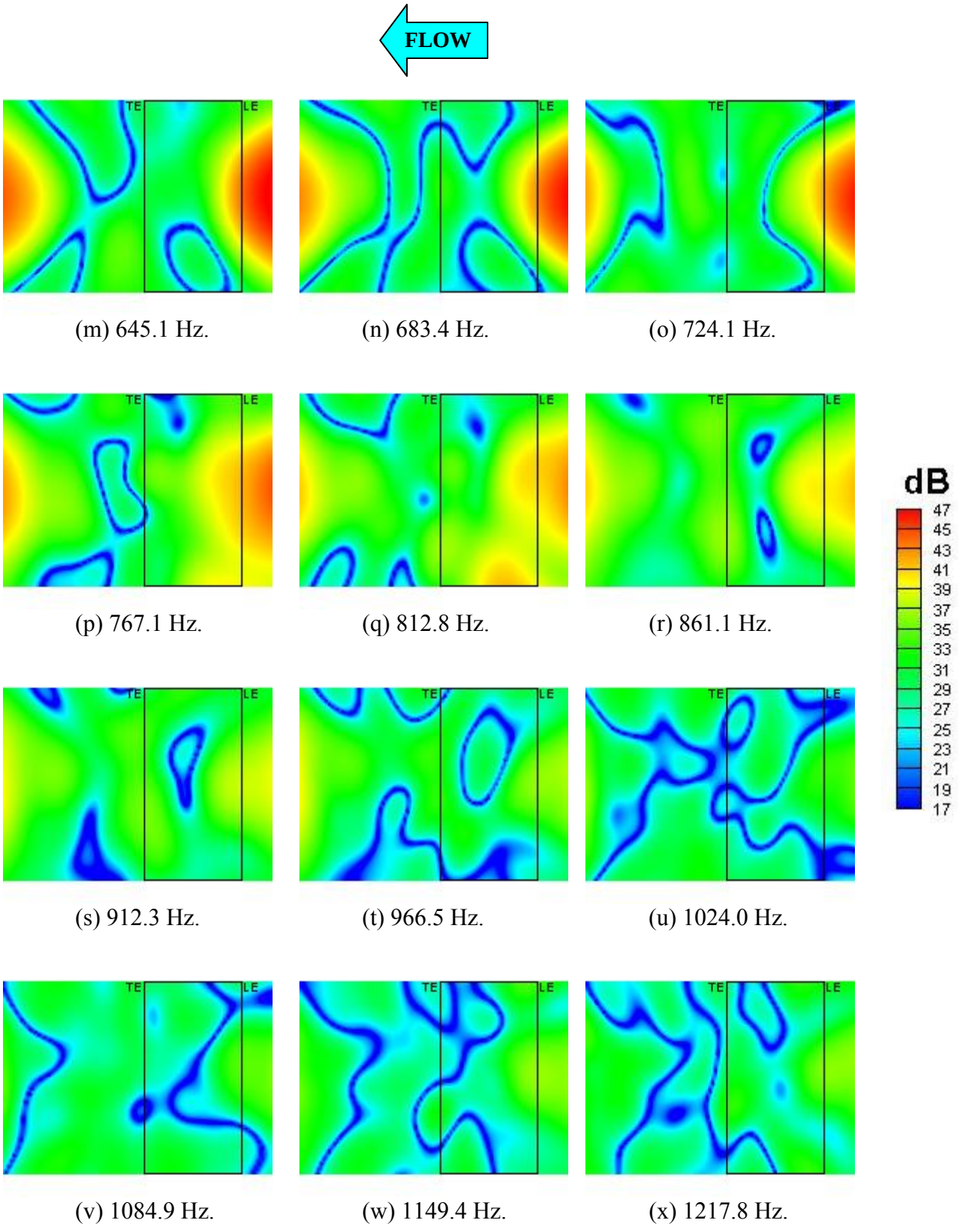

(m) 645.1 Hz. (n) 683.4 Hz. (o) 724.1 Hz.

(p) 767.1 Hz. (q) 812.8 Hz. (r) 861.1 Hz.

(s) 912.3 Hz. (t) 966.5 Hz. (u) 1024.0 Hz.

(v) 1084.9 Hz. (w) 1149.4 Hz. (x) 1217.8 Hz.

Figure 9. 1/12-Octave band beamform maps for Run009
(Airfoil at α = -3˚, U=31.21 m/s, Tripped BL, phased array on pressure side).

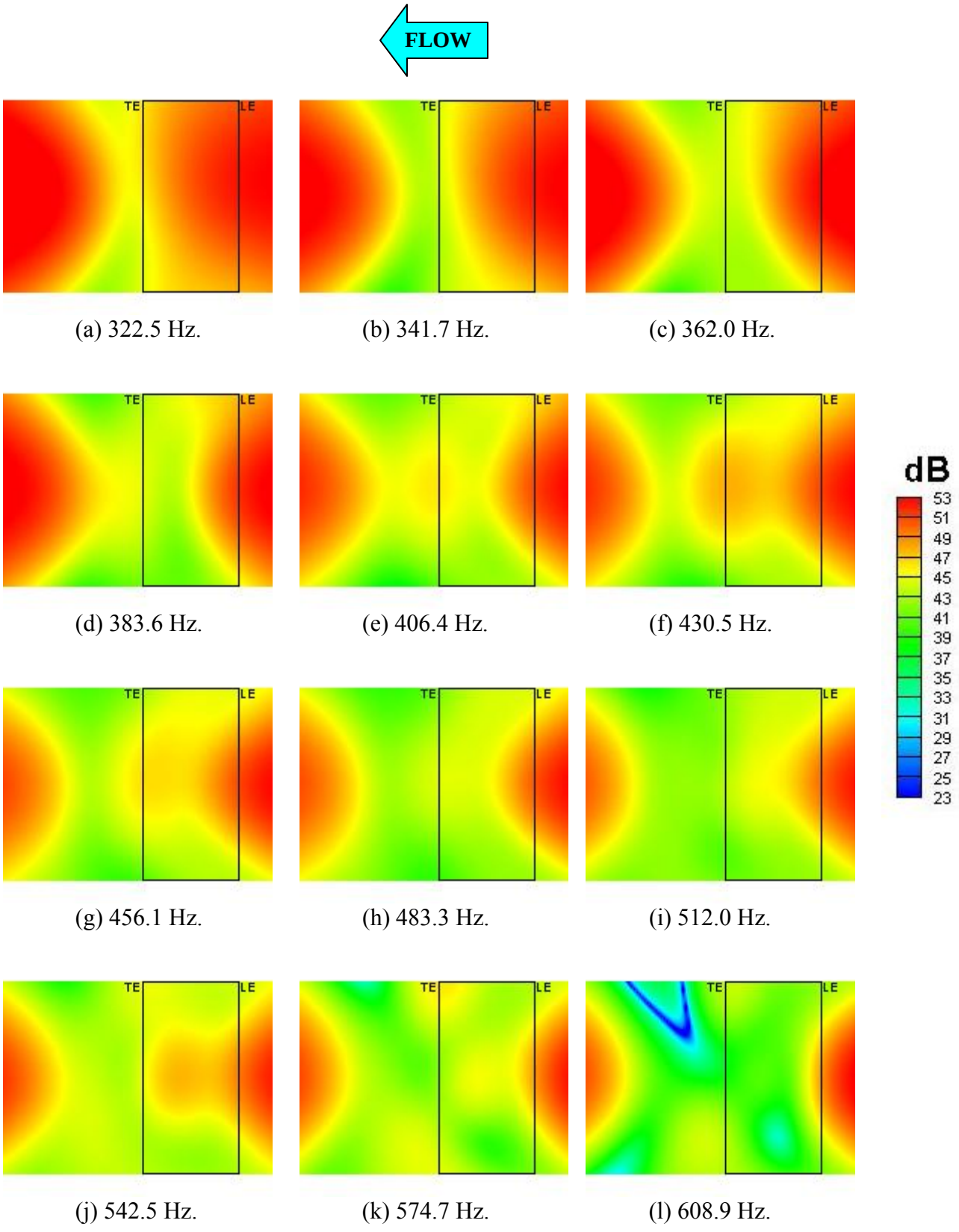

(a) 322.5 Hz. (b) 341.7 Hz. (c) 362.0 Hz.

(d) 383.6 Hz. (e) 406.4 Hz. (f) 430.5 Hz.

(g) 456.1 Hz. (h) 483.3 Hz. (i) 512.0 Hz.

(j) 542.5 Hz. (k) 574.7 Hz. (l) 608.9 Hz.

Figure 10. 1/12-Octave band beamform maps for Run010
(Airfoil at α = -3˚, U=38.99 m/s, Tripped BL, phased array on pressure side).

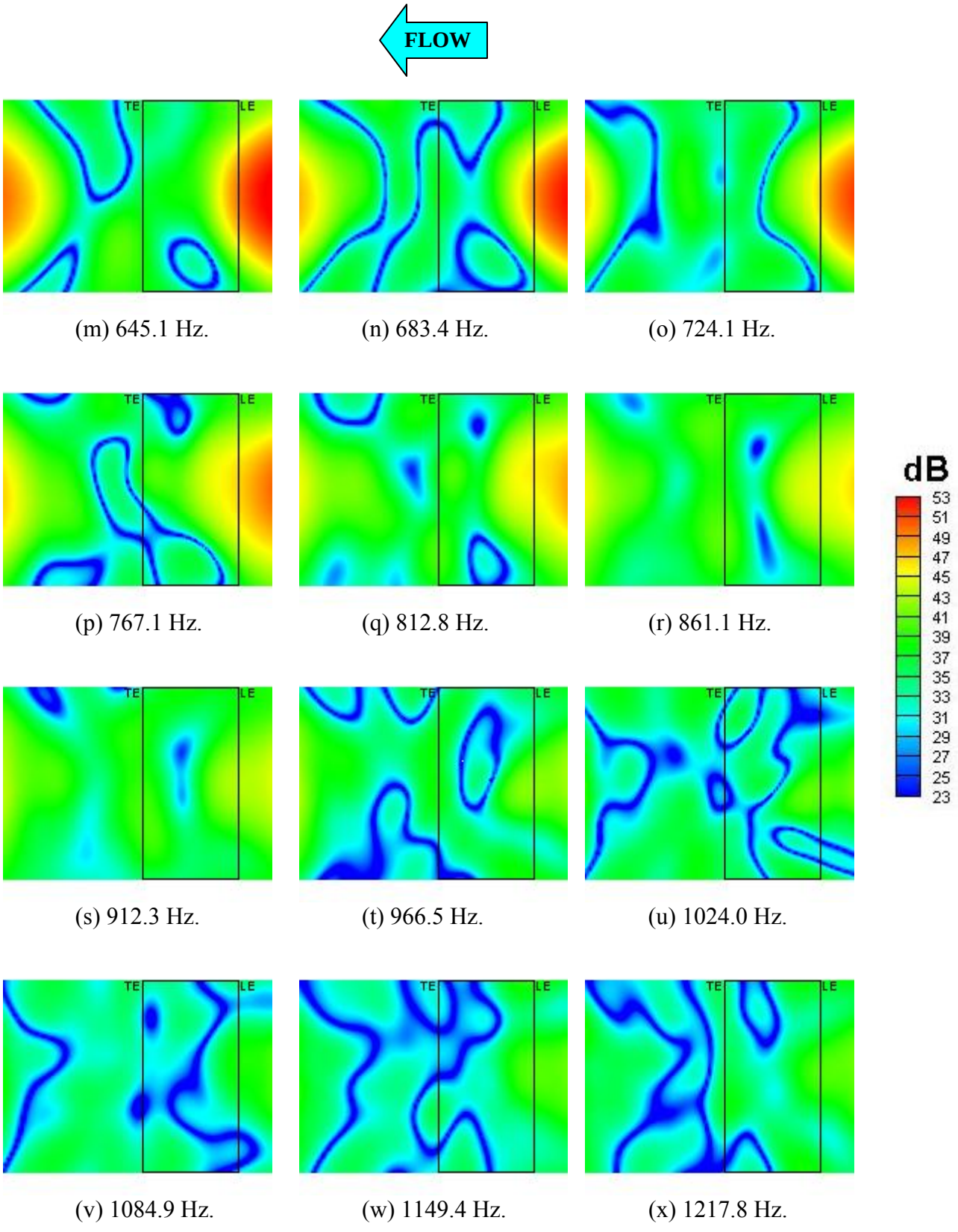

(m) 645.1 Hz. (n) 683.4 Hz. (o) 724.1 Hz.

(p) 767.1 Hz. (q) 812.8 Hz. (r) 861.1 Hz.

(s) 912.3 Hz. (t) 966.5 Hz. (u) 1024.0 Hz.

(v) 1084.9 Hz. (w) 1149.4 Hz. (x) 1217.8 Hz.

Figure 10. 1/12-Octave band beamform maps for Run010
(Airfoil at α = -3˚, U=38.99 m/s, Tripped BL, phased array on pressure side).

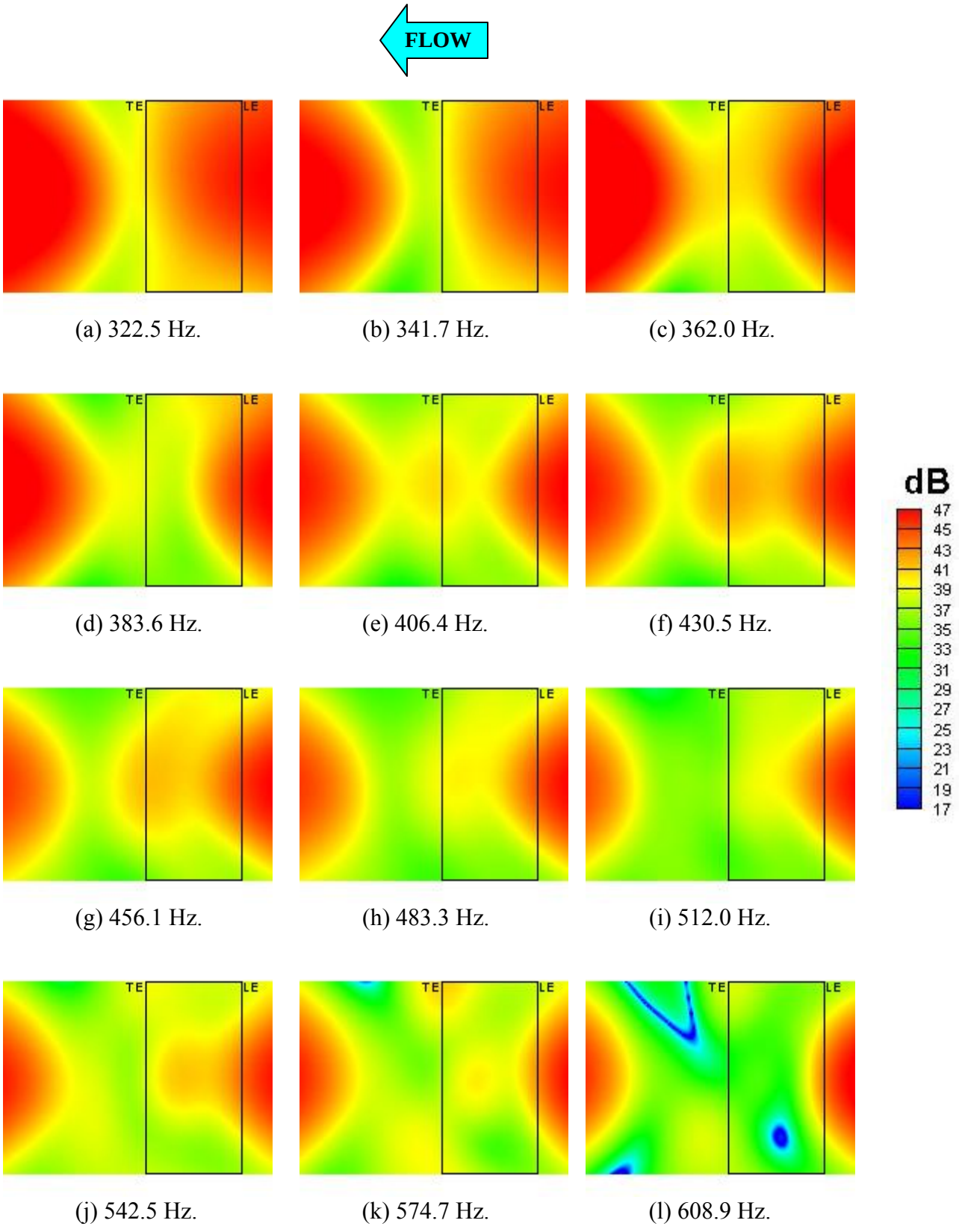

(a) 322.5 Hz. (b) 341.7 Hz. (c) 362.0 Hz.

(d) 383.6 Hz. (e) 406.4 Hz. (f) 430.5 Hz.

(g) 456.1 Hz. (h) 483.3 Hz. (i) 512.0 Hz.

(j) 542.5 Hz. (k) 574.7 Hz. (l) 608.9 Hz.

Figure 11. 1/12-Octave band beamform maps for Run012
(Airfoil at α = -5˚, U=31.21 m/s, Tripped BL, phased array on pressure side).

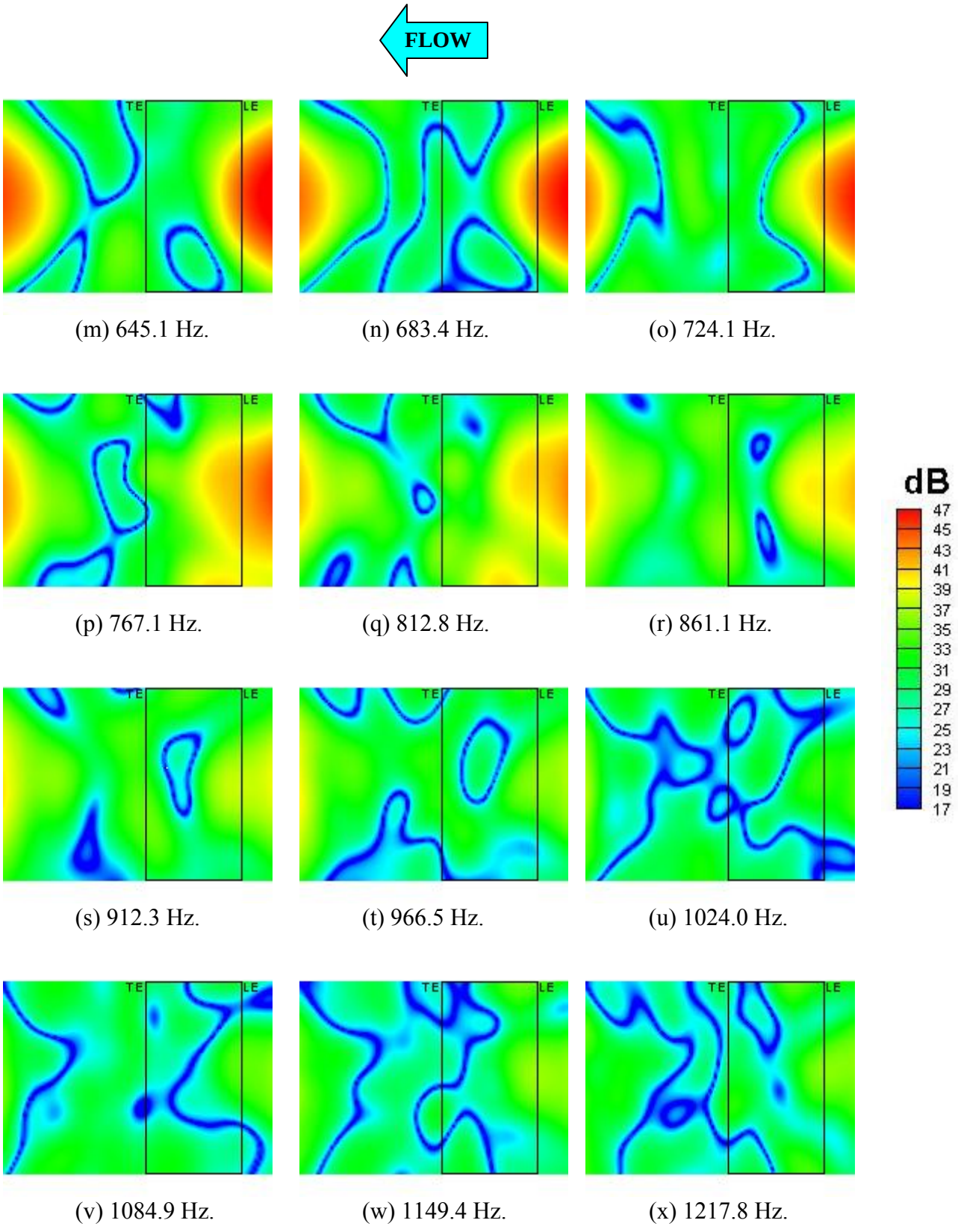

(m) 645.1 Hz. (n) 683.4 Hz. (o) 724.1 Hz.

(p) 767.1 Hz. (q) 812.8 Hz. (r) 861.1 Hz.

(s) 912.3 Hz. (t) 966.5 Hz. (u) 1024.0 Hz.

(v) 1084.9 Hz. (w) 1149.4 Hz. (x) 1217.8 Hz.

Figure 11. 1/12-Octave band beamform maps for Run012
(Airfoil at α = -5˚, U=31.21 m/s, Tripped BL, phased array on pressure side).

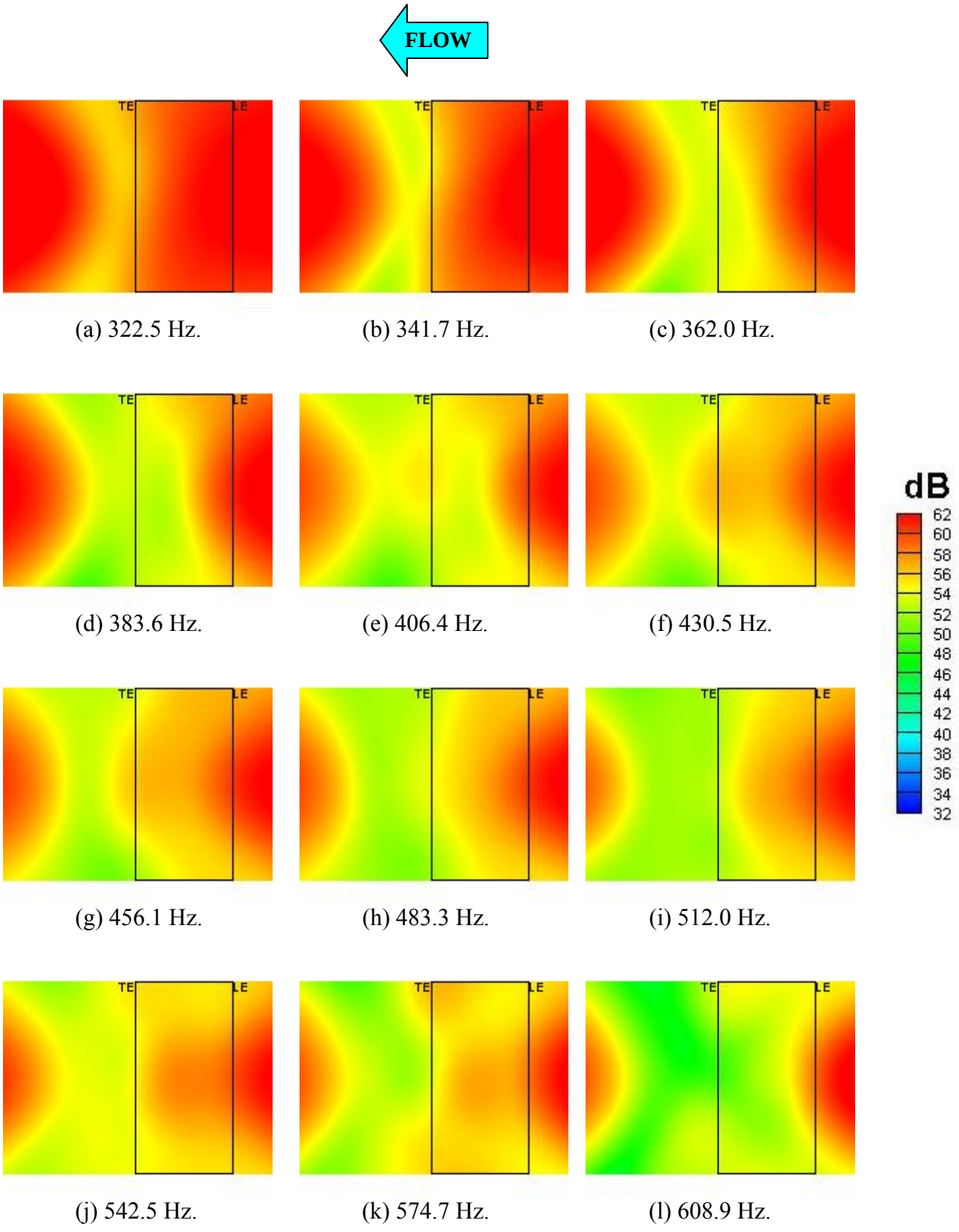

(a) 322.5 Hz. (b) 341.7 Hz. (c) 362.0 Hz.

(d) 383.6 Hz. (e) 406.4 Hz. (f) 430.5 Hz.

(g) 456.1 Hz. (h) 483.3 Hz. (i) 512.0 Hz.

(j) 542.5 Hz. (k) 574.7 Hz. (l) 608.9 Hz.

Figure 12. 1/12-Octave band beamform maps for Run014
(Airfoil at α = -5˚, U=54.79 m/s, Tripped BL, phased array on pressure side).

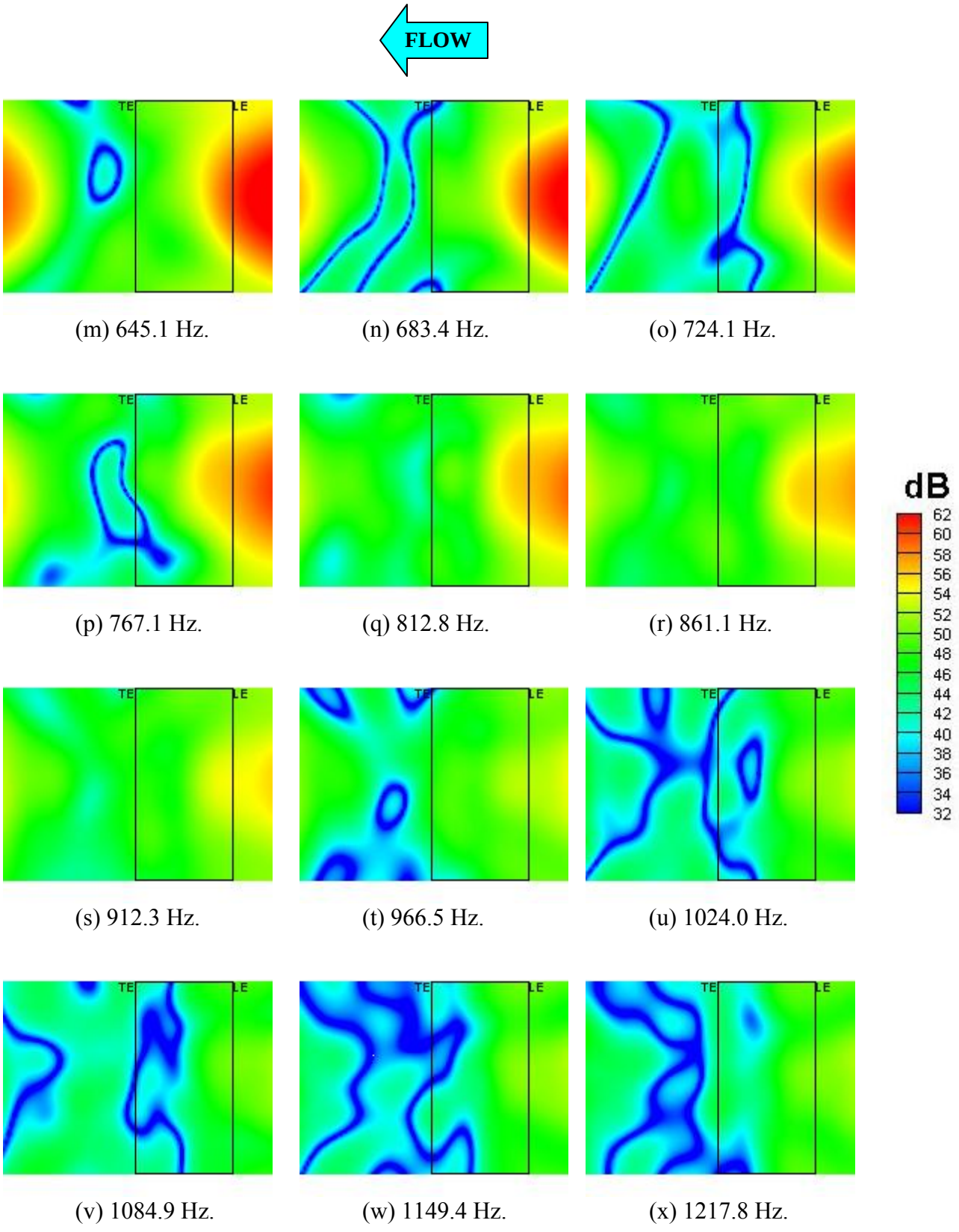

(m) 645.1 Hz. (n) 683.4 Hz. (o) 724.1 Hz.

(p) 767.1 Hz. (q) 812.8 Hz. (r) 861.1 Hz.

(s) 912.3 Hz. (t) 966.5 Hz. (u) 1024.0 Hz.

(v) 1084.9 Hz. (w) 1149.4 Hz. (x) 1217.8 Hz.

Figure 12. 1/12-Octave band beamform maps for Run014
(Airfoil at α = -5˚, U=54.79 m/s, Tripped BL, phased array on pressure side).

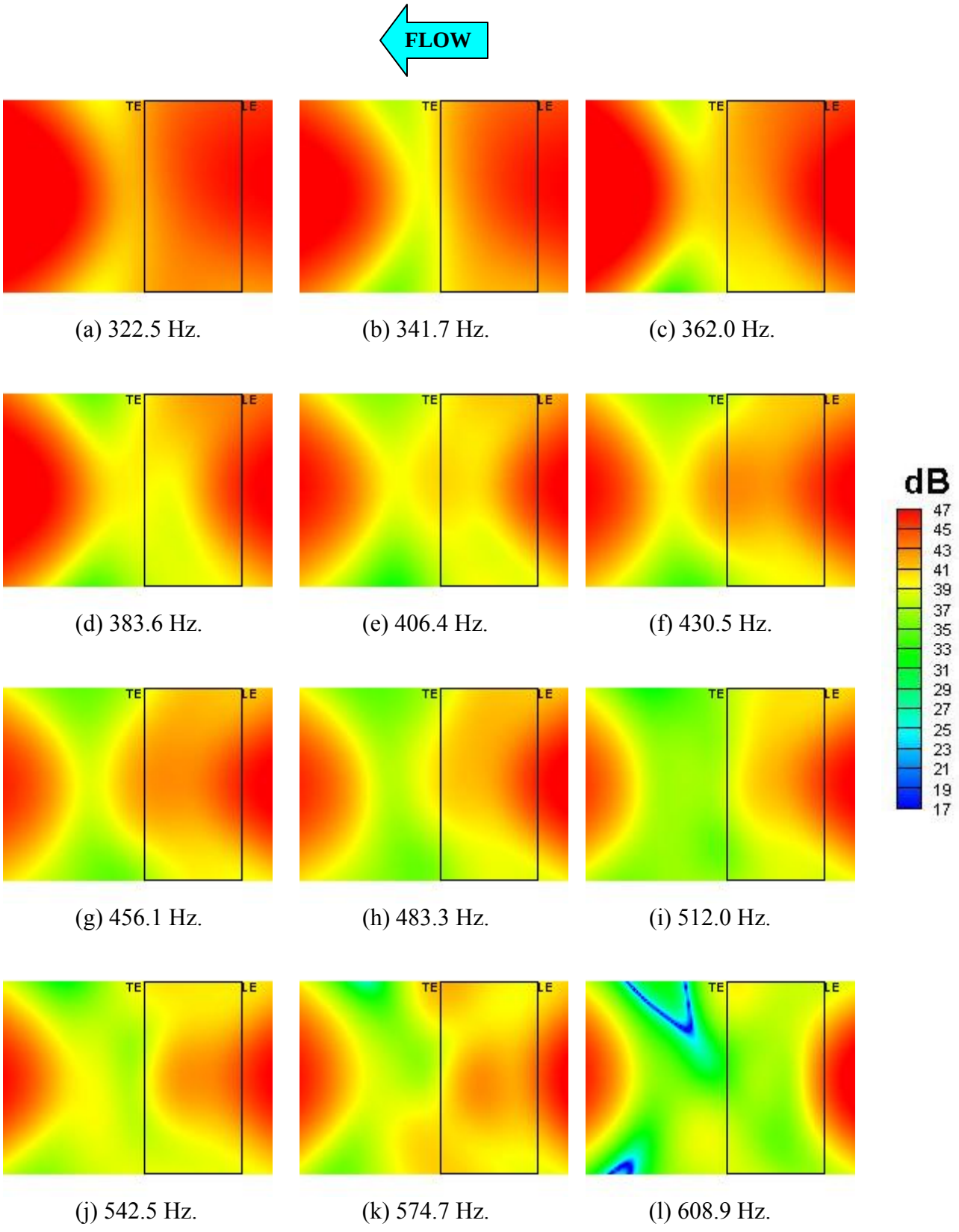

(a) 322.5 Hz. (b) 341.7 Hz. (c) 362.0 Hz.

(d) 383.6 Hz. (e) 406.4 Hz. (f) 430.5 Hz.

(g) 456.1 Hz. (h) 483.3 Hz. (i) 512.0 Hz.

(j) 542.5 Hz. (k) 574.7 Hz. (l) 608.9 Hz.

Figure 13. 1/12-Octave band beamform maps for Run015
(Airfoil at α = -7˚, U=31.18 m/s, Tripped BL, phased array on pressure side).

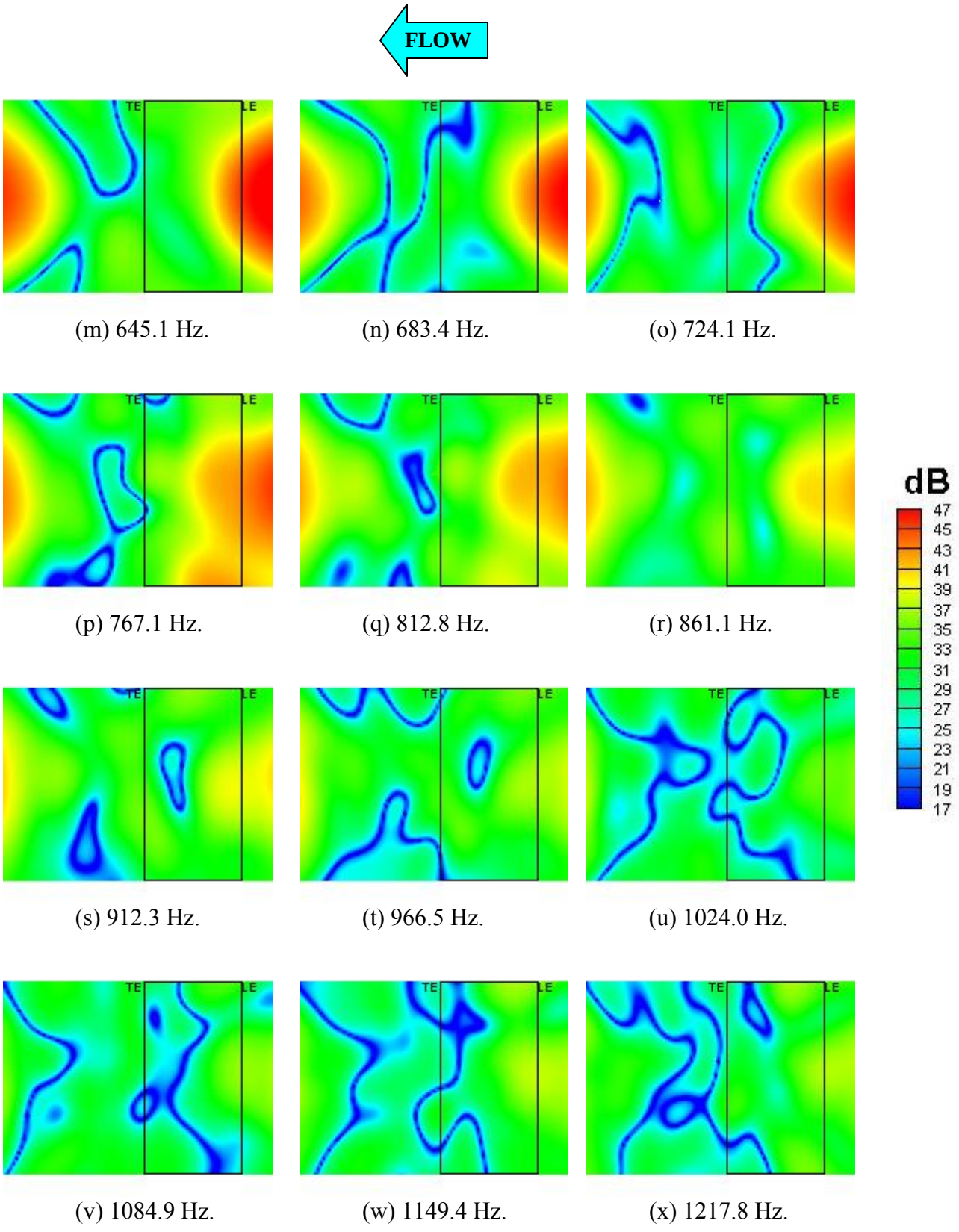

(m) 645.1 Hz. (n) 683.4 Hz. (o) 724.1 Hz.

(p) 767.1 Hz. (q) 812.8 Hz. (r) 861.1 Hz.

(s) 912.3 Hz. (t) 966.5 Hz. (u) 1024.0 Hz.

(v) 1084.9 Hz. (w) 1149.4 Hz. (x) 1217.8 Hz.

Figure 13. 1/12-Octave band beamform maps for Run015
(Airfoil at α = -7˚, U=31.18 m/s, Tripped BL, phased array on pressure side).

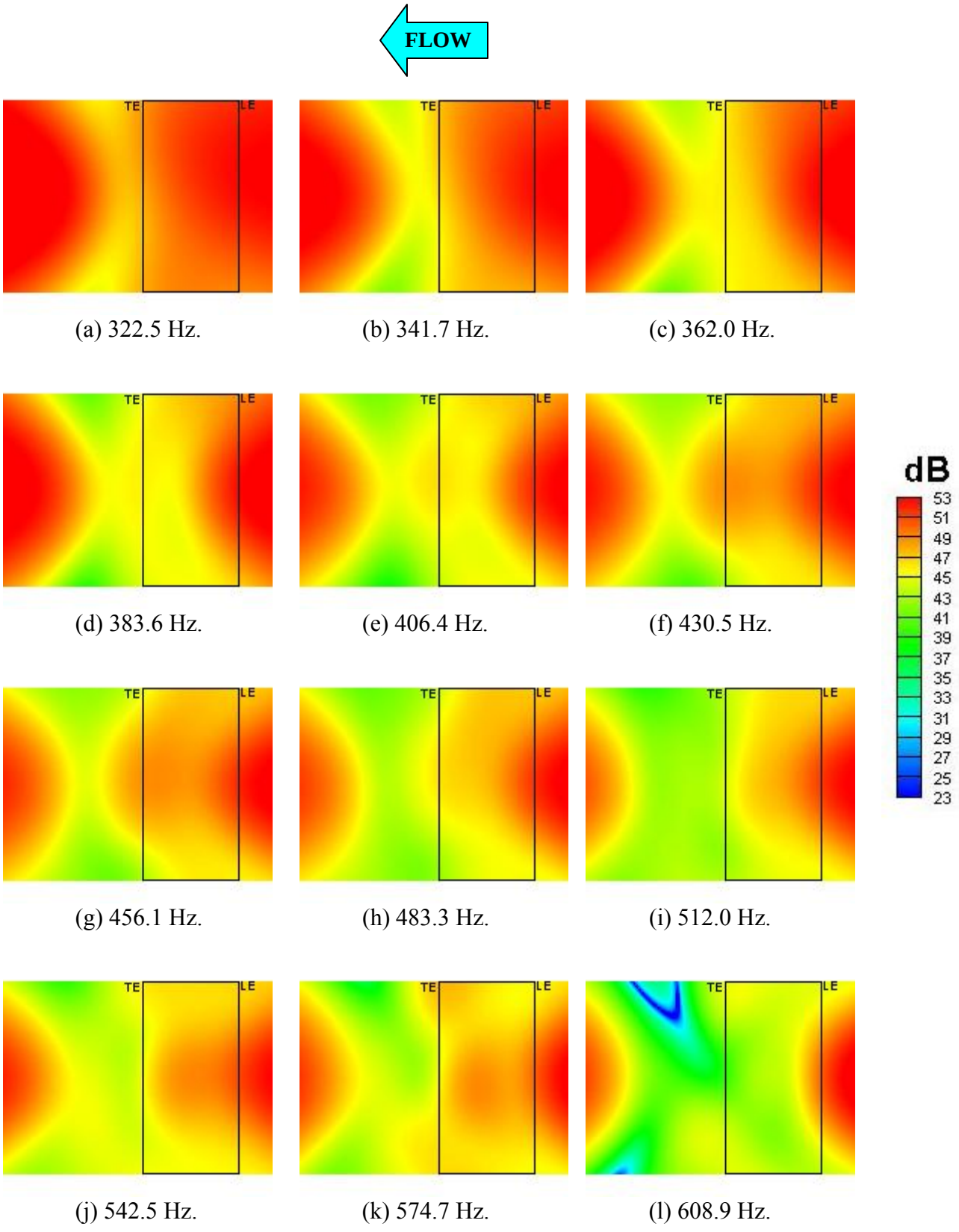

(a) 322.5 Hz. (b) 341.7 Hz. (c) 362.0 Hz.

(d) 383.6 Hz. (e) 406.4 Hz. (f) 430.5 Hz.

(g) 456.1 Hz. (h) 483.3 Hz. (i) 512.0 Hz.

(j) 542.5 Hz. (k) 574.7 Hz. (l) 608.9 Hz.

Figure 14. 1/12-Octave band beamform maps for Run016
(Airfoil at α = -7˚, U=39.14 m/s, Tripped BL, phased array on pressure side).

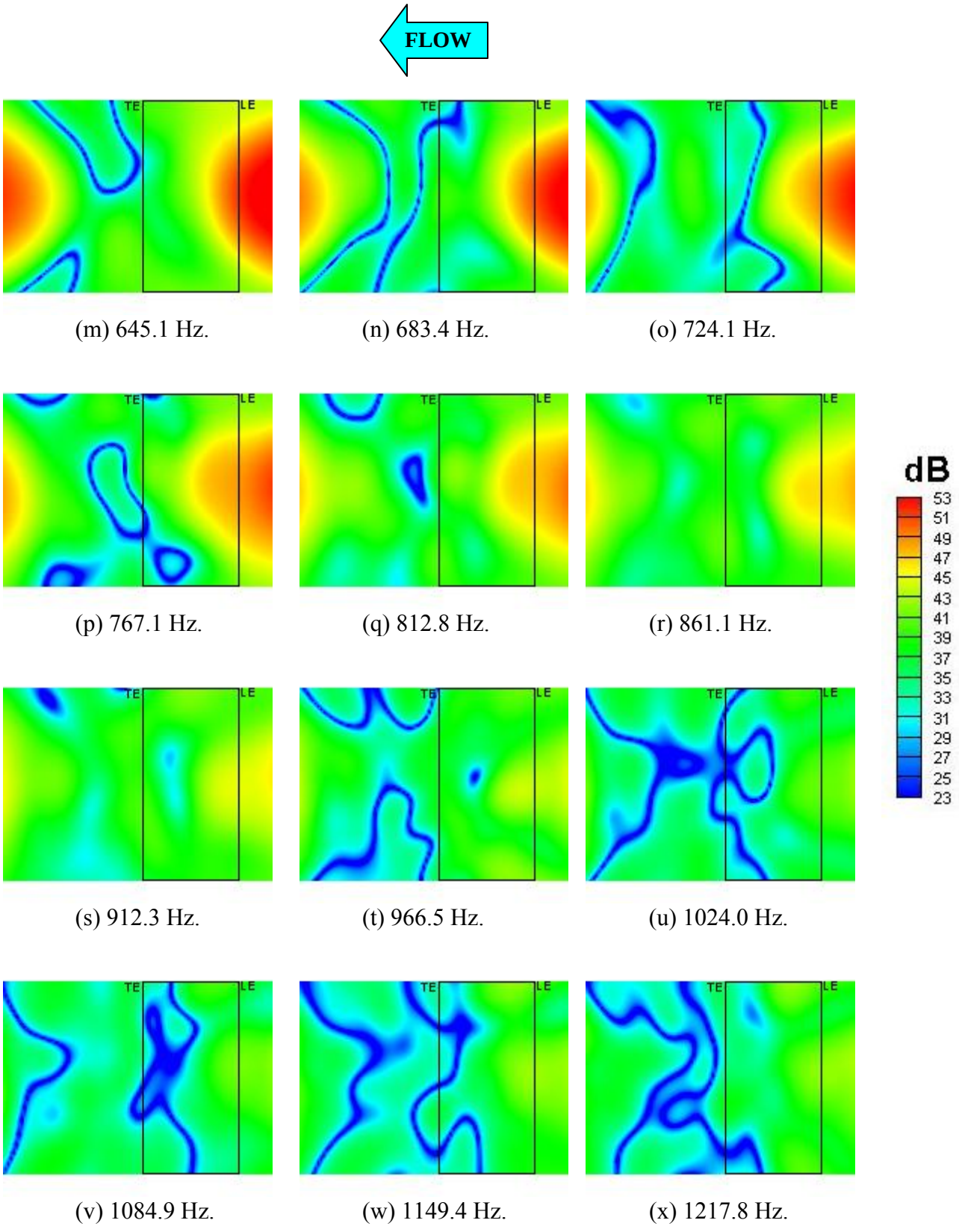

(m) 645.1 Hz. (n) 683.4 Hz. (o) 724.1 Hz.

(p) 767.1 Hz. (q) 812.8 Hz. (r) 861.1 Hz.

(s) 912.3 Hz. (t) 966.5 Hz. (u) 1024.0 Hz.

(v) 1084.9 Hz. (w) 1149.4 Hz. (x) 1217.8 Hz.

Figure 14. 1/12-Octave band beamform maps for Run016
(Airfoil at α = -7˚, U=39.14 m/s, Tripped BL, phased array on pressure side).

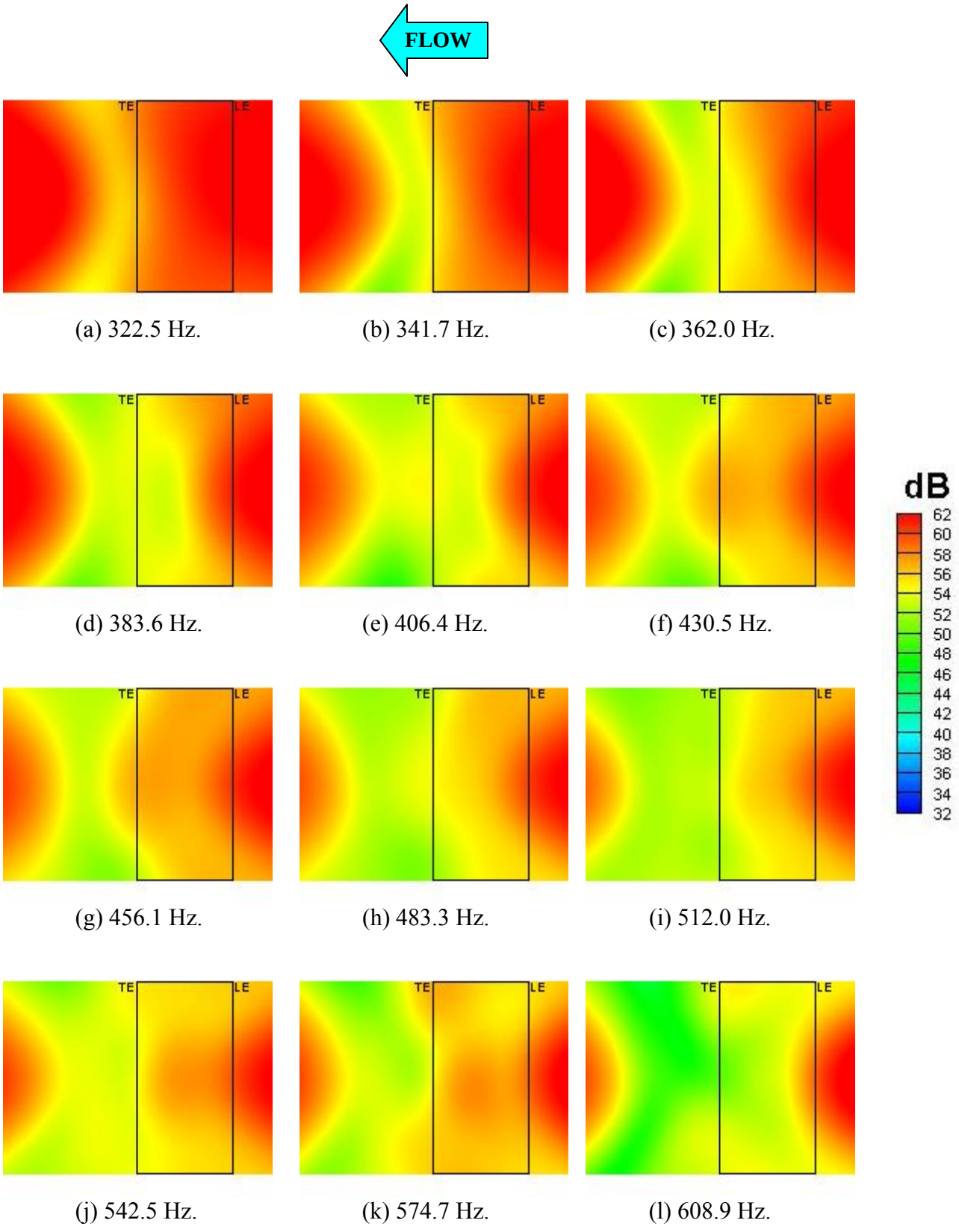

(a) 322.5 Hz. (b) 341.7 Hz. (c) 362.0 Hz.

(d) 383.6 Hz. (e) 406.4 Hz. (f) 430.5 Hz.

(g) 456.1 Hz. (h) 483.3 Hz. (i) 512.0 Hz.

(j) 542.5 Hz. (k) 574.7 Hz. (l) 608.9 Hz.

Figure 15. 1/12-Octave band beamform maps for Run017
(Airfoil at α = -7˚, U=54.72 m/s, Tripped BL, phased array on pressure side).

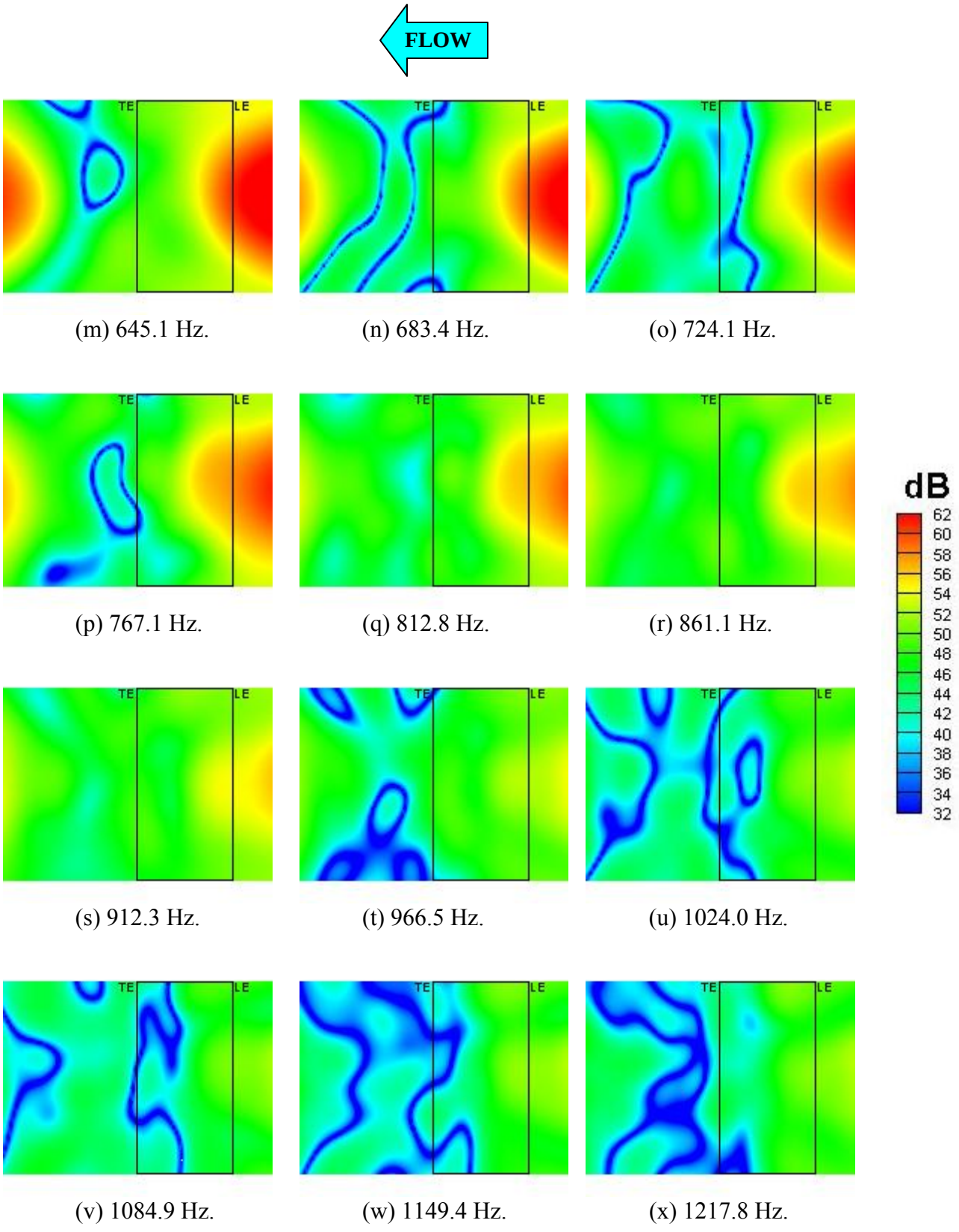

(m) 645.1 Hz. (n) 683.4 Hz. (o) 724.1 Hz.

(p) 767.1 Hz. (q) 812.8 Hz. (r) 861.1 Hz.

(s) 912.3 Hz. (t) 966.5 Hz. (u) 1024.0 Hz.

(v) 1084.9 Hz. (w) 1149.4 Hz. (x) 1217.8 Hz.

Figure 15. 1/12-Octave band beamform maps for Run017
(Airfoil at α = -7˚, U=54.72 m/s, Tripped BL, phased array on pressure side).

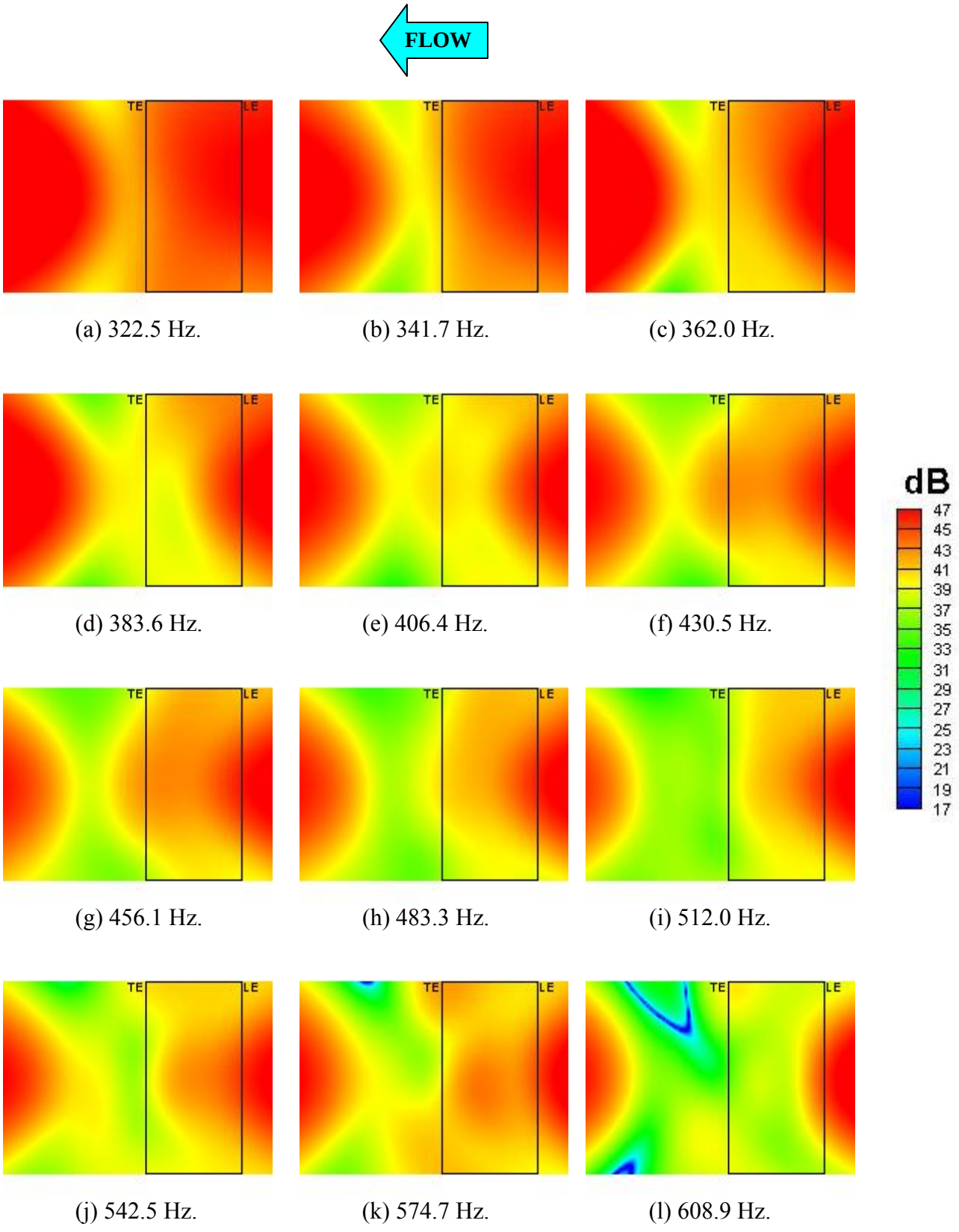

(a) 322.5 Hz. (b) 341.7 Hz. (c) 362.0 Hz.

(d) 383.6 Hz. (e) 406.4 Hz. (f) 430.5 Hz.

(g) 456.1 Hz. (h) 483.3 Hz. (i) 512.0 Hz.

(j) 542.5 Hz. (k) 574.7 Hz. (l) 608.9 Hz.

Figure 16. 1/12-Octave band beamform maps for Run018
(Airfoil at α = -9˚, U=31.18 m/s, Tripped BL, phased array on pressure side).

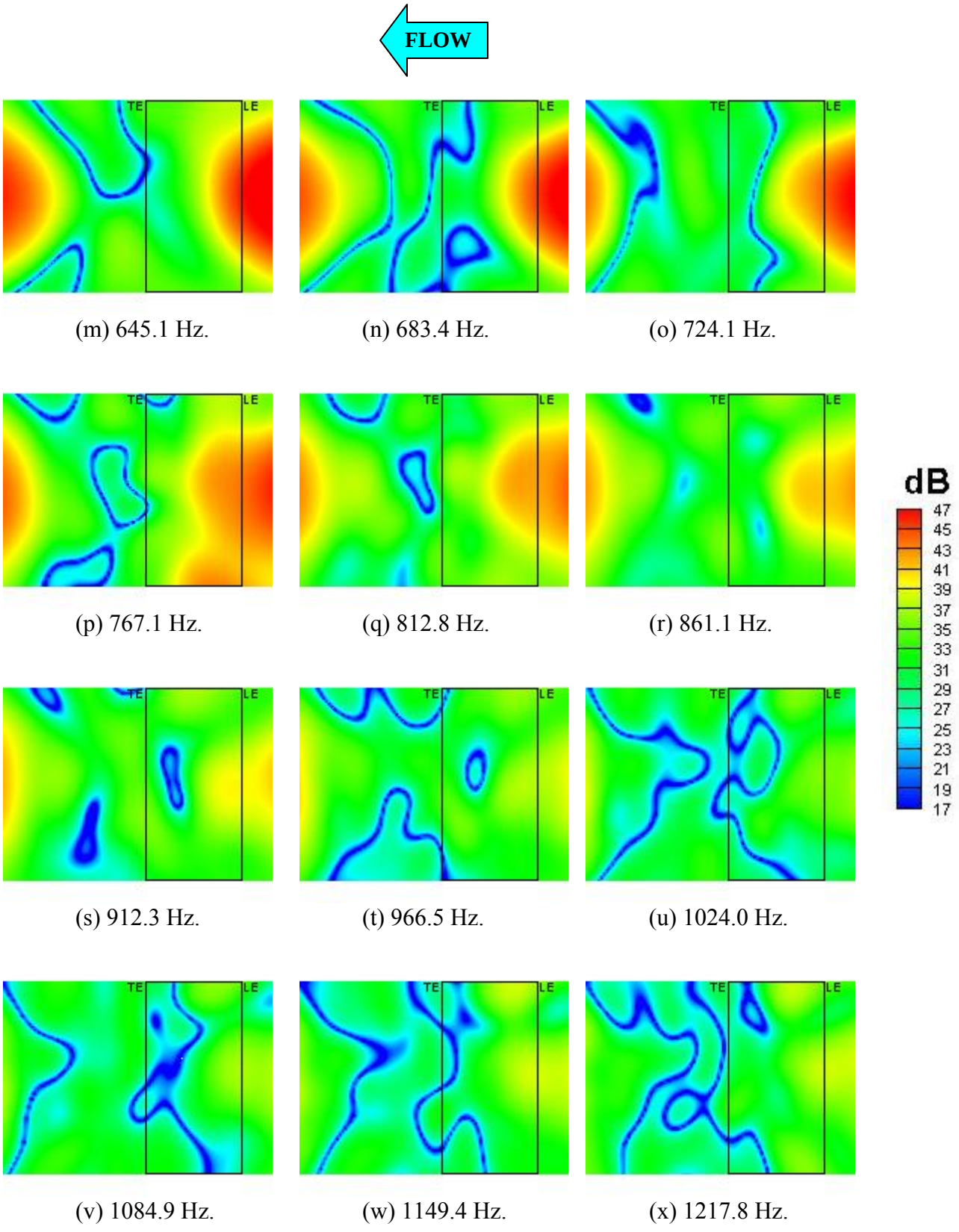

(m) 645.1 Hz. (n) 683.4 Hz. (o) 724.1 Hz.

(p) 767.1 Hz. (q) 812.8 Hz. (r) 861.1 Hz.

(s) 912.3 Hz. (t) 966.5 Hz. (u) 1024.0 Hz.

(v) 1084.9 Hz. (w) 1149.4 Hz. (x) 1217.8 Hz.

Figure 16. 1/12-Octave band beamform maps for Run018
(Airfoil at α = -9˚, U=31.18 m/s, Tripped BL, phased array on pressure side).

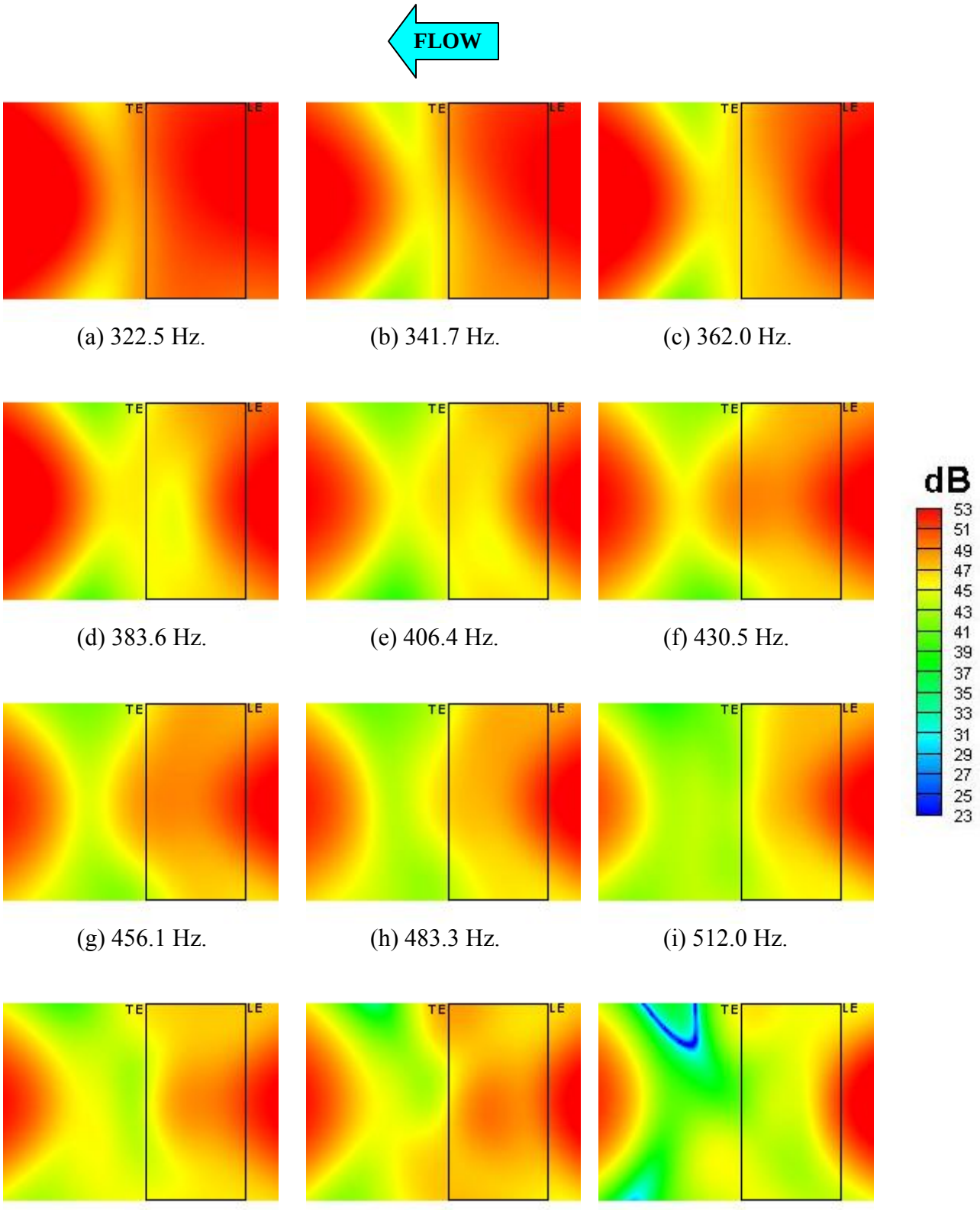

(a) 322.5 Hz. (b) 341.7 Hz. (c) 362.0 Hz.

(d) 383.6 Hz. (e) 406.4 Hz. (f) 430.5 Hz.

(g) 456.1 Hz. (h) 483.3 Hz. (i) 512.0 Hz.

(j) 542.5 Hz. (k) 574.7 Hz. (l) 608.9 Hz.

Figure 17. 1/12-Octave band beamform maps for Run019
(Airfoil at α = -9˚, U=39.02 m/s, Tripped BL, phased array on pressure side).

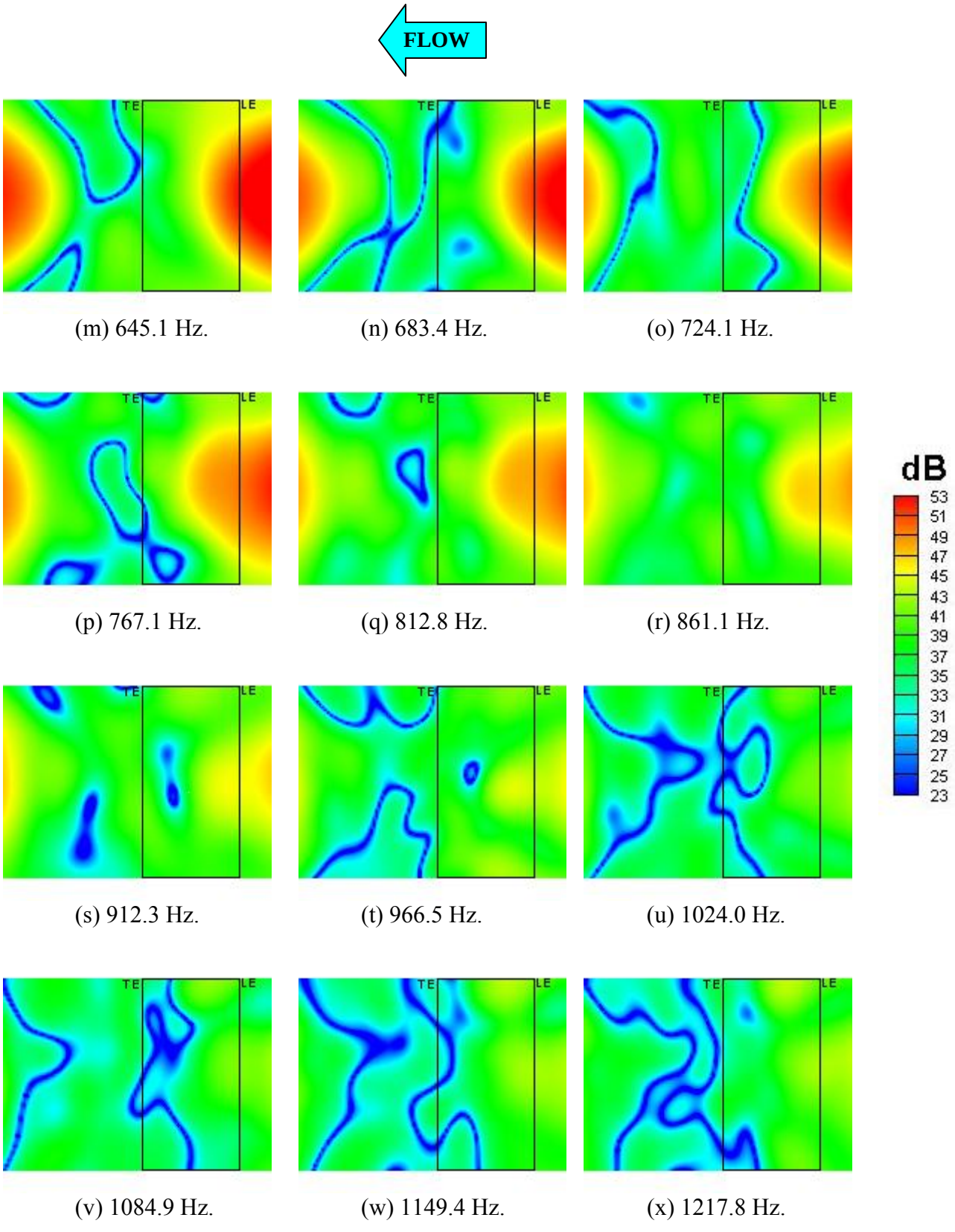

(m) 645.1 Hz. (n) 683.4 Hz. (o) 724.1 Hz.

(p) 767.1 Hz. (q) 812.8 Hz. (r) 861.1 Hz.

(s) 912.3 Hz. (t) 966.5 Hz. (u) 1024.0 Hz.

(v) 1084.9 Hz. (w) 1149.4 Hz. (x) 1217.8 Hz.

Figure 17. 1/12-Octave band beamform maps for Run019
(Airfoil at α = -9˚, U=39.02 m/s, Tripped BL, phased array on pressure side).

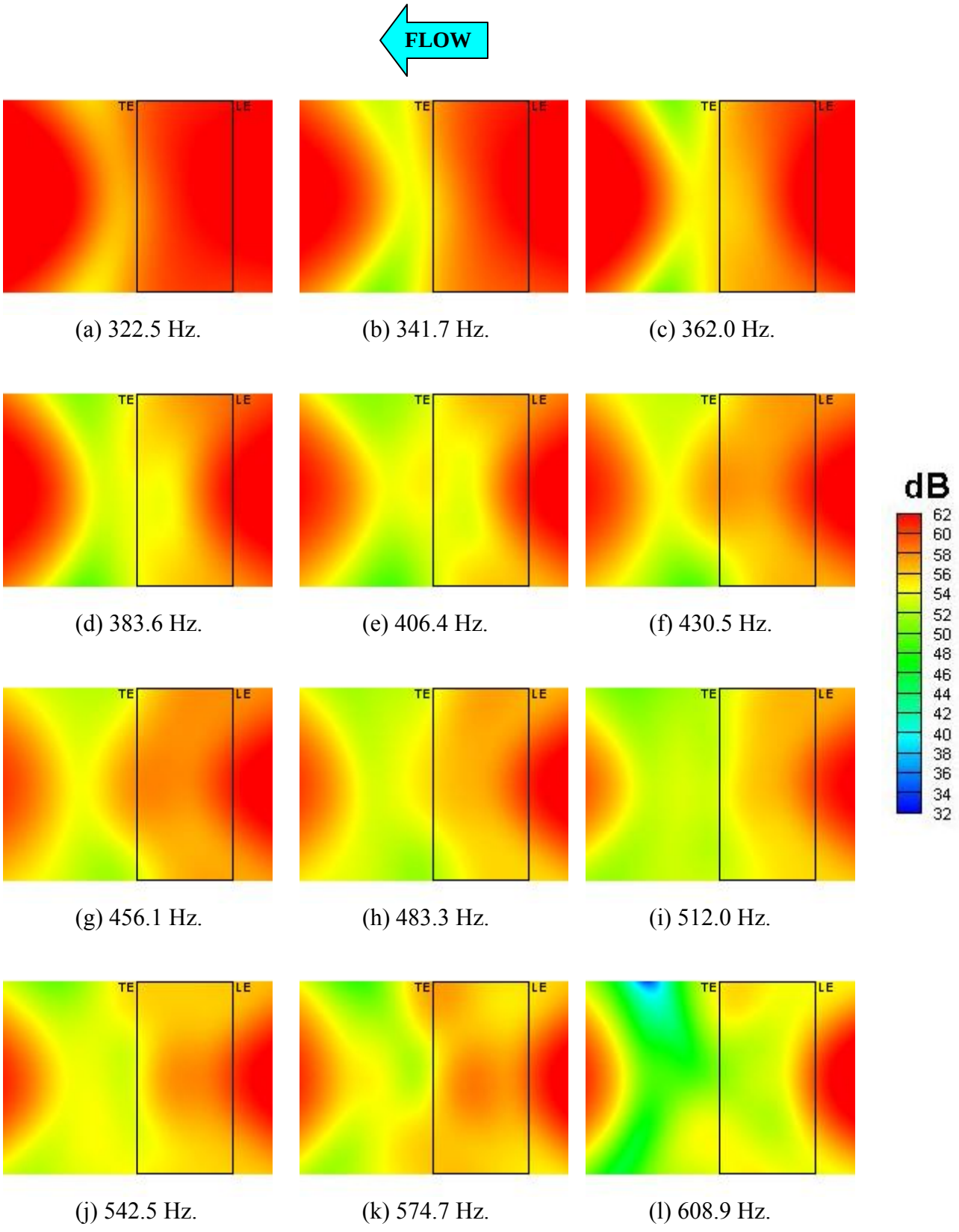

(a) 322.5 Hz. (b) 341.7 Hz. (c) 362.0 Hz.

(d) 383.6 Hz. (e) 406.4 Hz. (f) 430.5 Hz.

(g) 456.1 Hz. (h) 483.3 Hz. (i) 512.0 Hz.

(j) 542.5 Hz. (k) 574.7 Hz. (l) 608.9 Hz.

Figure 18. 1/12-Octave band beamform maps for Run020
(Airfoil at α = -9˚, U=54.73 m/s, Tripped BL, phased array on pressure side).

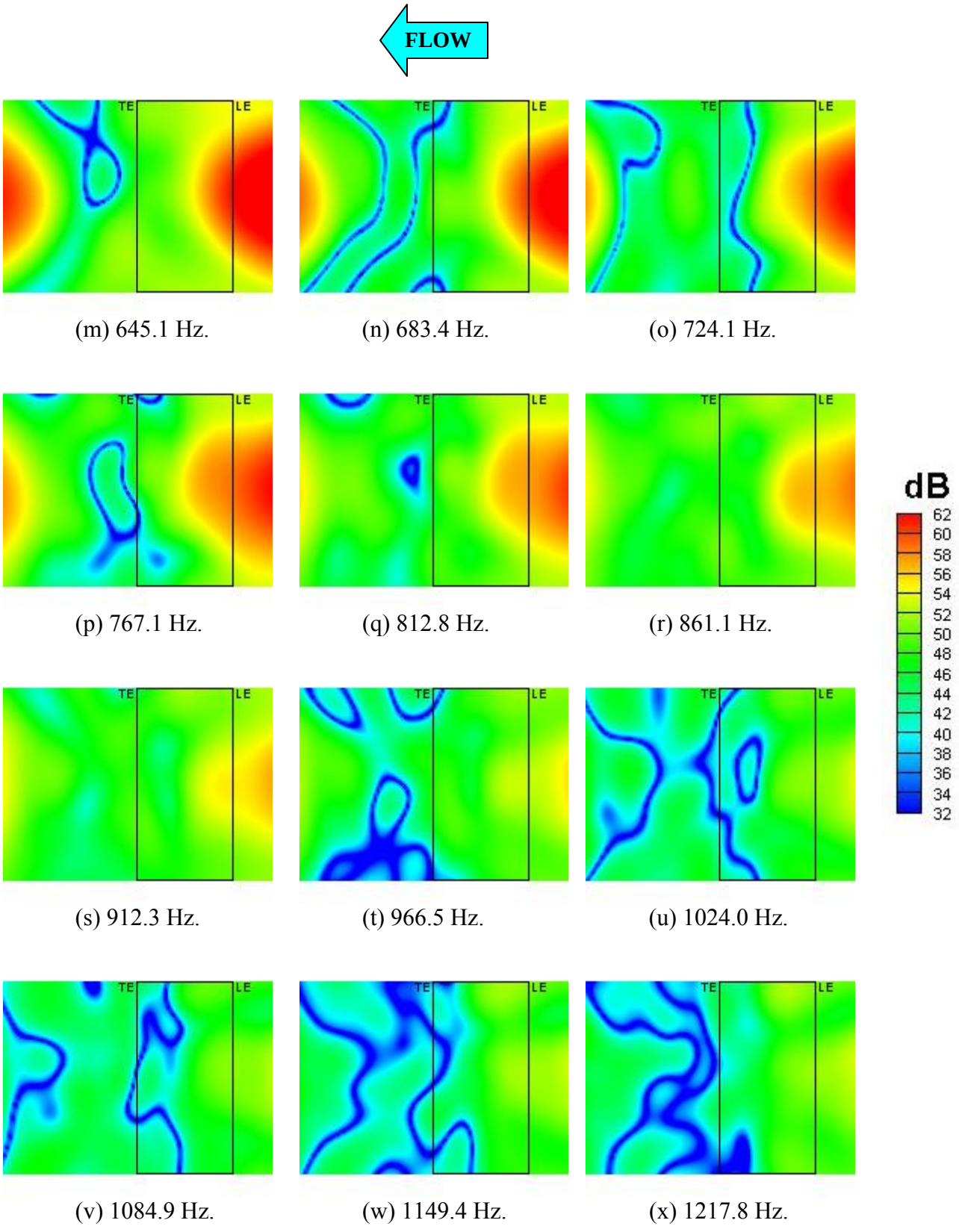

(m) 645.1 Hz. (n) 683.4 Hz. (o) 724.1 Hz.

(p) 767.1 Hz. (q) 812.8 Hz. (r) 861.1 Hz.

(s) 912.3 Hz. (t) 966.5 Hz. (u) 1024.0 Hz.

(v) 1084.9 Hz. (w) 1149.4 Hz. (x) 1217.8 Hz.

Figure 18. 1/12-Octave band beamform maps for Run020
(Airfoil at α = -9˚, U=54.73 m/s, Tripped BL, phased array on pressure side).

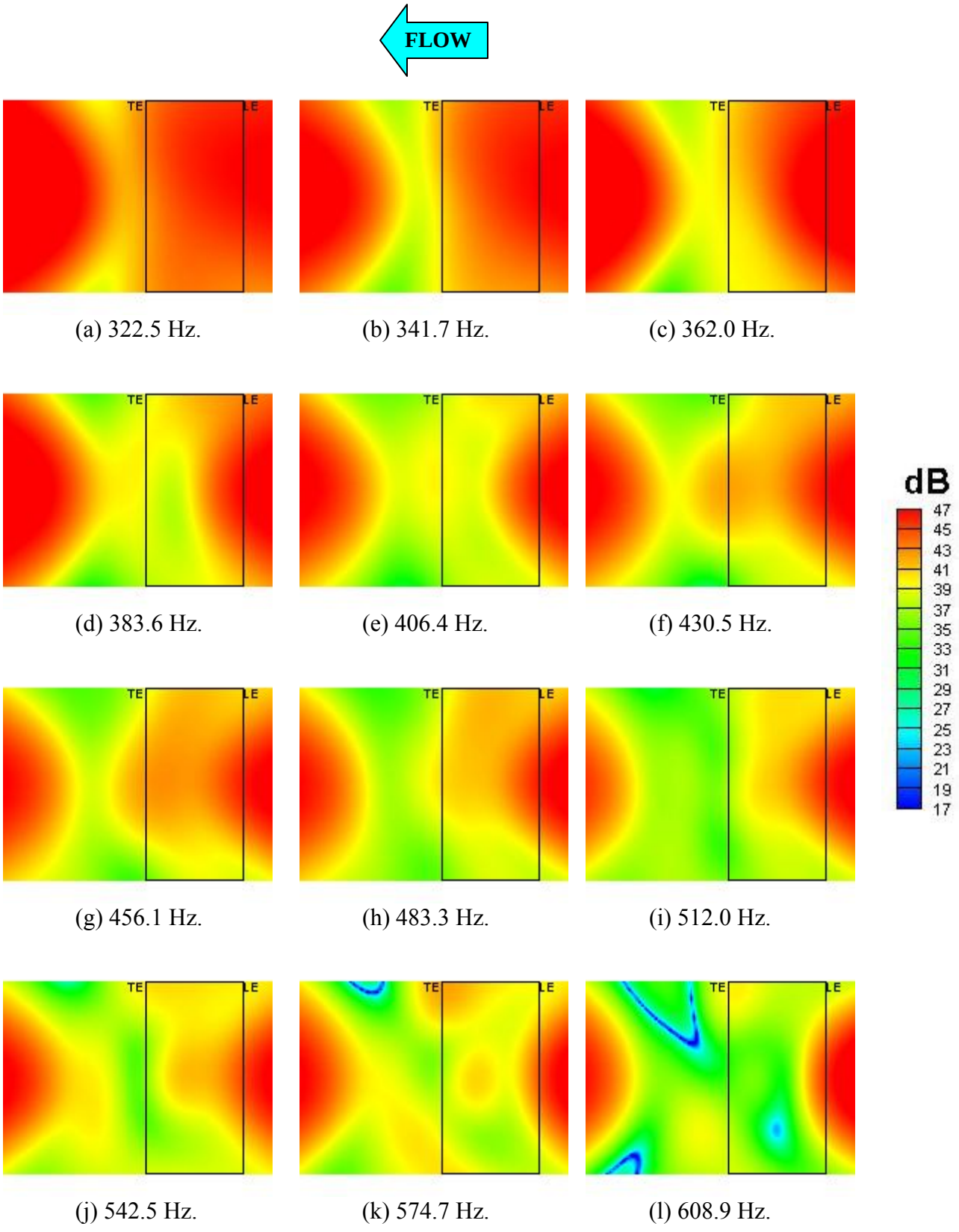

(a) 322.5 Hz. (b) 341.7 Hz. (c) 362.0 Hz.

(d) 383.6 Hz. (e) 406.4 Hz. (f) 430.5 Hz.

(g) 456.1 Hz. (h) 483.3 Hz. (i) 512.0 Hz.

(j) 542.5 Hz. (k) 574.7 Hz. (l) 608.9 Hz.

Figure 19. 1/12-Octave band beamform maps for Run021
(Airfoil at α = -11˚, U=31.18 m/s, Tripped BL, phased array on pressure side).

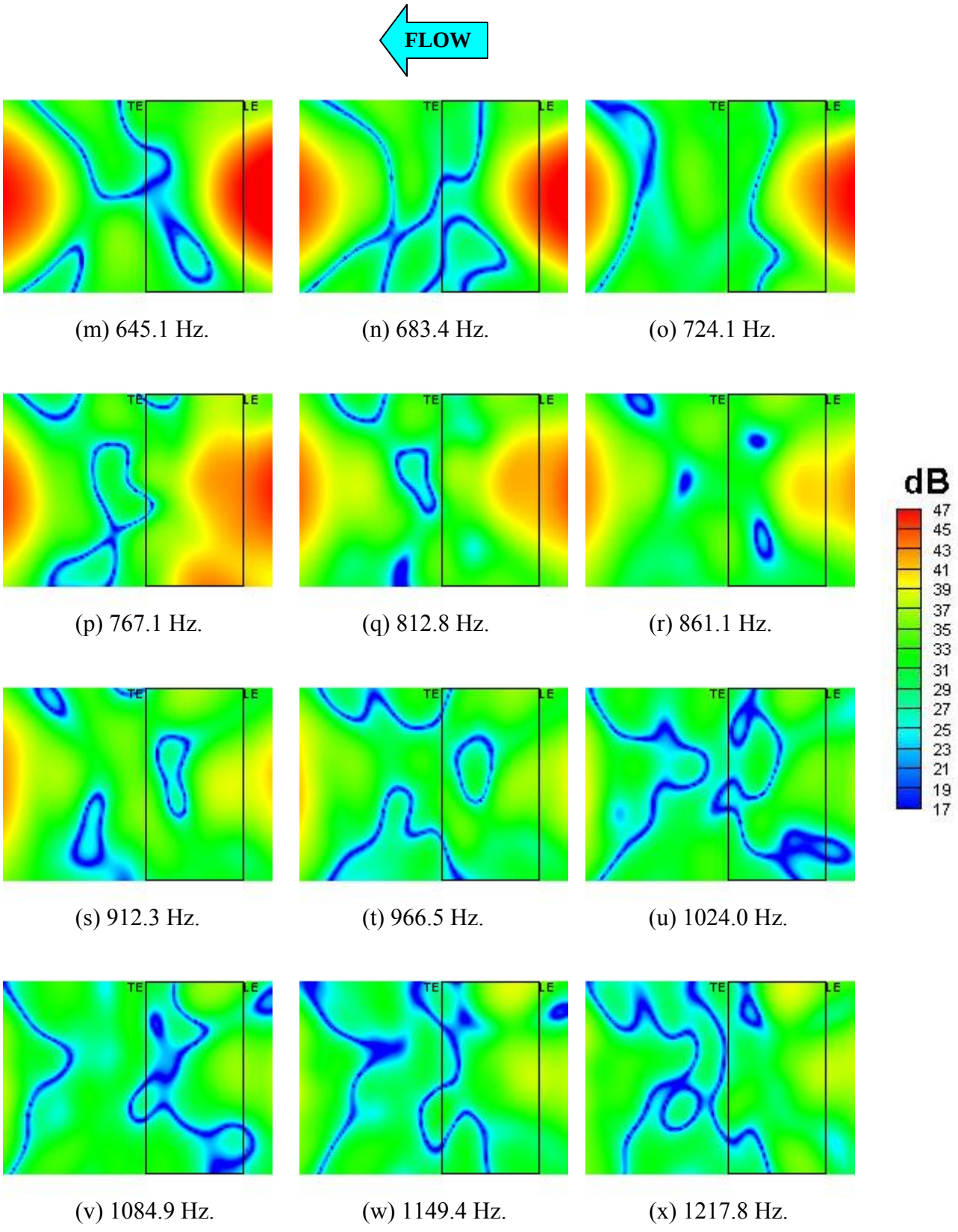

(m) 645.1 Hz. (n) 683.4 Hz. (o) 724.1 Hz.

(p) 767.1 Hz. (q) 812.8 Hz. (r) 861.1 Hz.

(s) 912.3 Hz. (t) 966.5 Hz. (u) 1024.0 Hz.

(v) 1084.9 Hz. (w) 1149.4 Hz. (x) 1217.8 Hz.

Figure 19. 1/12-Octave band beamform maps for Run021
(Airfoil at α = -11˚, U=31.18 m/s, Tripped BL, phased array on pressure side).

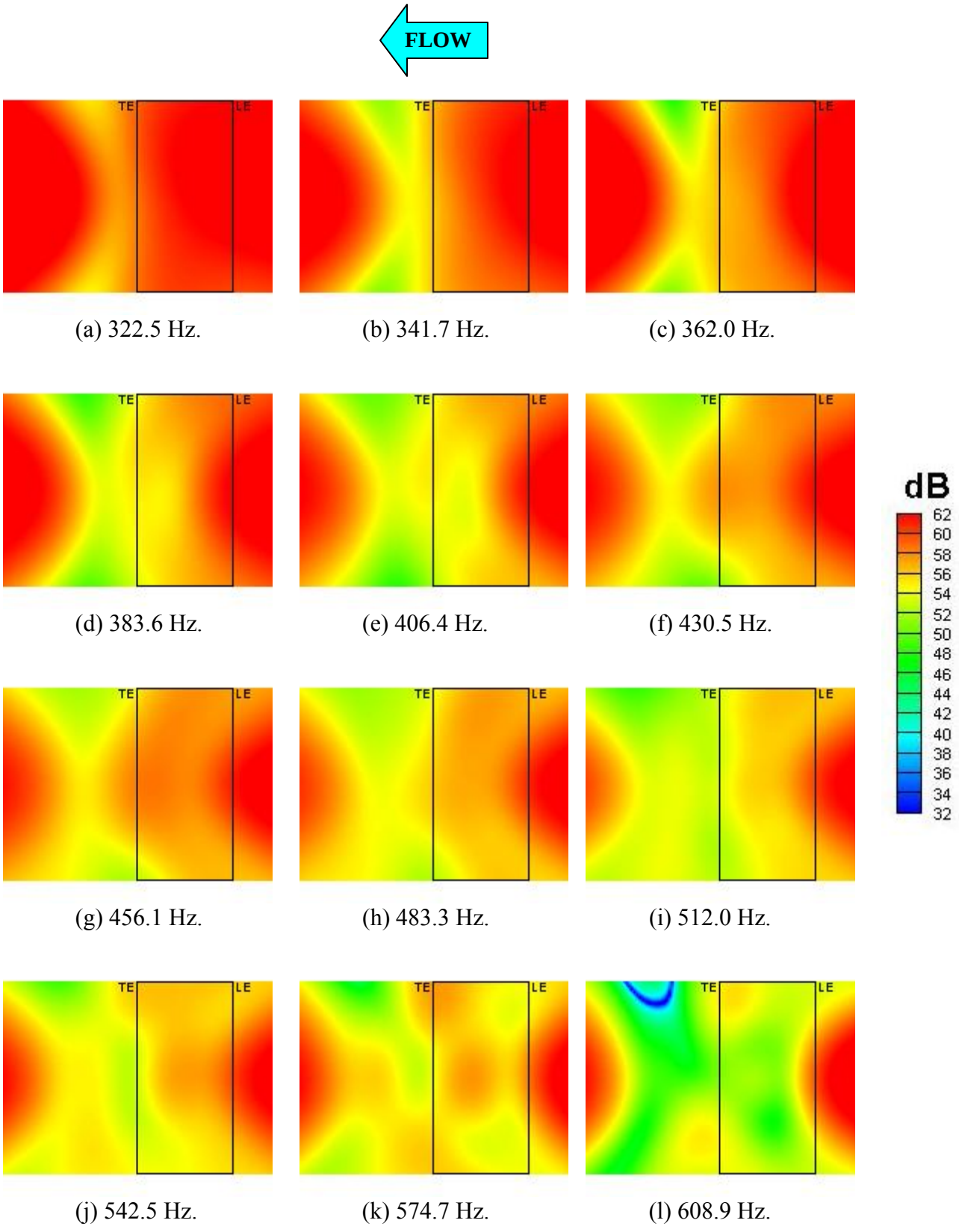

(a) 322.5 Hz. (b) 341.7 Hz. (c) 362.0 Hz.

(d) 383.6 Hz. (e) 406.4 Hz. (f) 430.5 Hz.

(g) 456.1 Hz. (h) 483.3 Hz. (i) 512.0 Hz.

(j) 542.5 Hz. (k) 574.7 Hz. (l) 608.9 Hz.

Figure 20. 1/12-Octave band beamform maps for Run023
(Airfoil at α = -11˚, U=54.69 m/s, Tripped BL, phased array on pressure side).

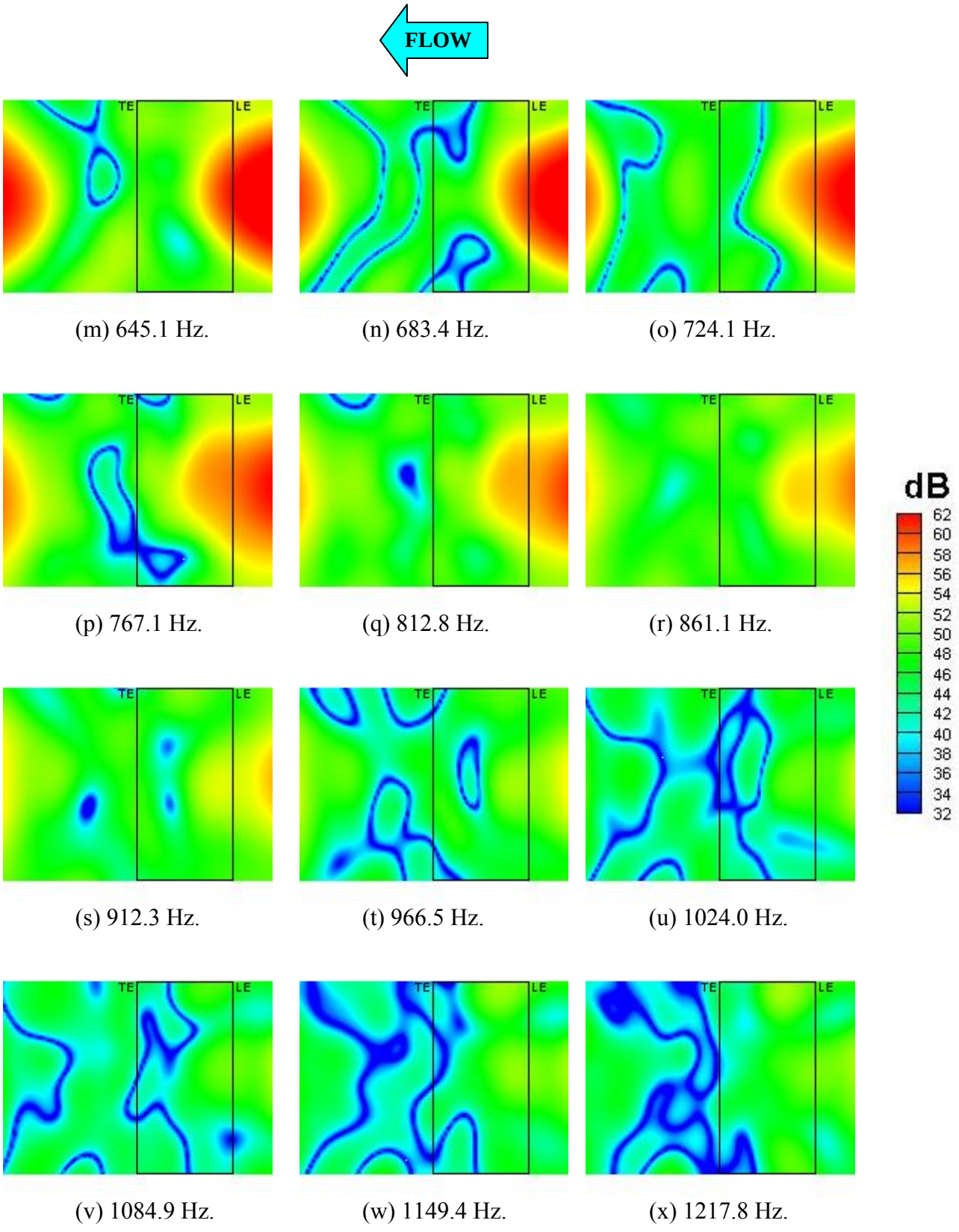

(m) 645.1 Hz. (n) 683.4 Hz. (o) 724.1 Hz.

(p) 767.1 Hz. (q) 812.8 Hz. (r) 861.1 Hz.

(s) 912.3 Hz. (t) 966.5 Hz. (u) 1024.0 Hz.

(v) 1084.9 Hz. (w) 1149.4 Hz. (x) 1217.8 Hz.

Figure 20. 1/12-Octave band beamform maps for Run023
(Airfoil at α = -11˚, U=54.69 m/s, Tripped BL, phased array on pressure side).

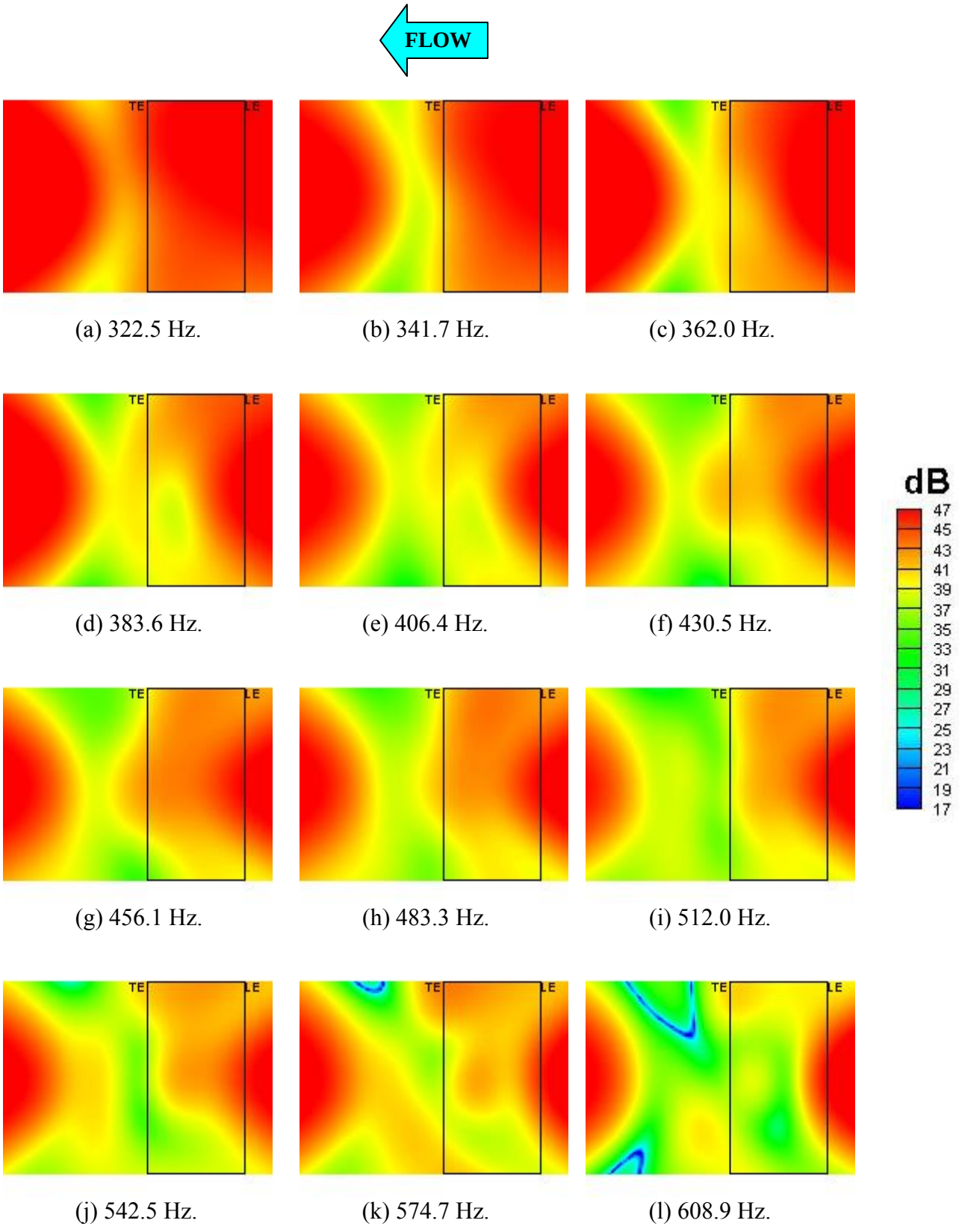

(a) 322.5 Hz. (b) 341.7 Hz. (c) 362.0 Hz.

(d) 383.6 Hz. (e) 406.4 Hz. (f) 430.5 Hz.

(g) 456.1 Hz. (h) 483.3 Hz. (i) 512.0 Hz.

(j) 542.5 Hz. (k) 574.7 Hz. (l) 608.9 Hz.

Figure 21. 1/12-Octave band beamform maps for Run024
(Airfoil at α = -15˚, U=31.15 m/s, Tripped BL, phased array on pressure side).

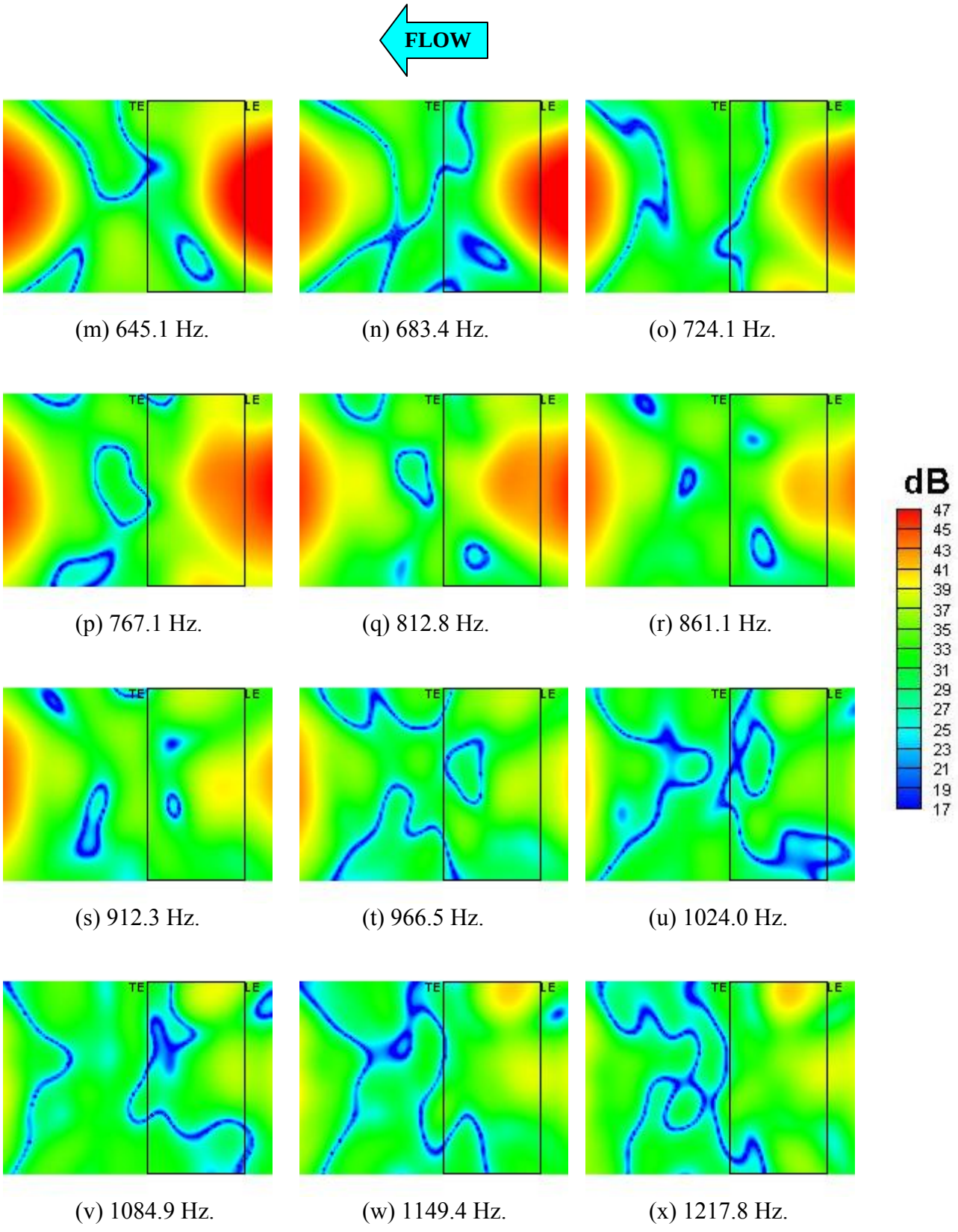

Figure 21. 1/12-Octave band beamform maps for Run024
(Airfoil at α = -15˚, U=31.15 m/s, Tripped BL, phased array on pressure side).

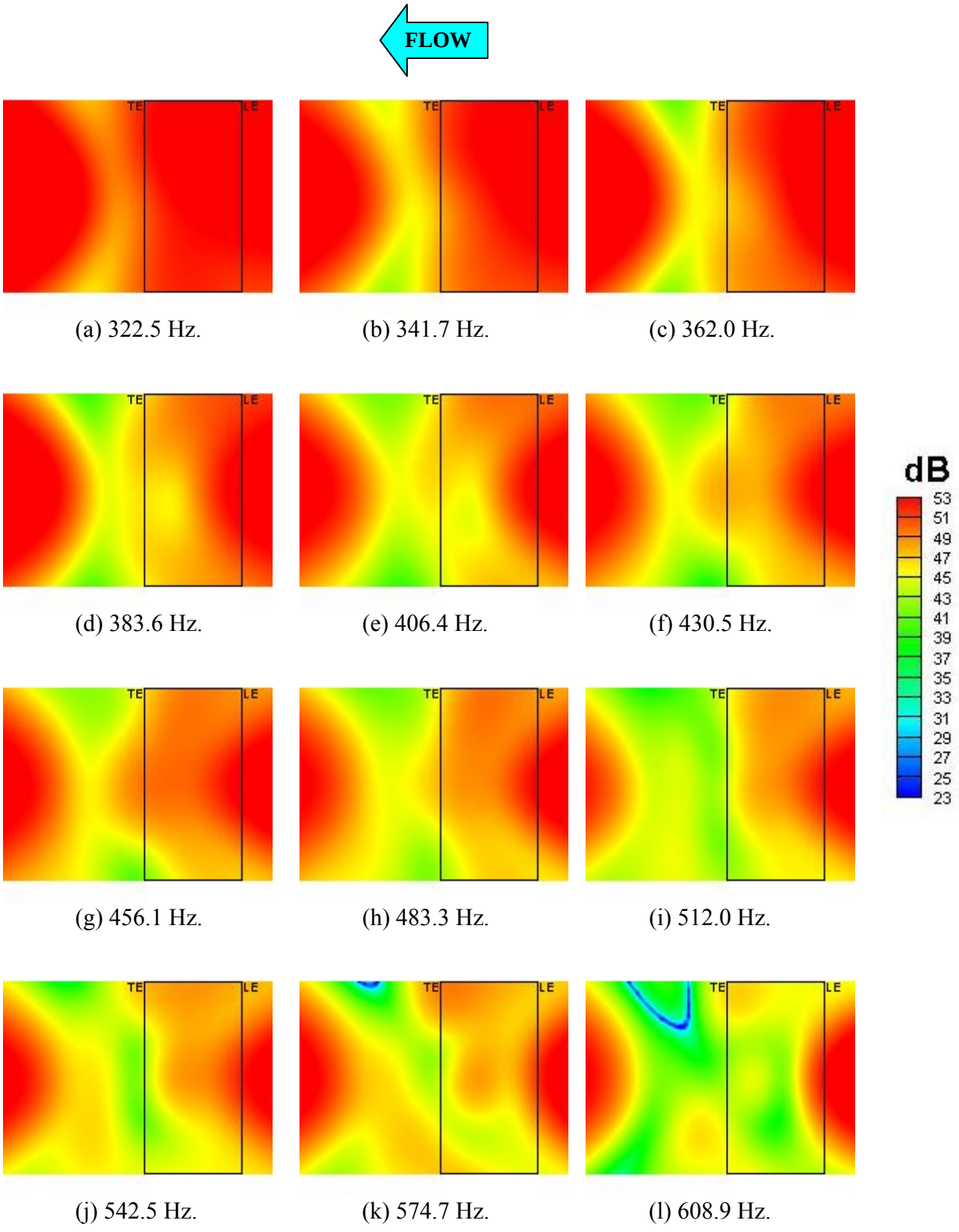

(a) 322.5 Hz. (b) 341.7 Hz. (c) 362.0 Hz.

(d) 383.6 Hz. (e) 406.4 Hz. (f) 430.5 Hz.

(g) 456.1 Hz. (h) 483.3 Hz. (i) 512.0 Hz.

(j) 542.5 Hz. (k) 574.7 Hz. (l) 608.9 Hz.

Figure 22. 1/12-Octave band beamform maps for Run025
(Airfoil at α = -15˚, U=38.95 m/s, Tripped BL, phased array on pressure side).

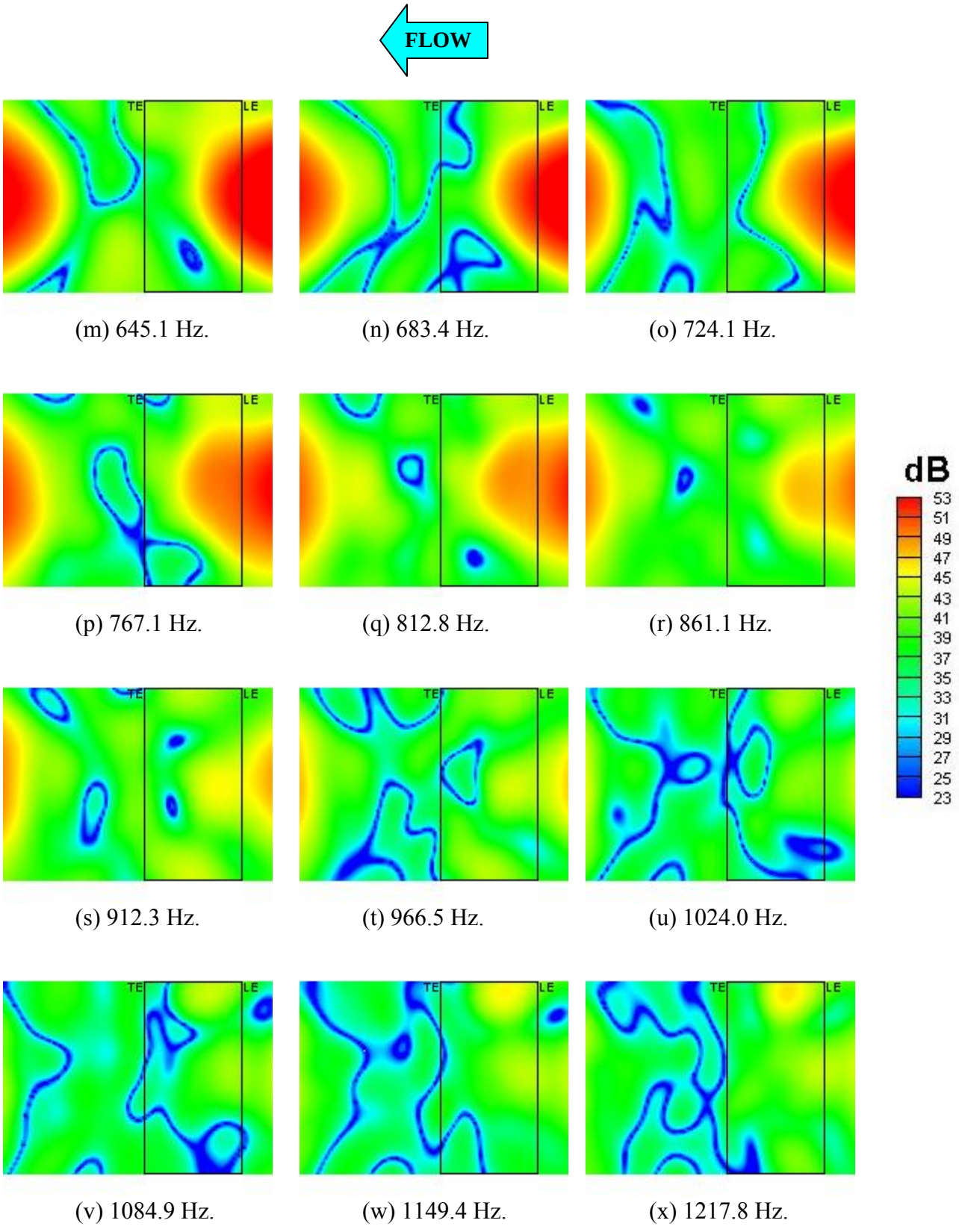

(m) 645.1 Hz. (n) 683.4 Hz. (o) 724.1 Hz.

(p) 767.1 Hz. (q) 812.8 Hz. (r) 861.1 Hz.

(s) 912.3 Hz. (t) 966.5 Hz. (u) 1024.0 Hz.

(v) 1084.9 Hz. (w) 1149.4 Hz. (x) 1217.8 Hz.

Figure 22. 1/12-Octave band beamform maps for Run025
(Airfoil at α = -15˚, U=38.95 m/s, Tripped BL, phased array on pressure side).

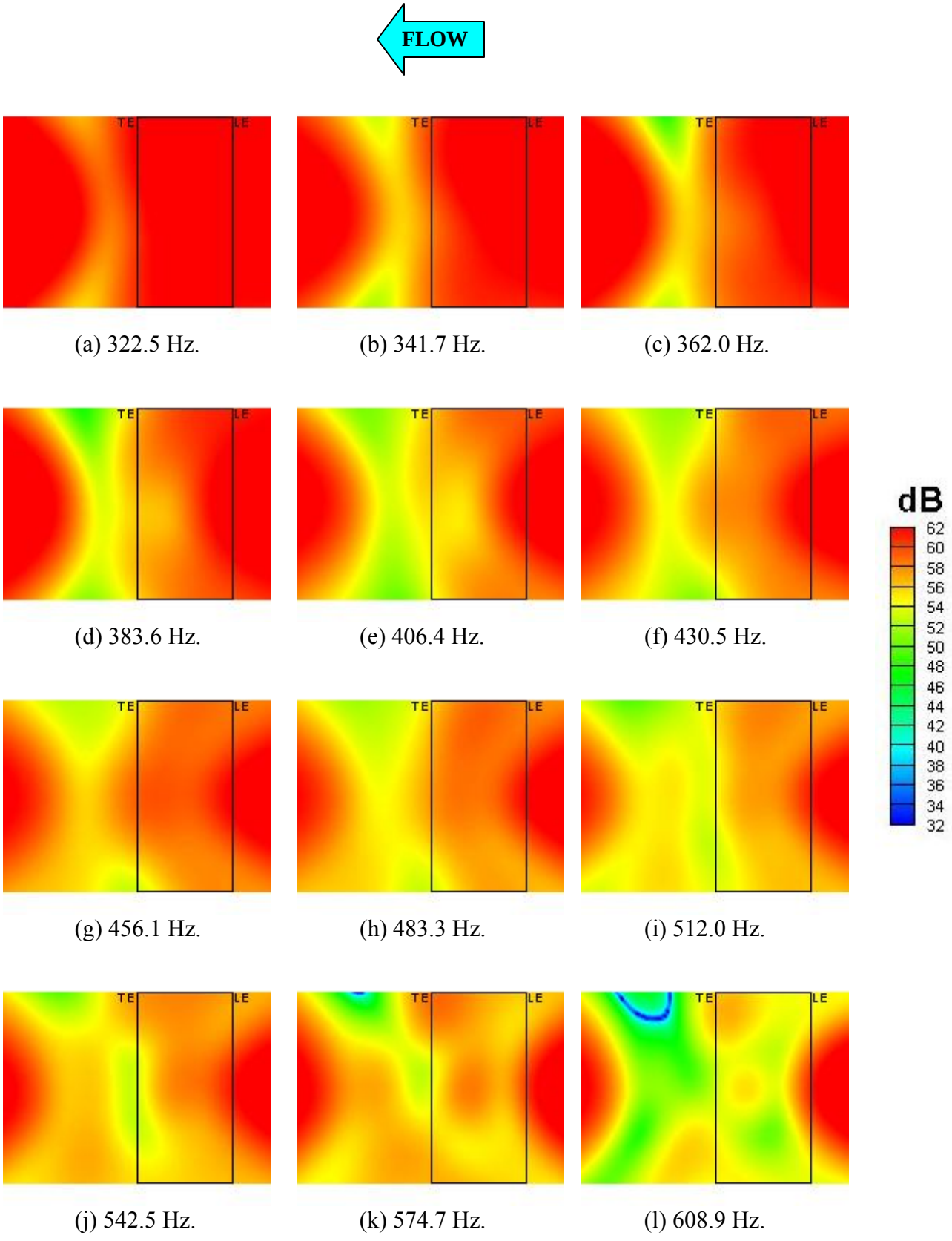

(a) 322.5 Hz. (b) 341.7 Hz. (c) 362.0 Hz.

(d) 383.6 Hz. (e) 406.4 Hz. (f) 430.5 Hz.

(g) 456.1 Hz. (h) 483.3 Hz. (i) 512.0 Hz.

(j) 542.5 Hz. (k) 574.7 Hz. (l) 608.9 Hz.

Figure 23. 1/12-Octave band beamform maps for Run026
(Airfoil at α = -15˚, U=54.69 m/s, Tripped BL, phased array on pressure side).

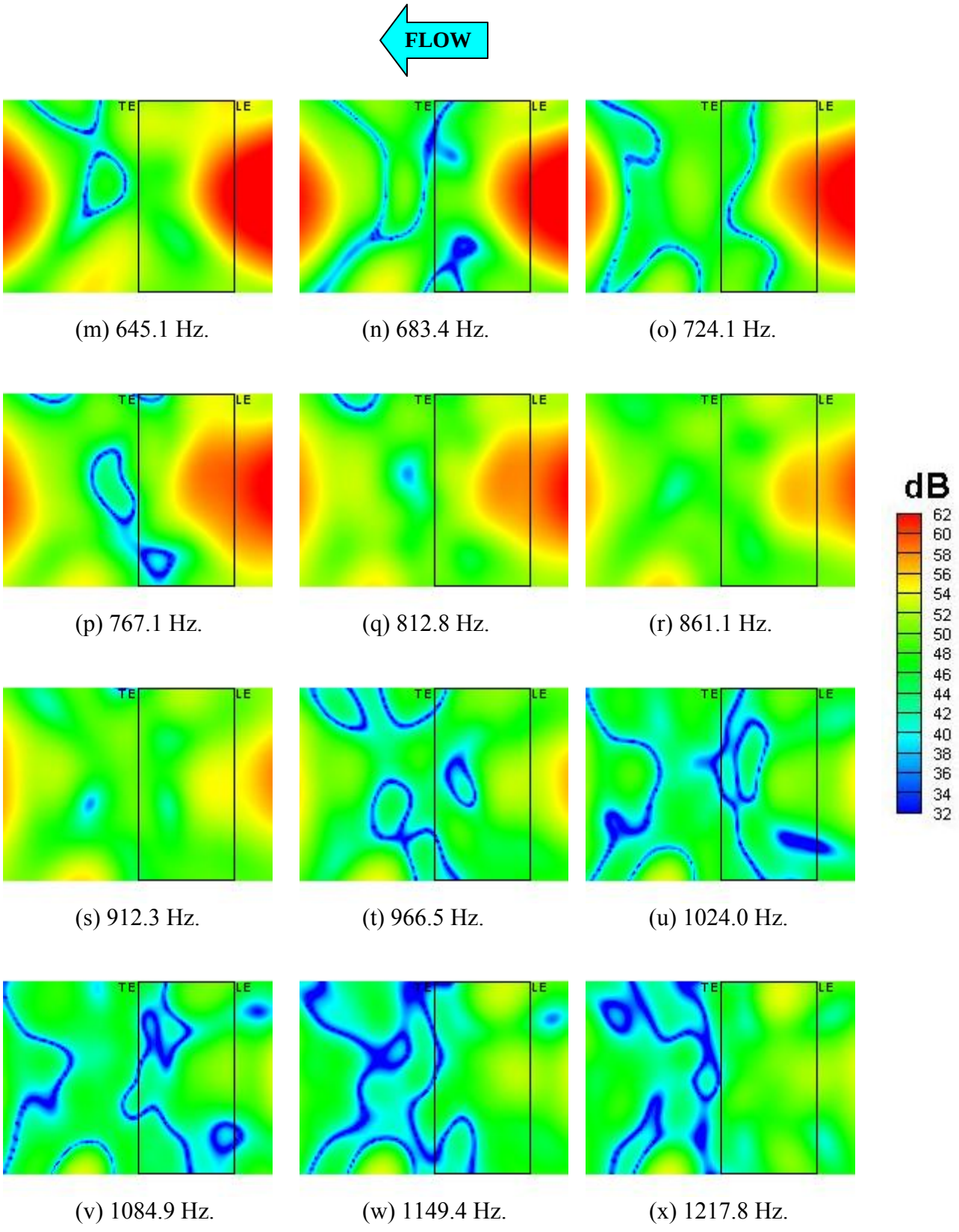

(m) 645.1 Hz. (n) 683.4 Hz. (o) 724.1 Hz.

(p) 767.1 Hz. (q) 812.8 Hz. (r) 861.1 Hz.

(s) 912.3 Hz. (t) 966.5 Hz. (u) 1024.0 Hz.

(v) 1084.9 Hz. (w) 1149.4 Hz. (x) 1217.8 Hz.

Figure 23. 1/12-Octave band beamform maps for Run026
(Airfoil at α = -15˚, U=54.69 m/s, Tripped BL, phased array on pressure side).

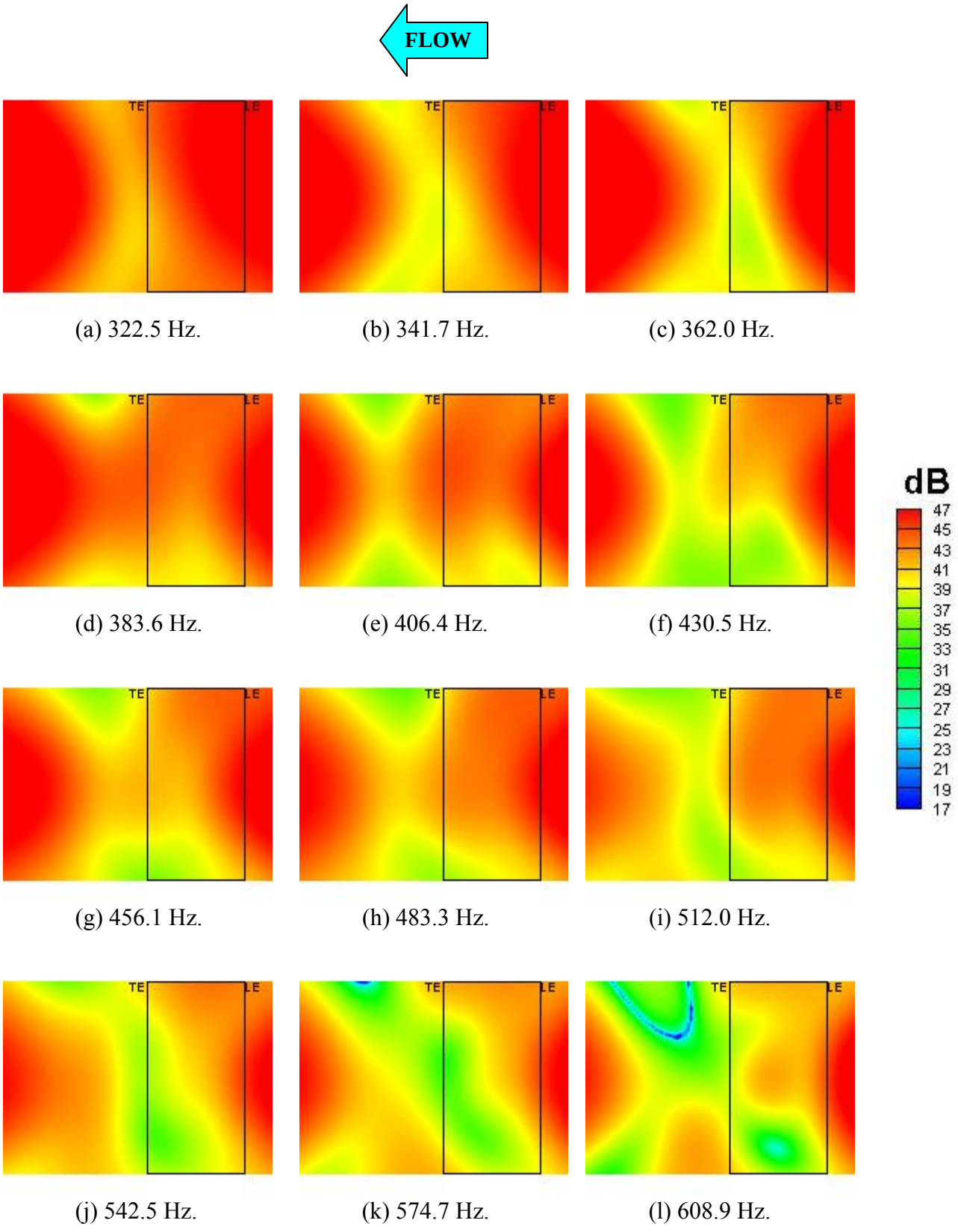

(a) 322.5 Hz. (b) 341.7 Hz. (c) 362.0 Hz.

(d) 383.6 Hz. (e) 406.4 Hz. (f) 430.5 Hz.

(g) 456.1 Hz. (h) 483.3 Hz. (i) 512.0 Hz.

(j) 542.5 Hz. (k) 574.7 Hz. (l) 608.9 Hz.

Figure 24. 1/12-Octave band beamform maps for Run027
(Airfoil at α = 15˚, U=30.85 m/s, Tripped BL, phased array on suction side).

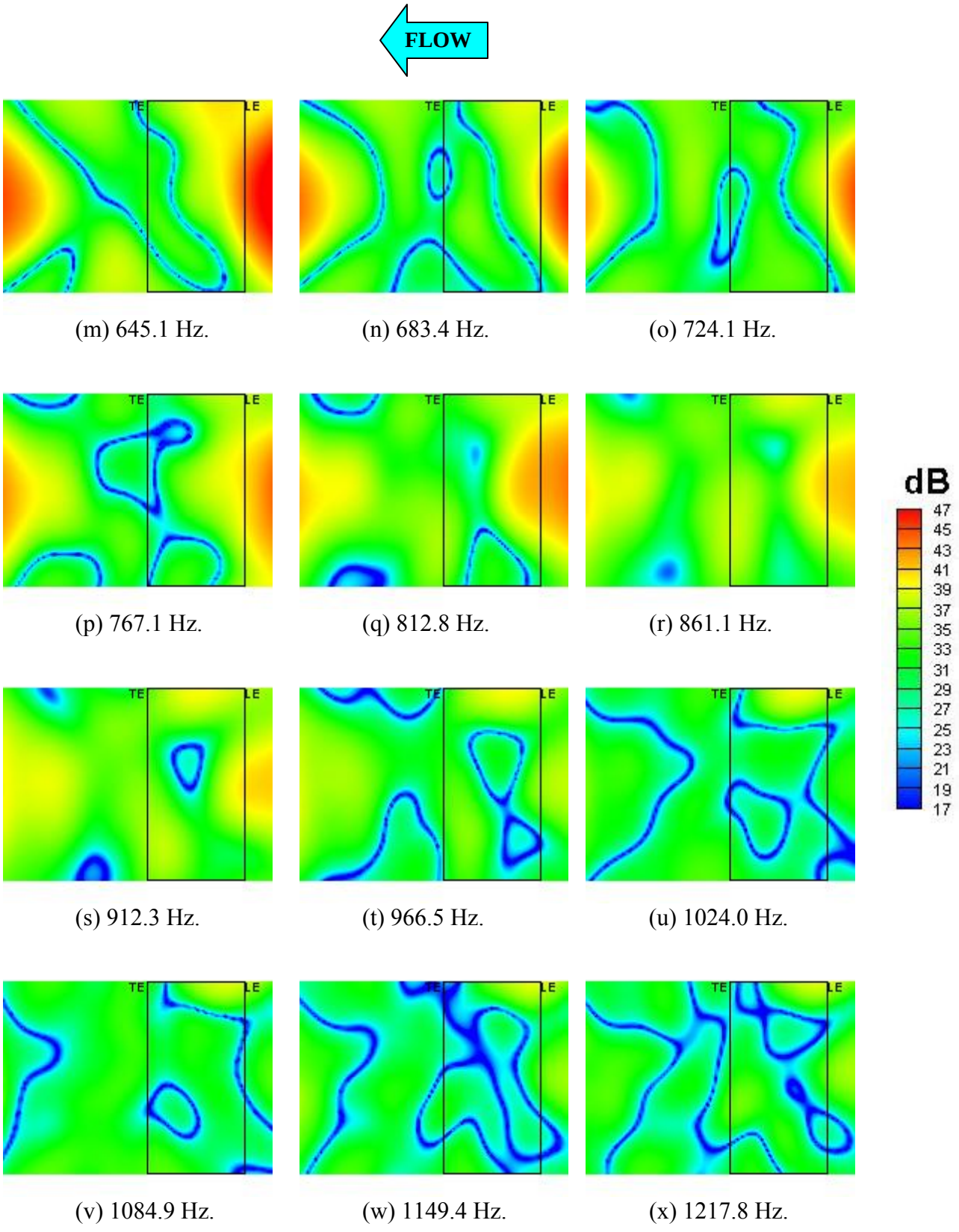

(m) 645.1 Hz. (n) 683.4 Hz. (o) 724.1 Hz.

(p) 767.1 Hz. (q) 812.8 Hz. (r) 861.1 Hz.

(s) 912.3 Hz. (t) 966.5 Hz. (u) 1024.0 Hz.

(v) 1084.9 Hz. (w) 1149.4 Hz. (x) 1217.8 Hz.

Figure 24. 1/12-Octave band beamform maps for Run027
(Airfoil at α = 15˚, U=30.85 m/s, Tripped BL, phased array on suction side).

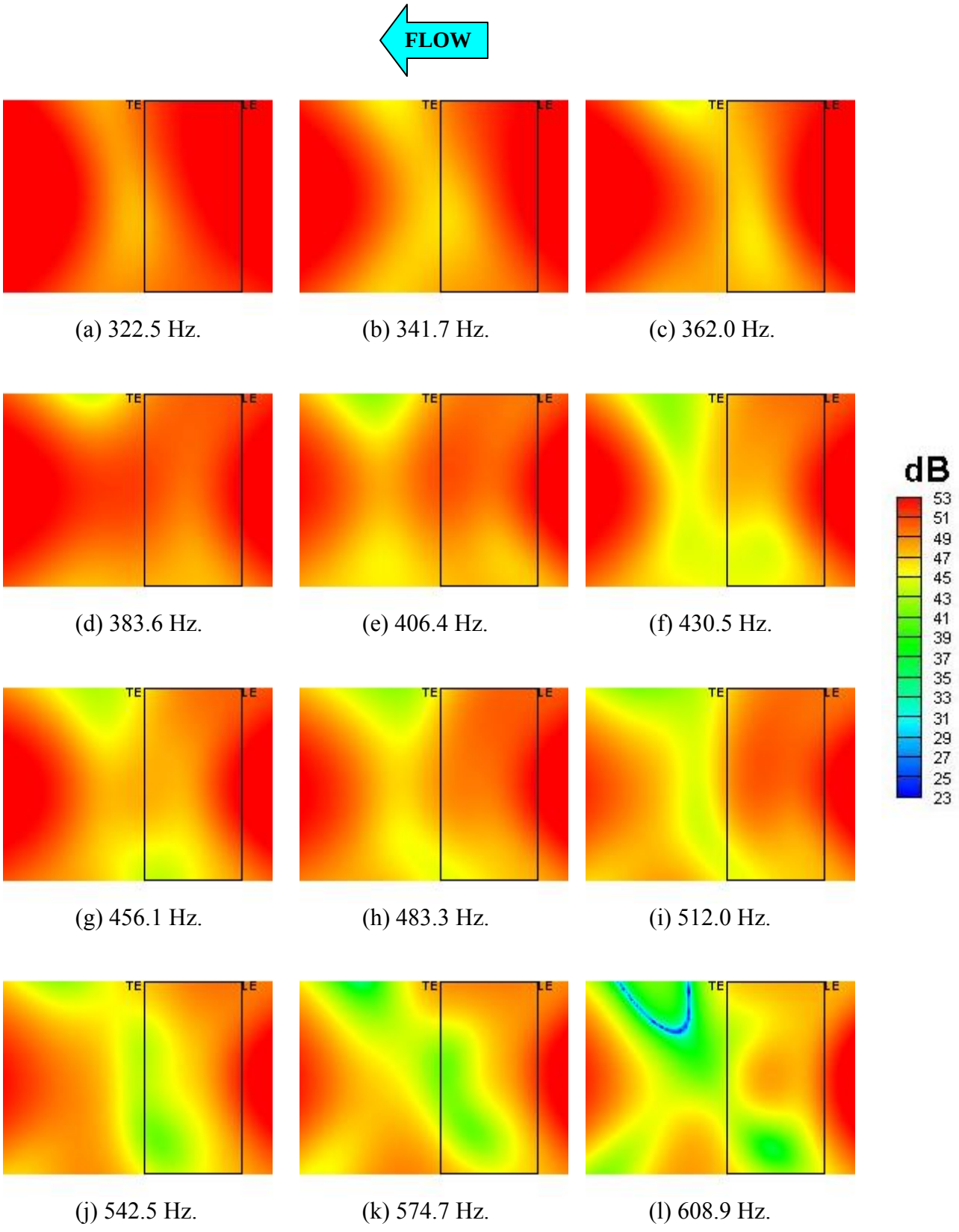

(a) 322.5 Hz. (b) 341.7 Hz. (c) 362.0 Hz.

(d) 383.6 Hz. (e) 406.4 Hz. (f) 430.5 Hz.

(g) 456.1 Hz. (h) 483.3 Hz. (i) 512.0 Hz.

(j) 542.5 Hz. (k) 574.7 Hz. (l) 608.9 Hz.

Figure 25. 1/12-Octave band beamform maps for Run028
(Airfoil at α = 15˚, U=38.69 m/s, Tripped BL, phased array on suction side).

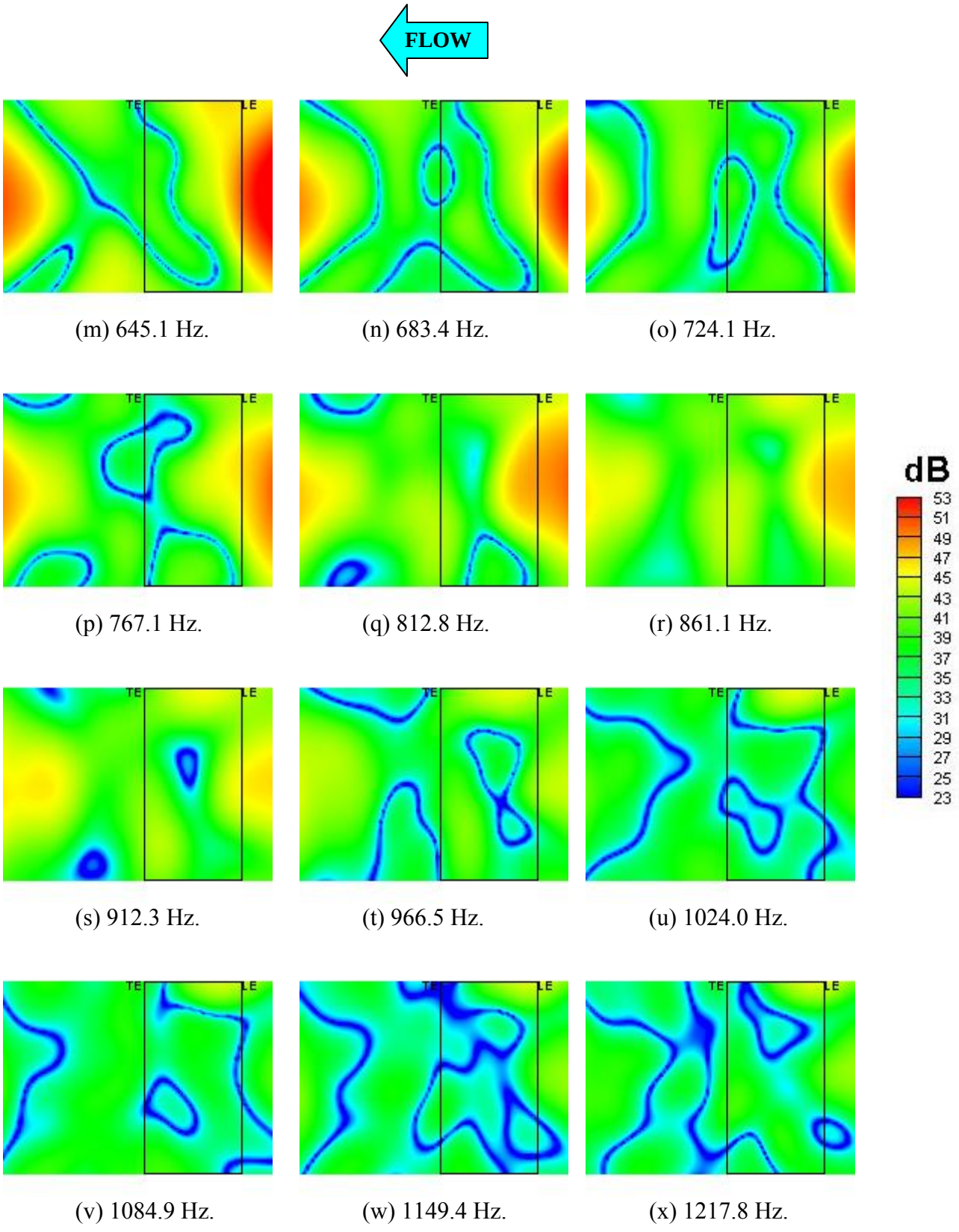

(m) 645.1 Hz. (n) 683.4 Hz. (o) 724.1 Hz.

(p) 767.1 Hz. (q) 812.8 Hz. (r) 861.1 Hz.

(s) 912.3 Hz. (t) 966.5 Hz. (u) 1024.0 Hz.

(v) 1084.9 Hz. (w) 1149.4 Hz. (x) 1217.8 Hz.

Figure 25. 1/12-Octave band beamform maps for Run028
(Airfoil at α = 15˚, U=38.69 m/s, Tripped BL, phased array on suction side).

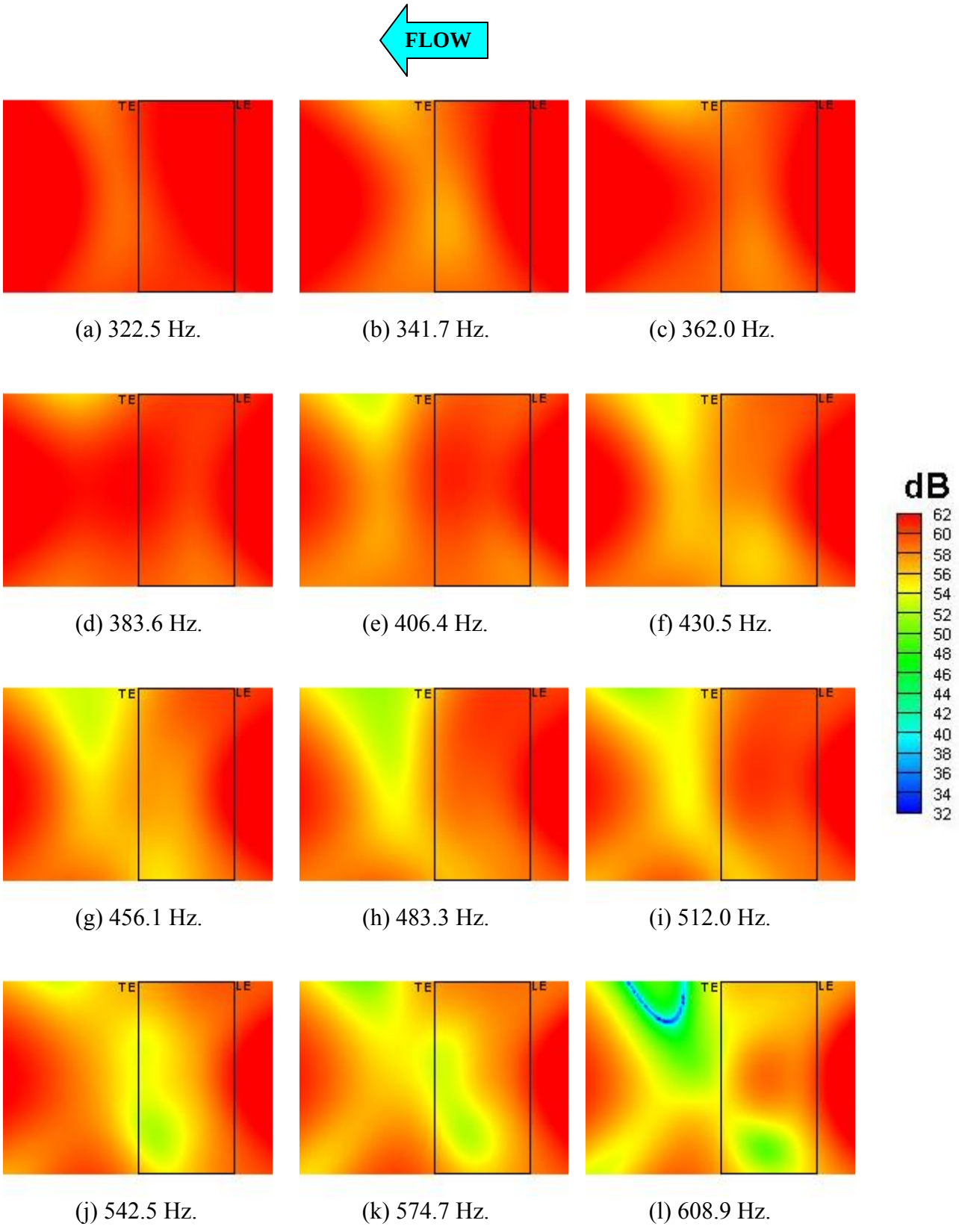

(a) 322.5 Hz. (b) 341.7 Hz. (c) 362.0 Hz.

(d) 383.6 Hz. (e) 406.4 Hz. (f) 430.5 Hz.

(g) 456.1 Hz. (h) 483.3 Hz. (i) 512.0 Hz.

(j) 542.5 Hz. (k) 574.7 Hz. (l) 608.9 Hz.

Figure 26. 1/12-Octave band beamform maps for Run029
(Airfoil at α = 15˚, U=54.23 m/s, Tripped BL, phased array on suction side).

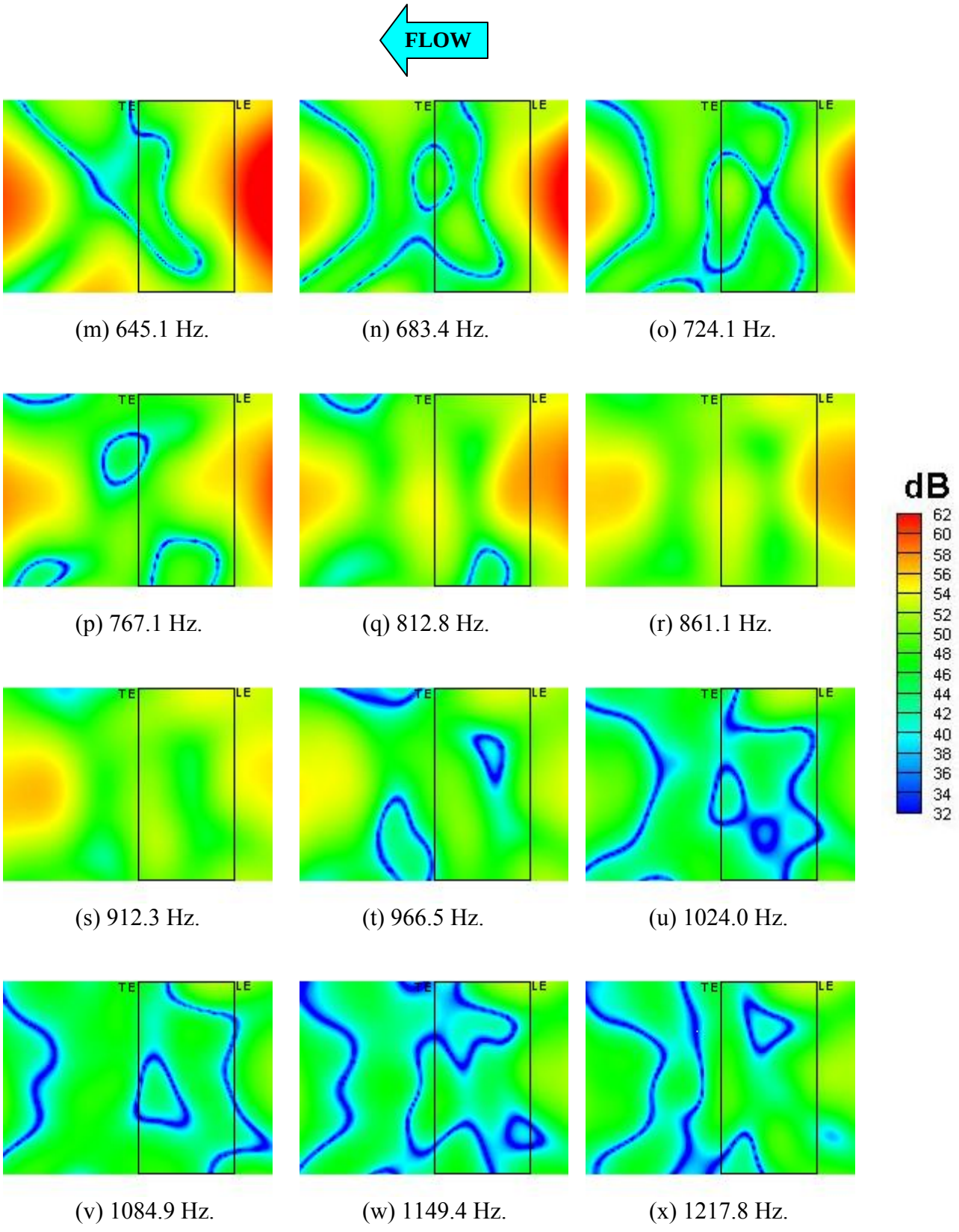

(m) 645.1 Hz. (n) 683.4 Hz. (o) 724.1 Hz.

(p) 767.1 Hz. (q) 812.8 Hz. (r) 861.1 Hz.

(s) 912.3 Hz. (t) 966.5 Hz. (u) 1024.0 Hz.

(v) 1084.9 Hz. (w) 1149.4 Hz. (x) 1217.8 Hz.

Figure 26. 1/12-Octave band beamform maps for Run029
(Airfoil at α = 15˚, U=54.23 m/s, Tripped BL, phased array on suction side).

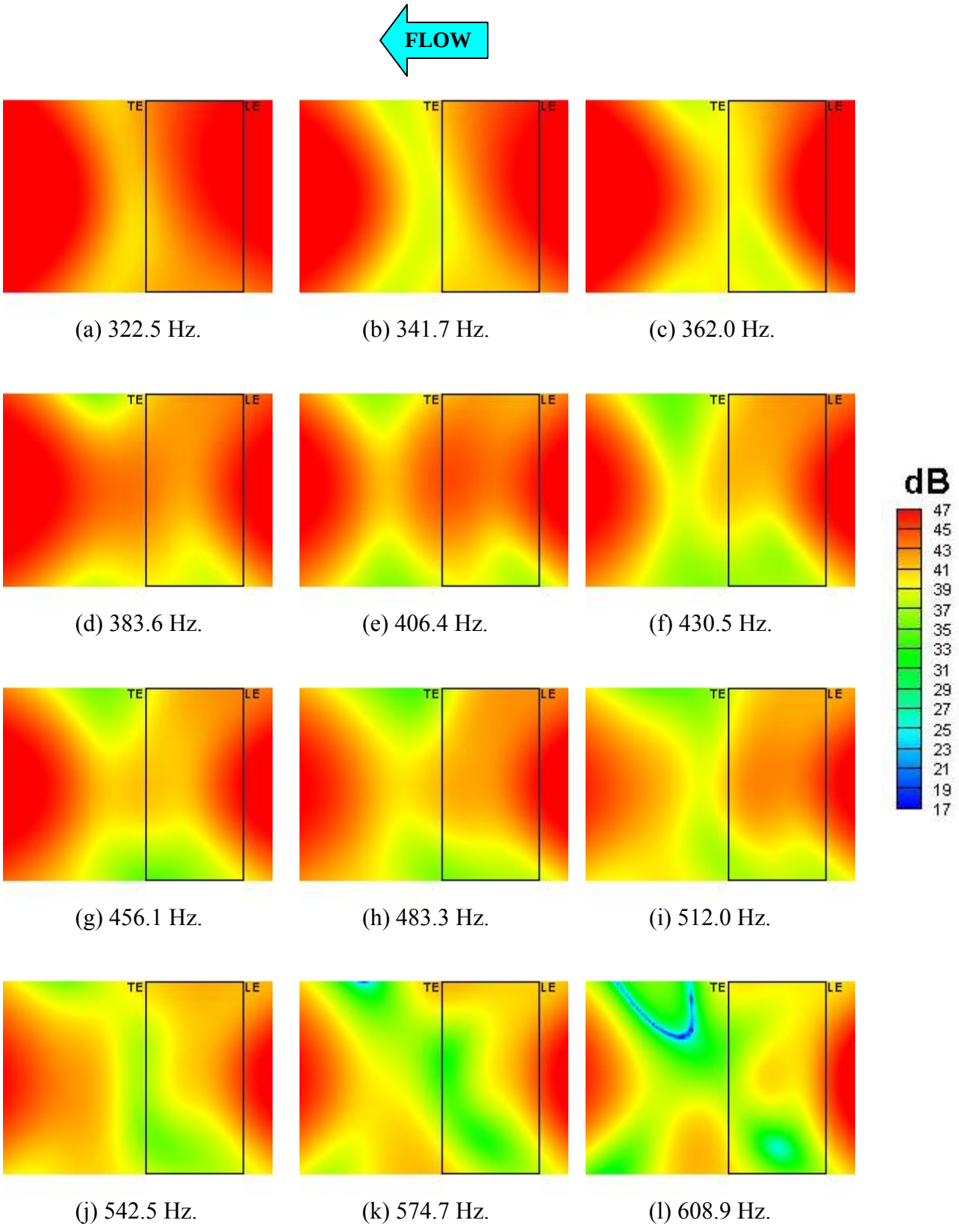

(a) 322.5 Hz. (b) 341.7 Hz. (c) 362.0 Hz.

(d) 383.6 Hz. (e) 406.4 Hz. (f) 430.5 Hz.

(g) 456.1 Hz. (h) 483.3 Hz. (i) 512.0 Hz.

(j) 542.5 Hz. (k) 574.7 Hz. (l) 608.9 Hz.

Figure 27. 1/12-Octave band beamform maps for Run030
(Airfoil at α = 11˚, U=30.98 m/s, Tripped BL, phased array on suction side).

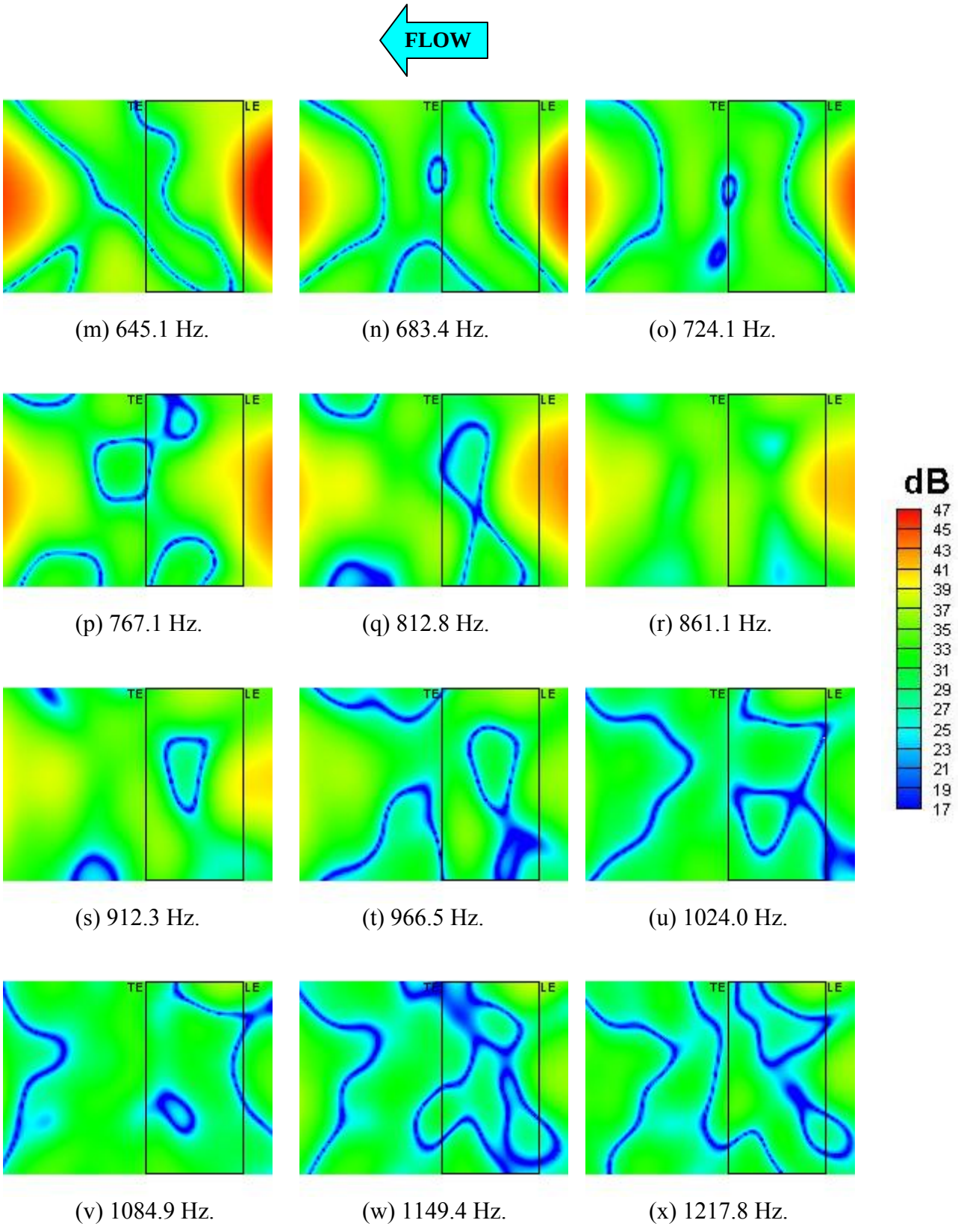

(m) 645.1 Hz. (n) 683.4 Hz. (o) 724.1 Hz.

(p) 767.1 Hz. (q) 812.8 Hz. (r) 861.1 Hz.

(s) 912.3 Hz. (t) 966.5 Hz. (u) 1024.0 Hz.

(v) 1084.9 Hz. (w) 1149.4 Hz. (x) 1217.8 Hz.

Figure 27. 1/12-Octave band beamform maps for Run030
(Airfoil at α = 11˚, U=30.98 m/s, Tripped BL, phased array on suction side).

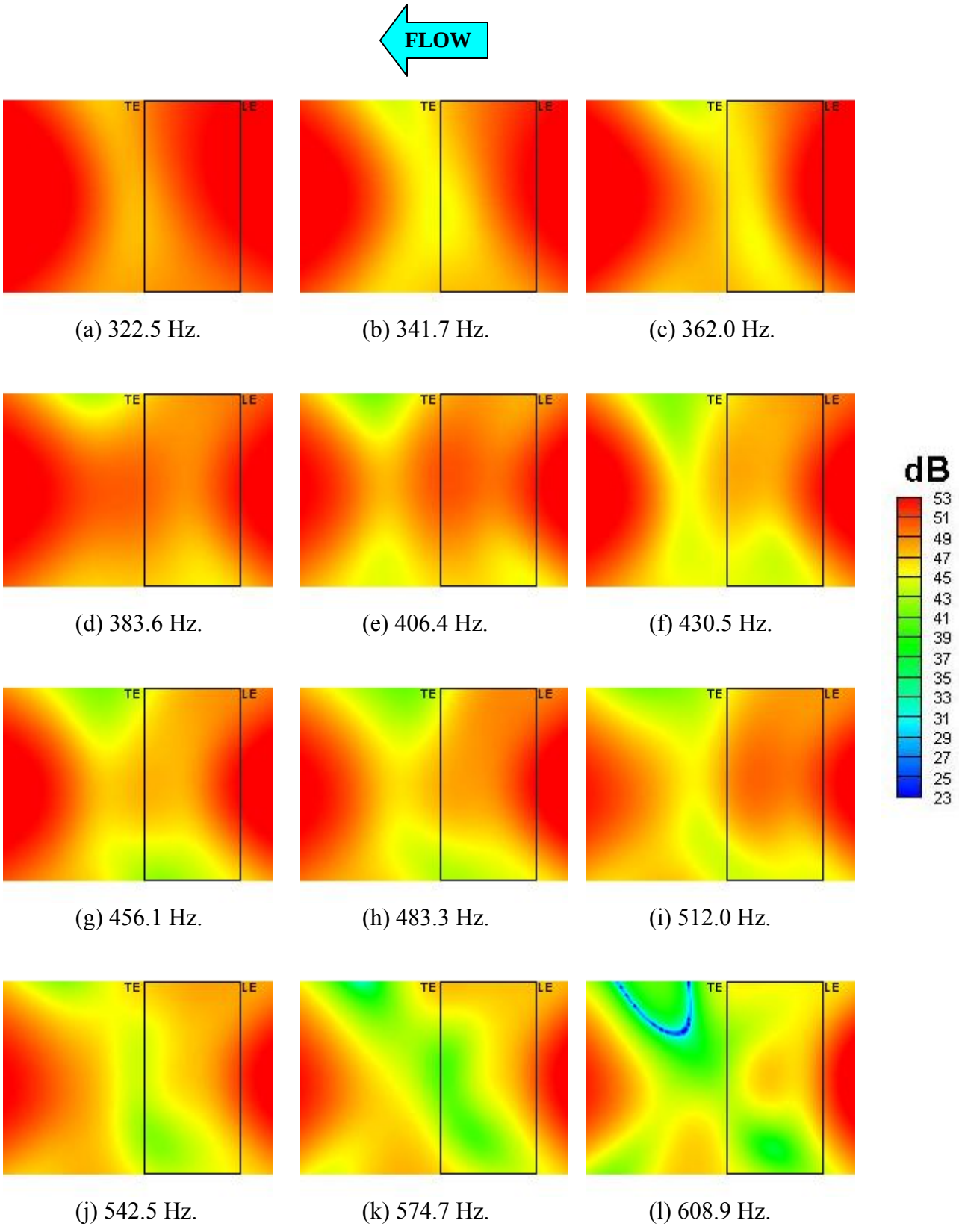

Figure 28. 1/12-Octave band beamform maps for Run031
(Airfoil at α = 11˚, U=38.87 m/s, Tripped BL, phased array on suction side).

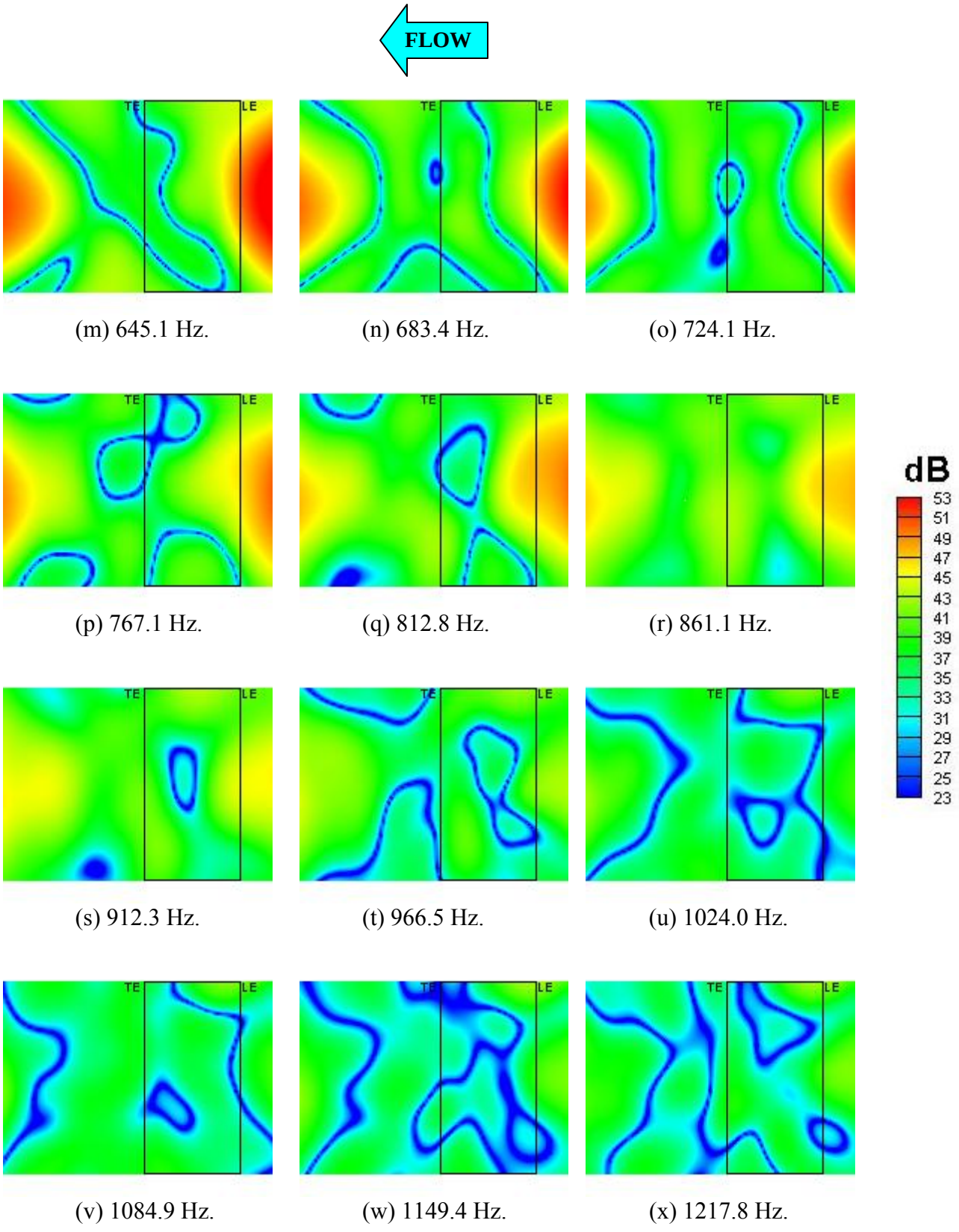

(m) 645.1 Hz. (n) 683.4 Hz. (o) 724.1 Hz.

(p) 767.1 Hz. (q) 812.8 Hz. (r) 861.1 Hz.

(s) 912.3 Hz. (t) 966.5 Hz. (u) 1024.0 Hz.

(v) 1084.9 Hz. (w) 1149.4 Hz. (x) 1217.8 Hz.

Figure 28. 1/12-Octave band beamform maps for Run031
(Airfoil at α = 11˚, U=38.87 m/s, Tripped BL, phased array on suction side).

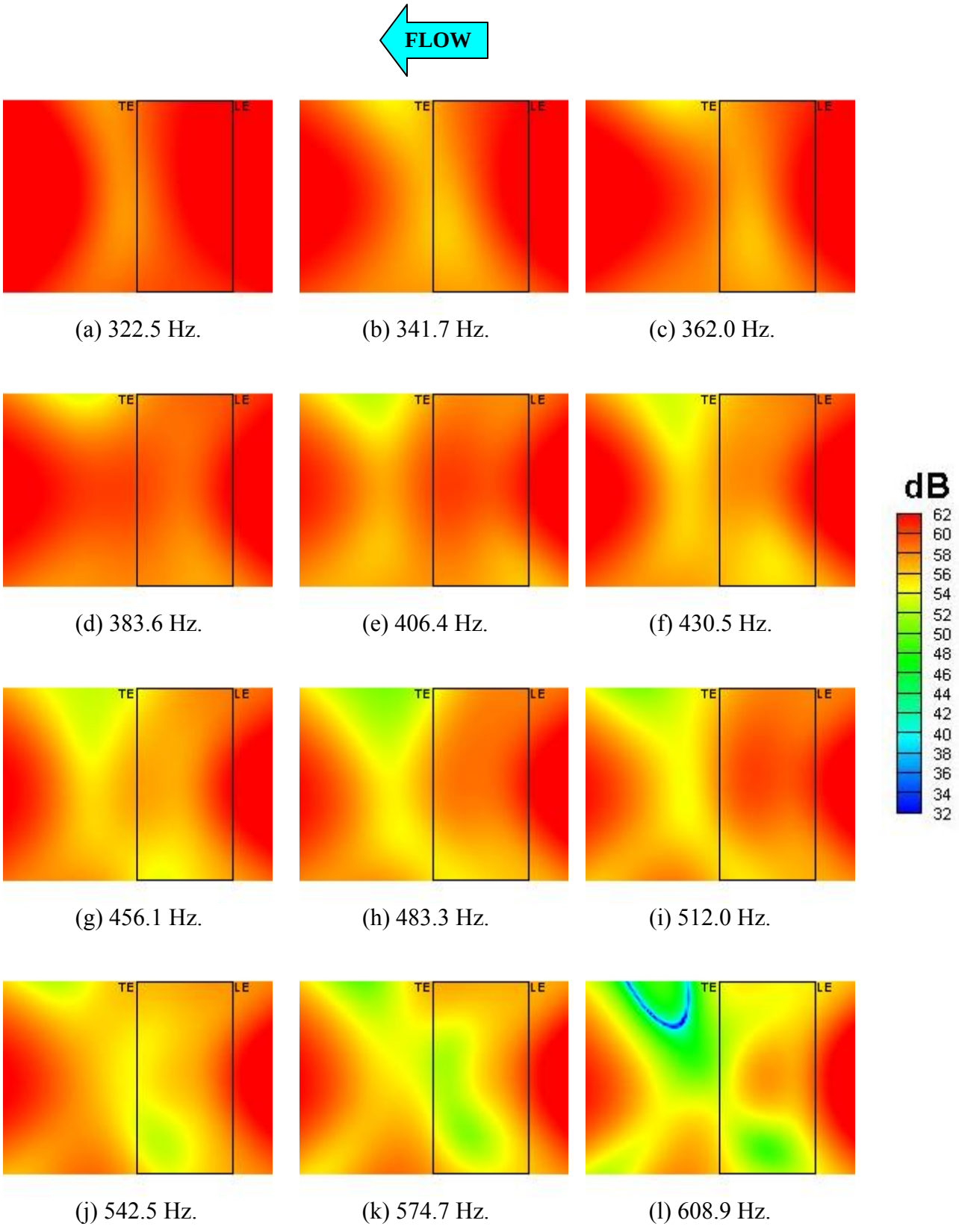

(a) 322.5 Hz. (b) 341.7 Hz. (c) 362.0 Hz.

(d) 383.6 Hz. (e) 406.4 Hz. (f) 430.5 Hz.

(g) 456.1 Hz. (h) 483.3 Hz. (i) 512.0 Hz.

(j) 542.5 Hz. (k) 574.7 Hz. (l) 608.9 Hz.

Figure 29. 1/12-Octave band beamform maps for Run032
(Airfoil at α = 11˚, U=54.63 m/s, Tripped BL, phased array on suction side).

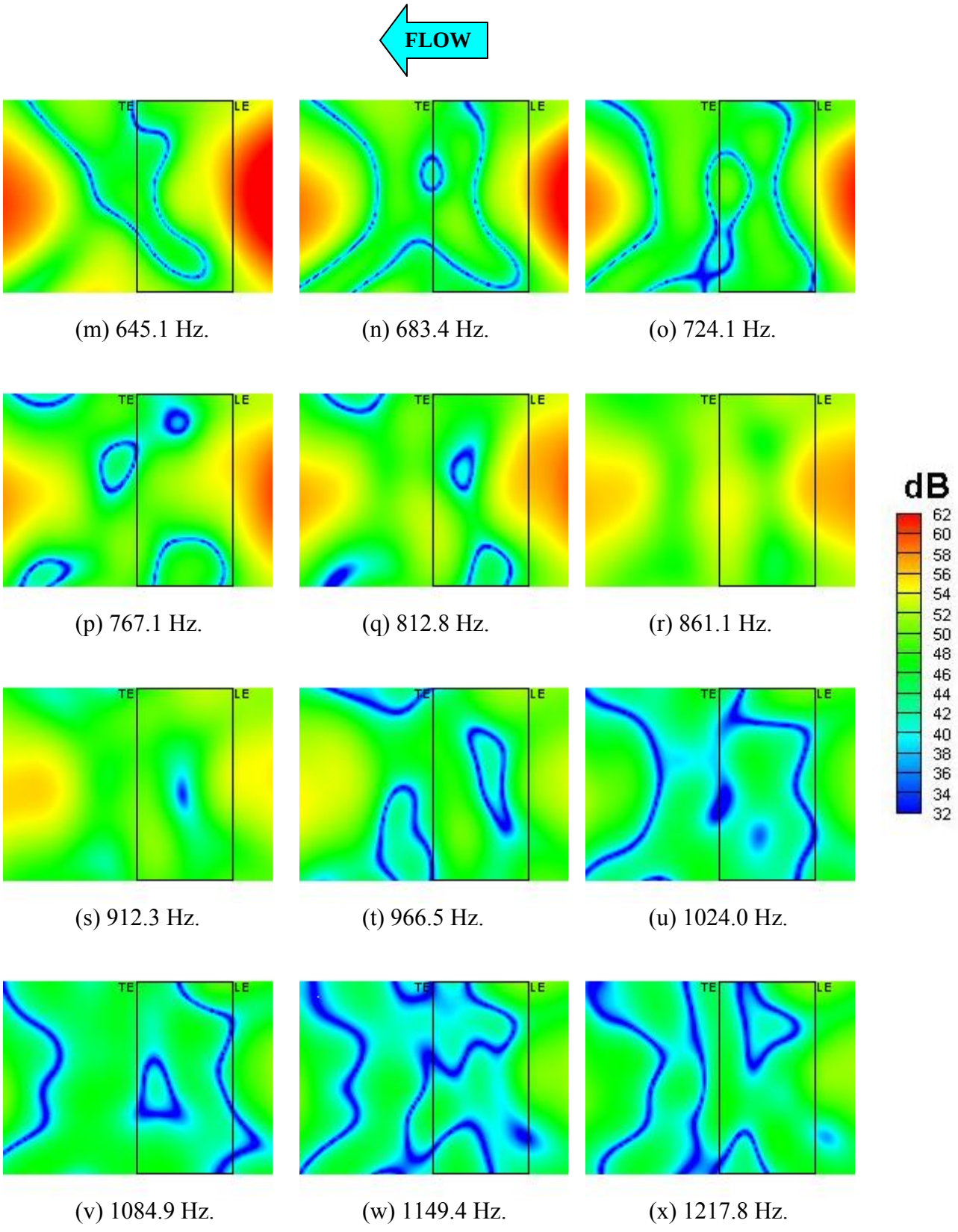

(m) 645.1 Hz. (n) 683.4 Hz. (o) 724.1 Hz.

(p) 767.1 Hz. (q) 812.8 Hz. (r) 861.1 Hz.

(s) 912.3 Hz. (t) 966.5 Hz. (u) 1024.0 Hz.

(v) 1084.9 Hz. (w) 1149.4 Hz. (x) 1217.8 Hz.

Figure 29. 1/12-Octave band beamform maps for Run032
(Airfoil at α = 11˚, U=54.63 m/s, Tripped BL, phased array on suction side).

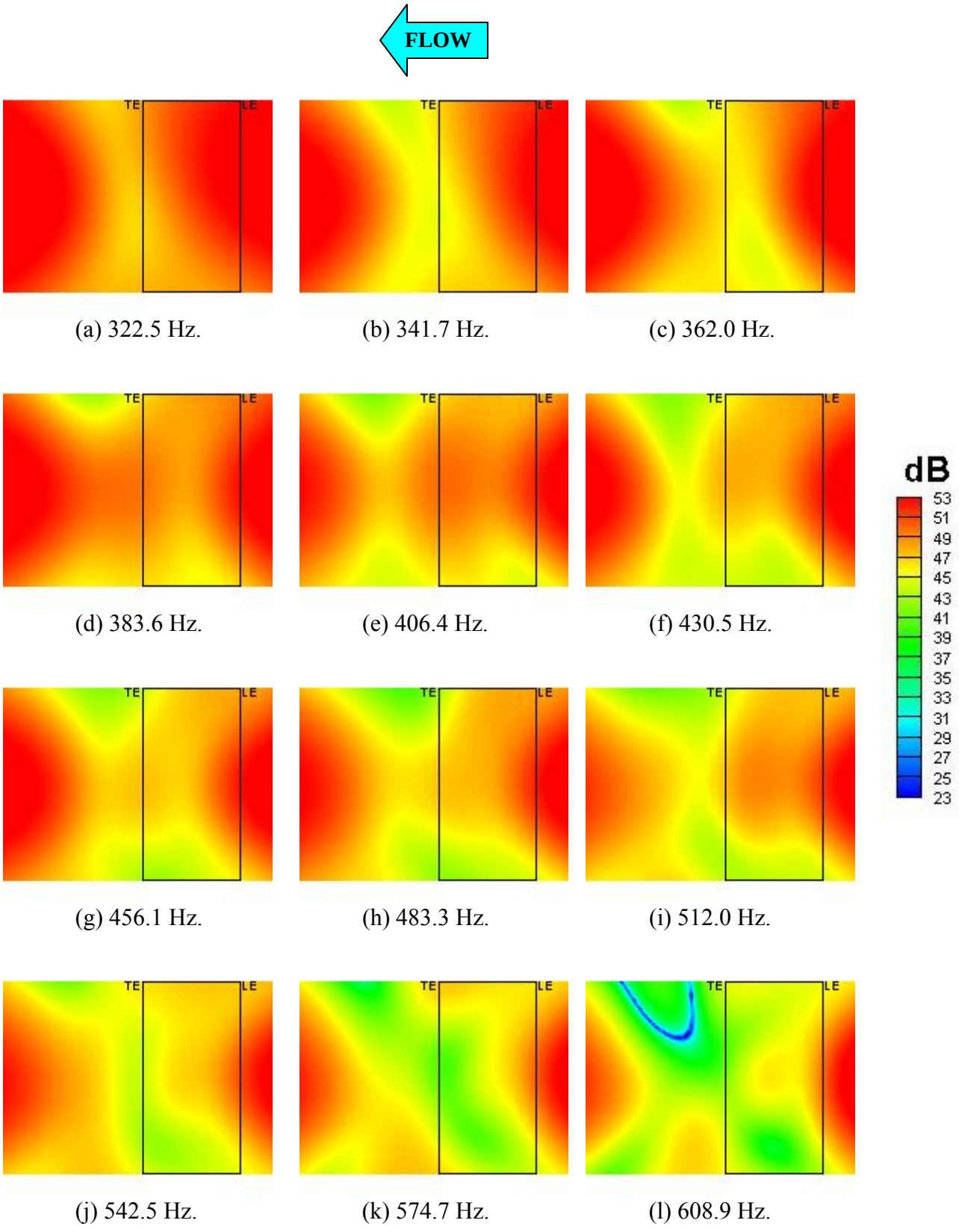

(a) 322.5 Hz. (b) 341.7 Hz. (c) 362.0 Hz.

(d) 383.6 Hz. (e) 406.4 Hz. (f) 430.5 Hz.

(g) 456.1 Hz. (h) 483.3 Hz. (i) 512.0 Hz.

(j) 542.5 Hz. (k) 574.7 Hz. (l) 608.9 Hz.

Figure 30. 1/12-Octave band beamform maps for Run034
(Airfoil at α = 9˚, U=38.87 m/s, Tripped BL, phased array on suction side).

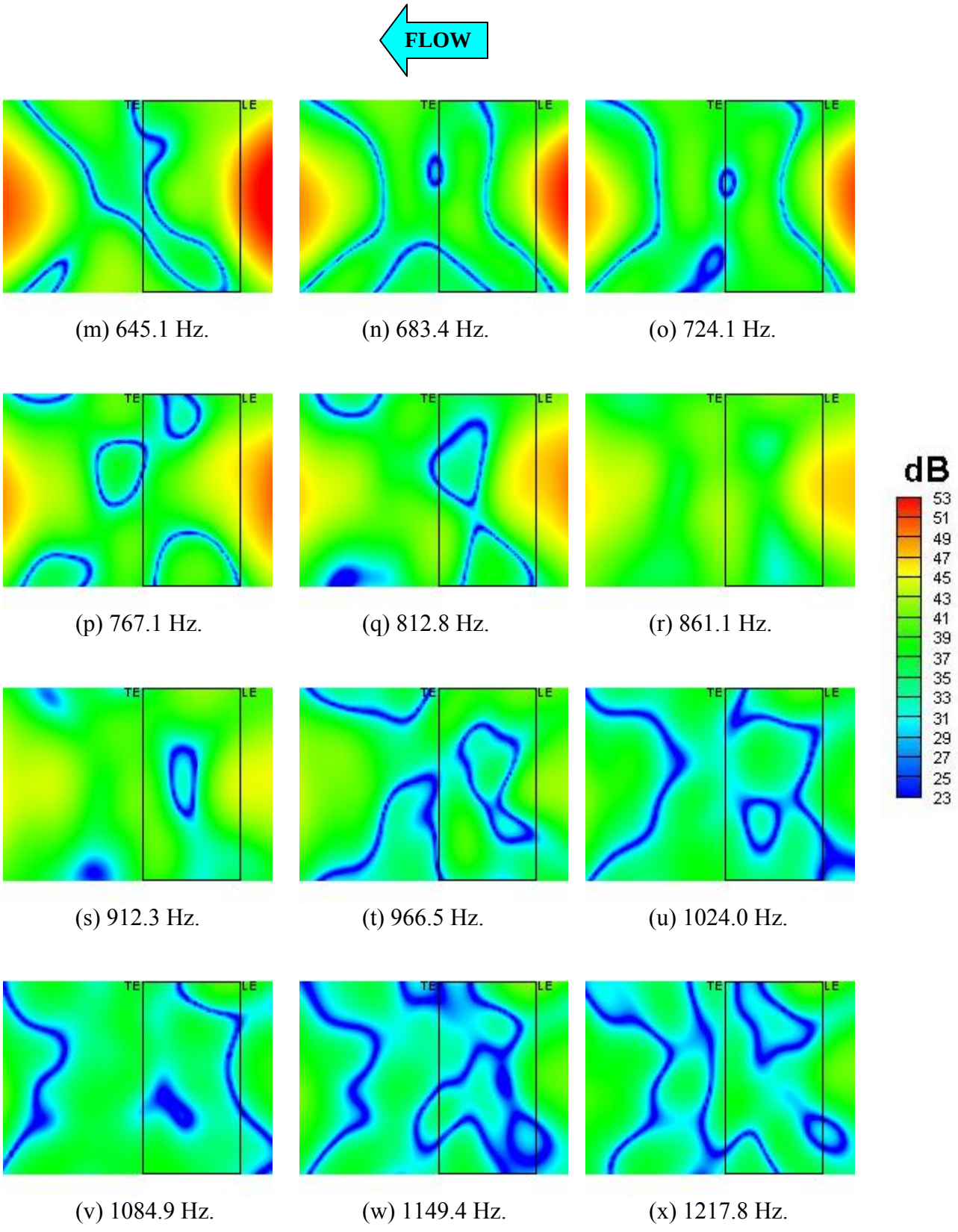

(m) 645.1 Hz. (n) 683.4 Hz. (o) 724.1 Hz.

(p) 767.1 Hz. (q) 812.8 Hz. (r) 861.1 Hz.

(s) 912.3 Hz. (t) 966.5 Hz. (u) 1024.0 Hz.

(v) 1084.9 Hz. (w) 1149.4 Hz. (x) 1217.8 Hz.

Figure 30. 1/12-Octave band beamform maps for Run034
(Airfoil at α = 9˚, U=38.87 m/s, Tripped BL, phased array on suction side).

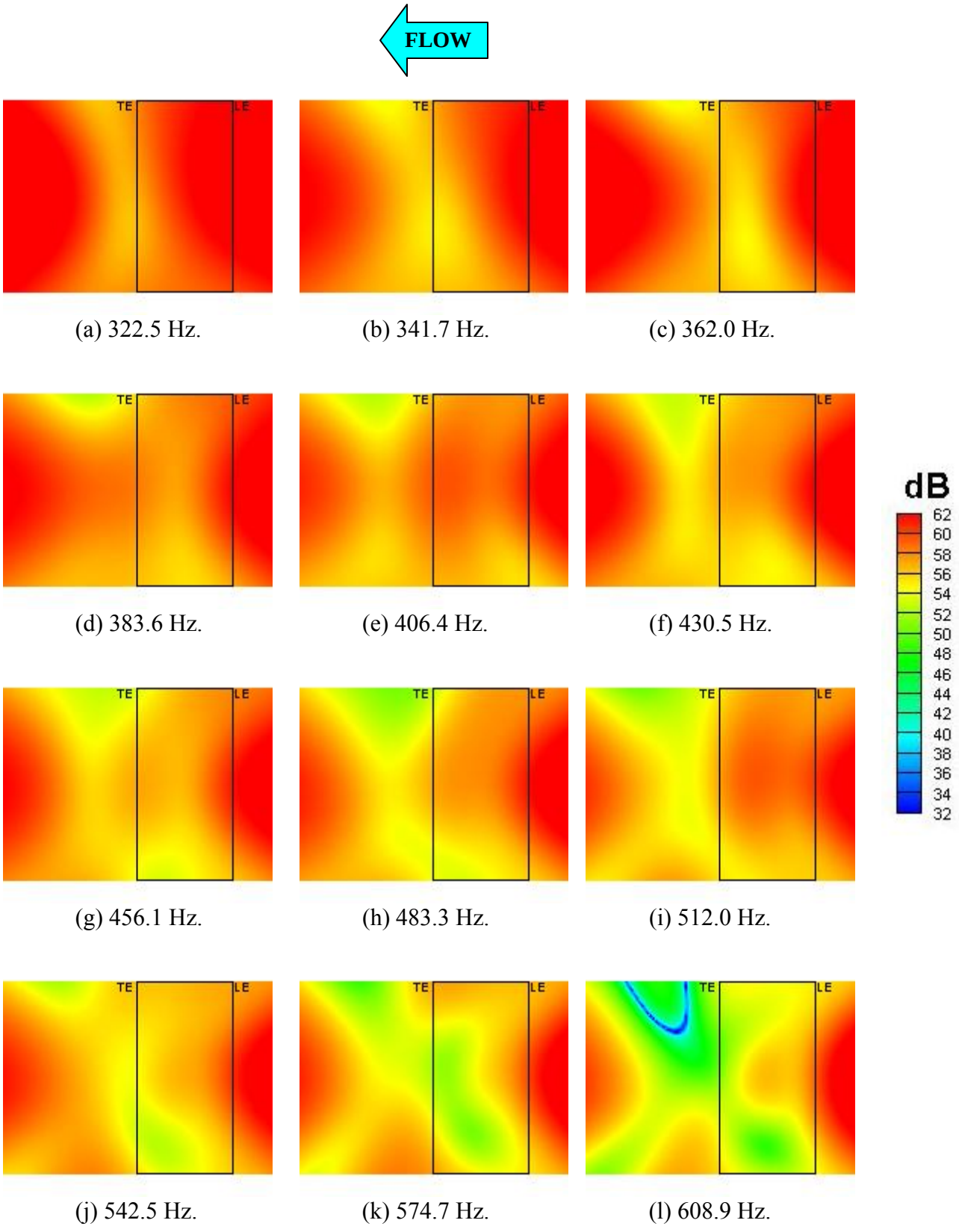

(a) 322.5 Hz. (b) 341.7 Hz. (c) 362.0 Hz.

(d) 383.6 Hz. (e) 406.4 Hz. (f) 430.5 Hz.

(g) 456.1 Hz. (h) 483.3 Hz. (i) 512.0 Hz.

(j) 542.5 Hz. (k) 574.7 Hz. (l) 608.9 Hz.

Figure 31. 1/12-Octave band beamform maps for Run035
(Airfoil at α = 9˚, U=54.58 m/s, Tripped BL, phased array on suction side).

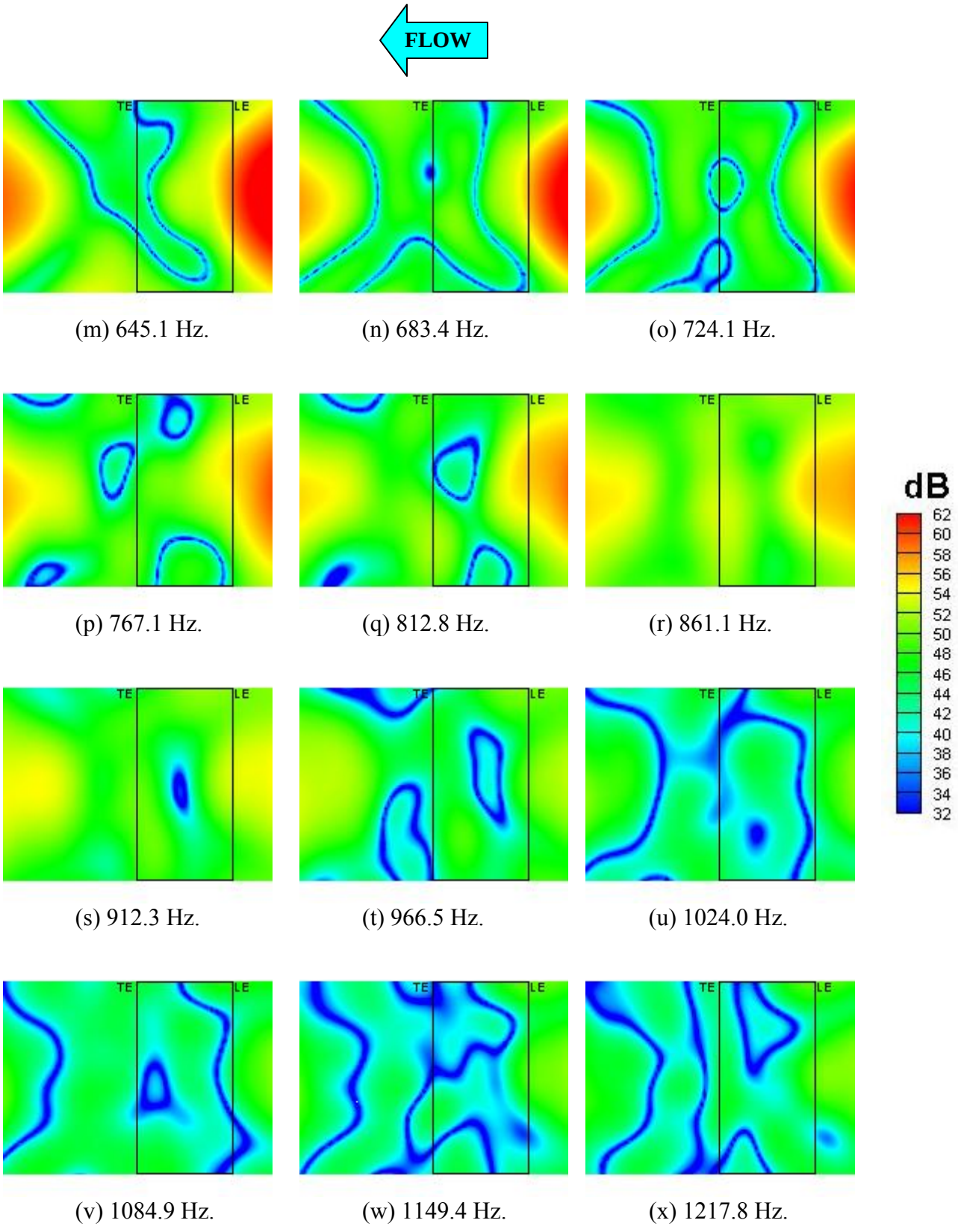

(m) 645.1 Hz. (n) 683.4 Hz. (o) 724.1 Hz.

(p) 767.1 Hz. (q) 812.8 Hz. (r) 861.1 Hz.

(s) 912.3 Hz. (t) 966.5 Hz. (u) 1024.0 Hz.

(v) 1084.9 Hz. (w) 1149.4 Hz. (x) 1217.8 Hz.

Figure 31. 1/12-Octave band beamform maps for Run035
(Airfoil at α = 9˚, U=54.58 m/s, Tripped BL, phased array on suction side).

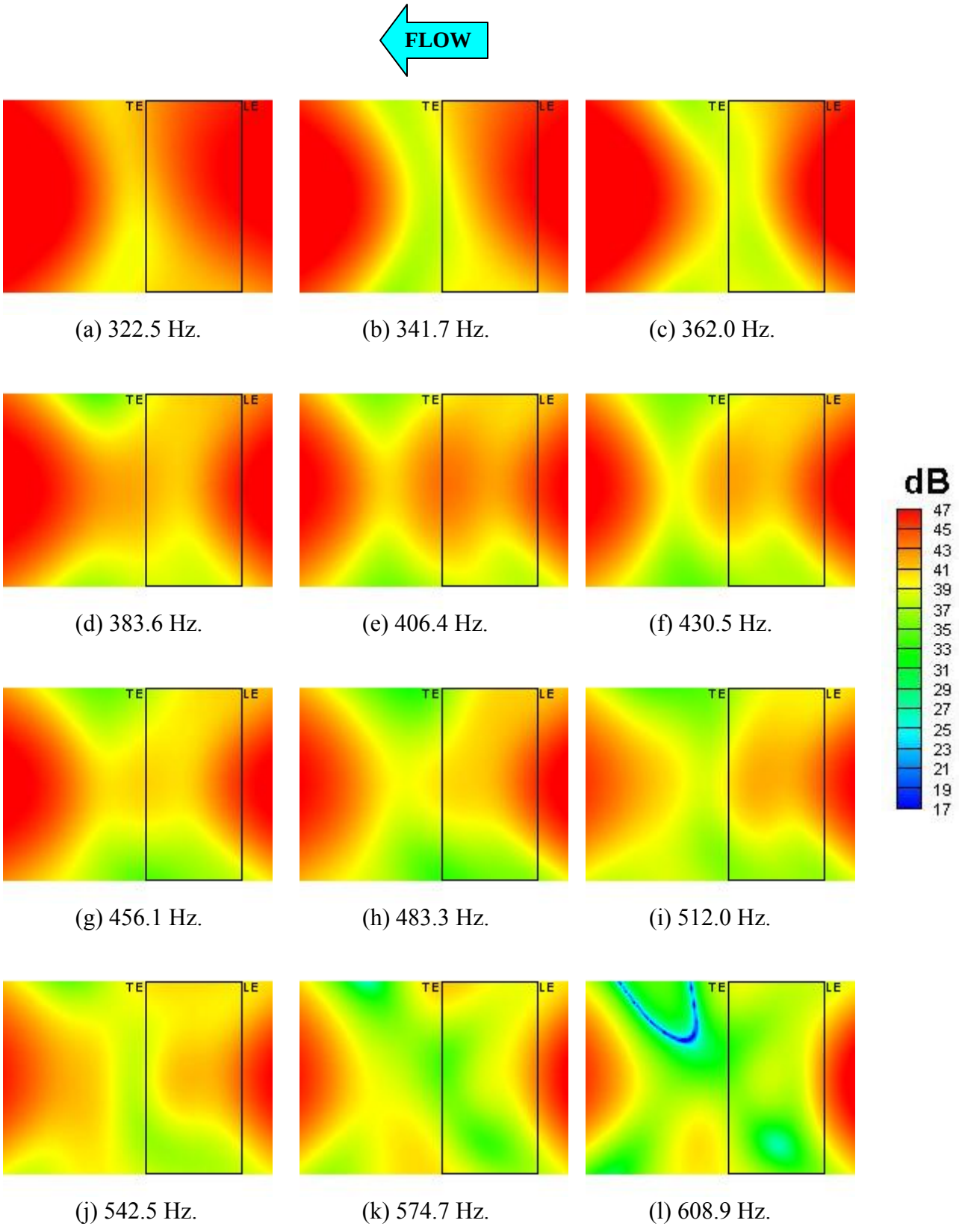

(a) 322.5 Hz. (b) 341.7 Hz. (c) 362.0 Hz.

(d) 383.6 Hz. (e) 406.4 Hz. (f) 430.5 Hz.

(g) 456.1 Hz. (h) 483.3 Hz. (i) 512.0 Hz.

(j) 542.5 Hz. (k) 574.7 Hz. (l) 608.9 Hz.

Figure 32. 1/12-Octave band beamform maps for Run036
(Airfoil at α = 7˚, U=30.88 m/s, Tripped BL, phased array on suction side).

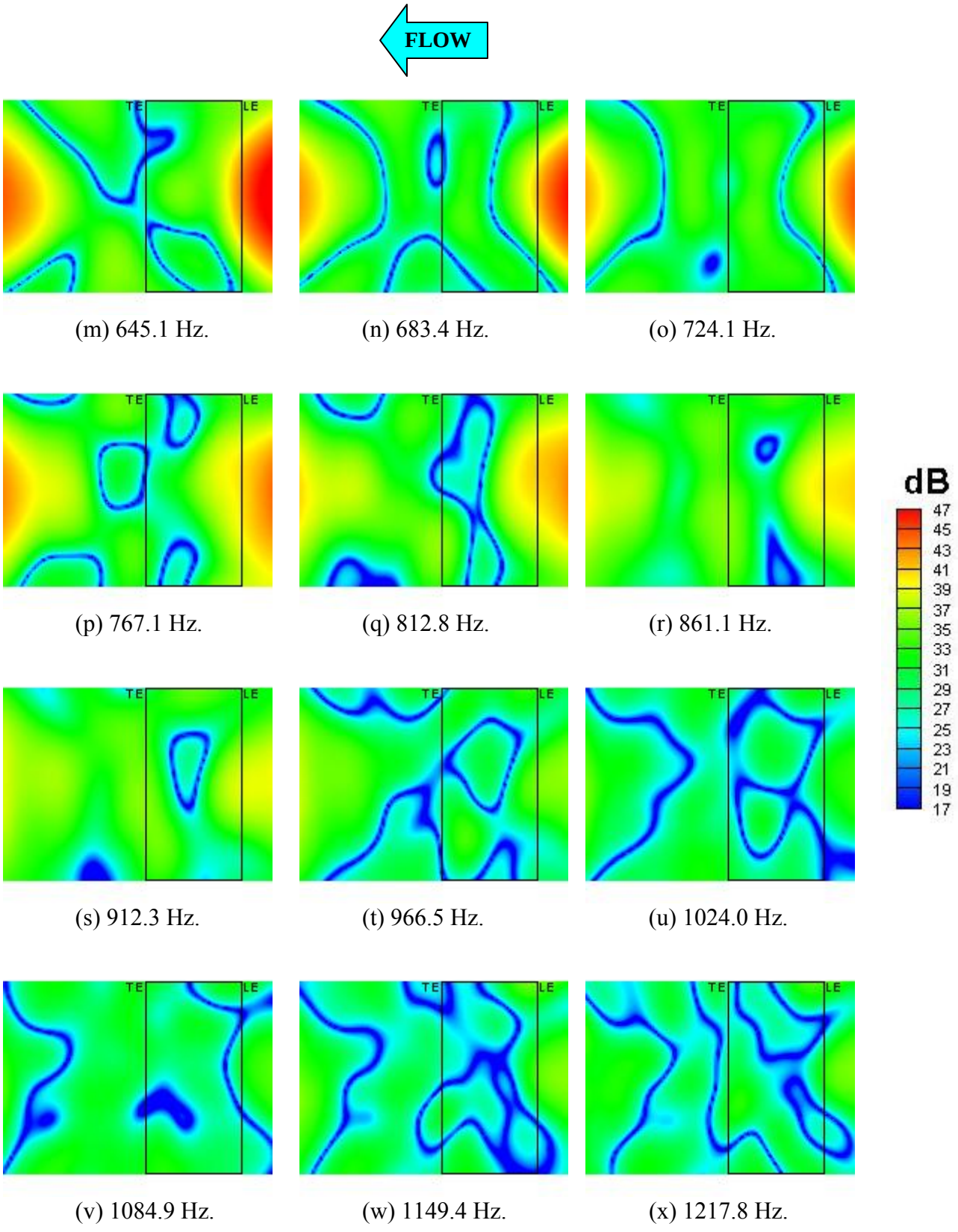

(m) 645.1 Hz. (n) 683.4 Hz. (o) 724.1 Hz.

(p) 767.1 Hz. (q) 812.8 Hz. (r) 861.1 Hz.

(s) 912.3 Hz. (t) 966.5 Hz. (u) 1024.0 Hz.

(v) 1084.9 Hz. (w) 1149.4 Hz. (x) 1217.8 Hz.

Figure 32. 1/12-Octave band beamform maps for Run036
(Airfoil at α = 7˚, U=30.88 m/s, Tripped BL, phased array on suction side).

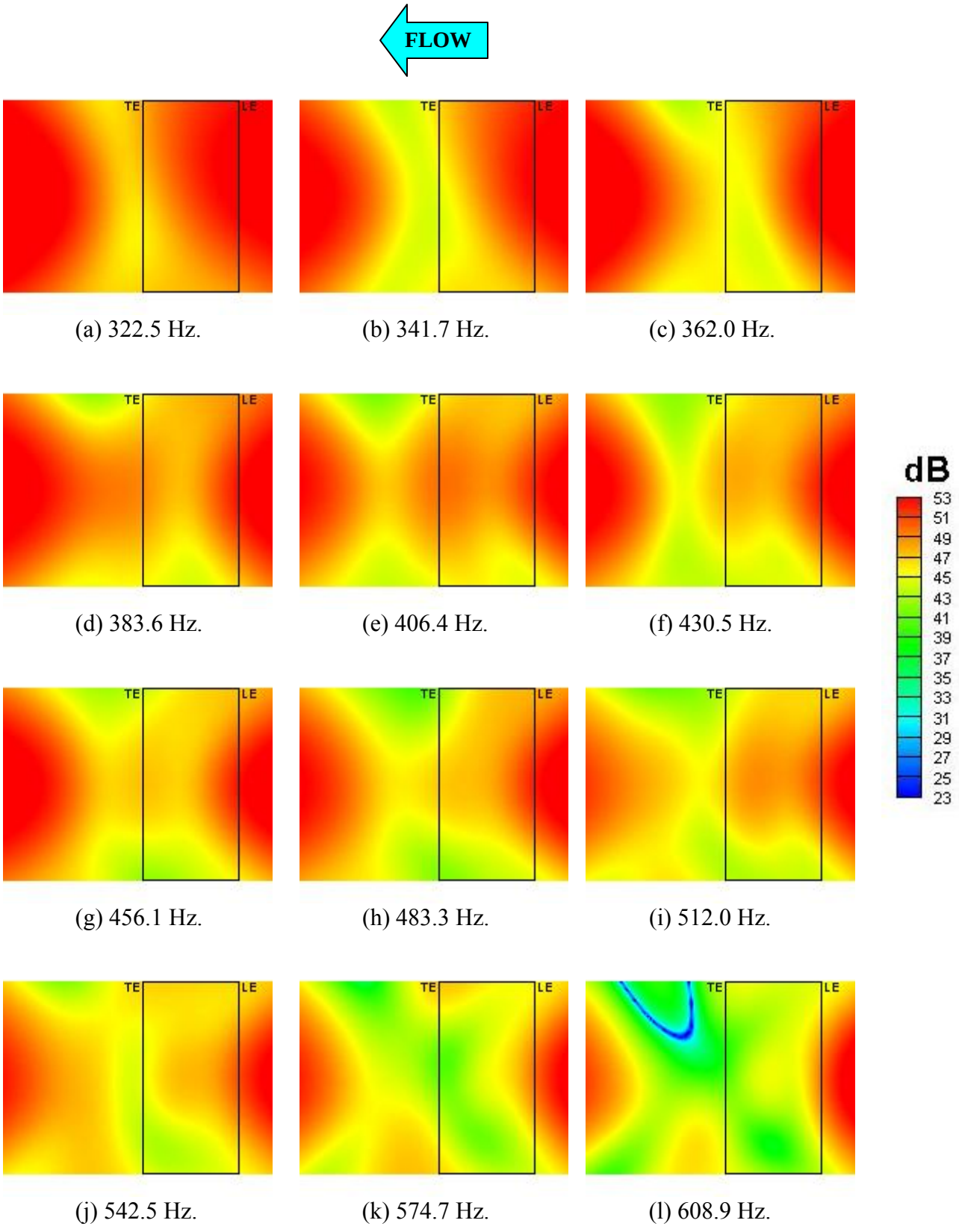

(a) 322.5 Hz. (b) 341.7 Hz. (c) 362.0 Hz.

(d) 383.6 Hz. (e) 406.4 Hz. (f) 430.5 Hz.

(g) 456.1 Hz. (h) 483.3 Hz. (i) 512.0 Hz.

(j) 542.5 Hz. (k) 574.7 Hz. (l) 608.9 Hz.

Figure 33. 1/12-Octave band beamform maps for Run037
(Airfoil at α = 7˚, U=38.99 m/s, Tripped BL, phased array on suction side).

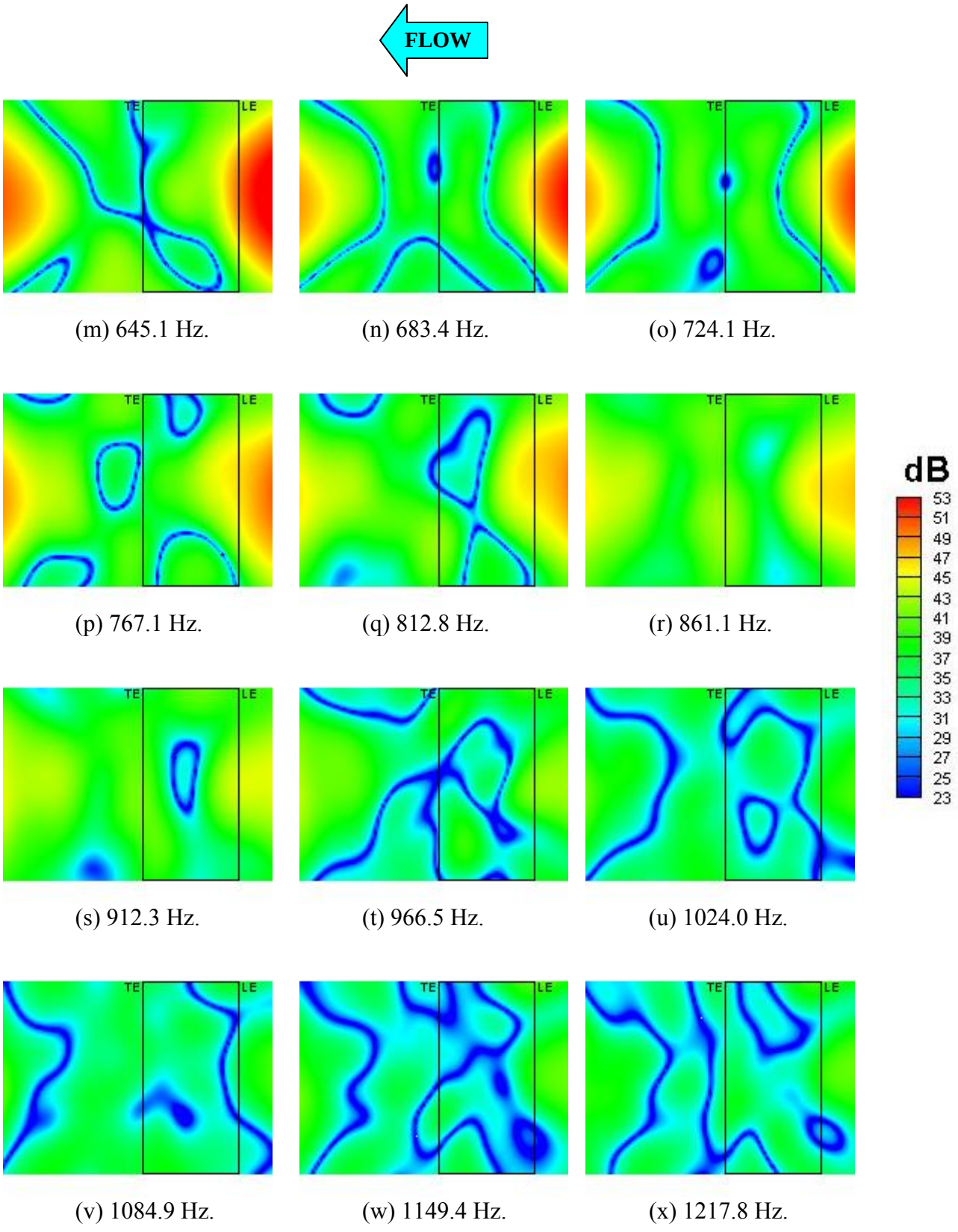

(m) 645.1 Hz. (n) 683.4 Hz. (o) 724.1 Hz.

(p) 767.1 Hz. (q) 812.8 Hz. (r) 861.1 Hz.

(s) 912.3 Hz. (t) 966.5 Hz. (u) 1024.0 Hz.

(v) 1084.9 Hz. (w) 1149.4 Hz. (x) 1217.8 Hz.

Figure 33. 1/12-Octave band beamform maps for Run037
(Airfoil at α = 7˚, U=38.99 m/s, Tripped BL, phased array on suction side).

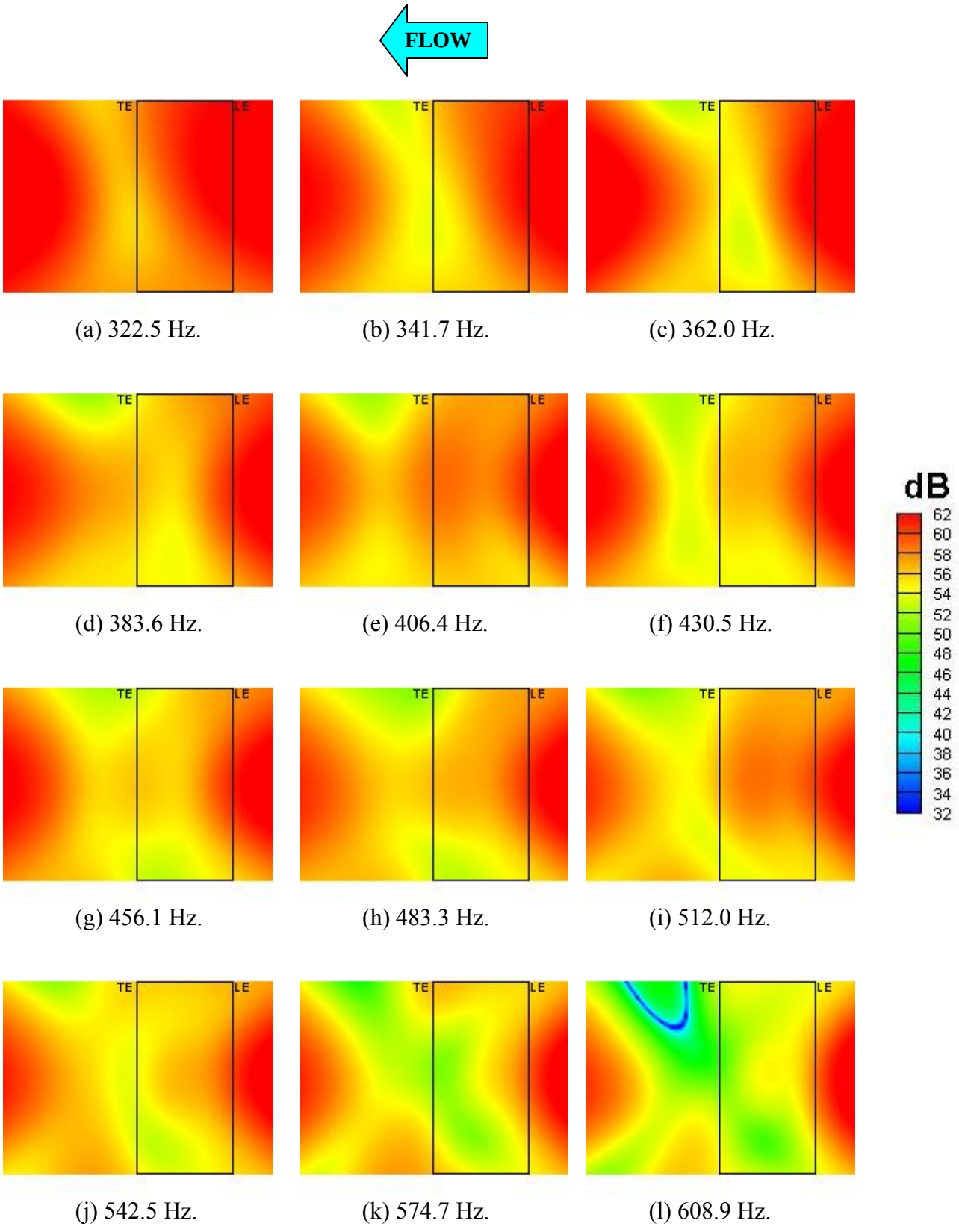

Figure 34. 1/12-Octave band beamform maps for Run038
(Airfoil at α = 7˚, U=54.58 m/s, Tripped BL, phased array on suction side).

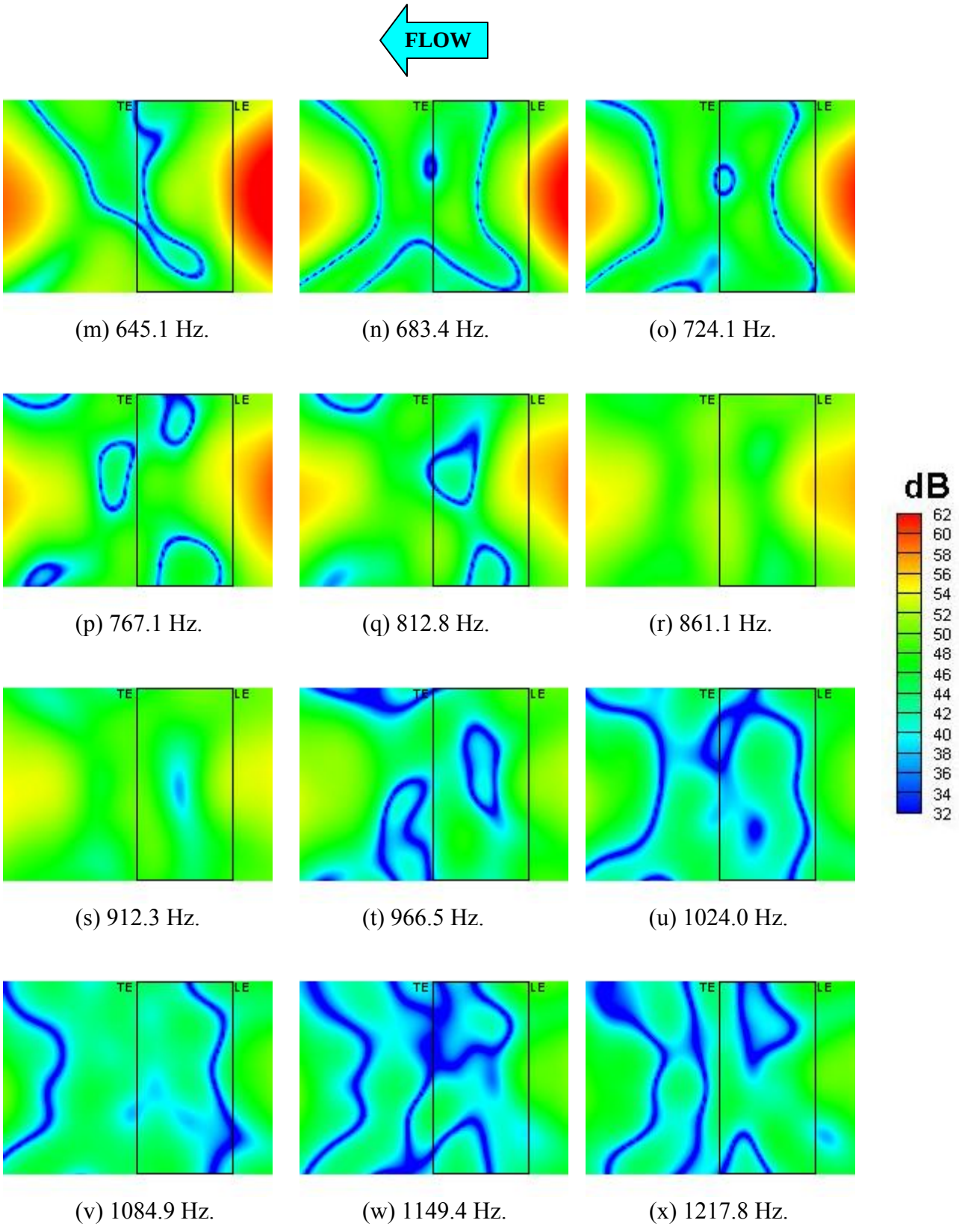

(m) 645.1 Hz. (n) 683.4 Hz. (o) 724.1 Hz.

(p) 767.1 Hz. (q) 812.8 Hz. (r) 861.1 Hz.

(s) 912.3 Hz. (t) 966.5 Hz. (u) 1024.0 Hz.

(v) 1084.9 Hz. (w) 1149.4 Hz. (x) 1217.8 Hz.

Figure 34. 1/12-Octave band beamform maps for Run038
(Airfoil at α = 7˚, U=54.58 m/s, Tripped BL, phased array on suction side).

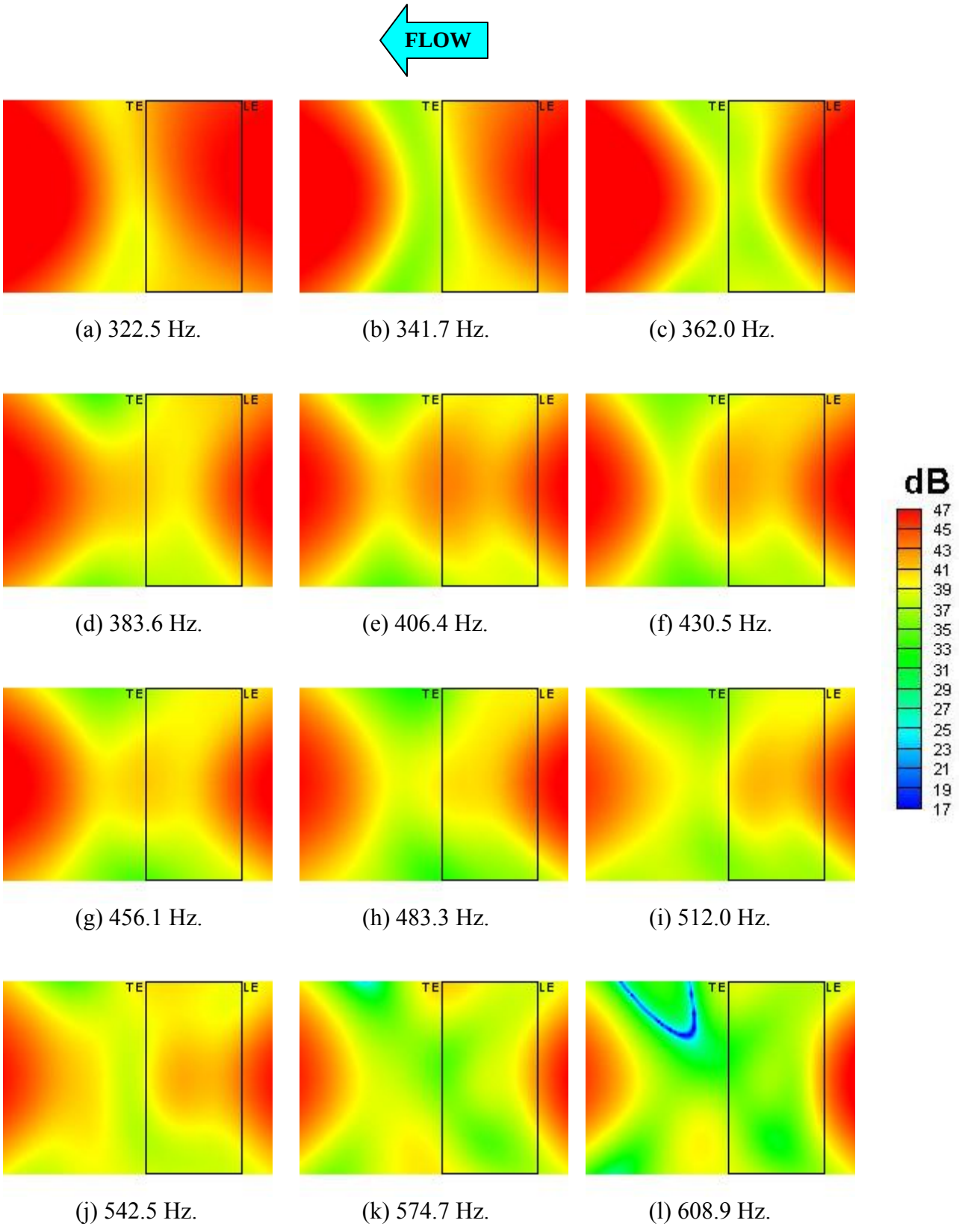

(a) 322.5 Hz. (b) 341.7 Hz. (c) 362.0 Hz.

(d) 383.6 Hz. (e) 406.4 Hz. (f) 430.5 Hz.

(g) 456.1 Hz. (h) 483.3 Hz. (i) 512.0 Hz.

(j) 542.5 Hz. (k) 574.7 Hz. (l) 608.9 Hz.

Figure 35. 1/12-Octave band beamform maps for Run039
(Airfoil at α = 5˚, U=31.09 m/s, Tripped BL, phased array on suction side).

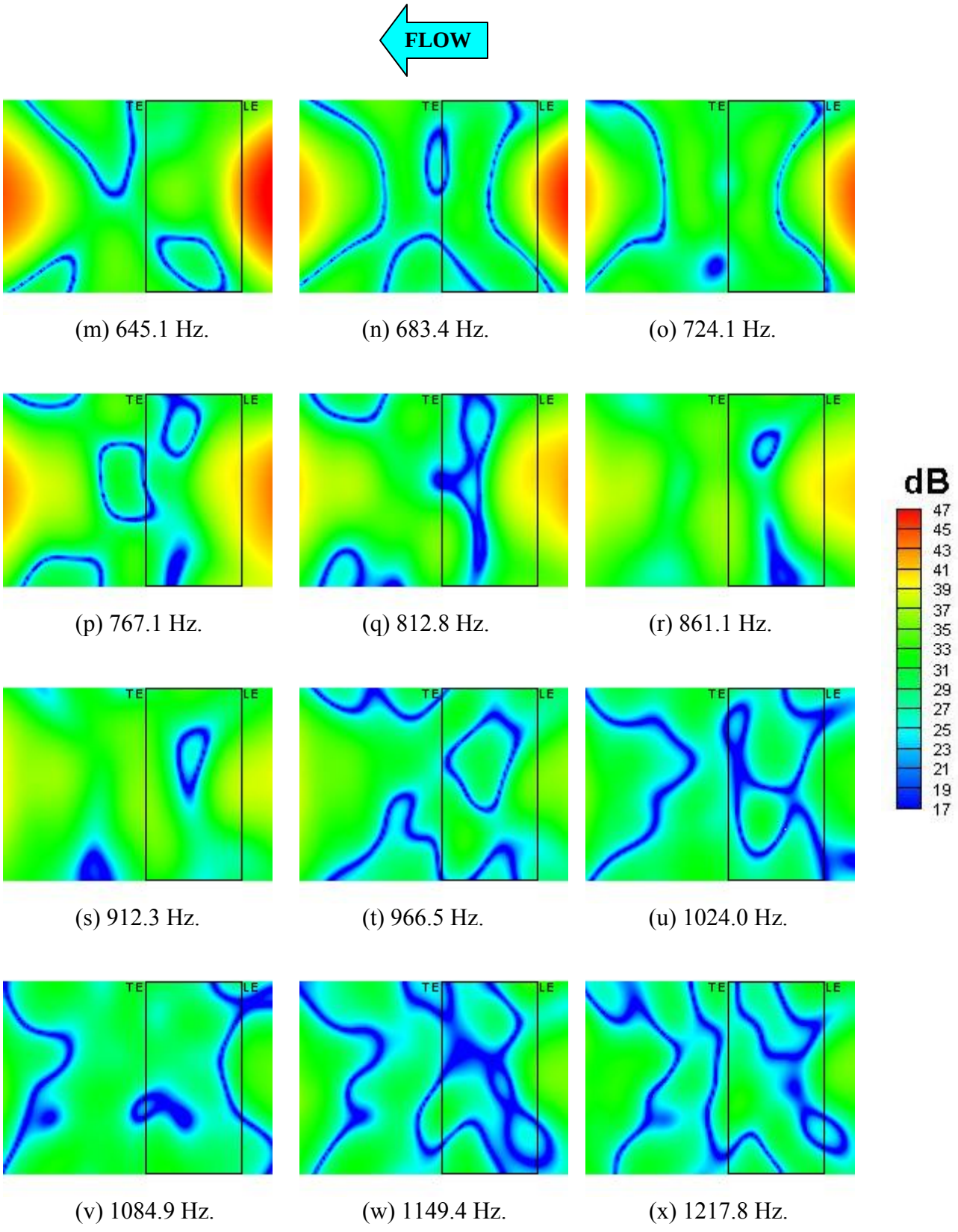

(m) 645.1 Hz. (n) 683.4 Hz. (o) 724.1 Hz.

(p) 767.1 Hz. (q) 812.8 Hz. (r) 861.1 Hz.

(s) 912.3 Hz. (t) 966.5 Hz. (u) 1024.0 Hz.

(v) 1084.9 Hz. (w) 1149.4 Hz. (x) 1217.8 Hz.

Figure 35. 1/12-Octave band beamform maps for Run039
(Airfoil at α = 5˚, U=31.09 m/s, Tripped BL, phased array on suction side).

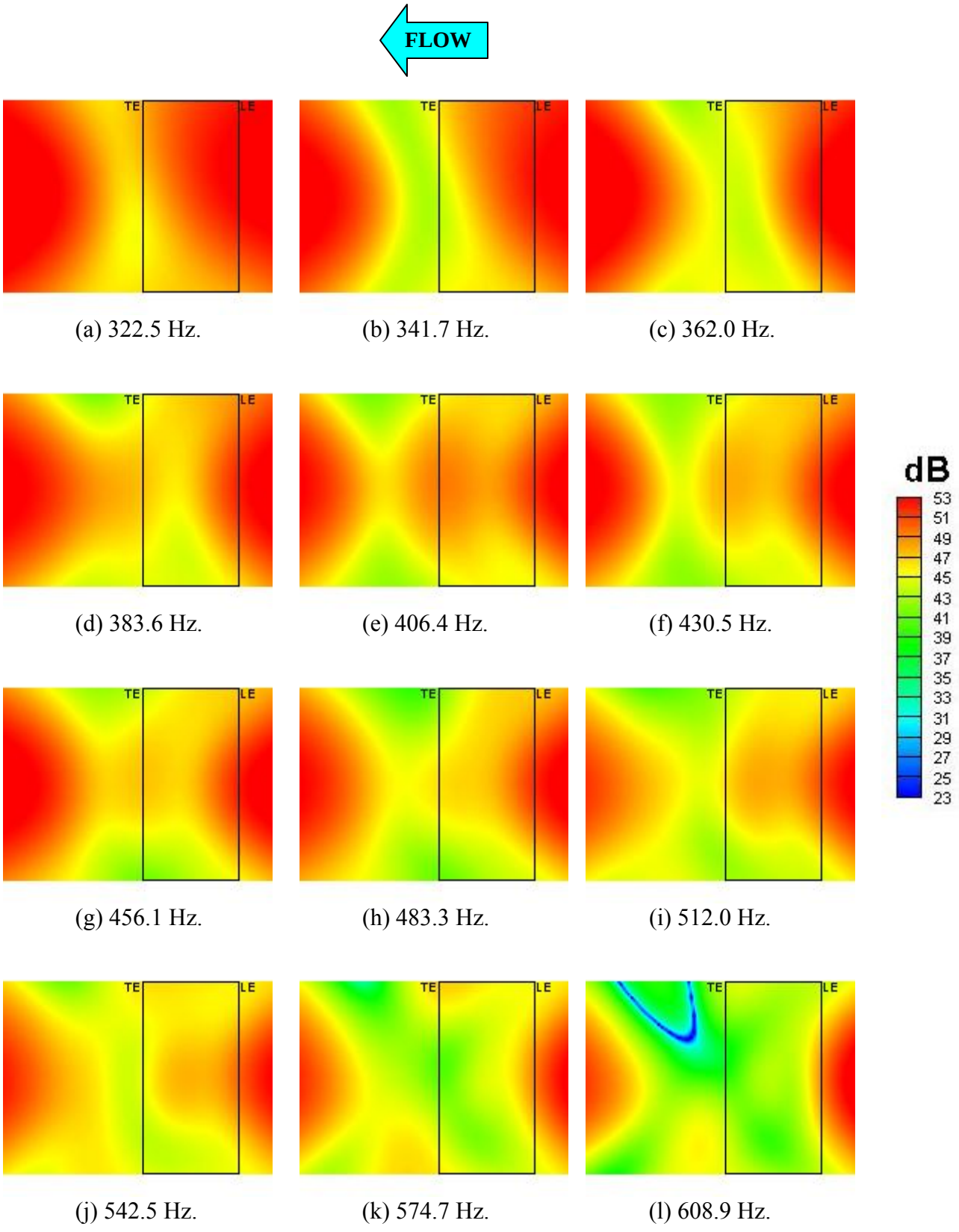

(a) 322.5 Hz. (b) 341.7 Hz. (c) 362.0 Hz.

(d) 383.6 Hz. (e) 406.4 Hz. (f) 430.5 Hz.

(g) 456.1 Hz. (h) 483.3 Hz. (i) 512.0 Hz.

(j) 542.5 Hz. (k) 574.7 Hz. (l) 608.9 Hz.

Figure 36. 1/12-Octave band beamform maps for Run040
(Airfoil at α = 5˚, U=38.87 m/s, Tripped BL, phased array on suction side).

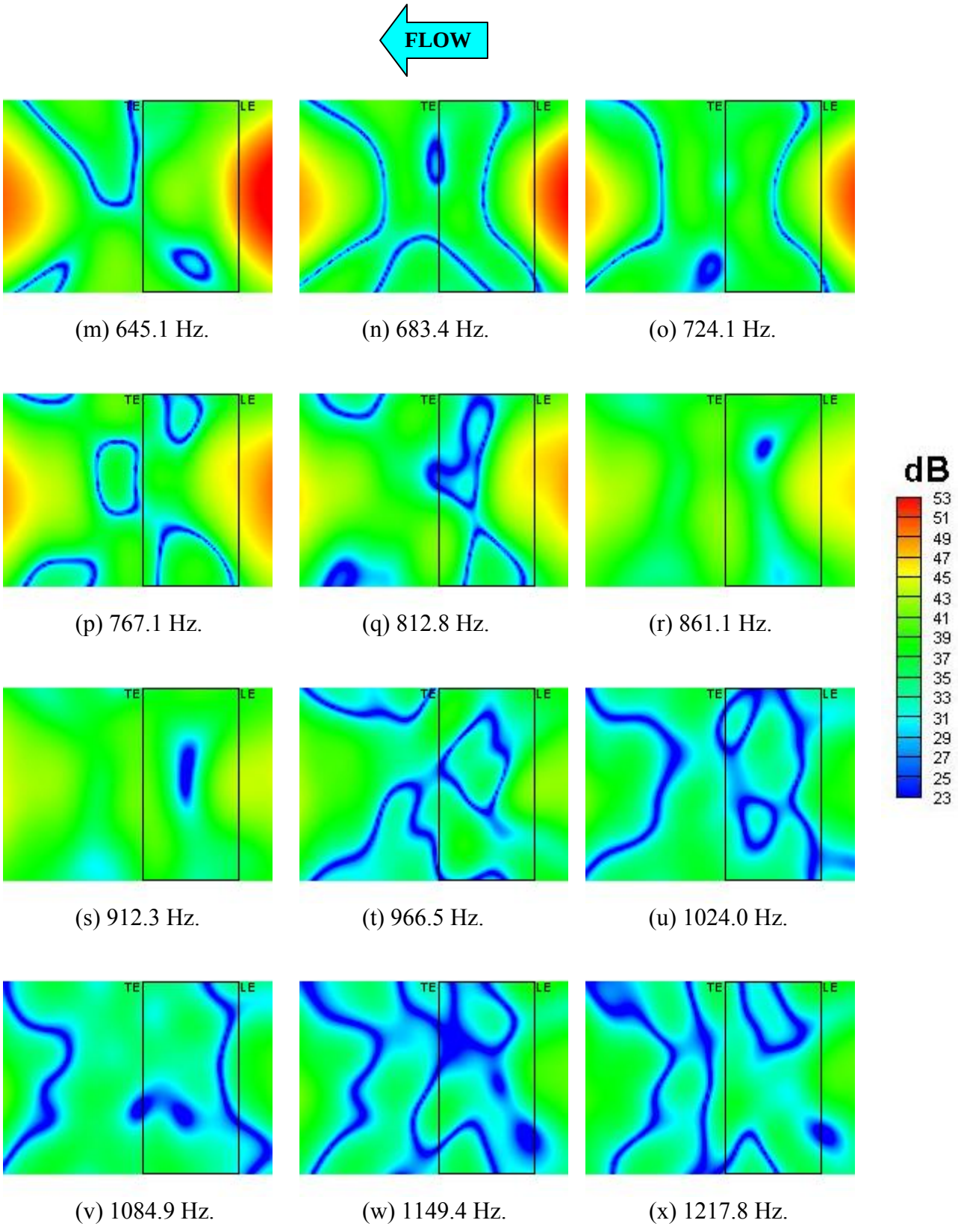

(m) 645.1 Hz. (n) 683.4 Hz. (o) 724.1 Hz.

(p) 767.1 Hz. (q) 812.8 Hz. (r) 861.1 Hz.

(s) 912.3 Hz. (t) 966.5 Hz. (u) 1024.0 Hz.

(v) 1084.9 Hz. (w) 1149.4 Hz. (x) 1217.8 Hz.

Figure 36. 1/12-Octave band beamform maps for Run040
(Airfoil at α = 5˚, U=38.87 m/s, Tripped BL, phased array on suction side).

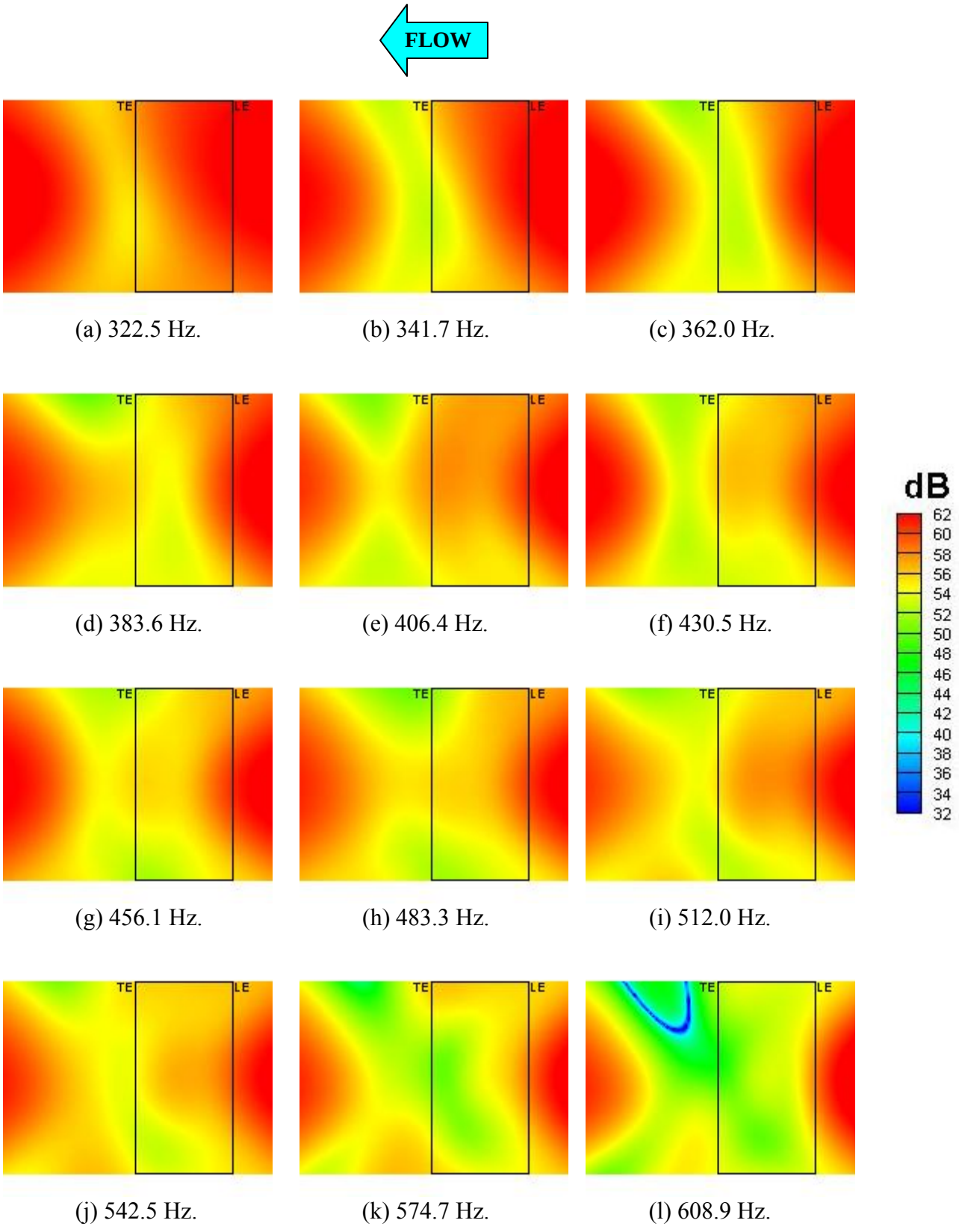

(a) 322.5 Hz. (b) 341.7 Hz. (c) 362.0 Hz.

(d) 383.6 Hz. (e) 406.4 Hz. (f) 430.5 Hz.

(g) 456.1 Hz. (h) 483.3 Hz. (i) 512.0 Hz.

(j) 542.5 Hz. (k) 574.7 Hz. (l) 608.9 Hz.

Figure 37. 1/12-Octave band beamform maps for Run041
(Airfoil at α = 5˚, U=54.58 m/s, Tripped BL, phased array on suction side).

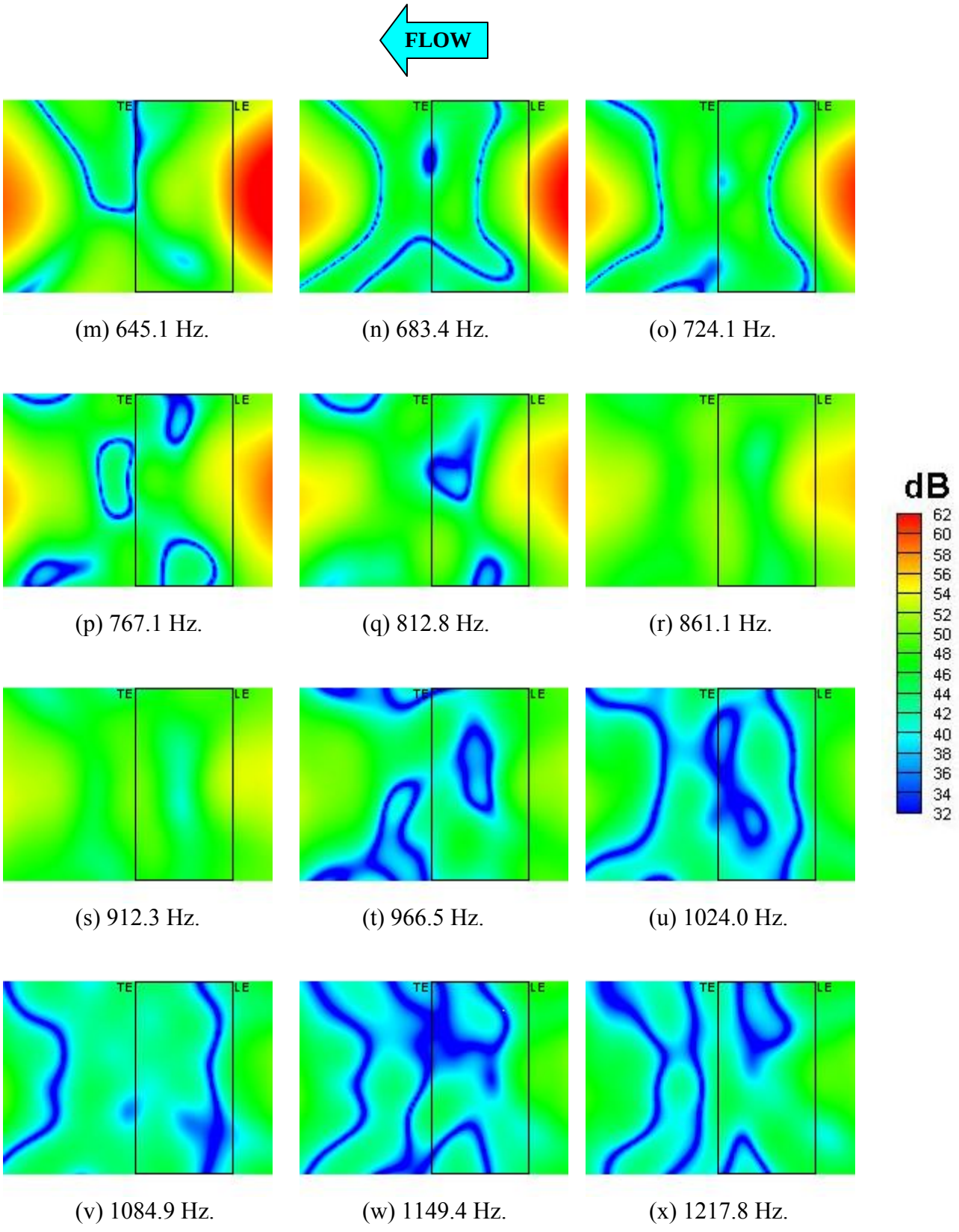

(m) 645.1 Hz. (n) 683.4 Hz. (o) 724.1 Hz.

(p) 767.1 Hz. (q) 812.8 Hz. (r) 861.1 Hz.

(s) 912.3 Hz. (t) 966.5 Hz. (u) 1024.0 Hz.

(v) 1084.9 Hz. (w) 1149.4 Hz. (x) 1217.8 Hz.

Figure 37. 1/12-Octave band beamform maps for Run041
(Airfoil at α = 5˚, U=54.58 m/s, Tripped BL, phased array on suction side).

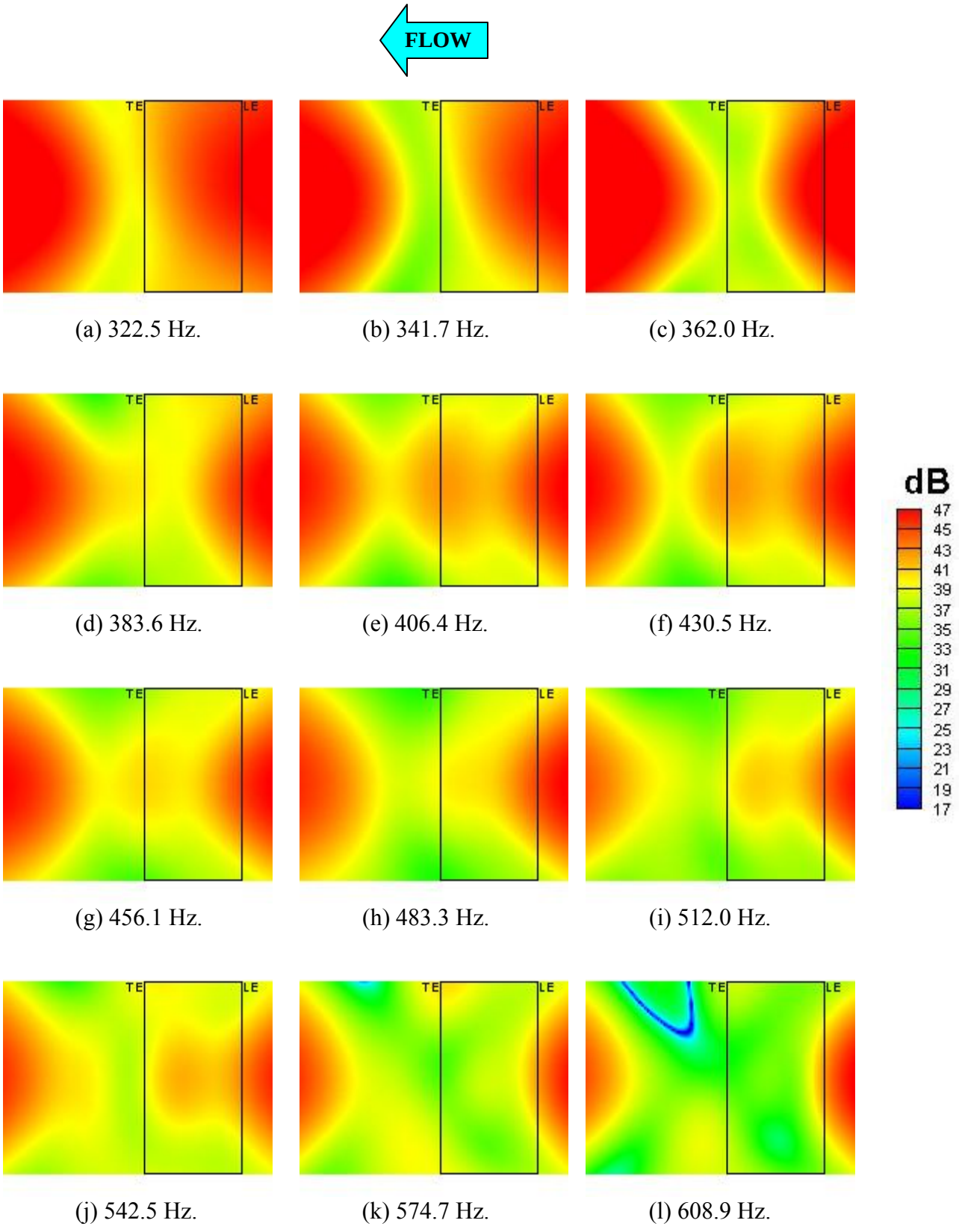

(a) 322.5 Hz. (b) 341.7 Hz. (c) 362.0 Hz.

(d) 383.6 Hz. (e) 406.4 Hz. (f) 430.5 Hz.

(g) 456.1 Hz. (h) 483.3 Hz. (i) 512.0 Hz.

(j) 542.5 Hz. (k) 574.7 Hz. (l) 608.9 Hz.

Figure 38. 1/12-Octave band beamform maps for Run042
(Airfoil at α = 3˚, U=30.92 m/s, Tripped BL, phased array on suction side).

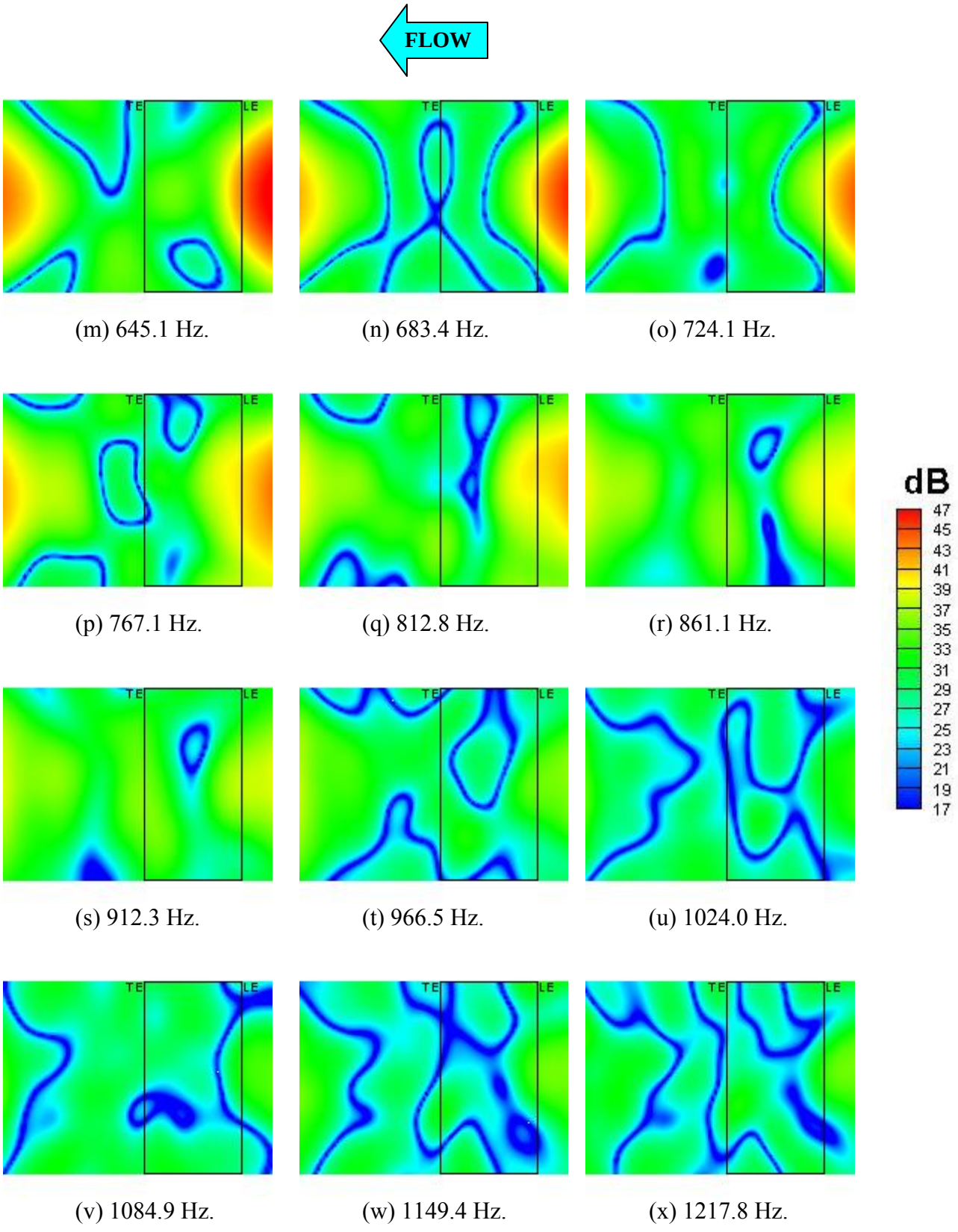

(m) 645.1 Hz. (n) 683.4 Hz. (o) 724.1 Hz.

(p) 767.1 Hz. (q) 812.8 Hz. (r) 861.1 Hz.

(s) 912.3 Hz. (t) 966.5 Hz. (u) 1024.0 Hz.

(v) 1084.9 Hz. (w) 1149.4 Hz. (x) 1217.8 Hz.

Figure 38. 1/12-Octave band beamform maps for Run042
(Airfoil at α = 3˚, U=30.92 m/s, Tripped BL, phased array on suction side).

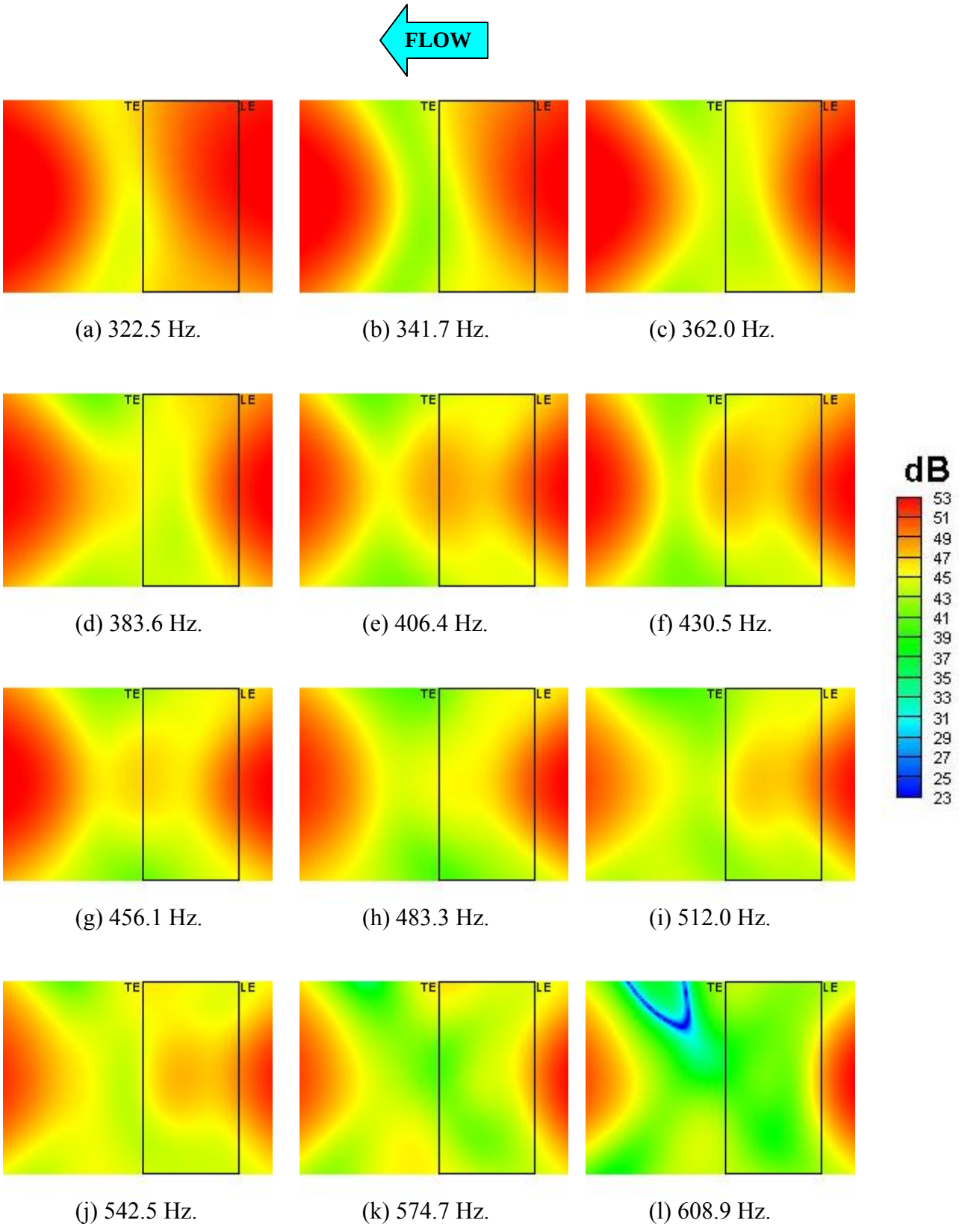

Figure 39. 1/12-Octave band beamform maps for Run043
(Airfoil at α = 3˚, U=38.84 m/s, Tripped BL, phased array on suction side).

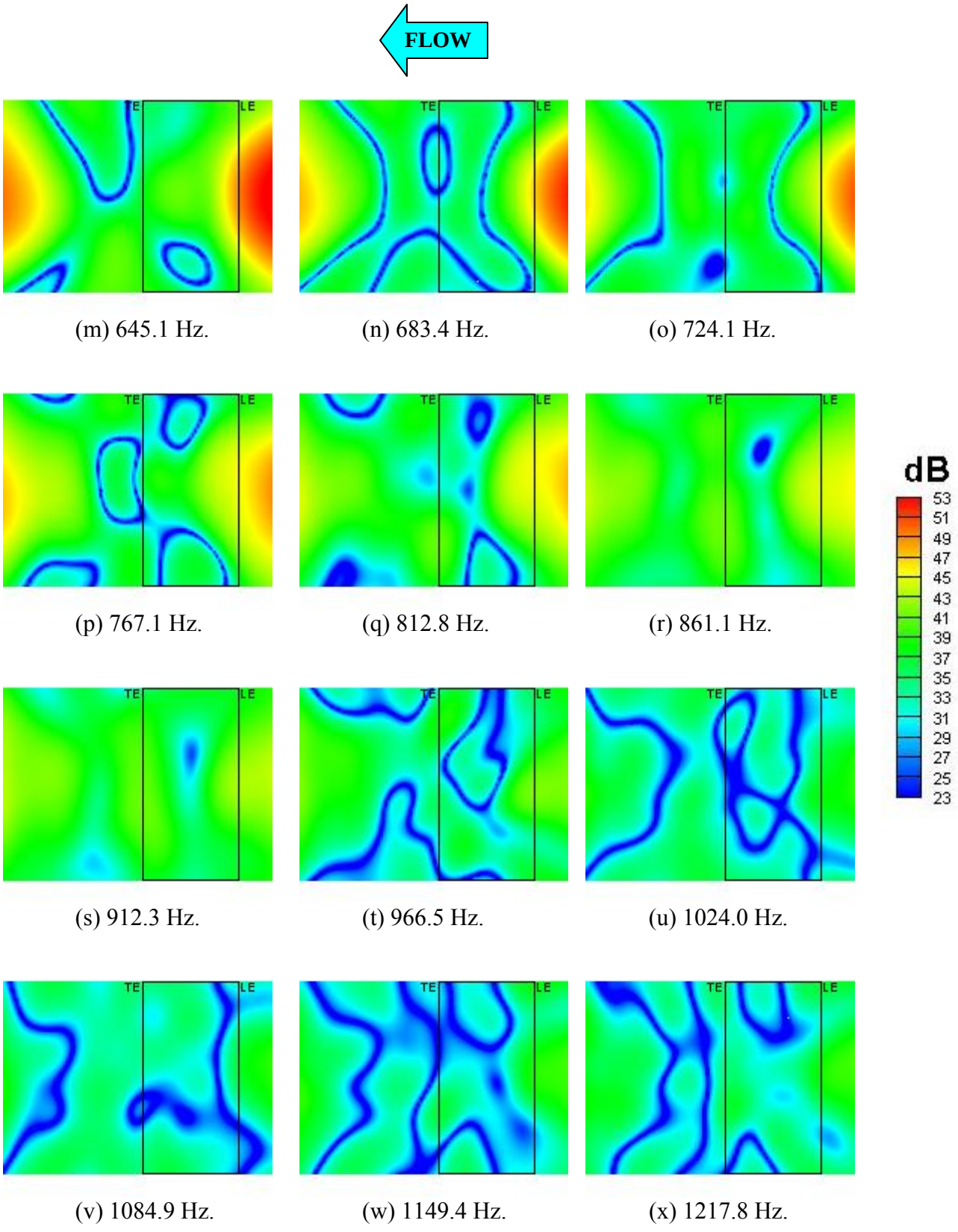

(m) 645.1 Hz. (n) 683.4 Hz. (o) 724.1 Hz.

(p) 767.1 Hz. (q) 812.8 Hz. (r) 861.1 Hz.

(s) 912.3 Hz. (t) 966.5 Hz. (u) 1024.0 Hz.

(v) 1084.9 Hz. (w) 1149.4 Hz. (x) 1217.8 Hz.

Figure 39. 1/12-Octave band beamform maps for Run043
(Airfoil at α = 3˚, U=38.84 m/s, Tripped BL, phased array on suction side).

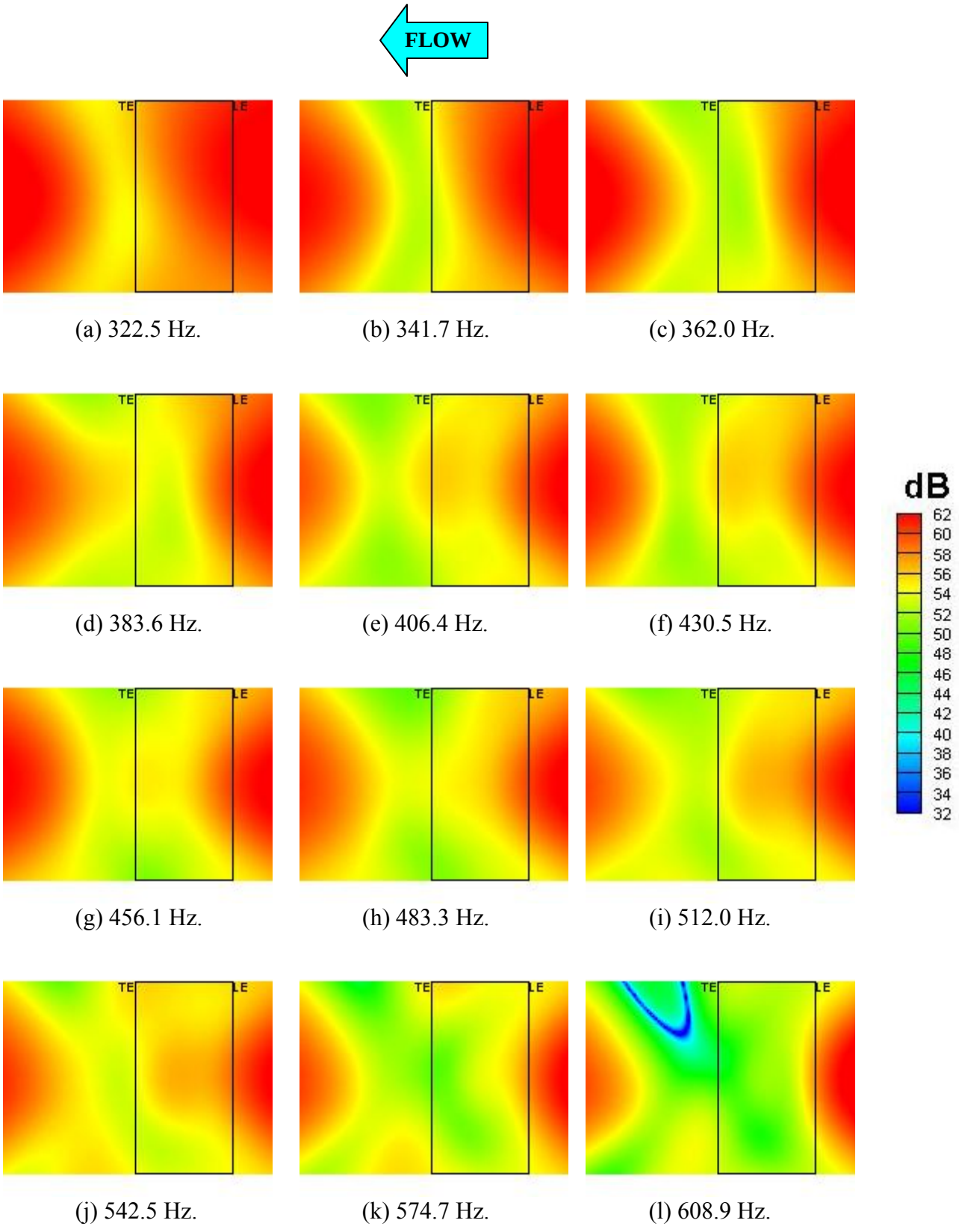

(a) 322.5 Hz. (b) 341.7 Hz. (c) 362.0 Hz.

(d) 383.6 Hz. (e) 406.4 Hz. (f) 430.5 Hz.

(g) 456.1 Hz. (h) 483.3 Hz. (i) 512.0 Hz.

(j) 542.5 Hz. (k) 574.7 Hz. (l) 608.9 Hz.

Figure 40. 1/12-Octave band beamform maps for Run044
(Airfoil at α = 3˚, U=54.49 m/s, Tripped BL, phased array on suction side).

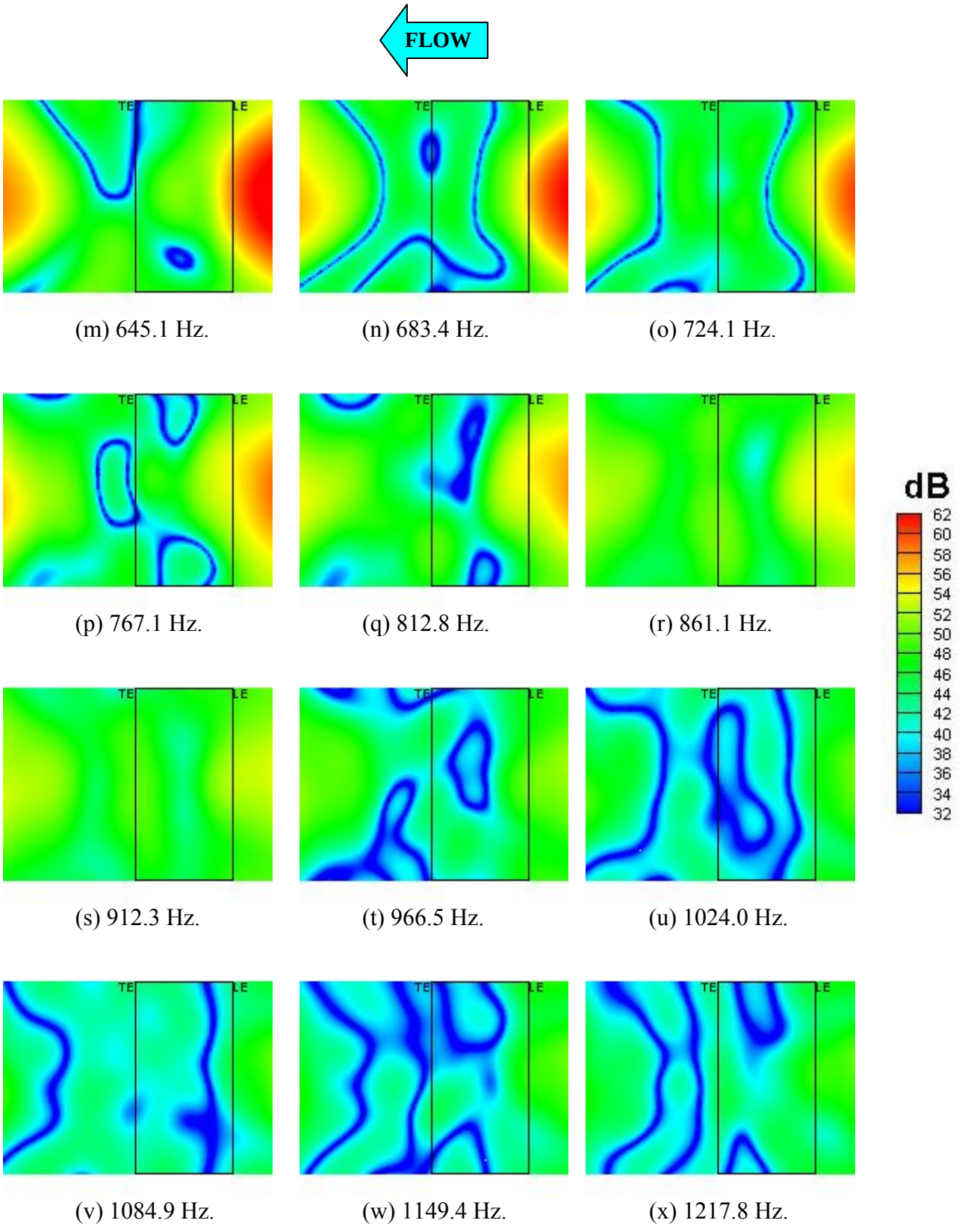

(m) 645.1 Hz. (n) 683.4 Hz. (o) 724.1 Hz.

(p) 767.1 Hz. (q) 812.8 Hz. (r) 861.1 Hz.

(s) 912.3 Hz. (t) 966.5 Hz. (u) 1024.0 Hz.

(v) 1084.9 Hz. (w) 1149.4 Hz. (x) 1217.8 Hz.

Figure 40. 1/12-Octave band beamform maps for Run044
(Airfoil at α = 3˚, U=54.49 m/s, Tripped BL, phased array on suction side).

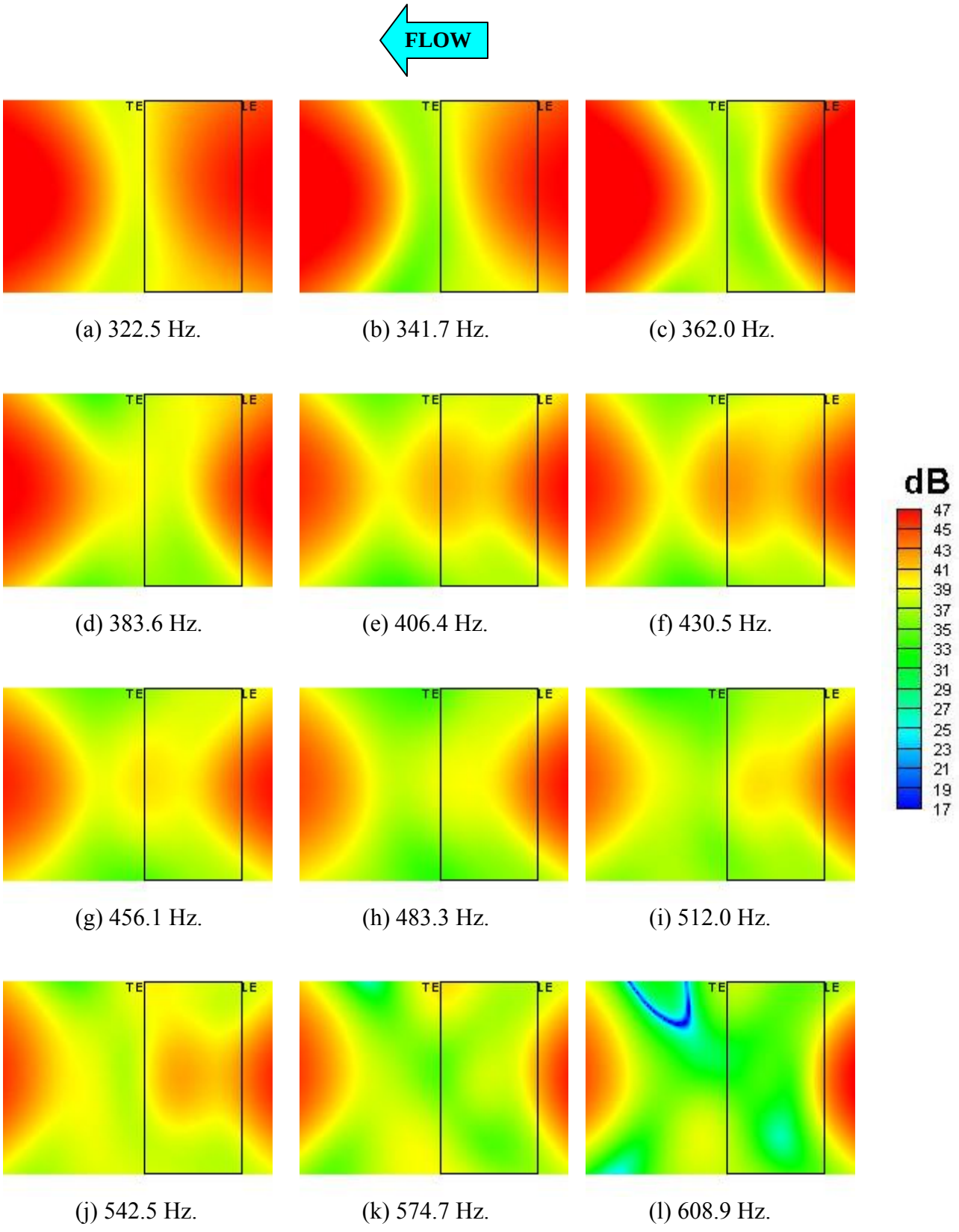

(a) 322.5 Hz. (b) 341.7 Hz. (c) 362.0 Hz.

(d) 383.6 Hz. (e) 406.4 Hz. (f) 430.5 Hz.

(g) 456.1 Hz. (h) 483.3 Hz. (i) 512.0 Hz.

(j) 542.5 Hz. (k) 574.7 Hz. (l) 608.9 Hz.

Figure 41. 1/12-Octave band beamform maps for Run045
(Airfoil at α = 1.5˚, U=31.03 m/s, Tripped BL, phased array on suction side).

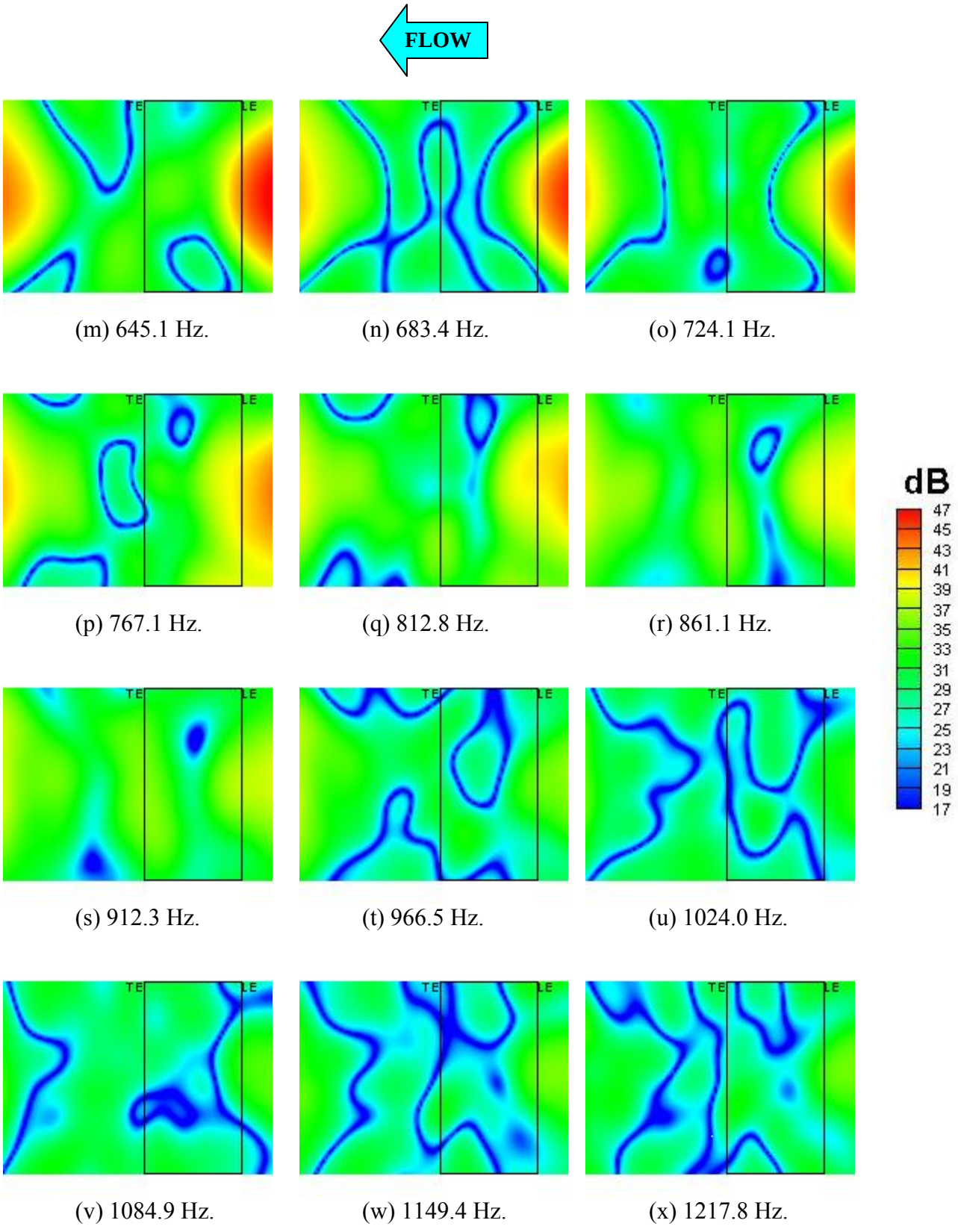

(m) 645.1 Hz. (n) 683.4 Hz. (o) 724.1 Hz.

(p) 767.1 Hz. (q) 812.8 Hz. (r) 861.1 Hz.

(s) 912.3 Hz. (t) 966.5 Hz. (u) 1024.0 Hz.

(v) 1084.9 Hz. (w) 1149.4 Hz. (x) 1217.8 Hz.

Figure 41. 1/12-Octave band beamform maps for Run045
(Airfoil at α = 1.5˚, U=31.03 m/s, Tripped BL, phased array on suction side).

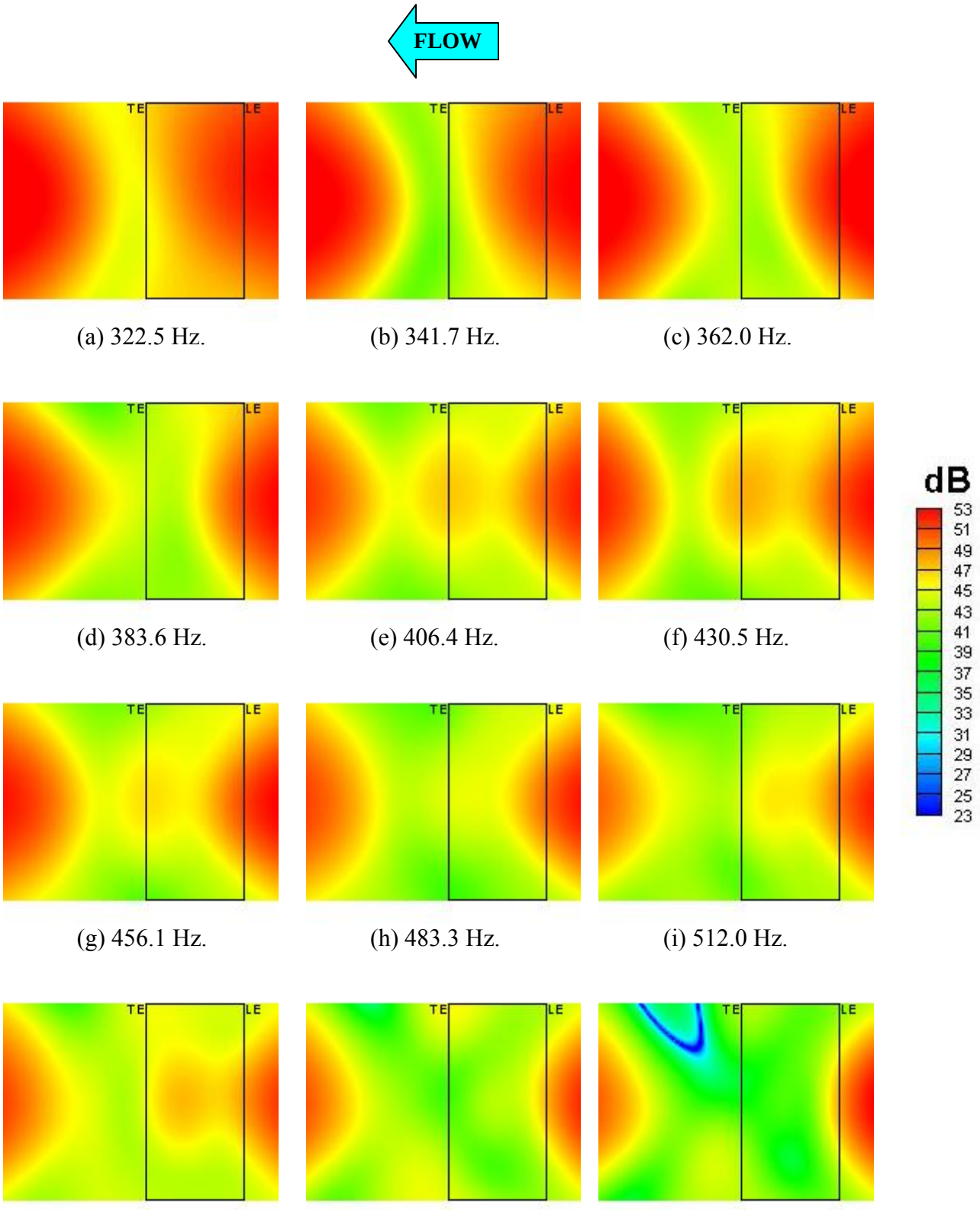

(a) 322.5 Hz. (b) 341.7 Hz. (c) 362.0 Hz.

(d) 383.6 Hz. (e) 406.4 Hz. (f) 430.5 Hz.

(g) 456.1 Hz. (h) 483.3 Hz. (i) 512.0 Hz.

(j) 542.5 Hz. (k) 574.7 Hz. (l) 608.9 Hz.

Figure 42. 1/12-Octave band beamform maps for Run046
(Airfoil at α = 1.5˚, U=38.80 m/s, Tripped BL, phased array on suction side).

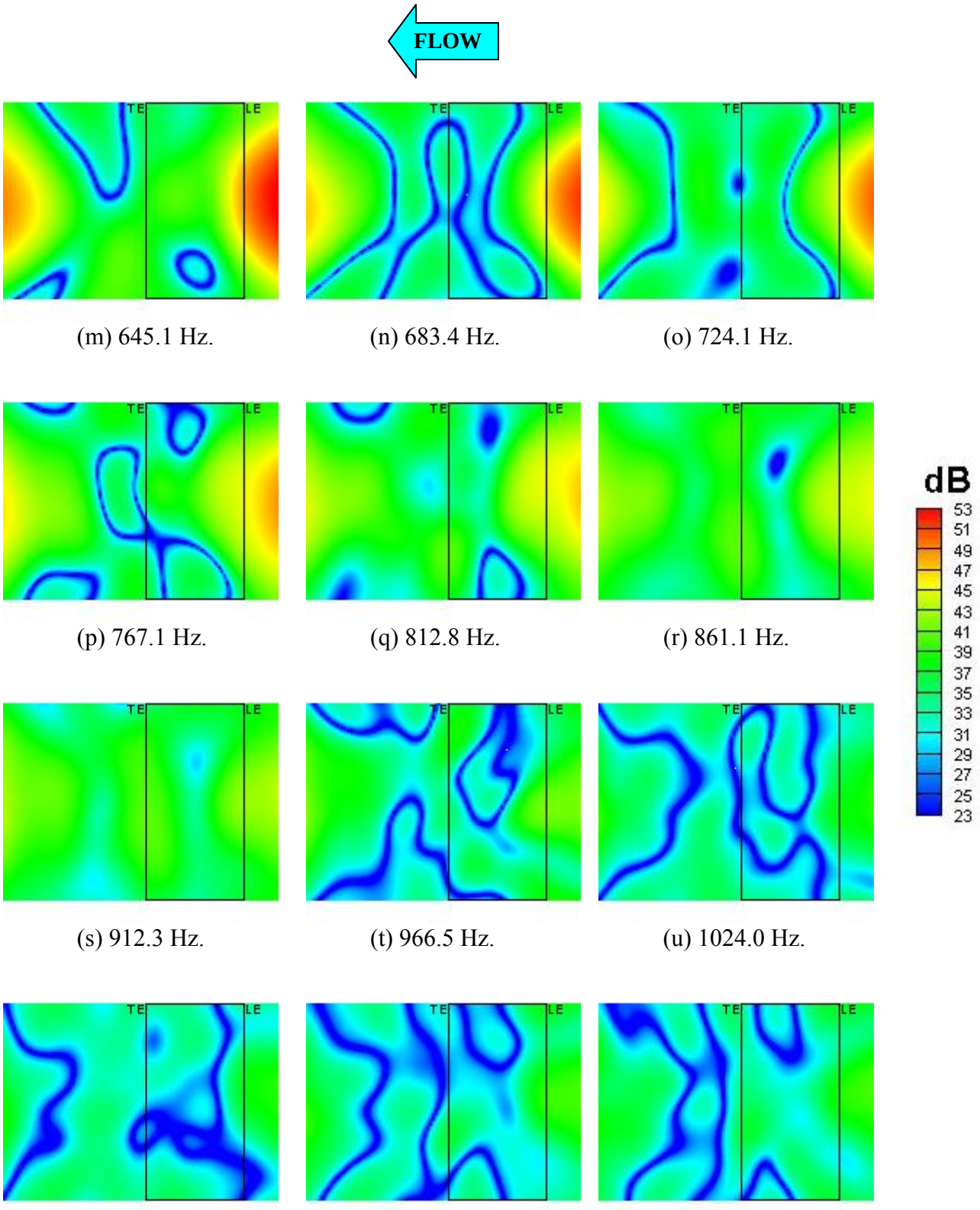

(m) 645.1 Hz. (n) 683.4 Hz. (o) 724.1 Hz.

(p) 767.1 Hz. (q) 812.8 Hz. (r) 861.1 Hz.

(s) 912.3 Hz. (t) 966.5 Hz. (u) 1024.0 Hz.

(v) 1084.9 Hz. (w) 1149.4 Hz. (x) 1217.8 Hz.

Figure 42. 1/12-Octave band beamform maps for Run046
(Airfoil at α = 1.5˚, U=38.80 m/s, Tripped BL, phased array on suction side).

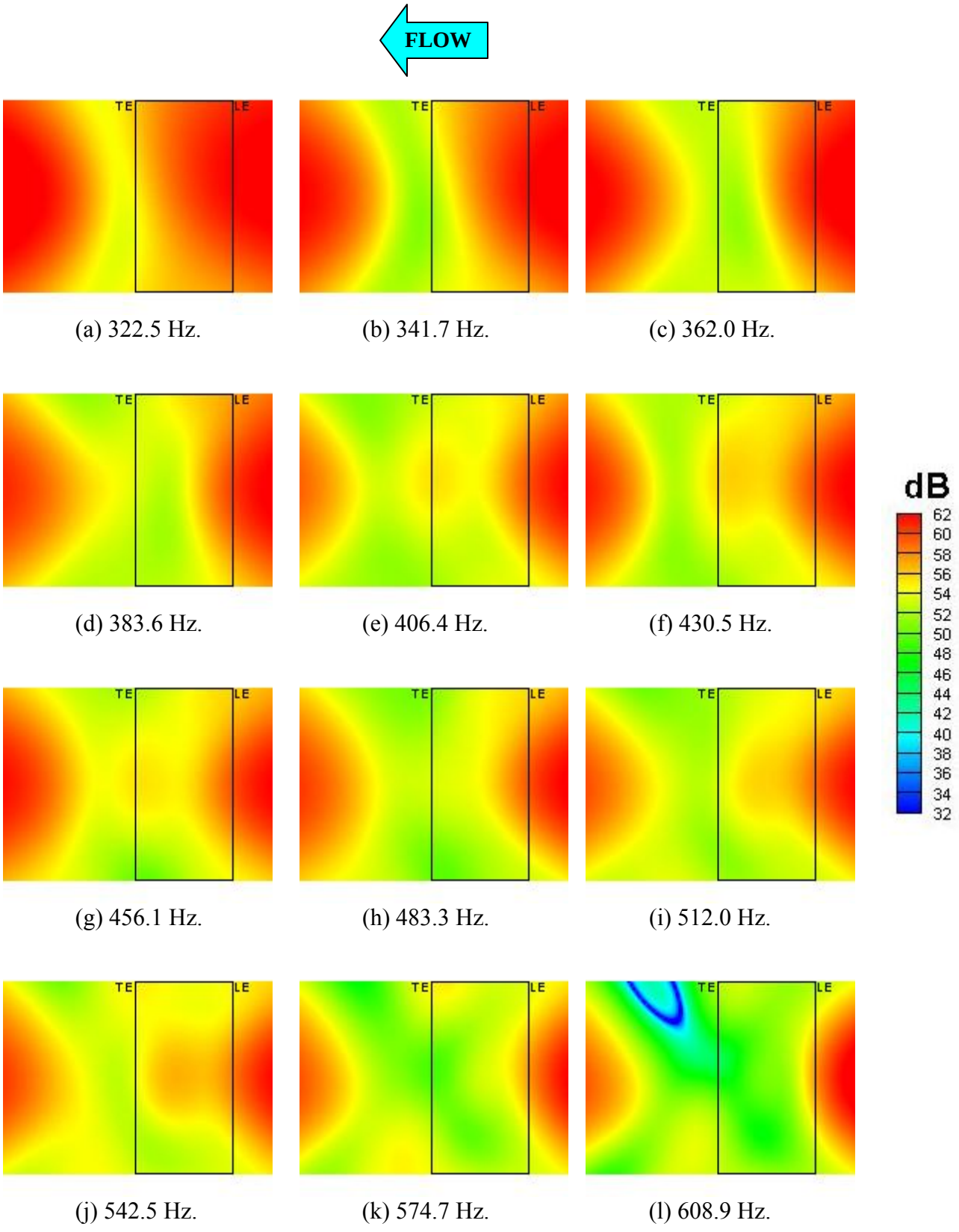

(a) 322.5 Hz. (b) 341.7 Hz. (c) 362.0 Hz.

(d) 383.6 Hz. (e) 406.4 Hz. (f) 430.5 Hz.

(g) 456.1 Hz. (h) 483.3 Hz. (i) 512.0 Hz.

(j) 542.5 Hz. (k) 574.7 Hz. (l) 608.9 Hz.

Figure 43. 1/12-Octave band beamform maps for Run047
(Airfoil at α = 1.5˚, U=54.44 m/s, Tripped BL, phased array on suction side).

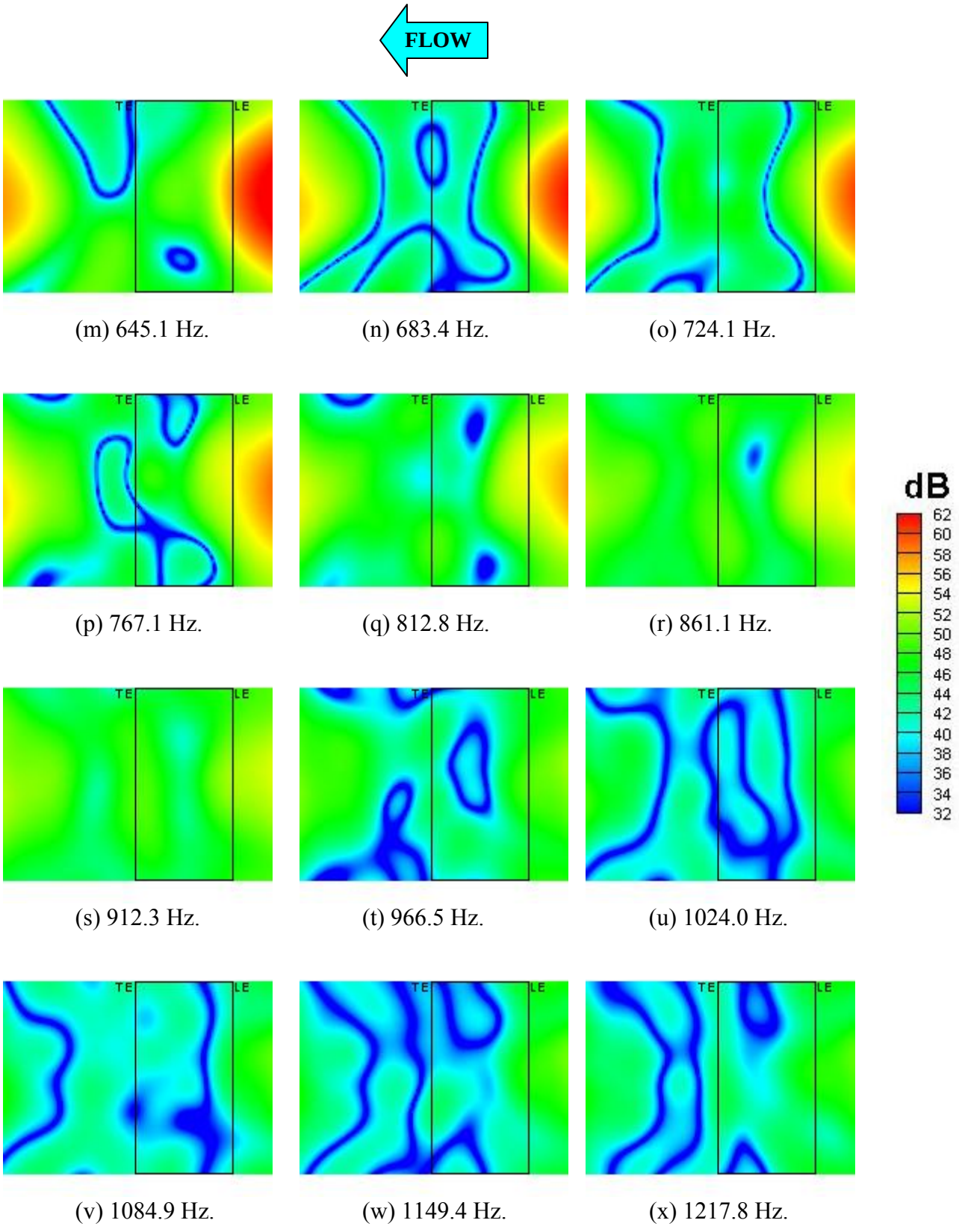

(m) 645.1 Hz. (n) 683.4 Hz. (o) 724.1 Hz.

(p) 767.1 Hz. (q) 812.8 Hz. (r) 861.1 Hz.

(s) 912.3 Hz. (t) 966.5 Hz. (u) 1024.0 Hz.

(v) 1084.9 Hz. (w) 1149.4 Hz. (x) 1217.8 Hz.

Figure 43. 1/12-Octave band beamform maps for Run047
(Airfoil at α = 1.5˚, U=54.44 m/s, Tripped BL, phased array on suction side).

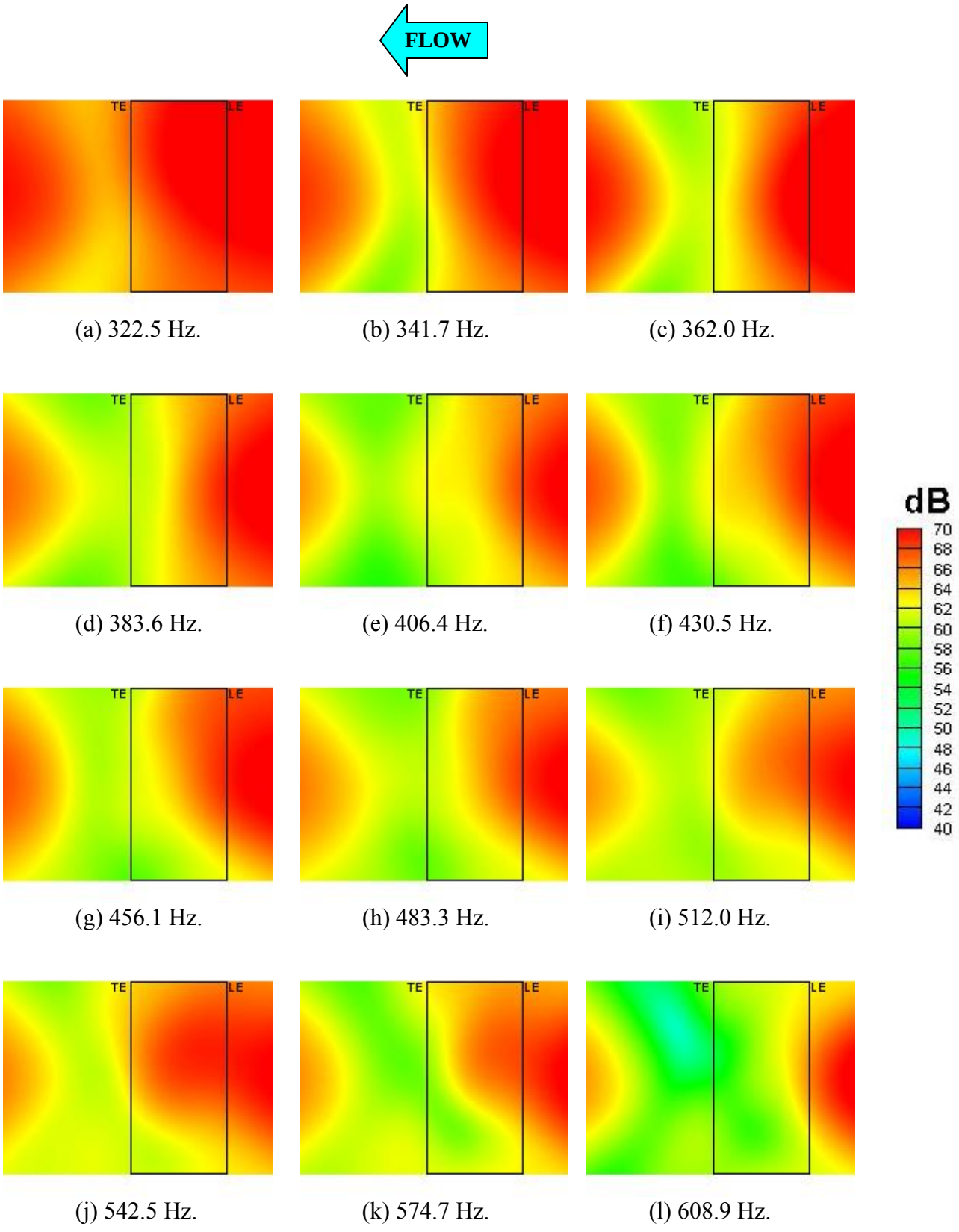

(a) 322.5 Hz. (b) 341.7 Hz. (c) 362.0 Hz.

(d) 383.6 Hz. (e) 406.4 Hz. (f) 430.5 Hz.

(g) 456.1 Hz. (h) 483.3 Hz. (i) 512.0 Hz.

(j) 542.5 Hz. (k) 574.7 Hz. (l) 608.9 Hz.

Figure 44. 1/12-Octave band beamform maps for Run048
(Airfoil at α = 1.5˚, U=70.36 m/s, Tripped BL, phased array on suction side).

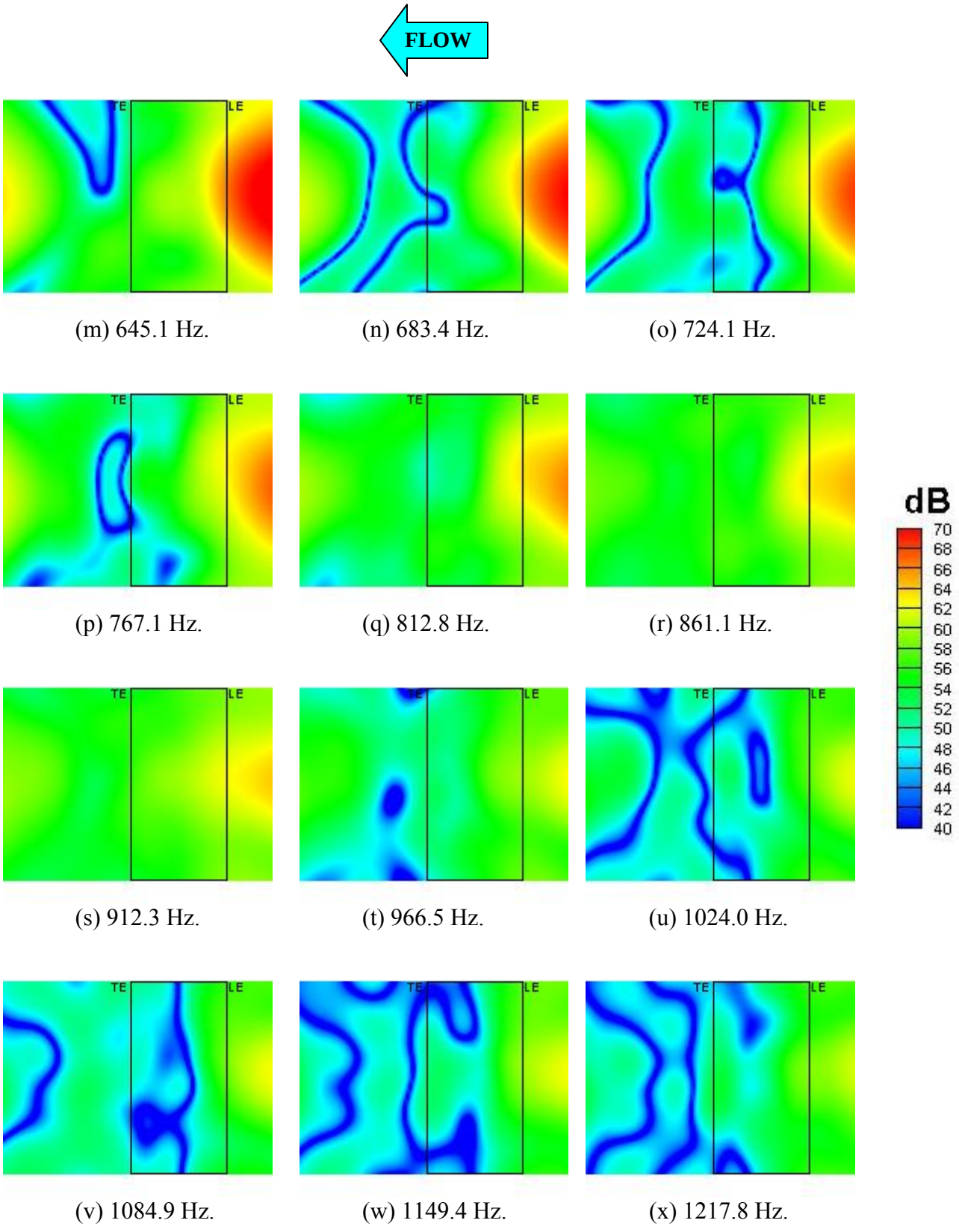

(m) 645.1 Hz. (n) 683.4 Hz. (o) 724.1 Hz.

(p) 767.1 Hz. (q) 812.8 Hz. (r) 861.1 Hz.

(s) 912.3 Hz. (t) 966.5 Hz. (u) 1024.0 Hz.

(v) 1084.9 Hz. (w) 1149.4 Hz. (x) 1217.8 Hz.

Figure 44. 1/12-Octave band beamform maps for Run048
(Airfoil at α = 1.5˚, U=70.36 m/s, Tripped BL, phased array on suction side).

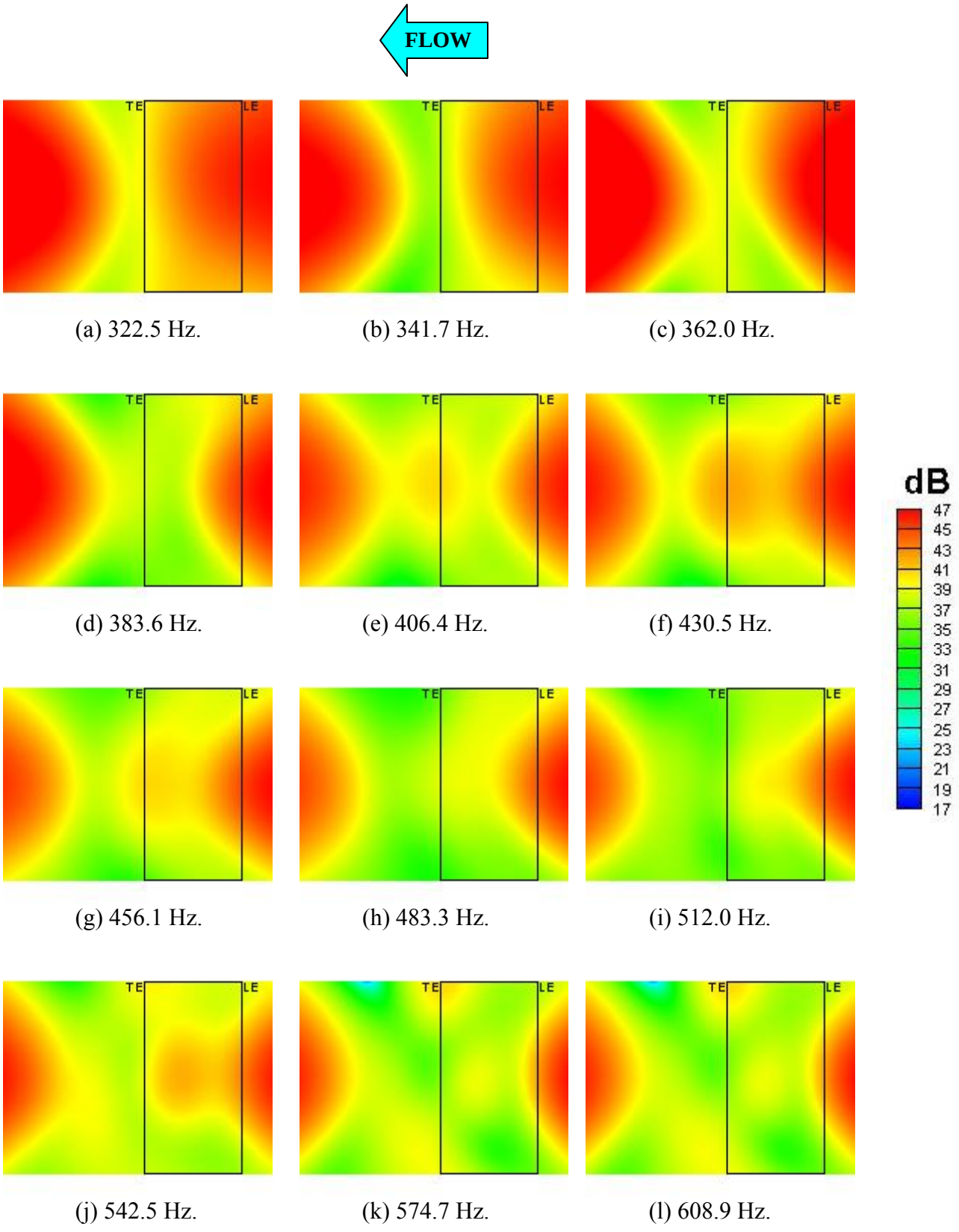

(a) 322.5 Hz. (b) 341.7 Hz. (c) 362.0 Hz.

(d) 383.6 Hz. (e) 406.4 Hz. (f) 430.5 Hz.

(g) 456.1 Hz. (h) 483.3 Hz. (i) 512.0 Hz.

(j) 542.5 Hz. (k) 574.7 Hz. (l) 608.9 Hz.

Figure 45. 1/12-Octave band beamform maps for Run049
(Airfoil at α = -3˚, U=30.86 m/s, Untripped BL, phased array on pressure side).

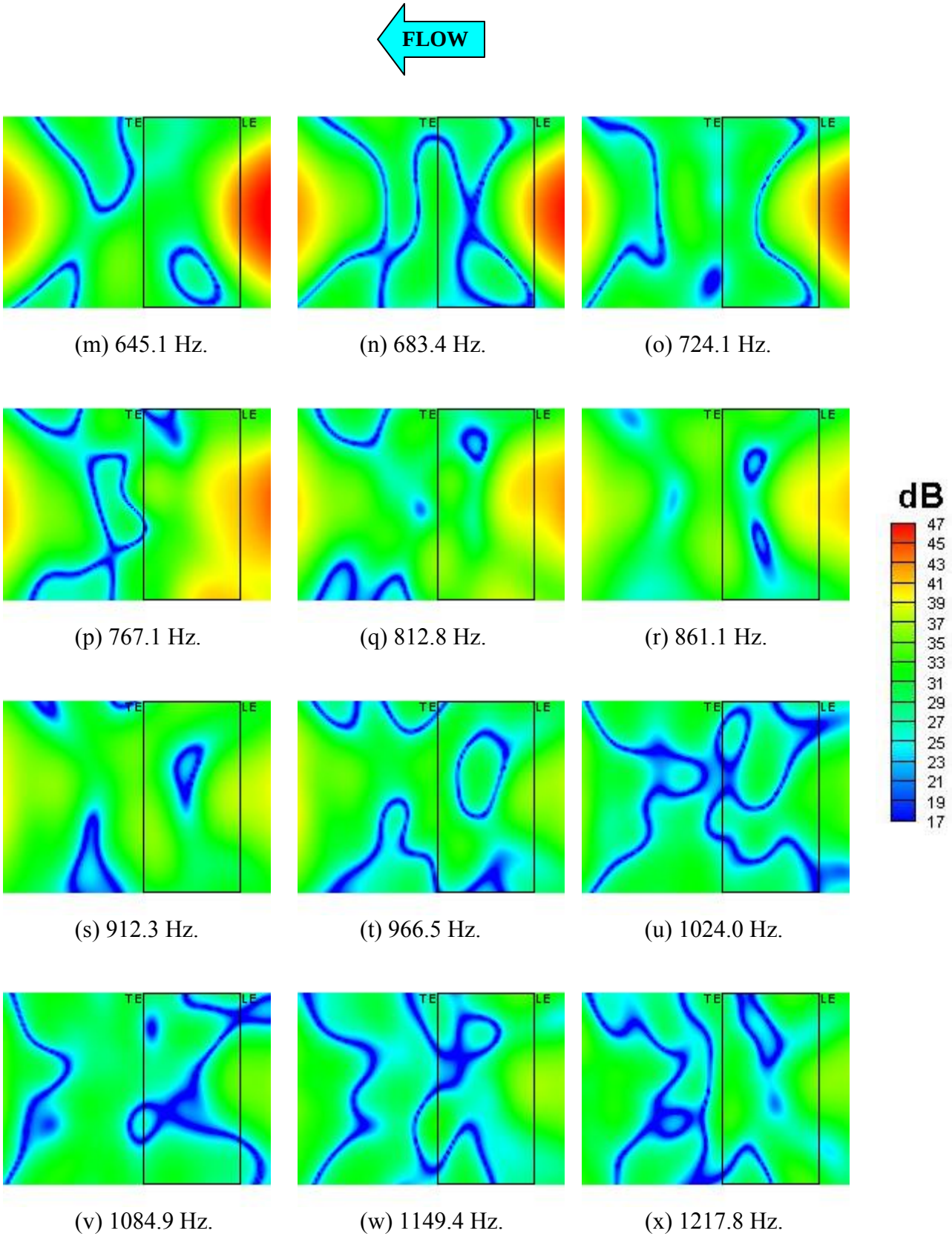

(m) 645.1 Hz. (n) 683.4 Hz. (o) 724.1 Hz.

(p) 767.1 Hz. (q) 812.8 Hz. (r) 861.1 Hz.

(s) 912.3 Hz. (t) 966.5 Hz. (u) 1024.0 Hz.

(v) 1084.9 Hz. (w) 1149.4 Hz. (x) 1217.8 Hz.

Figure 45. 1/12-Octave band beamform maps for Run049
(Airfoil at α = -3˚, U=30.86 m/s, Untripped BL, phased array on pressure side).

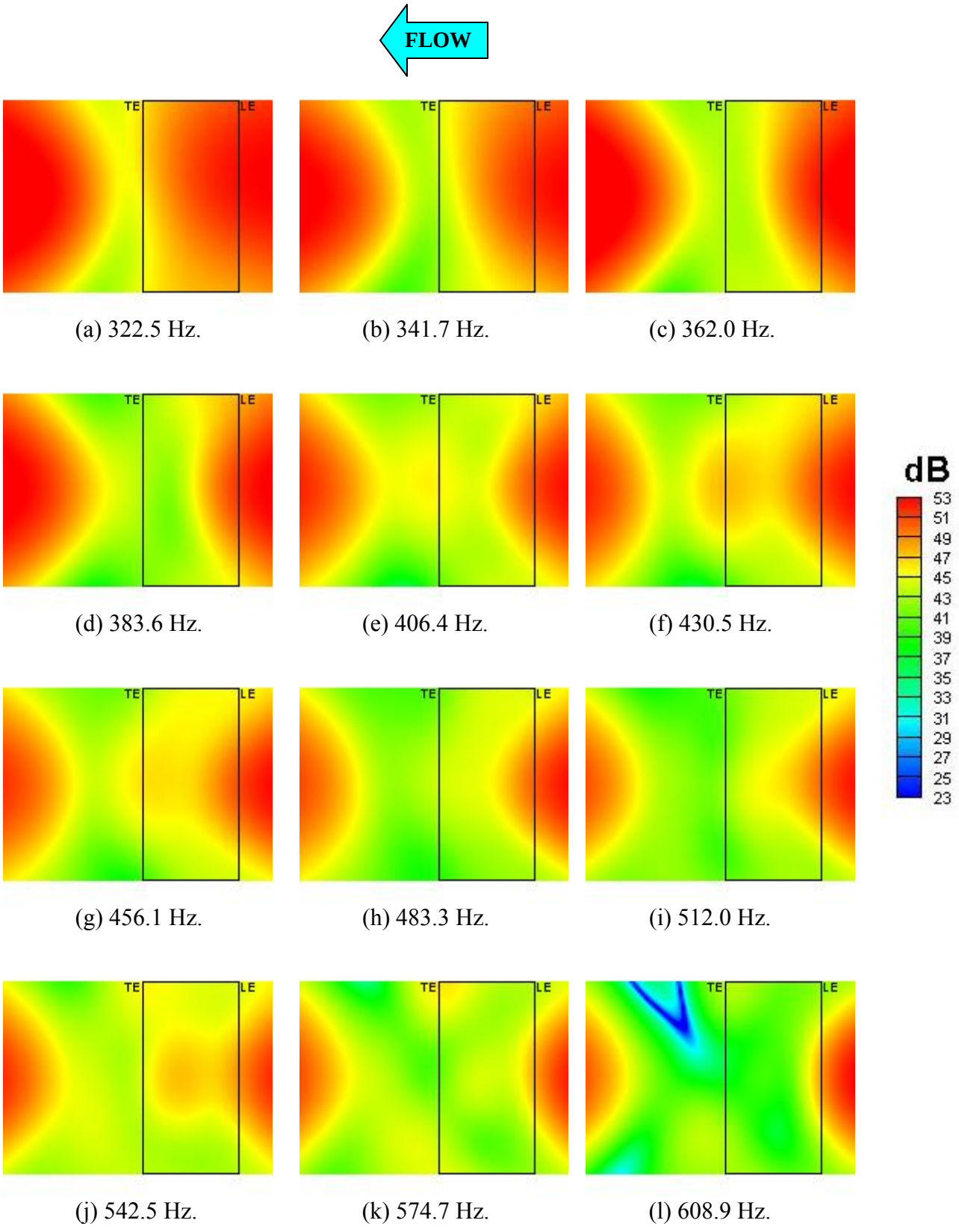

(a) 322.5 Hz. (b) 341.7 Hz. (c) 362.0 Hz.

(d) 383.6 Hz. (e) 406.4 Hz. (f) 430.5 Hz.

(g) 456.1 Hz. (h) 483.3 Hz. (i) 512.0 Hz.

(j) 542.5 Hz. (k) 574.7 Hz. (l) 608.9 Hz.

Figure 46. 1/12-Octave band beamform maps for Run050
(Airfoil at α = -3˚, U=38.77 m/s, Untripped BL, phased array on pressure side).

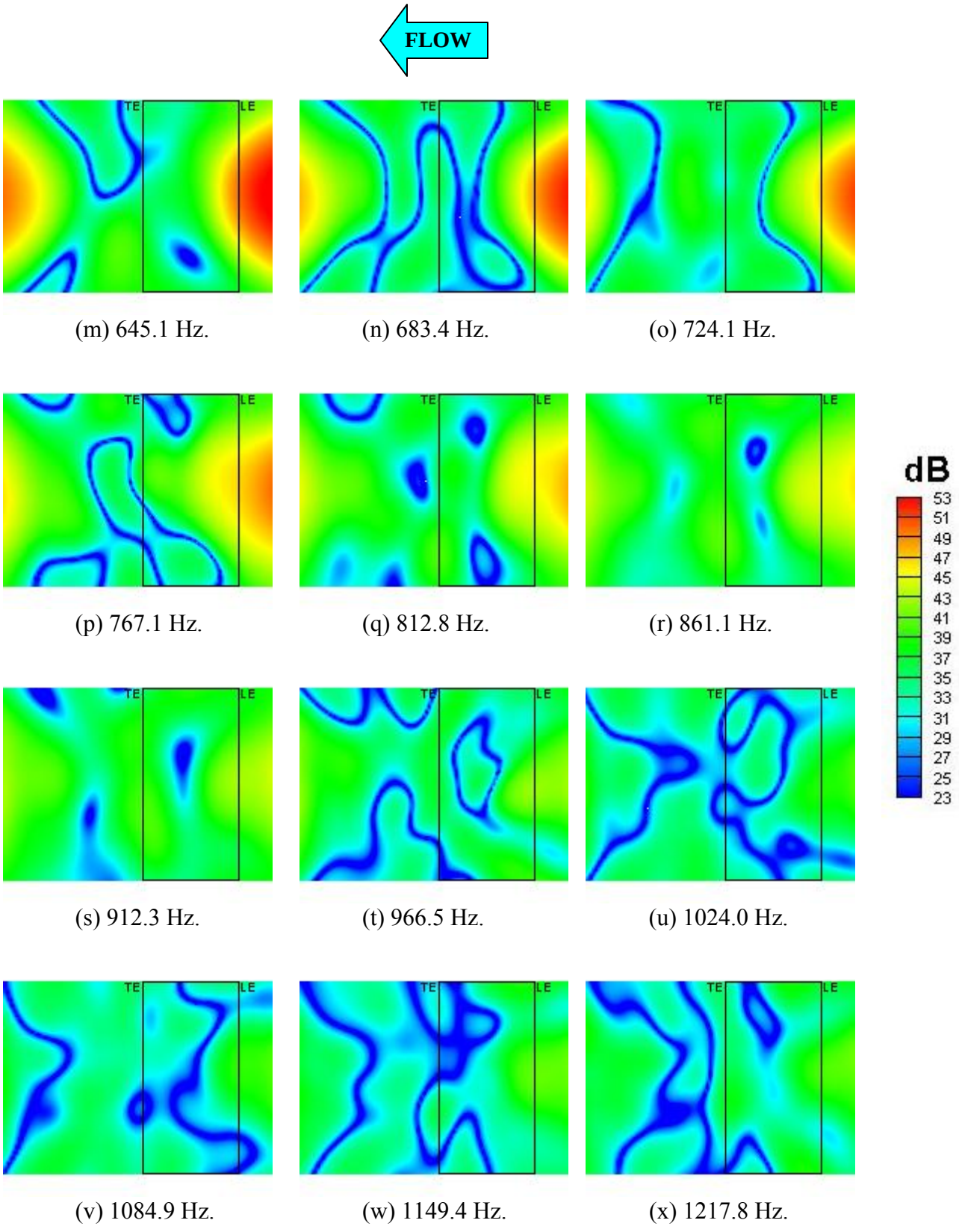

(m) 645.1 Hz. (n) 683.4 Hz. (o) 724.1 Hz.

(p) 767.1 Hz. (q) 812.8 Hz. (r) 861.1 Hz.

(s) 912.3 Hz. (t) 966.5 Hz. (u) 1024.0 Hz.

(v) 1084.9 Hz. (w) 1149.4 Hz. (x) 1217.8 Hz.

Figure 46. 1/12-Octave band beamform maps for Run050
(Airfoil at α = -3˚, U=38.77 m/s, Untripped BL, phased array on pressure side).

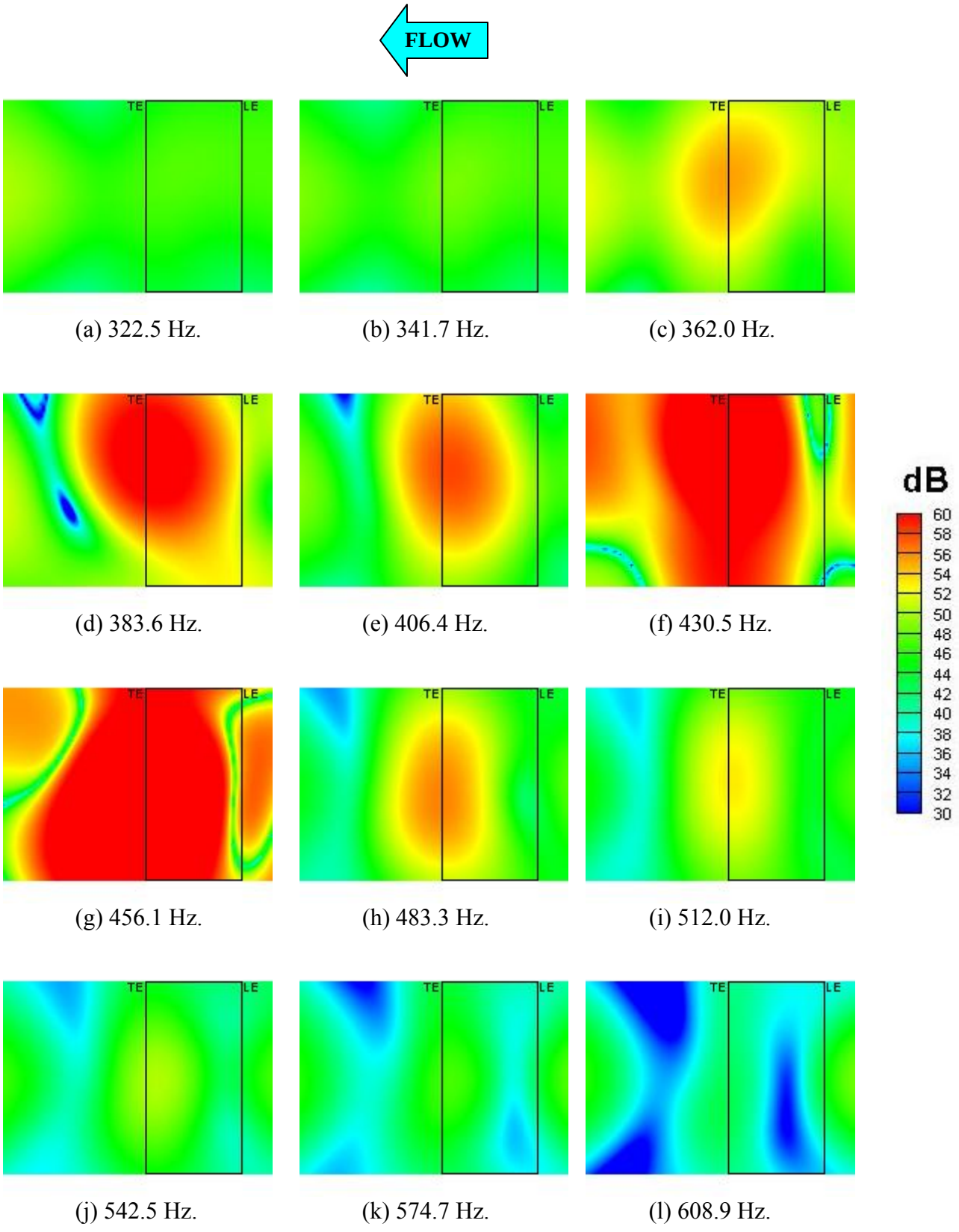

(a) 322.5 Hz. (b) 341.7 Hz. (c) 362.0 Hz.

(d) 383.6 Hz. (e) 406.4 Hz. (f) 430.5 Hz.

(g) 456.1 Hz. (h) 483.3 Hz. (i) 512.0 Hz.

(j) 542.5 Hz. (k) 574.7 Hz. (l) 608.9 Hz.

Figure 47. 1/12-Octave band beamform maps for Run051
(Airfoil at α = -7˚, U=31.00 m/s, Untripped BL, phased array on pressure side).

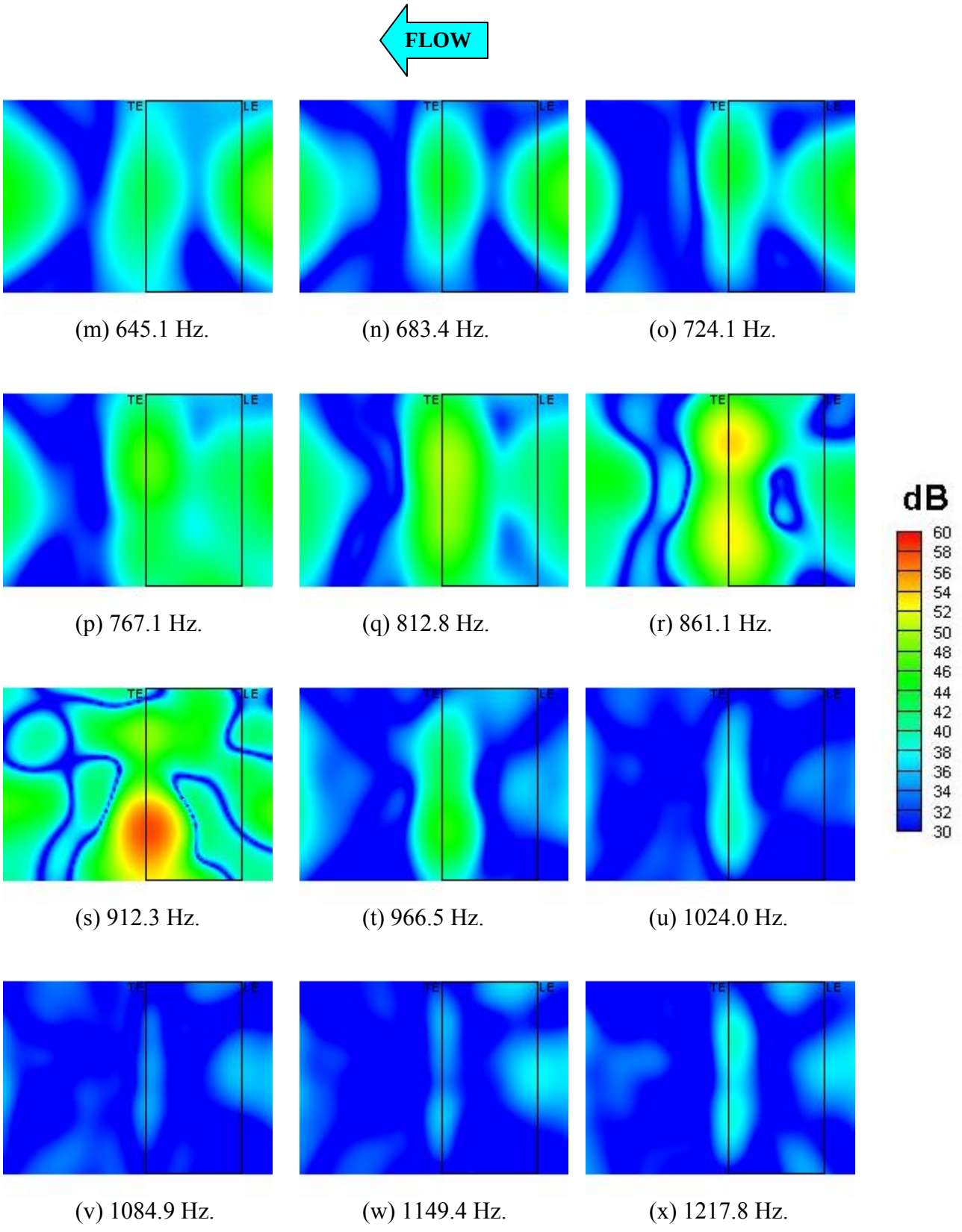

(m) 645.1 Hz. (n) 683.4 Hz. (o) 724.1 Hz.

(p) 767.1 Hz. (q) 812.8 Hz. (r) 861.1 Hz.

(s) 912.3 Hz. (t) 966.5 Hz. (u) 1024.0 Hz.

(v) 1084.9 Hz. (w) 1149.4 Hz. (x) 1217.8 Hz.

Figure 47. 1/12-Octave band beamform maps for Run051
(Airfoil at α = -7˚, U=31.00 m/s, Untripped BL, phased array on pressure side).

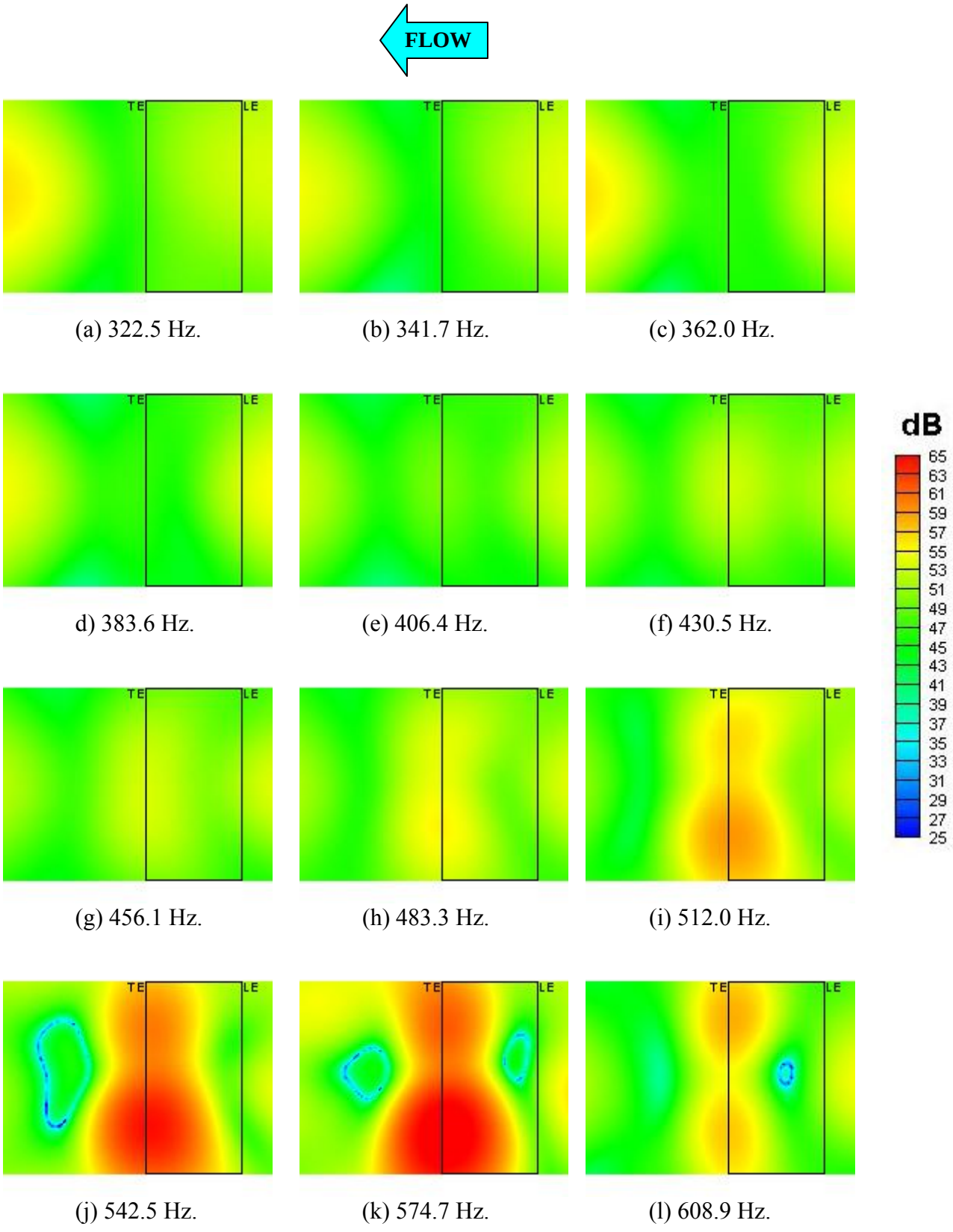

(a) 322.5 Hz. (b) 341.7 Hz. (c) 362.0 Hz.

d) 383.6 Hz. (e) 406.4 Hz. (f) 430.5 Hz.

(g) 456.1 Hz. (h) 483.3 Hz. (i) 512.0 Hz.

(j) 542.5 Hz. (k) 574.7 Hz. (l) 608.9 Hz.

Figure 48. 1/12-Octave band beamform maps for Run052
(Airfoil at α = -7˚, U=38.76 m/s, Untripped BL, phased array on pressure side).

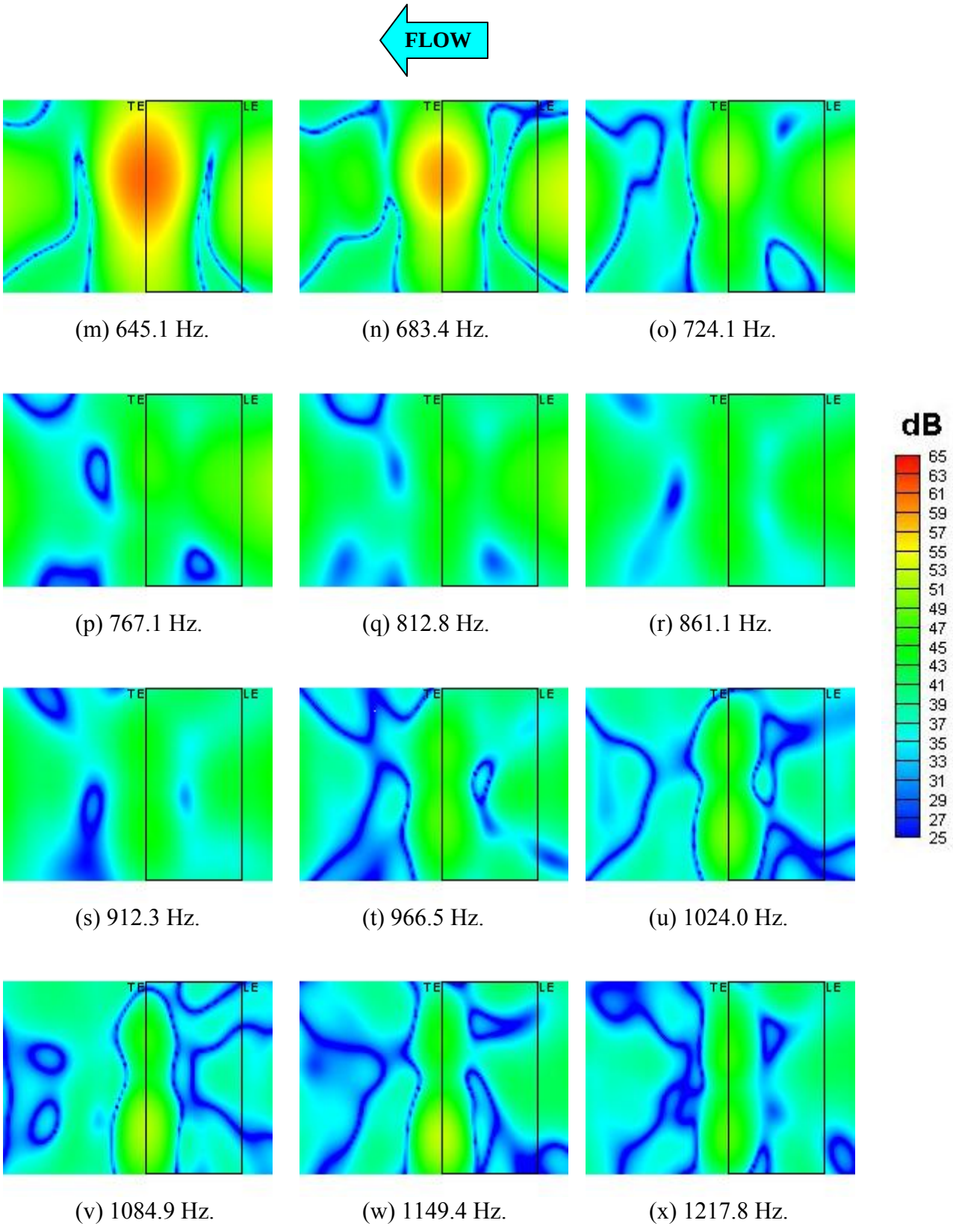

(m) 645.1 Hz. (n) 683.4 Hz. (o) 724.1 Hz.

(p) 767.1 Hz. (q) 812.8 Hz. (r) 861.1 Hz.

(s) 912.3 Hz. (t) 966.5 Hz. (u) 1024.0 Hz.

(v) 1084.9 Hz. (w) 1149.4 Hz. (x) 1217.8 Hz.

Figure 48. 1/12-Octave band beamform maps for Run052
(Airfoil at α = -7˚, U=38.76 m/s, Untripped BL, phased array on pressure side).

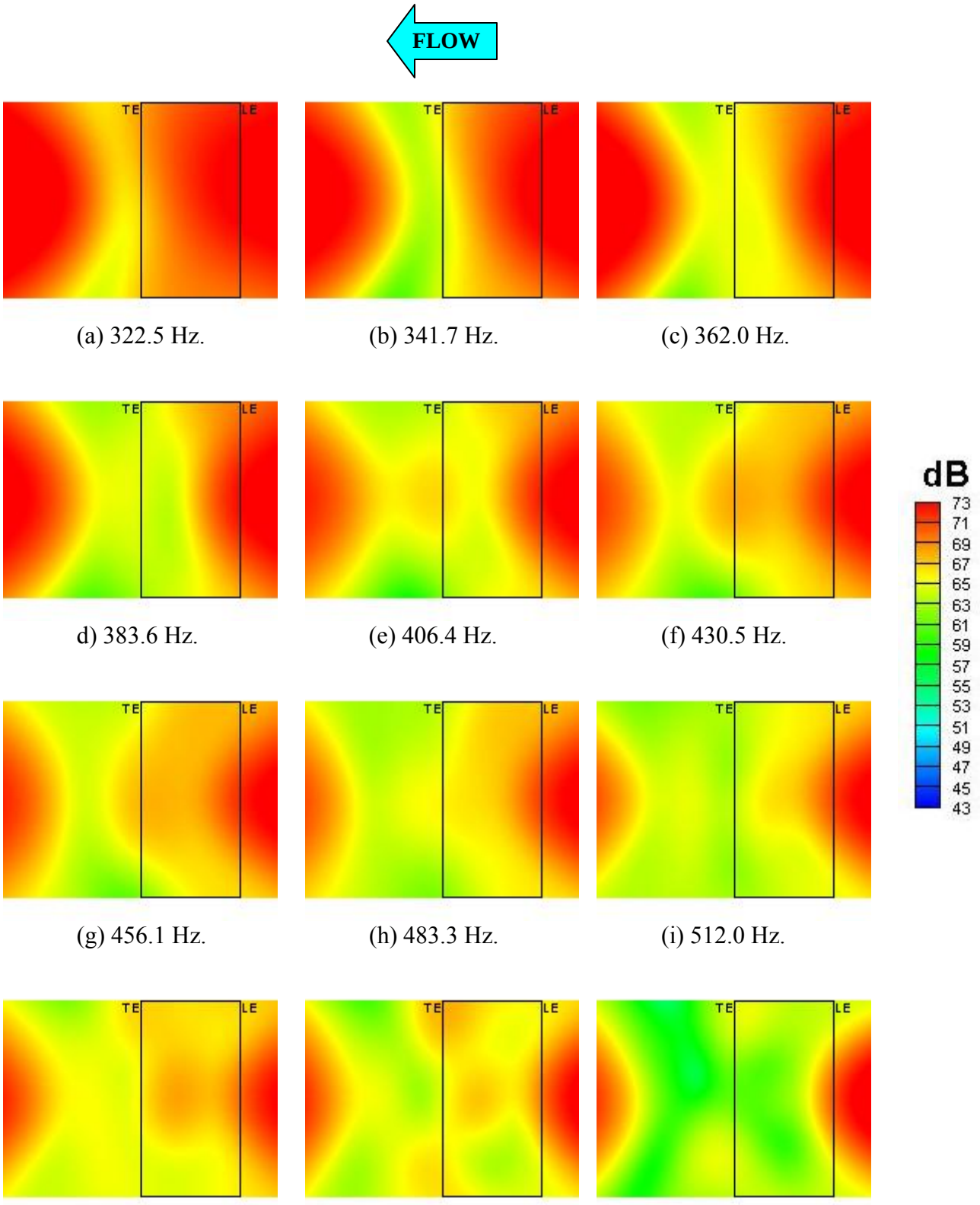

(a) 322.5 Hz. (b) 341.7 Hz. (c) 362.0 Hz.

d) 383.6 Hz. (e) 406.4 Hz. (f) 430.5 Hz.

(g) 456.1 Hz. (h) 483.3 Hz. (i) 512.0 Hz.

(j) 542.5 Hz. (k) 574.7 Hz. (l) 608.9 Hz.

Figure 49. 1/12-Octave band beamform maps for Run053
(Airfoil at α = -7˚, U=54.37 m/s, Untripped BL, phased array on pressure side).

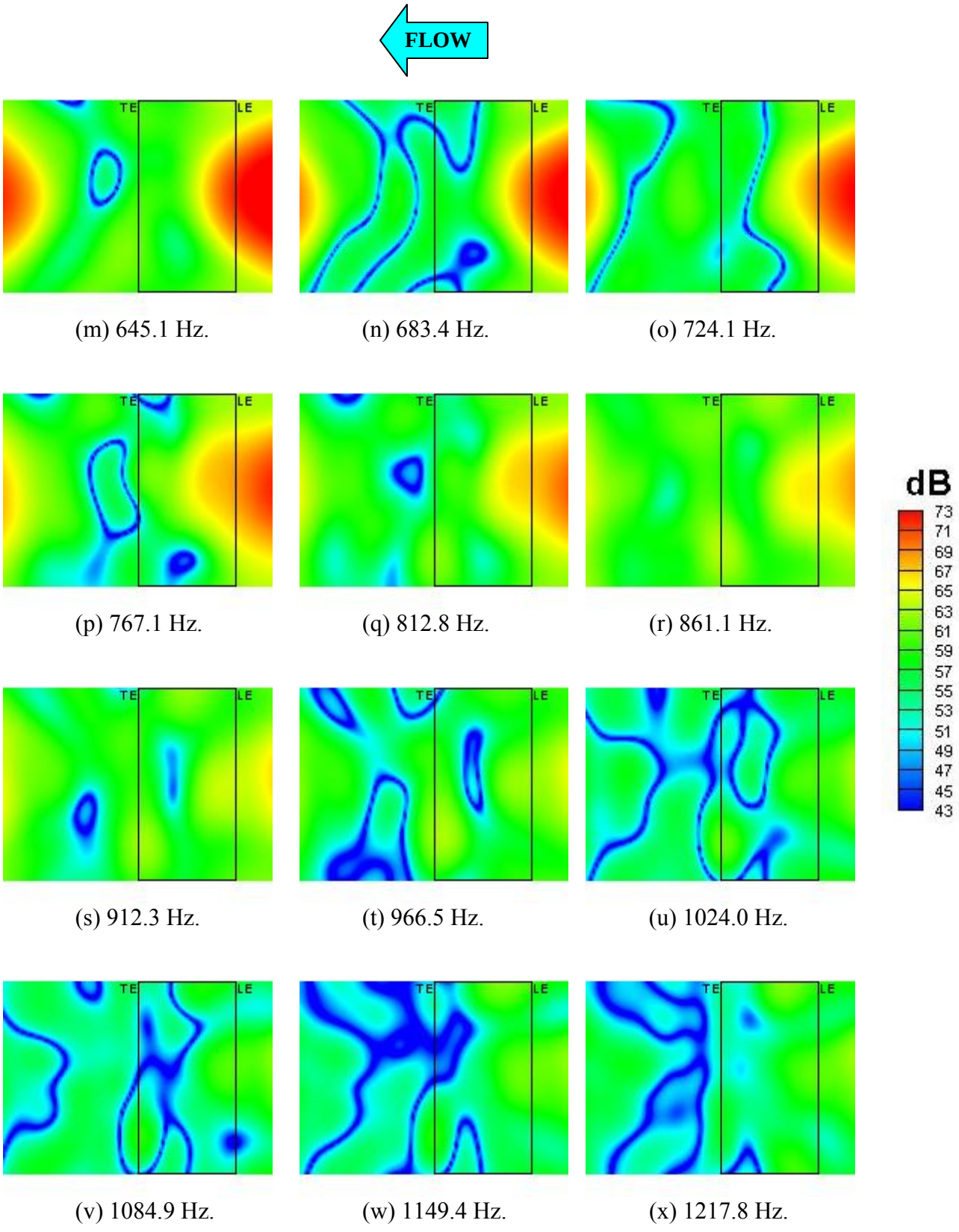

(m) 645.1 Hz. (n) 683.4 Hz. (o) 724.1 Hz.

(p) 767.1 Hz. (q) 812.8 Hz. (r) 861.1 Hz.

(s) 912.3 Hz. (t) 966.5 Hz. (u) 1024.0 Hz.

(v) 1084.9 Hz. (w) 1149.4 Hz. (x) 1217.8 Hz.

Figure 49. 1/12-Octave band beamform maps for Run053
(Airfoil at α = -7˚, U=54.37 m/s, Untripped BL, phased array on pressure side).

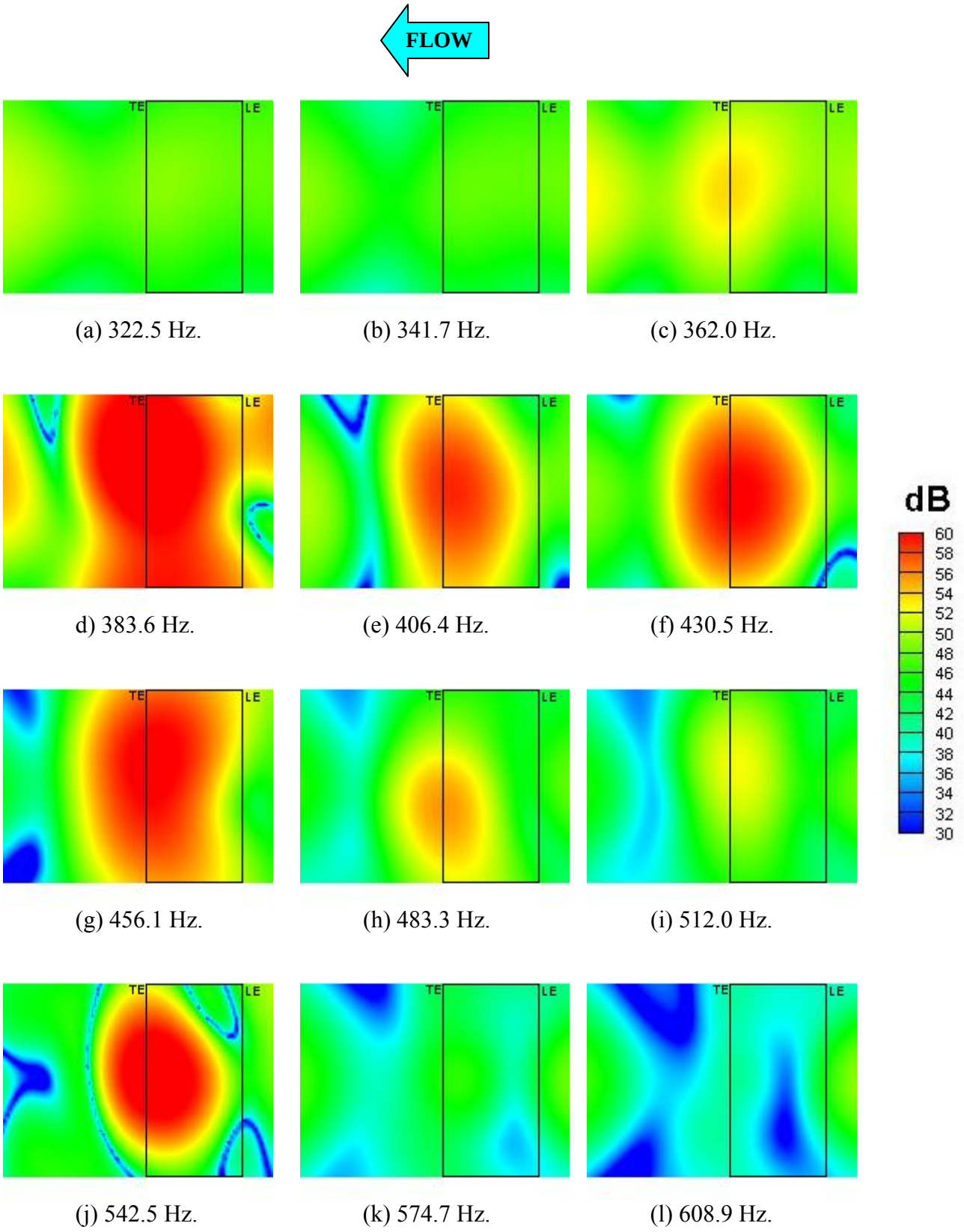

(a) 322.5 Hz. (b) 341.7 Hz. (c) 362.0 Hz.

d) 383.6 Hz. (e) 406.4 Hz. (f) 430.5 Hz.

(g) 456.1 Hz. (h) 483.3 Hz. (i) 512.0 Hz.

(j) 542.5 Hz. (k) 574.7 Hz. (l) 608.9 Hz.

Figure 50. 1/12-Octave band beamform maps for Run054
(Airfoil at α = -9˚, U=30.98 m/s, Untripped BL, phased array on pressure side).

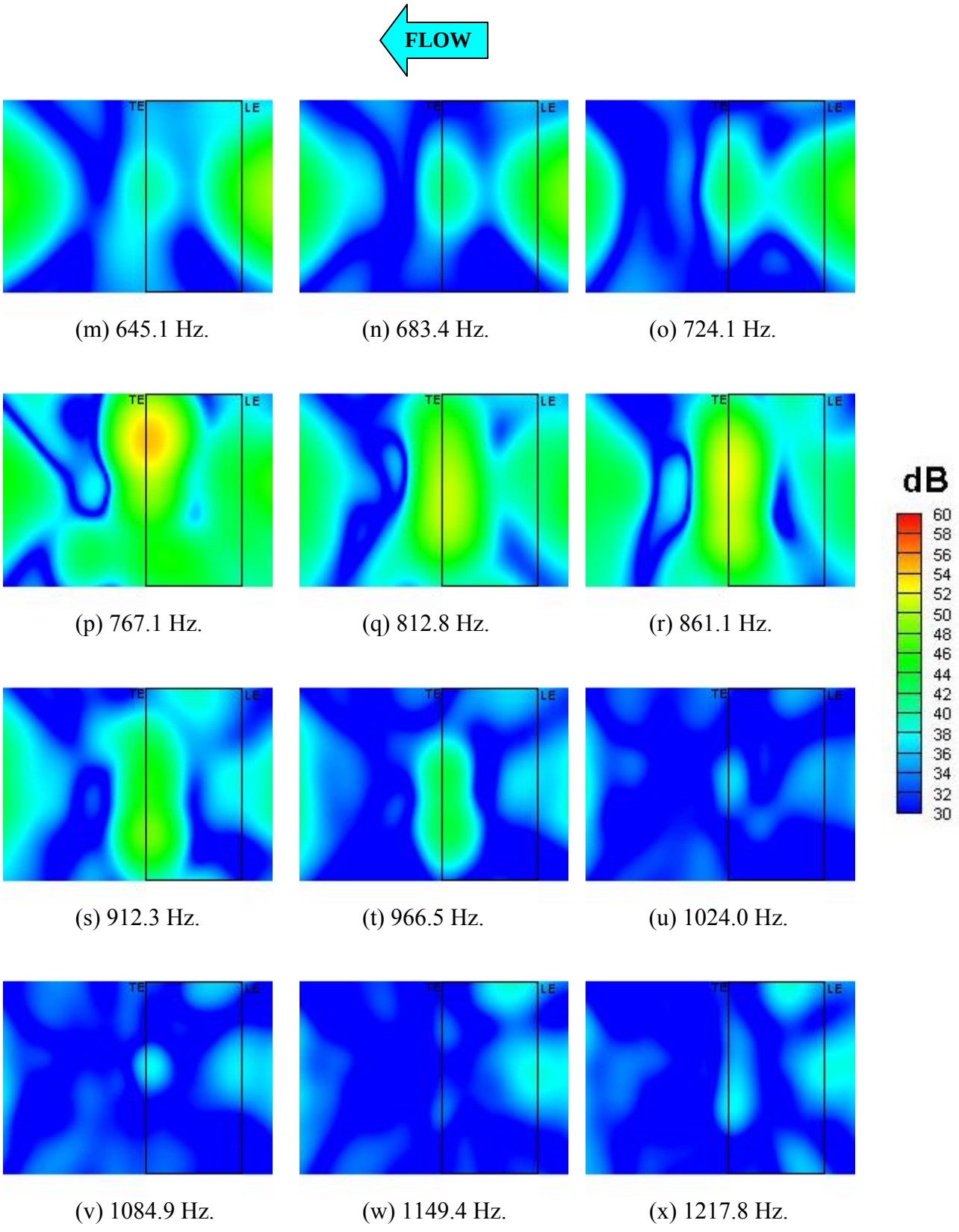

(m) 645.1 Hz. (n) 683.4 Hz. (o) 724.1 Hz.

(p) 767.1 Hz. (q) 812.8 Hz. (r) 861.1 Hz.

(s) 912.3 Hz. (t) 966.5 Hz. (u) 1024.0 Hz.

(v) 1084.9 Hz. (w) 1149.4 Hz. (x) 1217.8 Hz.

Figure 50. 1/12-Octave band beamform maps for Run054
(Airfoil at α = -9˚, U=30.98 m/s, Untripped BL, phased array on pressure side).

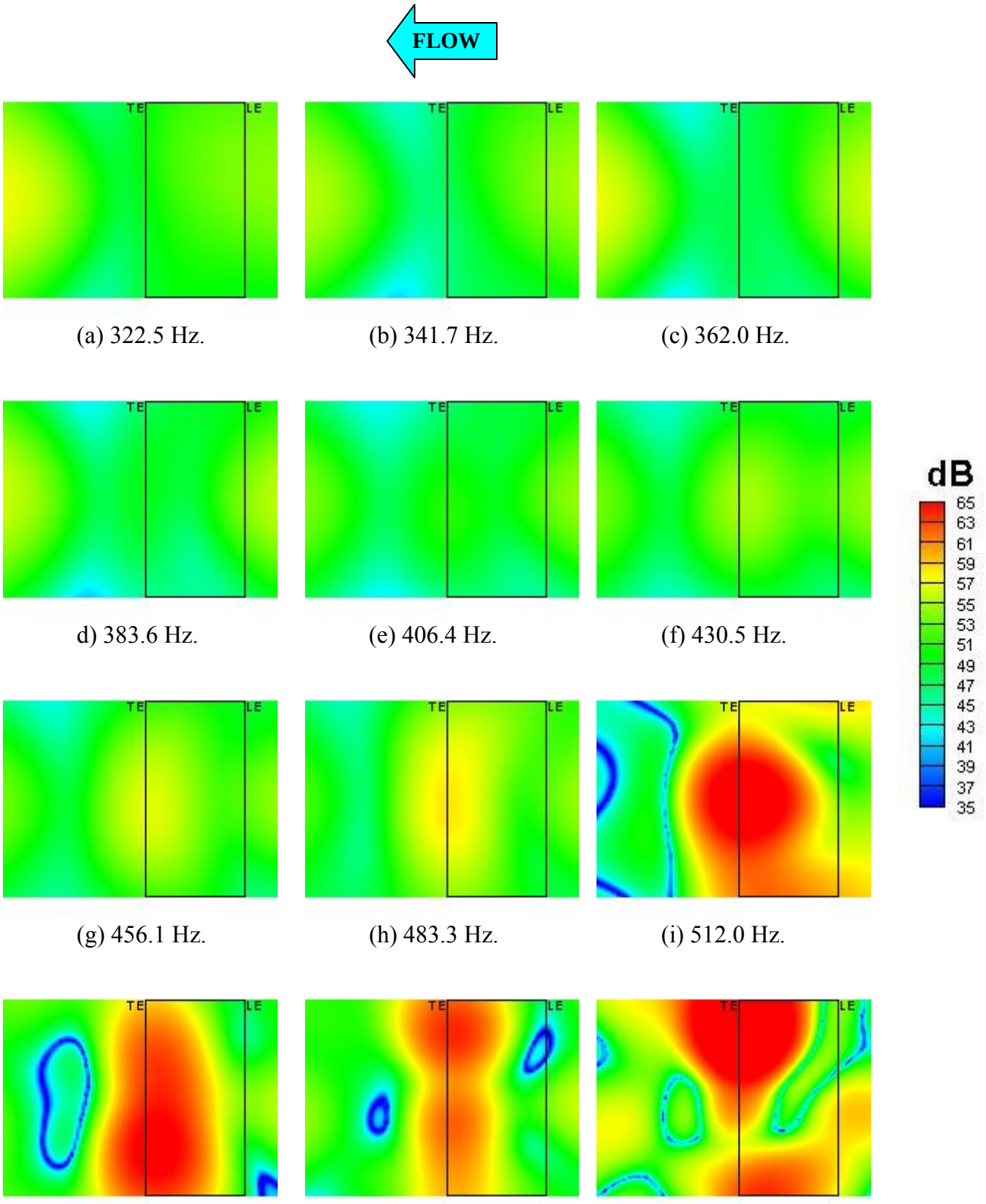

(a) 322.5 Hz. (b) 341.7 Hz. (c) 362.0 Hz.

d) 383.6 Hz. (e) 406.4 Hz. (f) 430.5 Hz.

(g) 456.1 Hz. (h) 483.3 Hz. (i) 512.0 Hz.

(j) 542.5 Hz. (k) 574.7 Hz. (l) 608.9 Hz.

Figure 51. 1/12-Octave band beamform maps for Run055
(Airfoil at α = -9˚, U=38.84 m/s, Untripped BL, phased array on pressure side).

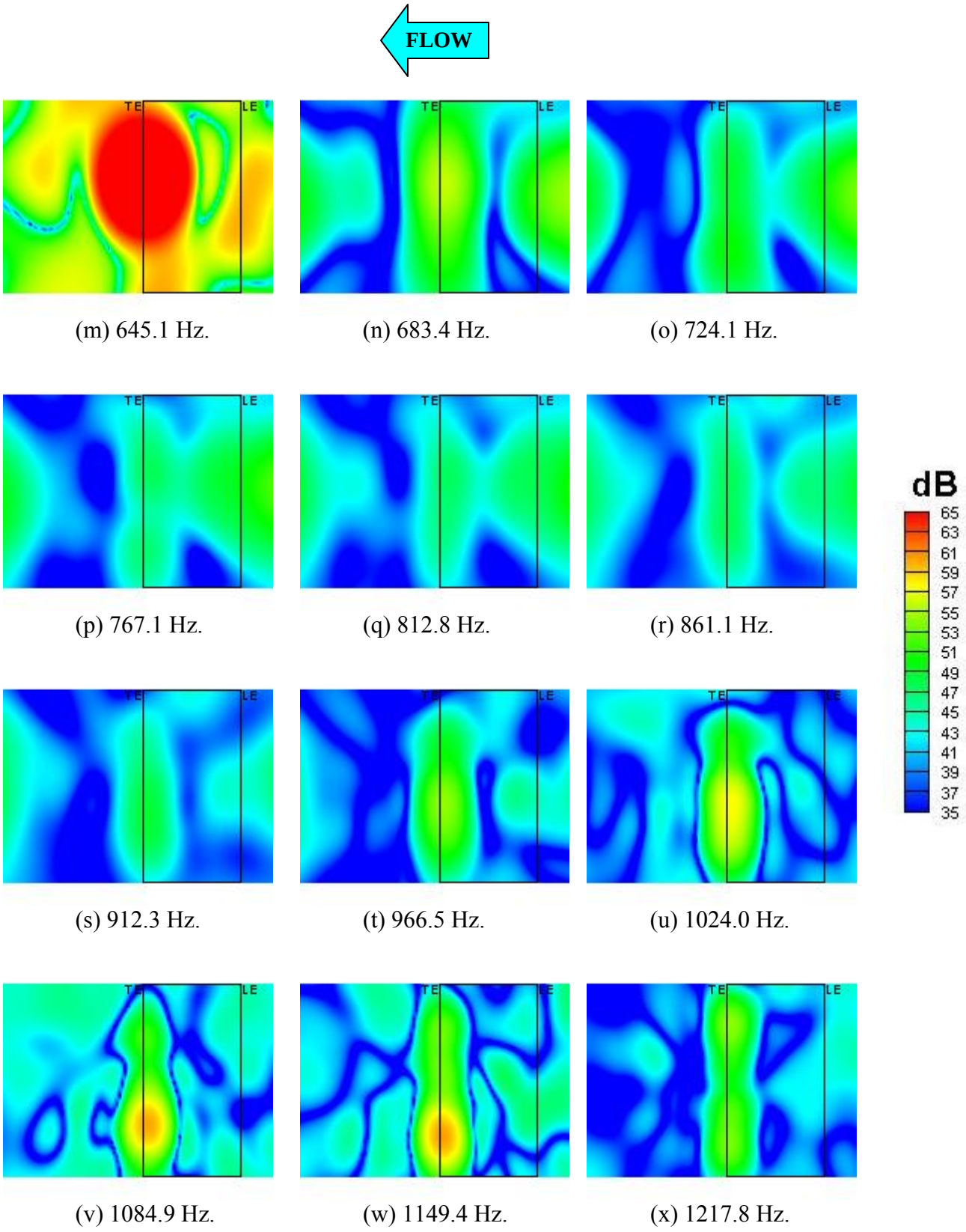

(m) 645.1 Hz. (n) 683.4 Hz. (o) 724.1 Hz.

(p) 767.1 Hz. (q) 812.8 Hz. (r) 861.1 Hz.

(s) 912.3 Hz. (t) 966.5 Hz. (u) 1024.0 Hz.

(v) 1084.9 Hz. (w) 1149.4 Hz. (x) 1217.8 Hz.

Figure 51. 1/12-Octave band beamform maps for Run055
(Airfoil at α = -9˚, U=38.84 m/s, Untripped BL, phased array on pressure side).

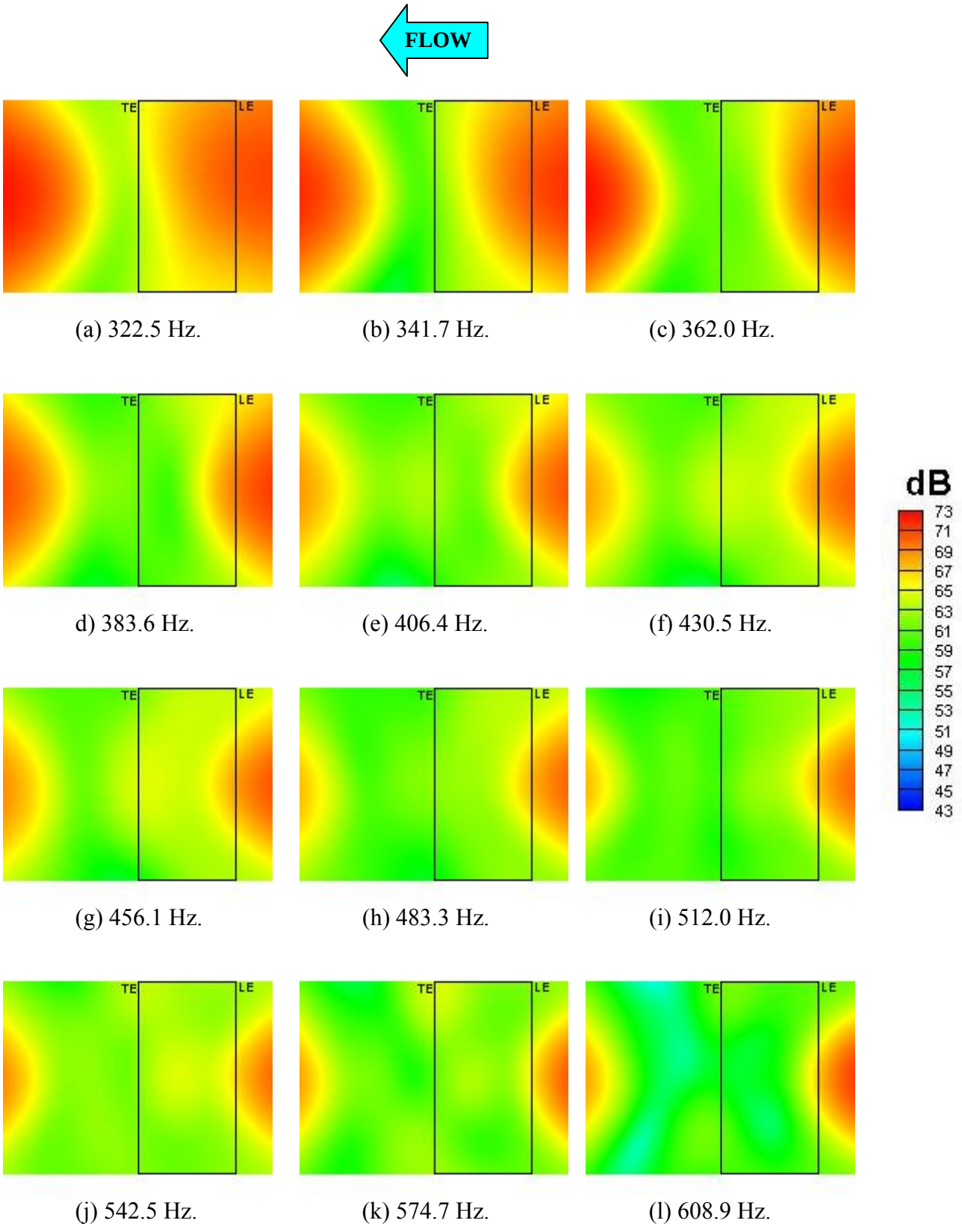

(a) 322.5 Hz. (b) 341.7 Hz. (c) 362.0 Hz.

d) 383.6 Hz. (e) 406.4 Hz. (f) 430.5 Hz.

(g) 456.1 Hz. (h) 483.3 Hz. (i) 512.0 Hz.

(j) 542.5 Hz. (k) 574.7 Hz. (l) 608.9 Hz.

Figure 52. 1/12-Octave band beamform maps for Run056
(Airfoil at α = -7˚, U=53.62 m/s, Untripped BL, phased array on pressure side).

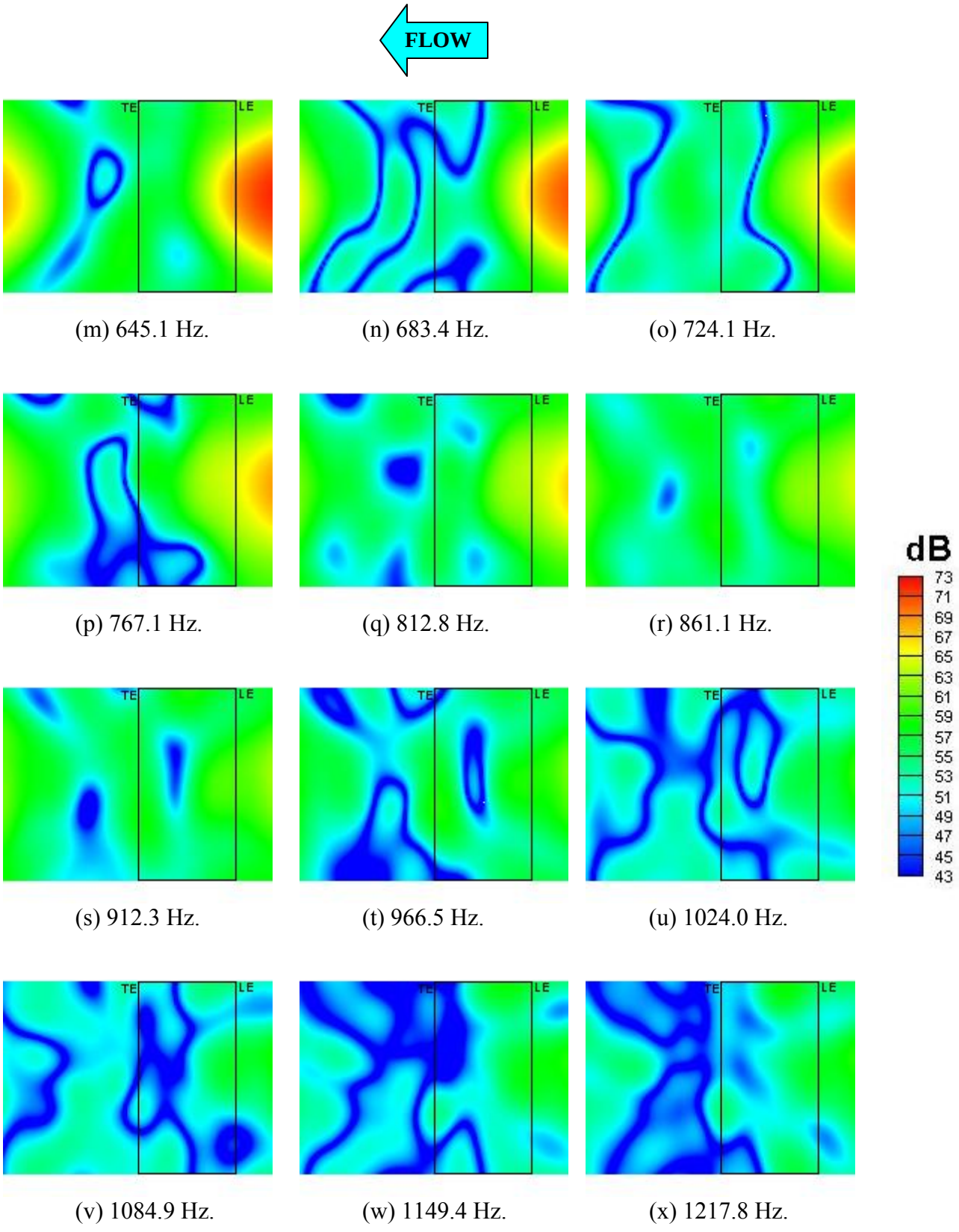

(m) 645.1 Hz. (n) 683.4 Hz. (o) 724.1 Hz.

(p) 767.1 Hz. (q) 812.8 Hz. (r) 861.1 Hz.

(s) 912.3 Hz. (t) 966.5 Hz. (u) 1024.0 Hz.

(v) 1084.9 Hz. (w) 1149.4 Hz. (x) 1217.8 Hz.

Figure 52. 1/12-Octave band beamform maps for Run056
(Airfoil at α = -7˚, U=53.62 m/s, Untripped BL, phased array on pressure side).